Physics of Atomic Nuclei, Vol. 63, No. 3, 2000, pp. 323–327. Translated from Yadernaya Fizika, Vol. 63, No. 3, 2000, pp. 389–393.

NUCLEI
Experiment

Investigation of the Isomeric Ratio for ^{44m,g}Sc

V. A. Zheltonozhsky[1)] and V. M. Mazur

Institute for Electron Physics, National Academy of Sciences of Ukraine, Uzhgorod, Ukraine

Received January 26, 1999; in final form, April 16, 1999

Abstract—The isomeric ratios measured for ^{44m,g}Sc in (γ, n), (p, n), $(p, \alpha p3n)$, and $(\alpha, p3n)$ reactions are presented. The values obtained in this way are compared with the results of calculations within the cascade–evaporation model and with data coming from an investigation of reactions like $(n, 2n)$, and (d, t). © *2000 MAIK "Nauka/Interperiodica".*

1. INTRODUCTION

One of the ways to deduce information about the properties of nuclei consists in studying the excitation of isomeric nuclear states and measuring isomeric ratios in various nuclear reactions. These data are of interest both from the standpoint of their possible practical application—for example, in optimizing the conditions under which induced gamma radiation [1] can produce radioactive pharmaceuticals—and from the standpoint of studying reaction mechanisms and the viability of their theoretical description [2]. In this connection, comprehensive investigations that permit a comparison of data obtained in various nuclear reactions are of importance.

Among the few nuclide species that can be obtained experimentally, we would like to mention the ^{44}Sc nucleus. Owing to the availability of this nuclide, the excitation of its isomeric states can be studied in various nuclear reactions, including ^{45}Sc$(\gamma, n)^{44m,g}$Sc, ^{45}Sc$(n, 2n)^{44m,g}$Sc, ^{41}K$(\alpha, n)^{44m,g}$Sc, ^{44}Ca$(p, n)^{44m,g}$Sc, ^{44}Ca$(\alpha, p3n)^{44m,g}$Sc, and ^{46}Ti$(\gamma, pn)^{44m,g}$Sc. The present article reports on a continuation and a generalization of an investigation of the energy dependences of ^{44}Sc isomeric ratios in (γ, n), (p, n), $(p, \alpha p3n)$, and $(\alpha, p3n)$ reactions [3, 4].

2. EXPERIMENTAL PROCEDURE AND RESULTS

Methodologically, the activity of ^{44}Sc can be measured rather straightforwardly. The half-lives of the 6^+ isomeric (m) and the 2^+ ground (g) state of ^{44}Sc are $T^m_{1/2}$ = 2.44 days and $T^g_{1/2}$ = 3.92 h, respectively. The lines of gamma rays accompanying their decays have nearly 100% intensities. The decays of these states were identified by the photopeaks at 0.271 and 1.157 MeV, respectively. The isomeric ratios of the cross sections, $r = \sigma_m/\sigma_g$ [yields Y_m/Y_g for (γ, n) reactions], were calculated by the formula

$$r = \sigma_m/\sigma_g = (\lambda_g - \lambda_m) \times \left\{ \left[c\frac{N_g}{N_m}\frac{\varphi_m}{\varphi_g}(\lambda_g - \lambda_m) - p\lambda_g \right] \frac{\lambda_g f_m(t)}{\lambda_m f_g(t)} + p\lambda_m \right\}^{-1}. \quad (1)$$

Here, $\varphi_{m,g} = (\Omega/4\pi)\xi_{m,g}k_{m,g}\alpha_{m,g}$, $(\Omega/4\pi)\xi_{m,g}$, $k_{m,g}$, and $\alpha_{m,g}$ being, respectively, the photoefficiency, the line self-absorption factor in the sample under study, and the line intensity; N_g and N_m are the numbers of pulses in, respectively, the ground-state and the isomeric-state photopeak; and

$$f_{m,g}(t) = [1 - \exp(-\lambda_{m,g}t_{\text{irrad}})]\exp(-\lambda_{m,g}t_{\text{cool}}) \times [1 - \exp(-\lambda_{m,g}t_{\text{meas}})],$$

where t_{irrad}, t_{cool}, and t_{meas} are, respectively, the irradiation time, the time of cooling, and the time of measurements; $\lambda_{m,g}$ is the decay constant; and $c = c_1c_2$ is a factor representing corrections for pulses that were missed and for those that overlapped. The spectroscopic data were borrowed from [5]. The (γ, n) reaction was investigated in a beam of bremsstrahlung photons from the M-30 microtron installed at the Institute for Electron Physics (Uzhgorod, Ukraine), whereas the reactions induced by charged particles were studied at the U-240 and U-120 cyclotrons of the Institute for Nuclear Research (Kiev, Ukraine). Our experimental procedure was described in detail elsewhere [4, 6].

The isomeric ratios of the yields ($d = Y_m/Y_g$) from the reaction ^{45}Sc$(\gamma, n)^{44m,g}$Sc were measured in the energy range E = 12–21 MeV. Figure 1*a* shows the experimental values of d versus the endpoint energy of the bremsstrahlung spectrum $E_{\gamma,m}$ (closed circles). It can be seen that, above the threshold, d increases sharply, reaching a plateau at $E_{\gamma,m}$ = 21 MeV, its level there being that of 0.21 ± 0.01, a value that is compatible, within the errors, with the result obtained previously at $E_{\gamma,m}$ = 22 MeV (open circles) [7]. However, it is significantly larger than the isomeric ratio of the yields that was estimated in [8] as $d < 0.02$ for the reac-

[1)] Institute for Nuclear Research, National Academy of Sciences of Ukraine, pr. Nauki 47, Kiev, 252028 Ukraine.

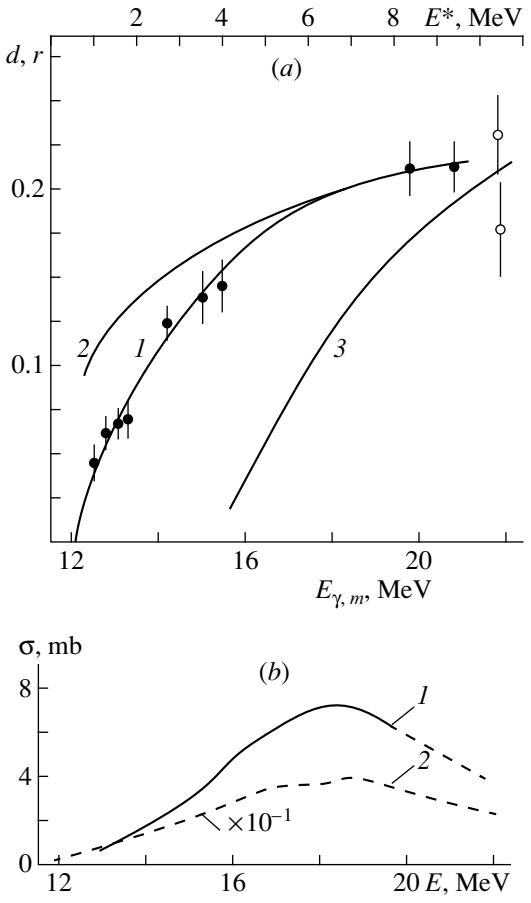

Fig. 1. (*a*) Isomeric ratios of the (curve *1*) yields and (curve *2*) cross sections versus energy for the reaction ^{45}Sc(γ, *n*)^{44m,g}Sc. Curve *3* was calculated within the cascade–evaporation model. (*b*) Cross section for the reaction ^{45}Sc(γ, *n*)^{44m,g}Sc (curve *1*) along with the total photoneutron cross section for this reaction (curve *2*).

tion ^{46}Ti(γ, *pn*)^{44m,g}Sc at $E_{\gamma,m}$ = 48 MeV. Curve *1* in Fig. 1*a* represents a least squares fit to the experimental dependence $d = f(E_{\gamma,m})$ in terms of the form $d = A\tanh[B(E - E_0)]$, the fitted parameter values being $A = 0.218 \pm 0.007$, $B = 0.228 \pm 0.02$ MeV^{-1}, and $E_0 = 11.6 \pm 0.07$ MeV.

The yield $Y(E_{\gamma,m})$ from (γ, *n*) reactions is known to be related to the cross section σ(*E*) by the equation

$$Y(E_{\gamma,m}) = k\int_{E_{\text{thr}}}^{E_{\gamma,m}} \sigma(E)W(E, E_{\gamma,m})dE, \qquad (2)$$

where $W(E, E_{\gamma,m})$ is the spectrum of bremsstrahlung photons, *k* is a normalization factor, E_{thr} is the reaction threshold, and $E_{\gamma,m}$ is the endpoint energy of the bremsstrahlung spectrum.

Using the total cross sections σ(*E*) for (γ, *n*) reactions from [9] and relation (2), we have calculated the absolute total yield from the (γ, *n*) reaction in question—that is, the sum $Y_n = Y_m + Y_g$, where Y_m and Y_g are the yields for the population of, respectively, the isomeric and the ground state. After that, the yield Y_m of the isomeric state was determined as $Y_m = dY_n/(d + 1)$ by using the measured isomeric ratios *d*, which correspond to curve *1* in Fig. 1*a*. The calculation was performed with a step of 0.5 MeV. On the basis of the values obtained in this way for the yield Y_m, we have then computed the cross section σ_m for the reaction ^{45}Sc(γ, *n*)^{44m,g}Sc (Fig. 1*b*) with the aid of the Penfold–Leiss inverse matrix [10]. The mean-square error in the cross section at its maximum was about 15%. For sake of comparison, the total cross section for the reaction ^{45}Sc(γ, *n*)^{44}Sc is also displayed in Fig. 1*b* (curve *2*). Since we have both the cross section σ_m and the cross section σ at our disposal, we can estimate the isomeric ratio $r = \sigma_m/\sigma_g$. As a result, we find that, in the range 14–16 MeV, the isomeric ratio σ_m/σ_g is greater than the yield ratio Y_m/Y_g by about 10% and that, at energies in excess of 20 MeV, these two ratios virtually coincide (curve *2* in Fig. 1*a*). That the ratios σ_m/σ_g and Y_m/Y_g for the reaction being considered behave in the way described above gives sufficient grounds to believe that a comparison of the experimental values of the isomeric yield and cross-section ratios (*d* and *r*, respectively) would be reasonable for other reactions as well.

In dealing with protons and alpha particles, we employed targets 10–15 mg/cm^2 thick manufactured from enriched $^{44}CaCO_3$ in the form of a powder pressed with polyethylene and then baked at *t* = 100°C.

Target assemblies were irradiated with a proton beam from the U-120 cyclotron, the primary beam energy being E_p = 6.7 MeV. The protons were moderated by aluminum foils. In order to study (α, *p*3*n*) reactions, target assemblies were exposed to alpha particles of beams extracted from the U-240 cyclotron. The primary beam energies of 80 and 100 MeV were reduced, in that case, with the aid of tantalum foils. The irradiated targets were transported to a semiconductor spectrometer by a pneumatic rabbit. The proton and α-particle ranges were calculated on the basis of data tabulated in [11].

We have also measured the isomeric ratios for the reaction ^{51}V(*p*, α*p*3*n*)^{44m,g}Sc implemented by exposing foils from natural vanadium to 50- and 70-MeV protons of U-240 internal beams.

All the measurements were performed with semiconductor spectrometers having a resolution of about 2.0 keV for the ^{60}Co gamma lines. The measurements were grouped into series with an interval of 2 to 3 h. In order to estimate the contribution of background admixtures, the residual activity was additionally measured after a lapse of a day since the completion of the exposure. The results obtained for the reactions ^{44}Ca(*p*, *n*)^{44m,g}Sc and ^{44}Ca(α, *p*3*n*)^{44m,g}Sc are displayed in Figs. 2 and 3, respectively. In these figures, the isomeric ratios for the reactions ^{45}Sc(*d*, *t*)^{44m,g}Sc [12] (Fig. 2) and ^{41}K(α, *n*)^{44m,g}Sc [13] (Fig. 3) are also shown for the sake of comparison. For the (*p*, α*p*3*n*) reaction in ques-

tion, it was found that $\sigma_m/\sigma_g = 1.4 \pm 0.2$ and 1.5 ± 0.2 at $E_p = 50$ and 70 MeV, respectively.

3. DISCUSSION OF THE RESULTS

A comparison of experimental data shows that the isomeric ratio r is one order of magnitude greater in the $(\alpha, p3n)$ reaction in question than in the (γ, n) reaction (see Figs. 1*a*, 3*a*). This distinction is compatible with the statistical pattern, because alpha particles introduce a significant angular momentum in the target nucleus, predominantly populating the 6^+ high-spin state.

A comparison of (γ, n), (p, n), and (d, t) reactions can be conveniently drawn in terms of the excitation energies of the residual nucleus. Figures 1–3 show the excitation energy $E^* = E - E_{\text{thr}}$ (top scale), where E_{thr} is the reaction threshold. It can be seen that, for the (γ, n) and (d, t) reactions, the values of σ_m/σ_g nearly coincide at close excitation energies of the residual nucleus. At the same time, the value of σ_m/σ_g for the (p, n) reaction is one order of magnitude less than that for the (γ, n) reaction. Qualitatively, this can be explained within the statistical approach by considering that the angular momentum of the input channel is $\mathbf{J} = \mathbf{1} + \mathbf{7}/2$ in the (γ, n) reaction and $\mathbf{J} = 0 + (\mathbf{1}/2 \text{ or } \mathbf{3}/2)$ in the (p, n) reaction. By merely taking into account equiprobable branching in gamma cascades from states with these spin values, we can find that the 6^+ state is populated in the (p, n) reaction with a probability that is 20–30 times less than that in the (γ, n) reaction.

In support of the above, we also note that recent studies of partial photonuclear channels (γ, n_i) and (γ, p_i) of giant-resonance decay that populate individual (ith) levels of the final nucleus $A - 1$ showed that, for ^{44}Sc, the statistical mechanism saturates 70 to 90% of all such decays [14]. In order to draw a comparison with experimental data, we have therefore estimated the isomeric ratios for the reaction $^{45}\text{Sc}(\gamma, n)^{44m,g}\text{Sc}$ within the cascade–evaporation model (CEM) [15, 16], which is based on the statistical approach. In these calculations, it was assumed that the ^{45}Sc nucleus absorbs a dipole photon. After the evaporation of a neutron, excited states of the daughter nucleus go over to the ground or the isomeric state via a cascade of $E1$ transitions. The density of nuclear levels was calculated by the Bethe–Bloch formula [17].

Curve *3* in Fig. 1*a* represents the results of these calculations. We note that consistent calculations within the above model [15, 16] fail to reproduce the experimental data. The agreement is achieved if the spin-cutoff parameter in the Bethe–Bloch formula is fixed at $\sigma = 3$ (curve *3* in Fig. 1*a*).

From Fig. 1*a*, it can be seen that, for the $(\gamma, n)^m$ reaction, the results obtained with $\sigma = 3$ are qualitatively similar to the corresponding experimental data. The calculation with $\sigma = 3$ agrees with the experimental data at $E = 20$ MeV. We note that, for the reaction $^{45}\text{Sc}(\gamma, n)^{44m,g}\text{Sc}$ at $E_{\gamma,m} = 45$ MeV, Völpel [18] obtained $\sigma_m/\sigma_g = 0.23$ and the spin-cutoff parameter of $\sigma = 2.8$, which is close to our value.

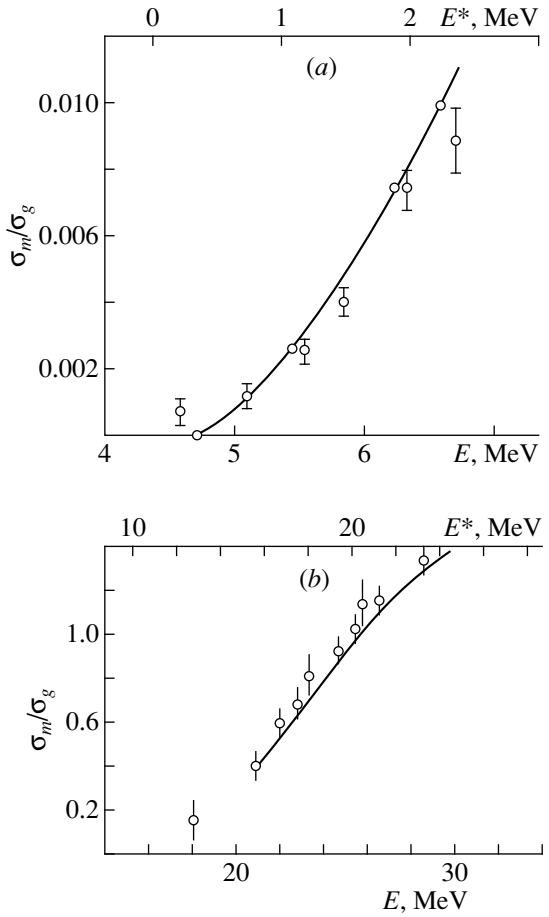

Fig. 2. Isomeric ratios for ^{44}Sc in the reactions (*a*) $^{44}\text{Ca}(p, n)^{44m,g}\text{Sc}$ and (*b*) $^{45}\text{Sc}(d, t)^{44m,g}\text{Sc}$.

Calculations within a similar model that were performed in a number of studies to determine theoretically the isomeric ratios for the neutron-induced reaction $^{45}\text{Sc}(n, 2n)^{44m,g}\text{Sc}$ also yielded close values for σ: for the $(n, 2n)^m$ reaction at $E_n = 15.0$ MeV, Karolyi and Csikai [19] obtained $\sigma_m/\sigma_g = 0.71$, the agreement between the calculated and measured values being achieved at $\sigma = 3.5 \pm 0.1$; at $E_n = 14.1$ MeV, Völpel [18] found the value of $r = 0.91$, with the spin-cutoff parameter being fixed at $\sigma = 3.68$; at the same value of $E_n = 14.1$ MeV, Tatarczuk and Medikus [8] arrived at $r = 0.72$ and the spin-cutoff parameter of $\sigma = 3.68$.

A more sophisticated version of the CEM was used in [20] to calculate isomeric ratios for reactions induced by massive particles. In this version, the isomeric pair is populated on the basis of the scheme according to which low-lying states deexcite and which is known from experiments; in particular, it is considered that an yrast trap can escape from states in the vicinity on an yrast line that have angular momenta exceeding those of metastable states, and an yrast line is introduced.

The yrast-line energy is represented as

$$Y(J) = \frac{h^2}{2\mathcal{J}} J(J+1), \tag{3}$$

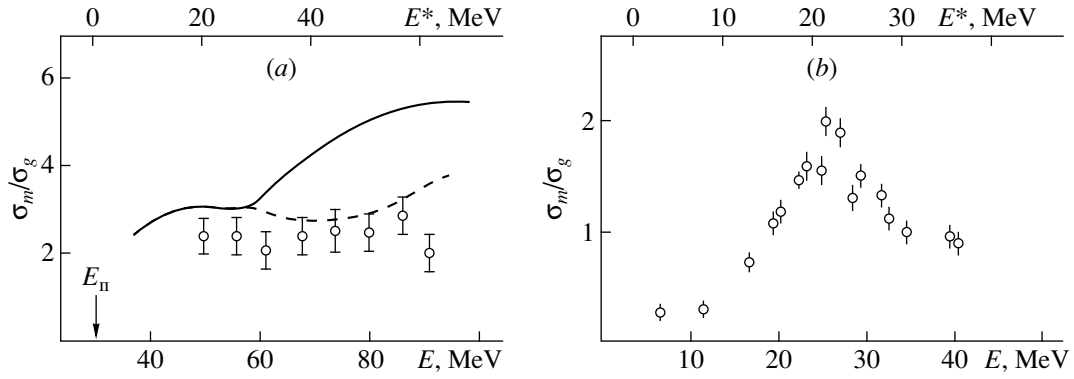

Fig. 3. Isomeric ratios versus energy for the reactions (*a*) ^{44}Ca(α, *p*3*n*)^{44m,g}Sc and (*b*) ^{41}K(α, *n*)^{44m,g}Sc.

where $\mathcal{J} = \mathcal{J}_{\text{rig}}[1 - b\exp(-0.693E/d)]$ is the moment of inertia of the nucleus. Here, *b* and *d* are numerical parameters (their commonly accepted values are $b = 0.5$ and $d = 6$ MeV), *E* is the excitation energy of the residual nucleus, and $\mathcal{J}_{\text{rig}}$ is the moment of inertia of a rigid body. The bracketed expression takes into account deviations of the moment of inertia from the rigid-body value at low excitation energies.

The density of nuclear levels was calculated on the basis of the expression prescribed by the back-shifted Fermi gas model; that is,

$$\rho(E, J) = \frac{2J+1}{24\sqrt{2}a^{1/4}(E-\delta)^{5/4}\sigma^3} \times \exp\left\{2\sqrt{a(E-\delta)} - \frac{(J+1/2)^2}{2\sigma^2}\right\}, \quad (4)$$

where δ is a correction for even–odd distinctions and

$$\sigma^2 = 0.0888(\pi^2/6)[1 - b\exp(-0.693E/d)] \times \sqrt{a(E-\delta)}A^{2/3}, \quad (5)$$

For the energy dependence of the level-density parameter *a*, we employed the phenomenological representation

$$a = \tilde{a}(1 + f(E)\delta W/E), \quad (6)$$

where $\delta W = M_{\text{expt}}(Z, A) - M_{\text{LD}}(Z, A)$ (*Z* is the charge of the nucleus, and *A* is the number of nucleons in it) is the experimental value of the shell correction to the mass formula, $M_{\text{expt}}(Z, A)$ and $M_{\text{LD}}(Z, A)$ being, respectively, the experimental value of the nuclear mass and the binding energy of the nucleus in the liquid-drop model; $\tilde{a}$ is the asymptotic value of the level-density parameter at high excitation energies,

$$\tilde{a}/A = \alpha + \beta A$$

$$(\alpha = 0.154\ \text{MeV}^{-1}, \quad \beta = -6.3 \times 10^{-5}\ \text{MeV}^{-1});$$

and

$$f(E) = 1 - \exp(-\gamma E), \quad \gamma = 0.054\ \text{MeV}^{-1}.$$

Expression (5) is valid for $E \gg T$ (*T* is the temperature of the nucleus); in view of this, the model level density was matched with the mean experimental level density at excitation energies of 0–2 MeV. If there was no experimental information, the model level density was matched with the value of $\rho(E, J) = 1\ \text{MeV}^{-1}$ in the vicinity of the yrast line.

In simulating the (α, *p*3*n*) reaction, we took into account all possible sequences of particle emission (*p*3*n*, 2*npn*, and 3*np*). The results of the calculations are represented by solid curves in Figs. 2*a* and 3*a*. It can be seen that, for the reactions featuring charged particles, the experimental values in question are faithfully reproduced on the basis of the CEM version used here. This suggests that the reactions being discussed are governed predominantly by the statistical mechanism.

It should be noted that the yrast trap was not considered in the calculations. That the giant *E*1 resonance is split into two maxima (Fig. 1*b*) indicates that the ^{45}Sc nucleus is severely deformed. Figure 3*b* displays data on the isomeric ratios *r* of the cross sections for the (α, *n*) reaction [13]. We can see that, here, the ratio *r* begins to decrease as soon as the excitation energy of the residual nucleus reaches a value of $E^* \sim 30$ MeV. Concurrently, this is the excitation-energy value at which the ratio *r* calculated for the (α, *p*3*n*) reaction begins to deviate from experimental data. All these observations may be explained upon taking into account the yrast-line contribution.

Bogila and Kolomiets [21] showed that, from some value of the particle energy in the input channel, the populations of states in the vicinity of the yrast line in the residual nucleus affect significantly $\sigma_m(E^*)$. In the (α, *p*3*n*) reaction, the ^{48}Ti compound nucleus is produced in states whose angular momenta exceed $J_i^{\max}$ (^{44}Sc) for excitation energies E^* of the residual nucleus not less than 25 MeV. This leads to $\Gamma_\gamma \geq \Gamma_{\text{part}}$ (where Γ stands for the channel widths). In such situations, σ_m/σ_g changes significantly upon taking into account the competition of channels involving particle emission in the gamma deexcitation of ^{44}Sc in the vicin-

ity of the yrast line (Fig. 3*a*, dashed curve). We can see that, at energies up to 100 MeV, this can also improve considerably the quantitative agreement of the σ_m/σ_g values calculated for the (α, *p*3*n*) reaction with experimental data.

It should be emphasized that the statistical process is operative in the (*p*, α*p*3*n*) reaction as well, but the channel of quasielastic proton scattering must be additionally taken into account here. The fact that, for this reaction, the ratio σ_m/σ_g changes only slightly within the energy range 50–70 MeV can be explained in this case.

From the above, it follows that quite a vast body of experimental data on the excitation of the 6^+ isomeric state of the ^{44}Sc nucleus in various reactions is available at present. An analysis of these data shows that the statistical mechanism plays an important role over a wide range of excitation energies of the residual nucleus and a wide range of particle species. This result could seem important, but it should be taken with caution, because a direct mechanism can contribute significantly to (*d*, *t*) reactions, as well as to (*p*, *n*) reactions near the threshold, and because, in reactions featuring alpha particles, preequilibrium particle emission occurs at energies $E_\alpha > 25$ MeV.

REFERENCES

1. V. G. Alpatov, S. B. Borzakov, *et al.*, Yad. Fiz. **60**, 970 (1997) [Phys. At. Nucl. **60**, 867 (1997)].
2. Yu. P. Gangrsky, A. P. Tonchev, and N. P. Balabanov, Fiz. Élem. Chastits At. Yadra **27**, 1043 (1996) [Phys. Part. Nuclei **27**, 428 (1996)].
3. V. A. Zheltonozhsky, V. I. Lomonosov, V. M. Mazur, *et al.*, At. Énerg. **60**, 441 (1990).
4. E. A. Bogila, V. I. Gavrilyuk, V. A. Zheltonozhsky, *et al.*, Izv. Akad. Nauk SSSR, Ser. Fiz. **55**, 921 (1991).
5. C. M. Lederer and V. Shirley, *Table of Isotopes* (New York, 1978).
6. V. M. Mazur, I. V. Sokolyuk, and Z. M. Bigan, Yad. Fiz. **54**, 895 (1991) [Sov. J. Nucl. Phys. **54**, 541 (1991)].
7. M. G. Davydov, V. G. Magera, and A. V. Trukhov, At. Énerg. **58**, 47 (1985).
8. Y. R. Tatarczuk and H. A. Medikus, Phys. Rev. **143**, 818 (1966).
9. S. S. Deitrich and B. L. Berman, At. Data Nucl. Data Tables **38**, 199 (1988).
10. A. S. Penfold and I. E. Leiss, Phys. Rev. **114**, 1332 (1959); O. V. Bogdankevich and F. A. Nikolaev, *Operation with Bremsstrahlung Beams* (Atomizdat, Moscow, 1964).
11. N. N. Pucherov *et al.*, *Tables of Mass Stopping Power and Ranges of 1–100 MeV Charged Particles* (Naukova Dumka, Kiev, 1975).
12. A. Mocoroa, H. Vignau, M. C. Caracoche, *et al.*, J. Inorg. Nucl. Chem. **27**, 1719 (1965).
13. T. Matsuo, J. M. Matuszek, *et al.*, Phys. Rev. B **139**, 886 (1965).
14. B. S. Ishkhanov, I. M. Kapitonov, and I. A. Tutyn', Yad. Fiz. **58**, 1180 (1995) [Phys. At. Nucl. **58**, 1103 (1995)].
15. L. Ya. Arifov *et al.*, Yad. Fiz. **34**, 1028 (1981) [Sov. J. Nucl. Phys. **34**, 572 (1981)].
16. Z. M. Bigan, V. M. Mazur, and Z. Z. Torich, Preprint No. KIYaI-84-10, KINR (Kiev Institute for Nuclear Research, 1984).
17. H. Bethe, Phys. Rev. **50**, 332 (1936); A. V. Malyshev, *Level Density and Structure of Atomic Nuclei* (Atomizdat, Moscow, 1969).
18. R. Völpel, Nucl. Phys. **A182**, 411 (1972).
19. J. Karolyi and J. Csikai, Nucl. Phys. **A122**, 234 (1968).
20. E. A. Bogila and V. M. Kolomiets, Ukr. Fiz. Zh. **34**, 7 (1989).
21. E. A. Bogila and V. M. Kolomiets, Yad. Fiz. **53**, 120 (1991) [Sov. J. Nucl. Phys. **53**, 78 (1991)].

Translated by E. Kozlovskiĭ

Physics of Atomic Nuclei, Vol. 63, No. 3, 2000, pp. 328–335. Translated from Yadernaya Fizika, Vol. 63, No. 3, 2000, pp. 394–401.

NUCLEI
Theory

Two-Body Potential Model for the Doublet Neutron–Deuteron System and Effects of Long-Range Interaction

Yu. V. Orlov, Yu. P. Orevkov, and L. I. Nikitina

Institute of Nuclear Physics, Moscow State University, Vorob'evy gory, Moscow, 119899 Russia

Received March 1, 1999

Abstract—In order to describe the doublet nucleon–deuteron system at low energies, Tomio *et al.* [Phys. Rev. C **35**, 441 (1987)] proposed a two-body model featuring a potential whose asymptotic behavior is consistent with the Faddeev equation—that is, a potential involving a long-range component. The characteristics of the bound and the virtual triton and the position of the pole of $k\cot\delta$—these quantities were not considered in the above article of Tomio *et al.*—are calculated in the present study. A comparison of the results obtained in this way with analogous results for the short-range Hulthén and Yukawa potentials reveals that, for the doublet neutron–deuteron system, the effects of long-range interaction do not play a significant role—that is, the system in question is far from a state of the Efimov type. *© 2000 MAIK "Nauka/Interperiodica".*

1. INTRODUCTION

The spin-doublet neutron–deuteron system is a classical testing ground for three-body Faddeev equations featuring various versions of nucleon–nucleon forces. Numerous investigations demonstrate that the properties of the neutron–deuteron system depend greatly on the version of *NN* interaction. By way of example, we indicate that correlations of the Phillips line type [1] were discovered for the dependence of the triton binding energy ε_T on the doublet scattering length a_2 and that correlations of the Girard–Fuda type [2] were found for the dependence of the virtual-triton binding energy ε_{T^*} on the same variable. The opinion that, because of the smallness of the deuteron binding energy ε_d in relation to the triton binding energy ε_T, the three-body character of the neutron–deuteron system must play a decisive role even at energies below the threshold for deuteron breakup had long been prevalent in the literature. However, calculations within the *N*/*D* method revealed [3–5] that the low-energy features of the neutron–deuteron system can be described fairly well within the two-body model taking no account of the three-body cut of the *S* matrix in the complex plane of energy. It follows that a two-body potential model can also be used in this energy region.

The two-body potential model was proposed in [6, 7]. The first of these two studies relied on the Hulthén potential

$$V(r) = -V_0/[\exp(\mu r) - 1]. \quad (1)$$

The parameters V_0 and μ were determined by fitting data on the scattering length a_2 and the binding energy ε_T (for the neutron–deuteron system, the corresponding experimental values are $a_2 = 0.65$ and $\varepsilon_T = 8.48$ MeV). The nuclear vertex constant G_T^2 was calculated in [6], and the value obtained there complies well with that which was presented by Simenog *et al.* [8], who made use of the results of a phase-shift analysis of experimental data on elastic neutron–deuteron scattering. It should be recalled that the nuclear vertex constant G_T^2 and the asymptotic normalization factor C_T^2 in the radial wave function of the bound state are related by a linear equation (see below). In addition, it was shown in [6] that the proposed model reproduces fairly well the character of variations that the vertex constant calculated on the basis of Faddeev equations displays in response to changes in a_2 and ε_T values. Later on, it was indicated in [9, 10] that other low-energy features of the doublet neutron–deuteron system—such as the position of the virtual pole (binding energy ε_{T^*} of the virtual triton T*), the corresponding nuclear vertex constant ($G_{T^*}^2$), and the position of the pole of $k\cot\delta$ [zero of the partial scattering amplitude $f(k)$] [10]—can be described satisfactorily on the basis of the same model without further fitting the parameters of the Hulthén potential.

In order to assess the sensitivity of the results to a specific form of the neutron–deuteron interaction potential, we calculated [10] all the aforementioned quantities for the Yukawa potential

$$V(r) = -V_0(\mu r)^{-1}\exp(-\mu r) \quad (2)$$

and arrived at results that agree fairly well both with experimental data and with the results obtained with the Hulthén potential.

Two potentials were proposed in [7]; of these, one (version B) has the form

$$V(r) = -V_0(R/r)^2[\sin(r/R)]^2\exp(-\mu r). \quad (3)$$

1063-7788/00/6303-0328$20.00

In contrast to the potentials (1) and (2), the potential (3) involves three parameters—V_0, R, and μ—which were determined by fitting data on three quantities that include, in addition to a_2 and ε_T mentioned above, the ^{3}He binding energy. The objective of the study reported in [7] was to assess theoretically the doublet proton–deuteron scattering length associated with nuclear interaction. The aforementioned characteristics of the doublet neutron–deuteron system other than the analogous scattering length were not computed in [7]. The oscillating factor in (3) was introduced in order that the potential be regular at zero value of the radius. In the other potential version (A), which is not considered in the present study, regularization at zero was achieved by matching the potential being considered with a constant potential in the central region.

The present study is aimed at (i) filling the existing gaps by calculating all the aforementioned low-energy features of the doublet neutron–deuteron system for the potential (3), (ii) refining the parameters of the potential (3), and (iii) comparing the results of these calculations for the potentials (1)–(3) in order to assess the sensitivity of these physical quantities to the character of the asymptotic behavior of a potential of the form

$$V(r) \longrightarrow C(r)r^{-n}\exp(-\mu r), \tag{4}$$

where $C(r) < \text{const}$, while the exponent n takes the values of $n = 0$, 1, and 2 for, respectively, the Hulthén potential, the Yukawa potential, and the potential (3) (which was used in [7]). We note that the potential (3) was chosen on the basis of the fact that the Faddeev equations lead to an effective interaction of the form $V(r) \longrightarrow C/r^2$ when the scattering length in the two-body subsystem tends to infinity. In the two-body potential model, this corresponds to the limit $\mu \longrightarrow 0$.

In this study, we consider only the two-parameter problem, fixing the value of μR at 0.2646, as in [7]. This choice was motivated, on one hand, by the fact that there are correlations between the low-energy features of the doublet neutron–deuteron system and, on the other hand, by a desire to perform a systematic analysis of the potential models (1)–(3) at the same level of generality (that is, with two parameters). Varying μR is beyond the scope of the present study. We also made use of the scaling properties of the potential (3) (see [10]). This enabled us to consider such combinations of physical quantities (these combinations may include the potential parameters) that are invariant under the scaling transformations $r \longrightarrow \gamma r$ and $p \longrightarrow \gamma^{-1}p$. The combinations in question depend only on the interaction strength $g = K_0^2 R^2$, where $K_0^2 = (2m_{12}/\hbar^2)V_0$, $m_{1,2}$ being the reduced mass of the system. In the case of the neutron–deuteron system, which is considered here, the reduced mass is $m_{12} = (2/3)m$, where m is the nucleon mass. Specifically, we calculated the quantities

$$a\chi_1,\ \chi_1/\mu,\ \chi_2/\mu,\ \kappa_0/\mu,\ C_1,\ C_2, \tag{5}$$

where $\chi_n = (2m_{12}\varepsilon_n)^{1/2}/\hbar$, ε_1 and ε_2 being, respectively, the binding energy in the ground (real) state with principal quantum number $n = 1$ and the binding energy in the first excited (virtual in this case) state with principal quantum number $n = 2$; $\kappa_0 = (2m_{12}E_0)^{1/2}/\hbar$, E_0 being the position of the pole of $k\cot\delta$ in the complex plane of energy E; and C_1 and C_2 are asymptotic normalization factors. It is well known that the nuclear vertex constant G^2 and the asymptotic normalization factor C are related by the equation (see, for example, [9]; $\nu \equiv T^*$)

$$\begin{aligned}(G_{T,\nu})^2 &= 3\pi(3/2)^2(\hbar/mc)^2\chi_{1,2}(C_{T,\nu})^2,\\ (C_{T,\nu})^2 &= (2/3)(C_{1,2})^2.\end{aligned} \tag{6}$$

The distinction between $C_{T,\nu}$ and $C_{1,2}$ is associated with taking into account the identity of nucleons in the isospin formalism.

By eliminating the parameter g, we can obtain relations that involve the aforementioned scaling physical quantities—for example, C_1^2 and $a\chi_1$—but which are free from the potential parameters. Allowances for the scaling properties of the potential simplifies considerably the procedure for fitting the potential parameters to specific values of a and χ_1. In determining the parameters, we proceeded along the following chain:

$$a\chi_1 \longrightarrow g \longrightarrow \chi_1/\mu \longrightarrow \mu \longrightarrow R \longrightarrow V_0. \tag{7}$$

As matter of fact, the above scaling properties make it possible to reduce the two-parameter problem to a one-parameter problem. This facilitates considerably the fitting of parameters and a comparison of the results obtained with the different potentials.

The virtual triton represents the first excited state of the triton. Therefore, its features are determined by the same parameter set as the features of the triton; that is, the quantities χ_2 and κ_0—or, on the energy scale, ε_2 and E_0—as well as C_{T^*}, are determined simultaneously with χ_1 and C_1^2. The position of the virtual pole ($B_\nu = \varepsilon_2 = \varepsilon_T - \varepsilon_d$) and the position of the pole ($-E_0$) of the function $k\cot\delta$ are reckoned from the threshold for the neutron–deuteron scattering channel at $E = -\varepsilon_d$. A comparison of the $a\chi_1$ dependences of C_1^2 for all three potentials over a wide range of the interaction strengths, including those that correspond to the formation of the extremely light bound nuclear states [deuteron d, hypertriton $^3H_\lambda$, triton T(^{3}H)], is of particular interest, because such a comparison does not involve the potential parameters explicitly.

In our calculations, we relied on the integral Lippmann–Schwinger equation and the Schrödinger equation in the momentum representation. Here, the doublet proton–deuteron scattering length was not calculated, because the method used here cannot take properly into account Coulomb interaction.

Below, we consider such energies at which it is legitimate to retain only the *s* wave. We use the system of units where $\hbar = c = 1$.

2. EFFECTIVE POTENTIAL AND ANALYTIC PROPERTIES OF THE SCATTERING AMPLITUDE

That the pole Feynman diagram that corresponds to proton exchange between the deuteron and the neutron, the singularity of this diagram in momentum transfer lying closely to the physical region, plays an important role in neutron–deuteron scattering is a theoretical argument in favor of the two-body potential model. The corresponding singularities of the partial scattering amplitude are logarithmic branch points and the relevant cuts in the complex plane of momentum that go along the imaginary axis. The interval $(-ik_1, ik_1)$, where $k_1 = (2/3)\sqrt{m\varepsilon_d} = 0.154$ fm^{-1}—or, on the energy scale, $E_1 = -\varepsilon_d/3 = 0.738$ MeV—is the domain of analyticity of the partial amplitude. This character of singularity can be simulated by using Yukawa type potentials—that is, potentials whose asymptotic behavior is given by (4), in which case a dynamical singularity occurs at $k = \pm i\mu/2$ (see, for example, [11]). Setting $\mu = 2k_1$, we obtain the range $M = \mu^{-1}$ of about 3 fm.

The properties being discussed follow from the analytic structure of the kernel of the Faddeev equation (see, for example, [12]). Among other things, it follows that a long-range interaction of the $1/r^2$ type arises when the scattering length for a pair subsystem tends to infinity. It is well known that this results in the accumulation of Efimov levels. Following the study of Efimov [13], Tomio *et al.* [7] deem it necessary to introduce the factor $1/r^2$ in the potential of the two-body model as well. It should be emphasized, however, that this character of long-range interaction is indeed of importance if the physical system under study is close to a state where the Efimov effect manifests itself—that is, where $\mu \longrightarrow 0$. As a matter of fact, the actual parameters of the nucleon–nucleon interaction are such that the doublet neutron–deuteron system has only one bound state (triton). For this reason, it is natural to expect that a specific form of potential—and in particular, the value of the exponent *n* in (4)—does not play a very important role, provided that an exponential decrease of the potential at infinity is ensured. On this basis, we believe (see also [6]) that all the above potentials (1)–(3) can be used on equal terms to construct a model description of the characteristics of the doublet neutron–deuteron system. The oscillations of the potential (3) look somewhat unnatural. Tomio *et al.* [7] questioned the applicability of "conventional" short-range potentials—in particular, the exponential and the Yukawa potentials—to the problem being discussed, but the critical comments of those authors do not seem justified. For example, their general statements that experimental data on the virtual triton cannot be reproduced with short-range potentials and that such potentials give no way to determine correctly the pole of the function $k\cot\delta$ are invalid, because they are at odds with the results obtained in [9, 10]. The assertion that the virtual state of the triton is unobservable physically, another point advocated in [7], does not withstand experimental tests—in fact, the existence of the state in question was reliably established on the basis of experimental data via a phase-shift analysis of doublet neutron–deuteron scattering (see [8]) and was confirmed by numerous calculations relying on the Faddeev equations for various models of nuclear forces (see, for example, [14]); we admit, however, that it is rather hard to see this state in neutron–deuteron scattering directly.

In analyzing the results of our numerical calculations, we rely on what is known from quantum scattering theory, as well as on the theorem of symmetry for bound and virtual levels [15], and on its important corollary concerning the trajectories of the zeros of the partial scattering amplitude $f(k)$ [16]. Recall that, for Yukawa type potentials, whose asymptotic behavior is given by (4) (with $n \le 2$)), it was proven in [15] that the disposition of the points at which the trajectories of the poles for bound and virtual states intersect the lines of dynamical singularities is characterized by a mirror symmetry with respect to the zero-momentum axis. It was shown in [16] that these symmetry points also belong to the trajectories of the poles of $k\cot\delta$ [zeros of $f(k)$]. For Yukawa type potentials, the trajectories of the zeros of $f(k)$ issue from the points where the scattering length *a* is zero ($a = 0$) and intersect the lines of dynamical singularities simultaneously with the trajectories of the poles corresponding to bound and virtual levels—that is, at the same symmetry points.

3. COMPUTATIONAL METHOD, CHOICE OF PARAMETERS, AND RESULTS OF THE COMPUTATIONS

The low-energy features of the doublet neutron–deuteron system whose behavior is governed by the potential (3) were computed by solving the integral Lippmann–Schwinger and Schrödinger equations in momentum space. These calculations are completely analogous to those for the Yukawa potential (see [10]). In order to describe virtual states, we used analytic continuations of these integral equations to the unphysical sheet of energy (see, for example, [14]). These equations feature the Fourier transform $V(k, k')$ of the potential $V(r)$—in particular, its values at imaginary momenta and at zero momentum as well. The potential in the form (3) is convenient because the function $V(k, k')$ is known for it in an analytic form (see Appendix).

The results of the calculations for the scaling quantities in (5) are presented in Fig. 1 ($M = \mu^{-1}$) versus the potential strength. For the argument, we took the quantity $\rho = \sqrt{g/g_{cr}}$, where $g_{cr} = 1.4218$ is the *g* value at which the ground state becomes a bound state. It is interesting to note that, for the potential (3), the ρ

dependence of $\chi_1 M$ is nearly linear; a linear relation between $\chi_1 M$ and g holds approximately for the Yukawa potential and exactly for the Hulthén potential (see [6, 10]). The results obtained for the parameters of the potential (3) by fitting the experimental values of ε_T and a_2 for the doublet neutron–deuteron system are displayed in Table 1, along with the parameter values from [7]. The fitting was implemented according to the chain presented in (7). The R and μ values obtained in the present study are close to those from [7]. Our potential-depth value of $V_0 = 40.5$ MeV is somewhat greater than that presented in [7]. The slight difference of $\Delta V_0 \cong 0.7$ MeV affects, however, the value of the scattering length a_2, a quantity that shows the highest sensitivity to changes in parameter values. By using the parameter values from [7] (see Table 1), we obtained $a_2 = 0.82$ fm, the experimental value being 0.65 fm. For the position of the closest dynamical singularity at $k = \pm ip$, the value of $\mu \cong 0.15$ fm^{-1} found from fitting for the exponent in (3) yields $p = \mu/2 = 0.075$ fm^{-1}. The last value is approximately one-half as great as the momentum value that determines the position of the singularity associated with one-nucleon exchange ($k_1 = 0.154$ fm^{-1}).

The value of the potential range ($M = \mu^{-1}$) is of crucial importance for correctly describing the position of the virtual level of the triton. Indeed, the trajectory of the virtual level (of the energy of the first excited state), $\chi_2 M$, cannot intersect the line of the first dynamical singularity determined by $|pM| = 0.5$ until the trajectory of the bound level approaches this line—that is, until ρ reaches a value of about 1.12, in which case $\chi_1 M = 0.5$. The value of $\rho \cong 1.68$ corresponds to the experimental value of $a\chi_1 = 0.291$. This sets the constraint $\chi_2 \le \mu/2 = 0.0753$ fm^{-1}. On the energy scale, we accordingly have $B_v \le 0.18$ MeV, which is three times as small as the well-known estimate $B_v \cong 0.5$ MeV, which was deduced from experimental data, as well as from the calculations based on the Faddeev equations. A comparison of the characteristics of the doublet neutron–deuteron system for the potentials (1)–(3) is illustrated in Table 2. This table also displays the results of the phase-shift analysis of experimental data that was performed for this system by using the modified formula of effective-range theory for the function $k\cot\delta$, which has a pole at $k = \pm i\kappa_0$ and which involves (or which does not involve) a k^4 term:

$$k\cot\delta = (1 + k^2/\kappa_0^2)^{-1}(-1/a + C_2 k^2 + C_4 k^4). \quad (8)$$

For the asymptotic normalization constant, this yields (see [10] and references therein)

$$C^2 = (1 - \chi^2/\kappa_0^2)/(1 - 2C_2\chi - 3\chi^2/\kappa_0^2 + 4C_4\chi^3). \quad (9)$$

It is worth noting that the position of the dynamical singularity in modified effective-range theory [equation (8)] is close to the singularity of the Feynman diagram for one-nucleon exchange ($E_1 = 0.738$ MeV). The position of the dynamical singularity in the two-body model that employs the Hulthén potential [at $n = 0$ in (4), this singularity appears to be a spurious pole] also proves to be close to the position of the singularity of this diagram. In the case of the Yukawa potential, the corresponding point (on the energy scale) is offset from the physical region by a distance twice as large as those in the preceding examples. For the potential given by

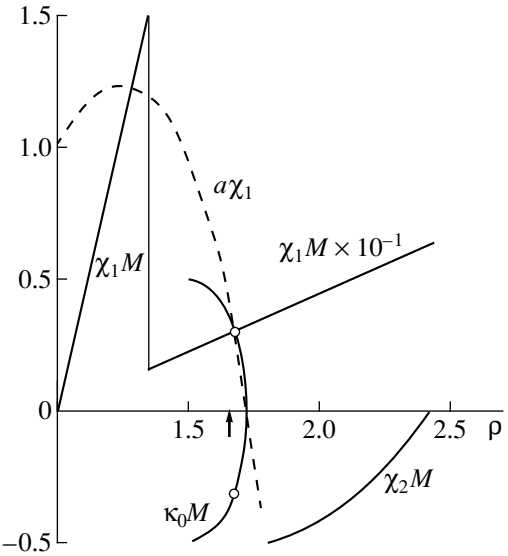

Fig. 1. Results of the calculations of the scaling quantities $a\chi_1$, $\chi_1 M$, $\chi_2 M$, and $\kappa_0 M$ with the potential (3) (introduced in [7]) versus the scaling variable $\rho = \sqrt{g/g_{cr}}$. Circles (and arrow) indicate those points on the curves that correspond to the experimental value of $a\chi_1 = 0.291$ for the doublet neutron–deuteron system. For the fast growing function $\chi_1 M$, the scale was changed by one order at $\rho = 1.35$.

Table 1. Parameters of the potential (3) and their fitted values

Potential \ Parameter	V_0, MeV	R, fm	μ, fm^{-1}	$\varepsilon_T - \varepsilon_d$, MeV	a_2, fm
Tomio *et al.*	39.839	1.7571	0.1506	6.013	0.822
Our study	40.495	1.7565	0.1507	6.260	0.650

Note: So large a number of decimal places have been presented only because this was done in [7] (since the model in question is quite rough, it is sufficient to calculate only three decimal places).

Table 2. Features of the doublet neutron–deuteron system

Model	G_T^2, fm	B_v, MeV	$-G_v^2$, fm	$-E_0$, MeV
Effective-range theory:				
[8, 10], $C_4 \neq 0$	1.48	0.530	0.0073	0.150
[17], $C_4 = 0$	0.33	0.482	0.008	0.047
Hulthén potential [9, 10]	1.48	0.75	0.018	0.20
Yukawa potential [10]	1.16	0.61	0.025	0.18
Potential of Tomio *et al*. from [7] [equation (3) in the present study]	1.47	0.176	–	0.063

(3), the dynamical singularity is one order of magnitude closer to the physical region than for the Yukawa potential. So great a distinction is due to the concerted effect of two factors, the different powers of r [$n = 2$ in the potential given by (3)] and the presence of the oscillating factor in the potential (3). Both these factors smooth out the attractive properties of the potential, but this is compensated by an increase in its range ($M = \mu^{-1}$) and an increase in its depth (V_0). For the potentials (1)–(3), the depth and range parameters are compared in Table 3. These parameters do not differ very strongly for the potentials (1) and (2). In the case of the potential (3), the depth V_0 is approximately twice as large as those for the potentials (1) and (2), the corresponding potential ranges being roughly in the ratios $M_3/M_1 \approx 3$ and $M_3/M_2 \approx 2$. From the point of view of practical applications in the theory of nuclear reactions, the most important quantity is the vertex constant G_T^2; its value obtained for the potential (3) is close to the results that are produced by the Hulthén potential and by modified effective-range theory according to equations (8) and (9) (see Table 2). The same can be seen in Fig. 2, which illustrates the relationship between the asymptotic normalization factor C_T^2 and the quantity $a\chi_1$. The results obtained with the potentials (1)–(3) are qualitatively similar, but they deviate drastically from the curve computed in the effective-range approximation {see equation (6) from the present study and equation (8) from [10]}:

$$C^2_{\text{eff.range}} = a\chi_1/(2 - a\chi_1). \quad (10)$$

The distinctions emerge immediately beyond the deuteron region, where $a\chi_1 = 1.26$. For the potential (3), the position of the pole of the function $k\cot\delta$ on the energy scale ($E_0 = 0.063$ MeV) is strongly underestimated in relation to the results produced by the Hulthén and Yukawa potentials (see Table 2), as well as in relation to the experimental value of $E_0 = 0.15$ MeV [8]. In all probability, this is also because the value obtained for the range M as the result of fitting is overly great, as was discussed above in connection with the position of the pole for T*. As can be seen from Fig. 1, the latter takes the maximum possible value at given M because the trajectory of $\chi_2 M$ tends to the dynamical-singularity line as ρ approaches 1.8, the experimental value of $a\chi_1$ for the doublet neutron–deuteron system corresponding to $\rho = 1.68$. We cannot rule out the possibility that,

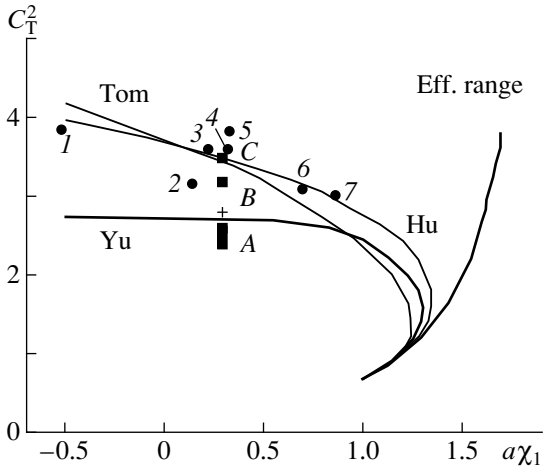

Fig. 2. Results of the calculation for the asymptotic normalization factor C_T^2 of the radial wave function of the ground bound state versus the product $a\chi_1$. The calculations were performed with the Hulthén potential (Hu); the Yukawa potential (Yu); and the potential in the form (3) (Tom), which was introduced in [7] and which takes into account long-range interaction. Closed circles represent the results of calculations based of the Faddeev equations with various nucleon–nucleon potentials (see references in [6]): (*1*) results obtained with the separable Yamaguchi potential, (*2*) results obtained on the basis of the quark-bag method, (*3*, *4*) results obtained with the rectangular-well potential, (*5*) results obtained with the Malfliet–Tjon potential, and (*6*, *7*) results obtained with soft-core Reid potential. Experimental data on C_T^2 were borrowed from (closed rectangle *A*) [18], (closed square *B*) [19], (closed square *C*) [8], and (cross) [20]. The error presented in [20] ($C_T^2 = 2.78 \pm 1.09$) corresponds to the scatter of the experimental data in Fig. 2.

in the case of the potential (3), the results for B_ν and E_0 can be refined by including the third parameter $R\mu$ in our fitting procedure.

It should be emphasized that, in effective-range theory, the G_T^2 value at $C_4 = 0$ differs dramatically from those at $C_4 \neq 0$. We note that, by formally extending equation (10) to the region where $a\chi_1 < 1$, we obtain the value of $G_T^2 = 0.17$. Adhikari [5], who derived formulas of the *N*/*D* method that correspond to expression (9) with $C_4 = 0$, also drew attention to the G_T^2 value strongly underestimated in relation to the results of the calculations from [2], which were based on the Faddeev equations. The conclusion of Adhikari was radical and incorrect: he asserted that the above implies the need for taking into account the three-body cut of the *S* matrix. In our opinion, the reason behind the aforementioned discrepancy is that, in [5], the number of terms retained in the expansion of the amplitude (or the function $k\cot\delta$) in power series in k was insufficient. In Table 2, a dash is placed instead of the G_ν^2 value for the case being discussed, because it is meaningless to calculate this quantity when the virtual-pole position found for the potential (3) differs very strongly from that which is known very well (the calculations for the region $\rho < 1.8$ have been performed, but their results are not presented here). Moreover, the fact that the position of the virtual pole nearly coincides with the position of the dynamical singularity generates purely technical problems in calculating the residue of the scattering amplitude at the virtual pole.

In solving the aforementioned integral equations, we used here the dimensionless variable $x = q/\mu$ (q is the wave number) and made the change of variable $x = e^t$. The latter guaranteed a correct cutoff at the lower and upper limits of the integrals involved and enabled us to evaluate these integrals by the method of rectangles. It is well known that, for functions taking the same values at the upper and lower limits of integration, other quadrature formulas provide no advantages over this method (in our case, the integrand tends to zero both at the lower and at the upper limit). The accuracy of the calculations was monitored by varying the width and the number of steps (up to the value of $N = 600$; usually, a reasonable accuracy was achieved at $N = 150$) and by verifying the behavior of the integrand over the entire interval of integration. For the bound state, the energy eigenvalues were determined by iterating the integral Schrödinger equation in momentum space. As a matter of fact, we solved the set of algebraic equations that emerged as the result of applying the method of rectangles to evaluating the integrals. The energies of virtual levels were found by solving the following set of equations (see [12, 14]) for the vertex function $g_l^{(n)}(q)$ (below, the superscript n, which represents the principal quantum number or the number of the level, and the orbital angular momentum l are suppressed for the sake of brevity):

Table 3. Parameters of the potentials (1)–(3) and position ($-E_1$) of the closest dynamical singularity

Potential \ Parameter	V_0, MeV	μ, fm^{-1}	$-E_1$, MeV
Hulthén [9, 10]	22.11	0.506	1.01
Yukawa [10]	17.43	0.360	2.01
Tomio *et al*. [7]	40.50	0.1507	0.352

Note: The one-nucleon-exchange diagram leads to a singularity at $E_1 = -0.738$ MeV

$$g(q) = (2\pi^2)^{-1}\int_0^\infty [V(q,k)g(k)/(z-k^2/2m_{12})]k^2dk + (i/\pi)m_{12}g(p)V(q,p), \quad (11)$$

$$g(p) = [1-(i/\pi)m_{12}pV(p,p)]^{-1}(2\pi^2)^{-1} \times \int_0^\infty [V(p,k)g(k)/(z-k^2/2m_{12})]k^2dk. \quad (12)$$

Here, $p = \sqrt{2m_{12}z}$ is the arithmetic value of the square root, z is the eigenvalue of energy E (it is real and negative for a virtual level), and $V(q, k)$ is the Fourier transform of the potential. The method that we used in dealing with this set of equations consisted in the following. First, we solved the nonhomogeneous equation (11), imposing the normalization condition $g(p) = 1$. After that, the eigenvalue of z was determined from equation (12). In order to find G_ν^2 [$G_\nu = g(i\chi_\nu)$], we used the generalized normalization condition [12, 14]

$$\int_0^\infty (q^2-p^2)^{-2}g^2(q)q^2dq + (i\pi/2p)g^2(p) \times \{1 + 2p[dg(k)/dk]|_{k=p}/g(p)\} = 2\pi^2(\hbar/2m_{12}c)^2. \quad (13)$$

In the case of a bound state, the second term is present neither on the right-hand side of (11) nor on the left-hand side of (13). The scattering length and the position of the zero of the amplitude $f(k)$ were determined by solving the conventional nonhomogeneous integral Lippmann–Schwinger equation (see, for example, [10]).

4. CONCLUSION

To summarize, we can state that the effects of long-range interaction are insignificant in the case of the doublet neutron–deuteron system and that the potential (3), which has a correct asymptotic behavior, does not show substantial advantages over short-range potentials usually used in nuclear physics, such as the

Yukawa and Hulthén potentials. It seems that the Hulthén potential provides quite a reasonable description of the low-energy properties of the doublet neutron–deuteron system; this potential is especially convenient because an analytic solution to the problem in the *s* wave is known for this case. It would be desirable to improve the precision to which the nuclear vertex constant G_T^2 is determined experimentally. This would make it possible to make a more motivated choice between various potentials of the two-body model that are used in describing the doublet neutron–deuteron system at low energies.

ACKNOWLEDGMENTS

This work was performed within the program "Universities of Russia: Basic Research" (project no. 5368, 1998).

APPENDIX

By definition, the Fourier transform of the potential $V(r)$ for an orbital angular momentum l is

$$V_l(q,k) = 4\pi\int_0^\infty j_l(qr)j_l(kr)V(r)r^2dr, \qquad (A.1)$$

where $j_l(x)$ is a spherical Bessel function [$j_0(x) = x^{-1}\sin x$]. For the potential (3), we can easily obtain (see [21, item 3.948]) the expression ($l = 0$)

$$\begin{aligned} V(q,k) &= -(\pi/2)[V_0R^2/\mu]v(x,y);\\ x &= q/\mu, \quad y = k/\mu, \quad \alpha = 2\mu R;\\ v(x,y) &= (xy)^{-1}[F_1(x,y,\alpha) + F_2(x,y,\alpha) - F_2(x,y,0)];\\ F_1(x,y,\alpha) &= w_1(x,y,0) - w_1(x,y,\alpha),\\ F_2(x,y,\alpha) &= w_2(x,y,\alpha) + w_2(x,y,-\alpha),\\ w_1(x,y,\alpha) &= [v_1(x,y,\alpha) + v_1(x,y,-\alpha)]/2,\\ w_2(x,y,\alpha) &= v_2(x,-y,\alpha) - v_2(x,y,\alpha), \end{aligned} \qquad (A.2)$$

where

$$\begin{aligned} v_1(x,y,\alpha) &= \ln\left|[1+(x-y+\alpha)^2]/[1+(x+y+\alpha)^2]\right|,\\ v_2(x,y,\alpha) &= (x+y+\alpha)\arctan(x+y+\alpha). \end{aligned} \qquad (A.3)$$

The absolute value is taken in the argument of the logarithm, since we need its real branch. It is worthwhile to present expressions for $v(x, ib)$ for the case where one of the arguments is purely imaginary. This function is required for calculating the asymptotic normalization factor; it is also needed for calculations on an unphysical sheet of energy in the case of a bound or a resonance state [see equations (11)–(13)]. By using expressions (A.2) and (A.3) and going over to the limit $y \longrightarrow ib$, we arrive at

$$\begin{aligned} v(x,ib) &= (2/xb)\{-v_3(x)\\ &+ 0.5[v_3(x+\alpha) + v_3(x-\alpha)]\\ &- \mathrm{Im}[v_4(x+\alpha) + v_4(x-\alpha) - 2v_4(x)]\}, \end{aligned} \qquad (A.4)$$

where

$$\begin{aligned} v_3(x) &= \arctan[2bx/(1+x^2-b^2)]\\ &+ \pi\theta(b^2-1-x^2), \end{aligned} \qquad (A.5)$$

$$v_4(x) = (x+ib)\arctan(x+ib). \qquad (A.6)$$

The second term on the right-hand side of (A.5)—it contains a Heaviside step function [$\theta(t) = 1$ for $t > 0$ and $\theta(t) = 0$ for $t < 0$]—has been introduced in order to ensure the continuity of the function $v_3(x)$ when the principal value of the arctangent (first term) is used. From (A.2) and (A.3), we can easily find that, at $x = y = ib$, the potential is given by

$$\begin{aligned} v(ib,ib) &= (-b^{-2})\{-\ln\left|1-4b^2\right| - \ln(1+\alpha^2)\\ &+ \ln\left|1+(\alpha+2ib)^2\right| + 2b\ln\left|(1-2b)/(1+2b)\right|\\ &+ 2\alpha\arctan\alpha - 2\mathrm{Re}[(\alpha+2ib)\arctan(\alpha+2ib)]\}. \end{aligned} \qquad (A.7)$$

In order to calculate the scattering length, we must have at our disposal an expression for the potential where one or both arguments are close to zero. These expressions can be obtained easily with the aid of equations (A.2) and (A.3), which can be used down to very small values of the arguments. In the limit $x \longrightarrow 0$ or $y \longrightarrow 0$, it is necessary evaluate an indefinite form of the 0/0 type. In particular, we have

$$v(0,0) = 4\alpha^2/(1+\alpha^2). \qquad (A.8)$$

REFERENCES

1. A. C. Phillips, Nucl. Phys. **A107**, 209 (1968).
2. B. A. Girard and M. G. Fuda, Phys. Rev. C **19**, 579 (1979).
3. G. Barton and A. C. Phillips, Nucl. Phys. **A132**, 97 (1969).
4. J. S. Whiting and M. G. Fuda, Phys. Rev. C **14**, 18 (1976).
5. S. K. Adhikari, Phys. Rev. C **30**, 31 (1984).
6. N. M. Petrov, Yad. Fiz. **48**, 50 (1988) [Sov. J. Nucl. Phys. **48**, 31 (1988)].
7. L. Tomio, A. Delfino, and S. K. Adhikari, Phys. Rev. C **35**, 441 (1987).
8. I. V. Simenog, A. I. Sitnichenko, and D. V. Shapoval, Yad. Fiz. **45**, 60 (1987) [Sov. J. Nucl. Phys. **45**, 37 (1987)].
9. Yu. V. Orlov, N. M. Petrov, and G. N. Teneva, Yad. Fiz. **55**, 38 (1992) [Sov. J. Nucl. Phys. **55**, 23 (1992)].

10. Yu. V. Orlov, Yu. P. Orevkov, and L. I. Nikitina, Izv. Akad. Nauk, Ser. Fiz. **60** (11), 152 (1996).
11. R. G. Newton, *Scattering Theory of Waves and Particles* (Transl. of 1st. Engl. ed., Mir, Moscow, 1969; Springer-Verlag, New York, 1982).
12. Yu. V. Orlov and V. V. Turovtsev, Zh. Éksp. Teor. Fiz. **86**, 1600 (1984) [Sov. Phys. JETP **59**, 934 (1984)].
13. V. Efimov, Nucl. Phys. **A362**, 45 (1981).
14. K. Möller and Yu. V. Orlov, Fiz. Élem. Chastits At. Yadra **20**, 1341 (1989) [Sov. J. Part. Nucl. **20**, 569 (1989)].
15. Yu. V. Orlov, Phys. Lett. B **163**, 25 (1985).
16. Yu. V. Orlov and L. I. Nikitina, Yad. Fiz. **61**, 833 (1998) [Phys. At. Nucl. **61**, 750 (1998)].
17. S. K. Adhikari and J. R. A. Torreaõ, Phys. Lett. B **132**, 257 (1983).
18. L. D. Blokhintsev, I. Borbely, and É. I. Dolinskiĭ, Fiz. Élem. Chastits At. Yadra **8**, 1189 (1977) [Sov. J. Part. Nucl. **8**, 485 (1977)].
19. L. D. Blokhintsev, A. M. Mukhamedzhanov, and A. N. Safronov, Fiz. Élem. Chastits At. Yadra **15**, 1296 (1984) [Sov. J. Part. Nucl. **15**, 580 (1984)].
20. A. I. Sattarov, M. K. Ubajdullaeva, and R. Yarmukhamedov, Yad. Fiz. **60**, 1221 (1997) [Phys. At. Nucl. **60**, 1096 (1997)].
21. I. S. Gradshteyn and I. M. Ryzhik, *Table of Integrals, Series, and Products* (5th ed., Nauka, Moscow, 1971; Transl. of 4th Russ. ed., Academic, New York, 1980).

Translated by A. Isaakyan

Physics of Atomic Nuclei, Vol. 63, No. 3, 2000, pp. 336–342. Translated from Yadernaya Fizika, Vol. 63, No. 3, 2000, pp. 402–408.

NUCLEI
Theory

${}^{6}_{\Lambda\Lambda}$He and ${}^{9}_{\Lambda}$Be Systems in the Three-Body Cluster Model Treated on the Basis of Differential Faddeev Equations

I. N. Filikhin* and S. L. Yakovlev

St. Petersburg State University, Universitetskaya nab. 7/9, St. Petersburg, 199164 Russia

Received April 29, 1998; in final form, February 19, 1999

Abstract—The ${}^{6}_{\Lambda\Lambda}$He and ${}^{9}_{\Lambda}$Be hypernuclei are treated as the $S = 0$, $T = 0$ (for the former) and $S = 1/2$, $T = 0$ (for the latter) bound states of the three-cluster systems $\Lambda\Lambda\alpha$ and $\Lambda\alpha\alpha$, respectively. The cluster-reduction method is used to solve the *s*-wave differential Faddeev equations for these systems. On the basis of the MT I–III model, the $\Lambda\Lambda$ interaction potential is specified in the form $V_{\Lambda\Lambda} = \frac{2}{3} V_{NN}$. Phenomenological potentials are used to describe $\Lambda\alpha$ and $\alpha\alpha$ interactions. The binding energies of the ${}^{6}_{\Lambda\Lambda}$He and ${}^{9}_{\Lambda}$Be hypernuclei and the parameters of low-energy Λ-hyperon and α-particle scattering on a ${}^{5}_{\Lambda}$He hypernucleus are calculated. It is shown that the proposed $\Lambda\Lambda$ interaction potential makes it possible to reproduce faithfully the binding energy of the ${}^{6}_{\Lambda\Lambda}$He hypernucleus and that scattering in the $\Lambda{}^{5}_{\Lambda}$He system is similar to neutron scattering on a deuteron.

1. INTRODUCTION

In recent years, much attention in nuclear physics has been given to three-particle systems consisting of two identical particles and a third particle different from the first two. Among the factors that provoke this interest, we would like to indicate the development of baryon models and attempts at obtaining a consistent description of the properties of baryons at different energies [1–4]. A feature peculiar to these realms is that experimental data on direct interactions of baryons at low energies are scanty. A calculation of the binding energies of mixed systems like $\Lambda(\Sigma)NN$ (hypertriton nucleus ${}^{3}_{\Lambda}$H) and $\Lambda\Lambda\alpha$ (${}^{6}_{\Lambda\Lambda}$He hypernucleus) may serve as a test for various model approaches. Theoretically, such systems are usually studied on the basis of Faddeev equations either in the integral or in the differential form [5]. In the case of three identical particles (for example, three nucleons), the set of Faddeev equations takes the simplest form. Broad experience gained in applying Faddeev equations to such systems was summarized in [6]. Since the number of coupled equations in Faddeev sets grows as soon as we embark on studies of nonidentical particles, relevant computational problems become more involved. The situation is further aggravated upon taking into account higher partial waves. Here, direct computational methods lead to algebraic problems of enormous dimension. These can hardly be solved without invoking supercomputers. Only in some recent studies were therefore systems like those mentioned above (ΛNN [1] and $nn\alpha$ [4]) analyzed on the basis of Faddeev equations with realistic interaction potentials.

In the present article, the three-particle systems $\Lambda\Lambda\alpha$ and $\alpha\alpha\Lambda$ are investigated on the basis of Faddeev equations in configuration space. In the *s*-wave approximation, which is used here, the equations for the coordinate parts of the Faddeev components take the same form for the two systems in question. The *s*-wave Faddeev equations are numerically solved by the cluster-reduction method. Previously, we used this method in [7–9] to study three- and four-nucleon systems and in [10] to study the Λnp system. In our calculations, the $\Lambda\alpha$ and $\alpha\alpha$ intercluster interactions are simulated by the phenomenological potentials from [11, 12]. The $\Lambda\Lambda$ interaction is specified on the basis of the *s*-wave model employing the MT I–III potential [13] modified as in [14], the singlet component of the $\Lambda\Lambda$ interaction potential being taken in the form $V_{\Lambda\Lambda} = \frac{2}{3} V_{NN}$. The hypothesis that the singlet $\Lambda\Lambda$ interaction is similar to the singlet nucleon–nucleon interaction has already been put forth in some previous studies. In our model, the proportionality factor between the $\Lambda\Lambda$ and *NN* potentials is chosen in such a way as to reproduce the experimental value of the ${}^{6}_{\Lambda\Lambda}$He binding energy.

The ensuing exposition is organized as follows. In Section 2, we describe the model and present the *s*-wave differential Faddeev equations for the $\Lambda\Lambda\alpha$ and $\alpha\alpha\Lambda$ systems. There, we also give a brief account of the

* e-mail: filikhin@cph10.phys.spbu.ru

method for solving these equations on the basis of cluster reduction. Section 3 contains the results of the calculations for the hyperon binding energy in the $^{6}_{\Lambda\Lambda}$He and $^{9}_{\Lambda}$Be nuclei. The rate at which the results of the calculations performed within the proposed approach converge is investigated in the same section. The wave functions of the hypernuclei are used to assess the degree of clustering in the systems being considered. Further, we investigate two-cluster scattering at energies below the three-body threshold—namely, $\Lambda\,^{5}_{\Lambda}$He scattering and $\alpha\,^{5}_{\Lambda}$He scattering. We calculate the relevant phase shifts and the parameters of the effective-range expansion. It is shown that the behavior of the function $p\cot(\delta)$ for $\Lambda\,^{5}_{\Lambda}$He scattering is similar to that in the case of *nd* scattering.

2. BASIC EQUATIONS AND METHOD FOR SOLVING THEM

We consider a three-particle system involving two identical charged particles. In order to describe this system, we make use of modified differential Faddeev equations, where the Coulomb potential of interaction between the charged particles is included in the unperturbed Hamiltonian. Specifically, we have

$$\begin{aligned}(H_0^u + V^{\mathrm{Coul}} + V_{12} - E)U &= -V_{12}(W + \epsilon P_{12}W),\\ (H_0^w + V^{\mathrm{Coul}} + V_{13} - E)W &= -V_{13}(U + \epsilon P_{12}W),\end{aligned} \tag{1}$$

where $\epsilon = -1$ (+1) for fermions (bosons), while the components U and W of the total wave function Ψ correspond to, respectively, the {12}3 and the {13}2 partition of the {123} system. The relevant kinetic-energy operators are denoted by H_0^u and H_0^w. By convention, the particles of the (12) pair are taken to be identical. We denote by P_{ik} the operator of particle permutation in the $\{ik\}$ pair, by V_{ik} the short-range pair interaction potentials, and by V^{Coul} the Coulomb potential of the {12} pair. The total wave function of the system can be represented as

$$\Psi = U + (I + \epsilon P_{12})W.$$

For the $\Lambda\Lambda\alpha$ and $\alpha\alpha\Lambda$ systems in the $S = 0$, $T = 0$ and $S = 1/2$, $T = 0$ spin–isospin states, respectively, the *s*-wave differential Faddeev equations form, in either case, a set of two coupled equations for the coordinate components of the spinors U and W; that is,

$$\begin{aligned}&[h_0^u + v_u^{\mathrm{Coul}}(x) + v_{12}(x) - E]U(x,y)\\ &\quad = -v_{12}(x)\int_{-1}^{1} du\,\frac{xy}{x'y'}W(x',y'),\\ &[h_0^u + v_w^{\mathrm{Coul}}(x,y) + v_{13}(x) - E]W(x,y)\end{aligned} \tag{2}$$

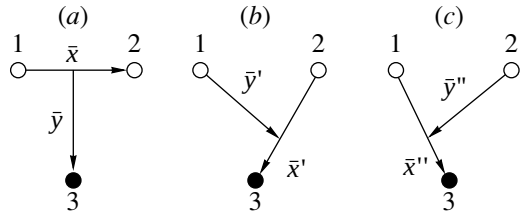

Fig. 1. Jacobi coordinates in the three-particle system.

$$= -\frac{1}{2}v_{13}(x)\left[\int_{-1}^{1} du\,\frac{xy}{x_1y_1}U(x_1,y_1) + \int_{-1}^{1} du\,\frac{xy}{x_2y_2}U(x_2,y_2)\right],$$

where

$$h_0^u = -\frac{1}{4}\frac{2m + m_3}{m_3}\partial_y^2 - \partial_x^2,$$

$$h_0^w = -\frac{1}{2}\frac{2m + m_3}{m + m_3}\partial_y^2 - \frac{m + m_3}{2m_3}\partial_x^2$$

are the kinetic-energy operators that are expressed in terms of the Jacobi coordinates and which correspond to, respectively, the {12}3 and the {13}2 partition of the {123} system. The Jacobi coordinates of the system being considered are schematically illustrated in Fig. 1.

For the $\Lambda\Lambda\alpha$ system, we have

$$m_3 = m_\Lambda, \quad m = m_\alpha, \quad v_{12}(x) = V_{\Lambda\Lambda}(x)\frac{m_\Lambda}{\hbar^2},$$

$$v_{13}(x) = V_{\Lambda\alpha}(x)\frac{m_\Lambda}{\hbar^2},$$

where m_Λ is the Λ-hyperon mass, m_α is the alpha-particle mass, $V_{\Lambda\Lambda}(x)$ is the singlet part of the $\Lambda\Lambda$ interaction potential, and $V_{\Lambda\alpha}(x)$ is the potential of interaction between the Λ hyperon and the alpha particle. There are no Coulomb potentials in the $\Lambda\Lambda\alpha$ system:

$$v_u^{\mathrm{Coul}}(x) = v_w^{\mathrm{Coul}}(x,y) = 0.$$

For the $\alpha\alpha\Lambda$ system, we have

$$m_3 = m_\alpha, \quad m = m_\Lambda, \quad v_{12}(x) = V_{\alpha\alpha}(x)\frac{m_\alpha}{\hbar^2},$$

$$v_{13}(x) = V_{\Lambda\alpha}(x)\frac{m_\alpha}{\hbar^2},$$

where $V_{\alpha\alpha}(x)$ is the $\alpha\alpha$-interaction potential. The Coulomb potentials $v_u^{\mathrm{Coul}}(x)$ and $v_w^{\mathrm{Coul}}(x,y)$ are given by

$$v_u^{\mathrm{Coul}}(x) = n/x, \quad v_w^{\mathrm{Coul}}(x,y) = n/r_>,$$

where $r_> = \max\{bx, y\}$ (the parameter b will be defined below). The transformations of the coordinates in the

integral terms of equations (2) are given by

$$x' = \left(\frac{1}{4}x^2 + y^2 + xyu\right)^{1/2},$$

$$y' = ((ax)^2 + (by)^2 - 2abxyu)^{1/2},$$

$$x_1 = ((bx)^2 + y^2 - 2bxyu)^{1/2},$$

$$y_1 = \left((ax)^2 + \frac{1}{4}y^2 + axyu\right)^{1/2},$$

$$x_2 = ((cx)^2 + y^2 + 2cxyu)^{1/2},$$

$$y_2 = (4(abx)^2 + (cy)^2 - 4abcxyu)^{1/2},$$

where $a = \frac{1}{2}\frac{2m + m_3}{m + m_3}$, $b = \frac{m_3}{m + m_3}$, and $c = \frac{m}{m + m_3}$ ($a = 0.615$, $b = 0.77$, and $c = 0.23$ for the $\Lambda\Lambda\alpha$ system and $a = 0.885$, $b = 0.23$, and $c = 0.77$ for the $\alpha\alpha\Lambda$ system).

The potential of interaction between two alpha particles is given by [11]

$$V_{\alpha\alpha}(r) = V_1 \exp\left(-\frac{r^2}{\beta_1^2}\right) + V_2 \exp\left(-\frac{r^2}{\beta_2^2}\right), \qquad (3)$$

where $V_1 = 125.0$ MeV, $\beta_1 = 1.53$ fm, $V_2 = -30.18$, and $\beta_1 = 2.85$ fm. The interaction between the Λ hyperon and the alpha particle has the form [12]

$$V_{\Lambda\alpha}(r) = V_0 \exp\left(-\frac{r^2}{\beta_0^2}\right),$$

where $V_0 = -47.97$ MeV and $\beta_0 = 1.566$ fm. Equations (2) must be supplemented with the asymptotic boundary conditions for the components U and W. States that belong to the discrete spectra of the systems being considered correspond to boundary-value problems with zero boundary conditions at $x = 0$, at $y = 0$, and at the boundary of the asymptotic region in the coordinates x and y. Further, we consider boundary-value problems for two-cluster scattering at energies of relative motion that do not exceed the threshold for the breakup of a bound cluster ($^5_\Lambda$He nucleus). The asymptotic boundary conditions for the scattering processes in the $\Lambda\,^5_\Lambda$He and $\alpha\,^5_\Lambda$He systems must be considered separately. In the case of hyperon scattering on a $^5_\Lambda$He nucleus, the asymptotic forms of the components $U(x, y)$ and $W(x, y)$ for $y \longrightarrow \infty$ are

$$U(x, y) \sim 0,$$

$$W(x, y) \sim \psi_0(x)[\chi_p(y) + a(p)\cos(py)],$$

where $\psi_0(x)$ is the wave function of the ground state of the $^5_\Lambda$He nucleus, while $\chi_p(y)$ is a function that describes the free relative motion of the Λ hyperon and a $^5_\Lambda$He nucleus in the initial state. For the latter function, we have $\chi_p(y) = \sin(py)/p$, where $ap^2 = E - \varepsilon_0$, ε_0 being the binding energy of the $^5_\Lambda$He nucleus. The phase shift δ is related to the amplitude $a(p)$ by the equation $a(p) = \tan(\delta)/p$.

In the problem of alpha-particle scattering on a $^5_\Lambda$He nucleus, the asymptotic expressions for the components $U(x, y)$ and $W(x, y)$ in the limit $y \longrightarrow \infty$ are given by

$$U(x, y) \sim 0,$$

$$W(x, y) \sim \psi_0(x)[\chi_p(y) - a(p)G_0(\eta, py)],$$

where $\chi_p(y) = F_0(\eta, py)$ and $\eta = \frac{1}{2}\frac{n}{ap}$ with $n = \frac{4m_\alpha e^2}{\hbar^2}$, $F_0(\eta, \rho)$ and $G_0(\eta, \rho)$ being, respectively, the regular and the singular Coulomb function. Here, we have considered that there is the Coulomb interaction between the alpha particles. The amplitude $a(p)$ is related to the phase shift by the equation $a(p) = -\tan(\delta)/pC_0^2$, where $C_0^2 = 2\pi\eta/[\exp(2\pi\eta) - 1]$.

The set of differential Faddeev equations (2) is solved here by the cluster-reduction method, which was proposed in [7–9] and which was used to calculate bound states and low-energy scattering states in three- and four-nucleon systems. Within this method, solutions to the original equations are expanded in the bases of eigenfunctions of the Hamiltonians of two-particle subsystems. Taking relevant projections, we arrive at a set of equations describing the relative motion of the clusters involved.

A solution to equations (2) can be represented as

$$U(x, y) = \sum_{l=0}^{N} \phi_l(x) f_l(y),$$
$$W(x, y) = \sum_{l=0}^{N} \psi_l(x) g_l(y), \qquad (4)$$

where the functions $\phi_l(x)$ and $\psi_l(x)$ are the solutions to the boundary-value problems for the Hamiltonians of the subsystems with zero boundary conditions; that is, these functions satisfy the equations

$$(-\partial_x^2 + v(x))\phi_l(x) = \varepsilon_l^u \phi_l(x), \qquad (5)$$

$$\left(-\frac{m + m_3}{2m_3}\partial_x^2 + v(x)\right)\psi_l(x) = \varepsilon_l^w \psi_l(x) \qquad (6)$$

and the boundary conditions $\phi_l(0) = \phi_l(R_x) = 0$ and $\psi_l(0) = \psi_l(R_x) = 0$. They form orthonormalized sets of functions. By taking relevant projections, we reduce the set of two-dimensional integro-differential equations (2) to a one-dimensional set of equations for the func-

tions $f_l(y)$ and $g_l(y)$ describing the relative motion of the clusters. These functions must satisfy asymptotic boundary conditions that are obtained by taking similar projections [7, 8].

3. RESULTS OF THE CALCULATION

In this section, we present the results that we obtained by solving numerically the effective equations for the functions $f_l(y)$ and $g_l(y)$ describing the relative motion of the clusters. We have considered boundary-value problems corresponding to the bound states in the $\Lambda\Lambda\alpha$ and $\alpha\alpha\Lambda$ systems and the problems of low-energy Λ-hyperon and alpha-particle scattering on a $_{\Lambda}^{5}$He hypernucleus. The equations for the functions $f_l(y)$ and $g_l(y)$ were solved by means of a finite-difference approximation on an equidistant mesh having N_y nodes. In these calculations, the number N_y of nodes, the radii R_x and R_y that specified the region where the asymptotic expressions for the sought solutions were used, and the number N of terms retained in expansions (4) were parameters to be chosen. For the bound state in the $\Lambda\Lambda\alpha$ system, a relative error at a level of 0.5% was achieved at $N_y = 100$, $R_x = 17$ fm, $R_y = 17$ fm, and $N = 10$. For the $\alpha\alpha\Lambda$ system, the same precision was obtained at $N_y = 100$, $R_x = 35$ fm, $R_y = 35$ fm, and $N = 30$. That the greater values of R_x, R_y, and N were required in the latter case was due to a slow decrease of the Coulomb interaction between the alpha particles. Figure 2 shows the binding energies of the $\alpha\alpha\Lambda$ and $\Lambda\Lambda\alpha$ systems as functions of N. The results of various calculations for the energy of hyperon separation from the $_{\Lambda\Lambda}^{6}$He hypernucleus are displayed in Table 1 along with the experimental value of this energy [in the three-body model, the separation energy $E(_{\Lambda\Lambda}^{6}\mathrm{He})$ coincides in magnitude with the binding energy of the $_{\Lambda\Lambda}^{6}$He hypernucleus, these two energies being opposite in sign]. Our result is seen to comply well with the experimental value. We note that the calculations performed in [15] by the method of hyperspherical harmonics in momentum space relied on model potentials and that the calculations performed in [2] employed the Faddeev equations with realistic potentials. For the root-mean-square radius of the $_{\Lambda\Lambda}^{6}$He hypernucleus, we obtained the value of $\langle r^2\rangle^{1/2} = 1.43$ fm. The calculation was based on the relation

$$\langle r^2\rangle^{1/2} = \left(\langle r_\alpha^2\rangle + \frac{m_\alpha}{m_\alpha + 2m_\Lambda}\langle R^2\rangle\right)^{1/2},$$

where $\langle r_\alpha^2\rangle^{1/2}$ is the root-mean-square radius of the alpha particle in the three-body system $\Lambda\Lambda\alpha$, while $\langle R^2\rangle^{1/2}$ is the root-mean-square radius of the alpha particle as the ^{4}He nucleus ($\langle R^2\rangle^{1/2} = 1.61$ fm). The results

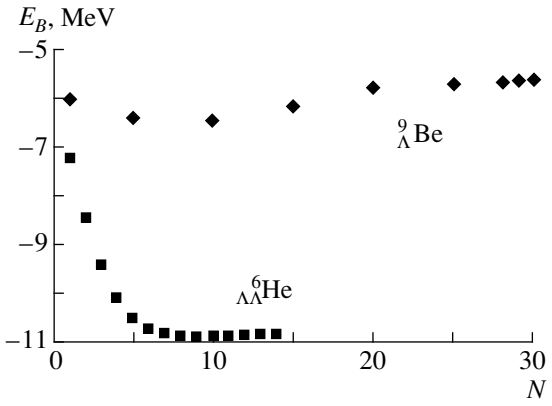

Fig. 2. Binding energies of the $_{\Lambda\Lambda}^{6}$He and $_{\Lambda}^{9}$Be hypernuclei as functions of the number N of terms retained in expansion (4).

of various calculations for the energy of Λ-hyperon separation from the $_{\Lambda}^{9}$Be hypernucleus are presented in Table 2. This separation energy, $E(_{\Lambda}^{9}\mathrm{Be})$, was calculated by the formula $E(_{\Lambda}^{9}\mathrm{Be}) = -E_B(_{\Lambda}^{9}\mathrm{Be}) + E_B(^8\mathrm{Be})$, where $E_B(_{\Lambda}^{9}\mathrm{Be})$ is the binding energy of the $_{\Lambda}^{9}$Be hypernucleus, while $E_B(^8\mathrm{Be})$ is the binding energy of the ^{8}Be nucleus [$E_B(^8\mathrm{Be}) = 0.09$ MeV]. The separation-energy value that resulted from our calculation is less than the experimental value by about 1.0 MeV, but the former complies well with the results obtained in [16, 17] on the basis of the three-body model. The calculation from [16] was performed by the method of hyperspherical functions in the momentum representation, model potentials being used there. The calculation from [17] was based on the differential Faddeev equations. In that study, the $\Lambda\alpha$ interaction was simulated by the potential from [18], while the $\alpha\alpha$ interaction potential was taken in the form (3).

The expansions in (4) are convenient for studying the degree of clustering in the three-particle systems $\Lambda\Lambda\alpha$ and $\alpha\alpha\Lambda$. Indeed, the probability P_{23} of finding the {123} system of particles in the 1{23} form, where the {23} pair appears to be a bound subsystem, can be

Table 1. Energy of Λ-hyperon separation from the $_{\Lambda\Lambda}^{6}$He hypernucleus and its root-mean-square radius

References	$E(_{\Lambda\Lambda}^{6}\mathrm{He})$, MeV	$\langle r^2\rangle^{1/2}$, fm
Our study	10.88	1.43
[15]	10.69	1.66
[2]	11.6	–
Experimental study reported in [2]	10.9 ± 0.6	–

Table 2. Energy of Λ-hyperon separation from the ${}^{9}_{\Lambda}$Be hypernucleus

References	$E({}^{9}_{\Lambda}\mathrm{Be})$, MeV
Our study	5.67
[16]	5.78
[17]	5.76
Experimental study reported in [16]	6.71 ± 0.4

Table 3. Probability of clustering in the ${}^{6}_{\Lambda\Lambda}$He and ${}^{9}_{\Lambda}$Be hypernuclei

System	$P_{\{23\}}$	P
Λ(Λα)	0.39	0.79
α(αΛ)	0.42	0.85

estimated as

$$P_{\{23\}} = \frac{\langle \psi_1 g_1 | \Psi \rangle}{\langle \Psi | \Psi \rangle},$$

where Ψ is the total wave function and where integration is performed with respect to the coordinates in Fig. 1*b*. The probability $P_{\{13\}}$ is defined is a similar way (integration is performed with respect to the coordinates in Fig. 1*c*). Since the particles in the {12} pair are taken to be identical, the total probability P that the system is clustered in the form *particle 1 (or 2) + a bound pair formed by particle 2 (or 1) and particle 3* is determined as the sum $P = P_{\{23\}} + P_{\{13\}}$. In addition, we have $P_{\{13\}} = P_{\{23\}}$. For the systems being considered, we are to deal with clustering of the form *Λ hyperon (alpha particle) +* ${}^{5}_{\Lambda}$*He*. The results of our calculations for $P_{\{23\}}$ and P are displayed in Table 3. For the sake of comparison, we indicate that, for the *nnp*(^{3}H) system, the quantity analogous to $P_{\{23\}}$ is estimated at 0.448 [1]. The method of cluster reduction makes it possible to go over easily to scattering problems. Here, we have studied low-energy scattering in the $\alpha\,{}^{5}_{\Lambda}$He and $\Lambda\,{}^{5}_{\Lambda}$He systems within the *s*-wave approximation. By virtue of the asymptotic boundary conditions, expansions of the form (4) are valid at energies of the relative motion of the clusters below the threshold for the disintegration of the bound subsystem (${}^{5}_{\Lambda}$He). By numerically solving the equations for the functions $f_l(y)$ and $g_l(y)$, we evaluated the relevant phase shifts at energies of relative motion (in the c.m. frame) that do not exceed the binding energy of the ${}^{5}_{\Lambda}$He hypernucleus ($E < 3.12$ MeV).

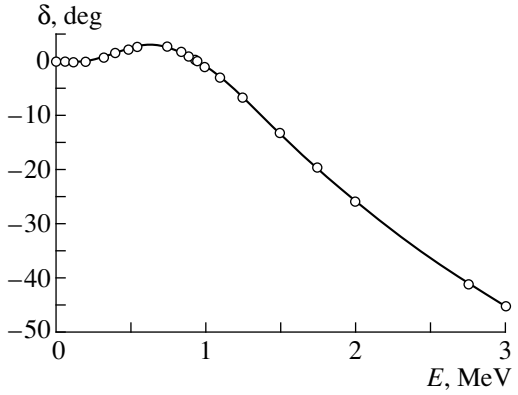

Fig. 3. Phase shift for alpha-particle scattering by a ${}^{5}_{\Lambda}$He hypernucleus: (points) values obtained on the basis of a numerical solution to equations (1) and (curve) phase shifts obtained by formula (7) with the aid of approximation (8) for the function $K_c(E)$.

An analysis of the energy dependence of the *s*-wave phase shift for $\alpha\,{}^{5}_{\Lambda}$He scattering shows that this phase shift behaves anomalously at energies of relative motion below 1 MeV. There, the phase shifts are small and positive. It is well known that, in the case of charged-particle scattering, the effective-range expansion holds for the function

$$K_{\mathrm{Coul}}(E) = C_0^2(\eta)\, p \cot(\delta(p)) + \frac{\eta}{a} h(\eta), \qquad (7)$$

where $h(\eta) = -\ln\eta + \mathrm{Re}\,\psi(1 + \eta i)$, $\psi(z)$ being a digamma function, while $p^2 = \frac{m_\alpha}{\hbar^2}\frac{E}{a}$. The function $K_{\mathrm{Coul}}(E)$ can be closely approximated by a modified effective-range expansion in the form

$$K_{\mathrm{Coul}}(E) = \frac{-1/A + r p^2 + q p^4}{1 + p^2/p_0^2}. \qquad (8)$$

For the coefficients A, r, q, and p_0^2, we obtained the numerical values of $A = -10^3$ fm, $r = 0.59$ fm, $q = -4.55$ fm^3, and $p_0^2 = -0.94$ MeV. Here, the parameter A has the meaning of the scattering length for alpha-particle interaction with the ${}^{5}_{\Lambda}$He nucleus. The phase shift for $\alpha\,{}^{5}_{\Lambda}$He scattering is displayed in Fig. 3, where the circles represent its calculated values, while the solid curve corresponds to the use of approximation (8) in the calculation based on expression (7). In accordance with (8), the scattering length for $\alpha\,{}^{5}_{\Lambda}$He interaction is large in magnitude and negative. This circumstance can be attributed to the presence of a virtual level in the Λαα system near the threshold for scattering [19]. On the basis of expansion (8), we find the effective range r_0

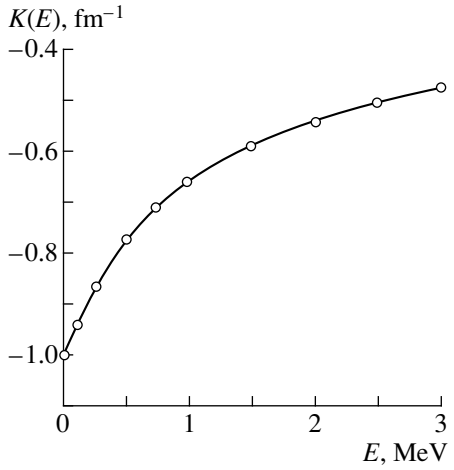

Fig. 4. Function $K(E) = p\cot(\delta)$ for Λ-hyperon scattering by a $_{\Lambda}^{5}$He hypernucleus: (curve) approximation (8) for the function $K(E)$ and (points) results obtained for $p\cot(\delta)$ from a numerical solution to equation (1).

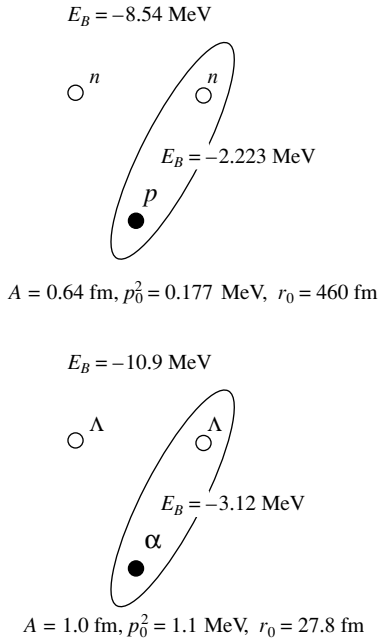

Fig. 5. *nnp* and ΛΛα systems. The scheme depicted in this figure is explained in the main body of the text. For the *nnp* system, the parameter values were obtained in [8].

for $\alpha\,_{\Lambda}^{5}$He interaction by using the formula

$$r_0 = 2\frac{dK_{\mathrm{Coul}}}{dp^2} \quad \text{for} \quad p^2 \longrightarrow 0. \tag{9}$$

The result is $r_0 = 1.2$ fm.

Further, we investigated the applicability of the effective-range approximation to describing the scattering process in the $\Lambda\,_{\Lambda}^{5}$He system. For this purpose, we evaluated the function $K(E) = p\cot(\delta)$ at low energies. This function is closely approximated by a modified effective-range expansion of the form (8) with the parameter values of $A = 1.002$ fm, $r = -5.5$ fm, $q = 0$ fm^3, and $p_0^2 = 1.1$ MeV $\left(p^2 = \dfrac{m_{\Lambda}}{\hbar^2}\dfrac{E}{a}\right)$. In Fig. 4, the approximation of $K(E)$ by (8) is represented by the solid curve, while the calculated values of $p\cot(\delta)$ are shown by circles. Here, we can clearly see the analogy with the thoroughly studied low-energy behavior of the function $K(E)$ in doublet neutron–deuteron scattering [8, 20]. The expansion given by (8) is usually associated with the presence of a virtual level in the *nd* system. The energy of the virtual level (pole of the S matrix) is determined [19] by solving the equation

$$K(E) - ip = 0 \text{ at } p = -i\kappa, \quad \kappa > 0. \tag{10}$$

If a representation of the form (8) is used in (10) for the function $K(E)$, the energy of the virtual level is 2.38 MeV. For specific values of the parameters in the effective-range expansion (8) for Λ-hyperon scattering on a $_{\Lambda}^{5}$He hypernucleus, the scattering length is 1.0 fm, while the effective range calculated for this interaction by equation (9) is 28.8 fm. Further, we note that the behavior of the function $p\cot(\delta)$ for the $\Lambda\,_{\Lambda}^{5}$He system is similar to the behavior of this function for *nd* scattering (the binding energies of the entire systems and the binding energies of the corresponding subsystems are also similar); therefore, we can construct a direct analogy between the ΛΛα and *nnp* systems. This analogy is illustrated by the scheme in Fig. 5, where we present the parameters of the *nnp* system that were obtained in [8]. Obviously, this similarity is due to the compactness of the alpha particle.

ACKNOWLEDGMENTS

This work was supported in part by the Contest Center of the Ministry for Higher Education of the Russian Federation (grant no. 97-0-14.3-23).

REFERENCES

1. K. Miyagawa, H. Kamada, W. Glöckle, *et al.*, Phys. Rev. C **51**, 2905 (1995).
2. S. B. Carr, I. R. Afnan, and B. F. Gibson, Contributed Papers of 15th International IUPAP Conference on Few Body Problems in Physics, Groningen, 1997; nucl-th/9712054.
3. T. Ueda, K. Tominaga, M. Yamaguchi, *et. al.*, Contributed Papers of 15th International IUPAP Conference on Few Body Problems in Physics, Groningen, 1997.
4. A. Gobis, D. V. Fedorov, and A. S. Jensen, J. Phys. G **23**, 401 (1997).
5. S. P. Merkuriev and S. L. Yakovlev, Dokl. Akad. Nauk SSSR **262**, 591 (1982); Teor. Mat. Fiz. **56**, 60 (1983);

S. P. Merkuriev and L. D. Faddeev, *Quantum Scattering Theory for Few-Particle Systems* (Nauka, Moscow, 1985).
6. A. A. Kvitsinskiĭ, Yu. A. Kuperin, *et al.*, Fiz. Élem. Chastits At. Yadra **17**, 267 (1986) [Sov. J. Part. Nucl. **17**, 113 (1986)].
7. S. L. Yakovlev and I. N. Filikhin, Vestn. S.-Peterb. Univ., Ser. 4, No. 3, 24 (1992).
8. S. L. Yakovlev and I. N. Filikhin, Yad. Fiz. **56** (12), 98 (1993) [Phys. At. Nucl. **56**, 1676 (1993)].
9. S. L. Yakovlev and I. N. Filikhin, Yad. Fiz. **58**, 817 (1995) [Phys. At. Nucl. **58**, 754 (1995)]; **60**, 1962 (1997) [**60**, 1794 (1997)].
10. I. N. Filikhin and S. L. Yakovlev, Yad. Fiz. **63**, 278 (2000) [Phys. At. Nucl. **63**, 223 (2000)].
11. S. Ali and A. R. Bodmer, Nucl. Phys. **80**, 99 (1966).
12. B. Buck, H. Friedrich, and C. Wheatley, Nucl. Phys. **A275**, 246 (1977).
13. R. A. Malfliet and J. A. Tjon, Ann. Phys. (New York) **61**, 425 (1970).
14. N. W. Schellingerhout, J. J. Schut, and L. P. Kok, Phys. Rev. C **46**, 1192 (1992).
15. R. I. Dzhibuti, T. Ya. Mikhelashvili, and K. V. Shitikova, Yad. Fiz. **45**, 670 (1987) [Sov. J. Nucl. Phys. **45**, 419 (1987)].
16. R. I. Dzhibuti and Sh. M. Tsiklauri, Yad. Fiz. **36**, 1387 (1982) [Sov. J. Nucl. Phys. **36**, 805 (1982)].
17. Y. Sunami and H. Narumi, Prog. Theor. Phys. **66**, 355 (1981).
18. R. C. Herndon and Y. C. Tang, Phys. Rev. **153**, 1091 (1967).
19. L. D. Landau and E. M. Lifshitz, *Quantum Mechanics: Non-Relativistic Theory* (4th ed., Nauka, Moscow, 1989; Transl. of 3rd Russ. ed., Pergamon, Oxford, 1977).
20. C. R. Chen, G. L. Payne, J. L. Friar, *et al.*, Phys. Rev. C **39**, 1261 (1989).

Translated by A. Isaakyan

Physics of Atomic Nuclei, Vol. 63, No. 3, 2000, pp. 343–352. Translated from Yadernaya Fizika, Vol. 63, No. 3, 2000, pp. 409–418.

NUCLEI
Theory

^{16}O Nucleus in the 4α Cluster Model

I. N. Filikhin* and S. L. Yakovlev

St. Petersburg State University, Universitetskaya nab. 7/9, St. Petersburg, 199164 Russia

Received February 16, 1999; in final form, May 28, 1999

Abstract—The ^{16}O nucleus is treated as a bound state of the four-alpha-particle system showing 3α + α clustering. The pair interaction of the alpha particles involved is simulated by a phenomenological potential. Additional three-particle potentials are introduced in order that the entire system and its three-particle subsystems be bound. The parameters of these potentials are determined by fitting the experimental values of the binding energies and the root-mean-square radii of the ^{12}C and ^{16}O nuclei. The calculations are performed on the basis of the *s*-wave differential equations for the Faddeev and Yakubovsky components. The ground and the first excited state of the ^{16}O nucleus are investigated. The most probable spatial arrangement of the alpha-particle clusters in the system is determined. The charge form factors are calculated for the ^{12}C and ^{16}O nuclei. The results of our model calculations comply well with experimental data. © *2000 MAIK "Nauka/Interperiodica".*

1. INTRODUCTION

It is commonly accepted at present that correlations of the alpha-particle-cluster type exist in the light nuclei ^{12}C and ^{16}O. However, a complete theoretical description of the properties of these nuclei that takes into account clustering of the above type has yet to be obtained [1–5]. Meanwhile, the idea of using a three-body potential in treating the ^{12}C nucleus as a system of three alpha particles made it possible to reproduce [4] the experimental values of the parameters of the 0_2^+ resonance state in the ^{12}C nucleus. This was done by constructing solutions to the differential Faddeev equations at positive energies. From the studies reported in [6], which implemented the microscopic variational approach, it can be seen that, by taking into account three-body forces, the experimentally observed behavior of the ^{16}O charge form factor is reproducible within this approach as well; in particular, a second diffraction minimum, which did not arise in models relying on pair nucleon–nucleon interaction potential, could be described upon the inclusion of three-body interactions.

In the present study, we address the question of whether it is possible to choose the parameters of the three-body potential in such a way that the properties of the ^{16}O nucleus could be described on the basis of the 4α cluster model. In our analysis, we employ the Faddeev equations for the 3α subsystem and the four-particle Yakubovsky equations in the differential form [7]. The *s*-wave Faddeev and Yakubovsky equations are solved numerically by the cluster-reduction method [8]. The short-range interaction between two alpha particles is simulated by the phenomenological potential from [9].

The ensuing exposition is organized as follows. In Section 2, we describe the model underlying our investigations and formulate basic equations. In Section 3, we give an account of the method used to solve the equations from Section 2 and present our numerical results. A brief summary of these results is given in the Conclusion.

2. DESCRIPTION OF THE MODEL

2.1. Potentials Used

For the pair potential of interaction between the alpha particles involved, we take the potential from [9] (version "a"), which makes it possible to reproduce faithfully the phase shifts for low-energy αα scattering. The *s*-wave projection of this potential has the form

$$V(r) = V_1 \exp(-r^2/\beta_1^2) + V_2 \exp(-r^2/\beta_2^2), \qquad (1)$$

where V_1 = 125.0 MeV, β_1 = 1.53 fm, V_2 = –30.18 MeV, and β_2 = 2.85 fm. Since a pair potential cannot bind the systems of three and four alpha particles because of the strong Coulomb repulsion, a three-body potential $V_3(\rho)$ is additionally introduced in the system of three alpha particles in order that the system be bound. Following [4], we specify this potential in the form

$$V_3(\rho) = V_3 \exp[-(\rho/\beta)^2], \qquad (2)$$

where $\rho^2 = \sum_{i=1}^{i=3} \mathbf{r}_i^2$, $\mathbf{r}_i$ being the radius vector of the *i*th particle (with respect to the center of mass of the system).

For the four-particle system, we introduce two-types of three-body potentials, $V_3^{\mathrm{I}}(\rho)$ and $V_3^{\mathrm{II}}(\rho)$. Of these, the first binds a three-particle cluster in the system, while the second specifies the interaction between

* e-mail: filikhin@cph10.phys.spbu.ru

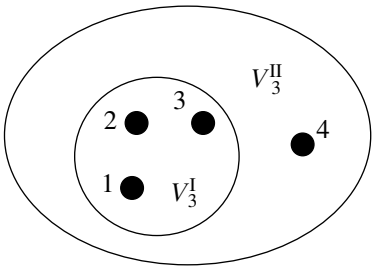

Fig. 1. Three-body potentials in the system of four alpha particles: $[V_3^I(\rho)]$ potential binding a three-particle cluster within the system and $[V_3^{II}(\rho)]$ potential simulating the interaction between the fourth particle and the pairs of the particles forming the three-particle cluster.

the fourth particle and each particle pair bound in the three-particle cluster. These potentials are chosen in the form (2), their parameters being denoted by V_3^I and β^I for the former and by V_3^{II} and β^{II} for the latter. In this way, the $3\alpha + \alpha$ cluster structure is explicitly singled out in the four-particle system. The three-body potentials in the system of four alpha particles are illustrated in Fig. 1. That the ^{16}O nucleus can be described within this scheme of clustering is confirmed by the calculations of Dubovichenko [10], who used the $^{12}C + \alpha$ two-cluster model to study the electromagnetic disintegration of the ^{16}O nucleus. By fitting the parameters of the intercluster potentials involving forbidden states, that author was able to reproduce the structure of the ^{16}O nucleus near the breakup threshold.

2.2. Three-Particle System

We consider the system of three charged particles having the same mass m_α. The particles are assumed to have neither internal structure nor spin. In order to describe this system, we make use of modified Faddeev equations in the differential form, with the Coulomb potential of particle interaction being included in the unperturbed Hamiltonian [7]. Since the particles of the system being considered are identical, the relevant Faddeev equations reduce to an equation for the U component of the total wave function. Specifically, we have

$$(H_0 + V^{\mathrm{Coul}} + V_3 + V - E)U = -V(P^+ + P^-)U,$$

where H_0 is the kinetic-energy operator, $P^\pm$ are the operators of cyclic permutations of the particles involved, V is the short-range potential of pair interaction between the particles, and V^{Coul} is the Coulomb potential of the system. The three-particle-interaction potential V_3 enters into the equations through the unperturbed Hamiltonian. The total wave function of the system can be represented as

$$\Psi = (I + P^+ + P^-)U.$$

The system can be described in terms of the Jacobi coordinates $\mathbf{x}$ and $\mathbf{y}$, which are related to the particle radius vectors $\mathbf{r}_k$ ($k = 1, 2, 3$) by the equations

$$\mathbf{x} = \mathbf{r}_2 - \mathbf{r}_1, \quad \mathbf{y} = (\mathbf{r}_1 + \mathbf{r}_2)/2 - \mathbf{r}_3.$$

The 3α subsystem is considered here in the s-wave approximation—that is, the total orbital angular momentum of the whole system and those for all of its subsystems are zero. The s-wave Faddeev equation represents an equation for the coordinate part $\mathcal{U}(x, y)$ of the Faddeev component U and has the form

$$(h_0 + v^{\mathrm{Coul}}(x) + v_{\alpha\alpha}(x) + v_3(\rho) - \varepsilon)\mathcal{U}(x, y) = -v_{\alpha\alpha}(x)\int_{-1}^{1} dv\,\frac{xy}{x_1 y_1}\mathcal{U}(x_1, y_1), \tag{3}$$

where $h_0 = -\frac{3}{4}\partial_y^2 - \partial_x^2$ is the kinetic-energy operator, $x = |\mathbf{x}|$, $y = |\mathbf{y}|$, and

$$x_1 = \left(\frac{x^2}{4} + y^2 + xyv\right)^{1/2},$$

$$y_1 = \left(\left(\frac{3}{4}x\right)^2 + \frac{y^2}{4} - \frac{3}{4}xyv\right)^{1/2}.$$

The s-wave projection $v^{\mathrm{Coul}}(x)$ of the Coulomb potential has the form

$$v^{\mathrm{Coul}}(x, y) = n/x + 2\frac{n}{r_>},$$

where $r_> = \max\{x/2, y\}$ and $n = 4m_\alpha e^2/\hbar^2$ ($n = 0.556$ fm^{-1}). The short-range potential of interaction between the alpha particles, $v_{\alpha\alpha}(x)$, is given by (1). The three-body interaction potential $v_3(\rho)$ has the form

$$v_3(\rho) = V_3^I \exp(-(\rho/\beta^I)^2)\frac{m_\alpha}{\hbar^2}, \tag{4}$$

where $\rho^2 = \frac{2}{3}y^2 + \frac{1}{2}x^2$, $V_3^I = -24.32$ MeV, $\beta^I = 3.795$ fm, and $\hbar^2/m_\alpha = 10.44$ MeV fm^2. The choice of values for the parameters V_3^I and β^I is explained in Section 3.

2.3. Four-Particle System

The system of four alpha particles represents a system of four identical bosons. For such systems, the differential Yakubovsky equations reduce to two equations for the components U^1 and U^2 of the wave function [7]. These equations can be written as

$$(H_0 + V + V^{\mathrm{Coul}} + V_3 - E)U^1 + V(P_4^+ + P_4^-)U^1 = -V((P_1^+ + P^+)U^1 + (P_1^+ + P_4^+)U^2),$$

$$(H_0 + V + V^{\mathrm{Coul}} + V_3 - E)U^2 + V(P^+P^+)U^2 = -V(P^+ + P_1^+)P^+U^1,$$

where V is the pair potential of particle interaction, V^{Coul} is the Coulomb interaction potential, V_3 is the three-body potential, H_0 is the kinetic-energy operator, $P^{\pm}$ are the operators of cyclic permutations of four particles, and $P_i^{\pm}$ are the operators of cyclic permutations of three particles (here, the subscript indicates the number of a particle that is not involved in a given permutation). The components U^1 and U^2 correspond to, respectively, 3 + 1 and 2 + 2 partitions of the system. The wave function of the system can be represented as

$$\Psi = (I + P^+ + P^+P^+ + P^-)(I + P_4^+ - P_4^-)U^1 + (I + P_1^+ + P_1^-)(I + P^+P^+)U^2.$$

In order to describe the system in configuration space, we make use of the Jacobi coordinates $\mathbf{X} = \{\mathbf{x}_i, \mathbf{y}_i, \mathbf{z}_i\}$, $i = 1, 2$, where the subscript i labels coordinates associated with the different partitions of the system, taking the values of $i = 1$ and 2 for the 3 + 1 and 2 + 2 partitions. The Jacobi coordinates are expressed in terms of the particle radius vectors $\mathbf{r}_k$ ($k = 1, 2, 3, 4$) as

$$\mathbf{x}_1 = \mathbf{r}_2 - \mathbf{r}_1, \quad \mathbf{y}_1 = (\mathbf{r}_1 + \mathbf{r}_2)/2 - \mathbf{r}_3,$$
$$\mathbf{z}_1 = (\mathbf{r}_1 + \mathbf{r}_2 + \mathbf{r}_3)/3 - \mathbf{r}_4, \quad \mathbf{x}_2 = \mathbf{r}_2 - \mathbf{r}_1,$$
$$\mathbf{y}_2 = \mathbf{r}_4 - \mathbf{r}_3, \quad \mathbf{z}_2 = (\mathbf{r}_1 + \mathbf{r}_2)/2 - (\mathbf{r}_3 + \mathbf{r}_4)/2.$$

We consider the system of four alpha particles in the s-wave approximation; that is, we assume that the orbital angular momentum of the whole system and the orbital angular momenta of all its subsystems are equal to zero. The s-wave differential equations for the coordinate parts $\mathcal{U}^1$ and $\mathcal{U}^2$ of the Yakubovsky components can be written as

$$(h_0^1 + v_{\alpha\alpha}(x) + v_1^{\mathrm{Coul}}(x, y, z) + v_3(\rho) - \varepsilon)\mathcal{U}^1(x, y, z) + v_{\alpha\alpha}(x)\int_{-1}^{1} dv\, \frac{xy}{x_1y_1}\mathcal{U}^1(x_1, y_1, z_1)$$
$$= -\frac{1}{2}v_{\alpha\alpha}(x)\int_{-1}^{1} du \int_{-1}^{1} dv \left(\frac{xyz}{x_2y_2z_2}\mathcal{U}^1(x_2, y_2, z_2) + \frac{xyz}{x_3y_3z_3}\mathcal{U}^2(x_3, y_3, z_3)\right), \quad (5)$$

$$(h_0^2 + v_{\alpha\alpha}(x) + v_2^{\mathrm{Coul}}(x, y, z) + v_3(\rho) - \varepsilon)\mathcal{U}^2(x, y, z) + v_{\alpha\alpha}(x)\mathcal{U}^2(y, x, z) = -v_{\alpha\alpha}(x)\int_{-1}^{1} dv\, \frac{xyz}{x_4y_4z_4}\mathcal{U}^1(x_4, y_4, z_4),$$

where $x = |\mathbf{x}|$, $y = |\mathbf{y}|$, $z = |\mathbf{z}|$, and

$$h_0^1 = -\left(\partial_x^2 + \frac{3}{4}\partial_y^2 + \frac{2}{3}\partial_z^2\right),$$
$$h_0^2 = -\left(\partial_x^2 + \partial_y^2 + \frac{1}{2}\partial_z^2\right).$$

The transformations of the coordinates appearing in (5) are given by

$$x_2 = x_1, \quad x_3 = x_1, \quad x_4 = y,$$
$$y_2 = \left(\left(\frac{y_1}{3}\right)^2 + z^2 + \frac{2}{3}y_1zu\right)^{1/2},$$
$$z_2 = \left(\left(\frac{8}{9}y_1\right)^2 + \frac{z^2}{9} - \frac{16}{27}y_1zu\right)^{1/2},$$
$$y_3 = \left(\left(\frac{2}{3}y_1\right)^2 + z^2 + \frac{4}{3}y_1zu\right)^{1/2},$$
$$z_3 = \left(\left(\frac{2}{3}y_1\right)^2 + \frac{z^2}{4} - \frac{2}{3}y_1zu\right)^{1/2},$$
$$y_4 = \left(\left(\frac{x}{2}\right)^2 + z^2 - xzu\right)^{1/2},$$
$$z_4 = \frac{2}{3}(x^2 + z^2 + 2xzu)^{1/2}.$$

The s-wave projection of the Coulomb interaction in the equation for the component of the 3 + 1 type has the form

$$v_1^{\mathrm{Coul}} = \frac{n}{x} + 2v_2^{(1)} + 2v_4^{(1)} + v_6^{(1)},$$
$$v_2^{(1)} = n\begin{cases} 2/x & \text{for} \quad x > 2y \\ 1/y & \text{for} \quad x < 2y, \end{cases}$$
$$v_4^{(1)} = n\begin{cases} \dfrac{1}{z} & \text{for} \quad z > \dfrac{x}{2} + \dfrac{y}{3} \\ \dfrac{1}{xy}\left(\dfrac{2}{3}\dfrac{1}{z}\left(z^2 - \left(\dfrac{3}{4}x - \dfrac{1}{2}y\right)^2\right) + 2\left(\dfrac{3}{4}x + \dfrac{1}{2}y - z\right)\right) & \text{for} \quad \left|\dfrac{1}{2}x - \dfrac{1}{3}y\right| < z < \dfrac{1}{2}x + \dfrac{1}{3}y \\ \dfrac{2}{x} & \text{for} \quad x > \dfrac{2}{3}y, \quad z < \left|\dfrac{1}{2}x - \dfrac{1}{3}y\right| \\ \dfrac{3}{y} & \text{for} \quad x < \dfrac{2}{3}y, \quad z < \left|\dfrac{1}{2}x - \dfrac{1}{3}y\right|, \end{cases}$$

$$v_6^{(1)} = n\begin{cases} \dfrac{1}{z} & \text{for} \quad x > \dfrac{2}{3}y \\ \dfrac{3}{2}\dfrac{1}{y} & \text{for} \quad x < \dfrac{2}{3}y. \end{cases}$$

The *s*-wave projection of the Coulomb interaction in the equation for the component of the 2 + 2 type is given by

$$v_2^{\text{Coul}} = \frac{n}{x} + \frac{n}{y} + 4v_2^{(2)},$$

where

$$v_2^{(2)} = n\begin{cases} \dfrac{1}{z} & \text{for} \quad z > \dfrac{x+y}{2} \\ \dfrac{1}{xy}\left(-\dfrac{1}{z}\left(\left(\dfrac{x-y}{2}\right)^2 + x + y - z\right)\right) & \\ & \text{for} \quad \left|\dfrac{x-y}{2}\right| < z < \dfrac{x+y}{2} \\ \dfrac{2}{x} & \text{for} \quad x > y, \quad z < \left|\dfrac{x-y}{2}\right| \\ \dfrac{2}{y} & \text{for} \quad x < y, \quad z < \left|\dfrac{x-y}{2}\right|. \end{cases}$$

As before, the short-range potential of interaction between the alpha particles, $v_{\alpha\alpha}(x)$, is taken in the form (1). The three-body interaction potential is simulated by the expression

$$v_3(\rho) = \frac{1}{4}\int_{-1}^{1}\int_{-1}^{1} dv\,du \sum_{a_2} v_{a_2}(\rho_{a_2}), \qquad (6)$$

where the subscript a_2 takes the values that correspond to the {123}{4}, {124}{3}, {134}{2}, and {234}{1} two-cluster partitions of the system. The potential for the {123}{4} partition is given above [see equation (4) in Subsection 2.2]. The remaining potentials $v_{a_2}(\rho_{a_2})$ are determined by expression (2) with the parameters V_3^{II} and β^{II}. In equation (6), the variables $\rho_{a_2}^2$ are expressed in terms of the Jacobi coordinates of the 3 + 1 type. Specifically, we have

$$\rho_{a_2}^2 = \frac{2}{3}\xi_{a_2}^2 + \frac{1}{2}\eta_{a_2}^2,$$

where

$$\xi_{\{124\}\{3\}}^2 = z^2 + \frac{1}{9}y^2 + \frac{2}{3}yzv, \quad \eta_{\{124\}\{3\}}^2 = x^2,$$

$$\xi_{\{134\}\{2\}}^2 = z^2 + \frac{1}{9}y_1^2 - \frac{2}{3}y_1zu, \quad \eta_{\{134\}\{2\}}^2 = x_1^2,$$

$$\xi_{\{234\}\{1\}}^2 = \xi_{\{134\}\{2\}}^2, \quad \eta_{\{234\}\{1\}}^2 = \eta_{\{134\}\{2\}}^2.$$

The expressions for the variables $\rho_{a_2}^2$ in terms of the Jacobi coordinates of the 2 + 2 type are given by

$$\rho_{a_2}^2 = \frac{2}{3}\xi_{a_2}^2 + \frac{1}{2}\eta_{a_2}^2,$$

$$\xi_{\{124\}\{3\}}^2 = z^2 - zyv + \frac{1}{4}y^2, \quad \eta_{\{124\}\{3\}}^2 = x^2,$$

$$\xi_{\{134\}\{2\}}^2 = z^2 - zxu + \frac{1}{4}x^2, \quad \eta_{\{134\}\{2\}}^2 = y^2,$$

$$\xi_{\{234\}\{1\}}^2 = \xi_{\{134\}\{2\}}^2, \quad \eta_{\{234\}\{1\}}^2 = \eta_{\{134\}\{2\}}^2.$$

For these potentials, the parameters V_3^{II} and β^{II} are chosen in such a way as to reproduce the experimental values of the binding energy of the ^{16}O nucleus and its root-mean-square radius.

2.4. Root-Mean-Square Radius of the 3α and 4α Systems

Since the above model is based on the three- and four-particle Faddeev and Yakubovsky equations, the internal structure of the alpha-particle clusters cannot be taken into account explicitly in this model. It is obvious that, in considering the geometric properties of the ^{12}O and ^{16}O nuclei, it is necessary to choose some way to take into account the geometric features of the alpha-particle clusters. From the literature, we know two models that allow for the internal structure of clusters in describing cluster systems. In the first model, all features of the clusters that are bound in some system are identical to their features in a free state. The second model admits modifications of some properties of the clusters when they are combined into a cluster system. Within the first model, Mikhelashvili *et al.* [1] treated the ^{12}C nucleus as a system of bound alpha particles, whereas Dubovichenko [10] studied the ^{12}C + α model of the ^{16}O nucleus. However, the experimental behavior of the charge form factor at high momentum transfers could be reproduced neither in [1] nor in [10]. A cluster-model modification that takes into account changes in the properties of bound clusters was considered by Kamada *et al.* [11], who studied the properties of the ^{6}Li nucleus treated as an α + *d* system. It turned out that the elastic form factor is faithfully reproduced for the lithium nucleus upon taking into account distortions of the deuteron cluster, its root-mean-square radius being a function of the intercluster coordinate [11]. Changes in the root-mean-square radii of the clusters were also taken into account by Bluge and Langanke [12], who studied α + *t* cluster systems, and by Dubovichenko and Dzhazairov-Kahramanov [13], who studied *n* + ^{3}He cluster systems. In [11–13], the cluster-deformation factor served as an adjustable parameter. Obviously, its choice cannot be substantiated rigorously within the cluster model.

Following [11–13], we assumed that the root-mean-square radius of the alpha-particle clusters in the ^{12}C and ^{16}O nuclei differs from that of a free alpha particle. We define the alpha-particle-deformation factor A as $A = (R_\alpha/R_c)^2$, where R_α is the charge radius of the alpha particle (R_α = 1.47 fm), while R_c is the root-mean-square radius of the alpha-particle cluster. By varying the deformation factor A, the experimentally observed behavior of the charge form factors for the ^{12}C and ^{16}O nuclei at high momentum transfers can be faithfully reproduced within the model outlined above. By using the deformation factor A, the root-mean-square radius of the systems of three and four alpha-particle clusters is calculated as

$$R = \sqrt{R_\alpha^2/A + r^2}, \quad (7)$$

where r stands for the root-mean-square radius of the system of structureless particles. We note once again that the parameters of the three-body potentials are determined by requiring that the potential models specified by equations (3) and (5) reproduce not only the relevant binding energies but also the experimental values of the root-mean-square radii of, respectively, the ^{12}C and ^{16}O nuclei. At a given value of the deformation factor A, equation (7) fixes the root-mean-square radius r. The adjustable parameters $V_3^{\mathrm{I}}(\rho)$ and $V_3^{\mathrm{II}}(\rho)$ of the potentials from (3) and (5) must lead to this value of r. Thus, the choice of values for the parameters of the three-body potentials depends on the cluster-deformation factor A.

Taking into account equation (7), we evaluated the form factor for either of the ^{12}C and ^{16}O nuclei as the product of the form factor $f(q)$ for the system of structureless particles and the form factor $F_\alpha(q/\sqrt{A})$ for the alpha-particle cluster; that is,

$$F(q) = F_\alpha(q/\sqrt{A})\, f(q). \quad (8)$$

According to [10], the charge form factor $F_\alpha(q)$ for the alpha-particle cluster can be parametrized as

$$F_\alpha(q) = (1 - (aq^2)^n)\exp(-bq^2),$$

where a = 0.09986 fm^2, b = 0.46376 fm^2, and n = 6. We use this parametrization here in calculating the form factors for the ^{12}C and ^{16}O nuclei by formula (8). For the deformation factor A, it was found here that, for the ^{12}C and ^{16}O nuclei, the values of, respectively, A = 3 and A = 4 must be substituted into equations (7) and (8).

3. METHOD FOR SOLVING EQUATIONS (3) AND (5) AND RESULTS OF THE CALCULATIONS

In the present study, the differential equations (3) and (5) for the Faddeev and Yakubovsky components were solved by the cluster-reduction method. Previously, this method was used in [8] to calculate the bound states of three- and four-nucleon systems and low-energy scattering in these systems. The cluster-reduction method alleviates considerably computational difficulties in solving relevant equations. Within this method, solutions to the original equations are sought in the form of expansions in the bases formed by the eigenfunctions of the Hamiltonians of two-particle (three-particle) subsystems. A transition to relevant projections leads to a set of equations for functions that describe the relative motion of the clusters. In this set, the dimensionality of each equation is less than the dimensionality of the original equations by unity. This reduction procedure was described in detail elsewhere [8]. The number N of basis functions that must be retained in the above expansions in order that the results of the calculations be convergent is the main parameter that determines the efficiency of the method. The point is that this parameter specifies the dimension of the algebraic problem that we are to solve in order to construct numerical solutions to the reduced equations. It is obvious that the smaller the value of N, the greater the gain in efficiency in relation to directly solving the original equations by the finite-difference method. This value is dependent on special features of the problem being solved. In particular, the value of N is reduced if the degree of clustering in the physical system under investigation is high.

Let us now proceed to describe the results obtained by numerically solving the differential equations (5) for the Yakubovsky components. The basis functions that are necessary for performing the above reduction were calculated as the eigenfunctions of the boundary-value problem for the Faddeev operator in (3) and the operator conjugate to it [8]. Equations (3) and (5) were solved within the rectangular domain Ω of configuration space. We denote by R_x, R_y, and R_z the parameters that specify the dimensions of this domain as

$$\Omega = \{x, y, z: x < R_x, y < R_y, z < R_z\}.$$

and set these parameters to $R_x = R_y = R_z$ = 25 fm. At the boundary of the domain Ω, we impose zero boundary conditions on solutions to equations (3) and (5).

Let us now address the problem of calculating the 3α system, whose bound state represents the ^{12}C nucleus. The three-body potential (4) makes it possible to reproduce the experimental value of the ^{12}C binding energy. The results of this calculation are displayed in Table 1 (here, the energy is reckoned from the threshold for the breakup of the system into separate alpha particles). For the sake of comparison, the corresponding values from [4] are indicated there for the parameters of the three-body potential and for the binding energy in the ground state of the 3α system. The distinctions between the potential parameters are explained by the use of the different models here and in [4], where the orbital angular momentum of the subsystems was taken into account up to that of the d wave. Table 1 also quotes the root-mean-square radius as calculated for the ^{12}C nucleus by formula (7) at A = 3. It can be seen

Table 1. Parameters of the three-body potential, binding energy of the ^{12}C nucleus, and its root-mean-square radius (the energy is reckoned from the threshold of the ^{12}C breakup into separate alpha particles)

References	V_3^{I}, MeV	β^{I}, fm	E_{B}, MeV	R, fm
[4]	–96.8	1.957	–6.81	2.36
Our study	–24.32	3.795	–7.27	2.47
Experimental data from [4]			–7.27	2.47

Table 2. Binding energies of the ^{12}C and ^{16}O nuclei versus the number N of basis functions taken into account in the cluster-reduction method

N	$E_{\mathrm{B}}(^{12}\mathrm{C})$, MeV	N	$E_{\mathrm{B}}(^{16}\mathrm{O})$, MeV	$E_{\mathrm{B}}^{*}(^{16}\mathrm{O})$, MeV
1	–5.32	1	–14.37	–8.48
5	–7.73	2	–14.39	–8.79
10	–8.10	3	–14.39	–8.79
15	–7.69	4	–14.40	–8.78
20	–7.39			
25	–7.28			
26	–7.27			
27	–7.27			

that this value complies well with the experimental result. The representation in (7) makes it possible to describe, on the basis of the 3α model, the experimentally observed behavior of the charge form factor for the ^{12}C nucleus at high momentum transfers (or the charge-distribution density in this nucleus at small distances). In Fig. 2, the form factor $f(q)$ for the 3α system is represented by the dashed curve. Closed circles in this figure show experimental data from [14]. The function $F(q)$ is depicted by the solid curve. The diffraction minimum of the function $F(q)$ is displaced with respect to its experimental position, but the behavior of this function at large values of q approximates closely the behavior of the ^{12}C form factor.

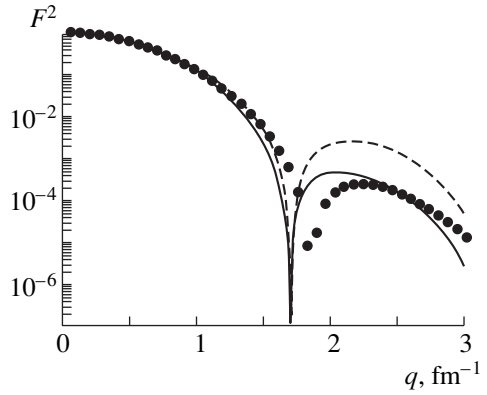

Fig. 2. Charge form factor for the ^{12}C nucleus: (closed circles) experimental values from [14], (dashed curve) results of the calculation for the system of three structureless alpha particles, and (solid curve) results obtained by taking into account the alpha-particle-cluster form factor by formula (8) at $A = 3$.

The results of the calculations for the binding energies of the 3α and 4α systems versus the number N of basis functions taken into account in the calculation are quoted in Table 2. The rate at which the results produced by the cluster-reduction method converge measures the degree of clustering in the subsystems. That the binding energy of the 4α system converges in N fast suggests that the degree of clustering of the 3α + α type is high, which is in accord with the results presented in [10]. The binding energies calculated for the ground and the first excited state of the 4α system are displayed in Table 3, along with relevant experimental data. The parameters of the three-body potentials used in the calculations are also quoted in this table.

The parameters of the potential $V_3^{\mathrm{I}}(\rho)$ in equation (4) were determined in calculating the ground state of the ^{12}C nucleus. In order to specify unambiguously the parameters V_3^{I} and β^{I}, we used the experimental values of the binding energy and the root-mean-square radius. We will illustrate the above by the graphs in Fig. 3, but we first redefine the parameters of the three-body potential $V_3^{\mathrm{I}}(\rho)$ via the relations $V_3^{\mathrm{I}} = V_0/\mu$ and $\nu = \beta^{\mathrm{I}}$, where $V_0 = 99$ MeV. Thus, the binding energy obtained in the calculation for the 3α system appears to be a function of two variables: $E = E(\mu, \nu)$. In Fig. 3*a*, we depicted a curve such that each point of it was obtained as a solution to the equation $E(\mu, \nu) = E^{\mathrm{expt}}$, where $E(\mu, \nu)$ is the binding energy calculated as described immediately above, while E^{expt} is the experimental value of the ^{12}C binding energy. As can be seen from this figure, the parameters μ and ν of the three-body potential cannot be fixed unambiguously on the basis of the ^{12}C binding energy alone. The calculated root-mean-square radius $r(\mu, \nu)$ of the 3α system is displayed in Fig. 3*b* as a function of ν at a μ value specified according to the data in Fig. 3*a*. By using the dependence in Fig. 3*b*, we can unambiguously determine the parameters μ and ν by requiring that the functional form of $r(\mu, \nu)$ correspond to (7)—that is, by taking it to be $r(\mu, \nu) = \sqrt{R^2 - R_\alpha^2/A}$, where we denote by R the experimental value of the root-mean-square radius of the ^{12}C nucleus ($R = 2.47$ fm). This illustrates the way in which the cluster-deformation factor A affects the choice of values for the parameters μ and ν. The situation here is such that, for various values of A, we can fit the binding energy and the root-mean-square radius of the 3α system to the corresponding experimental values for the ^{12}C nucleus, thereby fixing the parameters μ and ν for each given value of A. The ambiguity in choosing a

Table 3. Parameters of the three-body potentials, binding energies of the ^{16}O nucleus in the ground and in the first excited state (E_B and E_B^*, respectively; these energies are reckoned from the threshold of the ^{16}C breakup into separate alpha particles), and corresponding root-mean-square radii (R and R^*, respectively)

References	V_3^I, MeV	β^I, fm	V_3^{II}, MeV	β^{II}, fm	E_B, MeV	R, fm	E_B^*, MeV	R^*, fm
Our study	–24.32	3.795	–5.66	5.7	–14.4	2.7	–8.8	3.5
Experimental data from [10]					–14.4	2.71	–8.34	–

value for the deformation-factor A is removed by requiring that the form factor obtained for the relevant 3α system according to (8) reproduce the experimentally observed behavior of the ^{12}C form factor. For the 3α system, we deduced here the value of $A = 3$. The crosses in Fig. 3 show the values of μ and ν that correspond to $A = 3$. The parameters of the potential $V_3^{II}(\rho)$ were determined in a similar way from a fit to the binding energy in the ground state of the ^{16}O nucleus and to the experimental value of its root-mean-square radius taken to have the form (7). In that case, the cluster-deformation factor was chosen to be $A = 4$, which enabled us to reproduce the experimentally observed behavior of the ^{16}O form factor with the aid of representation (8) for the system of four alpha-particle clusters. The resulting s-wave potential model formulated in terms of equation (5) with the parameters specified as is described above has two bound states, the ground state and the first excited state. The ^{16}O nucleus also has two 0^+ levels in the discrete spectrum. It can be seen from Table 3 that, for the first excited state, the calculation yields an energy value close to the experimental one.

It is interesting to note that, geometrically, the 4α cluster model considered here is compatible with the simple $^{12}C + \alpha$ representation of the ground state of the ^{16}O nucleus. Let us demonstrate this explicitly. According to the two-cluster model, the root-mean-square distance d between the alpha-particle and ^{12}C clusters is calculated by the formula [15]

$$\frac{A_C}{A_O^2}d^2 = R^2 - \frac{A_C}{A_O}R_C^2 - \frac{1}{A_O}R_\alpha^2,$$

where $A_C = 3$ ($A_O = 4$) is the number of alpha particles in the ^{12}C (^{16}O) nucleus, while R, R_C, and R_α are the root-mean-square radii of, respectively, the ^{16}O nucleus, the ^{12}C nucleus, and the alpha particle. By using the experimental values of R, R_C, and R_α, we obtain $d = 3.4$ fm. Within our model, a natural choice for d is $(4/3)r$, where r is the root-mean-square radius of the alpha-particle cluster in the 4α system ($r = 2.58$ fm). It can easily be verified that $d \approx (4/3)r$.

Let us now discuss the results of the calculations for the ^{16}O form factor. These calculations were performed by formula (8) at $A = 4$. In Fig. 4, the dashed curve, points, and the solid curve represent, respectively, the form factor $f(q)$ for the 4α system, the experimental values from [16], and the function $F(q)$. The function $F(q)$ reproduces faithfully experimental data—in particular, the positions of the first and the second diffraction maximum, as well as the behavior of the charge form factor for the ^{16}O nucleus at high momentum transfers q. Figure 5 shows the charge-distribution density $\rho_{ch}(r)$ for systems formed by three and four alpha particles treated as structureless objects. The Fourier transforms of these functions appear to be the functions

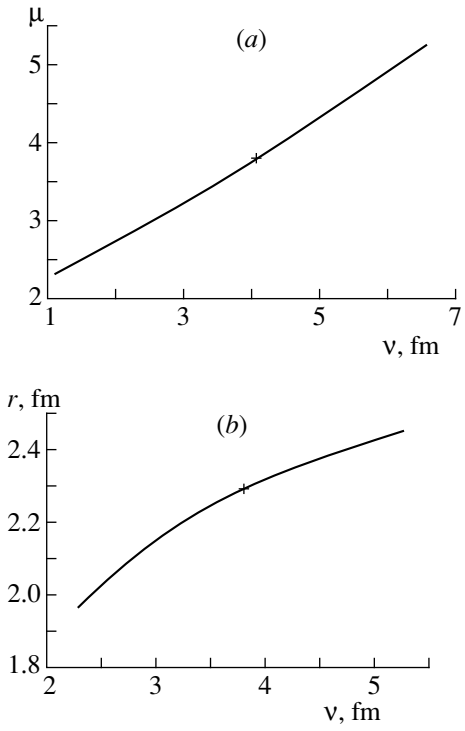

Fig. 3. Illustration of the procedure used here to fix the parameters in the three-body potential (4) for describing the properties of the ^{12}C nucleus: (*a*) relationship between the parameters μ ($V_3^I = V_0/\mu$) and ν ($\nu = \beta^I$) that was obtained from the condition requiring that the solution to equation (3) with the three-body potential specified by the parameters μ and ν lead to the experimental value of the ^{12}C binding energy and (*b*) root-mean-square radius r of the 3α system as a function of the parameter ν with allowance for the constraint imposed by the relationship between μ and ν in Fig. 3*a*. The crosses indicate the μ and ν values chosen in the present study.

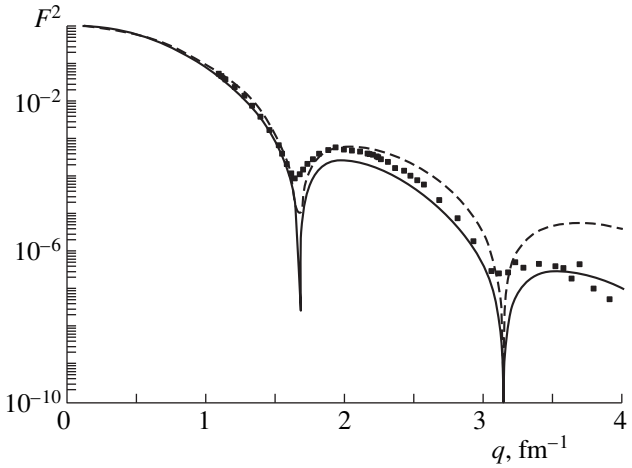

Fig. 4. Charge form factor for the ^{16}O nucleus: (closed squares) experimental values from [16], (dashed curve) results of the calculation for the system consisting of four structureless alpha particles, and (solid curve) results obtained by taking into account the alpha-cluster form factor by formula (8) at $A = 4$.

$f(q)$ in (8). In Fig. 5, the solid, the dotted, and the dashed curve correspond, respectively, to the ground state of the 4α system, to the first excited state of the 4α system, and to the ground state of the 3α system. The functions $\rho_{ch}(r)$ are normalized by the condition $\int_0^\infty \rho_{ch}(r)r^2dr = 1$. Let us compare the result obtained for the form factor of the 4α system at $A = 4$ with the corresponding result at $A = 1$, in which case the alpha particles in the nucleus are identical to a free alpha particle. The results of the calculations performed at $A = 1$ are presented in Fig. 6 (the notation there is identical to that in Fig. 4). In this case, the behavior of the resulting form factor differs drastically from the behavior of the ^{16}O form factor, especially at high momentum transfers. For the sake of completeness, we indicate that, in the calculation at $A = 1$, the fitted values of the parameters that appear in the potentials $V_3^{\mathrm{I}}(\rho)$ and $V_3^{\mathrm{II}}(\rho)$ are $V_3^{\mathrm{I}} = -82.5$ MeV, $\beta^{\mathrm{I}} = 2.35$ fm, $V_3^{\mathrm{II}} = -6.27$ MeV, and $\beta^{\mathrm{II}} = 5.95$ fm.

The wave functions obtained for the 4α and 3α systems by solving equations (5) and (3) were then used to study the spatial disposition of the alpha-particle clusters in the ^{16}O and ^{12}C nuclei. The coordinate component of the wave function of the 4α (3α) system depends on six (three) variables. These are the absolute values of the Jacobi coordinates—x, y, and z (x and y)—and the angles between the vectors **x**, **y**, and **z** (**x** and **y**)—$u = (\mathbf{x}, \mathbf{y})/xy$, $v = (\mathbf{x}, \mathbf{z})/xz$, and $w = (\mathbf{y}, \mathbf{z})/yz$. The most probable spatial configuration of the constituent alpha particles in the 4α or the 3α system is determined as that which is formed by the points at which the square of the total wave function of the system being considered peaks. Such configurations correspond to the values of $x = 2.9$ fm, $y = 2.5$ fm, and $u = 0$ for the 3α system; $x = 2.7$ fm, $y = 2.6$ fm, $z = 2.7$ fm, $u = 0$, $v = 0.5$, and $w = -0.4$ for the 4α system in the ground state; and $x = 2.5$ fm, $y = 2.6$ fm, $z = 2.7$ fm, $u = 0.5$, $v = 0.86$, and $w = 0$ for the 4α system in the first excited state. Figure 7 illustrates these configurations.

In the ^{12}C nucleus, the centers of mass of the alpha-particle clusters are situated at the vertices of an equilateral triangle with a side length of 2.9 fm (see Fig. 7*a*). This result is close to that from [4], where the corresponding side length is 2.98 fm; in contrast to

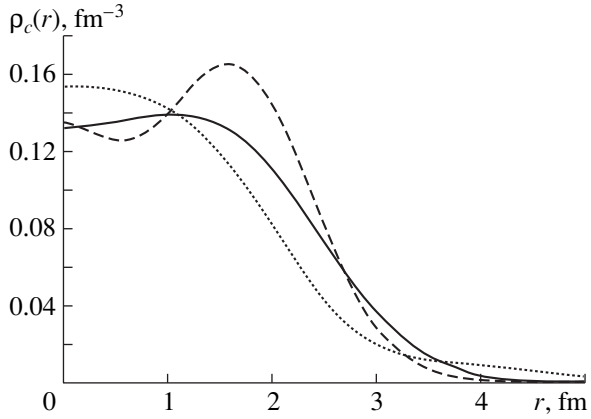

Fig. 5. Charge-distribution density in (solid curve) the ground state of the system of four alpha particles, (dotted curve) the first excited state of the system of four alpha particles, and (dashed curve) the ground state of the system of three alpha particles.

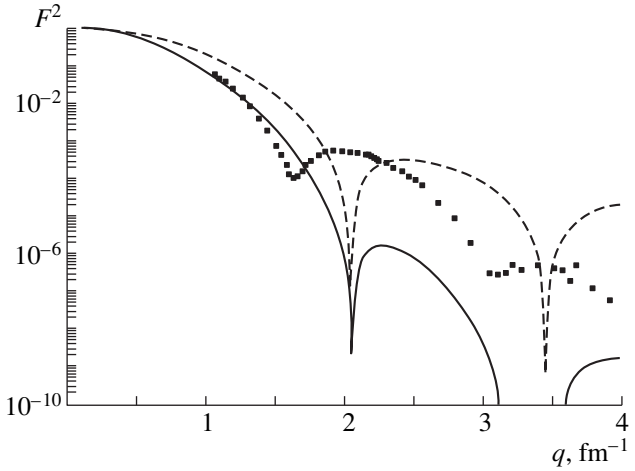

Fig. 6. Charge form factor for the ^{16}O nucleus: (closed squares) experimental values from [16], (dashed curve) results of the calculation for the system consisting of four structureless alpha particles, and (solid curve) results obtained by taking into account the alpha-cluster form factor by formula (8) at $A = 1$.

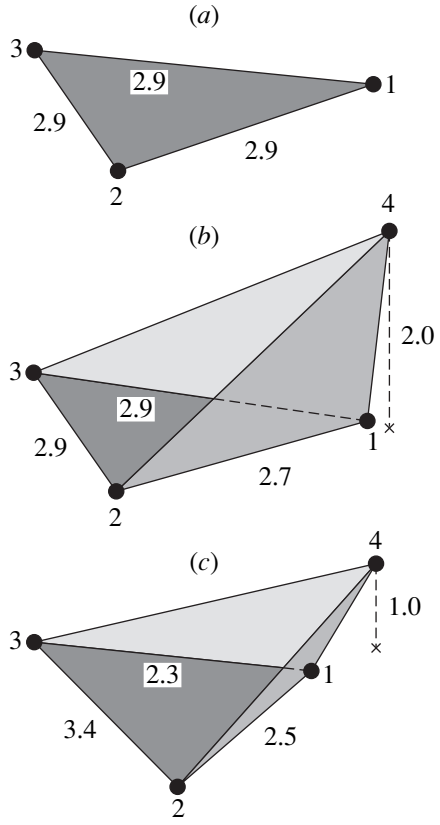

Fig. 7. Most probable disposition of the alpha-particle clusters in (*a*) the ground state of ^{12}C nucleus, (*b*) the ground state of ^{16}O nucleus, and (*c*) the first excited state (0^+) of the ^{16}O nucleus. The figures at the vertices indicate the numbers of the clusters, while the figure by the sides of the triangle in Fig. 7*a* and the figure by the edges of the tetrahedra in Figs. 7*b* and 7*c* indicate the distances (in fm) between the clusters.

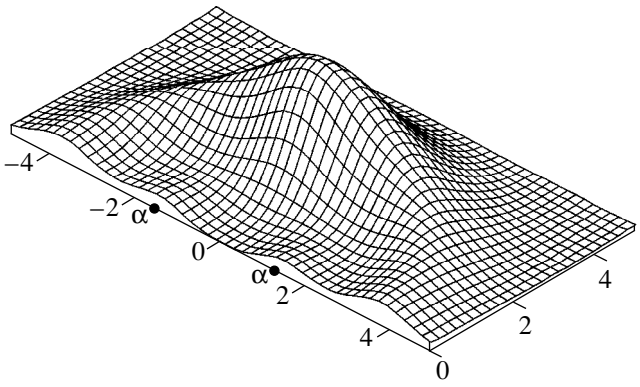

Fig. 8. Square of the wave function, $\Psi^2(x, y, u)$, of the system of three alpha particles for the ground state of the ^{12}C nucleus. The distance x between two alpha particles is fixed at $x = 2.93$ fm (closed circles indicate the positions of the centers of mass of the alpha-particle clusters). The function is expressed in terms of the coordinates yu and $y\sqrt{1-u^2}$ plotted along the axes in fm.

what was obtained in the present study, however, the binding energy in [4] is less in magnitude than the experimental value by 0.5 MeV. Figure 8 provides a clear view of the spatial disposition of the alpha-particle clusters in the ^{12}C nucleus. There, we can see the square of the wave function, $\Psi^2(x, y, u)$, of the 3α system. The distance between two alpha particles is fixed at $x = 2.9$ fm, and the function itself is plotted in terms of the coordinates yu and $y\sqrt{1-u^2}$.

In the ground state of the ^{16}O nucleus, the centers of mass of three alpha-particle clusters are situated at the vertices of an isosceles triangle with side lengths of 2.7, 2.9, and 2.9 fm (see Fig. 7*b*). The point offset from the center of mass of the 3α cluster by a distance of 2.7 fm in the direction determined by the angles $\theta_{xz} = 60°$ and $\theta_{yz} = 65°$ between the vectors **x** and **z** and between the vectors **y** and **z**, respectively, corresponds to the most probable position of the fourth alpha particle. For the first excited state of the ^{16}O nucleus, the disposition of the alpha-particle clusters is illustrated in 7*c*. The spatial configuration of the alpha-particle clusters was investigated in [2, 3, 17, 18], where the authors considered primarily a regular tetrahedron and a linear chain of alpha particles. Our calculations reveal that neither of these is realized in the ^{16}O nucleus. By way of example, we compare our results for the ground state of the ^{16}O nucleus with the corresponding results of Dufour *et al.* [3], who used the method of generator coordinates and who considered the disposition of the alpha-particle clusters at the vertices of a regular tetrahedron with an edge length of 2.39 fm. The calculations of Dufour *et al.* [3] underestimate greatly the root-mean-square radius of the ^{16}O nucleus, leading to the value of $R = 2.25$ fm. At the same time, their results for the ^{12}C nucleus are consistent with ours—namely, the disposition of the alpha-particle clusters in the ^{12}C nucleus is in accord with their disposition at the vertices of an equilateral triangle with a side length of 2.8 fm. We would also like to mention the study of Bauhoff *et al.* [18], who relied on the shell model of the nucleus. By employing the "Rhomb" configuration of the alpha-particle clusters in the ^{16}O nucleus, those authors were able to reproduce closely the position of the first excited (0^+) level. The above configuration from [18] is similar to the configuration obtained here for the excited 0^+ state of the ^{16}O nucleus.

4. CONCLUSION

The ^{16}O nucleus has been treated here as a bound state of the system consisting of four alpha-particle clusters. In addition to pair short-range potentials of interaction between the alpha particles, we have also considered three-body interaction potentials of two types. Of these, interaction of the first type binds three alpha particles into a cluster, while interaction of the second type simulates coupling between the fourth alpha-particle cluster and the pairs of the alpha parti-

cles bound into the above three-particle subsystem. As a matter of fact, this means that we have introduced a four-body interaction. The potential parameters have been determined by fitting the experimental values of the binding energies and of the root-mean-square radii for the ^{12}C and ^{16}O nuclei. The potential model obtained in this way on the basis of equations for the Yakubovsky components reproduces faithfully the first excited (0^+) state of the ^{16}O nucleus. Following [11–13], where in-medium changes in the root-mean-square radii of the clusters involved were considered in dealing with cluster systems, we have assumed here that the root-mean-square radius of the alpha-particle cluster in the 3α and 4α bound systems differs considerably from that of a free alpha particle. By calculating, within this framework, the charge form factors for the ^{12}C and ^{16}O nuclei treated as the 3α and 4α systems, respectively, we have been able to reproduce the experimentally observed behavior of these form factors and their magnitudes. Based on the results of our calculations for the wave function of the ^{16}O nucleus, we have found that the most probable disposition of four alpha-particle clusters in this nucleus is that at the vertices of a deformed tetrahedron.

ACKNOWLEDGMENTS

We are grateful to M.V. Zhukov for enlightening discussions on the results of this study.

Our work was supported in part by the Contest Center of the Ministry for Higher Education of the Russian Federation (project no. 97-0-14.3-23).

REFERENCES

1. T. Ya. Mikhelashvili, Yu. F. Smirnov, and A. M. Shirokov, Yad. Fiz. **48**, 969 (1988) [Sov. J. Nucl. Phys. **48**, 617 (1988)]; R. I. Dzhibuti, T. Ya. Mikhelashvili, and K. V. Shitikova, Yad. Fiz. **45**, 345 (1987) [Sov. J. Nucl. Phys. **45**, 217 (1987)].
2. N. Itagaki, A. Ohnishi, and K. Kato, nucl-th/9606056.
3. M. Dufour, P. Descouvemont, and D. Baye, Phys. Rev. C **50**, 795 (1994).
4. D. V. Fedorov and A. S. Jensen, Phys. Lett. B **389**, 631 (1996).
5. R. Pichler, H. Oberhummer, A. Csótó, *et al.*, Nucl. Phys. **A618**, 55 (1997).
6. J. H. Heisenberg and B. Mihaila, nucl-th/9802031; nucl-th/9802032.
7. S. P. Merkuriev and S. L. Yakovlev, Dokl. Akad. Nauk SSSR **262**, 591 (1982); Teor. Mat. Fiz. **56**, 60 (1983); S. P. Merkuriev and L. D. Faddeev, *Quantum Scattering Theory for Few-Particle Systems* (Nauka, Moscow, 1985).
8. S. L. Yakovlev and I. N. Filikhin, Yad. Fiz. **56** (12), 98 (1993) [Phys. At. Nucl. **56**, 1676 (1993)]; **58**, 817 (1995) [**58**, 754 (1995)]; **60**, 1962 (1997) [**60**, 1794 (1997)]; Contributed Papers of 16th European Conference on Few-Body Problems in Physics (Autrans, France, 1998); Few-Body Syst. Suppl. (in press); nucl-th/9809041.
9. S. Ali and A. R. Bodmer, Nucl. Phys. **88**, 99 (1966).
10. S. B. Dubovichenko, nucl-th/9802081.
11. H. Kamada *et al.*, Nucl. Phys. **A386**, 285 (1982); Prog. Theor. Phys. **72**, 368 (1984).
12. G. Bluge and K. Langanke, Few-Body Syst. **11**, 137 (1991).
13. S. B. Dubovichenko and A. V. Dzhazairov-Kakhramanov, Yad. Fiz. **56** (4), 45 (1993) [Phys. At. Nucl. **56**, 447 (1993)].
14. H. De Vries *et al.*, At. Data Nucl. Data Tables **36**, 495 (1987).
15. H. Walliser and D. Fliessbach, Phys. Rev. C **31**, 2242 (1985).
16. I. Sick and J. S. McCarthy, Nucl. Phys. **A150**, 631 (1970).
17. D. Robson, Phys. Rev. C **25**, 1108 (1982); M. Beiner *et al.*, Nucl. Phys. **A238**, 29 (1975); H. Fridrich, H. Husken, and A. Weiguny, Phys. Lett. B **38**, 199 (1972).
18. W. Bauhoff, H. Schultheis, and R. Schultheis, Phys. Rev. C **29**, 1046 (1984).

Translated by A. Isaakyan

Physics of Atomic Nuclei, Vol. 63, No. 3, 2000, pp. 353–364. Translated from Yadernaya Fizika, Vol. 63, No. 3, 2000, pp. 419–430.

NUCLEI
Theory

Lower and Upper Variational Bounds in Calculations of Coulomb and Nuclear Systems

A. G. Donchev, N. N. Kolesnikov and V. I. Tarasov[1)]

Department of Physics, Moscow State University, Vorob'evy gory, Moscow, 119899 Russia

Received August 28, 1998; in final form, April 27, 1999

Abstract—All formulas that are necessary for deriving not only upper (E_U) but also lower (E_L) variational bounds on the energy of systems featuring a few nonrelativistic particles are obtained with trial functions in the form of expansions in multidimensional Gaussian functions or exponentials. For potentials that are used most widely, all matrix elements are expressed in terms of known functions, a circumstance that simplifies considerably relevant numerical calculations. This is so for systems featuring an arbitrary number of particles in the case of a Gaussian basis and for three-particle systems in the case of an exponential basis. Numerical results for E_U and E_L, which are characterized by record accuracies, are presented for some Coulomb and nuclear systems such as the He atom; the $e^+e^-e^-$, $pp\mu^-$, 3α, and 4α systems; and hypertritium ($pn\Lambda$). Lower bounds with exponential trial functions are obtained for the first time (the corresponding formulas are presented for the first time as well); for a Gaussian basis, lower bounds for Coulomb systems have not been known either. Given E_L and E_U, limits within which the exact value of energy, E_0, lies can be indicated with confidence. Moreover, an analysis of the correlation between E_L and E_U with increasing number of terms in the expansion of the trial function makes it possible to improve the accuracy (at least by one order of magnitude) of the value E_∞ extrapolated to infinity. By considering specific examples, it is shown that the exponential basis is advantageous in relation to the Gaussian one. © *2000 MAIK "Nauka/Interperiodica".*

1. INTRODUCTION

Investigation of systems involving three and more particles is of paramount importance for theory because this makes it possible to reveal qualitatively new effects of multiparticle forces and multiparticle correlations that are absent in two-particle systems. Moreover, such investigations contribute to understanding the role of relativistic effects in systems of more than two particles. Calculations for few-particle systems are important from the point of view of practical applications in rapidly developing realms of science such as spectroscopy of multiply charged ions and the physics of positronium atoms and positronium molecules, mesic molecules, exotic nuclear systems, hypernuclei, and other hadronic and quark objects.

In the most popular nonrelativistic potential approach, various methods—primarily, Faddeev's methods, the method of hyperspherical functions, and the Monte Carlo method—are commonly used to solve the Schrödinger equation. In calculating bound systems, the variational approach, which provides the highest accuracy, remains, however, the most universal one in what is concerned with the shape and the structure of the potential. The absence of oscillations of the resulting estimates around the true value and the possibility of finding both the upper (E_U) and the lower (E_L) bound on energy—in many cases, this ensures the accuracy and reliability of calculations—are important advantages of the method.

In the overwhelming majority of studies, the authors restrict themselves to a determination of an upper bound on the ground-state energy E_0,

$$E_U = \min_{\psi} \frac{\langle \psi | H | \psi \rangle}{\langle \psi | \psi \rangle}, \tag{1}$$

where H is the Hamiltonian of the system, and ψ is the trial function. But there is always the problem of assessing the proximity of E_U to E_0. In calculations featuring many parameters, it is possible to approach an exact value by taking an ever more involved trial function and by constructing the dependence $E_U = E_U(n)$, where n is the quantity directly related to the number of variational parameters. For n, we can take the number of terms in the general expansion

$$\psi = \sum_{i=1}^{n} a_i \phi_i(\alpha^i), \tag{2}$$

where ϕ_i are basis functions that are dependent on variational parameters a_i and α^i.

In order to obtain an extrapolated energy value that is closer to an exact value, the n dependence of E_U is usually approximated by the expression

$$E_U(n) = E_\infty + f_U(n), \tag{3}$$

where f_U is some nonnegative function tending monotonically to zero as $n \longrightarrow \infty$, while E_∞ is the sought

[1)] Nuclear Safety Institute, Russian Academy of Sciences, Bol'shaya Tul'skaya ul. 52, Moscow, 113191 Russia.

extrapolated estimate of energy. However, the results of this procedure are open to criticism. In order to clarify this point, we note that, if the set of functions under use is not complete or if variational parameters are sought over some part of the full admissible region, E_∞ will not coincide with E_0, remaining only some far or close approximation of it.

Provided that a lower bound is derived along with E_U, the variational method frequently makes it possible to answer the most difficult question, that of the accuracy of the results it yields. If, in particular, the energy E_1 of the first excited state[2)] (or its lower bound) is known, then E_L can be found by the Temple formula [1]

$$E_L = \max_\psi \frac{E_1\langle\psi|H|\psi\rangle - \langle\psi|H^2|\psi\rangle}{E_1 - \langle\psi|H|\psi\rangle}, \quad (4)$$

which is valid for all trial functions ensuring fulfillment of the inequality $\langle\psi|H|\psi\rangle < E_1$. It can be seen easily that, at $\psi = \psi_0$, this formula yields the exact value for the energy of the system (as the expression for E_U does). Moreover, it can be shown (see, for example, [2]) that, if there is no a priori information other than that about $\langle H\rangle$, $\langle H^2\rangle$, and E_1, equation (4) leads to the best lower bound on E_0.

The calculations of few-nucleon nuclei from [3–6] show that E_L is a rougher estimate of E_0 than E_U. For example, the quantity

$$\eta = \frac{E_0 - E_L}{E_U - E_0}, \quad (5)$$

which is often used in comparing various estimates, proved to be 50–100 in calculating ^{3}He and ^{4}He nuclei bound by simple *NN* potentials featuring a hard core [3]. In calculating tritium with the Hamada–Johnston potentials, Delves *et al.* [4] obtained the value of $\eta \sim 800$ and arrived at the conclusion that η tends to ascend with increasing number of variational parameters. At the same time, η values appear to be much less in the case of potentials characterized by a simpler radial dependence. In particular, it was found in [5] that $\eta \approx 40$ for three-particle systems bound by the soft-core Ali–Bodmer $\alpha\alpha$ potential [7] and that $\eta \approx 5$–10 for three- and four-nucleon systems governed by the purely attractive Baker potential.

2. CHOICE OF TRIAL FUNCTIONS

Variational calculations prove successful if the choice of basis functions having good approximating capabilities is combined with a highly efficient procedure for optimizing parameters in order to ensure a fast convergence of energy estimates. At the same time, it is important that matrix elements of the Hamiltonian of the system and of its square have a form as simple as is possible.

For *S* states of the system of particles—and we investigate here precisely such states—these requirements are met by taking the functions

$$\phi_i(\alpha^i) = \exp\left(-\sum_{k>l=1}^{N} \alpha_{kl}^i r_{kl}^2\right), \quad (6)$$

$$\phi_i(\alpha^i) = \exp\left(-\sum_{k>l=1}^{N} \alpha_{kl}^i r_{kl}\right), \quad (7)$$

where r_{kl} is the distance between the kth and lth particles, while N is the number of particles.

For the function in (6), the matrix elements of the Hamiltonian and of its square for systems featuring an arbitrary number of particles bound by potentials used extensively can be computed analytically, whereby numerical calculations of both the upper and the lower bound are simplified considerably. All formulas required for such calculations (see also [5]) are presented in Appendix 1.

For the functions in (7), the needed matrix elements can be calculated analytically only for three-particle systems. Some relevant calculations—both for nuclear and for atomic systems—can be found in the literature (see, for example, [8–12]), but these refer to upper bounds E_U exclusively. This is not only because a determination of lower bounds is laborious but also because some necessary formulas have not yet been derived. In the next section and in Appendix 2, we present all formulas required for calculating both the upper and the lower bound on the energy of a three-particle system.

3. UPPER AND LOWER BOUNDS ON THE ENERGY OF A THREE-PARTICLE SYSTEM IN AN EXPONENTIAL BASIS

Upon separating the center of mass, the Hamiltonian of the three-particle system reduces to the form

$$H = \frac{\mathbf{P}_1^2}{2\mu_{23}} + \frac{\mathbf{P}_2^2}{2\mu_{31}} - \frac{\mathbf{P}_1\cdot\mathbf{P}_2}{m_3} + V,$$

where $\mathbf{P}_1 \equiv \mathbf{p}_{23}$ and $\mathbf{P}_2 \equiv \mathbf{p}_{31}$ are the momentum operators for relative motion, V is the potential-energy operator, and

$$\frac{1}{\mu_{23}} = \frac{1}{m_2} + \frac{1}{m_3} = \frac{1}{\mu} - \frac{1}{m_1},$$

$$\frac{1}{\mu_{31}} = \frac{1}{m_3} + \frac{1}{m_1} = \frac{1}{\mu} - \frac{1}{m_2}.$$

For coordinates, it is convenient to choose the interparticle distances $R_1 \equiv r_{23}$, $R_2 \equiv r_{31}$, and $R_3 \equiv r_{12}$ and the Euler angles. In the case of central forces

[2)] Here, we mean an excited state corresponding to the same symmetry of the wave function and the same angular momentum as in the ground state.

$[V = \sum_{i \neq j = 1}^{3} V_{ij}(r_{ij})]$, the ground-state wave function depends only on the relative coordinates, whereas the kinetic-energy operator can be represented in the form

$$T = -\frac{\hbar^2}{2}\left\{\sum_{k=1}^{3}\left(\frac{1}{\mu}-\frac{1}{m_k}\right)\frac{1}{R_k^2}\frac{\partial}{\partial R_k}\left(R_k^2\frac{\partial}{\partial R_k}\right)\right.$$
$$\left.-\sum_{k\neq l=1}^{3}\left(\frac{1}{\mu}-\frac{1}{m_k}-\frac{1}{m_l}\right)(\mathbf{n}_k\cdot\mathbf{n}_l)\frac{\partial^2}{\partial R_k\partial R_l}\right\},$$

where $\mathbf{n}_k$ is a unit vector aligned with the vector $\mathbf{R}_k$.

In our notation, the basis functions (7) are written as

$$|i\rangle \equiv \phi_i = \exp\left(-\sum_{k=1}^{3}\alpha_k^i R_k\right),$$

while the normalization condition for the trial function (2) is given by

$$\langle\psi|\psi\rangle = \sum_{i,j} a_i a_j \langle i|j\rangle,$$

where

$$\langle i|j\rangle = 8\pi^2\int_0^\infty R_1 dR_1\int_0^\infty R_2 dR_2$$
$$\times\int_{|R_1-R_2|}^{R_1+R_2} R_3 dR_3 \exp\left(-\sum_{k=1}^{3}(\alpha_k^i+\alpha_k^j)R_k\right).$$

The expressions for the upper and lower variational bounds on the energy can be found by differentiating the fundamental integrals

$$I^{000}(x_1x_2x_3)$$
$$\equiv 8\pi^2\int_0^\infty dR_1\int_0^\infty dR_2\int_{|R_1-R_2|}^{R_1+R_2} dR_3\exp\left(-\sum_{k=1}^{3}x_kR_k\right), \quad (8)$$

$$U_1^{000}(x_1x_2x_3)$$
$$\equiv 8\pi^2\int_0^\infty dR_1 V(R_1)\int_0^\infty dR_2\int_{|R_1-R_2|}^{R_1+R_2} dR_3\exp\left(-\sum_{k=1}^{3}x_kR_k\right) \quad (9)$$

with respect to the parameters x_k $(=\alpha_k^i + \alpha_k^j)$.

The integral

$$I^{klm}(x_1x_2x_3)$$
$$\equiv 8\pi^2\int_0^\infty R_1^k dR_1\int_0^\infty R_2^l dR_2\int_{|R_1-R_2|}^{R_1+R_2} R_3^m dR_3\exp\left(-\sum_{j=1}^{3}x_jR_j\right) \quad (10)$$

can be evaluated by using the relation

$$I^{klm}(x_1x_2x_3)$$
$$= \left(-\frac{\partial}{\partial x_1}\right)^k\left(-\frac{\partial}{\partial x_2}\right)^l\left(-\frac{\partial}{\partial x_3}\right)^m I^{000}(x_1x_2x_3),$$

while the integral

$$U_1^{klm}(x_1x_2x_3) \equiv 8\pi^2\int_0^\infty V(R_1)R_1^k dR_1\int_0^\infty R_2^l dR_2$$
$$\times\int_{|R_1-R_2|}^{R_1+R_2} R_3^m dR_3\exp\left(-\sum_{k=1}^{3}x_kR_k\right) \quad (11)$$

is taken with the aid of the relation

$$U_1^{klm}(x_1x_2x_3)$$
$$= \left(-\frac{\partial}{\partial x_1}\right)^k\left(-\frac{\partial}{\partial x_2}\right)^l\left(-\frac{\partial}{\partial x_3}\right)^m U_1^{000}(x_1x_2x_3).$$

The integral in (8) can be calculated easily, the result being

$$I^{000}(x_1x_2x_3) = \frac{16\pi^2}{(x_1+x_2)(x_2+x_3)(x_3+x_1)},$$

while the integral in (9) for arbitrary $V(R_1)$ reduces to the form

$$U_1^{000}(x_1x_2x_3) = \frac{16\pi^2}{(x_2+x_3)(x_2-x_3)}$$
$$\times\int_0^\infty V(R_1)dR_1(e^{-(x_3+x_1)R_1}-e^{-(x_1+x_2)R_1}).$$

For the sake of convenience, we now introduce the notation

$$t_1 \equiv 2(\mathbf{n}_2\cdot\mathbf{n}_3) = \frac{R_2^2+R_3^2-R_1^2}{R_2R_3},$$
$$t_2 \equiv 2(\mathbf{n}_3\cdot\mathbf{n}_1), \quad t_3 \equiv 2(\mathbf{n}_1\cdot\mathbf{n}_2);$$
$$T_p \equiv \langle i|t_p|j\rangle, \quad G_p \equiv \langle i|1/R_p|j\rangle,$$
$$I^{klm} \equiv I^{klm}(x_1x_2x_3).$$

We also introduce the operator O_{pq} implementing a permutation of any pair of coordinates x_p and x_q, for example,

$$O_{12}f(x_1x_2x_3) \equiv f(x_2x_1x_3),$$

and satisfying the condition $O_{pp} \equiv 1$, $p = 1, 2, 3$. It follows that

$$G_p = O_{p1}I^{011}, \quad T_p = O_{p1}(I^{120}+I^{102}-I^{300}),$$
$$p = 1, 2, 3.$$

After some simple algebra, we find that the matrix elements of the operator T between the states i and j can

be represented as

$$\langle i|T|j\rangle = \sum_{p=1}^{3}(s_p^i G_p - d_p^i T_p) - u^i I^{111},$$

where

$$s_1^i = \frac{\hbar^2}{\mu_{23}}\alpha_1^i, \quad s_2^i = \frac{\hbar^2}{\mu_{31}}\alpha_2^i, \quad s_3^i = \frac{\hbar^2}{\mu_{12}}\alpha_3^i,$$

$$u^i = s_1^i\alpha_1^i + s_2^i\alpha_2^i + s_3^i\alpha_3^i,$$

$$d_1^i = \frac{\hbar^2}{2m_1}\alpha_2^i\alpha_3^i, \quad d_2^i = \frac{\hbar^2}{2m_2}\alpha_3^i\alpha_1^i, \quad d_3^i = \frac{\hbar^2}{2m_3}\alpha_1^i\alpha_2^i.$$

The matrix elements for potentials used extensively are given by quite simple expressions. In particular, we have

$$\langle i|1/R_1|j\rangle = I^{011}(\alpha_1^i + \alpha_1^j, \alpha_2^i + \alpha_2^j, \alpha_3^i + \alpha_3^j)$$

for the Coulomb interaction $V(R_1) = 1/R_1$,

$$\langle i|\exp(-\lambda_1 R_1)|j\rangle = I^{111}(\alpha_1^i + \alpha_1^j + \lambda_1, \alpha_2^i + \alpha_2^j, \alpha_3^i + \alpha_3^j)$$

for the exponential potential $V(R_1) = \exp(-\lambda_1 R_1)$, and

$$\langle i|\exp(-\lambda_1 R_1)/R_1|j\rangle = I^{011}(\alpha_1^i + \alpha_1^j + \lambda_1, \alpha_2^i + \alpha_2^j, \alpha_3^i + \alpha_3^j)$$

for the Yukawa potential $V(R_1) = \exp(-\lambda_1 R_1)/R_1$. The expressions for the matrix elements of $V(R_2)$ and $V(R_3)$ are similar.

A determination of the lower variation bound (4) requires additionally calculating the matrix elements of the operators T^2, V^2, and VT. For this purpose, it is convenient to introduce the quantities

$$J_{pq} \equiv \langle i|1/R_p R_q|j\rangle, \quad W_{pq} \equiv \langle i|t_p/R_q|j\rangle,$$
$$Q_{pq} \equiv \langle i|t_p t_q|j\rangle.$$

A calculation of the matrix elements of T^2 leads to the expression

$$\langle i|T^2|j\rangle = u^i u^j I^{111} - \sum_{p=1}^{3}(s_p^i u^j + s_p^j u^i)G_p + \sum_{p=1}^{3}(d_p^i u^j + d_p^j u^i)T_p - \sum_{p,q=1}^{3}(s_q^i d_p^j + s_q^j d_p^i)W_{pq} + \sum_{p,q=1}^{3} s_p^i s_q^j J_{pq} + \sum_{p,q=1}^{3} d_p^i d_q^j Q_{pq},$$

where

$$W_{pp} = O_{p1}(I^{020} + I^{002} - I^{200}),$$

$$W_{pq} = O_{p1}O_{q2}(I^{1-12} + I^{110} - I^{3-10}),$$

$$Q_{pp} = O_{p1}(I^{5-1-1} + I^{13-1} + I^{1-13} - 2I^{31-1} - 2I^{3-11} + 2I^{111}),$$

$$Q_{pq} = O_{p1}O_{q2}(2I^{22-1} - I^{04-1} - I^{40-1} + I^{003}),$$

$$J_{pp} = O_{p1}I^{-111},$$

$$J_{pq} = O_{p1}O_{q2}I^{001}, \quad p \neq q.$$

The integrals in (10) with positive indices k, l, and m represent algebraic functions of combinations of the parameters $(\alpha_k^i + \alpha_k^j)$. The case of negative indices in (10) can be interpreted in terms of integrals with respect to the parameters x_k. In the presence of at least one negative index in I^{klm}, this leads to the emergence of logarithmic terms in the ratios of nonlinear parameters; for example, we have

$$I^{-100} = \frac{16\pi^2}{x_2 - x_3}\ln\frac{x_1 + x_2}{x_1 + x_3}.$$

In the case of two negative indices, there arise dilogarithmic functions, but they lead to divergences at no finite parameters values. In particular, the integral

$$I^{1-10} = \frac{16\pi^2}{x_3}\int_0^{x_3/x_2}\frac{d\eta}{\eta^2 - 1}\ln\frac{\eta(x_1 + x_3)}{\eta x_1 + x_3}$$

remains finite.

In numerical calculations, an accurate evaluation of integrals featuring negative indices nonetheless caused the greatest difficulties, which were sidestepped by means of special expansions whose form depended on the relations between the parameters α_k^i. The integrals appearing in the expressions for E_U and E_L are presented in Appendix 2.

A calculation of the matrix elements of V^2 is similar to the procedure for determining $\langle i|V|j\rangle$. In particular, we have

$$\langle i|1/R_1^2|j\rangle = I^{-111}(\alpha_1^i + \alpha_1^j, \alpha_2^i + \alpha_2^j, \alpha_3^i + \alpha_3^j),$$
$$\langle i|1/R_1 R_2|j\rangle = I^{001}(\alpha_1^i + \alpha_1^j, \alpha_2^i + \alpha_2^j, \alpha_3^i + \alpha_3^j)$$

for the Coulomb interaction,

$$\langle i|\exp(-2\lambda_1 R_1)|j\rangle = I^{111}(\alpha_1^i + \alpha_1^j + 2\lambda_1, \alpha_2^i + \alpha_2^j, \alpha_3^i + \alpha_3^j),$$

$$\langle i|\exp(-\lambda_1 R_1 - \lambda_2 R_2)|j\rangle = I^{111}(\alpha_1^i + \alpha_1^j + \lambda_1, \alpha_2^i + \alpha_2^j + \lambda_2, \alpha_3^i + \alpha_3^j)$$

for the exponential potential, and

$$\langle i|\exp(-2\lambda_1 R_1)/R_1^2|j\rangle = I^{-111}(\alpha_1^i + \alpha_1^j + 2\lambda_1, \alpha_2^i + \alpha_2^j, \alpha_3^i + \alpha_3^j),$$

$$\langle i|\exp(-\lambda_1 R_1 - \lambda_2 R_1)/R_1 R_2|j\rangle$$
$$= I^{001}(\alpha_1^i + \alpha_1^j + \lambda_1, \alpha_2^i + \alpha_2^j + \lambda_2, \alpha_3^i + \alpha_3^j)$$

for the Yukawa potential.

Further, the matrix element of the operator $V(R_1)T + TV(R_1)$ can be represented in the form

$$\langle i|V(R_1)T + TV(R_1)|j\rangle = s_1^j U_1^{011} + s_2^j U_1^{101} + s_3^j U_1^{110} - u^j U_1^{111} + d_3^j(U_1^{003} - U_1^{201} - U_1^{021}) + d_1^j(U_1^{300} - U_1^{120} - U_1^{102}) + d_2^j(U_1^{030} - U_1^{012} - U_1^{210}).$$

We have

$$U_1^{klm} = I^{k-1,l,m}(\alpha_1^i + \alpha_1^j, \alpha_2^i + \alpha_2^j, \alpha_3^i + \alpha_3^j)$$

for the Coulomb potential $V(R_1) = 1/R_1$,

$$U_1^{klm} = I^{k,l,m}(\alpha_1^i + \alpha_1^j + \lambda_1, \alpha_2^i + \alpha_2^j, \alpha_3^i + \alpha_3^j)$$

for the exponential potential $V(R_1) = \exp(-\lambda_1 R_1)$, and

$$U_1^{klm} = I^{k-1,l,m}(\alpha_1^i + \alpha_1^j + \lambda_1, \alpha_2^i + \alpha_2^j, \alpha_3^i + \alpha_3^j)$$

for the Yukawa potential $V(R_1) = \exp(-\lambda_1 R_1)/R_1$.

4. NUMERICAL CALCULATIONS

In our numerical calculations, the trial function was taken in the form of expansion (2) in the basis functions (6) or (7). Optimal values of the variational parameters were determined by means a procedure that combined step-by-step and global searches [13, 14]. According to this procedure, the trial function is constructed by successively adding terms to the expansion in (2). At each step, only the nonlinear parameters of the added term are determined at fixed parameters of the terms found previously by minimizing an upper bound. For this purpose, we invoke the Monte Carlo method with a distribution function that is deduced in each calculation from an analysis of the distribution that is actually being formed (learning algorithm). The nonlinear parameters obtained in this way can be used for the lower bound as well. At each step, the linear parameters are determined for E_U and E_L independently by means of conventional methods. Specific calculations reveal (examples are given below) that, at a fixed degree of precision, this approach makes it possible to reduce considerably (by a factor of 2 or more) the number of terms in expansion (2) in relation to the case where nonlinear parameters are fixed at some preset grid, chosen in one way or another rather than varied. Stochastic searches become more advantageous as the number of functions increases.

Given an upper bound, a determination of a lower bound is of importance, above all, for it fixes an interval where the exact value of the energy lies. Although lower bounds usually show more pronounced deviations from E_0 than upper bounds, a determination of the two bounds may refine the results of variational calculations. This concerns primarily calculations in which a trial function is gradually complicated by increasing the number of variational parameters. In such cases, an analysis of the parametric relationship between E_L and E_U at various values of n may be very informative [2]. Let us clarify this point further. If an expression similar to (3) is used for the lower bound, then the upper and the lower bound are related by the equation

$$E_U = E_\infty + (E_\infty - E_L)/\eta(n), \tag{12}$$

where $\eta = -f_L/f_U$ is the quantity introduced in (5). It can be seen from (12) that, if the two bounds are characterized by approximately the same character of convergence [so that $f_L(n) \propto f_U(n)$; hence, η = const], equation (12) is linear. It should be emphasized that this is so for any law of convergence, which is unknown, as a rule. It is obvious that, in this case, the estimate of E_0 is of the highest reliability. In actual practice, however, η is not strictly constant, slowly growing, in the majority of cases, as we approach the exact solution (see, for example, [4]). Nevertheless, the use of relation (12) simplifies considerably the extrapolation procedure in relation to that based on formulas of the type (3).

The convergence of variational bounds is often approximated by the power-law dependence

$$f_U(n) \propto n^{-\gamma_U}, \quad f_L(n) \propto n^{-\gamma_L}, \tag{13}$$

where γ_U and γ_L are adjustable parameters. In this case, relation (12) can be recast into the form

$$E_U \approx E_\infty + \text{const} \times (E_U - E_L)^{1+\gamma}, \tag{14}$$

where $\gamma \equiv (\gamma_U - \gamma_L)/\gamma_L$. In deriving this formula, we have replaced E_∞ by E_U on the right-hand side of it, assuming that $\eta \gg 1$. It may be used to extrapolate the results of the calculations in order to refine them.

5. GAUSSIAN FUNCTIONS

Figures 1 and 2 show an upper and a lower bound on the energies of the 3α and 4α systems, respectively, for various numbers n of terms in expansion (2) with the basis functions (6). Table 1 displays the upper and lower bounds obtained at maximal n and the corresponding extrapolated values (the probable extrapolation error at the last decimal place is given there in parentheses). The same table also quotes the expectation values of the kinetic- and potential-energy operators and the root-mean-square radii.[3)] Here and below, all energy values and all dimensions are given in MeV and fm, respectively, for the nuclear systems and in atomic units (a.u.) for the atomic systems.

The calculations were performed with the Ali–Bodmer potential (the d_0 version featuring no Coulomb

[3)]The radius values are listed for the purpose of reference exclusively—a dedicated analysis of the character of their convergence was not performed for nuclear systems, so that the number of decimal places retained in the table was not matched, in general, with the accuracy of the energy bounds.

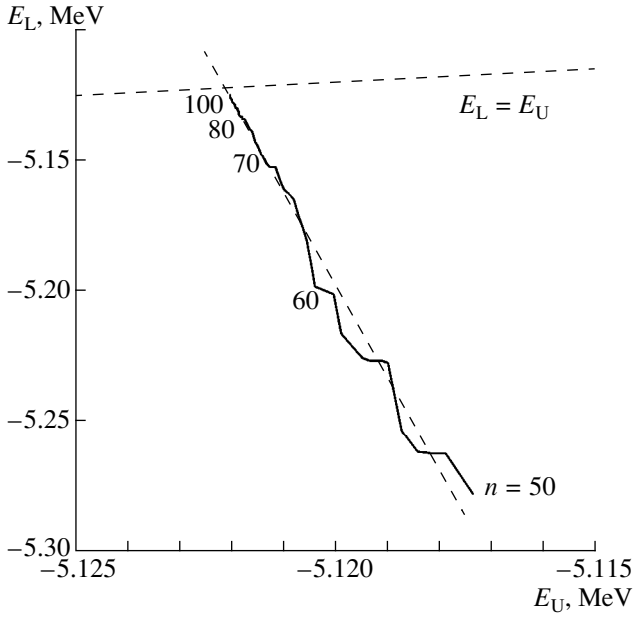

Fig. 1. Relation between the upper and lower bounds on the energy of the 3α system (Gaussian basis).

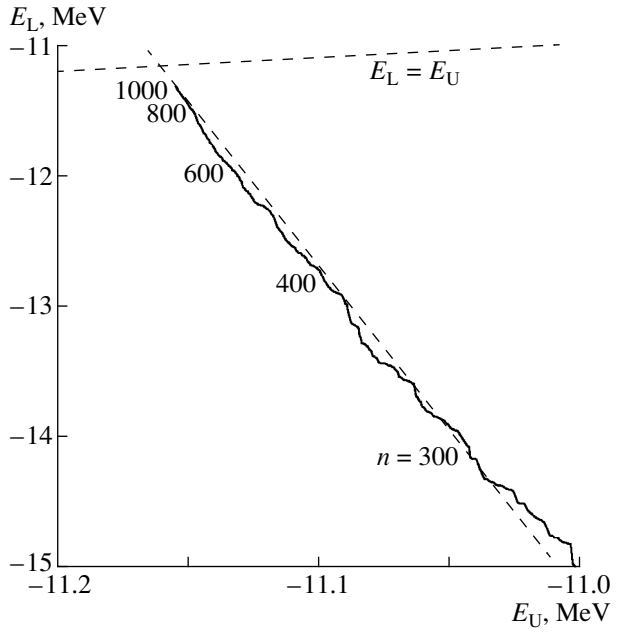

Fig. 2. Relation between the upper and lower bounds on the energy of the 4α system (Gaussian basis).

interaction; $\hbar/M_\alpha$ = 10.4465 MeV fm^2). In order to determine E_L, we used the energy of the first excited state; it is equal to zero in the 3α system (there is no excited bound states with zero angular momentum in the 3α system) and to the binding energy of the 3α system in the 4α system.

An analysis of the results revealed that the two bounds converge similarly; that is, their convergence can be approximated by a power-law dependence of the type (13) with $\gamma_U \approx \gamma_L \approx 3.7$ for three-particle systems and $\gamma_U \approx \gamma_L \approx 2.3$ for four-particle systems. Hence, the dependence $E_L = E_L(E_U)$ is close to a linear one, so that uncertainties in the calculation can be reduced considerably. Indeed, the extrapolation errors are estimated at about 10^{-5} MeV in the three-particle case, the difference between the estimates being 0.003 MeV. In the four-particle case, the accuracy of the calculations is much poorer. This is due above all to the doubled number of interparticle couplings in the presence of strong repulsion at small distances. It should be noted that η is close to 35 for the 3α system and to 24 for the 4α system. At present, the results that we obtained for the 3α and 4α systems are the most precise (compare with [6] and [13], respectively).

It can be seen from (4) that, in general, the lower the energy of the first excited state, the poorer the accuracy of the lower bound. By way of example, we present the results of our calculations for hypertritium, the three-particle system $pn\Lambda$ with an anomalously low excitation energy, which is equal to the binding energy B_Λ^{expt} = 0.13 MeV (the total binding energy of the system is 2.35 MeV). In the calculations, we used the semirealistic *NN* potential from [5] and the simplest Λ*N* potential from [15], the latter being corrected in such a way as to obtain a correct value for the ${}^3_\Lambda$H binding energy. The energy of the first excited state is equal to the deuteron binding energy (in our calculations, $E_1 = E_d = 2.221$ MeV).

The results of the calculations are displayed in Table 2 [row (a)] and in Fig. 3. It can be seen that, as in the case of alpha-particle systems, the dependence $E_L = E_L(E_U)$ is close to a linear one, but the η value is about 2800. Nevertheless, even so rough a lower bound makes it possible to determine one more decimal place by means of the extrapolation procedure ($E_\infty = -2.3689 \pm 0.0003$ MeV, which corresponds to $B_\Lambda = 0.1479 \pm 0.0003$ MeV).

As an example of the calculation for Coulomb systems, we quote the results for the He atom with an infinitely heavy nucleus (∞He). The calculations were performed up to n = 525. As might have been expected, the convergence of the variational procedure proved to be much poorer than in the case of nuclear systems. This was associated above all with the difficulties in describing the asymptotic behavior of the wave function in terms of the Gaussian basis. Apart from this, the convergence of the lower bound is poorer than that of the upper bound because of the special features of the spectrum of Coulomb systems (in calculating E_L, the E_1 value was chosen on the basis of the results of the calculations with exponential functions; see below). By way of illustration, we indicate that, in the present calculation, $\gamma_U \approx 1$, while $\gamma_L \approx 0.3$. Figure 4 displays the relation between E_U and E_L and its approximation according to (14) (dashed curve). The extrapolated value appeared to be –2.9039, whereas $E_U(525)$ = –2.9031 and $E_L(525) = -5.18$, η being about 4200.

Table 1. Upper and lower bounds on the energies of the 3α and 4α systems, extrapolated values of these energies, and mean kinetic and potential energies and root-mean-square radii for these systems

System	E_∞	E_U	E_L	$\langle T\rangle$	$\langle V\rangle$	$\langle r^2\rangle^{1/2}$
3α (n = 100)	–5.12212(1)	–5.122038	–5.125085	7.62	–12.74	2.44
4α (n = 1000)	–11.161(1)	–11.154	–11.322	14.51	–25.67	2.562

Table 2. Upper and lower bounds on the energy of the ${}^{3}_{\Lambda}\mathrm{H}$ system, extrapolated values of this energy, and mean kinetic and potential energies and root-mean-square radii for this system

	E_∞	E_U	E_L	$\langle T\rangle$	$2\langle V_{\Lambda N}\rangle$	$\langle V_{NN}\rangle$	$\langle r_\Lambda^2\rangle^{1/2}$	$\langle r_N^2\rangle^{1/2}$
(a)	–2.3689(3)	–2.3677	–5.72	18.96	–4.30	–17.03	6.15	4.05
(b)	–2.3586114(2)	–2.3586111	–2.3641	18.00	–4.75	–15.62	6.62	4.33

Note: (a) Gaussian basis, n = 500; (b) exponential basis, n = 300.

6. EXPONENTIAL FUNCTIONS

As a first example of the calculation with exponential functions, we present the results for the helium atom with an infinitely heavy nucleus (∞He) (see Table 3). At n = 100, we obtained E_U = –2.903724364 and E_L = –2.903741. In calculating E_L, we used the value of E_1 = –2.1753, which is obviously smaller than the energy of the first excited state.[4)] It can be seen that the results are much more accurate (by a few orders of magnitude) than those in the case of a Gaussian basis. The sought value of energy is constrained in a relatively narrow energy interval whose width can be further reduced by increasing the number of terms in (2).

Figure 5, which shows a correlation between the upper and lower bounds on the energy of the helium atom ∞He for various numbers of terms in expansion (2) with the basis functions (7), illustrates the procedure of extrapolation in accordance with equation (14). An analysis of convergence of variational bounds reveals that the dependences $E_U = E_U(n)$ and $E_L = E_L(n)$ can be approximated by power-law functions with power-law exponents γ_U = 6.7 and γ_L = 5.1, the extrapolated value being E_∞ = –2.903724377(2). Despite the large value of $\eta \approx 1300$ (owing to fast convergence of variational bounds), an extrapolation makes it possible to reduce computational errors by 1.5 orders of magnitude. It should also be noted that the virial theorem holds to a high accuracy (which increases further with increasing n). By way of example, we indicate that, at n = 200, the ratio $|2\langle T\rangle/\langle V\rangle|$ differs from unity only at the eleventh decimal place.

As to the upper bound, the most precise results for it are presently thought to be those of Frankowski and Pekeris [16] (E_U = –2.9037243770326, E_∞ = –2.9037243770333), which were obtained at n = 246 by using a rather cumbersome basis of the exponential type, including, in particular, logarithmic terms. We would also like to indicate the study of Schwarz [17], who combined exponential and power-law bases. Purely exponential bases were used in [9, 11], but the accuracy of calculations were poorer there. We emphasize that, at a given number of terms in expansion (2), our results for E_U are the most precise ones. Among other things, this shows that the accuracy of the calculation is more sensitive to the choice of procedure for determining extrema of variational estimates than to taking into account logarithmic terms in the trial function.

Finally, we have calculated the energies of some helium isotopes—^{3}He, ^{4}He, ^{6}He, and ^{8}He—and determined thereby mass effects. It is interesting to note that the specific mass effect is quite large here. The specific

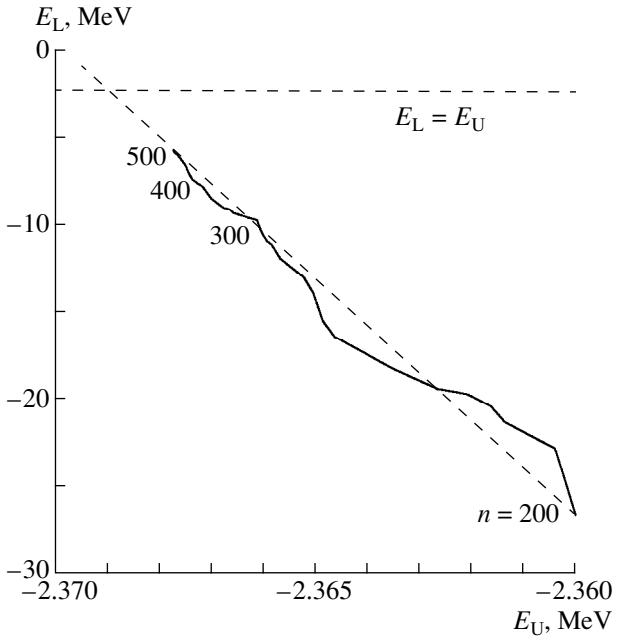

Fig. 3. Relation between the upper and lower bounds on the energy of hypertritium (Gaussian basis).

[4)]The energy of the first excited state was determined as that eigenvalue of the energy matrix which follows the eigenvalue corresponding to the ground state; at n = 200, we have E_1 = –2.17522938.

Table 3. Upper and lower bounds on the energy of the $^{\infty}$He system, extrapolated values of this energy, and mean kinetic and potential energies and root-mean-square radius for this system (exponential basis, $n = 100$)

E_∞	E_U	E_L	
–2.903724377(2)	–2.903724364	–2.903741	
$\langle T\rangle$	$\langle 2V_{ee}\rangle$	$\langle V_{e\alpha}\rangle$	$\langle r_e^2\rangle^{1/2}$
2.9037243770	0.9458184488	–3.3766336014	1.0924664734

Table 4. Total and specific mass effects in helium atoms (in 10^{-4} a.u.)

^{3}He	^{4}He	^{6}He	^{8}He	^{3}He	^{4}He	^{6}He	^{8}He
5.57166	3.98036	2.79175	2.09148	5.1878%	5.1887%	5.1904%	5.1906%

Table 5. Upper and lower bounds on the energy of the $e^+e^-e^-$ system, extrapolated value of this energy, and mean kinetic and potential energies and root-mean-square radii for this system (exponential basis, $n = 150$)

E_∞	E_U	E_L	$\langle T\rangle$
–0.2620050699(2)	–0.2620050694	–0.26200561	0.2620050700
$\langle V_{e^-e^-}\rangle$	$2\langle V_{e^-e^+}\rangle$	$\langle r_{e^-}^2\rangle^{1/2}$	$\langle r_{e^+}^2\rangle^{1/2}$
0.1556319057	–0.6796420457	5.1074695	3.3416086

mass effect with respect to the total mass effect is given in Table 4, all restrictions on the accuracy being due to the experimental uncertainties in nuclear masses.

Another example is provided by the exotic system $e^+e^-e^-$. Here, the calculations were performed up to $n = 150$, the results being presented in Table 5. A correlation between E_U and E_L over a final segment of the curve is illustrated in Fig. 6 (in atomic units). The character of convergence is specified by the values of $\gamma_U = 5.6$ and $\gamma_L = 4.7$, the extrapolated estimate being $E_\infty = -0.2620050698(2)$, $\eta \approx 900$. In deriving the lower bound, the value of –0.25, which corresponds to the breakup of the system into e^+e^- and e^-, was chosen for the energy of the first excited state.

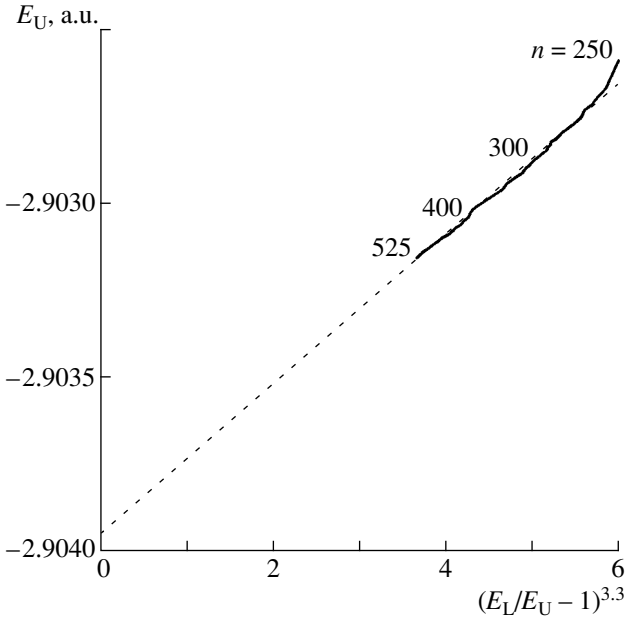

Fig. 4. Relation between the upper and lower bounds on the energy of the $^{\infty}$He atom (Gaussian basis).

Presented below are additionally the results of the calculations for the mesic hydrogen molecule:

$$E_U(100) = -102.223723,$$
$$E_L(100) = -102.2258,$$
$$E_\infty = -102.223742(3).$$

A calculation with the aid of the Gaussian basis again yields the rougher results

$$E_U(400) = -102.14,$$
$$E_\infty = -102.20(4).$$

As an example of what can be obtained from a calculation of three-body nuclear systems in an exponential basis, we present our results for hypertritium. In this calculation, we employed the simplest nuclear potentials of the exponential form $V(r) = -V_0\exp(-\nu r)$ with the same parameters as in [15]:

$$V_0 = 192.7 \text{ MeV}, \ \nu = 1.506 \text{ fm}^{-1}$$

for the NN potential;

$$V_0 = 711 \text{ MeV}, \ \nu = 4.44 \text{ fm}^{-1}$$

for the ΛN potential.

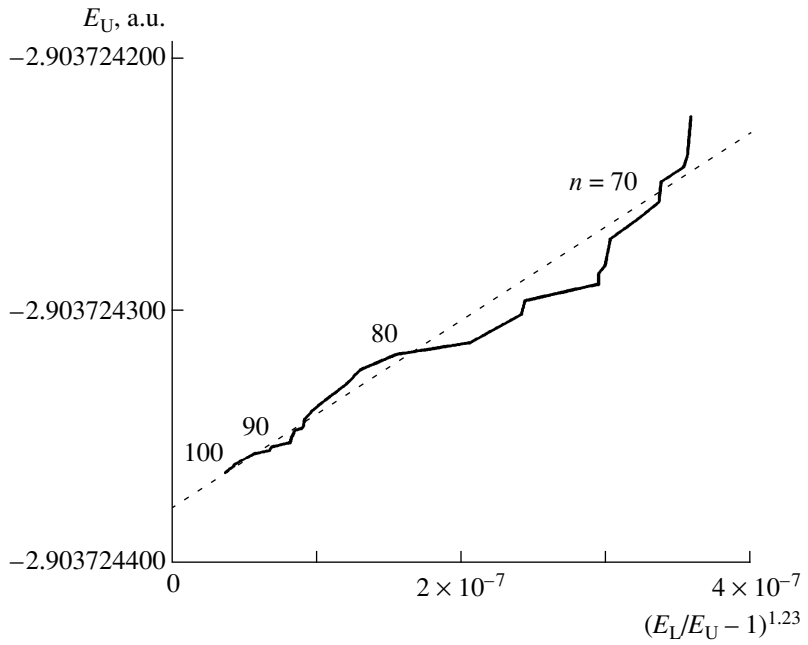

Fig. 5. Relation between the upper and lower bounds on the energy of the $^{\infty}$He atom (exponential basis).

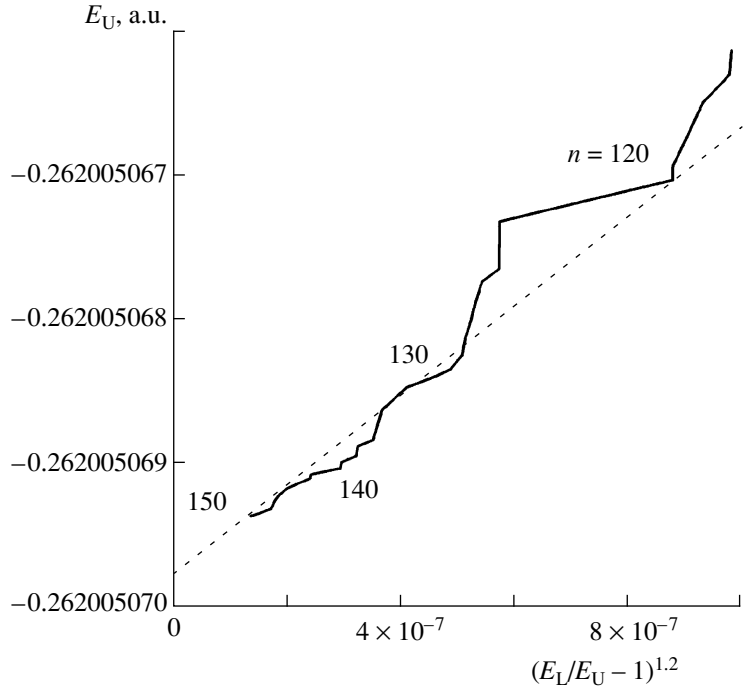

Fig. 6. Relation between the upper and lower bounds on the energy of the $e^+e^-e^-$ system (exponential basis).

Although these potentials differ from those used in the calculations of $^{3}_{\Lambda}$H with a Gaussian basis, the results are also presented in Table 2 [(b) row]. The relation between E_L and E_U for various n values is illustrated in Fig. 7 [here, the extrapolated value is E_∞ = –2.3586114(2) MeV]. In just the same way as in the case of atomic systems, the exponential basis ensures here a faster convergence and more precise results in relation to the Gaussian basis. For example, a precision of about 10^{-3} MeV is achieved only at $n \approx 300$ with the Gaussian basis and at a much smaller value of $n \approx 100$ with the exponential basis.

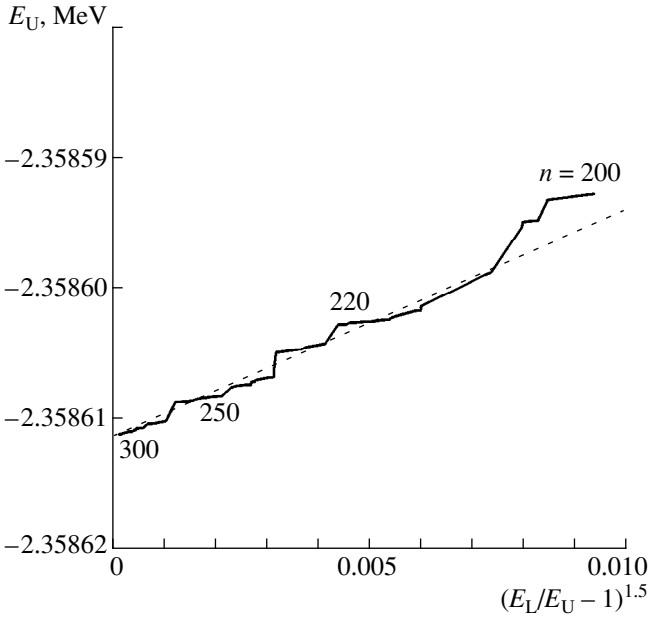

Fig. 7. Relation between the upper and lower bounds on the energy of hypertritium (exponential basis).

ACKNOWLEDGMENTS

We are grateful to A. M. Frolov for stimulating discussions.

APPENDIX 1

Gaussian Basis: Matrix Elements of the Hamiltonian and Its Square for Systems Featuring an Arbitrary Number of Particles

It is convenient to represent Gaussian functions as

$$\phi_i(\alpha^i) \equiv |i\rangle = \exp(-\mathbf{R}^+ A^i \mathbf{R}),$$

where $\mathbf{R}$ is the $(N-1)\times 1$ vector column $\{\mathbf{R}_{1N}, \mathbf{R}_{2N}, \ldots, \mathbf{R}_{N-1,N}\}$, while the elements of the $(N-1)\times(N-1)$ matrix A^i are related to the variational parameters α^i by the equations

$$A^i_{kk} = \sum_{l\neq k=1}^{N} \alpha^i_{lk}, \quad A^i_{kl} = -\alpha^i_{kl},$$
$$k \neq l = 1, 2, \ldots, N-1.$$

Overlap Integral

For the overlap integral, we have

$$\langle i|j\rangle = \int \exp\{-\mathbf{R}^+(A^i + A^j)\mathbf{R}\} d\mathbf{R}_{1N}\ldots d\mathbf{R}_{N-1,N}$$
$$= \pi^{3(N-1)/2}/D^{3/2},$$

where

$$D \equiv \det(A^i + A^j).$$

Kinetic Energy

For the matrix element of the kinetic-energy operator, the result is

$$\langle i|T|j\rangle = \langle i|j\rangle \mathcal{T}(\alpha^i, \alpha^j),$$

where

$$\mathcal{T}(\alpha, \beta) \equiv \sum_{klm}^{N} \mu_k \alpha_{km} \beta_{lm} (L_{kl} + L_{lm} - L_{kl}),$$

$$\mu_k \equiv 3\hbar^2/2m_k,$$
$$L_{kl} \equiv (\partial/\partial\alpha_{kl}) \ln D;$$

here, we formally set

$$\alpha_{kk} = 0, \quad \beta_{kk} = 0, \quad L_{kk} = 0; \quad k = 1, 2, \ldots, N.$$

Potential Energy

For the potential $V_{kl}(r_{kl})$ of interaction between the kth and lth particles, we have

$$\langle i|V_{kl}(r_{kl})|j\rangle = \langle i|j\rangle \frac{4}{\pi}\int_0^\infty V_{kl}(\sqrt{L_{kl}}x) e^{-x^2} x^2 dx.$$

From here, it is easy to calculate the matrix elements for all widely used potentials (see [5]). In particular, the results for the Gaussian and Coulomb potentials are

$$\langle i|\exp(-\nu r_{kl}^2)|j\rangle = \langle i|j\rangle (1 + \nu L_{kl})^{-3/2},$$
$$\langle i|1/r_{kl}|j\rangle = \langle i|j\rangle 2/\sqrt{\pi L_{kl}}.$$

Matrix Elements of the Squared Hamiltonian

For the relevant matrix elements, we have

$$\langle i|T^2|j\rangle = \langle i|j\rangle \Bigg[\mathcal{T}^2(\alpha^i, \alpha^j) - \frac{2}{3} \sum_{klmk'l'm'} \mu_m \mu_{m'} \alpha^i_{km}$$
$$\times \alpha^i_{lm} \alpha^j_{k'm'} \alpha^j_{l'm'} (4L_{kmk'm'} - 2L_{klk'm'} - 2L_{kmk'l'} + L_{klk'l'}) \Bigg],$$

$$\langle i|V_{kl}V_{mn}|j\rangle = \langle i|j\rangle \frac{2(1-g_{klmn})^{3/2}}{\pi g_{klmn}}$$
$$\times \int_{-\infty}^{\infty}\int_{-\infty}^{\infty} \exp(-x^2 + 2g_{klmn}xy - y^2) xy\, dx\, dy$$
$$\times V_{kl}(\sqrt{L_{kl}(1-g_{klmn})}|y|) V_{mn}(\sqrt{L_{mn}(1-g_{klmn})}|x|),$$

$$\langle i|TV_{kl} + V_{kl}T|j\rangle = 2\mathcal{T}(\alpha^i, \alpha^j)\langle i|V_{kl}|j\rangle$$

$$+\frac{8\langle i|j\rangle}{3\sqrt{\pi}L_{kl}}\int_0^\infty V_{kl}(\sqrt{L_{kl}}x)\left(x^2-\frac{3}{2}\right)x^2dx$$

$$\times\sum_{mnq}\mu_q(\alpha^i_{mq}\alpha^i_{nq}+\alpha^j_{mq}\alpha^j_{nq})(L_{mqkl}+L_{nqkl}-L_{mnkl}).$$

Here, we have introduced the additional notation

$$L_{klmn}\equiv\frac{\partial^2}{\partial\alpha_{kl}\partial\alpha_{kl}}\ln D,$$

$$g_{klmn}\equiv\sqrt{-L_{klmn}/L_{kl}L_{mn}}.$$

APPENDIX 2

Integrals I^{klm}

The integrals $I^{klm}(x_1, x_2, x_3)$ with nonnegative indices are homogeneous polynomials of degree $k+l+m+3$ in the variables

$$A_1\equiv(x_2+x_3)^{-1},\quad A_2\equiv(x_3+x_1)^{-1},$$

$$A_3\equiv(x_1+x_2)^{-1}.$$

In order to obtain upper variational bounds in problems involving Coulomb, exponential, or Yukawa potentials, we must calculate the following integrals and their combinations:

$$I^{000}=16\pi^2A_1A_2A_3,$$

$$I^{111}=2I^{000}((A_1+A_2)(A_2+A_3)(A_3+A_1)-A_1A_2A_3),$$

$$I^{011}=I^{000}(A_1A_2+A_2A_3+A_3A_1+2A_1^2),$$

$$T_1=2I^{111}-8I^{000}A_2A_3(A_2+A_3).$$

To deal with similar integrals featuring negative indices, it is convenient to introduce the notation

$$B_1\equiv(x_2-x_3)^{-1},\quad B_2\equiv(x_3-x_1)^{-1},\quad B_3\equiv(x_1-x_2)^{-1},$$

$$S^{[n]}_{C1}=B_1^n\ln\frac{A_2}{A_3}-B_1^{n-1}A_3-\ldots-\frac{B_1A_3^{n-1}}{n-1},$$

$$S^{[n]}_{E1}=B_1^n\ln\frac{A_2}{A_3}-B_1^{n-1}A_2+\ldots+(-1)^{n-1}\frac{B_1A_2^{n-1}}{n-1},$$

$$S^{[n]}_1=S^{[n]}_{C1}+S^{[n]}_{E1},$$

$$N^{[n]}=\frac{1}{n}\left(A_3^n\ln\frac{A_1}{A_2}-A_2^n\ln\frac{A_3}{A_1}-S^{[n]}_{C3}+(-1)^{n-1}S^{[n]}_{E2}\right).$$

In order to deduce lower variational bounds, we need the following integrals and their combinations:

$$I^{001}=I^{000}(A_1+A_2),$$

$$I^{-111}=A_1^3S^{[1]}_1-A_1S^{[3]}_1+I^{000}(A_1+(A_2+A_3)/2),$$

$$W_{11}=2I^{011}-4I^{000}A_2A_3,$$

$$W_{12}=2I^{000}A_1(A_3+2A_2)+4A_2^3S^{[2]}_2-4A_2^2S^{[3]}_2,$$

$$Q_{12}=4I^{111}-16I^{000}A_3(A_1^2+A_2^2)-32A_3^3S^{[3]}_3,$$

$$Q_{11}=12A_2(-2S^{[1]}_{E2}A_2^4+3S^{[2]}_{E2}A_2^3-3S^{[4]}_{E2}A_2+2S^{[5]}_{E2})$$
$$+12A_3(-2S^{[1]}_{C3}A_3^4-3S^{[2]}_{C3}A_3^3+3S^{[4]}_{C3}A_3+2S^{[5]}_{C3})$$
$$+4(T_1-I^{111})+I^{5-1-1},$$

$$I^{5-1-1}$$
$$=60\left\{\frac{1}{x_1}\left[N^{[5]}-A_2A_3\left(\frac{A_2^3}{4}+\frac{A_2^2A_3}{6}+\frac{A_2A_3^2}{6}+\frac{A_3^3}{4}\right)\right]\right.$$
$$+\frac{1}{x_1^2}\left[N^{[4]}-A_2A_3\left(\frac{A_2^2}{3}+\frac{A_2A_3}{4}+\frac{A_3^2}{3}\right)\right]$$
$$+\frac{1}{x_1^3}\left[N^{[3]}-A_2A_3\left(\frac{A_2}{2}+\frac{A_3}{2}\right)\right]$$
$$+\frac{1}{x_1^4}[N^{[2]}-A_2A_3]+\frac{1}{x_1^5}N^{[1]}+\frac{1}{x_1^6}\left[\mathrm{Li}_2\left(1-\frac{A_2}{A_1}\right)\right.$$
$$\left.\left.+\mathrm{Li}_2\left(1-\frac{A_3}{A_1}\right)+\frac{1}{2}\ln^2\frac{A_2}{A_3}+\frac{\pi^2}{6}\right]\right\}.$$

Here, Li_2 is a dilogarithmic function.

In the case where the parameters $u=x_1/x_2$ and $v=x_1/x_3$ are small simultaneously, we can use the expansions

$$I^{5-1-1}=x_2^{-6}\sum_{n=0}^\infty u^nP_{n+5}(w)\frac{(n+5)!}{n!(n+6)}$$
$$+x_3^{-6}\sum_{n=0}^\infty v^nP_{n+5}(w^{-1})\frac{(n+5)!}{n!(n+6)},$$

$$P_k(\alpha)=P_{k-2}(\alpha)-\frac{(-\alpha)^k}{k},\quad k=2,3,\ldots,$$

$$P_0=-\ln(1+\alpha),\quad P_1=1,\quad w=\frac{x_2}{x_3}.$$

These expressions are employed for $\max(u,v)<0.3$.

REFERENCES

1. G. Temple, Proc. R. Soc. London, Ser. A **119**, 276 (1928).
2. L. M. Delves, Adv. Nucl. Phys. **5**, 1 (1973).
3. Y. C. Tang, E. W. Schmid, and R. C. Herndon, Nucl. Phys. **65**, 203 (1965).
4. L. M. Delves, J. M. Blatt, and C. Pask, Phys. Lett. B **28**, 472 (1969).
5. N. N. Kolesnikov and V. I. Tarasov, Yad. Fiz. **35**, 609 (1982) [Sov. J. Nucl. Phys. **35**, 354 (1982)].

6. S. Nakaishi-Maeda, Y. Akaishi, and H. Tanaka, Prog. Theor. Phys. **64**, 1315 (1980).
7. S. Ali and A. R. Bodmer, Nucl. Phys. **80**, 99 (1966).
8. R. H. Dalitz and B. W. Downs, Phys. Rev. **110**, 958 (1958).
9. A. J. Thakkar and V. H. Smith, Phys. Rev. A **15**, 16 (1977).
10. N. N. Kolesnikov and V. A. Kopylov, Izv. Vyssh. Uchebn. Zaved., Fiz., No. 5, 36 (1983).
11. V. A. Kopylov, A. M. Frolov, and N. N. Kolesnikov, Izv. Vyssh. Uchebn. Zaved., Fiz., No. 10, 114 (1985).
12. A. M. Frolov and V. H. Smith, J. Phys. B **28**, L449 (1995).
13. V. I. Kukulin and V. M. Krasnopol'sky, J. Phys. G **3**, 795 (1977).
14. N. N. Kolesnikov, V. I. Tarasov, and M. I. Starostnikov, Available from VINITI, No. 3832-80 (Moscow, 1980).
15. N. N. Kolesnikov and V. I. Tarasov, Vestn. Mosk. Univ., Ser. 3: Fiz., Astron. **18** (6), 8 (1977).
16. K. Frankowski and C. L. Pekeris, Phys. Rev. **146**, 46 (1966).
17. C. Schwarz, Phys. Rev. **128**, 1146 (1962).

Translated by A. Isaakyan

Physics of Atomic Nuclei, Vol. 63, No. 3, 2000, pp. 365–372. Translated from Yadernaya Fizika, Vol. 63, No. 3, 2000, pp. 431–439.

NUCLEI
Nuclei

Studying Parity-Nonconservation Effect in the Conversion Transition between the Levels of the $(5/2)^{\pm}$ Doublet in the ^{229}Pa Nucleus

D. I. Grechukhin† and A. V. Lomonosov*

Russian Research Centre Kurchatov Institute, pl. Kurchatova 1, Moscow, 123182 Russia

Received April 8, 1999

Abstract—Effects of weak nucleon interaction are calculated for the ground-state doublet of $5/2^{\pm}$ levels of the strongly deformed nucleus $^{229}Pa_{91}$. A parity-nonconservation effect in the doublet states can be observed in the conversion spectrum for the isomeric transition between the doublet levels. By using a generalized model of the nucleus, the matrix element of the effective one-nucleon weak-interaction potential, which determines the weight of the opposite parity admixture in the doublet components is estimated in the single-particle approximation. The reduced probabilities of the $E1$ and $M1$ nuclear transitions between the doublet states are calculated within various models of the deformed nuclear potential. The effect of Coriolis forces on the dipole electric transition in question is considered. The lifetime of the upper doublet state is estimated. © *2000 MAIK "Nauka/Interperiodica".*

1. INTRODUCTION

It was predicted theoretically in [1] and established experimentally in [2, 3] that the ground state of the strongly deformed protoactinium nucleus ^{229}Pa actually represents a doublet of $I = 5/2$ states characterized by opposite parities (±), their energy splitting and the lifetime of the upper level being respectively, $\Delta E = 220 \pm 50$ eV and $\tau_{expt} = 0.6 \times 10^{-6}$ s.[1)]

In the interactions of ^{229}Pa nuclei with electrons, this unique situation can be used to observe parity-nonconservation effect in the doublet states—namely, in the conversion spectrum for the isomeric transition between the doublet levels and in the differential cross section for inelastic electron scattering leading to the excitation of this transition. The parity-mixed ($E1$ + $M1$) nuclear transition is almost completely saturated by the contribution of conversion channels (the internal-conversion ratio is about 10^4) featuring the upper electron shells $5d_{3/2}$, $5d_{5/2}$, $6s_{1/2}$, $6p_{1/2}$, $6p_{3/2}$, $6d_{3/2}$, $5f_{5/2}$, and $7s_{1/2}$ of the atom.

Among the effects that can be observed experimentally, there are those that are linear in the weak-interaction coupling constant G_F—for example, the helicity of conversion electrons in the multipolarity-mixed nuclear transition and the circular polarization of primary photons of atomic radiation that accompanies this transition under the condition that the momentum vector of a conversion electron is fixed—and those that are quadratic in G_F—for example, the effect that the admixture of the magnetic $M1$ multipole to the basic electric $E1$ multipole exerts on the intensities of the lines associated with the excitation of electron orbits of the ^{229}Pa atom via the conversion of the ($E1$ + $M1$) nuclear transition.

In the present study, we estimate the lifetime of the upper isomeric state of the doublet, thereby verifying the hypothesis of the one-nucleon structure of the doublet states. The wave functions of the orbitals involved were derived in the form of expansions in terms of a single-particle basis in a spherical Woods–Saxon potential, the expansion coefficients being taken from the tables presented by Gareev *et al.* [7]. In order to test the sensitivity of the results to the form of nuclear potential, we compare them with analytic estimates obtained on the basis of the Nilsson model with functions of the spherical oscillator basis [8].

We calculate here the reduced probabilities of the basic $E1$ and the admixed $M1$ nuclear transition and present a tentative estimate for the possible variations of the mixing amplitude in the ($E1$ + $M1$) transition that are due to uncertainties in the parameters appearing in the model of the nucleus used and to the possible complications of the structure of the doublet (because of Coriolis mixing).

2. MODEL WAVE FUNCTIONS OF THE $(5/2)^{\pm}$ DOUBLET OF STATES OF THE ^{229}Pa NUCLEUS

In order to describe the states of the strongly deformed nucleus ^{229}Pa, we make use of the generalized model of the nucleus due to Bohr and Mottelson [9]. In accordance with the experimental results pre-

† Deceased.

* e-mail: lomon@cerber.mbslab.kiae.ru

1) On the basis of their experiments, Levon *et al.* [4] questioned the existence of this doublet and proposed an alternative diagram of ^{229}Pa levels, but Sheline [5] and Ahmad [6] furnish additional evidence for the existence of the above doublet.

sented in [2], the ground state of the $^{229}Pa_{91}$ nucleus is interpreted here as the doublet of single-particle proton orbits with quantum numbers [523]5/2, –, 5/2 and [642]5/2, +, 5/2 (we follow here the $[Nn_Z\Lambda]\Omega, \Pi, I$ classification of orbits according to Nilsson [8]). The shape of the nucleus is determined by the expression

$$R(\vartheta', \varphi') = r_0 A^{1/3}\left[1 + \sum_{\lambda\mu}\beta_{\lambda\mu}Y_{\lambda\mu}(\vartheta', \varphi')\right], \quad (1)$$

where r_0 =1.28 fm, $Y_{\lambda\mu}(\vartheta', \varphi')$ are normalized spherical harmonics [$Y^*_{LM}(\vartheta, \varphi) = (-1)^M Y_{L-M}(\vartheta, \varphi)$], and $\beta_{\lambda\mu}$ are deformation parameters. In the laboratory frame, the wave function of a deformed nucleus has the form [8, 9]

$$\Psi_{IMK}(\mathbf{r}) = \sqrt{\frac{2I+1}{16\pi^2}}\varphi_{\text{vib}}\{\chi_{\Omega_p}(\mathbf{r}')\mathcal{D}^I_{MK}(\theta_i) + (-1)^{I-\sum j_p}\chi_{-\Omega_p}(\mathbf{r}')\mathcal{D}^I_{M-K}(\theta_i)\}, \quad (2)$$

where I is the total angular momentum of the nucleus, M is its projection onto the z axis that is fixed in space, and K is its projection onto the symmetry axis z' of the nucleus. The total angular momentum of the nucleus, **I**, is the sum of the angular momentum of the odd nucleon, **J**, and the angular momentum of the nuclear core, **R**, Ω_p being the projection of **J** onto the symmetry axis z' of the nucleus ($K \geq \Omega \geq 0$). The quantities $\mathcal{D}^I_{MK}(\theta_i)$ are the normalized elements of the rotation matrix [8, 9]. The single-particle wave function $\chi_{\Omega_p}(\mathbf{r}')$ is a solution to the Schrödinger equation in the strongly deformed model Woods–Saxon nuclear potential [7, 10] or in the Nilsson oscillator potential [8]. Within the model used in [7, 10], we have

$$\chi_{\Omega_p}(\mathbf{r}') = \sum_{nlj} c^{(\Omega_p)}_{nlj} F^{(\Omega_p)}_{nlj}(\mathbf{r}'), \quad (3)$$

where $F^{(\Omega_p)}_{nlj}(\mathbf{r}')$ are solutions to the Schrödinger equation in the spherically symmetric ($\beta_{\lambda\mu} \equiv 0$) Woods–Saxon potential, n is the radial quantum number, l is the orbital angular momentum of the nucleon, and j is the total angular momentum of the nucleon (**j** = **l** + **s**). The above solutions can be represented as

$$F^{(\Omega_p)}_{nlj}(\mathbf{r}') = R_{nlj}(r')\Omega_{jl\Omega_p}(\mathbf{r}'/r'), \quad (4)$$

where $\Omega_{jl\Omega_p}(\mathbf{r}'/r')$ is a spherical spinor of the form

$$\Omega_{jl\Omega_p}(\mathbf{r}'/r') = \sum_{\Lambda\Sigma} C^{j\Omega_p}_{l\Lambda s\Sigma} Y_{l\Lambda}(\mathbf{r}'/r')\phi_{s\Sigma}. \quad (5)$$

Here, Σ is the projection of the nucleon spin **s** onto the symmetry axis z' of the nucleus, Λ is the projection of the nucleon orbital angular momentum **l** onto the same axis, $C^{j\Omega_p}_{l\Lambda s\Sigma}$ is the relevant Clebsch–Gordan coefficient, and $\phi_{s\Sigma}$ is the nucleon spin wave function. The coefficients $c^{(\Omega_p)}_{nlj}$ were calculated in [7] and were presented in [10]; they satisfy the normalization condition

$$\sum_{nlj}\left|c^{(\Omega_p)}_{nlj}\right|^2 = 1. \quad (6)$$

The effective potential of weak interaction, $\hat{V}^N_{\text{PNC}}$, leads to the mixing of the doublet states, which is taken here into account in the first order of perturbation theory. The resulting states are then represented as

$$\widetilde{\left|\frac{5}{2}^-\right\rangle} = \left|[523]\frac{5}{2}, -, \frac{5}{2}\right\rangle + ib\left|[642]\frac{5}{2}, +, \frac{5}{2}\right\rangle,$$
$$\widetilde{\left|\frac{5}{2}^+\right\rangle} = \left|[642]\frac{5}{2}, +, \frac{5}{2}\right\rangle + ib\left|[523]\frac{5}{2}, -, \frac{5}{2}\right\rangle, \quad (7)$$

where b is a factor that characterizes the admixture of an opposite-parity state. We have

$$ib = \frac{\left\langle [642]\frac{5}{2}, +, \frac{5}{2}\middle|\hat{V}^N_{\text{PNC}}\middle|[523]\frac{5}{2}, -, \frac{5}{2}\right\rangle}{\Delta E}, \quad (8)$$

where $\Delta E > 0$.

The phases of the wave functions are chosen in such a way that the relevant matrix elements are purely imaginary quantities:

$$\left\langle [523]\frac{5}{2}, -, \frac{5}{2}\middle|\hat{V}^N_{\text{PNC}}\middle|[642]\frac{5}{2}, +, \frac{5}{2}\right\rangle^* = -\left\langle [523]\frac{5}{2}, -, \frac{5}{2}\middle|\hat{V}^N_{\text{PNC}}\middle|[642]\frac{5}{2}, +, \frac{5}{2}\right\rangle. \quad (9)$$

3. MATRIX ELEMENTS OF THE SINGLE-PARTICLE *E*1 TRANSITION BETWEEN THE [523]5/2, –, 5/2 AND [642]5/2, +, 5/2 STATES OF THE DEFORMED NUCLEUS ^{229}Pa

In the laboratory frame, the operator of the electric dipole transition of a proton has the form

$$\hat{\mathcal{M}}_e(1\mu) = e\frac{N}{A}rY_{1\mu}(\vartheta, \varphi). \quad (10)$$

Going over to the reference frame comoving with the nucleus and taking into account the equalities $I_1 = I_2 = I$ and $K_1 = K_2 = \Omega_1 = \Omega_2 = \Omega$, we find that the matrix element of this operator between the deformed-nucleus states $|I_1M_1\Omega_1\rangle$ and $|I_2M_2\Omega_2\rangle$ can be represented as

$$\langle I_2M_2\Omega_2K_2\left|\hat{\mathcal{M}}_e(1\mu)\right|I_1M_1\Omega_1K_1\rangle$$

$$= C^{I_2M_2}_{I_1M_1 1\mu} e\left(\frac{N}{A}\sqrt{\frac{3}{4\pi}}\sqrt{\frac{2I_1+1}{2I_2+1}}C^{I_2K_2}_{I_1K_1 1\kappa}\right)$$
$$\times\left\{\sum_{n_1l_1j_1n_2l_2j_2}\sum c^{(\Omega_1)}_{n_1l_1j_1}c^{(\Omega_2)}_{n_2l_2j_2}\sqrt{\frac{2j_1+1}{2j_2+1}}C^{l_20}_{l_1010}C^{j_2\Omega_2}_{j_1\Omega_1 1\kappa}\right. \quad (11)$$
$$\left.\times u(1l_2j_1s;\, l_1j_2)\int_0^\infty dr' r'^3 R_{n_2l_2j_2}(r')R_{n_1l_1j_1}(r')\right\},$$

where $\kappa = K_2 - K_1 = \Omega_2 - \Omega_1$.

By using the above formulas, we have calculated the reduced probability $B(E1;\ (5/2)^- \longrightarrow (5/2)^+)$ of the electric dipole transition within the model relying on the Woods–Saxon potential and within the Nilsson model. The results are presented in Tables 1 and 2, respectively. An estimate of the reduced probability for this transition according to Weisskopf [9] yields the value of $B_W(E_1;\ I_1 \longrightarrow I_2) = 2.75\ e^2\ \text{fm}^2$. Hence, the $E1$ transition between the [523]5/2, –, 5/2 and [642]5/2, +, 5/2 states of the deformed nucleus ^{229}Pa is suppressed in proportion to $(2.8–6.4) \times 10^{-4}$. The model based on the deformed oscillator potential leads to a stronger suppression of the $E1$ transition between these states. We note that either model predicts the growth of the reduced probability $B(E1;\ (5/2)^- \longrightarrow (5/2)^+)$ of the above electric dipole transition with increasing quadrupole deformation β_{20} of the nucleus.

4. ESTIMATING THE LIFETIME OF THE UPPER [(5/2)⁻] DOUBLET STATE OF THE ^{229}Pa NUCLEUS

As was indicated above, the transition between the [532]5/2, –, 5/2 and [642]5/2, +, 5/2 states of the deformed nucleus ^{229}Pa is almost completely saturated by the contribution of conversion channels.

By calculating the intensity of the conversion lines of the $E1$ nuclear transition for all electron subshells involved in the conversion process, we can obtain the total probability of conversion and the lifetime of the upper doublet level, which is to be compared with the experimental value of $\tau_{expt} = 0.6 \times 10^{-6}$ s [2]. The wave functions of the conversion electron are determined within the relativistic Hartree–Fock–Slater method. In order to assess the stability of the effect magnitude to uncertainties in the parameters of the atomic potential, we vary both the form of the exchange atomic potential and the population of the valence zone of the atom (a simulation of the effect of chemical environments). The details of our calculation of the total conversion probability can be found in [11]. For the ^{229}Pa atom, the total conversion probability was also computed in [12, 13].

For the $E1$ nuclear transition, the total conversion probability (that is, that which is summed over all electron shells of the atom) per unit time [14, 15] is given by

$$W_c^{\text{tot}}\left(E1;\ \frac{5^-}{2} \longrightarrow \frac{5^+}{2};\ \varepsilon_1 \longrightarrow \varepsilon_2\right)$$
$$= \frac{e^2 m_e}{\hbar^3 a_0^2} B\left(E1;\ \frac{5^-}{2} \longrightarrow \frac{5^+}{2}\right) w_e^{\text{tot}}(E1, \Delta E = \hbar\omega), \quad (12)$$

where $w_e^{\text{tot}}(E1, \Delta E = \hbar\omega)$ is the dimensionless electron-conversion factor for the $E1$ multipole (this factor is defined, for example, in [11, 14]), $B(E1;\ (5/2)^- \longrightarrow (5/2)^+)$ is the reduced probability of the electric dipole transition in e^2 fm^2 units, $\Delta E = \hbar\omega$, ε is the electron energy, and a_0 is the Bohr radius for the electron. The contribution of the admixed $M1$ nuclear transition to the total conversion probability can be disregarded; hence, the lifetime of the [523]5/2, –, 5/2 isomer of $^{229}Pa_{91}$ is determined completely by the $E1$ conversion nuclear transition.

For various values of the transition energy ΔE, the calculated dimensionless conversion factor for the $E1$ multipole, $w_e^{\text{tot}}(E1;\ \hbar\omega)$, and the calculated total conversion probability $W_c^{\text{tot}}(E1,\ (5/2)^- \longrightarrow (5/2)^+;\ \varepsilon_1 \longrightarrow \varepsilon_2)$ per unit time for the $E1$ nuclear transition are displayed in Table 3 versus the parameter β_{20} of the quadrupole deformation of the nucleus.

Thus, the estimated lifetime of the [523]5/2, –, 5/2 isomer of $^{229}Pa_{91}$, τ_{calc}, falls between 4×10^{-6} and 1×10^{-5} s. So dramatic a deviation of those estimates from the experimental value of $\tau_{expt} = 0.6 \times 10^{-6}$ s, which requires, however, a further refinement, may be due to the disregard of some factors in τ_{calc}—such as Coriolis

Table 1. Reduced probability $B(E1;\ 5/2^- \longrightarrow 5/2^+)$ of the electric dipole transition (the calculations were performed on the basis of the model employing the Woods–Saxon potential; ($\beta_{40} = 0.08$)

β_{20}	$B(E1;\ 5/2^- \longrightarrow 5/2^+) \times 10^3$, e^2 fm^{-2}
0.20	0.77
0.23	1.31
0.25	1.80

Table 2. Reduced probability $B(E1;\ 5/2^- \longrightarrow 5/2^+)$ of the electric dipole transition (the calculations were performed on the basis of the Nilsson model)

β_{20}	η	$B(E1;\ 5/2^- \longrightarrow 5/2^+) \times 10^3$, e^2 fm^{-2}
≈0.1	2	0.14
≈0.2	4	0.25
≈0.3	6	0.28

Table 3. Total electron conversion factor $w_e^{\mathrm{tot}}(E1,\ \Delta E = \hbar\omega)$ [for $5f_{5/2})^2(6d_{3/2})^1(7s_{1/2})^2$, a normal configuration of the protoactinium atom] and total conversion probability $W_e^{\mathrm{tot}}(E1;\ 5/2^- \longrightarrow 5/2^+)$ per unit time

ΔE, eV	$w_e^{\mathrm{tot}}(E1,\ \Delta E = \hbar\omega)$	$W_e^{\mathrm{tot}}(E1;\ 5/2^- \longrightarrow 5/2^+) \times 10^{-5}$, s^{-1}		
		$\beta_{20} = 0.20$	$\beta_{20} = 0.23$	$\beta_{20} = 0.25$
170	9.91	1.12	2.00	2.63
220	8.86	1.01	1.79	2.35
270	8.32	0.95	1.68	2.21

mixing, core polarization, and admixtures of multiparticle configurations—that affect the structure of the doublet states, rendering it more complicated. In this study, we restrict ourselves to estimating the effect of Coriolis forces, which admix nucleon orbits within an interval of ±5 MeV to the $5/2^{\pm}$ doublet states.

5. CORIOLIS MIXING OF PROTON ORBITS IN THE STRONGLY DEFORMED NUCLEUS $^{229}Pa_{91}$

In the laboratory frame, the Hamiltonian of the Coriolis interaction has the form [16]

$$\hat{H}_{\mathrm{Cor}} = -\frac{\hbar^2}{\mathcal{J}_0}(\hat{\mathbf{I}}\cdot\hat{\mathbf{J}}), \tag{13}$$

where $\mathcal{J}_0$ is the moment of inertia of the nuclear core with respect to the x' axis of an axisymmetric nucleus ($\mathcal{J}_{x'} = \mathcal{J}_{y'} = \mathcal{J}_0$).

The operator $\hat{H}_{\mathrm{Cor}}$ mixes the orbits that differ in the projections Ω of the total angular momentum J of the particle by $|\Delta\Omega| = 1$ and in the projections K of the total angular momentum I of the nucleus by $\Delta K = 1$. The $\Delta\Omega = 0$ term leads to the shift of the level only for $\Omega \geq 3/2$ [16]. Thus, the orbits $[Nn_Z\Lambda]3/2,\ -,\ 5/2$ and $[Nn_Z\Lambda]3/2,\ +,\ 5/2$ can be admixed to the original doublet components [5233]5/2, –, 5/2 and [642]5/2, +, 5/2, respectively; here, $\Omega \leq I$, $K_1 = \Omega_1$, and $K_2 = \Omega_2$. Gareev *et al.* [7] indicate the following series of such $\Omega = 3/2$ orbits: [532]3/2, –, 5/2; [521]3/2, –, 5/2; [512]3/2, –, 5/2; [501]3/2, –, 5/2; [411]3/2, +, 5/2; [402]3/2, +, 5/2; and [651]3/2, +, 5/2. In the first order of perturbation theory in the small parameter $\frac{\hbar^2}{\mathcal{J}_0}\frac{I(I+1)}{|E_1+E_2|}$, the expression for the first level of the doublet has the form

$$\left|[523]\frac{5}{2},-,\frac{5}{2}\right\rangle_c = A_1\left\{\left|[523]\frac{5}{2},-,\frac{5}{2}\right\rangle + A^{[532]\frac{3}{2},-,\frac{5}{2}}_{[523]\frac{5}{2},-,\frac{5}{2}}\times\left|[523]\frac{3}{2},-,\frac{5}{2}\right\rangle + A^{[521]\frac{3}{2},-,\frac{5}{2}}_{[523]\frac{5}{2},-,\frac{5}{2}}\times\left|[521]\frac{3}{2},-,\frac{5}{2}\right\rangle + A^{[512]\frac{3}{2},-,\frac{5}{2}}_{[523]\frac{5}{2},-,\frac{5}{2}}\times\left|[512]\frac{3}{2},-,\frac{5}{2}\right\rangle + A^{[501]\frac{3}{2},-,\frac{5}{2}}_{[523]\frac{5}{2},-,\frac{5}{2}}\times\left|[501]\frac{3}{2},-,\frac{5}{2}\right\rangle\right\}. \tag{14}$$

For the second level of the doublet, we have

$$\left|[642]\frac{5}{2},+,\frac{5}{2}\right\rangle_c = A_2\left\{\left|[642]\frac{5}{2},+,\frac{5}{2}\right\rangle + A^{[411]\frac{3}{2},+,\frac{5}{2}}_{[642]\frac{5}{2},+,\frac{5}{2}}\times\left|[411]\frac{3}{2},+,\frac{5}{2}\right\rangle + A^{[402]\frac{3}{2},+,\frac{5}{2}}_{[642]\frac{5}{2},+,\frac{5}{2}}\times\left|[402]\frac{3}{2},+,\frac{5}{2}\right\rangle + A^{[651]\frac{3}{2},+,\frac{5}{2}}_{[642]\frac{5}{2},+,\frac{5}{2}}\times\left|[651]\frac{3}{2},+,\frac{5}{2}\right\rangle\right\}. \tag{15}$$

In these expressions, A_1 and A_2 are new normalization constants, and

$$A^{[N_2n_{Z_2}\Lambda_2]\Omega_2,\,\Pi_2,\,I_2}_{[N_1n_{Z_1}\Lambda_1]\Omega_1,\,\Pi_1,\,I_1} = \frac{\langle[N_2n_{Z_2}\Lambda_2]\Omega_2,\,\Pi_2,\,I_2|\hat{H}_{\mathrm{cor}}|[N_1n_{Z_1}\Lambda_1]\Omega_1,\,\Pi_1,\,I_1\rangle}{E_{[N_1n_{Z_1}\Lambda_1]\Omega_1,\,\Pi_1,\,I_1} - E_{[N_2n_{Z_2}\Lambda_2]\Omega_2,\,\Pi_2,\,I_2}}. \tag{16}$$

The matrix elements of the Coriolis interaction operator $\hat{H}_{\mathrm{Cor}}$ ($\Omega_1 = 5/2$, $\Omega_2 = 3/2$) has the form

$$\langle I_2M_2\Omega_2\Pi_2K_2|\hat{H}_{\mathrm{Cor}}|I_1M_1\Omega_1\Pi_1K_1\rangle = -\frac{\hbar^2}{\mathcal{J}_0}\delta_{I_1I_2}\delta_{M_1M_2}\delta_{\Pi_1\Pi_2}\sqrt{I(I+1)}C^{I_2K_2}_{I_1K_1\,1K_2-K_1} \times\sum_{nlj}c^{(\Omega_1)}_{nlj}c^{(\Omega_2)}_{nlj}\sqrt{j(j+1)}C^{j\Omega_2}_{j\Omega_1\,1\Omega_2-\Omega_1}. \tag{17}$$

In order to calculate the matrix element $\langle[642]5/2,\ +,\ 5/2|_c\ \hat{\mathcal{M}}_e(1\mu)|[642]5/2,\ +,\ 5/2\rangle_c$ for the electric dipole transition being considered, we make use of equation (11). In this calculation, we take into account only the $E1$ transitions to the dominant orbitals of the superposition.

In accordance with the asymptotic selection rules [9], the allowed $\Delta\Omega = 0$ single-particle $E1$ transitions correspond to $\Delta N = 1$, $\Delta n_Z = 1$, $\Delta\Lambda = 0$, and $\Delta\Sigma = 0$, while the allowed $\Delta\Omega = 1$ single-particle $E1$ transitions correspond to $\Delta N = 1$, $\Delta n_Z = 0$, $\Delta\Lambda = \pm1$, and $\Delta\Sigma = 0$. All the transitions being considered are forbidden.

The spectrum of nuclear states of the core has not yet received adequate study; therefore, its moment of inertia $\mathcal{J}_0$ is uncertain to a considerable extent. The present calculations have been performed with $\hbar^2/\mathcal{J}_0$ = 10, 15, and 20 eV. The contribution of the admixed $E1$ transitions to the reduced probability (see Table 4) is small (less than 5%); hence, it has virtually no effect on the estimate of the isomer lifetime.

6. MATRIX ELEMENT OF THE NUCLEAR-VOLUME-AVERAGED POTENTIAL $\hat{V}^N_{\rm PNC}(\mathbf{r}, \hat{\mathbf{p}}, \hat{\boldsymbol{\sigma}})$ OF PARITY-NONCONSERVING FORCES FOR THE DEFORMED NUCLEUS ^{229}Pa

The simplest Hermitian operator of the effective parity-nonconserving potential acting on the odd nucleon (proton) has the form [17]

$$\hat{V}^N_{\rm PNC}(\mathbf{r}, \hat{\mathbf{p}}, \hat{\boldsymbol{\sigma}}) = \frac{G_{\rm F}}{2m_p c}\alpha(N, Z)\{(\hat{\boldsymbol{\sigma}}\cdot\hat{\mathbf{p}})\rho(\mathbf{r}) + \rho(\mathbf{r})(\hat{\boldsymbol{\sigma}}\cdot\hat{\mathbf{p}})\}. \quad (18)$$

Here, $G_{\rm F} = 10^{-5}\hbar^3/m_p^2 c$ is the Fermi constant of weak interaction; m_p is the proton mass; $\hat{\mathbf{p}}$ is the nucleon-momentum operator; $\hat{\boldsymbol{\sigma}}$ is the nucleon-spin operator; $\rho(\mathbf{r})$ is the density of the nucleon distribution over the volume of the deformed nucleus—it is taken in the Woods–Saxon form

$$\rho(\mathbf{r}') = -\frac{\rho_0}{[1 + \exp\{(r' - R(\vartheta', \varphi'))/a\}]}, \quad (19)$$

where $\rho_0 = (3/4\pi)(1/r_0)^3$; and $\alpha(N, Z)$ is a numerical coefficient of about unity. Data on the effects of parity nonconservation in resonance-neutron interactions with heavy ions can be interpreted in such a way that this coefficient is enhanced by one to two orders of magnitude; this in turn enhances, in the same proportion, the effects being discussed (see, for example, [18]). Nonetheless, we set $\alpha(N, Z) = 1$ in our ensuing calculations. By using the expansion in (1) and equation (19), we obtain

$$\rho(\mathbf{r}') = \sum_{\xi\mu}\rho_0\mathcal{B}_{\xi\mu}(r')Y_{\xi\mu}(\vartheta', \varphi'). \quad (20)$$

For axisymmetric nuclei, $\mu = 0$ and the quantities represented by ξ are even.

Let us now calculate the matrix element of the parity-nonconserving potential (18) between the [523]5/2, –, 5/2 and [642]5/2, +, 5/2 states of the deformed nucleus ^{229}Pa ($\Omega_{p1} = \Omega_{p2} = \Omega_p$, $I_1 = I_2 = I$, $K_1 = K_2 = \Omega_p$).

Table 4. Reduced probability $B(E1; 5/2^- \longrightarrow 5/2^+)$ of the electric dipole transition with allowance for Coriolis mixing of orbitals ($\beta_{40} = 0.08$)

$\hbar^2/\mathcal{T}_0$, eV	$B(E1; 5/2^- \longrightarrow 5/2^+) \times 10^3$, e^2 fm^2		
	$\beta_{20} = 0.20$	$\beta_{20} = 0.23$	$\beta_{20} = 0.25$
10	0.72	1.22	1.75
15	0.69	1.17	1.63
20	0.67	1.13	1.56

In the case of the wave function taken in the form (2), we arrive at

$$\begin{aligned}
\left\langle I_2M_2K_2\middle|\hat{V}^N_{\rm PNC}(\mathbf{r}, \hat{\mathbf{p}}, \hat{\boldsymbol{\sigma}})\middle|I_1M_1K_1\right\rangle &= \frac{G_{\rm F}}{2m_p c}\alpha(N, Z)\rho_0 \\
&\times\frac{1}{2}\delta_{I_1I_2}\delta_{M_1M_2}\delta_{K_1K_2}\sum_{n_1l_1j_1}\sum_{n_2l_2j_2}\sum_{\xi = 0, 2, 4, \ldots} C^{(\Omega_p)}_{n_1l_1j_1}C^{(\Omega_p)}_{n_2l_2j_2} \\
&\times(-i\hbar)\left(-\sqrt{\frac{2\xi+1}{4\pi}}\sqrt{2}\right)\left(\frac{(-1)^{\cdots}}{\sqrt{2j_2+1}}C^{j_2\Omega_p}_{j_1\Omega_p\xi0}\right) \\
&\times\left\{\sqrt{l_1+1}C^{l_20}_{l_1+10\xi0}u(l_1(l_1+1)ss;\,1j_1)\right. \\
&\times u(\xi l_2j_1s;\,(l_1+1)j_2)\int_0^\infty dr'r'^2R_{n_2l_2j_2}(r')\mathcal{B}_{\xi0}(r') \\
&\times\left[\frac{\partial R_{n_1l_1j_1}(r')}{\partial r'} - l_1\frac{R_{n_1l_1j_1}(r')}{r'}\right] + \sqrt{l_2+1}C^{j_10}_{l_2+10\xi0} \\
&\times u(l_2(l_2+1)ss;\,1j_2)u(\xi l_1j_2s;\,(l_2+1)j_1) \\
&\times\int_0^\infty dr'r'^2R_{n_1l_1j_1}(r')\mathcal{B}_{\xi0}(r')\left[\frac{\partial R_{n_2l_2j_2}(r')}{\partial r'} - l_2\frac{R_{n_2l_2j_2}(r')}{r'}\right] \\
&- \sqrt{l_1}C^{l_20}_{l_1-10\xi0}u(l_1(l_1+1)ss;\,1j_1) \\
&\times u(\xi l_2j_1s;\,(l_1+1)j_2)\int_0^\infty dr'r'^2R_{n_2l_2j_2}(r')\mathcal{B}_{\xi0}(r') \\
&\times\left[\frac{\partial R_{n_1l_1j_1}(r')}{\partial r'} + (l_1+1)\frac{R_{n_1l_1j_1}(r')}{r'}\right] \\
&- \sqrt{l_2}C^{l_10}_{l_2-10\xi0}u(l_2(l_2-1)ss;\,1j_2) \\
&\times u(\xi l_1j_2s;\,(l_2-1)j_1)\int_0^\infty dr'r'^2R_{n_1l_1j_1}(r')\mathcal{B}_{\xi0}(r') \\
&\times\left.\left[\frac{\partial R_{n_2l_2j_2}(r')}{\partial r'} + (l_2+1)\frac{R_{n_1l_1j_1}(r')}{r'}\right]\right\}. \quad (21)
\end{aligned}$$

Table 5. Matrix element $-i\langle[642]\frac{5}{2},+,\ \frac{5}{2}|\hat{V}^N_{\rm PNC}|[523]\frac{5}{2},-,\ \frac{5}{2}\rangle$ of the effective parity-nonconserving potential (the calculations were performed on the basis of the model employing the Woods–Saxon potential; $\beta_{40} = 0.08$)

β_{20}	$-i\langle[642]\frac{5}{2},+,\ \frac{5}{2}\|\hat{V}^N_{\rm PNC}\|[523]\frac{5}{2},-,\ \frac{5}{2}\rangle$, eV
0.20	0.48
0.23	0.52
0.25	0.55

Table 6. Matrix element $-i\langle[642]\frac{5}{2},+,\ \frac{5}{2}|\hat{V}^N_{\rm PNC}|[523]\frac{5}{2},-,\ \frac{5}{2}\rangle$ of the effective parity-nonconserving potential (the calculations were performed on the basis of the Nilsson model)

β_{20}	η	$-i\langle[642]\frac{5}{2},+,\ \frac{5}{2}\|\hat{V}^N_{\rm PNC}\|[523]\frac{5}{2},-,\ \frac{5}{2}\rangle$, eV
≈ 0.1	2	0.11
≈ 0.2	4	0.21
≈ 0.3	6	0.27

For the model based on the single-nucleon potential in the Woods–Saxon form, Table 5 displays the calculated matrix element of the operator $\hat{V}^N_{\rm PNC}(\mathbf{r}',\ \hat{\mathbf{p}},\ \hat{\boldsymbol{\sigma}})$ (18) between the [523]5/2, –, 5/2 and [642]5/2, +, 5/2 states of the deformed nucleus ^{229}Pa. Table 6 presents the results of analogous calculations within the Nilsson model.[2)] The coefficient b (8), which characterizes the weight of the opposite-parity admixture, is depicted in Fig. 1 as a function of the spacing ΔE between the levels in question; it is seen to vary between 1.6×10^{-3} and 3.2×10^{-3}.

Thus, our calculations have revealed that the parity-nonconserving potential $\hat{V}^N_{\rm PNC}(\mathbf{r},\ \hat{\mathbf{p}},\ \hat{\boldsymbol{\sigma}})$ generates a sizable mixing of the doublet components since the relevant matrix element of this potential is not suppressed owing to the complicated structure of the proton orbits that form the $5/2^{\pm}$ doublet of states in the spectrum of the strongly deformed nucleus $^{229}\mathrm{Pa}_{91}$.

7. MATRIX ELEMENT OF THE OPERATOR OF THE SINGLE-PARTICLE $M1$ TRANSITION BETWEEN THE [523]5/2, –, 5/2 AND [642]5/2, +, 5/2 STATES OF THE DEFORMED NUCLEUS ^{229}Pa

Only states characterized by identical parities contribute to the matrix element of the operator of the magnetic dipole transition between the parity-mixed $|\widetilde{5^-/2}\rangle$ and $|\widetilde{5^+/2}\rangle$ states (7) of the deformed nucleus ^{229}Pa. Therefore, the matrix element of the $M1$ transition is proportional to the difference of the magnetic moments for the [523] and [642] orbits, the mixing constant b (8) being the proportionality factor:

$$\left\langle\widetilde{\frac{5}{2}^+}\left|\hat{\mathcal{M}}_m(1\mu)\right|\widetilde{\frac{5}{2}^-}\right\rangle$$

$$= ib\left\{\left\langle[642]\frac{5}{2},+,\frac{5}{2}\left|\hat{\mathcal{M}}_m(1\mu)\right|[642]\frac{5}{2},+,\frac{5}{2}\right\rangle\right. \qquad (22)$$

$$\left.-\left\langle[523]\frac{5}{2},-,\frac{5}{2}\left|\hat{\mathcal{M}}_m(1\mu)\right|[523]\frac{5}{2},-,\frac{5}{2}\right\rangle\right\}.$$

In the laboratory frame, the operator of the magnetic dipole moment for the deformed nucleus with one odd nucleon has the form

$$\hat{\mathcal{M}}_m(1\mu) = \sqrt{\frac{3}{4\pi}}\mu_N \times[(g_s-g_l)\hat{s}_\mu+(g_l-g_R)\hat{j}_\mu+g_R\hat{I}_\mu], \qquad (23)$$

where $\mu_N = e\hbar/2m_pc$ is the nuclear magneton, $\hat{\mathbf{I}} = \hat{\mathbf{R}} + \hat{\mathbf{j}}$ is the total angular momentum of the whole nucleus, and $\hat{\mathbf{j}} = \hat{\mathbf{I}} + \hat{\mathbf{s}}$ is the total angular momentum of the odd nucleon. For the proton, we have (provided that the spin polarization of the core is disregarded) $g_s = 5.585$, $g_l = 1$, and $g_R = Z/A$. The operator $\hat{\mathbf{I}}$ is a complete integral

[2)]Here, we took into account only the spherically symmetric term ($\rho = 0$) in the interaction operator.

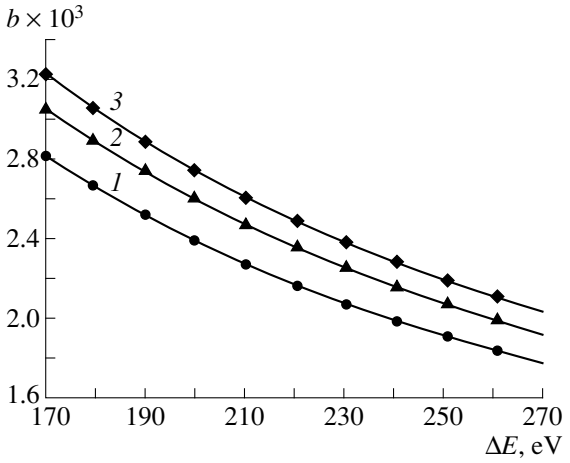

Fig. 1. Coefficient b (8), which characterizes the mixing of opposite-parity states, as a function of the spacing between these states for the quadrupole-deformation-parameter values of β_{20} = (*1*) 0.20, (*2*) 0.23, and (*3*) 0.25 (the calculations that yielded these results were based on the model employing the Woods–Saxon potential).

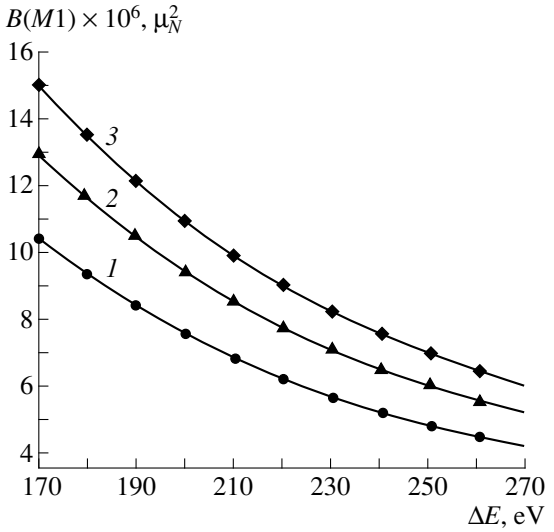

Fig. 2. Reduced probability $B(M1;\ \widetilde{5/2}^- \longrightarrow \widetilde{5/2}^+)$ of the magnetic dipole transition between the doublet states as a function of the spacing between these states for the quadrupole-deformation-parameter values of β_{20} = (*1*) 0.20, (*2*) 0.23, and (*3*) 0.25 (the calculations that yielded these results were based on the model employing the Woods–Saxon potential).

of the motion, whence it follows that, for the [523]5/2, –, 5/2 and [642]5/2, +, 5/2 orbits ($I_1 = I_2 = I = 5/2$), the relation

$$\langle IMK|\hat{\mathcal{M}}_m(1\mu)|I\tilde{M}K\rangle$$

$$= \sqrt{\frac{3}{4\pi}}\mu_B C^{IM}_{I\tilde{M}1\mu}\left\{g_R\sqrt{I(I+1)} + (g_l - g_R)\Omega_p C^{I\Omega_p}_{I\Omega_p 10}\right.$$

$$+ (g_s - g_l)\sqrt{s(s+1)}C^{I\Omega_p}_{I\Omega_p 10}\left[\sum_{nlj}\sum_{n'l'j'}\delta_{ll'}c^{(\Omega_p)}_{nlj}c^{(\Omega_p)}_{n'l'j'}\right. \quad (24)$$

$$\times(-1)^{j-j'}\sqrt{\frac{2j'+1}{2j+1}}u(j'l1s;\,sj)C^{j\Omega_p}_{j'\Omega_p 10}$$

$$\left.\left.\times\int_0^\infty dr' r'^2 R_{nlj}(r')R_{n'l'j'}(r')\right]\right\}$$

holds in the laboratory frame.

In the case being considered, we have $I_1 = I_2 = I$ and $\Omega_1 = \Omega_2 = \Omega$; therefore, the first two terms on the right-hand side of (24) do not contribute to the required difference.

Within the models relying on the Woods–Saxon potential and on the oscillator potential, we have calculated the reduced probability $B(M1;\ \widetilde{5/2}^- \longrightarrow \widetilde{5/2}^+)$ of the magnetic dipole transition between the $|\widetilde{5/2}^-\rangle$ and $|\widetilde{5/2}^+\rangle$ states of the deformed nucleus ^{229}Pa. The results of these calculations (in μ_N^2 units) are quoted in Tables 7 and 8 for the former and latter model versions, respectively. Either version predicts the growth of $B(M1;\ \widetilde{5/2}^- \longrightarrow \widetilde{5/2}^+)$ with increasing quadrupole-deformation parameter.

The resulting reduced probability $B(M1;\ \widetilde{5/2}^- \longrightarrow \widetilde{5/2}^+)$ of the magnetic dipole transition is on the same

Table 7. Reduced probability $B(M1;\ \widetilde{5/2}^- \longrightarrow \widetilde{5/2}^+)$ of the magnetic dipole transition (the calculations were performed on the basis of the model employing the Woods–Saxon potential; $\beta_{40} = 0.08$)

β_{20}	$B(M1;\ \widetilde{5/2}^- \longrightarrow \widetilde{5/2}^+)/b^2$, μ_N^2
0.20	1.31
0.23	1.39
0.25	1.44

Table 8. Reduced probability $B(M1;\ \widetilde{5/2}^- \longrightarrow \widetilde{5/2}^+)$ of the magnetic dipole transition (the calculations were performed on the basis of the Nilsson model)

β_{20}	η	$B(M1;\ \widetilde{5/2}^- \longrightarrow \widetilde{5/2}^+)/b^2$, μ_N^2
≈0.1	2	0.21
≈0.2	4	0.64
≈0.3	6	0.99

order of magnitude as the Weisskopf single-particle estimate $B_W(\widetilde{5/2}^- \longrightarrow \widetilde{5/2}^+) = 1.8\mu_N^2/b^2$; hence, the $M1$ transition between the states being considered is not suppressed. Figure 2 shows the reduced probability $B(M1; \widetilde{5/2}^- \longrightarrow \widetilde{5/2}^+)$ of the $M1$ transition as a function of the energy spacing between these levels.

8. CONCLUSION

Theoretical estimates of the parity-nonconserving single-particle nuclear potential depend on the scheme chosen for the formation of the weak interaction between nucleons. Quantitatively, estimates obtained within different schemes differ substantially. Available experimental data were obtained for nuclei having a complicated structure, and this reduces the reliability of quantitative data analysis. In the case of the $^{229}Pa_{91}$ nucleus, which is being considered here, there are grounds to interpret the levels of the $(5/2)^\pm$ doublet as single-particle ones. However, an additional experimental check upon this interpretation is required, the more so as an alternative diagram of protoactinium levels was proposed by Levon *et al.* [4] on the basis of their experimental study. It is also of interest to refine the lifetime of the [523]5/2, –, 5/2 isomer of the $^{229}Pa_{91}$ nucleus and to determine more precisely the energy splitting ΔE in the doublet.

It should be noted that, within this original interpretation of the $(5/2)^\pm$ doublet of states of the $^{229}Pa_{91}$ nucleus, the $E1$ transition is strongly suppressed, which leads to the estimated isomer lifetime of $\tau_{calc} \simeq 4 \times 10^{-6}$–$1 \times 10^{-5}$ s; at the same time, the experimental value, which requires, however, a refinement, is $\tau_{exp} \simeq 0.6 \times 10^{-6}$ s. We have shown that the inclusion of Coriolis forces does not remove this discrepancy. Possibly, the effect of nuclear-core polarization and the admixture of multiparticle configurations are factors that enhance the $E1$ transition in question.

We note that the above P-odd effect of mixing of the $(5/2)^\pm$ states in the spectrum of the $^{229}Pa_{91}$ nucleus can also be observed in the electron lines of conversion involving the outer $6s_{1/2}$, $6p_{1/2}$, $6p_{3/2}$, $6d_{3/2}$, $6d_{5/2}$, and $7s_{1/2}$ shells of the atom. By virtue of parity nonconservation, the $M1$ multipole is admixed to the dominant the $E1$ transition between the doublet states. From our calculations, it follows that the intensity of the $M1$ transition is suppressed in relation to the intensity of the $E1$ transition by four orders of magnitude. In the conversion channel, however, the $M1$ transition for some intense conversion lines is enhanced, according to our estimate, by a factor of about 10^2–10^3, which compensates, to a considerable extent, for the smallness of the doublet-mixing amplitude. A detailed discussion and estimates of parity-nonconservation effects accessible to observation will be presented elsewhere.

ACKNOWLEDGMENTS

We are grateful to A.L. Barabanov and B.V. Danilin for stimulating discussions on some aspects of this study and for some comments and suggestions.

This work was supported by the Russian Foundation for Basic Research (project no. 96-15-96548).

REFERENCES

1. R. R. Chasman, Phys. Lett. B **96**, 7 (1980).
2. I. Ahmad, J. E. Gindler, J. E. Betts, *et al.*, Phys. Rev. Lett. **49**, 1758 (1982).
3. I. Ahmad, R. R. Chasman, J. E. Gindler, *et al.*, Phys. Rev. Lett. **52**, 503 (1984).
4. A. I. Levon, J. de Boer, G. Grow, *et al.*, Nucl. Phys. **A576**, 267 (1994).
5. R. K. Sheline, Phys. Rev. C **48**, 1003 (1993).
6. I. Ahmad, in *Proceedings of the IV International Conference on Selected Topics in Nuclear Structure* (JINR, Dubna, 1994), No. E4-94-370, p. 193.
7. F. A. Gareev, S. P. Ivanova, and N. Yu. Shirkova, Preprint No. R4-5457, JINR (Joint Institute for Nuclear Research, 1970).
8. S. G. Nilsson, Mat. Fys. Medd. K. Dan. Vidensk. Selsk. **29** (16), 1 (1955).
9. A. Bohr and B. R. Mottelson, *Nuclear Structure* (Mir, Moscow, 1971, 1977; Benjamin, New York, 1969, 1975), Vols. 1, 2.
10. D. P. Grechukhin and A. V. Lomonosov, Preprint No. IAE-6117/2 (Russian Research Centre Kurchatov Inst., 1998).
11. D. P. Grechukhin and A. V. Lomonosov, Yad. Fiz. **62**, 2288 (1999) [Phys. At. Nucl. **62**, 2106 (1999)].
12. I. M. Band, M. A. Listengarten, and M. B. Trzhaskovskaya, Izv. Akad. Nauk, Ser. Fiz. **56** (11), 110 (1992).
13. O. Dragoun and M. Risavy, Phys. Rev. C **47**, 870 (1993).
14. D. P. Grechukhin and A. A. Soldatov, Preprint No. IAE-3174, IAE (Kurchatov Inst. of Atomic Energy, 1979).
15. A. I. Akhiezer and V. B. Berestetskiĭ, *Quantum Electrodynamics* (3rd ed., Nauka, Moscow, 1969; Wiley, New York, 1965).
16. J. M. Eisenberg and W. Greiner, *Nuclear Theory*, Vol. 1: *Nuclear Models, Collective and Single-Particle Phenomena* (Atomizdat, Moscow, 1975; North-Holland, Amsterdam, 1970).
17. R. J. Blin-Stoyle, *Fundamental Interactions and the Nucleus* (Mir, Moscow, 1976; North-Holland, Amsterdam, 1973).
18. J. J. Szhymansky, J. D. Bowman, M. Leuschner, *et al.*, Phys. Rev. C **49**, 3297 (1994).
19. F. A. Gareev, S. P. Ivanova, and B. N. Kalinkin, Preprint No. R4-3451, JINR (Joint Institute for Nuclear Research, 1967).

Translated by A. Isaakyan

Physics of Atomic Nuclei, Vol. 63, No. 3, 2000, pp. 373–376. Translated from Yadernaya Fizika, Vol. 63, No. 3, 2000, pp. 440–443.

NUCLEI
Theory

Nonconservation of the Quantum Number *K* and Phase Transitions in Rapidly Rotating Nuclei

A. M. Kamchatnov[1)] and V. G. Nosov

Russian Research Centre Kurchatov Institute, pl. Kurchatova 1, Moscow, 123182 Russia

Received June 25, 1998; in final form, March 12, 1999

Abstract—Three different effects observed in experiments with rotating nuclei—backbending, noncollective quadrupole transitions between different levels of the same band, and transitions that occur, in rapidly rotating nuclei, from large-*K* isomeric states immediately to the levels of a rotational band despite their strong forbiddenness in *K*—are explained in terms of nonconservation of the quantum number *K* in such nuclei. © *2000 MAIK "Nauka/Interperiodica".*

Shortly after the experimental discovery of backbending [1], it was assumed [2] that this phenomenon was due to the alignment of the angular momenta of constituent nucleons along the angular-velocity vector of the nucleus. However, the physics behind such alignment has not been clarified until now. That the above alignment is of a collective nature is supported by the entire body of data on the levels of rotational bands in various nuclei. In order to clarify this point in some detail, we can consider the frequency of a rotating nucleus as a function of the angular momentum *I*; from the graph of this function, which, at large values of *I*, has the form

$$\hbar\Omega = \frac{dE(I)}{dI}, \tag{1}$$

we can see that backbending is always accompanied by a fall of $\hbar\Omega$ below the rigid-body line

$$\hbar\Omega = \frac{\hbar^2}{\mathcal{J}_0}I, \tag{2}$$

where

$$\mathcal{J}_0 = \frac{2}{5}MR^2 \tag{3}$$

is the rigid-body value of the moment of inertia of the nucleus being considered, *M* and *R* being its radius and mass, respectively. For the first backbending, such a correlation is observed for each rotational band of a nonspherical nucleus. In contrast to this, secondary backbends occur completely under the rigid-body line, whereas so-called low-frequency anomalies [3, 4] show no correlation with this line. By way of illustration, the rotational frequency as a function of *I* is plotted in Fig. 1 for three rotational bands of the ^{160}Yb nucleus (experimental data on the transition energies for this nucleus were borrowed from [5]). For each of these bands, we see that, in the region of the first backbending, the rotational frequency as a function of *I* traverses the rigid-body line in the downward direction. In the rotational band built on the ground state of the ^{160}Y nucleus (that is, in the yrast line of this nucleus), the second backbending occurs below the rigid-body line. In the rotational band built on the $I^\pi = 6^-$ state, the low-*I* irregularity of Ω represents a low-frequency anomaly. Such anomalies are probably due to a noncollective alignment of an "odd" angular momentum, which is weakly coupled to the nuclear core [6, 7].

The above feature of the experimental *I* dependences of Ω suggests [8] that the first backbendings have a specific collective origin that distinguishes them both from higher backbendings and from low-frequency anomalies. Experimental data indicate that backbending has nothing to do with intersections of different bands; therefore, it may be viewed as an intrinsic property of a given band. In [8], we hypothesized that backbending results from nonconservation on the quantum number *K*, the projection of the total angular momentum onto the symmetry axis of the nucleus. Generally, the quantity $K = \mathbf{I}\cdot\mathbf{n}$ is well defined only in the limit $\Omega \longrightarrow 0$—that is, for a nucleus at rest. As soon as components with different values of *K* appear in the rotational density matrix of a nucleus, the angle ϑ between the direction of angular momentum **I** and the symmetry axis **n** of the nucleus becomes uncertain. For the spin of the nucleus in excess of some critical value, I_c, all *K* in the interval $-I \le K \le I$ become equiprobable. In this way, a smooth evolution of the scheme governing the coupling of angular momenta in a rotating nucleus is completed, resulting in a simple form of this coupling; the most typical mean values are then given by

$$\langle K\rangle = 0, \quad \langle K^2\rangle = \frac{I(I+1)}{3}, \quad \langle\cos^2\vartheta\rangle = \frac{1}{3}; \tag{4}$$

[1)] Institute of Spectroscopy, Russian Academy of Sciences, Troitsk, Moscow oblast, 142092 Russia.

1063-7788/00/6303-0373$20.00 © 2000 MAIK "Nauka/Interperiodica"

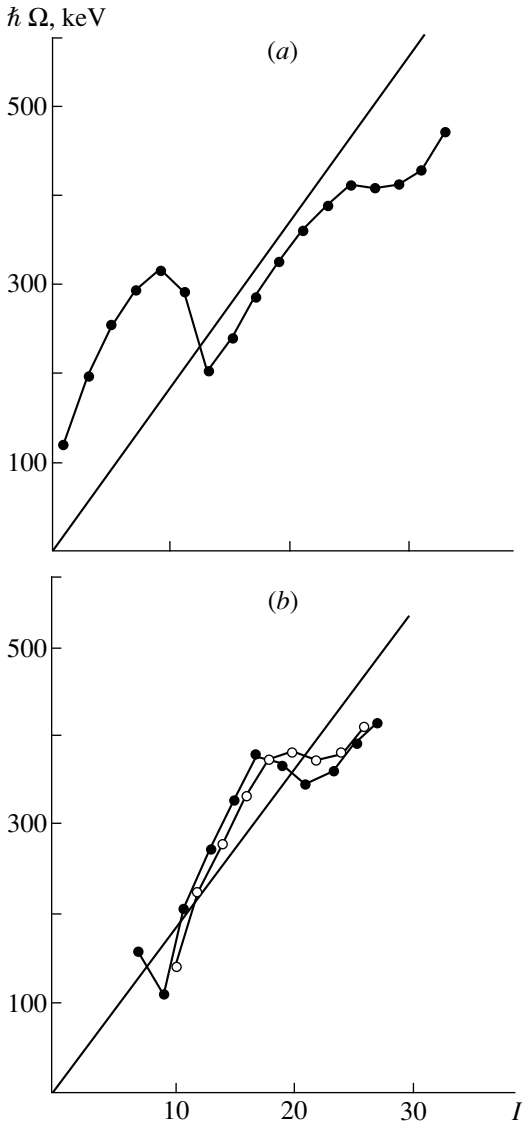

Fig. 1. Rotational frequency Ω as a function of the angular momentum I (*a*) for the yrast line of the ^{160}Yb nucleus and (*b*) for the I^{π} = (closed circles) 6^- and (open circles) 9^- bands of the same nucleus. For the yrast line of ^{160}Yb, the critical value of the angular momentum is 12.5. The straight line corresponds to the rigid-body approximation.

that is, we go over from a less symmetric to a more symmetric rotational state: in particular, the distribution of the angle ϑ becomes isotropic [see the last relation in (4)]. The critical value of the nuclear spin, I_c, corresponds to the first backbending of the rotational band being considered; experimentally, this backbending manifests itself as the above intersection of the rigid-body line.

The above collective (macroscopic) transition that involves a change in symmetry is naturally formulated within the theory of phase transitions due to Landau [9]. In [8, 10–12], the required formalism was developed in terms of the order parameter

$$\eta = 1 - \frac{3\langle K^2\rangle}{I(I+1)}, \tag{5}$$

which vanishes in the more symmetric $I \geq I_c$ phase—we refer to it as the *n* phase. At the point where $\Omega(I)$ intersects the rigid-body line in the region of the first backbending, we have

$$\hbar\Omega_{nc} = \frac{\hbar^2}{\mathcal{J}_0} I_c, \tag{6}$$

where Ω_{nc} is the value of the rotational frequency at I values just above I_c—that is, at the onset of the *n* phase.

Let us describe the situation in some detail. In the limit of adiabatically slow rotation, the wave function can be represented as

$$D^I_{KM}(\mathbf{n})\chi_K(\xi).$$

If, however, the values of I and $M = I_z$ are fixed, the total wave function of a nonspherical nucleus generally has the form

$$\Psi_{IM} = \sum_{K=-I}^{I} D^I_{KM}(\mathbf{n}) c^I_K \chi_K(\xi). \tag{7}$$

In order to obtain a self-consistent description in terms of the collective variable $\mathbf{n}$, we assume, as usual, that the extrinsic and intrinsic values of K coincide:

$$\mathbf{I}\cdot\mathbf{n} \equiv K_\xi. \tag{8}$$

Upon the convolution of the internal (nonrotational) variables ξ, the relevant density matrix takes the form

$$\rho(\mathbf{n},\mathbf{n}') = \sum_{K=-I}^{I} w(K) D^I_{KM}(\mathbf{n}) D^{I*}_{KM}(\mathbf{n}'),$$
$$w(K) = \left|c^I_K\right|^2. \tag{9}$$

In the representation of three angular-momentum variables I, M, and K, the rotational density matrix has the particularly simple form

$$\rho_{I_0M_0}(I, M, K;\ I', M', K') = \delta_{II_0}\delta_{I'I_0}\delta_{MM_0}\delta_{M'M_0}\delta_{KK'}w(K). \tag{10}$$

Generally, the rotational state $\delta_{KK'}w(K)$ is mixed—it becomes pure and factorizes only for the degenerate case where K assumes a definite value. In the region $I \geq I_c$, where the scheme of coupling of angular momenta is simplified, we have $w(K) = (2I+1)^{-1}$.

The proposed interpretation of the backbending phenomenon must be verified or disproved by confronting other predictions of the underlying approach with data. One of the possible checks was indicated in [8]. The probability w of electric quadrupole transitions between different levels of a band is known to depend on K^2. Therefore, a calculation of the lifetime of a state that picks up contributions characterized by different values of K necessarily involves averaging over the K

distribution. In the semiclassical approximation, the probability w for $I \gg 1$ was derived in [8, 12] as

$$w = \frac{e^2\omega^5}{360\hbar c^5}\left(1+\frac{\eta}{2}\right)^2 Q_0^2, \quad (11)$$

where $\omega = 2\Omega$ and Q_0 is the macroscopic quadrupole moment of the nucleus due to its deformation. At the same time, the result at $K = 0$ is

$$w = \frac{e^2\omega^5}{40\hbar c^5}\frac{I(I-1)}{(2I-1)(2I+1)}Q_0^2.$$

By somewhat formally defining the quantity Q_I as

$$Q_I^2 = \frac{4}{9}\left(1+\frac{\eta}{2}\right)^2 Q_0^2, \quad (12)$$

we finally arrive at the interpolation formula

$$w = \frac{e^2\omega^5}{40\hbar c^5}\frac{I(I-1)}{(2I-1)(2I+1)}Q_I^2, \quad (13)$$

which holds approximately for all values of I. We can see that, in the n phase ($I \geq I_c$), the effective quadrupole moment for radiative transitions, Q_I, amounts to only two-thirds of the quadrupole moment Q_0 for the lowest value of I in the yrast band of an even–even nucleus. The predictions are conveniently compared with the data in terms of the ratio Q_I^2/Q_0^2, where Q_0 is the quadrupole moment for the $2^+ \longrightarrow 0^+$ transition. We have

$$\zeta = \frac{Q_I^2}{Q_0^2} = \frac{2}{15}\frac{(2I-1)(2I+1)}{I(I-1)}\left(\frac{\omega_{2\to 0}}{\omega_{I\to I-2}}\right)^5 \frac{w_{I\to I-2}}{w_{2\to 0}}. \quad (14)$$

That the probability of quadrupole transitions in a rotational band decreases with increasing I was indeed observed experimentally (see, for example, [13]), but no attempt has been made to relate this phenomenon, referred to as the loss of collectivity, to nonconservation of K in rapidly rotating nuclei. The observed I dependence of the ratio ζ_I for the yrast line of the ^{160}Yb nucleus [14] is displayed in Fig. 2 along with our predictions. As a rule, $\zeta_I \leq 1$, and the experimental values of ζ_I tend to decrease with increasing I. Because of large uncertainties, the agreement with the prediction is not compelling.

Previously, there was one more experimental finding that supports the hypothesis of K nonconservation in rapidly rotating nuclei. We mean here the observation of direct radiative transitions from the large-K isomeric states of the ^{182}Os, ^{174}Hf, and ^{179}W nuclides to the levels of the rotational bands built on the corresponding ground states [15–19]. Had K been constant throughout the above bands, such radiative transitions would be strongly forbidden. That these transitions occur only to higher levels in the vicinity of backbending suggests that the amount of K nonconservation increases as I approaches the critical spin value I_c. Yet another important observation is that some transitions to different bands of the ^{174}Hf nucleus (namely, to the ground-state band, to the band built on the β-vibrational state of the nucleus, and to the octupole and hexadecapole bands) are characterized by very similar delay factors f_ν ($\nu = |K_i - K_f| - \lambda$ is the order of forbiddenness in K, λ being the multipolarity of the transition from the state i to the state f). This implies that violation of the quantum number K has a universal character independent of the structure of a particular band. Likewise, the data are consistent with the assumption that final states are broadly spread in K.

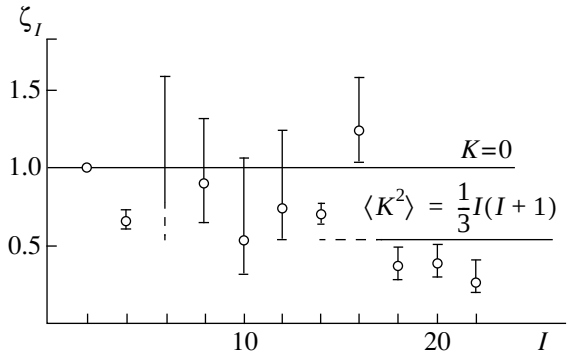

Fig. 2. Squared ratio of the effective quadrupole momentum in the yrast line of ^{160}Yb to the quadrupole momentum for the $2^+ \longrightarrow 0^+$ transition [see equation (14)] versus the angular momentum I.

To summarize, nonconservation of the quantum number K provides a clue to understanding the aforementioned phenomena. Experimental data suggest that K is violated because the scheme of coupling of angular momenta gradually evolves as I increases within a band.

REFERENCES

1. A. Johnson, H. Ryde, and J. Starkier, Phys. Lett. B **34**, 605 (1971).
2. F. S. Stephens and R. S. Simon, Nucl. Phys. **A183**, 257 (1972).
3. J. L. Durrell, D. G. Dracoulis, C. Fahlander, *et al.*, Phys. Lett. B **115**, 367 (1982).
4. J. C. Wells, N. R. Johnson, C. Baktash, *et al.*, Phys. Rev. C **36**, 431 (1987).
5. L. L. Riedinger, Phys. Scr. **5**, 36 (1983).
6. A. M. Kamchatnov, Zh. Éksp. Teor. Fiz. **98**, 754 (1990) [Sov. Phys. JETP **71**, 418 (1990)].
7. A. M. Kamchatnov, J. Phys. G **16**, 1203 (1990).
8. V. G. Nosov and A. M. Kamchatnov, Zh. Éksp. Teor. Fiz. **73**, 785 (1977) [Sov. Phys. JETP **46**, 411 (1977)].
9. L. D. Landau and E. M. Lifshitz, *Statistical Physics* (Nauka, Moscow, 1976; Pergamon, Oxford, 1980), Part 1.
10. V. G. Nosov and A. M. Kamchatnov, Zh. Éksp. Teor. Fiz. **76**, 1506 (1979) [Sov. Phys. JETP **49**, 765 (1979)].

11. V. G. Nosov and A. M. Kamchatnov, Zh. Éksp. Teor. Fiz. **80**, 433 (1981) [Sov. Phys. JETP **53**, 221 (1981)].
12. V. G. Nosov, *Macroscopic Quantum Effects in Atomic Nuclei* (Atomizdat, Moscow, 1980).
13. J. C. Lisle, D. Clarke, R. Chapman, *et al.*, Nucl. Phys. **A520**, 451 (1990).
14. M. P. Fewell, N. R. Johnson, F. K. McGowan, *et al.*, Phys. Rev. C **31**, 1057 (1985); **37**, 101 (1988).
15. J. Pedersen, B. B. Back, S. Bjornholm, *et al.*, Phys. Rev. Lett. **54**, 306 (1985).
16. P. Choudhury, B. Fabricius, C. Christensen, *et al.*, Nucl. Phys. **A485**, 136 (1988).
17. P. M. Walker, G. Sletten, N. L. Gjorup, *et al.*, Phys. Rev. Lett. **65**, 416 (1990).
18. G. Sletten, N. L. Gjorup, S. Juutinen, *et al.*, Nucl. Phys. **A520**, 325 (1990).
19. P. M. Walker, G. D. Dracoulis, A. P. Byrne, *et al.*, Phys. Rev. Lett. **67**, 433 (1991).

Translated by A. Asratyan

Physics of Atomic Nuclei, Vol. 63, No. 3, 2000, pp. 377–390. Translated from Yadernaya Fizika, Vol. 63, No. 3, 2000, pp. 444–458.

NUCLEI
Theory

Coupled-Channel Description of the Photodisintegration of ^{24}Mg, ^{28}Si, and ^{32}S Nuclei within the Intermediate-Coupling Scheme

E. N. Golovach, B. S. Ishkhanov, and V. N. Orlin

Institute of Nuclear Physics, Moscow State University, Vorob'evy gory, Moscow, 119899 Russia

Received January 25, 1999; in final form, April 23, 1999

Abstract—The coupled-channel method is used to calculate photonuclear reactions on ^{24}Mg, ^{28}Si, and ^{32}S nuclei within the intermediate-coupling scheme. The origin of relatively narrow peaks corresponding to photoabsorption on these nuclei is studied. Partial channels of giant-dipole-resonance decay are considered. It is shown that the splitting of the giant dipole resonance in the ^{24}Mg nucleus into two broad maxima is due to the deformation of its surface. © *2000 MAIK "Nauka/Interperiodica".*

1. INTRODUCTION

In light and medium-mass nuclei ($A \le 100$) with unfilled outer shells, giant multipole resonances (GMR) are formed from configurations of the *particle* + (*A – 1*) *core in an excited state* and *hole* + (*A + 1*) *core in an excited state* type rather than from configurations of the *particle + hole* type because particle and hole excitations of the valence shell that are generated by primary single-particle transitions (see Fig. 1) decay fast, transferring their energy to a large number of valence nucleons. This circumstance was partly taken into account in [1–3], where basis configurations of the *particle* + (*A – 1*) *core* type were used in calculating GMRs in 1*p*-shell nuclei within the so-called intermediate-coupling scheme, but where configurations corresponding to single-particle transitions from deep filled levels were disregarded.

Calculations within the intermediate-coupling scheme have not become popular because it is difficult to treat quantitatively low-lying states of heavy and medium-mass nuclei in the full configuration space of the valence shell. Recently, a method for computing low-lying nuclear states by consecutively adding nucleons to the nuclear system was proposed in [4]. In this method, a relatively small number of basis states are used at each step of the calculations. The method is applicable not only to light but also to medium-mass nuclei. Owing to this, a version of the coupled-channel method within the intermediate-coupling scheme could be developed in a form that is rather simple, but which is suitable for calculating the structure and decay features of GMRs in light and medium-mass nuclei with unfilled outer shells [5].

In [5], nucleon–nucleus scattering states $|(\alpha\mathcal{B})^{(\pm)}_\Lambda\rangle$ that feature diverging (+) or converging (–) spherical waves at infinity were represented in the form

$$|(\alpha\mathcal{B})^{(\pm)}_\Lambda\rangle = \sum_{\alpha'}\sum_{\mathcal{B}'}\langle(\alpha'\mathcal{B}')_\Lambda|(\alpha\mathcal{B})^{(\pm)}_\Lambda\rangle|(\alpha'\mathcal{B}')_\Lambda\rangle + \sum_{\gamma'}\sum_{\mathcal{A}'}\langle(\gamma'\mathcal{A}')_\Lambda|(\alpha\mathcal{B})^{(\pm)}_\Lambda\rangle|(\gamma'\mathcal{A}')_\Lambda\rangle, \quad (1)$$

where Λ is the total angular momentum of the nucleon system (if isospin is considered to be a good quantum number, Λ will represent the set of quantum numbers that includes the above angular momentum and the

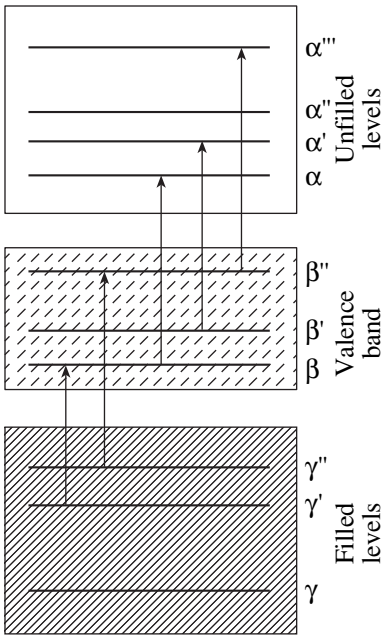

Fig. 1. Basic types of single-particle transitions leading to the formation of giant resonances in light and medium-mass nuclei.

1063-7788/00/6303-0377$20.00

isospin moment of the system); $\alpha \equiv \varepsilon_\alpha \vec{\alpha} \equiv \varepsilon_\alpha l_\alpha j_\alpha m_\alpha \tau_\alpha$, α', … stand for the quantum numbers characterizing unfilled single-particle states in the mean nuclear field $u(r)$; γ, γ', … are quantum numbers of filled single-particle states in the mean nuclear field $u(r)$; $|(\alpha\mathcal{B})_\Lambda\rangle \equiv (a_\alpha^+|\mathcal{B}\rangle)_\Lambda$, $|(\alpha'\mathcal{B}')_\Lambda\rangle$, … are basis wave functions that describe open and closed channels of the *particle* + (*A* – *1*) *core* type (by a channel, we mean here a partition of the nuclear system in question into two components); $|(\gamma\mathcal{A})_\Lambda\rangle \equiv (a_\gamma|\mathcal{A}\rangle)_\Lambda$, $|(\gamma'\mathcal{A}')_\Lambda\rangle$, … are basis wave function that describe closed channels of the *hole* + (*A* + *1*) *core* type; a_λ^+ and a_λ are the operators of, respectively, nucleon creation and annihilation in the single-particle state $|\lambda\rangle$; $|\mathcal{B}\rangle$, $|\mathcal{B}'\rangle$, … ($|\mathcal{A}\rangle$, $|\mathcal{A}'\rangle$, …) are low-lying natural-parity excited states of the $A - 1$ ($A + 1$) nucleus that diagonalize the nuclear Hamiltonian within the configuration space of the valence shell; and $\sum_x$ denotes summation over discrete quantum numbers and integration with respect to continuous quantum numbers *x*.

This approximation provides a natural generalization of the standard 1*p*1*h* approximation for light and medium-mass nuclei with unfilled shells; in just the same way as the latter, it takes no account of correlations in the ground state of the nucleus.

The expansion coefficients $\langle(\alpha'\mathcal{B}')_\Lambda|(\alpha\mathcal{B})_\Lambda^{(\pm)}\rangle$ and $\langle(\gamma'\mathcal{A}')_\Lambda|(\alpha\mathcal{B})_\Lambda^{(\pm)}\rangle$ characterize the contributions of various $\alpha'\mathcal{B}'$ and $\gamma'\mathcal{A}'$ channels to the scattering state $|(\alpha\mathcal{B})_\Lambda^{(\pm)}\rangle$. Coupling between the channels arises in the internal region of the reaction in question, where the residual nucleon–nucleon forces V_{res} are operative over distances $r < R_0 \approx 1.5A^{1/3}$. In a finite spatial region, single-particle states $|\alpha\rangle$ of the continuous spectrum can be expanded in terms of a discrete set of the oscillator functions $\{|n\vec{\alpha}\rangle\}$ as

$$|\alpha\rangle = \sum_n \langle n\vec{\alpha}|\alpha\rangle|n\vec{\alpha}\rangle \quad \text{for} \quad r < R_0, \tag{2}$$

where $n = 0, 1, 2, \ldots$ is the number of the oscillator quanta. For the channel amplitudes, we therefore have the relation

$$\langle(\alpha'\mathcal{B}')_\Lambda|(\alpha\mathcal{B})_\Lambda^{(\pm)}\rangle = \sum_{n'} \langle\alpha'|n'\vec{\alpha}'\rangle\langle(n'\vec{\alpha}', \mathcal{B}')_\Lambda|(\alpha\mathcal{B})_\Lambda^{(\pm)}\rangle \quad \text{for} \quad r < R_0. \tag{3}$$

The scalar products $\langle(n'\vec{\alpha}', \mathcal{B}')_\Lambda|(\alpha\mathcal{B})_\Lambda^{(\pm)}\rangle$ and $\langle(\gamma'\mathcal{A}')_\Lambda|(\alpha\mathcal{B})_\Lambda^{(\pm)}\rangle$ describe the configurational content of the scattering state in the internal region of the reaction being considered. They determine completely all the characteristics of the nuclear reaction. In particular, the amplitude of the probability for the transition of a nucleus from the ground state $|\Psi_0\rangle$ to the scattering state $|(\alpha\mathcal{B})_\Lambda^{(\pm)}\rangle$ under the effect of the multipole operator F_λ that is responsible for GMR excitation can be expressed in terms of these scalar products. In [5], a compact set of algebraic equations (equations of channel coupling) was derived for the quantities $\langle(n'\vec{\alpha}', \mathcal{B}')_\Lambda|(\alpha\mathcal{B})_\Lambda^{(\pm)}\rangle$ and $\langle(\gamma'\mathcal{A}')_\Lambda|(\alpha\mathcal{B})_\Lambda^{(\pm)}\rangle$. The matrix for this set of equations was obtained within standard shell-model calculations in the basis $\{|(\alpha\mathcal{B})_\Lambda\rangle, |(\gamma\mathcal{A})_\Lambda\rangle\}$, which in turn was computed by the procedure proposed in [4].

In the present study, the model in question is employed to describe the photodisintegration of ^{24}Mg, ^{28}Si, and ^{32}S nuclei in the giant-dipole-resonance (GDR) region.

2. DETAILS OF THE CALCULATIONS

The interaction of nuclei with an electromagnetic field can be taken into account by perturbation theory. In the absorption of a photon with energy *E* between about 8 and 30 MeV by a nucleus, a dominant role is played by electric-dipole-excitation processes leading to the formation of a GDR, which subsequently decays into a residual nucleus and a nucleon. In order to obtain the effective cross sections for photonuclear reactions, it is then sufficient to calculate the amplitudes of the probabilities for the electric-dipole transitions, $\langle(\alpha\mathcal{B})_\Lambda^{(-)}|(D|\Psi_0\rangle)_\Lambda$, where *D* is the electric-dipole-moment operator. These probability amplitudes can be represented as linear combinations of the scattering-state components $\langle(n'\vec{\alpha}', \mathcal{B}')_\Lambda|(\alpha\mathcal{B})_\Lambda^{(-)}\rangle$ and $\langle(\gamma'\mathcal{A}')_\Lambda|(\alpha\mathcal{B})_\Lambda^{(-)}\rangle$ in the internal region of the reaction [5].

In order to simplify the calculations, we assume that nuclear Hamiltonian is invariant under the charge-conjugation operation and that the isospin is a good quantum number. In actual nuclei, these assumptions are violated because neutrons and protons move in different potential wells and have different separation thresholds. Therefore, only proton features [in describing (γ, *p*) reactions] or only neutron features [in describing (γ, *n*) reactions] are usually included in calculations that take into account isospin conservation in light nuclei [6]. It should be emphasized, however, that the use of the same potential well for neutrons and for protons and of the same separation threshold for these particle species gives no way to take into account the effect of these factors on the competition between the neutron and proton channels of GDR decay. The fact that this procedure is not correct has an especially strong effect on the description of the photodisintegration of $N \neq Z$ nuclei (owing to the strong impact of the neutron excess on the nucleon-separation thresholds). Taking this into account, we restricted our consideration to three self-conjugate nuclei, ^{24}Mg, ^{28}Si, and ^{32}S, not belonging to close vicinities of the beginning or the end of the 1*d*2*s*

shell, in order to avoid dealing with strong correlations in the ground state of the nucleus.

For these nuclei, we have calculated the partial photoproton cross sections $\sigma(\gamma, p_i)$ corresponding to the ground state ($i = 0$), the first excited state ($i = 1$), and other states of the final nucleus, as well as the total cross section for $E1$ absorption, $\sigma_{abs} \approx 2[\sigma(\gamma, p_0) + \sigma(\gamma, p_1) + \sigma(\gamma, p_2) + \ldots]$. We did not consider the photoneutron cross sections because, within the isospin formalism, the reaction cross sections for the neutron channels of photodisintegration on self-conjugate nuclei are close to those for the proton channels.

2.1. Single-Particle States

For the $1d2s$ shell nuclei, the unfilled single-particle states $\{|\alpha\rangle\}$, the valence states $\{|\beta\rangle\}$, and the filled states $\{|\gamma\rangle\}$ correspond, respectively, to $1f_{7/2,\,5/2}$ and $2p_{3/2,\,1/2}$, to $1d_{5/2,\,3/2}$ and $2s_{1/2}$, and to $1p_{3/2,\,1/2}$ orbitals (see Fig. 1).

In calculating the single-particle states $|1f_{7/2,\,5/2}\rangle$ and $|2p_{3/2,\,1/2}\rangle$, we used the proton potential

$$u(r) = u_0 f_0(r) + (u_s/r)(df_s(r)/dr)\mathbf{l}\cdot\boldsymbol{\sigma} + u_{\mathrm{Coul}}(r), \quad (4)$$

where u_0 and u_s are amplitudes of, respectively, nuclear and spin–orbit interactions; $u_{\mathrm{Coul}}(r)$ is the Coulomb potential; and $f_0(r)$ and $f_s(r)$ are the Woods–Saxon form factors. With the exception of the nuclear-potential-well depth u_0, which is generally dependent on the orbital quantum number l, the parameters of these potentials were chosen to be identical to those in the global optical model [7]. On the basis of data presented in [8] for one-nucleon-transfer reactions, we can obtain an upper bound on the depth of the nuclear-potential well for f states (by using the energy of the $1f_{7/2}$ level): $u_{0f} \leq 64$, 60, and 58 MeV for ^{24}Mg, ^{28}Si, and ^{32}S, respectively. The eventual values of the parameters u_{0f} and u_{0p} were found by varying them in the course of calculations. They are presented in Table 1. The states $|1f_{7/2,\,5/2}\rangle$ and $|2p_{3/2,\,1/2}\rangle$ of the continuous spectrum correspond to these parameters.

For the single-particle states $|1d_{5/2,\,3/2}\rangle$, $|2s_{1/2}\rangle$, and $|1p_{3/2,\,1/2}\rangle$, we used spherical-oscillator functions with oscillator parameter $\nu = (\hbar/m\omega)^{1/2} = 1.005A^{1/6}$ fm ($\hbar\omega = 41A^{-1/3}$ MeV). These functions were also used as a basis for the expansion of the states $\{|\alpha\rangle\} = \{|1f_{7/2,\,5/2}\rangle$ and $|2p_{3/2,\,1/2}\rangle\}$ in the internal region of the reaction. The energies of the states $\{|\gamma\rangle\} = \{|1p_{3/2}\rangle, |1p_{1/2}\rangle\}$ appearing directly in the coupled-channels equations (see [5]) were considered as model parameters. They can be roughly estimated on the basis of data on quasielastic nucleon knockout. For example, it follows from the data of Arditi *et al.* [9] that, for ^{24}Mg, the energies $\varepsilon_{1p_{3/2}}$ and $\varepsilon_{1p_{1/2}}$ are equal, respectively, to 22 ± 2 and to 18 ± 2 MeV (if we assume that the maxima of the strength function that are observed experimentally at excitation energies of ^{23}Na nuclei equal to about 14.4, 9.9, and 2.5 MeV correspond to the three Nilsson orbits into which the $1p_{3/2}$ and $1p_{1/2}$ levels split in the deformed nucleus [10]). The parameters $\varepsilon_{1p_{3/2}}$ and $\varepsilon_{1p_{1/2}}$ were varied in the course of the calculations in order to obtain better agreement between the theoretical and experimental GDR structures. Their eventual values are presented in Table 1.

Table 1. Fitted parameters of the model used

Nucleus	u_{0f}, MeV	u_{0p}, MeV	$\varepsilon_{1p_{3/2}}$, MeV	$\varepsilon_{1p_{1/2}}$, MeV	V_0, MeV
^{24}Mg	62	62	–20	–17	50
^{28}Si	58	58	–23	–19	50
^{32}S	57	62	–24	–20	45

Strictly speaking, the single-particle basis described above is not orthonormalized, since the bound states $|1p_{3/2,\,1/2}\rangle$, which appear in it and which were approximated by the oscillator states $|113/2\rangle$ and $|111/2\rangle$, are not orthogonal to the states $|2p_{3/2,\,1/2}\rangle$ of the continuous spectrum. In discretizing the continuum, measures were therefore taken to restore the orthogonality of the basis—the oscillator states $|113/2\rangle$ and $|111/2\rangle$ were not included in the set of oscillator states in which we expanded the state $|2p_{3/2,\,1/2}\rangle$ in the internal region of the reaction.

The value chosen for the oscillator parameter ensures a fast convergence of the results of the calculations with increasing total number N of oscillator functions used in expanding the single-particle states of the continuous spectrum. This is illustrated in Fig. 2, where the estimates of the model photoabsorption cross section that were obtained for the truncated $\{|\mathcal{B}\rangle, |\mathcal{A}\rangle\}$ basis (10 + 10 states) are depicted at various values of N. It can be seen from this figure that the results prove to be reasonable even at $N = 1$ and that, from $N = 3$, the curves calculated for different N become virtually indistinguishable.

2.2. Low-Lying States of $A \mp 1$ Nuclei

Natural-parity low-lying states $\{|\mathcal{B}\rangle, |\mathcal{A}\rangle\}$ for the $A \mp 1$ nuclei were calculated by the method that relies on successively adding nucleons to the nuclear system in the configuration space of the $1d2s$ shell [4]. In these calculations, the energies of the single-particle valence states and the matrix elements of the effective two-particle interaction, which are dependent on the mass number A, were taken in just the same way as in [11].

In describing the photodisintegration of ^{24}Mg, ^{28}Si, and ^{32}S nuclei, we took into account all low-lying states $|\mathcal{B}\rangle$ and $|\mathcal{A}\rangle$ at excitation energies not exceeding 11 MeV. This made it possible to calculate the structure

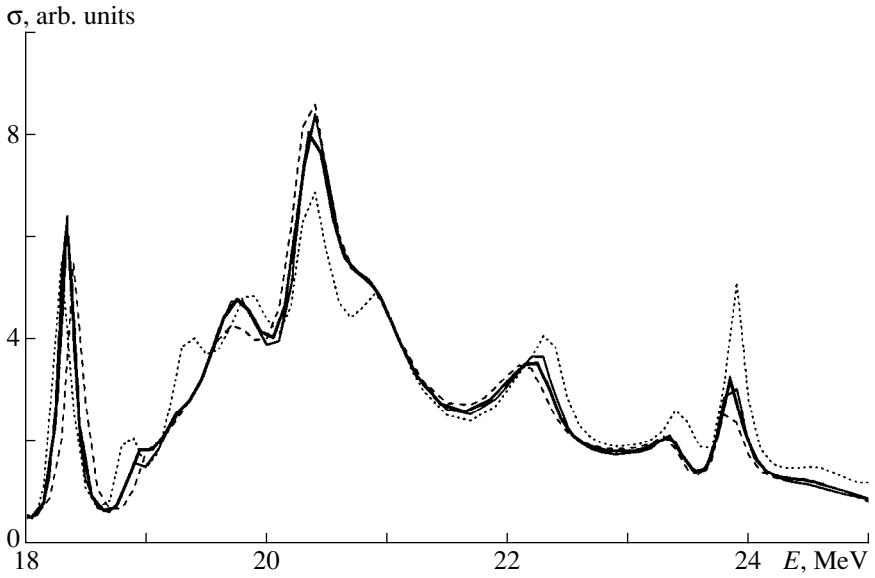

Fig. 2. Model cross section for photoabsorption as a function of energy for the cases where single-particle states were approximated by using N = (dotted curve) 1, (dashed curve) 2, (thin solid curve) 3, and (thick solid curve) 4 oscillator functions.

and the decay features of the GDR up to about 30–32 MeV (the last value is obtained as the sum 11 MeV + nucleon-separation threshold + energy of the highest single-particle resonance in a continuum).

2.3. Residual Nucleon–Nucleon Interaction

The coupled-channel equations (see [5]) do not involve the matrix elements of the effective two-particle interaction between nucleons belonging to the valence shell, nor do they contain explicitly the energies of single-particle valence levels. Therefore, it is not necessary to match the nuclear Hamiltonians used to describe the low-lying states $|\mathcal{B}\rangle$ and $|\mathcal{A}\rangle$ with those used to calculate the scattering states $|(\alpha\mathcal{B})^{(-)}_{\Lambda}\rangle$.

As was indicated above, the coupling of reaction channels is due to the residual nucleon–nucleon interaction V_{res}. This interaction must be chosen in such a way as to prevent the emergence of an additional mean field for particle α and hole γ^{-1} moving in the field of the $A \mp 1$ core; otherwise, expansion (1), which implies that the single-particle states $|\alpha\rangle$ and $|\,|\gamma\rangle$ correspond the true mean field of the nucleus, becomes meaningless.

Taking this into account, we choose the residual interaction V_{res} in the form

$$V_{\text{res}} = V - U_{\text{add}}, \qquad (5)$$

where

$$V = \frac{1}{4}\sum_{\kappa}\sum_{\lambda}\sum_{\mu}\sum_{\nu}\langle\kappa\lambda|v|\mu\nu\rangle_{\text{as}}a^{+}_{\kappa}a^{+}_{\lambda}a_{\nu}a_{\mu}$$

is the effective nucleon–nucleon interaction ($\langle\kappa\lambda|v|\mu\nu\rangle_{\text{as}}$ stands for antisymmetrized two-particle matrix elements), while

$$U_{\text{add}} = \sum_{\mu}\sum_{\nu}\Big[\sum_{\lambda}\langle\mu\lambda|v|\nu\lambda\rangle_{\text{as}}v_{\lambda}(\mathcal{C})\Big]a^{+}_{\mu}a_{\nu}$$

is the additional mean field that is generated for a particle (hole) by V forces if the $A \mp 1$ core is in the state $|\mathcal{C}\rangle = |\mathcal{B}\rangle, |\mathcal{B}'\rangle, \ldots$ ($|\mathcal{A}\rangle, |\mathcal{A}'\rangle, \ldots$) [12]. In the expression for U_{add},

$$v_{\lambda}(\mathcal{C}) = \left\langle\mathcal{C}\left|\sum_{m_{\lambda}}\sum_{\tau_{\lambda}}a^{+}_{\lambda}a_{\lambda}\right|\mathcal{C}\right\rangle[2(2j_{\lambda}+1)]^{-1}$$

is the occupation number for the single-particle level $|\lambda\rangle$.

In this study, we employed the Rosenfeld forces for the effective nucleon–nucleon forces V. The radial dependence of these forces is determined by the Yukawa potential of radius $1/\mu = 1.5$ fm. The amplitude of the forces, V_0, was considered as a model parameter and was varied to fit the energy position of the giant resonance. The resulting values of V_0 are presented in Table 1.

3. DISCUSSION OF THE RESULTS OF THE CALCULATIONS

The main results of our calculations are displayed in Figs. 3–9 and in Tables 2–5.

3.1. Intermediate Structure of GDRs

Figure 3 shows the calculated (thin solid curve) and experimental (thick solid curve) cross sections for $E1$ photoabsorption. Both theoretical results and experi-

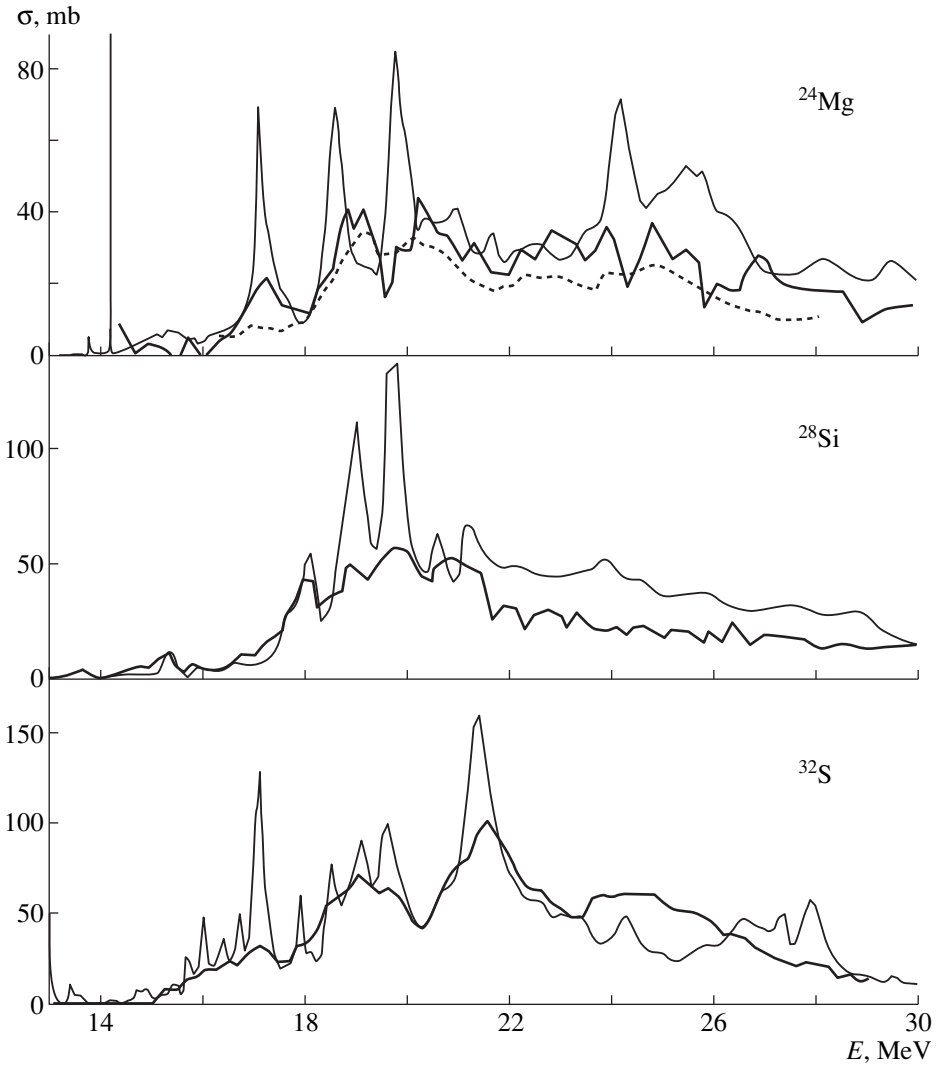

Fig. 3. Photoabsorption cross sections: (thin solid curve) theoretical cross section $\sigma_{abs} \approx 2[\sigma(\gamma, p_0) + \sigma(\gamma, p_1) + \sigma(\gamma, p_2) + \ldots]$ and (thick solid curve) experimental data {cross section for photoabsorption on a natural mixture of isotopes for Mg [13], cross section for photoabsorption on ^{28}Si [14], and the sum of the cross sections $\sigma(\gamma, p)$ [15] and $\sigma(\gamma, n)$ [16] for ^{32}S}. For the ^{24}Mg nucleus, the dashed curve represents the sum of the experimental cross sections $\sigma(\gamma, p)$ [17] and $\sigma(\gamma, n)$ [18].

mental data exhibit a pronounced intermediate structure of GDRs. This structure can be associated with the intrusion of closed $\gamma\mathcal{A}$ channels into the continuum of the nuclear system. Indeed, it was shown in a number of studies (see, for example, [19]) that discrete states superimposed on a continuous spectrum must generate a resonance structure in the reaction cross section.

The role of closed $\gamma\mathcal{A}$ channels corresponding to $1p \longrightarrow 1d2s$ dipole transitions in the formation of the intermediate structure of giant resonances is illustrated in Fig. 4, which displays the results of our calculations for the GDR in ^{24}Mg for the following cases:

(i) Effective interaction is switched off completely (dotted curve).

(ii) We take into account only the interaction between the configurations $|(\alpha\mathcal{B})_\Lambda\rangle$ corresponding to the $1d2s \longrightarrow 1f2p$ dipole transitions (dashed curve).

(iii) We take into account the interactions between all reaction channels (solid curve).

Figure 4 demonstrates how the residual nucleon–nucleon interaction forms a collective dipole state [case (ii)] from single-particle resonances [case (i)] and how the inclusion of closed channels increases the intensity (integrated cross section) of a GDR and leads to the emergence of many resonance states [case (iii)].

The importance of taking into account $\gamma\mathcal{A}$ channels in describing the intermediate structure of GDRs can be seen from the configurational content of resonance states. As was indicated above, the scalar products $\langle(n'\vec{\alpha}', \mathcal{B}')_\Lambda|(\alpha\mathcal{B})^{(-)}_\Lambda\rangle$ and $\langle(\gamma'\mathcal{A}')_\Lambda|(\alpha\mathcal{B})^{(-)}_\Lambda\rangle$, which characterize the configurational content of scattering states in the internal region of the reaction being considered, are found in solving the equations for channel

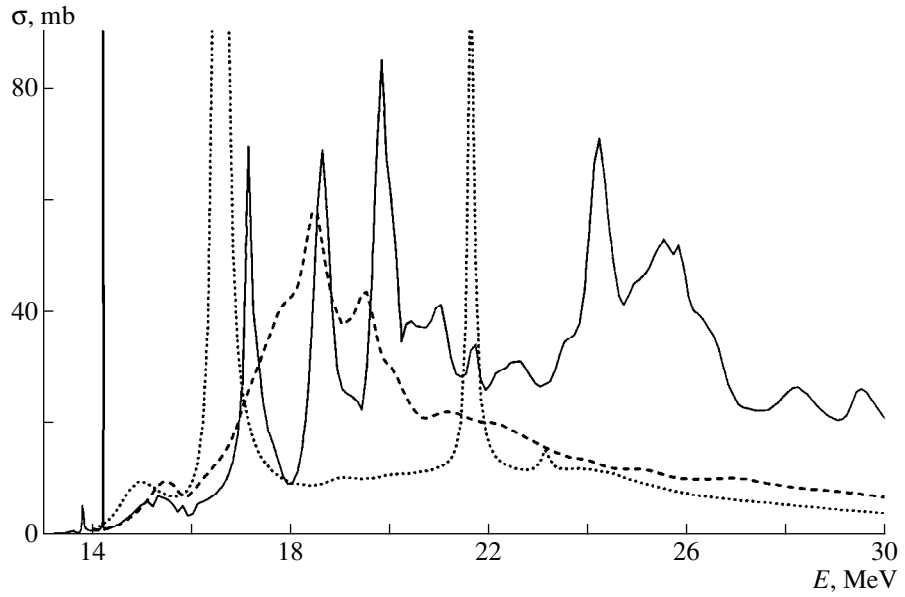

Fig. 4. Effect of channel coupling on the properties of the GDR in ^{24}Mg: (dotted curve) no coupling is taken into account, (dashed curve) only the coupling of channels that correspond to $1d2s \longrightarrow 1f2p$ transitions is taken into account, and (solid curve) all channel couplings are taken into account.

coupling. By using these quantities, the contribution of various configurations of the $|(\alpha\mathcal{B})_\Lambda\rangle$ and $|(\gamma\mathcal{A})_\Lambda\rangle$ types to the GDR can be estimated at any excitation energy E of the nucleus involved. For some dipole states of the nuclei considered in this study, the relevant data are given in Tables 2–4, which list the contributions of the ten most important configurations near resonance energies. From these data, it can be seen that the intermediate structure of the GDRs in $1d2s$-shell nuclei is of a collective origin and that it arises owing to the strong

Table 2. Main components of the GDR in ^{24}Mg near some photoabsorption resonances

E_{res} = 17.1 MeV		E_{res} = 18.6 MeV		E_{res} = 19.8 MeV		E_{res} = 24.2 MeV		E_{res} = 25.5 MeV	
configuration	contribution, %	configuration	contribution, %	configuration	contribution, %	configuration	contribution, %	configuration	contribution, %
$1p^1_{1/2}(8.80)$	17.14	$1f_{7/2}(0.45)$	7.00	$1p^1_{1/2}(6.01)$	5.90	$1p^1_{1/2}(7.62)$	4.33	$1p^1_{1/2}(10.19)$	3.65
$1p^1_{3/2}(7.88)$	11.36	$1p^1_{1/2}(4.56)$	4.33	$2p_{3/2}(5.51)$	4.09	$1p^1_{1/2}(6.76)$	2.57	$1p^1_{1/2}(10.54)$	2.69
$1p^1_{3/2}(7.77)$	7.04	$1p^1_{1/2}(6.01)$	3.83	$1p^1_{1/2}(6.76)$	4.01	$1p^1_{1/2}(9.09)$	2.02	$1f_{7/2}(8.80)$	2.54
$1f_{7/2}(0.45)$	5.46	$2p_{1/2}(4.54)$	3.80	$1p^1_{1/2}(5.63)$	3.59	$1f_{5/2}(0.45)$	1.90	$2p_{3/2}(8.36)$	1.92
$1p^1_{3/2}(2.91)$	3.60	$2p_{3/2}(5.51)$	3.42	$2p_{3/2}(6.09)$	3.45	$1p^1_{3/2}(6.28)$	1.85	$1f_{7/2}(8.37)$	1.88
$1p^1_{1/2}(6.01)$	3.48	$2p_{3/2}(4.54)$	3.13	$1f_{7/2}(0.45)$	3.04	$1f_{7/2}(5.80)$	1.82	$1p^1_{1/2}(9.39)$	1.84
$1p^1_{1/2}(4.56)$	2.95	$1f_{7/2}(5.51)$	2.85	$1f_{7/2}(5.51)$	2.93	$1f_{7/2}(7.54)$	1.79	$1f_{7/2}(8.88)$	1.80
$1p^1_{3/2}(7.62)$	2.78	$1p^1_{1/2}(9.92)$	2.81	$1p^1_{3/2}(0.00)$	2.57	$1p^1_{3/2}(7.62)$	1.77	$1f_{7/2}(7.83)$	1.79
$1p^1_{3/2}(9.92)$	2.65	$2p_{3/2}(2.42)$	2.64	$2p_{1/2}(2.76)$	2.46	$1f_{7/2}(8.80)$	1.50	$1f_{7/2}(8.64)$	1.64
$1f_{7/2}(5.51)$	2.40	$2p_{3/2}(2.76)$	2.33	$2p_{1/2}(4.54)$	2.38	$1p^1_{1/2}(9.20)$	1.36	$1p^1_{3/2}(6.76)$	1.63

Note: Here and in Tables 3–5, the theoretical excitation energies (in MeV) of states of the $A \mp 1$ cores are indicated in parentheses.

Table 3. Main components of the GDR in ^{28}Si near some photoabsorption resonances

E_{res} = 18.1 MeV		E_{res} = 19.0 MeV		E_{res} = 19.7 MeV		E_{res} = 20.6 MeV		E_{res} = 21.2 MeV	
configuration	contribution, %	configuration	contribution, %	configuration	contribution, %	configuration	contribution, %	configuration	contribution, %
$2p_{3/2}(7.89)$	5.46	$1p^{1}_{1/2}(9.52)$	11.95	$1f_{7/2}(0.00)$	6.95	$1p^{1}_{1/2}(11.67)$	6.04	$1p^{1}_{1/2}(11.08)$	3.58
$1p^{1}_{3/2}(2.35)$	4.90	$2p_{3/2}(5.68)$	5.68	$2p_{3/2}(6.22)$	3.94	$1p^{1}_{1/2}(5.18)$	3.03	$1f_{5/2}(1.23)$	1.89
$2p_{3/2}(4.00)$	4.65	$1f_{7/2}(0.00)$	5.60	$1f_{7/2}(2.72)$	3.81	$2p_{3/2}(6.45)$	2.84	$2p_{3/2}(7.08)$	1.83
$1f_{7/2}(2.72)$	4.49	$1f_{7/2}(2.36)$	3.74	$1p^{1}_{1/2}(9.52)$	3.43	$1p^{1}_{1/2}(10.32)$	2.22	$1p^{1}_{1/2}(11.67)$	1.83
$1f_{7/2}(4.78)$	4.16	$2p_{3/2}(5.49)$	3.18	$1p^{1}_{1/2}(10.32)$	3.39	$2p_{3/2}(0.81)$	2.15	$2p_{3/2}(7.04)$	1.83
$2p_{3/2}(4.11)$	3.61	$1p^{1}_{1/2}(1.49)$	2.82	$1f_{7/2}(6.45)$	2.99	$1p^{1}_{3/2}(8.40)$	1.99	$2p_{3/2}(6.81)$	1.77
$1f_{7/2}(2.36)$	3.58	$2p_{1/2}(2.70)$	2.18	$1f_{7/2}(3.15)$	2.74	$2p_{3/2}(7.08)$	1.91	$2p_{3/2}(8.70)$	1.75
$2p_{1/2}(3.65)$	3.34	$1f_{7/2}(6.74)$	2.08	$1p^{1}_{1/2}(1.49)$	2.69	$2p_{3/2}(5.68)$	1.79	$1p^{1}_{1/2}(6.86)$	1.59
$2p_{3/2}(2.72)$	3.19	$1p^{1}_{1/2}(5.18)$	1.99	$1p^{1}_{3/2}(10.32)$	2.67	$1f_{7/2}(0.00)$	1.68	$1p^{1}_{3/2}(8.40)$	1.55
$2p_{1/2}(1.23)$	3.18	$2p_{3/2}(2.70)$	1.94	$1f_{7/2}(2.36)$	2.05	$1f_{7/2}(6.45)$	1.67	$1f_{7/2}(5.51)$	1.46

Table 4. Main components of the GDR in ^{32}S near some photoabsorption resonances

E_{res} = 17.1 MeV		E_{res} = 19.1 MeV		E_{res} = 19.6 MeV		E_{res} = 21.4 MeV		E_{res} = 24.3 MeV	
configuration	contribution, %	configuration	contribution, %	configuration	contribution, %	configuration	contribution, %	configuration	contribution, %
$1f_{7/2}(2.49)$	7.58	$1f_{7/2}(6.73)$	4.87	$1f_{7/2}(7.28)$	5.87	$1f_{7/2}(7.55)$	9.33	$1f_{7/2}(5.28)$	4.46
$1f_{7/2}(4.43)$	4.61	$2p_{3/2}(7.55)$	4.49	$1f_{7/2}(6.50)$	4.66	$1f_{7/2}(6.19)$	3.96	$1p^{1}_{1/2}(5.82)$	3.31
$1f_{7/2}(5.82)$	4.03	$1f_{7/2}(7.28)$	4.05	$1f_{7/2}(6.99)$	3.80	$1f_{7/2}(8.10)$	3.14	$1p^{1}_{1/2}(6.81)$	3.25
$1f_{7/2}(5.13)$	3.45	$2p_{1/2}(7.61)$	3.74	$1p^{1}_{1/2}(2.17)$	3.72	$1f_{7/2}(6.84)$	2.74	$1f_{5/2}(7.35)$	2.75
$2p_{1/2}(5.96)$	3.18	$1f_{7/2}(6.51)$	3.09	$1f_{5/2}(5.13)$	2.86	$1p^{1}_{1/2}(3.73)$	2.67	$1p^{1}_{1/2}(4.58)$	2.51
$1p^{1}_{1/2}(5.10)$	2.99	$2p_{3/2}(8.41)$	3.04	$2p_{1/2}(7.89)$	2.68	$1f_{7/2}(5.28)$	2.37	$1f_{7/2}(7.50)$	2.11
$2p_{3/2}(6.99)$	2.88	$1p^{1}_{1/2}(0.00)$	2.75	$1f_{7/2}(6.51)$	2.49	$1f_{7/2}(2.49)$	2.29	$1f_{7/2}(5.60)$	2.07
$2p_{3/2}(7.00)$	2.80	$2p_{3/2}(7.61)$	2.70	$1f_{7/2}(6.22)$	2.01	$1f_{5/2}(4.71)$	2.15	$1p^{1}_{1/2}(4.67)$	2.05
$1f_{7/2}(8.53)$	2.74	$1f_{5/2}(2.49)$	2.09	$2p_{1/2}(7.00)$	2.01	$1f_{7/2}(6.99)$	1.98	$1p^{1}_{1/2}(6.41)$	1.92
$2p_{3/2}(6.38)$	2.62	$1f_{7/2}(6.99)$	2.09	$1f_{5/2}(5.82)$	1.99	$1f_{7/2}(6.50)$	1.84	$1f_{7/2}(7.78)$	1.86

mixing of the $|(\alpha\mathcal{B})_\Lambda\rangle$ and $|(\gamma\mathcal{A})_\Lambda\rangle$ configurations; of these, the configurations corresponding to the $1p^{-1}_{1/2}$ hole play the most important role in the formation of the intermediate structure of GDRs. Figure 5, which shows the energy dependences of those components in the cross sections for photoabsorption on ^{24}Mg, ^{28}Si, and ^{32}S that are associated with the (dashed curve) $|(\alpha\mathcal{B})_\Lambda\rangle$ and (dotted curve) $|(\gamma\mathcal{A})_\Lambda\rangle$ configurations, also illustrates the strong mixing of these configurations in dipole states.

In going over from ^{24}Mg to ^{28}Si and further to ^{32}S, the contribution to the photoabsorption cross section from the $|(\gamma\mathcal{A})_\Lambda\rangle$ configuration decreases steadily because the filling of the $1d2s$ valence shell leads to the blocking of $1p \longrightarrow 1d2s$ single-particle transitions. Nonetheless, these configurations continue to play a

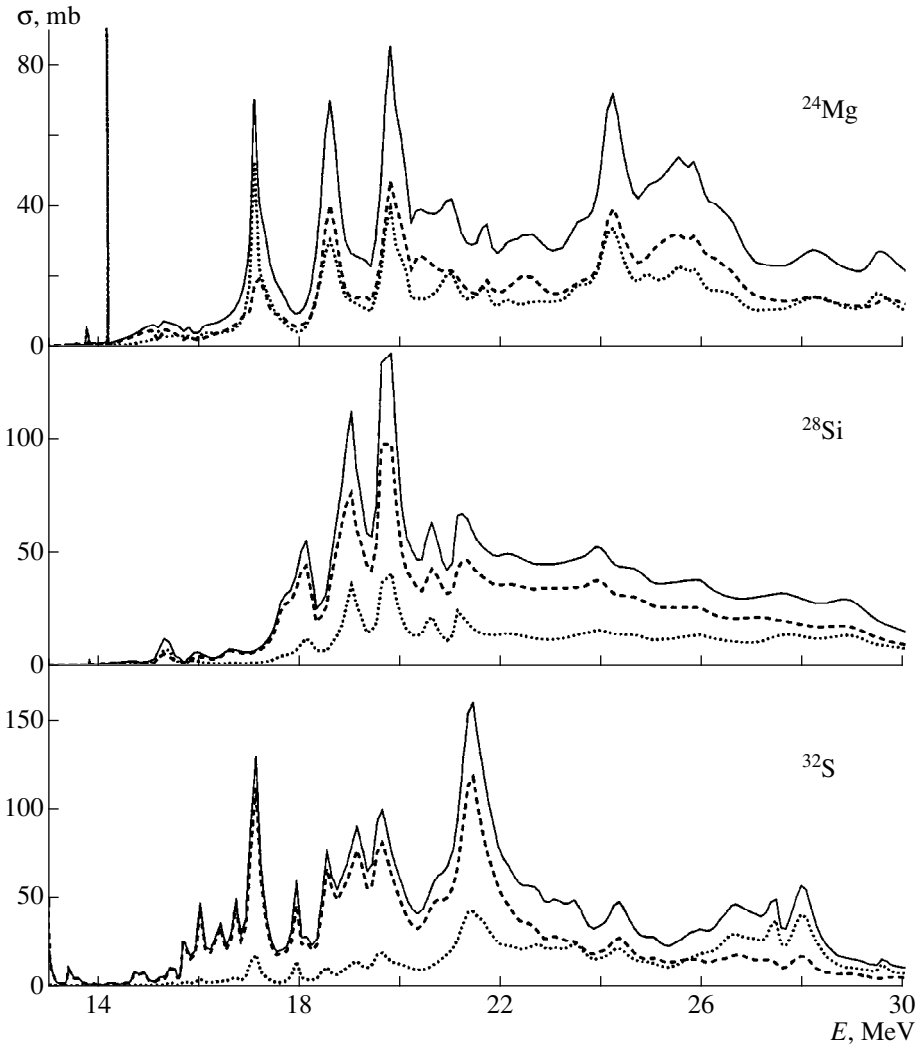

Fig. 5. Configurational content of the GDRs in the ^{24}Mg, ^{28}Si, and ^{32}S nuclei: (dashed curve) contribution of configurations corresponding to $1d2s \longrightarrow 1f2p$ transitions, (dotted curve) contribution of configurations corresponding to $1p \longrightarrow 1d2s$ transitions, and (solid curve) total photoabsorption cross section.

significant role in the formation of the intermediate structure of GDRs. This is confirmed by the data from Table 5, which displays the configurational content of the GDR in ^{32}S in the vicinity of the 17.1-MeV resonance. As can be seen from this table, the resonance correlates definitively with one of the $\gamma\mathcal{A}$ closed channels: as the excitation energy of the nucleus approaches the position of the resonance peak, the contribution of the $a_{1p_{1/2}}|\mathcal{A}; E_{\mathcal{A}} = 5.1$ MeV$\rangle$ configuration to the photoabsorption cross section increases sharply.

3.2. Gross Structure of GDRs

In addition to the intermediate structure, the cross section for photoabsorption on the ^{24}Mg nucleus shows a gross structure: it distinctly splits into two broad peaks localized in the regions 16–22 and 22–28 MeV. Usually, these features of the GDR in ^{24}Mg are explained by the deformation of the nuclear surface. Indeed, there are a few experimental factors indicating that the ^{24}Mg nucleus has the shape of a prolate spheroid of revolution.

The effect of nuclear deformations on the properties of GDRs in $1d2s$-shell nuclei was considered by Bassichis and Scheck [20], who first calculated single-particle states in an axisymmetric self-consistent Hartree–Fock potential in order to use them, at the next stage, in an analysis of a GDR within the $1p1h$ scheme. Those authors found that the dipole states in ^{24}Mg and ^{28}Si break down into two energy groups, the upper one, which is due primarily to $1p \longrightarrow 1d2s$ transitions, and the lower one, which is associated with $1d2s \longrightarrow 1f2p$ transitions. In addition, they established that the upper energy group of states corresponds primarily to $\Delta K = 1$ single-particle transitions, where K is the projection of the nucleon angular momentum onto the symmetry axis

Table 5. Changes in the configurational content of the GDR in ^{32}S in the vicinity of the 17.1-MeV resonance

E = 16.8 MeV		E = 16.9 MeV		E = 17.0 MeV		E = 17.1 MeV		E = 17.2 MeV	
configuration	contribution, %	configuration	contribution, %	configuration	contribution, %	configuration	contribution, %	configuration	contribution, %
$2p_{3/2}(6.19)$	7.09	$2p_{3/2}(6.19)$	7.26	$1f_{7/2}(2.49)$	6.61	$1f_{7/2}(2.49)$	7.58	$2p_{3/2}(6.99)$	5.34
$2p_{3/2}(6.38)$	6.75	$2p_{3/2}(6.38)$	4.41	$1f_{7/2}(4.43)$	4.34	$1f_{7/2}(4.43)$	4.61	$1f_{7/2}(2.49)$	4.86
$2p_{1/2}(5.22)$	5.14	$1f_{7/2}(2.49)$	4.20	$2p_{3/2}(6.19)$	3.96	$1f_{7/2}(5.82)$	4.03	$1f_{7/2}(4.43)$	4.12
$2p_{3/2}(8.53)$	4.60	$1f_{7/2}(4.43)$	3.63	$2p_{3/2}(7.00)$	3.78	$1f_{7/2}(5.13)$	3.45	$1f_{7/2}(5.60)$	3.85
$2p_{3/2}(5.28)$	3.17	$2p_{3/2}(7.00)$	3.22	$1f_{7/2}(5.82)$	3.70	$2p_{1/2}(5.96)$	3.18	$1f_{7/2}(5.82)$	3.66
$2p_{3/2}(7.35)$	3.09	$2p_{1/2}(5.22)$	3.18	$1p^{1}_{1/2}(5.10)$	3.35	$1p^{1}_{1/2}(5.10)$	2.99	$1f_{7/2}(8.53)$	3.14
$2p_{3/2}(7.00)$	2.92	$1f_{5/2}(1.22)$	2.70	$2p_{1/2}(5.96)$	3.31	$2p_{3/2}(6.99)$	2.88	$1f_{7/2}(5.13)$	2.95
$1f_{7/2}(5.13)$	2.74	$2p_{3/2}(8.53)$	2.59	$2p_{3/2}(6.38)$	2.99	$2p_{3/2}(7.00)$	2.80	$2p_{3/2}(7.35)$	2.83
$2p_{1/2}(4.93)$	2.73	$1f_{7/2}(5.13)$	2.59	$2p_{1/2}(4.93)$	2.32	$1f_{7/2}(8.53)$	2.74	$2p_{1/2}(5.65)$	2.73
$2p_{3/2}(6.84)$	2.64	$1p^{1}_{1/2}(5.10)$	2.55	$1f_{7/2}(5.13)$	2.20	$2p_{3/2}(6.38)$	2.62	$2p_{3/2}(6.84)$	2.66

of the nucleus and that the lower energy group corresponds to transitions leaving this quantum number unchanged ($\Delta K = 0$ transitions). On this basis, Bassichis and Scheck [20] concluded that there are configuration splitting of the giant resonance in these nuclei [21] and the splitting of it due to nuclear deformations.

The analysis performed in [20] is disadvantageous in that (i) it relies on a phenomenological two-particle interaction in evaluating the deformed self-consistent field, (ii) it covers only $1p1h$ configurations, and (iii) it takes no account of the continuum effect on giant-resonance formation. The present calculation also suggests that configurations associated with $1p \longrightarrow 1d2s$ transitions play an important role in the formation of the second, high-energy, maximum of photoabsorption on the ^{24}Mg nucleus (see Fig. 4). From Fig. 5, it can be seen, however, that these configurations come to be dominant above the second GDR maximum (their contribution grows significantly there)—that is, in the energy region $E \geq 28$ MeV, where the role of $1p_{3/2} \longrightarrow 1d2s$ transitions becomes more pronounced. This means that the observed gross structure of the GDR in ^{24}Mg is of a collective origin.

Let us consider the possibility of the splitting of the GDR in ^{24}Mg due to a deformation of the nuclear surface. We have already indicated that this GDR, as well as the other ones considered in the present study, possesses a high degree of collectivization. On the basis of the Danos–Okamoto model [22], it was deduced that, in a prolate axisymmetric nucleus, there can arise two types of collective dipole vibrations of neutrons with respect to protons—that, with a lower energy, along the symmetry axis of the nucleus and that, with a higher energy and doubled intensity (because there are two degenerate transverse modes), in the plane orthogonal to the symmetry axis. This is precisely the reason that the photoabsorption cross section is split into two peaks.

In the generalized model from [23], the collective transverse and longitudinal dipole vibrations of a spheroidal even–even nucleus can be described in terms of the wave functions $|\Psi^{\parallel}_{1M}\rangle$ and $|\Psi^{\perp}_{1M}\rangle$ that, in the laboratory frame, are given by

$$\begin{aligned} |\Psi^{\parallel}_{1M}\rangle &= \sqrt{\frac{1}{3}}q^{+}_{1M}|\Psi_0\rangle - \sqrt{\frac{2}{3}}(q^{+}_{1}|\Psi_2\rangle)_{1M}, \\ |\Psi^{\perp}_{1M}\rangle &= \sqrt{\frac{2}{3}}q^{+}_{1M}|\Psi_0\rangle + \sqrt{\frac{1}{3}}(q^{+}_{1}|\Psi_2\rangle)_{1M}, \end{aligned} \tag{6}$$

where q^{+}_{1M} is the operator of creation of collective dipole vibrations, $|\Psi_0\rangle$ is the ground state of the nucleus, and $|\Psi_2\rangle$ is the first excited ($J^{\pi} = 2^{+}$) state of the nucleus. {In going over to the intrinsic coordinate frame, formulas (6) are transformed into the conventional relations

$$|\Psi^{\parallel}_{1M}\rangle = \sqrt{\frac{3}{8\pi^2}}\mathcal{D}^{1}_{M0}(\theta_i)q^{+}_{10}|\Psi_0\rangle$$

and

$$\begin{aligned} |\Psi^{\perp}_{1M}\rangle &= \sqrt{\frac{3}{16\pi^2}}[(\mathcal{D}^{1}_{M1}(\theta_i)q^{+}_{11}|\Psi_0\rangle) \\ &+ \mathcal{D}^{1}_{M-1}(\theta_i)q^{+}_{1-1}|\Psi_0\rangle], \end{aligned}$$

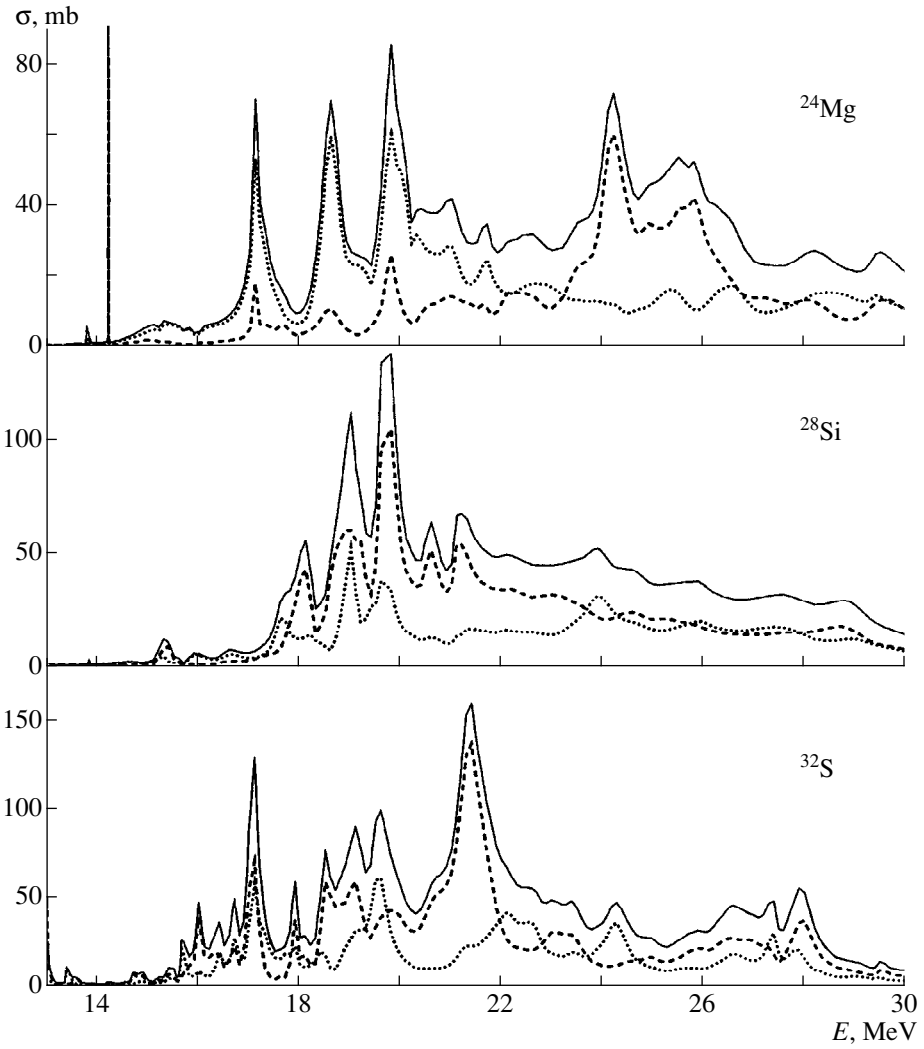

Fig. 6. Contributions of the longitudinal and transverse configurations to the GDRs in the ^{24}Mg, ^{28}Si, and ^{32}S nuclei: (dotted curve) longitudinal component, (dashed curve) transverse component, and (solid curve) total photoabsorption cross section.

since, for a deformed nucleus, the relation

$$|\Psi_{2M}\rangle = \sqrt{\frac{5}{8\pi^2}}\mathcal{D}^2_{M0}(\theta_i)|\Psi_0\rangle$$

holds in the strong-coupling approximation.}

In (6), we replace the operator q^+_{1M} by the dipole-moment operator $D(1M)$, considering that, if the giant resonance is fully collectivized, we have $D(1M) \propto [q^+_{1M} + (-1)^{1+M}q_{1-M}]$ and $q_1|\Psi_0\rangle = q_1|\Psi_2\rangle = 0$. We can then obtain the relation

$$\frac{\left|\langle(\alpha\mathcal{B})^{(-)}_\Lambda|\Psi^\parallel_\Lambda\rangle\right|^2}{\left|\langle(\alpha\mathcal{B})^{(-)}_\Lambda|\Psi^\perp_\Lambda\rangle\right|^2} = \frac{\left|\langle(\alpha\mathcal{B})^{(-)}_\Lambda|(D|\Psi_0\rangle)_\Lambda - \sqrt{2}\langle(\alpha\mathcal{B})^{(-)}_\Lambda|(D|\Psi_2\rangle)_\Lambda\right|^2}{\left|\sqrt{2}\langle(\alpha\mathcal{B})^{(-)}_\Lambda|(D|\Psi_0\rangle)_\Lambda + \langle(\alpha\mathcal{B})^{(-)}_\Lambda|(D|\Psi_2\rangle)_\Lambda\right|^2}, \quad (7)$$

which determines the ratio of the probabilities for the excitation of the longitudinal and transverse dipole vibrations in an arbitrary scattering state $|(\alpha\mathcal{B})^{(-)}_\Lambda\rangle$ with energy E and which makes it possible to break down the total photoabsorption cross section into the longitudinal and transverse components. The matrix elements $\langle(\alpha\mathcal{B})^{(-)}_\Lambda|(D|\Psi_2\rangle)_\Lambda$ and $\langle(\alpha\mathcal{B})^{(-)}_\Lambda|(D|\Psi_0\rangle)_\Lambda$, which are necessary for such calculations, can be expressed in terms of the intrinsic components of the scattering states $\langle(n'\vec{\alpha}', \mathcal{B}')_\Lambda|(\alpha\mathcal{B})^{(-)}_\Lambda\rangle$ and $\langle(\gamma'\mathcal{A}')_\Lambda|(\alpha\mathcal{B})^{(-)}_\Lambda\rangle$.

The results obtained by breaking down the photoabsorption cross section into the longitudinal and the transverse component are displayed in Fig. 6. It can be seen from this figure that, for ^{24}Mg, the longitudinal vibrational mode is indeed localized predominantly in the region of the low-energy photoabsorption maximum and that the transverse mode is localized in the

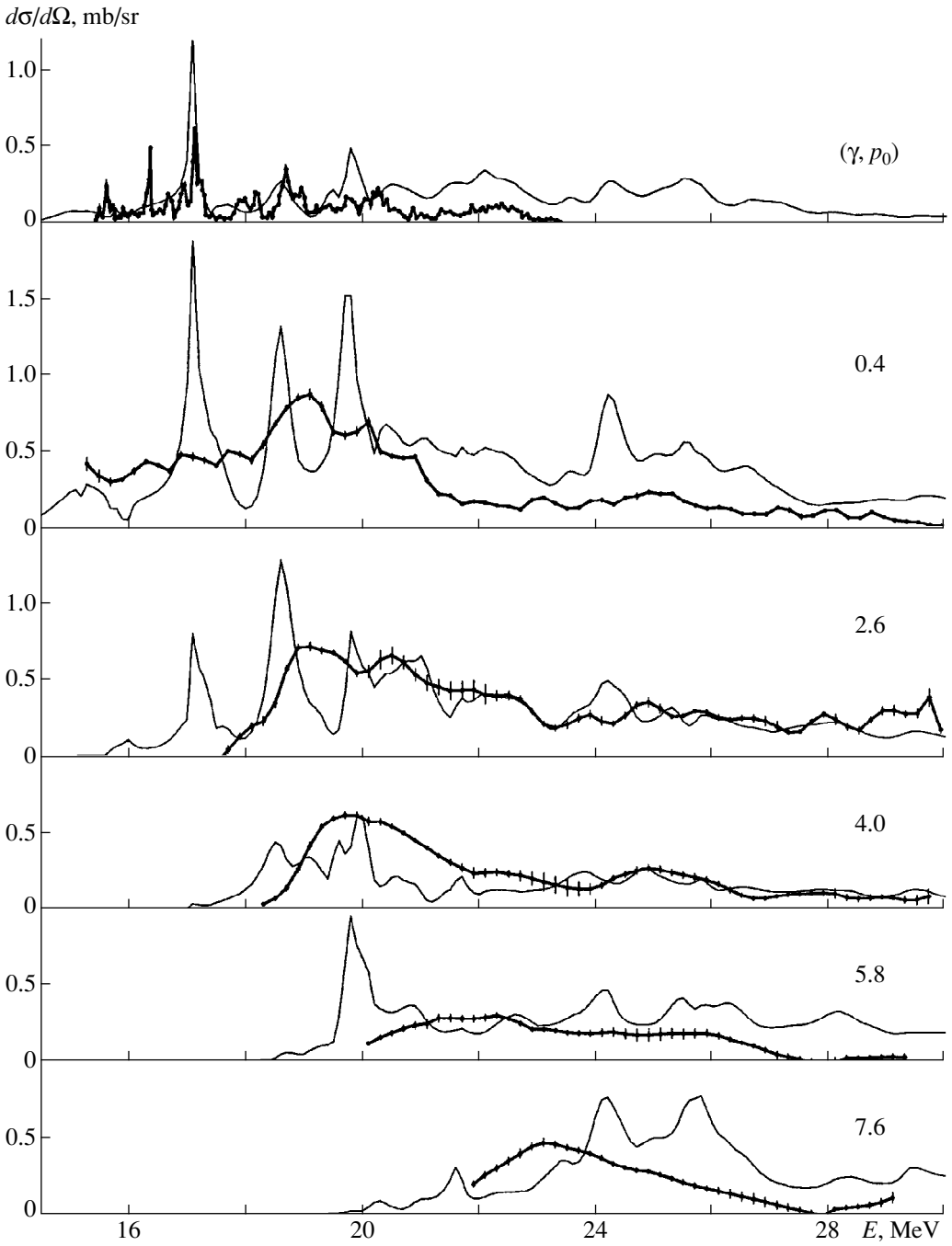

Fig. 7. Differential partial cross sections corresponding to proton emission at a right angle for the ^{24}Mg nucleus: (thin curve) theoretical results and (thick curve) experimental data. The figures indicate the mean energies (in MeV) for those groups of states of the final nucleus that were singled out in the experiment reported in [17]. The experimental cross section $d\sigma(\gamma, p_0)/d\Omega$ was rescaled from the cross section $d\sigma(p, \gamma_0)/d\Omega$ [24].

region of the high-energy maximum. This suggests a direct relationship between the gross structure of the GDR in ^{24}Mg and the nuclear deformation. For ^{28}Si and ^{32}S, on the contrary, it is impossible to separate the longitudinal and transverse photoabsorption peaks. This makes it possible to state that these nuclei are nearly spherical.

The dominance of the transverse component of ^{28}Si and ^{32}S photodisintegration at energies $E < 23$ MeV suggests that the strong inequality $|\langle(\alpha\mathcal{B})^{(-)}_{\Lambda}|(D|\Psi_0\rangle)_{\Lambda}| \gg |\langle(\alpha\mathcal{B})^{(-)}_{\Lambda}|(D|\Psi_2\rangle)_{\Lambda}|$ holds in this energy region (see formula (7)) and that the photoabsorption cross section is determined primarily by the giant resonance over the

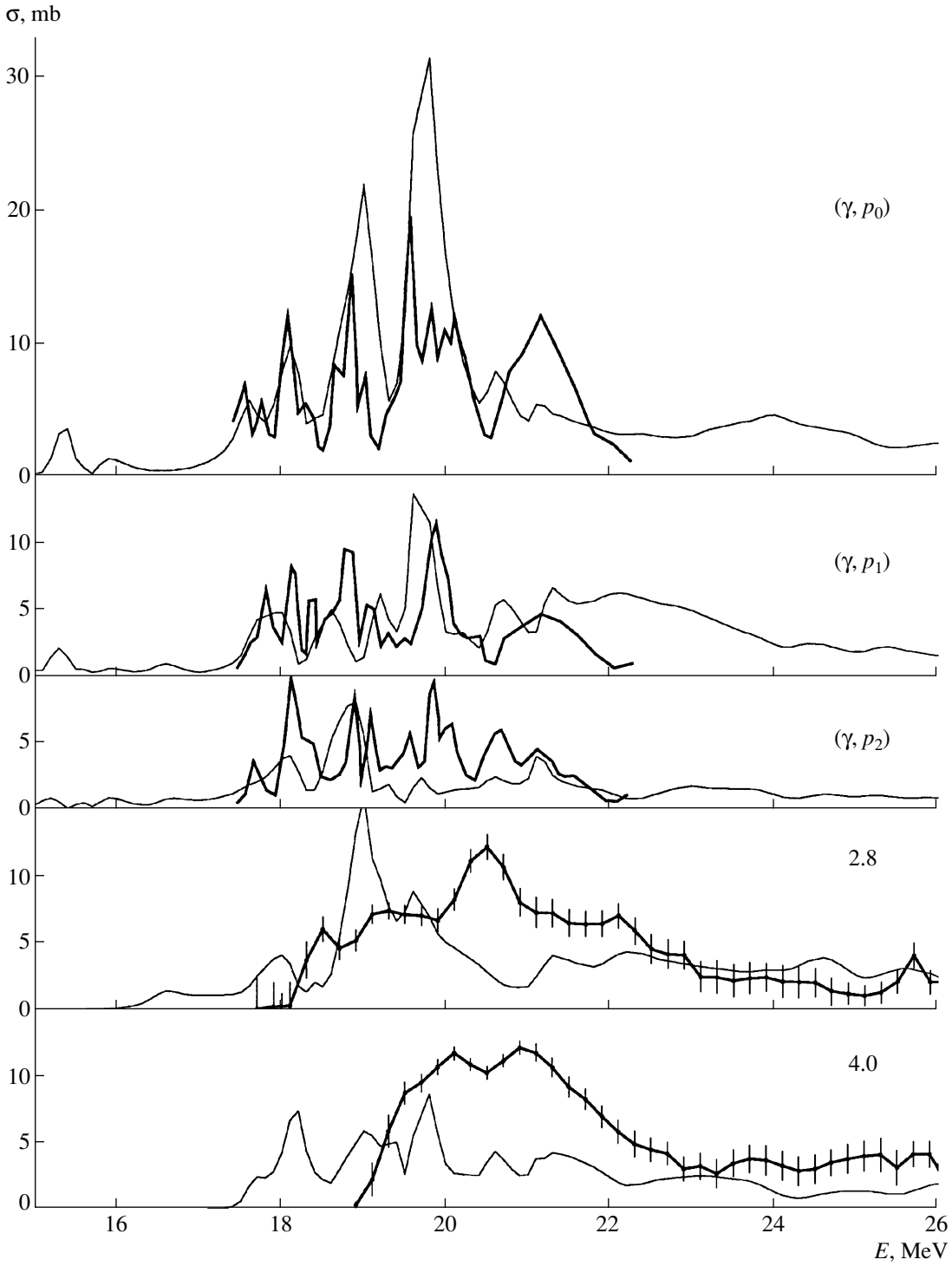

Fig. 8. Photoprotonic partial cross sections for the ^{28}Si nucleus. The notation is identical to that in Fig. 7. The experimental cross sections $\sigma(\gamma, p_i)$, $i = 1, 2$, were borrowed from [25], whereas the remaining experimental data were taken from [26].

ground state of the nucleus. At higher energies ($E >$ 23 MeV), the relative value of the longitudinal component of the photoabsorption cross section increases, which indicates that the effect of the giant resonance over the first excited ($J^\pi = 2^+$) state of the nucleus becomes more pronounced.

3.3. Partial Channels of GDR Decay

More detailed information about the character of nuclear photodisintegration is contained in partial photoprotonic cross sections that correspond to fixed states (or groups of states) of the final nucleus. The calculated

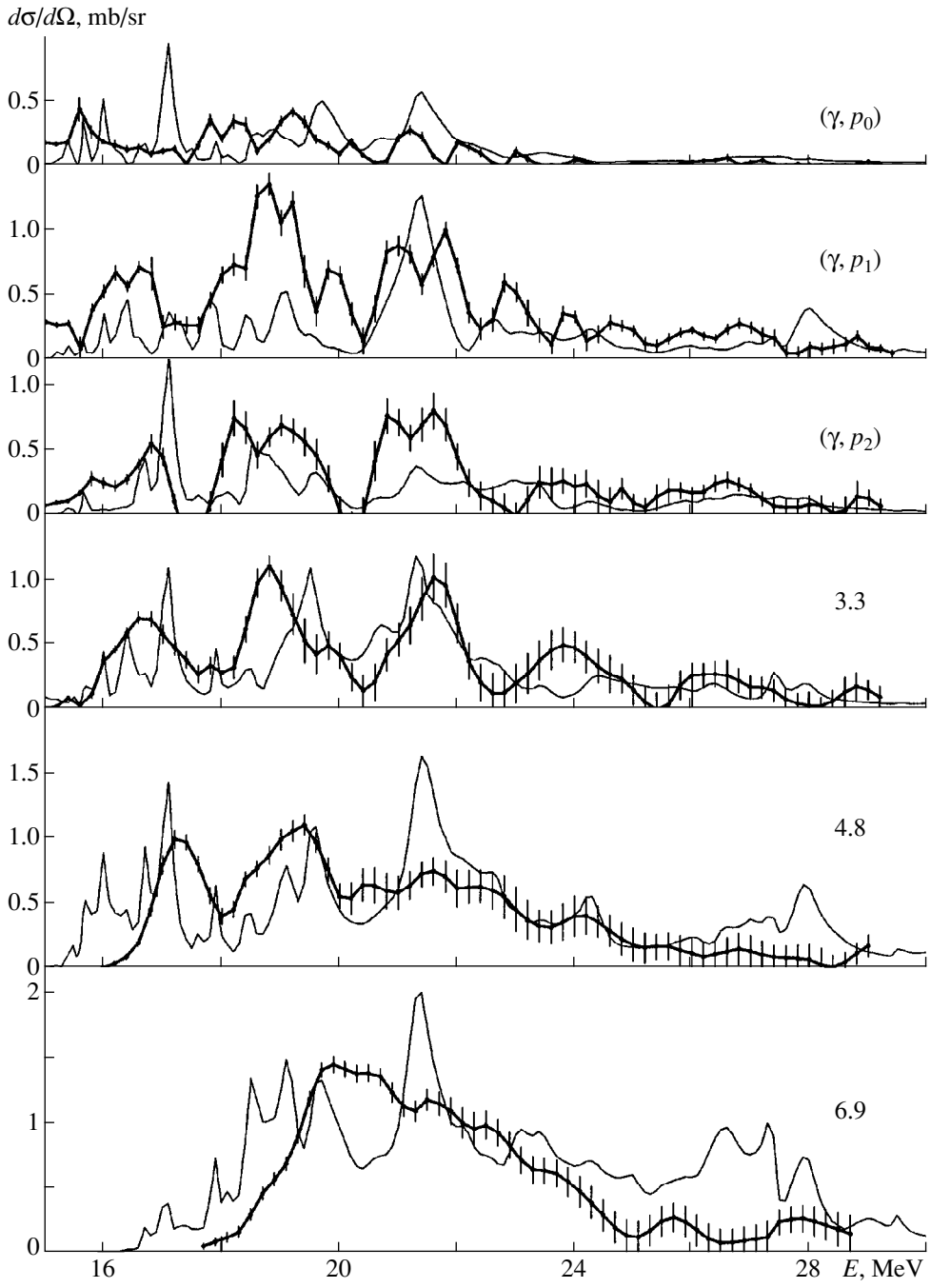

Fig. 9. Differential partial cross sections corresponding to proton emission at a right angle for the ^{32}S nucleus. The notation is identical to that in Fig. 7. Experimental data were taken from [15].

partial cross sections are presented in Figs. 7–9, where they are contrasted against experimental data.

In practice, partial cross sections are often employed to estimate the contributions of various shell configurations to giant resonances. However, some caution should be exercised in this case. In particular, it can be seen from Table 2 that, for ^{24}Mg, none of the ten most important configurations of the 17.1-MeV resonance corresponds to the ground state of the final nucleus. At the same time, the partial cross section $\sigma(\gamma, p_0)$ saturates about one-half of the total proton cross section $\sigma(\gamma, p) \approx \sigma_{abs}/2$ at the excitation energy E of the nucleus about 17.1 MeV (compare with Figs. 3 and 7). A similar pattern is observed at other resonance excitation energies of ^{24}Mg.

It is well known that partial cross sections are much more sensitive to the details of the calculation than the total reaction cross section. Therefore, they provide a

reliable criterion for testing various models. It can be seen from Figs. 7–9 that, by and large, the coupled-channel equations in the scheme of intermediate coupling describe fairly well partial channels of the photodisintegration of ^{24}Mg, ^{28}Si, and ^{32}S nuclei. This means that the approach in question takes into account the main factors that affect the formation and decay of giant resonances in light and medium-mass nuclei with unfilled outer shells.

4. CONCLUSION

We have demonstrated the capabilities of the coupled-channel method in the intermediate-coupling scheme by applying it to the photodisintegration of some 1*d*2*s*-shell nuclei. The results that we have obtained (see preceding section) reveal that the proposed model is able to describe satisfactorily the mechanism of GDR formation and its position on the energy scale, as well as its width, structure, and decay characteristics, in light and medium-mass nuclei with unfilled shells. This is the main result of our study.

It should be noted, however, that there are discrepancies between the theoretical results and experimental data and that these discrepancies are due to the model approximations used. As can be seen from Figs. 3 and 7–9, the calculations give the poorest fit to the experimental data at high excitation energies of the nucleus. One of the possible reasons for this is that the basis configurations $\{|\mathcal{B}\rangle, |\mathcal{A}\rangle\}$ were restricted to states with excitation energies of $E \lesssim 11$ MeV. The agreement with experimental data could probably be improved by expanding the basis, but this is hindered by difficulties in calculating the states $|\mathcal{B}\rangle$ and $|\mathcal{A}\rangle$ at high excitation energies, difficulties that stem from the fact that, in the region $E > 10$–11 MeV, mixing effects must be taken into account for different principal nuclear shells. It is possible that the results of the calculations are also affected by the disregard of ground-state correlations in nuclei (see [27]). First of all, this concerns the deformed nucleus ^{24}Mg, where deformed orbitals of opposite parities may approach. However, taking into account ground-state correlations in a nucleus would also require significantly expanding the basis used in the intermediate-coupling scheme.

ACKNOWLEDGMENTS

We are grateful to V. V. Varlamov, the head of the Center for Data from Photonuclear Studies at Moscow State University, for kind permission to copy several files from the database of this center.

REFERENCES

1. D. Kurath, Phys. Rev. **101**, 216 (1956).
2. J. Birkholz, Nucl. Phys. **A189**, 385 (1972).
3. N. G. Goncharova, H. R. Kissener, and R. A. Éramzhyan, Fiz. Élem. Chastits At. Yadra **16**, 773 (1985) [Sov. J. Part. Nucl. **16**, 337 (1985)]; A. N. Golzov, N. G. Goncharova, and H. R. Kissener, Nucl. Phys. **A562**, 76 (1987).
4. E. N. Golovach and V. N. Orlin, Yad. Fiz. **59**, 1948 (1996) [Phys. At. Nucl. **59**, 1879 (1996)].
5. E. N. Golovach and V. N. Orlin, Yad. Fiz. **62**, 247 (1999) [Phys. At. Nucl. **62**, 212 (1999)].
6. J. Raynol, M. A. Melkanoff, and T. Sawada, Nucl. Phys. **A101**, 369 (1967).
7. J. Rapaport, Phys. Rep. **87**, 25 (1982).
8. P. M. Endt and C. Van der Leun, Nucl. Phys. **A310**, 1 (1978).
9. M. Arditi, H. Doubre, M. Riou, *et al.*, Nucl. Phys. **A103**, 319 (1967).
10. S. G. Nilsson, Mat. Fys. Medd. K. Dan. Vidensk. Selsk. **29** (16) (1955).
11. B. H. Wildental, Prog. Part. Nucl. Phys. **11**, 5 (1984).
12. D. J. Rowe and C. Ngo-Trong, Rev. Mod. Phys. **47**, 471 (1975).
13. B. S. Dolbilkin, V. I. Korin, L. E. Lazareva, *et al.*, Nucl. Phys. **72**, 137 (1965).
14. N. Bezic, D. Jamnik, G. Kernel, *et al.*, Nucl. Phys. **A117**, 124 (1968).
15. V. V. Varlamov, B. S. Ishkhanov, I. M. Kapitonov, *et al.*, Yad. Fiz. **28**, 590 (1978) [Sov. J. Nucl. Phys. **28**, 302 (1978)].
16. B. I. Goryachev, B. S. Ishkhanov, V. G. Shevchenko, *et al.*, Yad. Fiz. **7**, 1168 (1968) [Sov. J. Nucl. Phys. **7**, 698 (1968)].
17. V. V. Varlamov, B. S. Ishkhanov, I. M. Kapitonov, *et al.*, Yad. Fiz. **30**, 1185 (1979) [Sov. J. Nucl. Phys. **30**, 617 (1979)].
18. S. C. Fultz, R. A. Álvarez, B. L. Berman, *et al.*, Phys. Rev. C **4**, 149 (1971).
19. F. Villars, *Fundamentals in Nuclear Theory* (Vienna, 1967), p. 269.
20. W. H. Bassichis and F. Scheck, Phys. Rev. **145**, 771 (1966).
21. V. G. Neudatchin and V. G. Shevchenko, Phys. Lett. **12**, 18 (1964); R. A. Eramzhyan, B. S. Ishkhanov, I. M. Kapitonov, *et al.*, Phys. Rep. **136**, 229 (1986).
22. M. Danos, Nucl. Phys. **5**, 23 (1958); K. Okamoto, Prog. Theor. Phys. **15**, 75L (1956).
23. A. Bohr and B. Mottelson, Mat. Fys. Medd. K. Dan. Vidensk. Selsk. **27** (16) (1953).
24. R. C. Bearse, L. Meyer-Schutzmeister, and R. E. Segel, Nucl. Phys. **A116**, 682 (1968).
25. S. Matsumoto, H. Yamashita, T. Kamae, *et al.*, J. Phys. Soc. Jpn. **20**, 1321 (1965).
26. V. V. Varlamov, B. S. Ishkhanov, I. M. Kapitonov, *et al.*, Izv. Akad. Nauk SSSR, Ser. Fiz. **43**, 186 (1979).
27. S. P. Kamerdzhiev and V. I. Tselyaev, Izv. Akad. Nauk SSSR, Ser. Fiz. **55**, 49 (1991); S. Kamerdzhiev, G. Tertychny, and J. Speth, Nucl. Phys. **A569**, 313 (1994).

Translated by A. Isaakyan

Physics of Atomic Nuclei, Vol. 63, No. 3, 2000, pp. 391–398. Translated from Yadernaya Fizika, Vol. 63, No. 3, 2000, pp. 459–467.

NUCLEI
Theory

Effect of Rescattering on Polarization Observables of the Reaction $\gamma d \longrightarrow pp\pi$ in the Delta-Resonance Region

A. Yu. Loginov, A. A. Sidorov, and V. N. Stibunov

Institute of Nuclear Physics, Tomsk Polytechnic University, Tomsk, Russia

Received December 16, 1998; in final form, February 24, 1999

Abstract—The effect of pion–nucleon and nucleon–nucleon rescatterings on polarization observables of the reaction $\gamma d \longrightarrow pp\pi^-$ are calculated in the delta-isobar region. Pion–nucleon and nucleon–nucleon rescatterings are considered on the basis of a diagrammatic approach. Lorentz invariant expressions are used for the operators of photoproduction and of pion scattering on a free nucleon. A unitarization procedure in the *K*-matrix approximation is used for resonance partial-wave amplitudes. It is shown that, in the delta-resonance region, rescattering has a sizable effect on polarization observables of the reaction $\gamma d \longrightarrow pp\pi^-$ at high momenta of final protons. © *2000 MAIK "Nauka/Interperiodica".*

1. In [1, 2], the reaction $e\vec{d} \longrightarrow e'pp\pi^-$ was studied at the photon point by using the internal polarized target of the VEPP-3 storage ring. In this experiment, protons with momenta in excess of 300 MeV/c were recorded in coincidence. The resulting differential cross sections and asymmetry components, especially a_{20}, differ significantly from the results obtained on the basis of the spectator model. In view of this, it seems necessary to take into account final-state interaction (FSI) for the reaction in question—that is, pion–nucleon and nucleon–nucleon rescatterings. In [3], a diagrammatic approach allowing for FSI was used to compute the spin-averaged differential cross sections for negative-pion photoproduction on a deuteron in the process

$$\gamma d \longrightarrow pp\pi^-. \qquad (1)$$

The effect of final-state interactions on polarization observables of the electro- and photodisintegration of deuterons was taken into account in [4–8]. In the present study, we calculate the effect of FSI on polarization observables of reaction (1). The results of these calculations can serve as a basis for simulating the behavior of polarization observables in specific elements of the phase space of reaction (1) and for planning polarization experiments at high proton momenta in an optimal way. These results can also be used for a direct comparison with available experimental data. Such a comparison can contribute to clarifying the question of whether it is necessary to consider more complicated mechanisms of reaction (1).

The present article is organized as follows. In Section 2, we describe the model used and derive expressions for the amplitudes corresponding to various rescattering mechanisms. In Section 3, we determine the relevant helicity amplitudes and polarization observables. The results of our calculations are presented in Section 4.

2. In order to obtain the amplitude for reaction (1), we make use of the diagrammatic approach developed in [9, 10]. In [3, 11], the diagrammatic approach was applied to the reaction of pion photoproduction on a deuteron. In our calculations, we take into account the contributions to the amplitude that come from the diagrams in Fig. 1 and from the diagrams that differ from those by the permutations of identical final-state nucleons. The first diagram corresponds to the spectator model, which describes well experimental data corresponding to kinematical conditions close to those of quasifree pion photoproduction. If the momenta of both nucleons are rather high (greater than 200 MeV/c), it is necessary to take into account the contributions of the remaining diagrams, which describe rescatterings in the final state. The need for taking these diagrams into account stems from the fact that, with increasing momentum of the spectator nucleon, the probability of finding it inside the deuteron decreases. Within the spectator model, this leads to the reduction of the reaction amplitude. At the same time, the rescattering amplitude is determined by an integral with respect to the momentum of the nucleon in the deuteron. Even at high momenta of the nucleons in the final state, the main contribution to this integral may come from the low-momentum component of the deuteron wave function. Therefore, the role of rescattering effects increases with increasing nucleon momenta.

In constructing analytic expressions corresponding to the diagrams in Fig. 1, Laget [3] and Blomqvist and Laget [11] took the photoproduction amplitude in the nonrelativistic form. In the delta-isobar region, this form is valid in an arbitrary reference frame at small values of p^2/m^2, where p and m are the nucleon mass and the nucleon momentum, respectively. In order to

1063-7788/00/6303-0391$20.00 © 2000 MAIK "Nauka/Interperiodica"

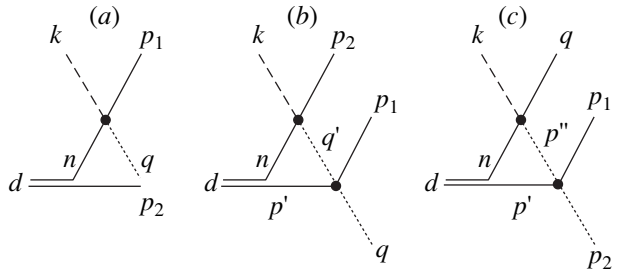

Fig. 1. Diagrams for the reaction $\gamma d \longrightarrow pp\pi^-$: (*a*) diagram of the spectator model, (*b*) diagram for pion–nucleon rescattering; and (*c*) diagram for nucleon–nucleon rescattering.

describe the resonance partial-wave amplitude $M_{1+}^{3/2}$, they took the delta-isobar mass with a small imaginary addition dependent on the isobar energy. The parametrization that those authors used for this dependence gave no way to obtain a unified description of the photoproduction of charged and neutral pions. We make use of the amplitude for pion photoproduction on nucleons from [12]. This amplitude is written in the Lorentz invariant and gauge-invariant form; it realizes the pseudovector version of pion–nucleon interaction and takes into account the contributions of the Born diagrams in the *s*, *t*, and *u* channels; the *s*- and the *u*-channel contribution of the delta isobar; and the contribution of the *t*-channel exchanges of rho and omega mesons. The unitarization procedure in the *K*-matrix approximation was used for the resonance partial-wave amplitudes $E_{1+}^{3/2}$ and $M_{1+}^{3/2}$. This made it possible to avoid introducing an imaginary addition to the delta-isobar mass and to obtain a unified description of the photoproduction of charged and neutral pions. Pion–nucleon scattering was described by the Lorentz invariant amplitude from [13]. This amplitude also realizes the pseudovector version of pion–nucleon interaction and takes into account the contribution of the Born terms in the *s*, *t*, and *u* channels; the contribution of the delta isobar in the *s* and *u* channels; and the contribution of the *t*-channel exchanges of σ and ρ mesons. In just the same way as in the case of pion photoproduction on nucleons, the unitarization procedure in the *K*-matrix approximation was used for the resonance partial-wave amplitude P_{33}.

The amplitude of nucleon–nucleon scattering was represented in the form of multipole expansion including partial waves to order $L = 2$ inclusive. The partial-wave phase shifts for nucleon–nucleon scattering were taken from [14].

For the final *NN* state, the wave function that satisfies the requirements of symmetry under nucleon permutations and which is written in terms of the coupled basis in spin and isospin spaces has the form

$$|\mathbf{p}_1, \mathbf{p}_2, sm_s, tm_t\rangle = \frac{1}{\sqrt{2}}(|\mathbf{p}_1\rangle^1|\mathbf{p}_2\rangle^2 + (-1)^{1+s+t}|\mathbf{p}_2\rangle^1|\mathbf{p}_1\rangle^2)|sm_s\rangle|tm_t\rangle, \quad (2)$$

where $\mathbf{p}_1$ and $\mathbf{p}_2$ are the nucleon momenta; *s* and m_s are, respectively, the nucleon-pair spin and its projection onto the *z* axis; and *t* and m_t are the nucleon-pair isospin and its projection onto the *z* axis. In the reference frame where the deuteron momentum is *d* and where the *z* axis coincides with the photon-momentum direction, the amplitude for reaction (1) in the spectator model then has the form [15]

$$T^{\text{spect}}(\mathbf{p}_1, \mathbf{p}_2, \mathbf{q}, s, m_s; \mathbf{k}, \lambda_\gamma, \mathbf{d}, m_d) = -\sum_{m_s'}\langle sm_s|\left[\sqrt{\frac{E_{\mathbf{p}_2}}{E_{\mathbf{d}-\mathbf{p}_2}}}T^1_{\gamma n\to p\pi^-}(\mathbf{p}_1, \mathbf{q}; \mathbf{d}-\mathbf{p}_2, \mathbf{k}, \lambda_\gamma)\times\Psi_{m_s', m_d}\left(\frac{1}{2}(\mathbf{d}-2\mathbf{p}_2)\right) + (-1)^s\sqrt{\frac{E_{\mathbf{p}_1}}{E_{\mathbf{d}-\mathbf{p}_1}}}\times T^1_{\gamma n\to p\pi^-}(\mathbf{p}_2, \mathbf{q}; \mathbf{d}-\mathbf{p}_1, \mathbf{k}, \lambda_\gamma)\Psi_{m_s', m_d}\left(\frac{1}{2}(\mathbf{d}-2\mathbf{p}_1)\right)\right]|1m_s'\rangle, \quad (3)$$

where $\mathbf{q}$ is the final-pion momentum; $\mathbf{k}$ and λ_γ are, respectively, the photon momentum and helicity; $\mathbf{d}$ and m_d are, respectively, the deuteron 3-momentum and the deuteron spin projection; *s* and m_s are the spin of the final-state nucleon pair and its projection on the *z* axis; m_s' is the projection of the total spin of the nucleons forming the deuteron onto the *z* axis; $E_{\mathbf{p}}$ is the on-shell energy of a nucleon with a momentum $\mathbf{p}$; and $T^1_{\gamma n\to p\pi^-}(\mathbf{p}_1, \mathbf{q}; \mathbf{d}-\mathbf{p}_2, \mathbf{k}, \lambda_\gamma)$ is the amplitude of negative-pion photoproduction on a neutron—this amplitude is treated as an operator that acts on the spin variables of the first nucleon, $|1m_s'\rangle$ and $|sm_s\rangle$, in two-nucleon systems. The quantities $\Psi_{m_s', m_d}(\mathbf{p})$ are expressed in terms of the *S*- and *D*-wave components of the deuteron wave function as [15]

$$\Psi_{m_s', m_d}(\mathbf{p}) = (2\pi)^{3/2}\sqrt{2E_d}\times\sum_{L=0,2}\sum_{m_L} i^L u_L(p)Y_{Lm_L}(\hat{\mathbf{p}})\left\langle Lm_L1m_s'\middle|1m_d\right\rangle, \quad (4)$$

where E_d is the deuteron energy, and $\hat{\mathbf{p}}$ is the unit vector in the direction of the momentum *p*. In the calculations, we use here the deuteron wave functions for the Bonn potential (full model) [16].

Pion–nucleon rescattering is described by the diagram in Fig. 1*b* and by the analogous diagram where the identical final-state nucleons are interchanged. In reaction (1), there can occur the charge-exchange-free pion–nucleon rescattering $\pi^-p \longrightarrow \pi^-p$ and the charge-exchange pion–nucleon rescattering $\pi^0n \longrightarrow \pi^-p$. With allowance for this and for the identity of final-state nucleons, the contribution of pion–nucleon rescattering to the amplitude of reaction (1) can be represented as

$$T^{\pi N}(\mathbf{p}_1, \mathbf{p}_2, \mathbf{q}, s, m_s; \mathbf{k}, \lambda_\gamma, \mathbf{d}, m_d)$$
$$= \int \frac{d^4p'}{(2\pi)^4} \sum_{m'_s} \frac{\langle sm_s|[T^1_{\pi N}(\mathbf{p}_1, \mathbf{q}; \mathbf{p}', \mathbf{q}')T^2_{\gamma N}(\mathbf{p}_2, \mathbf{q}'; \mathbf{d}-\mathbf{p}', \mathbf{k}, \lambda_\gamma)]|1m'_s\rangle}{(n^0 - E_{\mathbf{d}-\mathbf{p}'} + i\epsilon)(p'^0 - E_{\mathbf{p}'} + i\epsilon)(q'^2 - m_\pi^2 + i\epsilon)} V(\mathbf{d}-\mathbf{p}', \mathbf{p}'; m'_s, m_d) \quad (5)$$
$$+ (-1)^s \int \frac{d^4p'}{(2\pi)^4} \sum_{m'_s} \frac{\langle sm_s|[T^1_{\pi N}(\mathbf{p}_2, \mathbf{q}; \mathbf{p}', \mathbf{q}')T^2_{\gamma N}(\mathbf{p}_1, \mathbf{q}'; \mathbf{d}-\mathbf{p}', \mathbf{k}, \lambda_\gamma)]|1m'_s\rangle}{(n^0 - E_{\mathbf{d}-\mathbf{p}'} + i\epsilon)(p'^0 - E_{\mathbf{p}'} + i\epsilon)(q'^2 - m_\pi^2 + i\epsilon)} V(\mathbf{d}-\mathbf{p}', \mathbf{p}'; m'_s, m_d),$$

where $T^1_{\pi N}(\mathbf{p}_1, \mathbf{q}; \mathbf{p}', \mathbf{q}')$ $[T^2_{\gamma N}(\mathbf{p}_2, \mathbf{q}'; \mathbf{d}-\mathbf{p}', \mathbf{k}, \lambda_\gamma)]$ is the pion–nucleon scattering amplitude (pion-photoproduction amplitude) acting, as an operator, on the spin variables of the first (second) nucleon in two-nucleon systems $|1m'_s\rangle$ and $|sm_s\rangle$. The quantities n^0 and p'^0 ($E_{\mathbf{d}-\mathbf{p}'}$ and $E_{\mathbf{p}'}$) are the off-shell (on-shell) energies of nucleons with momenta $\mathbf{d} - \mathbf{p}'$ and $\mathbf{p}'$, respectively. The quantity $[T^1_{\pi N}T^2_{\gamma N}]$ stands for a sum over isospin variables in the two-particle operator; that is,

$$[T^1_{\pi N}T^2_{\gamma N}] = T^1_{\pi^- p \to \pi^- p}T^2_{\gamma n \to p\pi^-} - T^1_{\pi^0 n \to \pi^- p}T^2_{\gamma p \to p\pi^0}. \quad (6)$$

Since the deuteron isospin is zero, the amplitude of charge-exchange pion–nucleon scattering and the amplitude of charge-exchange-free pion–nucleon scattering appear in the rescattering amplitudes with opposite signs. The quantity $V(\mathbf{p}'', \mathbf{p}'; m'_s, m_d)$ is the *dnp* vertex function. In the nonrelativistic limit, it is related to $\Psi_{m'_s, m_d}$ as [3]

$$V(\mathbf{p}'', \mathbf{p}'; m'_s, m_d)$$
$$= (E_d - E_{\mathbf{p}'} - E_{\mathbf{p}''})\Psi_{m'_s, m_d}\left(\frac{1}{2}(\mathbf{p}'' - \mathbf{p}')\right), \quad (7)$$

where $\mathbf{p}'$ and $\mathbf{p}''$ are the momenta of nucleons constituting the deuteron. In expression (5), we decomposed the relativistic nucleon propagators into terms corresponding to virtual nucleons with positive and negative energies and retained only terms with positive energies. This was done because virtual nucleons with negative energies manifest themselves only from momenta higher than a value of about 1 GeV/c [17], but such momenta are not reached in the kinematical region of the delta isobar. In this kinematical region, the relativistic form must be used for the pion propagator. The integrand in (5) has four poles in the variable p'^0; of these, two lie in the upper half-plane of the complex variable p'^0, while the other two lie in its lower half-plane:

$$p'^0_{1+} = E_d - E_{\mathbf{d}-\mathbf{p}'} + i\epsilon, \quad p'^0_{2+} = p^0_\Delta - \omega_{\mathbf{q}'} + i\epsilon,$$
$$p'^0_{1-} = E_{\mathbf{p}'} - i\epsilon, \quad p'^0_{2-} = p^0_\Delta + \omega_{\mathbf{q}'} - i\epsilon. \quad (8)$$

Here, p^0_Δ is the energy of the pion–nucleon pair involved in the rescattering process, while $\omega_{\mathbf{q}'}$ is the on-shell energy of the pion with the momentum $\mathbf{q}'$. Integration with respect to energy in (5) is performed by closing the contour of integration in the lower half-plane. In evaluating the resulting contour integral, we take into account only the residue at the nucleon pole p'^0_{1-}. The residue at the pole p'^0_{2-} of the pion propagator is disregarded because of its smallness [3]. In performing integration with respect to the nucleon 3-momentum, the pion propagator can be represented in the form

$$\frac{1}{q'^2 - m_\pi^2 + i\epsilon} = P\frac{1}{q'^2 - m_\pi^2} - i\pi\delta(q'^2 - m_\pi^2). \quad (9)$$

The expression in (5) then decomposes into the sum of terms corresponding to the contribution of the delta function and the contribution of the principal value of the integral. Specifically, we have

$$T^{\pi N}(\mathbf{p}_1, \mathbf{p}_2, \mathbf{q}, s, m_s; \mathbf{k}, \lambda_\gamma, \mathbf{d}, m_d)$$
$$= T^{\pi N}_{\text{on}}(\mathbf{p}_1, \mathbf{p}_2, \mathbf{q}, s, m_s; \mathbf{k}, \lambda_\gamma, \mathbf{d}, m_d) \quad (10)$$
$$+ T^{\pi N}_{\text{off}}(\mathbf{p}_1, \mathbf{p}_2, \mathbf{q}, s, m_s; \mathbf{k}, \lambda_\gamma, \mathbf{d}, m_d),$$

where

$$T^{\pi N}_{\text{on}}(\mathbf{p}_1, \mathbf{p}_2, \mathbf{q}, s, m_s; \mathbf{k}, \lambda_\gamma, \mathbf{d}, m_d) = \frac{-1}{16\pi^2|\mathbf{p}_\Delta|}\int_0^{2\pi} d\phi' \int_{|p_-|}^{p_+} p'dp'$$
$$\times \sum_{m'_s} \langle sm_s|[T^1_{\pi N}(\mathbf{p}_1, \mathbf{q}; \mathbf{p}', \mathbf{q}')T^2_{\gamma N}(\mathbf{p}_2, \mathbf{q}'; \mathbf{d}-\mathbf{p}', \mathbf{k}, \lambda_\gamma)]|1m'_s\rangle$$
$$\times \Psi_{m'_s, m_d}\left(\frac{1}{2}(\mathbf{d} - 2\mathbf{p}')\right) + \frac{(-1)^{1+s}}{16\pi^2|\mathbf{p}_\Delta|}\int_0^{2\pi} d\phi' \int_{|p_-|}^{p_+} p'dp' \quad (11)$$

$$\times\sum_{m_s'}\langle sm_s|[T^1_{\pi N}(\mathbf{p}_2,\mathbf{q};\mathbf{p}',\mathbf{q}')T^2_{\gamma N}(\mathbf{p}_1,\mathbf{q}';\mathbf{d}-\mathbf{p}',\mathbf{k},\lambda_\gamma)]|1m_s'\rangle\Psi_{m_s',m_d}\left(\frac{1}{2}(\mathbf{d}-2\mathbf{p}')\right),$$

$$T^{\pi N}_{\rm off}(\mathbf{p}_1,\mathbf{p}_2,\mathbf{q},s,m_s;\mathbf{k},\lambda_\gamma,\mathbf{d},m_d)$$

$$= -iP\int\frac{d^3p'}{2\pi^3}\sum_{m_s'}\frac{\langle sm_s|[T^1_{\pi N}(\mathbf{p}_1,\mathbf{q};\mathbf{p}',\mathbf{q}')T^2_{\gamma N}(\mathbf{p}_2,\mathbf{q}';\mathbf{d}-\mathbf{p}',\mathbf{k},\lambda_\gamma)]|1m_s'\rangle}{\mathbf{q}'^2-m_\pi^2}\Psi_{m_s',m_d}\left(\frac{1}{2}(\mathbf{d}-2\mathbf{p}')\right) \quad (12)$$

$$+(-1)^{1+s}iP\int\frac{d^3p'}{2\pi^3}\sum_{m_s'}\frac{\langle sm_s|[T^1_{\pi N}(\mathbf{p}_2,\mathbf{q};\mathbf{p}',\mathbf{q}')T^2_{\gamma N}(\mathbf{p}_1,\mathbf{q}';\mathbf{d}-\mathbf{p}',\mathbf{k},\lambda_\gamma)]|1m_s'\rangle}{\mathbf{q}'^2-m_\pi^2}\Psi_{m_s',m_d}\left(\frac{1}{2}(\mathbf{d}-2\mathbf{p}')\right).$$

In expression (11), the quantities p_- and p_+ are given by

$$p_\pm = \frac{|\mathbf{P}_\Delta|}{Q}E_{\rm c.m.} \pm \frac{P^0_\Delta}{Q}|\mathbf{p}_{\rm c.m.}|, \quad (13)$$

where Q is the invariant mass of the pion–nucleon pair; $E_{\rm c.m.}$ and $\mathbf{p}_{\rm c.m.}$ are, respectively, the nucleon energy and momentum in the c.m. frame of the pion–nucleon pair; and P^0_Δ and $\mathbf{P}_\Delta$ are the energy and momentum of the pion–nucleon pair in the reference frame used. The quantities $|p_-|$ and p_+ represent, respectively, the minimal and the maximal values of the nucleon momentum in the reference frame where the energy and the momentum of the pion–nucleon pair are P^0_Δ and $\mathbf{P}_\Delta$. We note that p_+, p_-, and the kinematical variables appearing in (13) take different values for the first and the second term in (11). In the amplitude given by (11), integration with respect to the momentum $\mathbf{p}'$ is performed in the reference frame where the z axis is aligned with the momentum of the pion–nucleon pair; the integration with respect to $\cos\theta'$ is removed by the delta function, whereby the angle θ' is fixed.

The amplitude in (11) depends crucially on the integration limit $|p_-|$. Let us consider it in the laboratory frame. If the motion of the nucleons in the deuteron and the contribution of the D-wave component of the deuteron wave function are disregarded, each term in [11] is proportional to the integral

$$I_{\rm lab} = \int_{|p_-|}^{p_+} p'dp'u_0(p'). \quad (14)$$

In the kinematical region of the delta isobar, the upper limit p_+ is almost always greater than 300 MeV/c; at the same time, the lower limit $|p_-|$ depends greatly on the momenta of the nucleons and of the pion, varying between 0 and 300 MeV/c. Therefore, the integral in (14) increases strongly at small $|p_-|$ and depends only slightly on p_+. In the c.m. frame of reaction (1), the argument of the deuteron wave function develops an azimuthal dependence; as a result, each term in (11) now proves to be proportional to the integral

$$I_{\rm c.m.} = \int_0^{2\pi}d\phi'\int_{|p_-|}^{p_+}p'dp'u_0\left(\frac{1}{2}(|\mathbf{d}-2\mathbf{p}'|)\right), \quad (15)$$

which also depends primarily on the lower integration limit $|p_-|$.

In the amplitudes $T^{\pi N}_{\rm on}$ and $T^{\pi N}_{\rm off}$, the residue at the nucleon pole fixes one nucleon on the mass shell. Here, the second nucleon is not on the mass shell, but its off-mass-shellness is moderately small in the kinematical region being considered. In the amplitude $T^{\pi N}_{\rm on}$, relation (9) fixes the pion on the mass shell. In the amplitude $T^{\pi N}_{\rm off}$, the pion is not on the mass shell, but the main contribution to the integral comes from the region where we can use the on-shell amplitudes for pion photoproduction and pion–nucleon scattering. The amplitudes in (11) and (12) were determined by means of a numerical integration; in doing this, the approximation where the amplitude of pion photoproduction and the amplitude of pion–nucleon scattering are factored out of the integral sign at zero momenta of the nucleons within the deuteron was used to evaluate the principal value of the integral.

Nucleon–nucleon rescattering is described by the diagram in Fig. 1*c* and the analogous diagram with the interchanged identical final-state nucleons. The contributions of these diagrams to the amplitude of nucleon–nucleon rescattering are identical in magnitude, but they are opposite in sign. Since the diagrams with interchanged fermions enter into the amplitude with opposite signs, their contributions add up; as a result, the expression for the amplitude of nucleon–nucleon rescattering in the coupled-basis representation takes the form

$$T^{NN}(\mathbf{p}_1, \mathbf{p}_2, \mathbf{q}, s, m_s; \mathbf{k}, \lambda_\gamma, \mathbf{d}, m_d) = 2\int \frac{d^4p'}{(2\pi)^4}$$

$$\times \sum_{\substack{s''m_s'' \\ m_s'}} \frac{\langle sm_s|T^1_{pp\to pp}(\mathbf{p}_1, \mathbf{p}_2; \mathbf{p}', \mathbf{p}'')|s''m_s''\rangle\langle s''m_s''|T^2_{\gamma n\to p\pi^-}(\mathbf{p}'', \mathbf{q}; \mathbf{d}-\mathbf{p}', \mathbf{k}, \lambda_\gamma)|1m_s'\rangle}{(n^0 - E_{\mathbf{d}-\mathbf{p}'} + i\epsilon)(p'^0 - E_{\mathbf{p}'} + i\epsilon)(p''^0 - E_{\mathbf{p}''} + i\epsilon)} V(\mathbf{d}-\mathbf{p}', \mathbf{p}'; m_s', m_d), \tag{16}$$

where $T^1_{pp\to pp}(\mathbf{p}_1, \mathbf{p}_2; \mathbf{p}', \mathbf{p}'')$ [$T^2_{\gamma n\to p\pi^-}(\mathbf{p}'', \mathbf{q}; \mathbf{d}-\mathbf{p}', \mathbf{k}, \lambda_\gamma)$] is the proton–proton scattering amplitude (pion-photoproduction amplitude) acting, as an operator, on the spin variables of both nucleons (the second nucleon) of the two-nucleon systems $|sm_s\rangle$ and $|s''m_s''\rangle$ ($|1m_s'\rangle$ and $|s''m_s''\rangle$). In just the same way as in the case of pion–nucleon rescattering, integration with respect to the variable p'^0 is performed by closing the contour in the lower half-plane and by taking the residue at the nucleon pole $p'^0 = E_{p'} - i\epsilon$. Upon factoring the photoproduction amplitude and the amplitude of nucleon–nucleon scattering out of the integral sign and disregarding the contribution of the *D*-wave component of the deuteron wave function, we can represent the amplitude of nucleon–nucleon rescattering as [3]

$$T^{NN}(\mathbf{p}_1, \mathbf{p}_2, \mathbf{q}, s, m_s; \mathbf{k}, \lambda_\gamma, \mathbf{d}, m_d)$$

$$= -i\frac{4\pi W}{mp_{\text{c.m.}}} \sum_{m_n m_{p'} m_{p''}} \left\langle \frac{1}{2}m_n\frac{1}{2}m_{p'}\middle|1m_d\right\rangle \left\langle \frac{1}{2}m_{p''}\frac{1}{2}m_{p'}\middle|sm_s\right\rangle$$

$$\times T_{pp\to pp}\left(\mathbf{p}_1, \mathbf{p}_2, s, m_s; \frac{\mathbf{d}}{2}, \mathbf{p}'', s, m_s\right)$$

$$\times T_{\gamma n\to p\pi^-}\left(\mathbf{p}'', m_{p''}, \mathbf{q}; \frac{\mathbf{d}}{2}, m_n, \mathbf{k}, \lambda_\gamma\right) \tag{17}$$

$$\times \int \frac{d^3\xi}{(2\pi)^3} \frac{(2\pi)^{3/2}\sqrt{2E_d}u_0(|\boldsymbol{\xi} + \mathbf{P}/2|)}{\sqrt{4\pi}}$$

$$\times \frac{(p^2_{\text{c.m.}} + \beta^2)}{(p^2_{\text{c.m.}} - \xi^2 + i\epsilon)(\xi^2 + \beta^2)},$$

where m_n, $m_{p'}$, and $m_{p''}$ are the *z* projections of the spins of intermediate-state nucleons; *W* is the energy of the nucleon pair in its c.m. frame; $p_{\text{c.m.}}$ is the nucleon momentum in the same frame; $\mathbf{P} = \mathbf{p}_1 + \mathbf{p}_2 - \mathbf{d}$; $\mathbf{p}'' = \mathbf{p}_1 + \mathbf{p}_2 - \mathbf{d}/2$; and β = 241 MeV. The quantities $T_{pp\to pp}(\mathbf{p}_1, \mathbf{p}_2, s, m_s; \mathbf{p}', \mathbf{p}'', s, m_s)$ are the diagonal matrix elements of the *pp*-scattering amplitudes in the channel-spin representation; represented in the form of a multipole expansion, they are expressed in terms of the phase shifts for nucleon–nucleon scattering. The integral with respect to the variable ξ in (17) can be calculated analytically [3].

Double rescattering in reaction (1) can be represented by the diagrams in Fig. 2 and the analogous diagrams with the interchanged identical final-state nucleons. We have calculated the contribution of these diagrams to the squared modulus of the amplitude and found that, under the kinematical conditions being considered (that is, in the delta-resonance region and at high momenta of final nucleons), it is about 1% of the contribution from single rescattering. For this reason, we disregard the effects of double rescattering and represent the amplitude of reaction (1) in the form

$$T(\mathbf{p}_1, \mathbf{p}_2, \mathbf{q}, s, m_s; \mathbf{k}, \lambda_\gamma, \mathbf{d}, m_d)$$

$$= T^{\text{spect}}(\mathbf{p}_1, \mathbf{p}_2, \mathbf{q}, s, m_s; \mathbf{k}, \lambda_\gamma, \mathbf{d}, m_d)$$

$$+ T^{\pi N}(\mathbf{p}_1, \mathbf{p}_2, \mathbf{q}, s, m_s; \mathbf{k}, \lambda_\gamma, \mathbf{d}, m_d) \tag{18}$$

$$+ T^{NN}(\mathbf{p}_1, \mathbf{p}_2, \mathbf{q}, s, m_s; \mathbf{k}, \lambda_\gamma, \mathbf{d}, m_d).$$

The use of the amplitude for pion photoproduction on nucleons from [12] ensures gauge invariance of the amplitude in (18).

3. The amplitude in (18) is written in the mixed representation: the polarization of the initial-state particles is described in terms of the photon helicity λ_γ and the *z* projection m_d of the deuteron spin, while the polarization of the final state is described by the total spin *s* of the nucleon pair and its *z* projection m_s. In order to calculate polarization observables, it is more convenient to use helicity amplitudes [18]. In order to accomplish a transition to the helicity amplitudes of the reaction in question, we perform a unitary transformation from a coupled basis of the nucleon pair to its helicity basis and go over from the deuteron-spin projection onto the *z* axis (which is aligned with the direction of the photon

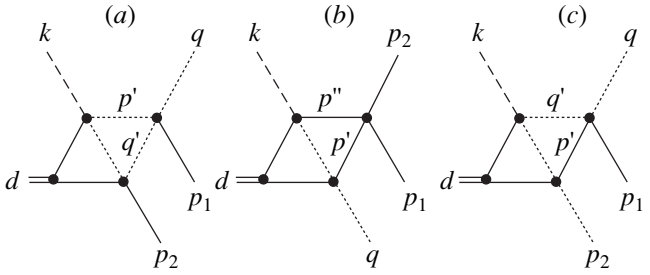

Fig. 2. Diagrams for double rescattering in the reaction $\gamma d \longrightarrow pp\pi^-$: (*a*) πN–πN rescattering, (*b*) πN–NN rescattering, and (*c*) NN–πN rescattering.

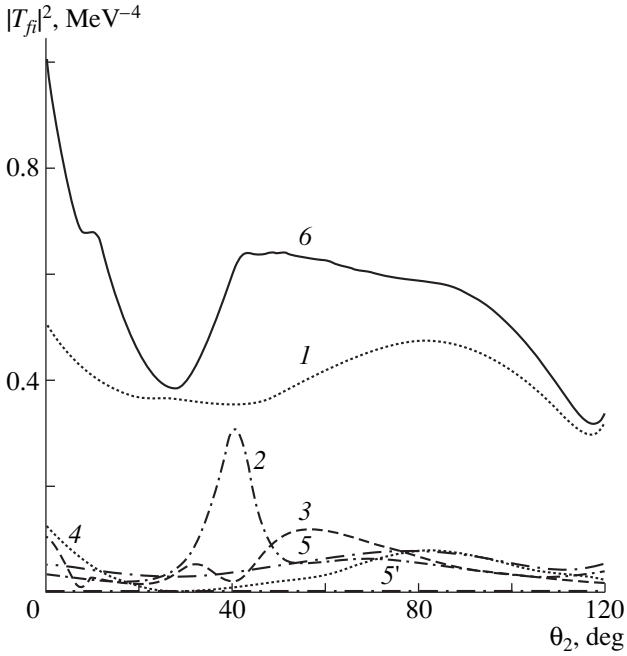

Fig. 3. Squared moduli of the amplitudes corresponding to the diagrams in Fig. 1 as functions of the proton emission angle θ_2 at $p_1 = 300$ MeV, $\theta_1 = 100°$, $\phi_1 = 0°$, $\phi_2 = 180°$, and $E_\gamma = 360$ MeV (all kinematical variables are taken in the c.m. frame of the reaction): (*1*) results produced by the spectator model, (*2*) contribution of on-shell pion–nucleon rescattering, (*3*) contribution of off-shell pion–nucleon rescattering, (*4*) contribution of nucleon–nucleon rescattering, (*5*) contribution of double rescattering, and (*6*) sum of all contributions.

momentum) to the deuteron helicity. Specifically, we have

$$\begin{aligned} &T(\mathbf{p}_1, \lambda_1, \mathbf{p}_2, \lambda_2, \mathbf{q}; \mathbf{k}, \lambda_\gamma, \mathbf{d}, \lambda_d) \\ &= \sum_{sm_s}\sum_{m_1m_2}\left\langle \frac{1}{2}m_1\frac{1}{2}m_2\middle| sm_s\right\rangle D^{*1/2}_{m_1\lambda_1}(\phi_1, \theta_1, 0) \\ &\quad\times D^{*1/2}_{m_2\lambda_2}(\phi_2, \theta_2, 0)(-1)^{1-\lambda_d} \\ &\quad\times T(\mathbf{p}_1, \mathbf{p}_2, \mathbf{q}, s, m_s; \mathbf{k}, \lambda_\gamma, \mathbf{d}, -\lambda_d), \end{aligned} \tag{19}$$

where $D^{1/2}_{m_i\lambda_i}(\phi_i, \theta_i, 0)$ are D functions defined according to [18], ϕ_i and θ_i being the Euler angles specifying a transition to the individual helicity frame of the ith nucleon. The helicity amplitudes in (19) are antisymmetric under the interchange of final protons. From the parity-conservation law, it follows that they also satisfy the relations

$$\begin{aligned} T(\mathbf{p}_1, \lambda_1, \mathbf{p}_2, \lambda_2, \mathbf{q}; \mathbf{k}, \lambda_\gamma, \mathbf{d}, \lambda_d) &= \prod_i \eta_i(-1)^{s_i-\lambda_i} \\ \times T(\mathbf{p}'_1, -\lambda_1, \mathbf{p}'_2, -\lambda_2, \mathbf{q}'; \mathbf{k}', -\lambda_\gamma, \mathbf{d}', -\lambda_d), \end{aligned} \tag{20}$$

where η_i and s_i are, respectively, the intrinsic parity and spin of the ith particle and where the momenta on the right-hand side are obtained from the original ones by means of a reflection with respect to the xz plane. In the case of coplanar kinematics, these relations coincide with those for two-body reactions. In all, there are 24 complex helicity amplitudes for reaction (1). In order to determine them, it is necessary to know 47 independent observables (the common phase factor remains indefinite). For coplanar kinematics, the number of independent helicity amplitudes of reaction (1) is halved by relations (20), so that we are left with the same number of these as that in the case of the two-body reaction $\gamma d \longrightarrow pn$.

According to [18], the general expression for polarization observables of the three-body reaction (1) is

$$F^{I_1M_1, I_2M_2}_{I_\gamma M_\gamma, I_dM_d} = \frac{\mathrm{tr}T\tau_{I_\gamma M_\gamma}\tau_{I_dM_d}T^\dagger\tau_{I_1M_1}\tau_{I_2M_2}}{\mathrm{tr}TT^\dagger}, \tag{21}$$

where T are the helicity amplitudes given by (19); $\tau_{I_iM_i}$ is the spherical spin–tensor for a nucleon with a momentum p_i; and $\tau_{I_\gamma M_\gamma}$ and $\tau_{I_dM_d}$ are the spherical spin–tensors of the photon and the deuteron, respectively. It should be noted that, at a given initial-state energy, polarization observables of the two-body reaction depend only on one kinematical variable, scattering angle; in the three-body reaction, however, the analogous observables depend on five variables, whose choice is ambiguous. Frequently, the momentum and two emission angles for one of the particles and two emission angles for a second particle are chosen for these.

4. In order to illustrate the effects of rescattering, we have calculated the squared moduli of the amplitudes corresponding to the diagrams in Fig. 1, the components of the analyzing power of reaction (1) with respect to beam and target polarizations ($T_{22,00}$ and $T_{00,20}$, respectively), and the polarization of one of the final protons ($P1_y$). The calculations were performed in the c.m. frame of reaction (1) under the conditions of coplanar kinematics. The results are presented below versus the proton-emission angle θ_2 at $p_1 = 300$ MeV/c, $\theta_1 = 100°$, $\phi_1 = 0°$, $\phi_2 = 180°$, and $E_\gamma = 360$ MeV.

Figure 3 shows the quantities obtained upon averaging the squared moduli of the amplitudes over the spins of the initial particles and summing the result of this averaging over the spins of final particles. At proton-emission angles θ_2 in excess of 120°, the effect of rescatterings is insignificant in relation to the contribution of the spectator mechanism. For this reason, these results are displayed only for θ_2 values between 0° and 120°. In these data, the most spectacular feature is that the squared modulus of the amplitude for on-shell pion–nucleon rescattering has a distinct maximum at $\theta_2 \sim 40°$. The main contribution to this maximum comes from the first term in the amplitude given by (11). This term corresponds to the case where the proton with the momentum $\mathbf{p}_1$ participates in the scattering process. In this kinematical domain, the value of $|p_-|$ is

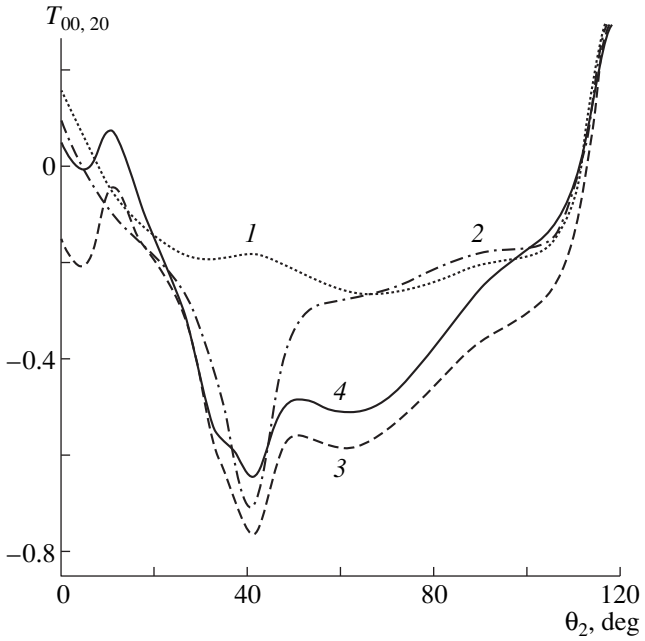

Fig. 4. Effect of rescatterings on the reaction analyzing power $T_{00,\,20}$ (the calculations were performed for the same kinematics as in Fig. 3): (*1*) results produced by the spectator model, (*2*) results taking into account on-shell pion–nucleon rescattering, (*3*) results taking into account on-shell and off-shell pion–nucleon rescatterings, and (*4*) results taking into account on-shell and off-shell pion–nucleon rescatterings and nucleon–nucleon rescattering.

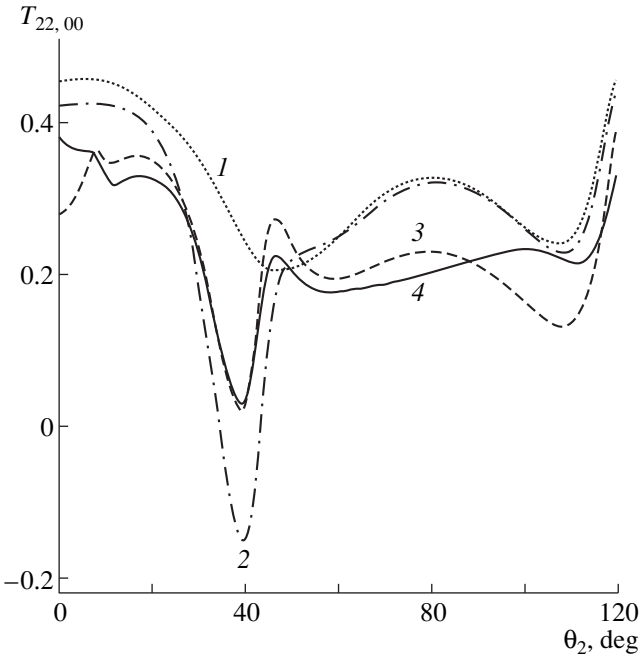

Fig. 5. Effect of rescatterings on the reaction analyzing power $T_{22,\,00}$ (the calculations were performed for the same kinematics as in Fig. 3). The notation for the curves is identical to that in Fig. 4.

small for the first term in (11), so that the integral in (15) is maximal. As to off-shell pion–nucleon rescattering, the main contribution to it comes from the first term in the amplitude given by (12). In just the same way as in the preceding case, this term corresponds to the rescattering of the proton with the momentum $\mathbf{p}_1$. The behavior of the amplitude for off-shell pion–nucleon rescattering is determined primarily by the dependence of the integral

$$I_{\text{off-shell}} = P\int d^3p' \frac{u_0\left(\frac{1}{2}(|\mathbf{d}-2\mathbf{p}'|)\right)}{q'^2 - m_\pi^2}$$

on the proton emission angle θ_2. The contribution of nucleon–nucleon rescattering increases fast with decreasing kinetic energy of the relative motion of final nucleons. This is because the $^1S_0$ phase shift increases in that case. In Fig. 3, this is manifested in the growth of the contribution from nucleon–nucleon rescattering in the region of small θ_2. With increasing kinetic energy of the relative motion of final nucleons, the contribution of $^1S_0$ scattering decreases, but this is accompanied by an increase in the contribution of scattering in $L = 1, 2$ states ($^3P_0$, $^3P_1$, $^3P_2$, $^1D_2$). In Fig. 3, an increase in the contribution from nucleon–nucleon rescattering in the region around the point $\theta_2 \sim 90°$ is due to rescatterings in the P and D states.

Figures 4 and 5 illustrate the effect of rescattering on, respectively, the tensor analyzing power with respect to target polarization, $T_{00,\,20} = F^{00,\,00}_{00,\,20}$, and the tensor analyzing power with respect to beam polarization, $T_{22,\,00} = F^{00,\,00}_{22,\,00}$. On-shell pion–nucleon rescattering has the most pronounced effect on these quantities, leading to the emergence of deep minima near a value of $\theta_2 \sim 40°$. Off-shell pion–nucleon rescattering and nucleon–nucleon rescattering reduce the depths of the minima, especially for $T_{22,\,00}$. It is interesting to note that a partial filling of the minimum for $T_{22,\,00}$ is caused by off-shell pion–nucleon rescattering, although the squared modulus of its amplitude has a minimum precisely in the region around $\theta_2 \sim 40°$. The main contribution to the reduction of the minimum depth for $T_{22,\,00}$ comes from the interference of the amplitudes for off- and on-shell pion–nucleon rescattering.

Figure 6 illustrates the effect of rescattering on the polarization of the final proton with the momentum $\mathbf{p}_1$ in the case of an unpolarized initial state. We define the above polarization as

$$P1_y = \frac{\mathrm{tr}TT^\dagger\sigma_y(1)}{\mathrm{tr}TT^\dagger},$$

where T are the helicity amplitudes given by (19), while $(1/2)\sigma_y(1)$ is the operator of the y projection of the pro-

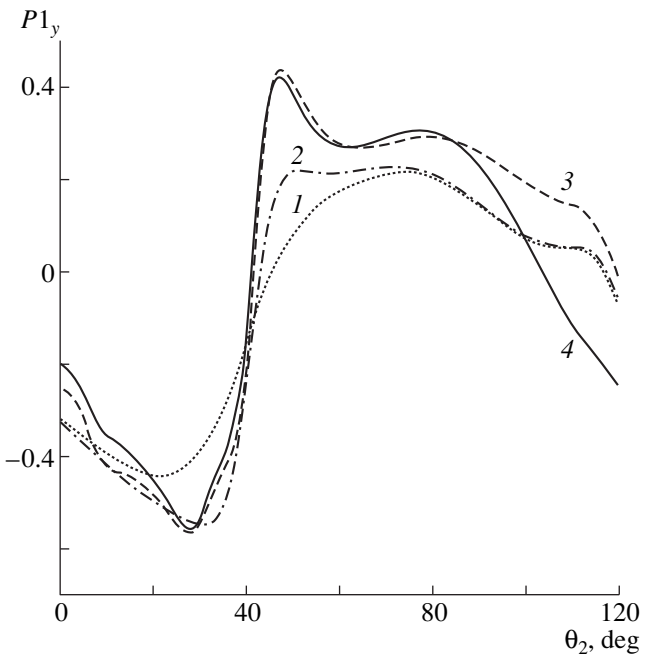

Fig. 6. Effect of rescatterings on the nucleon polarization $P1_y$ (the calculations were performed for the same kinematics as in Fig. 3). The notation for the curves is identical to that in Fig. 4.

ton spin; under the conditions of coplanar kinematics, the other components of the polarization vector vanish. It can be seen that rescattering affects considerably the behavior of $P1_y$, especially in the range $\theta_2 \sim 40°$–$60°$. It should be noted that, in the case of an unpolarized initial state, the polarization of the protons originating from reaction (1) is nonzero even within the spectator model (that is, without allowing for pion–nucleon and nucleon–nucleon rescatterings). This is because the description of pion photoproduction on a nucleon in the delta-isobar region requires taking into account, in addition to the Born terms, the *s*- and *u*-channel contributions of the delta isobar and the contribution of the *t*-channel exchanges of rho and omega mesons. Allowance for the delta-isobar contribution in the *s* channel induces an imaginary part in the amplitude of pion photoproduction on a nucleon; as a result, the final nucleon proves to be polarized even in the case of an unpolarized initial state. At the same time, the polarization of final nucleons from the reaction $e^-d \longrightarrow e'^-pn$ proceeding from an unpolarized initial state is nonzero only if proton–neutron rescattering is taken into account [4], since the amplitude of elastic electron–nucleon scattering is real-valued in the Born approximation.

In summary, we have used a diagrammatic approach to calculate the effect of pion–nucleon and nucleon–nucleon rescatterings on polarization observables of the reaction $\gamma d \longrightarrow pp\pi^-$. Our calculations have revealed that, at high momenta of final-state protons, these rescattering processes affect noticeably the behavior of the polarization observables in the kinematical region of the delta isobar. We would like to emphasize that rescattering effects must be taken into account in analyzing experimental data.

ACKNOWLEDGMENTS

This work was supported in part by the Russian Foundation for Basic Research (project nos. 98-02-17993 and 98-02-17949) and by the International Association for the Promotion of Cooperation with Scientists from the Independent States of the Former Soviet Union (grant no. 96-0424).

REFERENCES

1. A. Yu. Loginov, A. V. Osipov, A. A. Sidorov, *et al.*, Pis'ma Zh. Éksp. Teor. Fiz. **67**, 730 (1998).
2. A. Yu. Loginov, A. V. Osipov, A. A. Sidorov *et al.*, in *Proceedings of the XVI European Conference on Few-Body Problems in Physics, Autrans, France, 1998*, p. 84.
3. J. M. Laget, Nucl. Phys. **A296**, 388 (1978).
4. M. P. Rekalo, G. I. Gakh, and A. P. Rekalo, *Polarization Phenomena in the Interactions of High-Energy Electrons with Deuterons* (Tsentr. Nauch. Issled. Inst. Atominform, Moscow, 1987).
5. M. P. Rekalo, G. I. Gakh, and A. P. Rekalo, Yad. Fiz. **57**, 698 (1994) [Phys. At. Nucl. **57**, 659 (1994)].
6. M. P. Rekalo, G. I. Gakh, and A. P. Rekalo, Yad. Fiz. **59**, 996 (1996) [Phys. At. Nucl. **59**, 952 (1996)].
7. Yu. P. Mel'nik and A. V. Shebeko, Phys. Rev. C **48**, 1259 (1993).
8. M. I. Levchuk, Few-Body Syst. **19**, 77 (1995).
9. I. S. Shapiro, *Theory of Direct Nuclear Reactions* (Gosatomizdat, Moscow, 1963).
10. I. S. Shapiro, Usp. Fiz. Nauk **92**, 549 (1967) [Sov. Phys. Usp. **10**, 515 (1967)].
11. I. Blomqvist and J. M. Laget, Nucl. Phys. **A280**, 405 (1977).
12. R. M. Davidson, N. C. Mukhopadahyay, and R. S. Wittman, Phys. Rev. D **43**, 71 (1991).
13. M. G. Olsson and E. T. Osypowski, Nucl. Phys. B **101**, 136 (1975).
14. M. H. MacGregor, R. A. Arndt, and R. M. Wright, Phys. Rev. **169**, 1128 (1968).
15. R. Schmidt, H. Arenhövel, and P. Wilhelm, Z. Phys. A **355**, 421 (1996).
16. R. Machleidt, K. Holinde, and C. Elster, Phys. Rep. **149**, 1 (1987).
17. J. Hornstein and J. Gross, Phys. Lett. B **47**, 205 (1973).
18. O. F. Nemets and A. M. Yasnogorodskiĭ, *Polarization Studies in Nuclear Physics* (Naukova Dumka, Kiev, 1980).

Translated by A. Isaakyan

Physics of Atomic Nuclei, Vol. 63, No. 3, 2000, pp. 399–413. Translated from Yadernaya Fizika, Vol. 63, No. 3, 2000, pp. 468–483.

NUCLEI
Theory

Mean Field for the p + ^{90}Zr System in the Energy Range –60 MeV < E < +65 MeV and Single-Particle Features of Proton States in ^{90}Zr from a Dispersive Optical-Model Analysis

E. A. Romanovsky, O. V. Bespalova, S. A. Goncharov, D. V. Pleshkov, and T. I. Spasskaya

Institute of Nuclear Physics, Moscow State University, Vorob'evy gory, Moscow, 119899 Russia

Received December 16, 1998; in final form, April 16, 1999

Abstract—Data on the scattering of protons with energies 5 MeV < E < 65 MeV by ^{90}Zr nuclei and data on the energies of proton particle and hole levels in the A + 1 and A – 1 systems with A = 90 are analyzed within the dispersive optical model. The parameters of the mean proton field for ^{90}Zr are determined in the energy range –60 MeV < E < +65 MeV. The predicted single-particle features of the levels (root-mean-square radii of orbits, occupation numbers, spread widths, spectroscopic factors, and spectral functions) comply well with experimental data obtained in (d, ^{3}He), (^{3}He, d), (n, d), and (d, n) reactions for levels near the Fermi surface and in (e, $e'p$) and (p, $2p$) reactions for deep levels. © *2000 MAIK "Nauka/Interperiodica".*

1. INTRODUCTION

The shell and optical models are widely used in studying the structure of nuclei and nuclear reactions. In these models, nucleon–nucleus interaction is described on the basis of the mean-field concept. In traditional realizations of the models, the mean nuclear field is represented as a single-particle local potential that is complex in the optical model (optical potential) and real in the shell model (shell-model potential). These potentials are determined independently of each other in the energy regions $E > 0$ and $E < 0$ within, respectively, the optical and the shell model.

A unified approach to determining a mean field for nucleon–nucleus interaction was developed in recent years (see [1, 2] and references therein). This approach relies on the assumption that the optical and the shell-model potential are both complex-valued; it indicates a way to determine the shell-model potential by extrapolating some parameters found at positive energies to the region of negative energies. The extrapolation procedure is based on the use of dispersion relations between the real and imaginary parts of the mean field and is referred to as a dispersive optical-model analysis. The approach in question makes it possible to determine a unified mean field for both positive and negative energies by using simultaneously experimental data on scattering and on the positions of single-particle levels. This in turn permits a determination of single-particle features of levels such as root-mean-square radii, occupation numbers, spectroscopic factors, and spectral functions at energies well below the Fermi energy, where experimental data are very scanty as a rule.

The dispersive optical-model analysis also provides a physically reasonable description of scattering at energies below the Coulomb barrier, where the predictive power of the traditional optical model is questionable because of well-known continuous and discrete ambiguities. The region of subbarrier energies is interesting in that it is the region where the optical potential can be used to describe both scattering cross sections and the properties of quasistationary nucleon states in a nucleus. In particular, there arises the possibility of describing a direct nucleonic decay of subbarrier single-particle states [3, 4].

The dispersive optical model (see, for example, [5]) and the variational moment approach [6, 7], also known as DOM and VMA, respectively, are the main two versions implementing the above ideas. These versions differ by procedures for constructing the energy dependence of the parameters determining the mean-field potential. In the studies quoted above, these versions were applied to the interactions of neutrons and protons with ^{40}Ca, ^{90}Zr, and ^{208}Pb nuclei. These systems represent an important subject of theoretical and experimental studies, and a vast body of data for bound and scattering states are available in the literature for them. As a development of the DOM version from [5], a procedure was proposed in [8] for determining the parameters of the mean-field potential for protons in the mass-number region $40 \le A \le 208$ and in the energy region –60 MeV < E < +65 MeV on the basis of global systematizations of the potential parameters in the traditional (nondispersive) optical model. In particular, use was made of the CH-89 systematization [9], which was based on an analysis of rich experimental information about differential cross sections for scattering, $\sigma(\theta)$, and the polarization $P(\theta)$ for the above class of nuclei in the energy range 10 MeV < E < 65 MeV. By additionally including data on reaction cross section from [10] in the above analysis, the A dependence of the parameters appearing in the imaginary part of the

1063-7788/00/6303-0399$20.00

potential was determined more precisely (CH-89* version [11]).

In the present study, the DOM version proposed in [8] is used to analyze the $p + {}^{90}$Zr system. We pursue here the following goals.

(i) Within this DOM version, the procedure for determining the mean geometric parameters of the imaginary part of the mean-field potential differs from that in [5]. In contrast to what was done in [5], the data set analyzed here contains data on scattering at low energies (6 MeV < E < 25 MeV); at the same time, the energy range included in our analysis is bounded from above by a value of 65 MeV. Experimental and estimated information about the total proton cross sections for $p + {}^{90}$Zr interactions is used at the initial stage of the analysis. A comparison of the parameter values found in the present study and in [5] is important for assessing the accuracy in determining the parameters.

(ii) In the present study, the calculated features of single-particle states are compared both with the experimental data used in [5] and with the results of the most comprehensive and precise investigation of deep hole states in ^{90}Zr that was performed at the Petersburg Nuclear Physics Institute by the method quasielastic proton scattering at 1 GeV [12]. Owing to this, the predicted and measured features of deep hole states could be compared for the first time.

The present article is organized as follows. In Section 2, we give a brief account of the DOM version used here. In Section 3, we determine the average parameters of the mean-field potential within the DOM version proposed in [8]. Problems that arise in determining the energy dependence of the Hartree–Fock component of the mean-field potential for the $p + {}^{90}$Zr system in the energy range –60 MeV < E < +65 MeV are discussed in Section 4. Proton scattering by ^{90}Zr nuclei for E < 20 MeV is analyzed in Section 5. In Section 6, we compare the calculated and measured features of the bound states in ^{90}Zr. In Section 7, we compare the mean-field parameters for the ^{40}Ca, ^{90}Zr, and ^{208}Pb nuclei. The results of our study are summarized in the Conclusion (Section 8).

2. DISPERSIVE OPTICAL MODEL

The most justified DOM version was applied in [5]. The method developed in [8] for determining the average parameters of the mean field relies on the DOM version from [5]. Given below is a brief description of this version.

The proton–nucleus potential, both in the traditional and in the dispersive version of the optical model, is represented as the sum of three components; that is,

$$U(r, E) = -U_p(r, E) - U_{so}(r, E) + V_{Coul}(r), \quad (2.1)$$

where $U_p(r, E)$ is a central potential, $U_{so}(r, E)$ is the spin–orbit potential, and $V_{Coul}(r)$ is the Coulomb potential.

In the region E < 65 MeV, the real and imaginary parts of the central potential and the spin–orbit potential in the traditional optical model are usually expressed in terms of the Woods–Saxon form as

$$U_p(r, E) = V_R(r, E) + iW_I(r, E)$$
$$= V_R(E) f(r, r_R, a_R) + iW_s(E) f(r, r_s, a_s) \quad (2.2)$$
$$- i \times 4a_d W_d(E) \frac{d}{dr} f(r, r_d, a_d),$$

$$U_{so}(r, E) = 2V_{so}(E) \frac{1}{r} \frac{d}{dr} f(r, r_{so}, a_{so}) \mathbf{l} \cdot \mathbf{s}, \quad (2.3)$$

where

$$f(r, r_i, a_i) = \frac{1}{1 + \exp[(r - r_i A^{1/3})/a_i]}$$
$$(i = R, s, d, so)$$

is the Woods–Saxon function. The Coulomb interaction is simulated by the potential of a uniformly charged sphere of radius $R_{Coul} = r_{Coul} A^{1/3}$. The subscripts s and d label, respectively, the volume and the surface part of the imaginary potential. Within the DOM, the central component of the mean-field potential can be represented as the sum of two components, a static and a dynamical one. The former is a smooth function of E determined by the local approximation. Physically, it corresponds to the Hartree–Fock potential for the system of A nucleons; therefore, it is usually referred to as the Hartree–Fock component of the mean field (V_{HF}). The dynamical component is a complex quantity dependent sharply on energy near E_F. It is assumed that this component carries information about correlation (for $E < E_F$) and dynamical polarization (for $E > E_F$) effects. By virtue of analytic properties, its real and imaginary parts (ΔV and W, respectively) are related by a dispersion equation. In view of this, the dynamical component is often referred to as a dispersive term. It is precisely this component that determines the important energy dependence of the central component (V_R):

$$U_p(r, E) = V_R(r, E) + iW_I(r, E)$$
$$= V_{HF}(r, E) + \Delta V_s(r, E) + \Delta V_d(r, E) + iW_I(r, E). \quad (2.4a)$$

For this component, we also use the Woods–Saxon parametrization

$$U_p(r, E) = V_{HF}(E) f(r, r_{HF}, a_{HF})$$
$$+ \Delta V_s(E) f(r, r_s, a_s) - 4a_d \Delta V_d(E) \frac{d}{dr} f(r, r_d, a_d) \quad (2.4b)$$
$$+ iW_s(E) f(r, r_s, a_s) - i \times 4a_d W_d(E) \frac{d}{dr} f(r, r_d, a_d).$$

The volume and the surface dispersive components of the real potential [$\Delta V_s(r, E)$ and $\Delta V_d(r, E)$, respectively] can be calculated with the aid of the dispersive relation,

provided that the corresponding components of the imaginary part are known. Specifically, we have

$$\Delta V_{s(d)}(r, E) = (E_F - E)\frac{P}{\pi}\int_{-\infty}^{\infty}\frac{W_{s(d)}(r, E')}{(E' - E_F)(E - E')}dE', \quad (2.5)$$

where the symbol P denotes the principal value of an improper integral.

Various applications of the optical potential are often based on the traditional Woods–Saxon form of the real potential. In order to go over from the parameters of $V_R^{DOM}(r, E)$ to the parameters of the effective real Woods–Saxon potential, $V_R^{eff}(E)$ and $r_R^{eff}(E)$, we can proceed as in [6], requiring invariability of the volume integral of the real potential and invariability of the real-potential value at $r = 0$. The diffuseness a_R of the effective potential then coincides with the parameter a_{HF} for the Hartree–Fock component of the real dispersive optical potential.

We note that, in (2.4b), the same geometric shape of $f(r, r_i, a_i)$ $(i = s, d)$ is assumed for the corresponding components of the dispersive part and the imaginary part of the potential. This follows from fulfillment of the dispersion relation between these components, provided that the geometric shape of $f(r, r_i, a_i)$ $(i = s, d)$ is independent of (or dependent very slightly on) energy, or, in other words, provided that the same is true for geometric parameters $r_{s(d)}$ and $a_{s(d)}$, which determine this function.

Experimental data on scattering can be conveniently analyzed in terms of the volume integrals of the potential components being considered:

$$J_i(E) = \frac{4\pi}{A}\int_0^{\infty}V_i(r, E)r^2dr, \quad i = R, HF; \quad (2.6)$$

$$J_{\Delta V_i}(E) = \frac{4\pi}{A}\int_0^{\infty}\Delta V_i(r, E)r^2dr; \quad (2.7)$$

$$J_i(E) = \frac{4\pi}{A}\int_0^{\infty}W_i(r, E)r^2dr, \quad i = s, d; \quad (2.8)$$

$$J_I(E) = J_s(E) + J_d(E). \quad (2.9)$$

The dispersion relation (2.5) remains in force for these volume integrals as well:

$$J_{\Delta V_i}(E) = (E_F - E) \times \frac{P}{\pi}\int_{-\infty}^{\infty}\frac{J_i(E')}{(E' - E_F)(E - E')}dE', \quad i = s, d. \quad (2.10)$$

The volume integrals $J_i(E)$ (2.8) and J_I (2.9) of the imaginary potential are determined on the basis of the parameters W_s, W_d, r_s, a_s, r_d, and a_d found within the conventional optical model from an analysis of data on elastic scattering for each energy value E_k individually. In order to determine the dispersive contributions $J_{\Delta V_s}(E)$ and $J_{\Delta V_d}(E)$ according to (2.10), the resulting sets $J_s(E_k)$, $J_d(E_k)$, and $J_I(E_k)$ are approximated by dependences that are integrable analytically. Various expressions for $J_I(E)$ and $J_s(E)$ were considered in [1, 2]. Here, in just the same way as in [5, 8], $J_I(E_k)$ and $J_s(E_k)$ are approximated by the JM formulas [1]

$$J_i^{JM}(E) = \alpha_i\frac{(E - E_F)^4}{(E - E_F)^4 + \beta_i^4}, \quad i = I, s; \quad (2.11)$$

$$J_d^{JM}(E) = J_I^{JM}(E) - J_s^{JM}(E). \quad (2.12)$$

The parameters α_I and β_I are determined by minimizing the functional χ^2 in fitting $J_I^{JM}(E)$ to the set $J_I(E_k)$, while the parameter β_s is determined by fitting $J_s^{JM}(E)$ to the set $J_s(E_k)$ (in doing this, it is assumed that $\alpha_I = \alpha_s$). Upon this parametrization, the integral in (2.10) is calculable analytically. The results are

$$J_{\Delta V}(E) = \frac{\alpha_I\beta_I(E - E_F)[(E - E_F)^2 + \beta_I^2]}{\sqrt{2}[(E - E_F)^4 + \beta_I^4]}, \quad (2.13)$$

$$J_{\Delta V_s}(E) = \frac{\alpha_I\beta_s(E - E_F)[(E - E_F)^2 + \beta_s^2]}{\sqrt{2}[(E - E_F)^4 + \beta_s^4]}, \quad (2.14)$$

$$J_{\Delta V_d}(E) = J_{\Delta V}(E) - J_{\Delta V_s}(E). \quad (2.15)$$

A transition to the strength parameters of the potential is accomplished by using the formulas

$$W_s(E) = \frac{J_s(E)}{\int f(r, r_s, a_s)d\mathbf{r}}, \quad W_d(E) = \frac{J_d(E)}{4a_d\int\frac{df(r, r_d, a_d)}{dr}d\mathbf{r}}, \quad (2.16)$$

$$\Delta V_s(E) = \frac{J_{\Delta V_s}(E)}{\int f(r, r_s, a_s)d\mathbf{r}}, \quad \Delta V_d(E) = \frac{J_{\Delta V_d}(E)}{4a_d\int\frac{df(r, r_d, a_d)}{dr}d\mathbf{r}}. \quad (2.17)$$

In analyzing $\sigma^{expt}(\theta)$, $P^{expt}(\theta)$, and σ_r^{expt} on the basis of the DOM, the substitution of (2.16) and (2.17) into (2.2) makes it possible to find, for each value of E_k, ten parameters of the mean-field potential. These are V_{HF}, r_{HF}, a_{HF}, r_s, a_s, r_d, a_d, V_{so}, r_{so}, and a_{so}. From individual parameter sets, we then determine the energy-averaged

geometric parameters r_{HF}, a_{HF}, r_s, a_s, r_d, a_d, r_{so}, and a_{so}, as well as the energy dependence of the strength parameter $V_{so}(E)$. Further, the fitting procedure is applied once again in order to derive the optimal parameters $V_{HF}(E_k)$ at fixed averaged parameters listed above. On the basis of the set $V_{HF}(E_k)$, we can determine the averaged energy dependence $V_{HF}(E)$ for $E > 0$.

In order to find $V_{HF}(E)$ for $E < 0$, we use experimental information about the energies of particle and hole levels E_{nlj}^{expt} in the $A + 1$ and $A - 1$ systems, respectively. In solving the Schrödinger equation for bound states,

$$\left[-\frac{\nabla^2}{2m} + V(r, E_{nlj})\right]\Phi_{nlj}(\mathbf{r}) = E_{nlj}\Phi_{nlj}(\mathbf{r}), \quad (2.18)$$

where

$$\begin{aligned} -V(r, E_{nlj}) &= V_{HF}(r, E_{nlj}) + \Delta V_s(r, E_{nlj}) \\ &+ \Delta V_d(r, E_{nlj}) + U_{so}(r, E_{nlj}), \end{aligned} \quad (2.19)$$

the method that relies on fitting the well depth is used to determine the strength parameters $V_{HF}(E_{nlj})$ and the single-particle wave functions for the subshell having the quantum numbers n, l, and j:

$$\Phi_{nlj}(\mathbf{r}) = \frac{u_{nlj}(r)}{r}Y_{lm}(\mathbf{\Omega}). \quad (2.20)$$

The parameters $\Delta V_s(E)$ and $\Delta V_d(E)$ of the potential (2.19) are calculated by formulas (2.17); for the geometric parameters, we take averaged results from the analysis of scattering data. In the following, the wave functions (2.20) are used to determine the single-particle features of the levels.

3. $p + {}^{90}$Zr SYSTEM: DETERMINATION OF AVERAGED PARAMETERS

As in [5], we analyze here the $p + {}^{90}$Zr system. In this analysis, we included data from [13] at $E_k = 6.35$ and 8.38 MeV; data from [14] at 9.7, 9.8, 10.75, 12.7, 16.0, 18.8, 19.08, 20.25, 20.37, 22.04, 22.5, 22.9, 40.0, 49.39, and 61.4 MeV; and data from [5] at 30 and 65 MeV. In contrast to [5], we restricted our analysis to the energy region $E \le 65$ MeV, but we included a vast body of data from the energy region $E < 20$ MeV.

In [5], the average values of the geometric parameters $r_{s(d)}$ and $a_{s(d)}$ were fixed by using the parameter sets determined in the conventional optical model individually for each specific energy value E_k. The parameters r_s and a_s were averaged over the interval 80 MeV $< E <$ 135 MeV, where surface absorption is negligibly small, while the parameters r_d and a_d were averaged over the region $E < 80$ MeV. This way is well validated, but it is difficult to implement it for the majority of $40 < A < 208$ nuclei, because the main body of experimental data for these nuclei was obtained for energies in the region $E < 65$ MeV. We note that the individual analysis from [5] did not invoke data on total reaction cross sections σ_r. The values obtained in [5] for $J_I(E_k)$ in the energy interval 20–65 MeV differ from their arithmetic mean of $\langle J_I(E_k)\rangle_{20-65\,\mathrm{MeV}} = 107$ MeV fm^3 by more than 10%.

In analyzing data on the $p + {}^{40}$Ca system within the VMA version, Maxaux and Sartor [6] showed that the mean parameters of the conventional optical model can be used for the mean values of the parameters $r_{s(d)}$ and $a_{s(d)}$. In [8], it was proposed to determine the parameters $r_{s(d)}$ and $a_{s(d)}$ by using the global systematization CH-89* [9], which was composed for the parameters of the conventional optical model and which included data on total reaction cross section measured to within 3% [10]. For the $p + {}^{90}$Zr system, the dependence $\sigma_r^{est}(E)$ in the region $20 < E < 65$ MeV was estimated in [11] to within 5%. The result proved to be in fairly good agreement with that which was found within the conventional optical model with the parameter values from the CH-89* systematization ($a_d^* = 0.61$ fm). For the imaginary volume integral $J_I \le (E)$, the mean value obtained in [11] for this energy interval is $\langle J_I^{CH\text{-}89^*}(E)\rangle = 100 \pm 2$ MeV fm^3.

In accordance with what was said in Section 2, the first stage of our analysis involves determining the parameters α_I, β_I, and β_s, which appear in (2.11) and which are used to calculate, by means of dispersion relations, the strength parameters of the components of the dispersive term in the real part of the mean-field potential [see equations (2.13)–(2.17)].

First of all, we note that, at sufficiently high energies, the approximate relation $\alpha_I \approx J_I(E)$ follows from (2.11). From the results presented in [5, 8, 11], it can be seen that, in the approximation given by (2.11), the dependence $J_I(E)$ for $p + {}^{90}$Zr at $\beta \approx 10$ MeV approaches a nearly constant value for $E > 20$ MeV. Therefore, it is expedient to fix the parameter α_I at the value equal to $\langle J_I^{CH\text{-}89^*}(E)\rangle$; that is,

$$\alpha_I = 100 \text{ MeV fm}^3. \quad (3.1)$$

(The value of $\alpha_I = 106.97$ MeV fm^3 was found in [5].) Thus, it is seen that, by additionally invoking, at the initial stage of the analysis, data on total reaction cross sections, we were able to refine the α_I value fixed in the ensuing calculations. The parameter β_I is determined by the values of $J_I(E_k)$ in the region $E_k \le 20$ MeV. At $E \approx 10$ MeV, reliable values of the volume integrals $J_I(E_k)$ within the conventional optical model are clustered in the interval 75–90 MeV fm^3, which corresponds to the interval 9.4 MeV $\le \beta_I \le$ 12.2 MeV. The value of $\beta_I = 12.208$ MeV was obtained in [5]. In the present study, the calculations were performed at $\beta_I = 12.2$ and 9.4 MeV. The dependence $J_I^{JM}(E)$ according to (2.11) at the above two β_I values and at $\alpha_I = 100$ MeV fm^3 is displayed in Fig. 1, along with the dependence

$J_I^{\text{CH-89*}}(E)$. In Section 5, it will be shown that the above ambiguity in β_I does not have a pronounced effect on the agreement between the calculated and measured values of the cross sections. The results presented below were obtained at

$$\beta_I = 12.2 \text{ MeV}, \tag{3.2}$$

unless otherwise stated.

The results of numerous analyses within the conventional optical model reveal that, because of ambiguities inherent in multiparametric fits, the quantities $J_s(E_k)$ show a wider scatter than $J_I(E_k) = J_s(E_k) + J_d(E_k)$ do. For some nuclei with mass numbers between 40 and 124, the scatter of the empirical values of $J_s(E_k)$ often goes beyond the corridor within which the dependences $J_s^{\text{CH-89*}}(E)$ predicted for these nuclei lie. Therefore, the parameter β_s extracted from a fit of $J_s^{\text{JM}}(E_k)$ to the set of empirical values of $J_s(E_k)$ (this procedure was employed in [5]) is determined with large uncertainties. In the present study, the value of β_s was found from the condition requiring that the deviation of $J_s^{\text{JM}}(E)$ from $J_s^{\text{CH-89*}}(E)$ be minimal in the interval 20–65 MeV (see Fig. 1). The value of

$$\beta_s = 60.3 \text{ MeV}, \tag{3.3}$$

which was deduced in this way, is 30% greater than the value of β_s = 46.695 MeV, which was obtained in [5]. The distinctions between the β_s and α_I values from this study and those from [5] lead to a 30% decrease in $J_{\Delta V_s}(E)$ (2.14) for energies of $E \le 30$ MeV in relation to the result presented in [5]. In the energy region 30 MeV < E < 60 MeV, the dependence $J_{\Delta V_s}(E)$ obtained here is close to that in [5].

At the next stage, we determine the mean values of the geometric parameters of the spin–orbit potential and a smooth energy dependence of the strength parameter $V_{\text{so}}(E)$. The CH-89 systematization of the potential parameters was based not only on the analysis of a vast body of data on elastic-scattering cross sections but also on analyses of polarizations. For the p + ^{90}Zr system, the mean values of the parameters of the spin–orbit potential in the CH-89 systematization are close to values obtained in [5]. In the present study, we employed the mean values of the parameters of the spin–orbit potential both from [5] and from [9]. The calculations revealed that the small distinctions between the values obtained in [5] and in [9] for the parameters of the spin–orbit potential have only a slight effect on the determination of the parameters of the Hartree–Fock component. Wiesel *et al.* [15] studied changes in the positions E_{nlj} of single-particle levels in response to variations in the parameter V_{so} between 5.3 and 7.3 MeV and in response to variations in the parameter r_{so} between 1.03 and 1.23 fm at a fixed value of a_{so}.

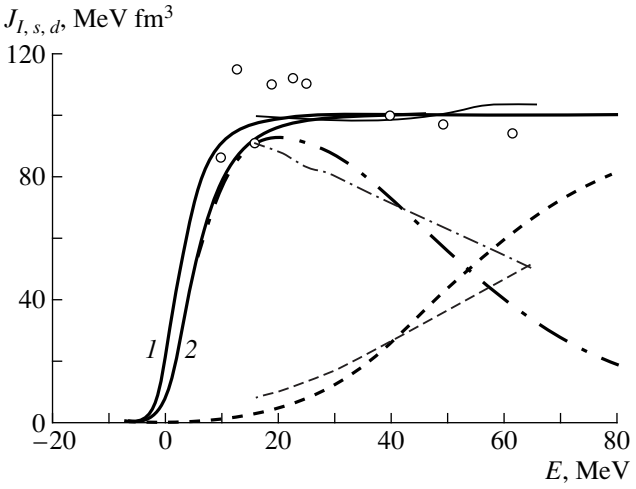

Fig. 1. Volume integrals of the imaginary potential for the p + ^{90}Zr system: (thick solid curves *1* and *2*) $J_I^{\text{JM}}(E)$ at β_I = 9.4 and 12.2 MeV, respectively; (thin solid curve) $J_I^{\text{CH-89*}}(E)$; (thick dashed curve) $J_s^{\text{JM}}(E)$; (thin dashed curve) $J_s^{\text{CH-89*}}(E)$; (thick dash-dotted curve) $J_d^{\text{JM}}(E)$; (thin dash-dotted curve) $J_d^{\text{CH-89*}}(E)$; and (points) empirical value of J_I^{DOM} within the conventional optical model.

The calculations performed there for the n + ^{208}Pb system showed that, for particle and for hole states, the values of E_{nlj} undergo virtually no changes for j < 7/2, depending noticeably on V_{so} and r_{so} only for j > 7/2. Because these regularities are observed both for protonic and for neutronic systems and because our calculations were performed only for $j \le 9/2$, moderately small uncertainties in choosing the parameters of the spin–orbit potential must not affect the results of the calculations for E_{nlj}. For this reason, we will henceforth fix the parameters of the spin–orbit potential in accordance with [9], setting them to

$$\begin{aligned} V_{\text{so}}(E) &= 5.9 \text{ MeV fm}^2, \\ r_{\text{so}} = 1.072 \text{ fm}, &\quad a_{\text{so}} = 0.63 \text{ fm}. \end{aligned} \tag{3.4}$$

The next step consists in determining the parameters of the Hartree–Fock component of the potential given by (2.4a) and (2.4b). For this purpose, we first fix the geometric parameters of the imaginary part of this potential at the CH-89* values of

$$r_d = r_s = 1.24 \text{ fm}, \tag{3.5}$$

$$a_d = a_s = 0.61 \text{ fm} \tag{3.6}$$

and calculate the parameters W_s, W_d, ΔV_s, and ΔV_d at

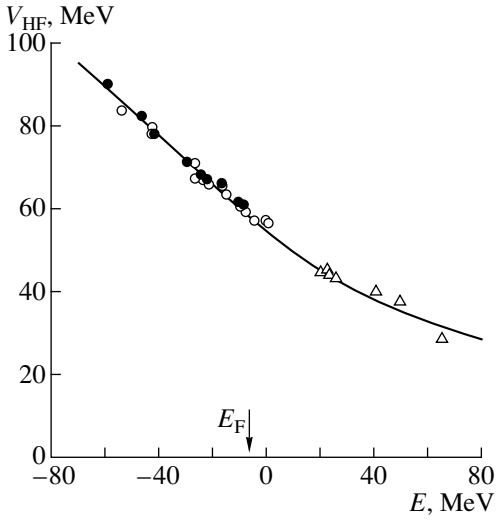

Fig. 2. Strength parameter of the Hartree–Fock component of the dispersive optical potential for the $p + {}^{90}$Zr system: (solid curve) dependence specified by equations (4.1) and (4.4) with the parameters set to the values from (4.2), (4.3), (4.6), and (4.7); (closed circles) $V_{HF}(E_{nlj})$ values for E_{nlj} from [12]; (open circles) $V_{HF}(E_{nlj})$ values for E_{nlj} from [16–21]; and (open triangles) our data for $E_k > 0$.

each energy value E_k according to the equations

$$W_s(E_k) = \frac{J_s^{JM}(E_k)}{\int f(r, r_s, a_s)d\mathbf{r}},$$
$$W_d(E_k) = \frac{J_d^{JM}(E_k)}{4a_d\int \frac{df(r, r_d, a_d)}{dr}d\mathbf{r}}, \quad (3.7)$$

$$\Delta V_s(E_k) = \frac{J_{\Delta V_s}(E_k)}{\int f(r, r_s, a_s)d\mathbf{r}},$$
$$\Delta V_d(E_k) = \frac{J_{\Delta V_d}(E_k)}{4a_d\int \frac{df(r, r_d, a_d)}{dr}d\mathbf{r}}. \quad (3.8)$$

The values of $J_s^{JM}(E)$, $J_d^{JM}(E)$, $J_{\Delta V_s}(E)$, and $J_{\Delta V_d}(E)$ were found on the basis of equations (2.11)–(2.15). The parameters $V_{HF}(E_k)$, $r_{HF}(E_k)$, and $a_{HF}(E_k)$ were established by means of two procedures. Within the first of these, all three parameters were varied freely, and their set was determined, for each individual energy value E_k, by minimizing the χ^2 functional in fitting the computed values $\sigma^{DOM}(\theta)$, $P^{DOM}(\theta)$, and $\sigma_r^{DOM}(E_k)$ to the corresponding experimental results in the range 20 MeV < E < 65 MeV. Within the second procedure, the strength parameter of the Hartree–Fock component was estimated by using the CH-89 systematization of the parameters:

$$V_{HF}(E_k) = \frac{J_{HF}(E_k)}{\int f(r, r_{HF}, a_{HF})d\mathbf{r}} = \frac{J_R^{CH\text{-}89}(E_k) - J_{\Delta V}(E_k)}{\int f(r, r_{HF}, a_{HF})d\mathbf{r}}. \quad (3.9)$$

The last equality is based on the results presented in [11], where it was shown that, to within 3–5%, the empirical values of J_R corresponding to those parameter sets that make it possible to reproduce not only $\sigma^{expt}(\theta)$ and $P^{expt}(\theta)$ but also $\sigma_r^{expt}(E_k)$ are consistent with the values $J_R^{CH\text{-}89}$ for $40 < A < 124$ and 20 MeV < E < 65 MeV. At this step, the geometric parameters $r_{HF}(E_k)$ and $a_{HF}(E_k)$ remained free. As within the first procedure, their values were determined for each individual value of E_k. The calculations relied on the modified SPI-GENOA code, which makes it possible to vary the geometric parameters of the potential at fixed values of the corresponding volume integrals. In either case, we used the values from (3.1)–(3.6) and r_{Coul} = 1.264 fm [9]. The values of $V_{HF}(E_k)$, $r_{HF}(E_k)$, and $a_{HF}(E_k)$ as determined by applying the above two procedures are consistent within 1 to 2%. On the basis of the resulting parameter sets, we found the mean values of the geometric parameters of the Hartree–Fock components in the energy range 20–65 MeV. The results are

$$r_{HF} = 1.24 \pm 0.04 \text{ fm}, \quad (3.10)$$
$$a_{HF} = 0.68 \pm 0.02 \text{ fm}. \quad (3.11)$$

4. $p + {}^{90}$Zr SYSTEM: DETERMINATION OF THE ENERGY DEPENDENCE $V_{HF}(E)$ IN THE ENERGY RANGE –60 MeV < E < +60 MeV

The energy dependence $V_{HF}(E)$ was determined on the basis of data on $V_{HF}(E_k)$ for 20 MeV < E_k < 65 MeV and data on $V_{HF}(E_{nlj})$ for $E < 0$ at r_{HF} and a_{HF} values fixed according to (3.10) and (3.11). For 20 MeV < E_k < 65 MeV, $V_{HF}(E_k)$ values are presented in Fig. 2. In order to determine $V_{HF}(E)$ for $E < 0$, we used experimental information from [12, 16–21] on the energies of particle and hole states in the systems $A + 1$ and $A - 1$ systems ($A = 90$), respectively, which was obtained from an analysis of various nuclear reactions and which is displayed in Table 1.

The energies of bound states were computed with the aid of subroutines from the DRUCK-4 package [22]. The strength parameter $V_{HF}(E_{nlj})$ was determined by fitting the energies E_{nlj} calculated for single-particle states in solving the Schrödinger equation (2.18) with the potential (2.19) to the corresponding experimental values. In doing this, the parameters r_{HF} and a_{HF} were set to the values in (3.10) and (3.11) and were not varied, while the spin–orbit potential was fixed in accordance with (3.4). The fitted values of $V_{HF}(E_{nlj})$ are given

Table 1. Energies E_{nlj} (in MeV) of single-particle proton states in ^{90}Zr

nlj	Experimental data							Results of the calculations	
	$(e, e'p)$ [16]	$(p, 2p)$ [17]**	$(p, 2p)$ [12]	$(d, {}^3\mathrm{He})$ [18]	(n, d) [19]	$({}^3\mathrm{He}, d)$ [20]	(d, n) [21]	our study	[5]
$2d_{5/2}$						–1.30	–1.09	–0.05	–0.45
$1g_{7/2}$						–0.34		>0	>0
$1g_{9/2}$						–5.11	–5.16	–5.10	–4.87
$2p_{1/2}$	–8.36		–9.1(0.4)*	–8.36	–8.36			–8.10	–8.60
$2p_{3/2}$	–10.4 (0.2)			–9.87	–9.87			–9.66	–10.30
$1f_{5/2}$	–10.8 (0.2)		–11.0 (0.4)	–10.11	–10.11			–9.84	–9.68
$1f_{7/2}$	–17.0 (0.5)		–17.2 (0.5)	–15.56				–15.38	–15.69
$2s_{1/2}$	–21.8 (0.4)		–22.3 (0.5)					–23.8	–24.01
$1d_{3/2}$	–23.8 (0.5)*	–27.0 (0.8)*	–24.8 (0.6)					–25.78	–25.19
$1d_{5/2}$			–30.2 (0.8)					–31.72	–30.39
$1p_{1/2}$		–43.0 (0.8)*	–41.9 (1.1)					–43.03	–41.81
$1p_{3/2}$			–46.8 (1.5)					–45.24	–44.40
$1s_{1/2}$		–54.0 (0.8)	–59.4 (2.1)					–57.62	–59.88

* Mean value for the n_l orbits.

** Data from [17] were borrowed from Table 2 of the study of Vorob'ev [12].

in Fig. 2. On the basis of this data on $V_{\mathrm{HF}}(E_{nlj})$, we approximated it in the region $E < E_{\mathrm{F}}$ by the dependence

$$V_{\mathrm{HF}}(E) = V_{\mathrm{HF}}(E_{\mathrm{F}}) - \lambda(E - E_{\mathrm{F}}), \quad (4.1)$$

where the parameters found on the basis of a least squares fit are

$$V_{\mathrm{HF}}(E_{\mathrm{F}}) = 58.06 \pm 0.81 \text{ MeV}, \quad (4.2)$$

$$\lambda = 0.591 \pm 0.035. \quad (4.3)$$

Information about $V_{\mathrm{HF}}(E_{nlj})$ values that was deduced from an analysis of experimental data presented in [12] for the energy region –60 MeV ≤ E ≤ –9 MeV suggests that, for –60 MeV ≤ E ≤ E_{F}, $V_{\mathrm{HF}}(E)$ is a linear function of energy to within 5%. The parameter values in (4.2) and (4.3) are close to the values of $V_{\mathrm{HF}}(E_{\mathrm{F}})$ = 60.8 MeV and λ = 0.606, which were found in [5] under the assumption of a linear behavior of $V_{\mathrm{HF}}(E)$ in the region –25 MeV ≤ E ≤ E_{F}.

In a number of studies (see [1] and references therein), it is assumed that $V_{\mathrm{HF}}(E)$ is a linear function of energy for E > 0 as well. From Fig. 2, it can be seen, however, that the functional form of $V_{\mathrm{HF}}(E)$ for $E < E_{\mathrm{F}}$ is different from that for $E > E_{\mathrm{F}}$. That $V_{\mathrm{HF}}(E)$ is a linear function of energy for $E > E_{\mathrm{F}}$ leads to the reversal of the sign of the real potential at $E \approx 90$ MeV rather than in the region $E \approx$ 350–500 MeV, as is predicted by an analysis of scattering data within the relativistic version of the conventional optical model [23].

In just the same way as in [5], $V_{\mathrm{HF}}(E)$ for $E > E_{\mathrm{F}}$ is approximated here by the dependence

$$V_{\mathrm{HF}}(E) = V^1_{\mathrm{HF}}(E_{\mathrm{F}}) + V^2_{\mathrm{HF}}(E_{\mathrm{F}}) \exp\left[\frac{-\lambda(E - E_{\mathrm{F}})}{V^2_{\mathrm{HF}}(E_{\mathrm{F}})}\right], \quad (4.4)$$

$$V_{\mathrm{HF}}(E_{\mathrm{F}}) = V^1_{\mathrm{HF}}(E_{\mathrm{F}}) + V^2_{\mathrm{HF}}(E_{\mathrm{F}}), \quad (4.5)$$

where the parameter values are

$$V^1_{\mathrm{HF}}(E_{\mathrm{F}}) = 15.16 \text{ MeV}, \quad (4.6)$$

$$V^2_{\mathrm{HF}}(E_{\mathrm{F}}) = 42.90 \text{ MeV}. \quad (4.7)$$

In Figs. 3*b* and 3*c*, the elastic-scattering differential cross sections and polarizations calculated with the parameter values from (3.1)–(3.6), (3.10), (3.11), (4.3), (4.6), and (4.7) are contrasted against relevant experimental data over a broad energy region not covering, however, near-barrier and subbarrier energies. It can be seen from these figures that, in the region E > 20 MeV, the computed dependences $\sigma^{\mathrm{DOM}}(\theta)/\sigma_R$ and $P^{\mathrm{DOM}}(\theta)$ comply well with the experimental angular distributions $\sigma^{\mathrm{expt}}(\theta)/\sigma_R$ and $P^{\mathrm{expt}}(\theta)$.

5. p + ^{90}Zr SYSTEM: ANALYSIS OF SCATTERING DATA IN THE REGION E < 20 MeV

It was shown in [6, 24] that, in the region of near-threshold and subthreshold energies, the assumption that the mean geometric parameters $r_s = r_d$ and $a_s = a_d$ are independent of energy leads to an overestimation of

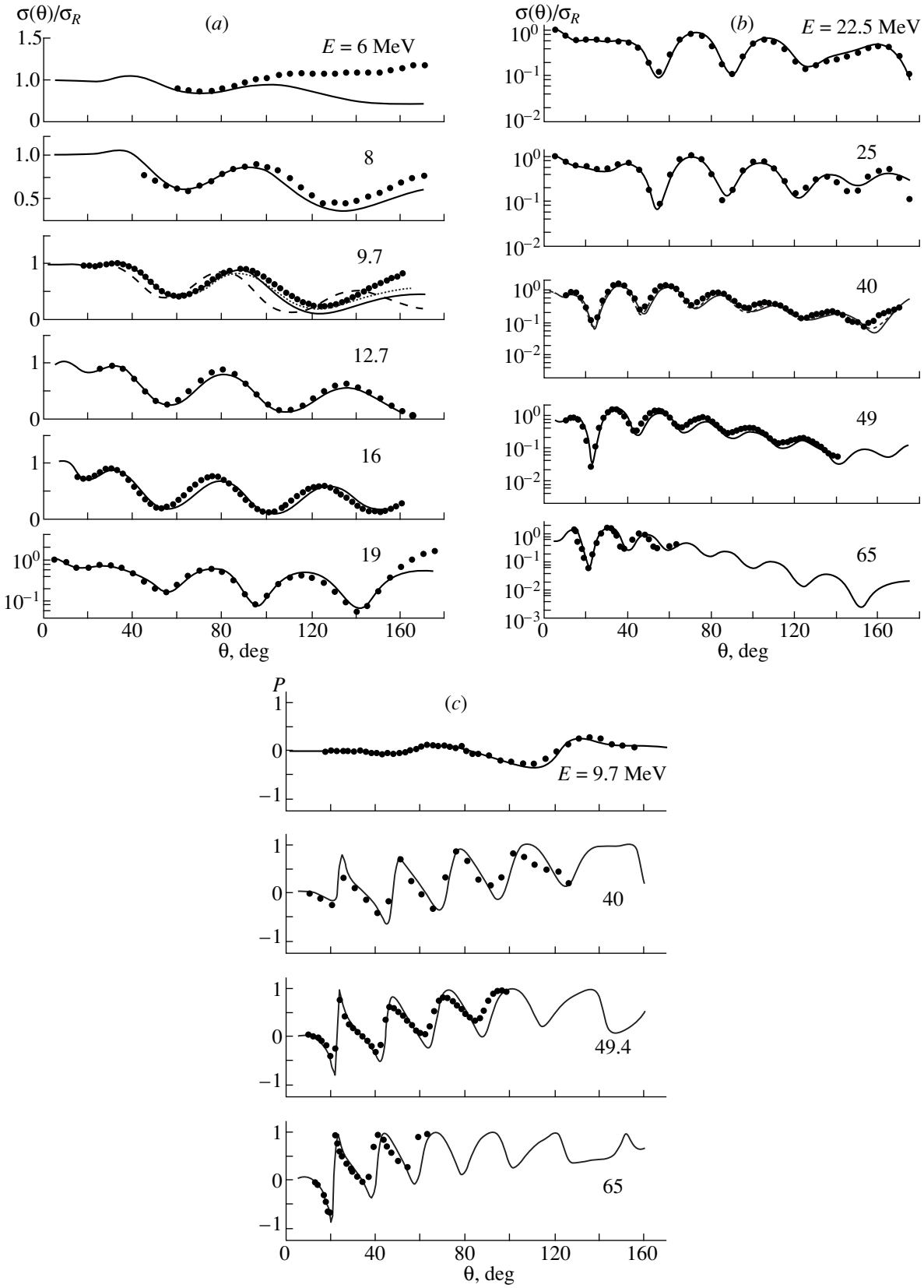

Fig. 3. Differential cross sections for elastic scattering in the energy regions (*a*) $E < 20$ MeV and (*b*) 20 MeV $< E <$ 65 MeV: (points) experimental data, (solid curves) results of the calculations with the average parameters from the present study ($\beta_I = 12.2$ MeV), (dotted curve) results of the calculations with the average parameters from the present study ($\beta_I = 9.4$ MeV), and (dashed curves) results of the calculations with the average parameters from [5]; (*c*) polarizations (the notation here is identical to that in Figs. 3*a* and 3*b*).

the total reaction cross sections and to considerable deviations of $\sigma^{DOM}(\theta)$ and $P^{DOM}(\theta)$ from $\sigma^{expt}(\theta)$ and $P^{expt}(\theta)$. Since the main contribution to absorption at low energies comes from the surface term, σ_r^{DOM} and σ_r^{expt} can be brought into closer proximity by introducing an energy dependence in the geometric parameters r_d and a_d of the imaginary potential at the volume integrals $J_{I,s,d}(E)$ fixed in accordance with (2.11) and (3.1)–(3.3). Agreement with the values $\sigma_r^{est}(E)$ estimated in [11, 25, 26] for $E < 20$ MeV is then achieved by reducing the parameter a_d and by slightly increasing r_d with decreasing energy. As to the volume integrals $J_{I,s,d}(E)$, they still remain fixed in accordance with (2.11) and (3.1)–(3.3), whereas the dispersive surface component is computed with the parameters r_d and a_d set to the values in (3.5) and (3.6).

Following [27], we parametrized the energy dependences of the geometric parameters $r_d(E_k)$ and $a_d(E_k)$ of the imaginary potential (see Fig. 4) for 5 MeV < E < 20 MeV as

$$r_d(E) = r_1 - \frac{r_2(E-E_F)^4}{(E-E_F)^4 + r_3^4}, \quad (5.1)$$

$$a_d(E) = a_1 + \frac{a_2(E-E_F)^4}{(E-E_F)^4 + a_3^4}, \quad (5.2)$$

where

$$r_1 = 1.5 \text{ fm}, \quad r_2 = 0.28 \text{ fm}, \quad r_3 = 12 \text{ MeV},$$
$$a_1 = 0.1 \text{ fm}, \quad a_2 = 0.61 \text{ fm}, \quad a_3 = 18 \text{ MeV}. \quad (5.3)$$

From the dispersion relations, it follows that, if the surface-absorption form is dependent on energy, the potentials $W_d(r(E), E)$ and $\Delta V_d(r(E), E)$ cease to be identical. The estimates presented in [25] give sufficient reason to believe, however, that, in the energy range 5 MeV < E < 20 MeV, the effective real potential $V_R^{eff}(r, E)$ that, in the conventional optical model, corresponds to the DOM potential featuring a dispersive component modified by the energy dependence of the form of the potential $W_d(r(E), E)$ changes insignificantly (by less than 1%) in relation to the potential computed with the parameters r_d and a_d independent of E.

Figure 3*a* shows the cross sections $\sigma^{DOM}(\theta)/\sigma_R$ and $\sigma^{expt}(\theta)/\sigma_R$ for $E < 20$ MeV. The calculations here were performed with the mean values of r_d and a_d from (5.1)–(5.3). At E_k = 6.35, 8.38, and 9.7 MeV, the distinctions between the calculated and measured values of the cross sections for scattering angles in the region $\theta < 90°$ may be due to the contribution of elastic scattering through a compound nucleus. The values calculated for the total reaction cross section on the basis of the DOM, σ_r^{DOM}, agree with the corresponding values

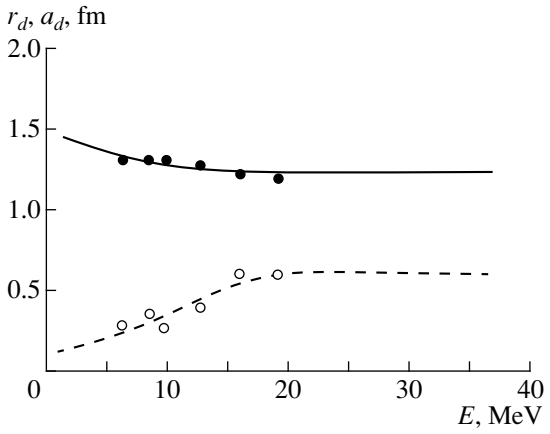

Fig. 4. Geometric parameters of the imaginary surface potential for 5 MeV < E < 20 MeV as functions of energy: (solid curve) $r_d(E)$, (dashed curve) $a_d(E)$, and (points) results of fitting from the present study.

estimated in [26] with allowance for the compound-nucleus contribution, σ_r^{est}, within the errors of the estimate. For E_k = 9.7 MeV, Fig. 3*a* displays two computed dependences $\sigma^{DOM}(\theta)/\sigma_R$ at β_I = 9.4 and 12.2 MeV. It can be seen that these computed angular distributions are close. The computed total reaction cross sections also differ only slightly from each other. In view of this, it proves impossible to remove the ambiguity in β_I by comparing the computed angular dependences $\sigma^{DOM}(\theta)/\sigma_R$ and the computed total reaction cross section with available experimental or estimated values.

The cross section $\sigma_r^{DOM}(E)$ calculated with the mean parameter values found in this study is displayed in Fig. 5 along with the experimental values from [10], the estimates from [11, 28], and the predictions from [5]. From this figure, it can be seen that the cross sections σ_r^{DOM} as computed within our DOM version comply with the experimental data and with the estimates.

6. BOUND STATES

The mean-field parameters were used to calculate the features of single-particle bound protonic states in the A + 1 and A – 1 nuclei at A = 90.

6.1. Energies of Single-Particle Levels in ^{90}Zr

The positions (energies) of single-particle bound states in the mean-field potential were calculated by the method of fitting. The Schrödinger equation (2.18) was solved with the potential $V(r, E_i)$ (2.19) computed by using equation (3.8) with the parameters set to the values in (3.1)–(3.6), (3.10), (3.11), and (4.1)–(4.7); this was done at some energy E_i playing the role of a free parameter. In fitting E_i, the difference between the

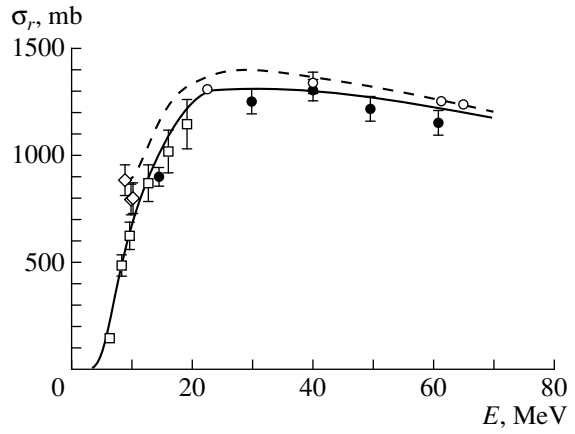

Fig. 5. Total reaction cross section: (closed circles and open diamonds) experimental data from [10] for ^{90}Zr and ^{nat}Zr, respectively; (open squares) estimate from [11]; (open circles) estimate from [28]; (solid curve) results of the calculations with the average parameters from the present study; and (dashed curve) results of the calculations with the average parameters from [5].

resulting eigenvalue $E^{(i)}_{nlj}(E_i)$ and E_i, $\Delta^{(i)}_{nlj} = |E^{(i)}_{nlj}(E_i) - E_i|$, decreases with increasing number i of iterations. By analogy with [29], the value of E_i is treated here as the eigenvalue E_{nlj} as soon as $\Delta^{(i)}_{nlj}$ ceases to exceed 10 keV. The results of seeking E_{nlj} in this way are quoted in Table 1.

We note that, for the levels from the $1g_{9/2}$ to the $1s_{1/2}$ one, the E_{nlj} values computed here agree with those from [5] to within 3%. An experimental investigation of the hole states in ^{90}Zr was performed in [12]. Within the experimental errors, the calculated values of E_{nlj} agree with those measured in [12].

6.2. Effective Proton Mass

The energy dependence of the mean field can be taken into account by introducing the concept of the effective nucleon mass in the real central potential of the nucleus. This quantity is used in the ensuing calculations of the root-mean-square radii, of the occupation numbers for nucleon shells, of spectroscopic factors, and of spectral functions. The ratio of the total effective mass m^* to the bare nucleon mass m is expressed in terms of the derivative of the potential as

$$m^*(r, E)/m = 1 - \frac{d}{dE}V(r, E). \tag{6.1}$$

The Hartree–Fock effective mass $m^*_{\rm HF}$ is defined in a similar way:

$$m^*_{\rm HF}(r, E)/m = 1 - \frac{d}{dE}V_{\rm HF}(r, E). \tag{6.2}$$

The so-called E mass $\bar{m}(r, E)$ is related to m^* and $m^*_{\rm HF}$ by the equation

$$\begin{aligned}\bar{m}(r, E)/m &= m^*(r, E)/m^*_{\rm HF}(r, E)\\ &= 1 - [m/m^*_{\rm HF}(r, E)]\frac{d}{dE}\Delta V(r, E).\end{aligned} \tag{6.3}$$

In evaluating quantities characterizing the single-particle motion of nucleons in a nucleus, the effects of nonlocality can be taken into account in terms of the wave function [1]

$$\bar{u}_{nlj}(r) = C_{nlj}P_{nlj}(r)u_{nlj}(r), \tag{6.4}$$

where

$$P_{nlj}(r) = [m^*_{\rm HF}(r, E_{nlj})/m]^{1/2} \tag{6.5}$$

is the Perey factor and where the normalization factor C_{nlj} is determined from the condition

$$\int_0^\infty \bar{u}^2_{nlj}(r)dr = 1. \tag{6.6}$$

The expectation value of the ratio of the total effective proton mass to the free-proton mass was calculated by the formula

$$\langle m^*_{nlj}/m\rangle = \int_0^\infty \bar{u}^2_{nlj}(r)[m^*(r, E_{nlj})/m]dr. \tag{6.7}$$

The $\langle m^*_{nlj}/m\rangle$ values as computed by this formula are quoted in Table 2, along with the corresponding results from [5] and the estimates from [30]. The values presented in [30] were obtained by fitting the results of the calculations performed in the spherical approximation with sets of parameters of the effective Skyrme interaction to the measured energies of single-particle proton states. The values of $\langle m^*_{nlj}/m\rangle$ from this study proved close to the corresponding values from [5] for all levels, with the exception of the $1s_{1/2}$ one; for this level, our results are in better agreement with the estimates from [30], which comply with our present results and with data from [5] to within 10–15%.

6.3. Root-Mean-Square Radii of Orbits

From an analysis of the spectral functions for the reaction ^{90}Zr$(e, e'p)$, Den Herder *et al.* [16] determined the root-mean-square radii of single-particle orbits for some states. Below, the predictions of the DOM involving the mean-field potential obtained here will be compared with data from [16].

The root-mean-square radii of single-particle orbits were computed here according to the standard prescrip-

tions of quantum mechanics:

$$R_{nlj}^{\mathrm{rms}} = \left[\int_0^\infty \bar{u}_{nlj}^2(r) r^2 dr\right]^{1/2}. \quad (6.8)$$

The root-mean-square radii calculated with the mean parameters of the potential (2.19) are listed in Table 3, along with the corresponding results from [5] and the experimental and theoretical values of these radii from [16] and [31], respectively. From this table, it can be seen that our results comply with those from [5] to within 1% for high-lying levels and to within 1 to 2% for deep levels; our results also agree with those from [16, 31] to a precision not poorer than 5%.

6.4. Shell Occupation Numbers

For single-particle orbits, the occupation numbers were calculated by the formulas

$$N_{nlj}^{<} = \int_0^\infty \bar{u}_{nlj}^2(r)\left[1 + \left\{m_{\mathrm{HF}}^*/m(r, E_{nlj})\right\}^{-1}\pi^{-1} \times \int_{E_{\mathrm{F}}}^\infty \frac{W(r, E')}{(E' - E_{nlj})^2} dE'\right] dr \quad \text{for} \quad E_{nlj} < E_{\mathrm{F}}, \quad (6.9)$$

$$N_{nlj}^{>} = -\int_0^\infty \bar{u}_{nlj}^2(r)\left[\left\{m_{\mathrm{HF}}^*/m(r, E_{nlj})\right\}^{-1}\pi^{-1} \times \int_{-\infty}^{E_{\mathrm{F}}} \frac{W(r, E')}{(E' - E_{nlj})^2} dE'\right] dr \quad \text{for} \quad E_{nlj} > E_{\mathrm{F}}. \quad (6.10)$$

The expressions for $N_{nlj}^{<,>}$ were obtained with the aid of the REDUCE system for analytic calculations [32]. Approximate expressions for $N_{nlj}^{<,>}$ can also be found in [7].

The results of the calculations according to formulas (6.9) and (6.10) are presented in Table 4, along with experimental data from [16], the results from [5], and the theoretical predictions from [33–35]. In the microscopic calculations, Brand *et al*. [33] used the *G*-matrix approach allowing for short-range calculations, Kumar and Gunye [34] relied on the Hartree–Fock–Bogolyubov formalism for quadrupole-plus-pair interaction, and Van Neck *et al.* [35] took into account the coupling single-particle and vibrational degrees of freedom to short-range correlations. The present calculation and that from [5] somewhat underestimate the occupation numbers for the levels from the $2p_{3/2}$ to the $1s_{1/2}$ one and overestimate them for particle levels in relation to the theoretical values. We note that our results comply with the theoretical values from [35] to within 5%. We also note that, in [16], the occupation numbers were determined with the aid of the sum rule in the independent-particle model: $N_{nlj} = S_{nlj}/(2j + 1)$. The spectroscopic factors S_{nlj} extracted from data on $(e, e'p)$ reactions are dependent on the choice of model. Presently, there are no experimental methods that would make it possible to determine occupation numbers in a model-independent way. The discontinuity Z between the occupation numbers for particle and hole orbits at $E = E_{\mathrm{F}}$ is found here to be 0.47 (see Fig. 6). It was 0.53 in [5].

Table 2. Effective proton mass on the *nlj* orbit in ^{90}Zr

nlj	$\langle m^*/m\rangle_{nlj}$		
	our study	[5]	[30]
$2d_{5/2}$	1.07	1.10	
$1g_{7/2}$	1.06		
$1g_{9/2}$	0.97	0.947	
$2p_{1/2}$	0.91	0.902	
$2p_{3/2}$	0.94	0.917	
$1f_{5/2}$	0.90	0.844	0.75
$1f_{7/2}$	0.84	0.814	0.68
$2s_{1/2}$	0.49	0.543	0.65
$1d_{3/2}$	0.51	0.554	0.63
$1d_{5/2}$	0.54	0.571	0.59
$1p_{1/2}$	0.57	0.544	0.54
$1p_{3/2}$	0.57	0.525	0.53
$1s_{1/2}$	0.50	0.384	0.50

Table 3. Root-mean-square radii R_{nlj}^{rms} (in fm) of single-particle proton orbits in ^{90}Zr

nlj	Results of the calculation			Experimental data [16]
	our study	[5]	[31]*	
$2d_{5/2}$	5.60	5.63		
$1g_{9/2}$	4.99	5.01	4.93	4.97(10)
$2p_{1/2}$	4.70	4.77	4.63	4.57(9)
$2p_{3/2}$	4.68	4.66	4.57	4.48(7)
$1f_{5/2}$	4.55	4.51	4.52	4.54(7)
$1f_{7/2}$	4.38	4.39	3.91	4.51(11)
$2s_{1/2}$	3.85	3.90	4.01	3.87
$1d_{3/2}$	3.91	3.90	4.08	3.99(10)**
$1d_{5/2}$	4.06	3.99	4.01	
$1p_{1/2}$	3.57	3.46		
$1p_{3/2}$	3.65	3.53		
$1s_{1/2}$	3.03	2.86		

* The theoretical estimates of Negele and Vautherin [31] were borrowed from the study of Den Herder *et al*. [16] (Table 11).

** Mean value for the 1*d* orbits.

Table 4. Occupation numbers N_{nlj} for single-particle proton orbits in ^{90}Zr

nlj	Results of the calculation					Experimental data [16]	*nlj*	Results of the calculation					Experimental data [16]
	our study	[5]	[33]	[34]	[35]			our study	[5]	[33]	[34]	[35]	
$2d_{5/2}$	0.134	0.131	0.054	0.02			$2s_{1/2}$	0.873	0.880	0.96		0.84	0.64
$1g_{7/2}$			0.04	0.02			$1d_{3/2}$	0.877	0.880	0.95		0.84	0.71*
$1g_{9/2}$	0.251	0.210	0.08	0.19	0.04		$1d_{5/2}$	0.892	0.891	0.96		0.85	
$2p_{1/2}$	0.768	0.790	0.86	0.65	0.76	0.36	$1p_{1/2}$	0.909	0.910	0.97			
$2p_{3/2}$	0.794	0.813	0.88	0.88	0.77	0.56	$1p_{3/2}$	0.912	0.913	0.97			
$1f_{5/2}$	0.779	0.804	0.90	0.86	0.78	0.60	$1s_{1/2}$	0.922	0.928	0.98			
$1f_{7/2}$	0.830	0.845	0.93	0.97	0.80	0.68							

* Mean value for the 1*d* orbits.

6.5. Spectroscopic Factors of States

The spectroscopic factors for *nlj* single-particle states were computed by the formula [1]

$$S_{nlj} = \int_0^\infty \bar{u}^2_{nlj}(r)[m/\bar{m}(r, E_{nlj})]dr. \qquad (6.11)$$

The S_{nlj} values obtained in the present study are quoted in Table 5, along with the results of the calculations from [5] and the experimental data from [16, 18–21]. Our predictions are close to those from [5] for all levels, with the exception of the $1s_{1/2}$ one. The values S^{expt}_{nlj} show a wide scatter and deviate strongly from the calculated values. Among the reasons behind the wide scatter of S^{expt}_{nlj}, we can indicate the following. Spectroscopic factors extracted from data on one-nucleon-transfer reactions are sensitive to the parameters (in particular, to geometric parameters) of the potential for the proton bound state in a nucleus and to the parameters of the optical potentials for incident and scattered particles. In practice, it is impossible to take into account all transitions in sum rules, since it is difficult to detect weak transitions. Moreover, different definitions for spectroscopic factors extracted from experimental data are used in different studies. Therefore, a comparison of S^{theor}_{nlj} and S^{expt}_{nlj} should be performed with caution. The spectroscopic factors S_{nlj} calculated on the basis of (6.11) are "absolute" ones [1], but there is no experimental information about the absolute spectroscopic factors for the $p + {}^{90}$Zr system.

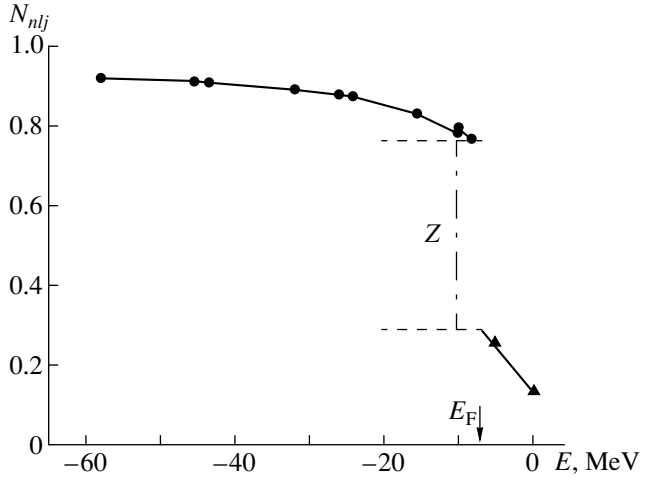

Fig. 6. Occupation numbers for (closed triangles) particle and (closed circles) hole orbits. The lines were drawn to guide the eye.

6.6. Spectroscopic Functions and Widths of Levels

For *nlj* single-particle states, the spectroscopic functions, which appear to be averaged energy distributions of spectroscopic factors, were calculated by the formula [1]

$$\zeta_{nlj}(E) = \pi^{-1}\frac{S_{nlj}\langle W_{nlj}(E)\rangle/\langle m^*_{nlj}/m\rangle}{(E-E_{nlj})^2 + [\langle W_{nlj}(E)\rangle/\langle m^*_{nlj}/m\rangle]^2}, \qquad (6.12)$$

where

$$\langle W_{nlj}(E)\rangle = \int_0^\infty \bar{u}^2_{nlj}(r)W_I(r, E)dr. \qquad (6.13)$$

For the $1f_{7/2}$, $1d_{3/2} + 1d_{5/2}$, and $2s_{1/2}$ states, the spectral functions calculated with the aid of (6.12) are shown in Fig. 7, along with the corresponding results from [5] and experimental data from [16].

The full spread widths at half maximum, Γ_{nlj}, of *nlj* single-particle states were calculated by the formula

$$\Gamma_{nlj} = 2\langle W_{nlj}(E_{nlj})\rangle/\langle m^*_{nlj}/m\rangle. \qquad (6.14)$$

Table 6 presents the results of these calculations and the corresponding experimental data from [12, 16] for deep hole levels in ^{90}Zr. We can see that the Γ_{nlj} values calculated in the present study for the $1f_{7/2}$, $1p_{1/2}$, $1p_{3/2}$, and $1s_{1/2}$ states comply well with experimental data deter-

Table 5. Spectroscopic factors S_{nlj} for single-particle proton orbits in ^{90}Zr

nlj	Results of the calculation		Experimental data				
	our study	[5]	(e, $e'p$) [16]	(d, ^{3}He) [18]	(n, d) [19]	(^{3}He, d) [20]	(d, n) [21]
$2d_{5/2}$	0.670	0.682				0.83	0.435
$1g_{7/2}$						0.38	
$1g_{9/2}$	0.627	0.666				1.0	0.97
$2p_{1/2}$	0.665	0.680	0.36(4)	0.90	0.85(3)		
$2p_{3/2}$	0.649	0.660	0.56(6)	0.98	0.45(13)		
$1f_{5/2}$	0.622	0.665	0.60(8)	1.48	0.13(7)		
$1f_{7/2}$	0.637	0.670	0.68(9)	1.41			
$2s_{1/2}$	1.070	0.959	0.64(8)				
$1d_{3/2}$	0.989	0.896	0.71(10)*				
$1d_{5/2}$	0.939	0.876					
$1p_{1/2}$	0.811	0.833					
$1p_{3/2}$	0.824	0.870					
$1s_{1/2}$	0.880	1.114					

* Mean value for the 1d orbits.

mined for the first time in [12]. The calculated widths Γ_{nlj} of the $2s_{1/2}$, $1d_{3/2}$, and $1d_{5/2}$ states are greater than the corresponding experimental values from [12] by nearly 50%, but they agree well with data on (e, $e'p$) [16]. On the basis of this comparison, we conclude that the degrees of fragmentation of deep hole states can be reliably predicted on the basis of the DOM.

7. COMPARISON OF THE MEAN-FIELD PARAMETERS FOR THE p + ^{40}Ca, ^{90}Zr, ^{208}Pb SYSTEMS

It is of interest to compare the mean-field parameters for the p + ^{90}Zr system that were obtained here and in [5] with the corresponding parameters for the p + ^{40}Ca, ^{208}Pb systems from [7, 36]. For all of these systems, the values of the parameters r_{HF} and a_{HF} are displayed in Table 7.

Although the parameters in the dependence $V_{\mathrm{HF}}(E)$ [$V^1_{\mathrm{HF}}(E_{\mathrm{F}}), V^2_{\mathrm{HF}}(E_{\mathrm{F}})$, and λ] take different values in this study and in [5], the corresponding volume integrals agree to within 3%. The values of r_{HF} as determined here and in [5] agree to the same degree of precision, whereas the values of a_{HF} differ by more than 10%. The mean geometric parameters of the Hartree–Fock component that were evaluated in the present study are close to the geometric parameters of the real part of the conventional-optical-model potential for the p + ^{90}Zr system (r_V = 1.23 fm, a_V = 0.68 fm) [37].

It should be noted that the total reaction cross sections calculated with the mean parameters from [5], $\sigma_r^{\mathrm{DOM}}(E_k)$, are larger than σ_r^{est} from [11, 28] by about 10%. This indicates that the mean parameters from [5] should be refined. The values $\sigma_r^{\mathrm{DOM}}(E_k)$ as computed with the mean parameters from the present study comply with the corresponding estimates from [11, 28] to within 3%.

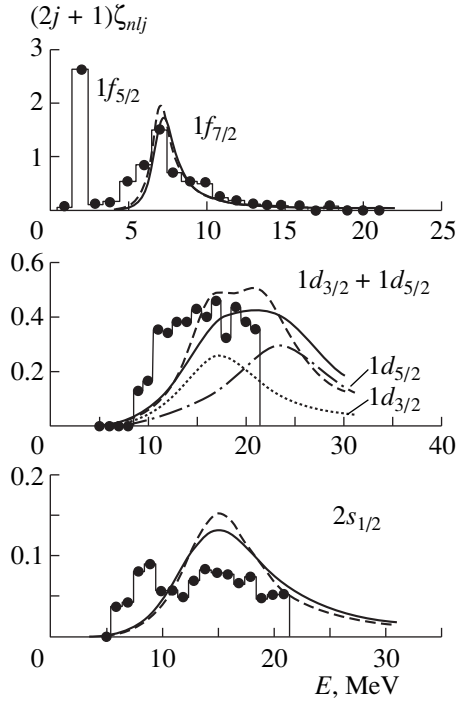

Fig. 7. Spectral functions for the $1f_{7/2}$, $1d_{3/2}$ + $1d_{5/2}$, and $2s_{1/2}$ single-particle orbits: (solid curves) results of our present calculation, (dashed curves) results of the calculations from [5], (dash-dotted curve) our present results for the $1d_{5/2}$ orbit, (dotted curve) our present results for the $1d_{3/2}$ orbit, and (points on the histogram) experimental data from [16].

Table 6. Total widths Γ_{nlj} (in MeV) of single-particle proton levels in ^{90}Zr

nlj	Results of our calculation	Experimental data	
		[12]	[16]
$1f_{7/2}$	1.91	2.03(0.89)	6.7(1)
			3.1(6)
$2s_{1/2}$	10.59	3.65(0.63)	10(1)
			8(2)
$1d_{3/2}$	9.79	4.46(0.79)	7(2)
$1d_{5/2}$	12.18	7.57(0.76)	13
$1p_{1/2}$	10.65	9.18(0.88)	
$1p_{3/2}$	12.04	15.55(0.95)	
$1s_{1/2}$	17.94	18.78(1.0)	

Table 7. Parameters r_{HF} and a_{HF} of the Hartree--Fock component of the mean field

Nucleus	r_{HF}, fm	a_{HF}, fm	References
^{40}Ca	1.20	0.73	[36]
^{90}Zr	1.217	0.76	[5]
^{90}Zr	1.24 ± 0.04	0.68 ± 0.02	Our study
^{208}Pb	1.225	0.71	[7]

A detailed analysis of $\sigma^{expt}(\theta)$ and $\sigma_r^{est}(E_k)$ for the energy range 6.35 MeV $\le E \le$ 16 MeV was performed in [25]. Processes leading to compound-nucleus formation and to the excitation of isobaric analogous resonances were taken into account there at low energies. All the parameters of the dispersive optical potential, with the exception of r_{HF}, a_{HF}, r_d, and a_d, were fixed in accordance with [5]. In varying these four parameters, the volume integral $J_{HF}^{JM}(E)$ was required to be fixed at the values corresponding to the parametrization from [5]. The parameter values were tabulated in [25], and graphs illustrating the qualities of relevant fits were also presented there. The values averaged over the sets $r_{HF}(E_k)$ and $a_{HF}(E_k)$ proved to be $r_{HF} = 1.26 \pm 0.02$ fm and $a_{HF} = 0.65 \pm 0.04$ fm; that is, they are consistent with the results obtained here.

The results of Mahaux and Sartor [6], who used the variational moment approach to determine the mean parameters of the Hartree–Fock potential for the p + ^{40}Ca system, also agree with the value of a_{HF} from the present study. It should be recalled that, in the variational moment approach, the parameter a_{HF} is a priori introduced as the mean value of the diffuseness of a real conventional-optical-model potential and that the parameter r_{HF} and the dependence $V_{HF}(E)$ are obtained on the basis of a variational procedure (see [6]). Within the variational moment approach, the correctness of a determination of a_{HF} is tested by requiring that the calculated and measured values of E_{nlj}, $\sigma(\theta)$, $P(\theta)$, and σ_r be in agreement, and it was established in [23] that this is indeed the case. In the CH-89 systematization of global parameters [9], a unified value of $a_R = 0.69 \pm 0.006$ fm of the diffuseness of the real potential was established for all $40 \le A \le 208$ nuclei. We can thus see that it is close to the value of $a_{HF} = 0.68 \pm 0.02$ fm found in the present study.

8. CONCLUSIONS

(i) We have analyzed data on proton scattering by ^{90}Zr nuclei and data on the energies of protonic particle and hole states in the $A + 1$ and $A - 1$ ($A = 90$) systems. This analysis was performed within the dispersive optical-model version proposed in [8]. In order to determine the average parameters of the mean-field potential, we have used the geometric parameters of the imaginary potential from the CH-89 and CH-89* systematizations (see [9] and [11], respectively). In a free determination of the remaining three parameters of the Hartree–Fock component, this has made it possible to reduce considerably the ambiguity in evaluating the mean-field parameters and to achieve agreement between the calculated and measured differential cross sections for elastic scattering, polarizations, total reaction cross sections, and positions of single-particle levels to a precision better than 5%. The predictions that we have obtained here for single-particle properties of bound states agree with the results presented by Wang *et al.* [5], who deduced the parameters of the mean field by averaging the individual parameters for the p + ^{90}Zr system.

That the results of our calculations comply well with experimental data both for $E > 0$ and for $E < 0$ gives sufficient grounds for using the proposed dispersive optical-model version to deduce information about the average parameters of the Hartree–Fock component of the mean-field potential for $40 < A < 208$ nuc-lei in the energy range –60 MeV $< E <$ +65 MeV.

(ii) An analysis of (p, $2p$) data on the positions (energies) of hole levels in ^{90}Zr has revealed that the Hartree–Fock component of the mean-field potential, $V_{HF}(E)$, is a linear function of energy in the range –60 MeV $< E < E_F$.

(iii) The method proposed in [8] for determining the parameters of the proton mean field has enabled us to predict the features of single-particle proton states in the $A + 1$ and $A - 1$ systems ($A = 90$) down to deep ones. The predicted features of proton states in ^{90}Zr are in good agreement with currently available experimental information.

ACKNOWLEDGMENTS

We are grateful to E. Stephenson for valuable consultations; P. Kunz for kind permission to use the DWUCK-4 code and for advice; M.G. Urin, V.G. Neudatchin, and N.P. Yudin for enlightening discussions;

and to G.D. Satchler for stimulating our investigations along these lines.

ACKNOWLEDGMENTS

This work was supported by the Russian Foundation for Basic Research (project no. 96-02-17402a).

REFERENCES

1. C. Mahaux and R. Sartor, Adv. Nucl. Phys. **20**, 1 (1991).
2. G. R. Satchler, Phys. Rep. **199**, 147 (1991).
3. M. G. Urin and G. A. Chekomazov, Izv. Akad Nauk, Ser. Fiz. **59** (5), 2 (1995); G. A. Chekomazov and M. G. Urin, Phys. Lett. B **349**, 400 (1995).
4. M. G. Urin and G. A. Chekomazov, Yad. Fiz. **61**, 435 (1998) [Phys. At. Nucl. **61**, 375 (1998)].
5. Y. Wang *et al.*, Phys. Rev. C **47**, 2677 (1993).
6. C. Mahaux and R. Sartor, Nucl. Phys. **A528**, 253 (1991).
7. C. Mahaux and R. Sartor, Nucl. Phys. **A503**, 525 (1989).
8. E. A. Romanovsky *et al.*, Izv. Akad. Nauk, Ser. Fiz. **63**, 980 (1999).
9. R. L. Varner, Phys. Rep. **201**, 57 (1991).
10. R. F. Carlson, At. Data Nucl. Data Tables **68**, 93 (1996).
11. E. A. Romanovsky *et al.*, Yad. Fiz. **61**, 37 (1998) [Phys. At. Nucl. **61**, 32 (1998)].
12. A. A. Vorob'ev *et al.*, Yad. Fiz. **58**, 1923 (1995) [Phys. At. Nucl. **58**, 1817 (1995)].
13. K. P. Lieb, J. J. Kent, and C. F. Moore, Phys. Rev. **175**, 1482 (1968).
14. C. M. Perey and F. G. Perey, At. Data Nucl. Data Tables **17**, 1 (1976).
15. G. J. Weisel *et al.*, Phys. Rev. C **54**, 2410 (1996).
16. J. W. A. den Herder, H. P. Blok, E. Jans, *et al.*, Nucl. Phys. **A490**, 507 (1988).
17. A. N. James *et al.*, Z. Phys. A **138**, 145 (1969).
18. A. Stuirbrink *et al.*, Z. Phys. A **297**, 307 (1980).
19. K. Bharuth-Ram, A. C. Bawa, and W. R. McMurray, Phys. Rev. C **36**, 1749 (1987).
20. G. Finkel *et al.*, Nucl. Phys. **A217**, 197 (1973).
21. J. L. Horton *et al.*, Nucl. Phys. **A190**, 362 (1972).
22. P. D. Kunz, Code DWUCK-4 (unpublished).
23. C. Mahaux and R. Sartor, Nucl. Phys. **A484**, 205 (1988).
24. E. A. Romanovsky *et al.*, Izv. Akad. Nauk, Ser. Fiz. **57** (10), 161 (1993).
25. E. A. Romanovsky *et al.*, Izv. Akad. Nauk, Ser. Fiz. **60** (5), 32 (1996).
26. E. A. Romanovsky *et al.*, Izv. Akad. Nauk, Ser. Fiz. **62**, 1056 (1998).
27. Y. Wang, C. C. Foster, E. J. Stephenson, *et al.*, Phys. Rev. C **45**, 2891 (1992).
28. E. D. Cooper *et al.*, Phys. Rev. C **47**, 297 (1993).
29. J. P. Delaroche, Y. Wang, and J. Rapaport, Phys. Rev. C **39**, 391 (1989).
30. Yu. V. Dotsenko, Doctoral Dissertation in Mathematical Physics (St. Petersburg, 1996).
31. J. W. Negele and D. Vautherin, Phys. Rev. C **5**, 1472 (1972).
32. A. C. Hearn, REDUCE User's Manual, version 3.6 [RAND Publ. CP78 (Rev. 7/95)].
33. M. G. E. Brand, G. A. Rijsdik, F. A. Muller, *et al.*, Nucl. Phys. **A531**, 253 (1991).
34. A. Kumar and M. R. Gunye, Phys. Rev. C **32**, 2116 (1985).
35. D. van Neck, M. Waroquier, and J. Ryckebusch, Phys. Lett. B **249**, 157 (1990).
36. W. Tornow, Z. P. Chen, and J. P. Delaroche, Phys. Rev. C **42**, 693 (1990).
37. A. J. Koning, J. J. van Wijk, and J. P. Delaroche, in *Proceedings of a Specialists Meeting on Nucleon–Nucleus Optical Model up to 200 MeV, Bruyéres-le-Châtel, France* (1996), p. 111.

Translated by A. Isaakyan

Physics of Atomic Nuclei, Vol. 63, No. 3, 2000, pp. 414–421. Translated from Yadernaya Fizika, Vol. 63, No. 3, 2000, pp. 484–491.

NUCLEI
Theory

Temperature Dependence of Radiative Strength Functions and Isomeric Cross Sections

O. T. Grudzevich*

Institute of Atomic Power Engineering, Obninsk, Kaluga oblast, 249020 Russia

Received September 28, 1998; in final form, March 23, 1999

Abstract—The effect of a parametrization of the temperature dependence of radiative strength functions for electric dipole transitions on the cross sections for isomer excitation in (n, γ), $(n, 2n)$, (n, p), (n, α), (γ, γ'), (γ, n), (γ, p), and $(\gamma, 2n)$ reactions is investigated. It is shown that the agreement of the results of calculations with the observed isomeric cross sections can be considerably improved by using the proposed method. © *2000 MAIK "Nauka/Interperiodica".*

1. INTRODUCTION

Investigation of mechanisms that populate isomeric levels in nuclear reactions is of great topical interest in nuclear physics, since this makes it possible to obtain answers to some important questions concerning the structure of nuclei and the ways of isomer deexcitation and to refine methods for calculating theoretically the features of nuclear reactions. An accumulation of a vast body of experimental data on the cross sections for the production of nuclei in specific states provides a testing ground for new theoretical approaches that extends over wide ranges of excitation energies and target mass numbers.

According to [1], isometric states are populated predominantly via a cascade deexcitation of a nucleus excited in some reaction and via a direct population of an isomeric level upon the emission of primary particles or photons. These mechanisms, which saturate, respectively, 80–90 and 10–20% of relevant cross section, are operative even in reactions where nonstatistical effects dominate the formation of the total reaction cross section. Although being different in some details, current theoretical methods for calculating isomeric cross sections all employ two functionals to evaluate the population probability for a specific nuclear state, the level density in a nucleus and radiative strength functions. Most often, physicists involved in relevant investigations attribute discrepancies between the results of calculations and experimental cross-section values to uncertainties in the spin-dependence of the level density, assuming that radiative strength functions have a less pronounced effect on the results of the calculations in question and that they have been determined to a higher precision than the level density of nuclei with high angular momenta, which is based on theoretical predictions alone. By analyzing experimental data on the spectra of photons from the deexcitation of nuclei formed in neutron-induced reactions, it was shown, however, [2] that it is necessary to refine methods for calculating radiative strength functions. The method for calculating $E1$ radiative strength functions $f_{E1}(E_\gamma, T)$ that takes into account quasiparticle fragmentation and which was proposed by Kadmensky, Markushev, and Furman [3] (KMF method) can be modified by introducing a parametrization of $f_{E1}(E_\gamma, T)$ in such a way as to describe the features of the observed radiative transitions between discrete levels. It turned out that, when the temperature of the residual nucleus, T = const, is used as an adjustable parameter, which has the same value for all excitation energies (KMF method of constant temperature, quoted in the following as KMF–CT), the upper limit on the experimental values of radiative strength functions is reproduced satisfactorily for photon energies $E_\gamma \leq 3$ MeV.

Among the models that were invoked to calculate relevant cross sections, we would like to mention the statistical model of nuclear reactions that takes into account the laws of total-angular-momentum and parity conservation, the cascade–evaporation model of the decay of an excited nucleus [4], and the generalized superfluid model [5] (it is used to calculate the level density together with parameters appearing in it). Typical examples illustrating changes exhibited by the photon spectra in response to modifications in the method for calculating f_{E1} are given in Fig. 1. For all four isotopes of tungsten, the use of the KMF–CT method improves considerably the agreement with the experimental spectra of photons [6], a result that can hardly be achieved within the other methods. By way of example, we indicate that a reduction of the slope of the computed spectrum as great as is needed for this would require changing the level-density parameters by 10–20%, but this is incompatible with available data on the density of neutron resonances. By using strength functions as determined on the basis of the KMF–CT method, the agreement with experimental data was improved for a wide range of target nuclei in (n, γ) and

* e-mail: grudz@iate.obnisk.ru

1063-7788/00/6303-0414$20.00 © 2000 MAIK "Nauka/Interperiodica"

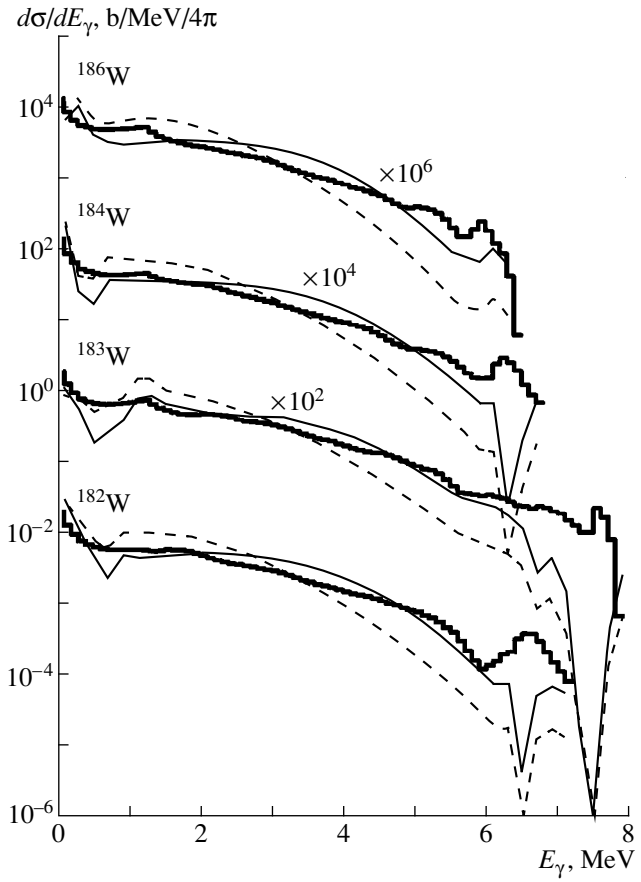

Fig. 1. Spectra of photons from the (n, γ) reactions on tungsten isotopes $^{182, 183, 184, 186}$W at $E_n = 0.5$ MeV: (histogram) experimental data from [6], (dashed curves) results of the calculations employing $E1$ strength functions as determined on the basis of the KMF method, and (solid curves) results of the calculations employing $E1$ strength functions as determined on the basis of the KMF–CT method (T = 0.1 MeV).

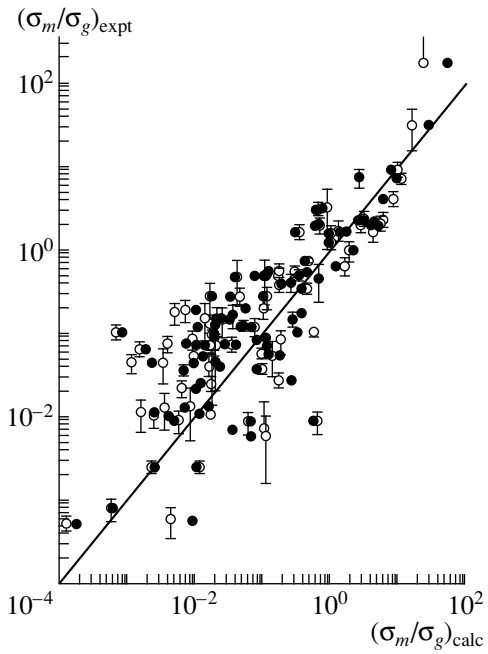

Fig. 2. Comparison of the measured and calculated ratios of isomeric cross sections (σ_m/σ_g) for radiative thermal-neutron capture. Experimental data were borrowed from [7]. Open and closed circles represent a comparison of experimental data with the results of the calculations employing $E1$ strength functions as determined on the basis of, respectively, the KMF and the KMF–CT (T = 0.1 MeV) method.

$(n, n'\gamma)$ reactions and for a wide range of incident-neutron energies (10 keV–14 MeV). The results of the calculations of the isomeric ratios for radiative thermal-neutron capture were also improved radically in this way [2].

The present article reports on a continuation of a series of studies devoted to developing theoretical methods for calculating isomeric ratios [1, 2]. It is aimed at further verifying the applicability of the KMF–CT method via an analysis of isomeric cross sections for neutron-induced and photonuclear reactions.

2. NEUTRON-INDUCED REACTIONS

In radiative thermal-neutron capture, isomeric ratios may undergo giant variations whose scale amounts to ten orders of magnitude. In view of this, the most serious difficulties arise in interpreting these observable isomeric cross sections. Agreement between the measured and calculated values within a factor of 2 would be a great success, but this has not yet been achieved [1]. In an attempt at improving the agreement between theoretical and experimental results, it therefore seems natural to use the KMF–CT method in calculating, above all, isomeric ratios $r = \sigma_m/\sigma_g$ for (n, γ) reactions induced by thermal neutrons. A display of the general situation is given in Fig. 2, which shows, along with experimental data from [7] and theoretical results from [1], results obtained with the strength functions calculated by the KMF–CT method (T = 0.1 MeV) for 89 isomeric states of nuclei from ^{24}Na to ^{210}Bi. Perfect agreement has not yet been reached, but the calculated values have a clear tendency to change in the desired direction. Indeed, some points moved along the abscissa toward the bisectrix corresponding to the coincidence of the calculated and experimental values. Figure 2 shows neither data on the reaction ^{189}Os$(n, \gamma)^{190}$Os$^m(10^-)$—here, the measured isomeric-ratio value is 10^{-5}, while the corresponding values calculated on the basis of the KMF and KMF–CT methods are 8×10^{-7} and 6×10^{-6}, respectively—nor data on the reaction ^{177}Hf$(n, \gamma)^{178}$Hf$^{m2}(16^+)$, which were discussed in [2]. It is for these two isomers, which are characterized by high spin values, that the experimental isomeric-ratio values can be reproduced with no reasonable variations in the spin dependence of the level density.

Of course, the partial cross sections for (n, p) and (n, α) reactions leading to the formation of nuclei in

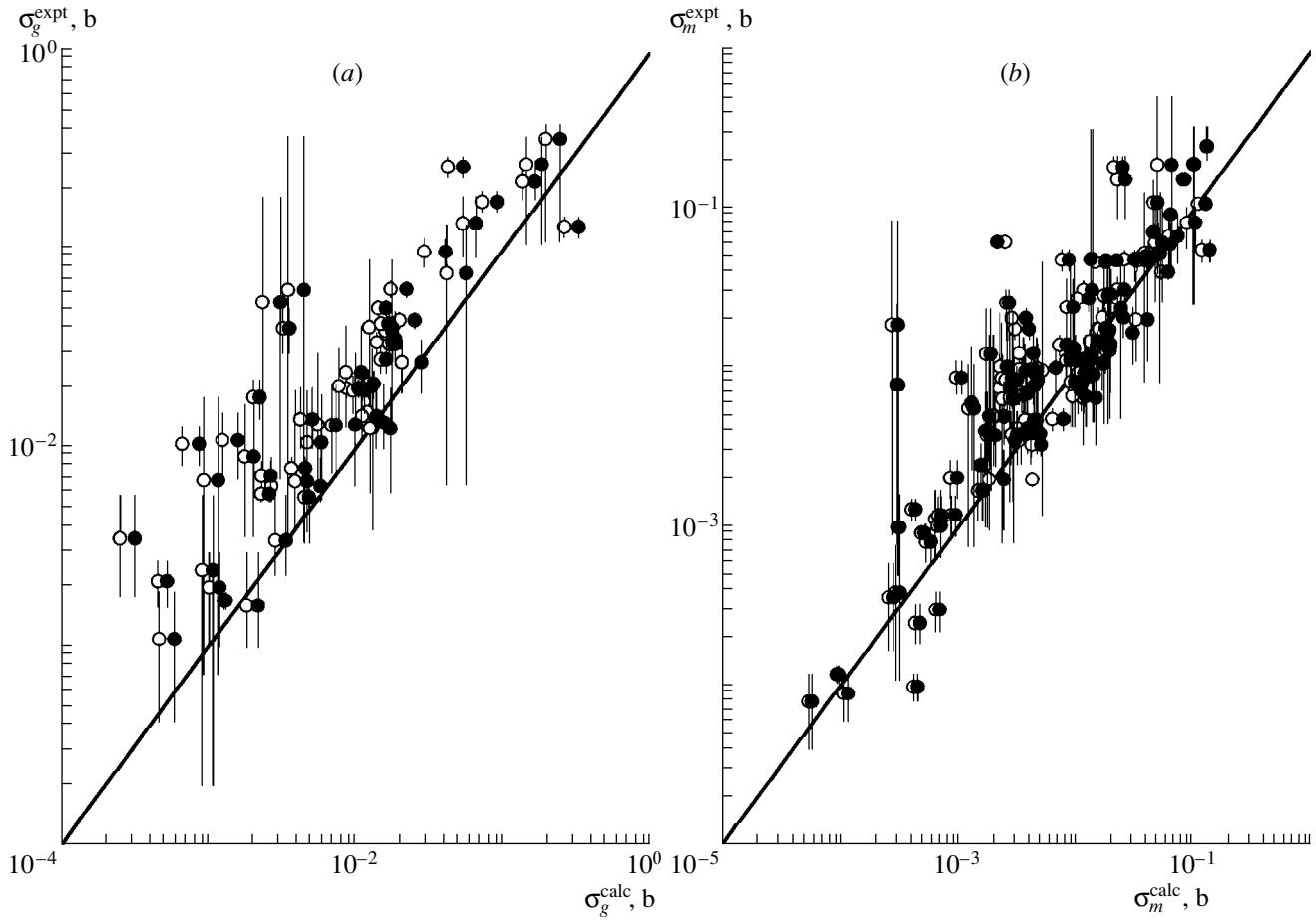

Fig. 3. Comparison of experimental and calculated values of the cross sections for (n, p) reactions leading to the formation of residual nuclei in (*a*) ground and (*b*) isomeric states. The notation for the points is identical to that in Fig. 2.

ground and isomeric states are less sensitive to modifications in the method for calculating radiative strength functions. This is because, in such reactions, the formation of a compound nucleus by neutrons having a broad spectrum of orbital angular momenta is accompanied by a substantial averaging of the features of the isomer population over the total angular momentum. The same occurs when the residual nucleus is populated by emitted particles having broad energy spectra and, hence, broad angular-momentum spectra. This explains isomeric-ratio values, which lie, as a rule, in the interval 0.1–1.0, and a weak sensitivity of the results to some parameter or functional of the model. Nonetheless, modifications in the method for calculating radiative strength functions affect the results of the calculations for isomeric cross sections. As a rule, the modified results are in better agreement with experimental data (see Figs. 3 and 4). Errors indicated in Figs. 3 and 4 are not experimental uncertainties proper; in fact, they represent the scatter of cross-section values quoted by different authors. The present comparison was performed not only for neutron energies E_n between 14 and 15 MeV but also for other energy values from the region $E_n < 20$ MeV scanned with a step of 1 MeV. Thus, each point in Figs. 3 and 4 represents a comparison of the calculated and experimental partial cross sections for neutrons with energies from E_{n1} to E_{n2} for a reaction resulting in the formation of a given residual nucleus. Of course, the statistical significance and the meaning of different points are different, but I think that this way of comparison is the most appropriate one for qualitatively representing the situation for a given reaction over the entire interval of energy.

For testing the method being discussed, $(n, 2n)$ reactions are less suitable, but representative examples can be found in this case as well. Quoted below are typical cases of desirable and undesirable changes in the calculated cross sections. An example where the modification to the method for calculating the $E1$ radiative strength function leads to a change improving the agreement between the theoretical and experimental values of the isomeric ratio is given in Fig. 5, while some examples where there are no such changes—although they are expected for the reactions ^{115}In$(n, 2n)$ and ^{87}Rb$(n, 2n)$—are illustrated in Fig. 6.

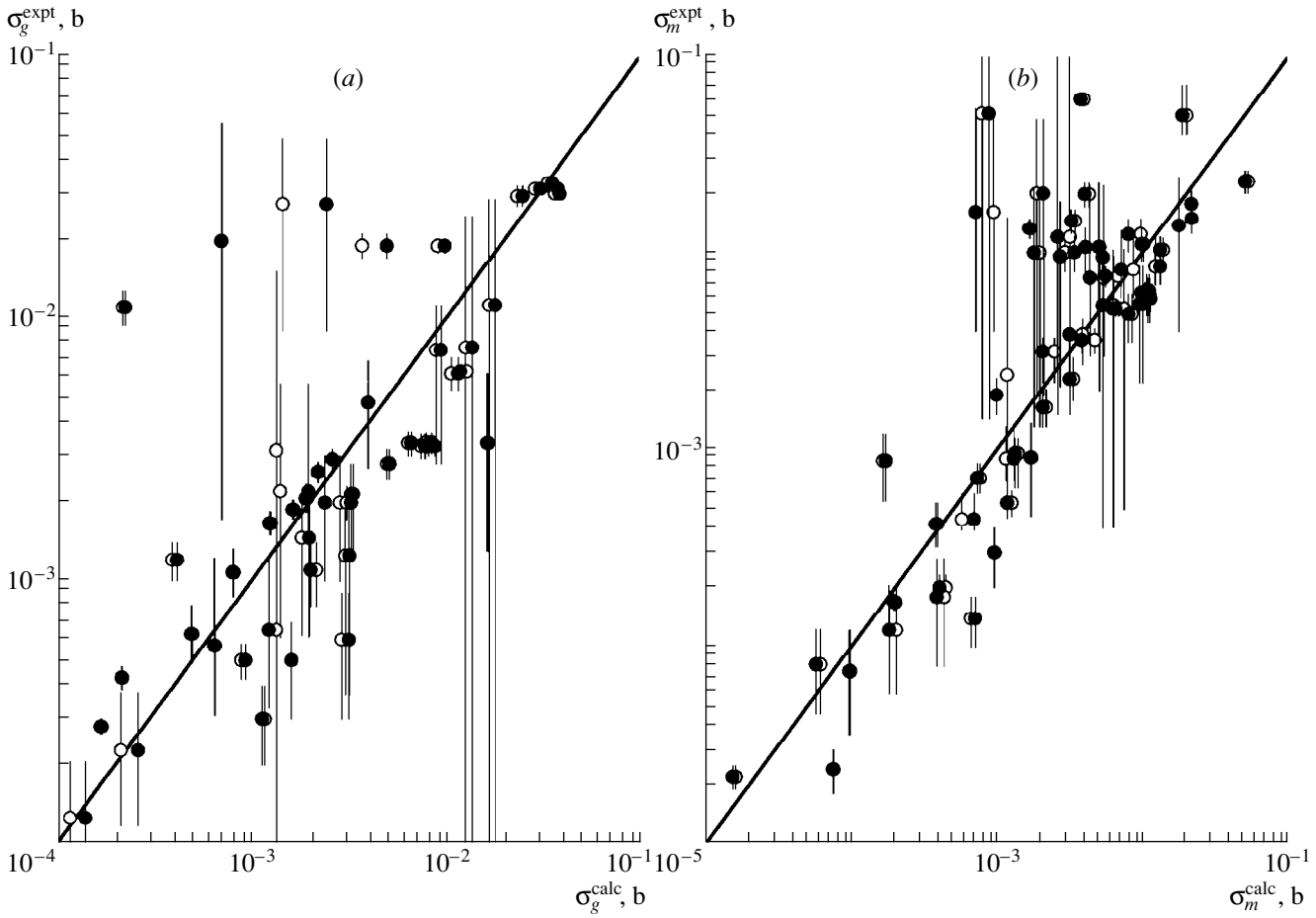

Fig. 4. As in Fig. 3, but for (n, α) reactions. The notation for the points is identical to that in Fig. 2.

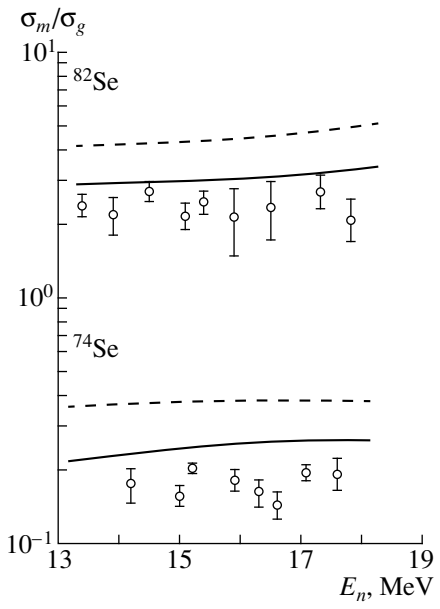

Fig. 5. Ratios of the isomeric cross sections (σ_m/σ_g) for the (n, $2n$) reactions on ^{82}Se and ^{74}Se nuclei as functions of the incident-neutron energy. Points represent experimental data from [8, 9]. The notation for the curves is identical to that in Fig. 1.

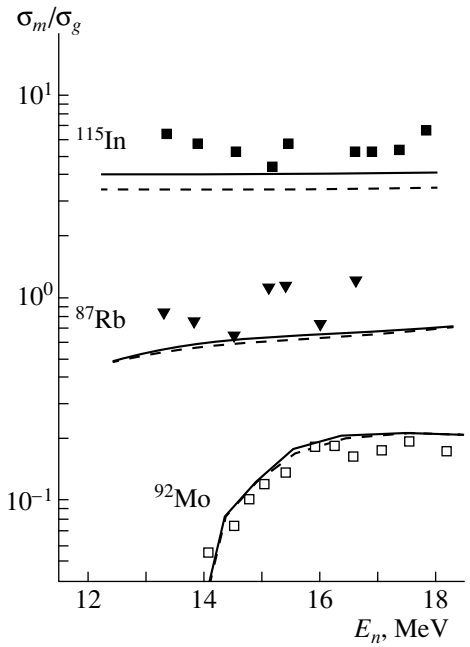

Fig. 6. As in Fig. 5, but for ^{92}Mo, ^{87}Rb, and ^{115}In target nuclei. Points represent experimental data from [8–10]. The notation for the curves is identical to that in Fig. 1.

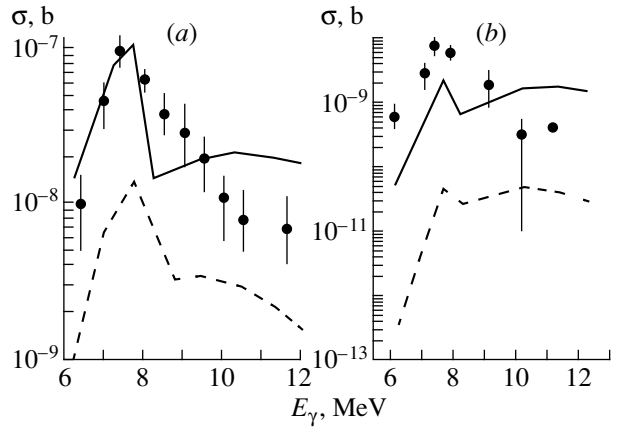

Fig. 7. Isomer excitation functions for the (γ, γ') reactions on (*a*) ^{180}Hf and (*b*) ^{190}Os nuclei. Points represent experimental data from [12]. The notation for the curves is identical to that in Fig. 1. The computed cross sections were not averaged over the bremsstrahlung spectrum.

Thus, evidence that the new method for calculating radiative strength functions makes it possible to remove some pronounced discrepancies between the theoretical and experimental values of isomeric cross sections has been obtained for neutron-induced reactions. In many cases, the new values deduced for the cross sections are closer to the experimental values.

3. PHOTONUCLEAR REACTIONS

A vaster part of experimental data on photonuclear reactions leading to the excitation of isomeric levels come from experiments employing bremsstrahlung photons [11–16]. This circumstance complicates a theoretical analysis of such data, since the observed energy dependence is smoothed, so that information about the bremsstrahlung spectrum is required for averaging the computed cross sections. Nonetheless, the data in question are of considerable interest for the following reasons: (i) The input reaction channel is unique. (ii) The possibility of constructing a consistent description of isomeric cross sections can be extended to a wider set of data. (iii) The data in question furnish fundamentally new information about the excitation of high-spin isomers and about reactions occurring on isomeric targets [11].

That the sensitivity of photonuclear reactions to the spin characteristics of both target nuclei and residual nuclei is increased because there are only two dominant waves—those of multipole orders $\lambda = 1$ and 2—in the input reaction channel is a property common to all such reactions viewed as a source of information about the population isomeric levels. Hence, the populations of isomeric levels of the residual nucleus that differ in spin by a few units provide some sort of a proving ground for methods used to calculate radiative strength functions. In implementing such tests, however, it is necessary to be confident that the deexcitation of the residual nucleus via radiative and radiation-free transitions has been simulated correctly. The method for mixing the states of the decaying nucleus that belong to bands having different values of the projection K of the total angular momentum on the symmetry axis (selection rules in K) may be an additional source of errors in the model used. It is well known that transitions between such states are characterized by the forbiddenness degree dependent on the difference $\Delta K = K_1 - K_2$, but it is very difficult to take into account these selection rules in practical calculations. At this stage of our analysis of data on photonuclear reactions, we will therefore ignore the selection rules in K (that is, we assume perfect mixing of states) and try to find out whether it is necessary to take them into account in describing the observed isomeric cross sections, especially in reactions of inelastic photon scattering. In part, the answer to this question was given in [2], where agreement with experimental data on the cross sections for the reactions ^{167}Er(γ, γ')^{167}Er^m and ^{179}Hf(γ, γ')^{179}Hf^m was achieved without taking into account selection rules in K. Data that are presented in Fig. 7 and which show that agreement with experimental data from [12] is achieved by modifying the method for calculating the strength function f_{E1} provide further evidence in favor of strong mixing of bands with different K values. It is obvious that, had the selection rules that forbid transitions between bands with different K values been introduced in the computational scheme, the calculated isomeric cross sections would be reduced considerably because isomers having high K values and appearing to be levels on which the corresponding bands are built (bandheads) are populated via a large number of successive gamma transitions between the states of various bands. Thus, we confirmed the qualitative conclusion of Oganessian and Karamian [13] that the states in question are strongly mixed. That agreement with isomeric cross sections of so small a magnitude (10^{-7}–10^{-9} b) was achieved is a merit of the method for evaluating $E1$ strength functions that is tested here.

In establishing the mechanism of isomer population, it is always hazardous to rely on an analysis of only one reaction—for example, ^{180}Hf(γ, γ')^{180}Hf^m—because the model parameters can be strongly biased in this specific case. The model itself then loses its original meaning, and the mechanism underlying it is in fact not tested via a comparison with measured cross sections. A consistent description of the population of the same isomer in two or more reactions [say, ^{190}Os^m(10$^-$) in the (n, γ) and (γ, γ') reactions] is free from this flaw and is more reliable from the viewpoint of testing theoretical methods.

We continue our consistent analysis by considering one more example, the excitation of the ^{89}Zr^m(1/2$^-$) isomer in the (γ, n) and (n, 2n) reactions (Fig. 8). For the first reaction, the results of the calculations with the conventional KMF strength function deviate strongly from experimental data, but the above change in the method for calculating f_{E1} leads to quite reasonable

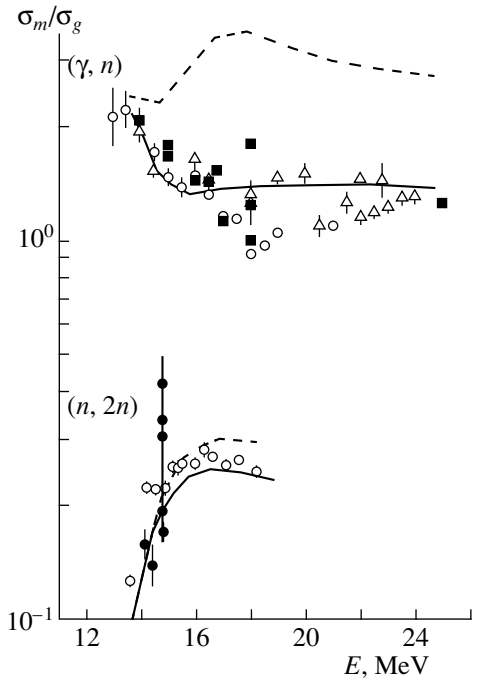

Fig. 8. Ratios of the isomeric cross sections (σ_{m1}/σ_g) for the (γ, *n*) and (*n*, 2*n*) reactions leading to the population of the isomeric pair of the ^{89}Zr nucleus as functions of primary energy [E_γ for (γ, *n*) and E_n for (*n*, 2*n*)]. Points represent experimental data from [9, 14]. The notation for the curves is identical to that in Fig. 1.

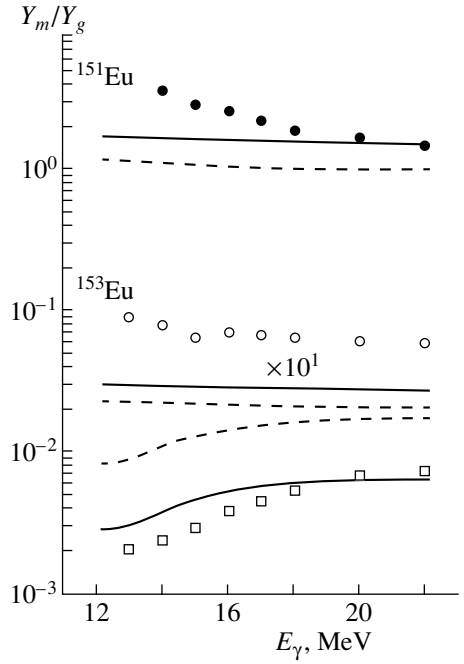

Fig. 9. Ratios of the isomeric yields from the (γ, *n*) reactions on ^{151}Eu and ^{153}Eu (in the middle for σ_{m1}/σ_g and at the bottom for σ_{m2}/σ_g) target nuclei: (points) experimental data from [15], (dashed curves) results of the calculations with $\sigma^2 = \sigma^2_{\text{rigid}}$, and (solid curves) results of the calculations with $\sigma^2 = \sigma^2_{\text{rigid}}/2$.

agreement. Improving the agreement for the (γ, *n*) reaction, the use of the radiative strength functions calculated by the KMF–PT method does not spoil it for the (*n*, 2*n*) reaction.

The proposed method is not universal—in particular, it does not of course supersede the conventional method for describing the isomeric cross sections and yields by varying the spin-cutoff parameter of the level density, σ^2. For example, it was shown in [1] that a consistent description of the isomeric ratios for ^{152}Eu^m(8$^-$) from (*n*, γ) and (*n*, 2*n*) reactions can be obtained by reducing σ^2 in relation to its value corresponding to the rigid-body value of the moment of inertia of the nucleus, σ^2_{rigid}. This method is additionally validated by the data in Fig. 9, where the experimentally determined ratio Y_m/Y_g of the yields from the reactions ^{151,153}Eu(γ, *n*) [15] are reproduced precisely upon changing σ^2. That changing this parameter is a viable procedure is further evinced by the data in Fig. 10, where we can see that the modification to the method for calculating radiative strength functions affects the results only slightly, but that the reduction of σ^2 leads to satisfactory agreement with experimental data [16].The modification to the method for calculating *E*1 strength functions has virtually no effect on the results of the calculations for isomeric cross sections in Fig. 10 because the differ-

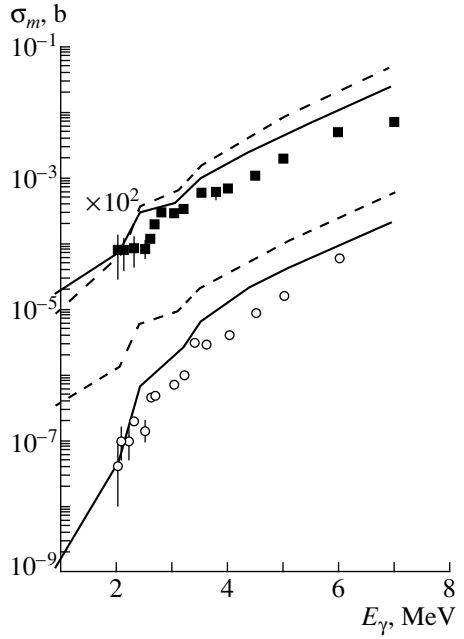

Fig. 10. Excitation functions for the reactions (at the top) ^{191}Ir(γ, γ′)^{191}Ir^m and (at the bottom) ^{197}Au(γ, γ′)^{197}Au^m: (points) experimental data from [16], (dashed curves) results of the calculations with $\sigma^2 = \sigma^2_{\text{rigid}}$, and (solid curves) results of the calculations with $\sigma^2 = \sigma^2_{\text{rigid}}/3$.

Table 1. Features of ground and isomeric levels populated in the reactions analyzed in the present article

Reaction	J^π_t	J^π_g	J^π_m	Reaction	J^π_t	J^π_g	J^π_m
^{82}Se(n, 2n)^{81}Se^m	0^+	$1/2^-$	$7/2^+$	^{151}Eu(γ, n)^{150}Eu^m	$5/2^+$	5^-	0^-
^{84}Se(n, 2n)^{83}Se^m	0^+	$9/2^+$	$3/2^-$	^{153}Eu(γ, n)^{152}Eu^{m,m2}	$5/2^+$	3^-	0^-, 8^-
^{115}In(n, 2n)^{114}In^m	$9/2^+$	1^+	5^+	^{190}Os(γ, γ')^{190}Os^m	0^+	0^+	10^-
^{87}Rb(n, 2n)^{86}Rb^m	$3/2^-$	2^-	6^-	^{191}Ir(γ, γ')^{191}Ir^m	$3/2^+$	$3/2^+$	$11/2^-$
^{92}Mo(n, 2n)^{91}Mo^m	0^+	$9/2^+$	$1/2^-$	^{197}Au(γ, γ')^{197}Au^m	$3/2^+$	$3/2^+$	$11/2^-$
^{90}Zr(γ, n)^{89}Zr^m	0^+	$9/2^+$	$1/2^-$				

Table 2. Ratio of the yields of isomeric and ground states (Y_m/Y_g) from photonuclear reactions on Ta and Hf isotopes

Reaction	J^π_t	J^π_g	J^π_m	$(Y_m/Y_g)_{\text{expt}}$	$(Y_m/Y_g)_{\text{calc1}}$	$(Y_m/Y_g)_{\text{calc2}}$
^{180}Hf(γ, γ')^{180}Hf^m	0^+	0^+	8^-	0.0029	2×10^{-6}	3×10^{-5}
^{180}Ta^m(γ, 2n)^{178}Ta^m	9^-	1^+	7^-	3.0	15	14
^{180}Ta^m(γ, p)^{179}Hf^{m2}	9^-	$9/2^+$	$25/2^-$	0.09	0.045	0.045
^{179}Hf(γ, γ')^{179}Hf^{m2}	$9/2^+$	$9/2^+$	$25/2^-$	0.0014	2×10^{-7}	7×10^{-6}
^{178}Hf(γ, p)^{177}Lu^m	0^+	$7/2^+$	$23/2^-$	<0.005	9×10^{-7}	2×10^{-6}
^{178}Hf^{m2}(γ, n)^{177}Hf^{m2}	16^+	$7/2^-$	$37/2^-$	0.12	0.19	0.19

Note: The experimental data quoted in this table were borrowed from [11]; the calculations were performed with the radiative strength functions as determined on the basis of the (calc1) KMF and (calc2) KMF–CT methods. Presented in the table are the spin–parities J^π_t, J^π_g, and J^π_m of the target nuclei, ground states of residual nuclei, and isomeric states of residual nuclei, respectively.

ence of the spins between the ground and isomeric levels of the ^{191}Ir and ^{197}Au nuclei is moderately small (see Table 1). For this reason, it does not seem reasonable to introduce the above selection rules in K.

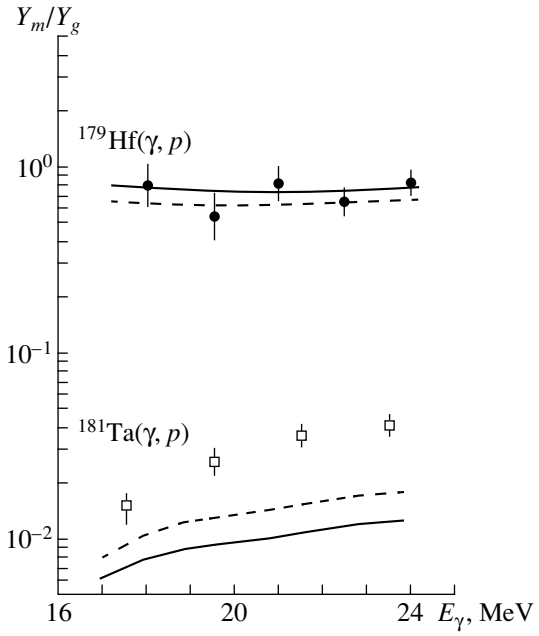

Fig. 11. Ratio of the yields of the isomeric state ^{178}Lu^m(9$^-$) and the ground state ^{178}Lu^g(1$^+$) from the reaction ^{179}Hf(γ, p) and ratio of the yields of the isomeric state ^{180}Hf^m(8$^-$) and the ground state ^{180}Hf^g(0$^+$) from the reaction ^{181}Ta(γ, p). Points represent experimental data from [11]. The notation for the curves is identical to that in Fig. 1.

A theoretical analysis of the isomeric cross sections for (γ, p) reactions is complicated by nonstatistical effects and by proton emission. At the same time, it can be hoped that selection rules in K for transitions in the residual nucleus are less important for these reactions, as well as for all other reactions featuring particle emission, than for photon scattering. That a satisfactory description of the isomeric ratios for the reaction ^{181}Ta(γ, p)^{180}Hf^m was obtained and that good agreement with experimental data was achieved for the reaction ^{179}Hf(γ, p)^{178}Lu^m (see Fig. 11) support this assumption.

As can be seen from Figs. 7–11, our theoretical model faithfully reproduces the energy dependence of the isomeric cross sections for photonuclear reactions; therefore, an analysis of data from [11], which were obtained for one value of the photon energy, the endpoint energy of the spectrum, seems quite informative. These data make it possible to study further the effect of the spin characteristics of nuclei on the mechanism responsible for the excitation of partial levels of residual nuclei. For some reactions, the measured and computed yields of the isomeric and ground states are quoted in Table 2, which shows that the use of the KMF–CT method improves, by and large, the agreement with experimental data. There remain, however, glaring discrepancies for four reactions. It seems strange that, despite a good description of the isomeric cross section for the reaction ^{180}Hf(γ, γ') (see Fig. 7*a*), the corresponding values $(Y_m/Y_g)_{\text{expt}}$ and $(Y_m/Y_g)_{\text{calc}}$ differ by nearly two orders of magnitude. Hence, the calculated value of the cross section for the population of the ground state is strongly overestimated. In all probability, the cross section σ_g for the reaction

^{179}Hf(γ, γ′)^{179}Hf^{m2} is also overestimated, since the isomeric cross section for ^{179}Hf(γ, γ′)^{179}Hf^{m} is reproduced quite reasonably [2]. Following the same line of reasoning, we can assume that the calculated cross sections for the population of states whose spins are close to the spin J_t of the ground state of the target nucleus [this is σ_m for ^{180}Ta(γ, 2n)^{178}Ta^m and σ_g for ^{178}Hf(γ, p)^{177}Lu^m] exceed the corresponding experimental values. This overestimation can be explained by the existence of some barrier [13] above which states having different K values are mixed freely, but below which selection rules in K are operative. Indeed, a high-spin state is populated through a cascade of a large number of low-energy transitions; hence, these transitions proceed between highly excited levels—that is, they are unaffected by selection rules in K. States whose spins are close to J_t are populated with the highest probability via one or two high-energy transitions, and these transitions must involve subbarrier levels—that is, they are quenched by selection rules in K.

4. CONCLUSION

We have tested the method for calculating radiative strength functions for electric dipole transitions that relies on the particle-fragmentation approach having a sound theoretical basis and on experimental information about transitions between discrete levels; it is referred to as the KMF–CT method.

The results of the calculations have been compared with a vast body of data on the cross sections for neutron- and photon-induced reactions occurring on A = 90–180 target nuclei and leading to the population of isomeric levels.

It has been shown that the method that was proposed by the present author with the aim of improving the description of the experimental spectra of photons from neutron-induced reactions and which is based on a specific parametrization of the temperature dependence of the $E1$ strength functions $f_{E1}(E_\gamma, T)$ appears to be quite an effective means for removing some significant discrepancies between the experimental and theoretical values of isomeric cross sections. For cases where there are relevant experimental data, a consistent description of the cross sections for isomer population in two reactions has been obtained, which renders the testing of the method more reliable.

A considerable discrepancy (up to two orders of magnitude) between the measured and calculated ratios of the yields of isomeric and ground states was found for four photonuclear reactions leading to the population of high-spin states. Possible reasons behind these discrepancies have been analyzed, and the most probable one has been indicated: it is the presence of a potential barrier affecting transitions between states having different values of the projection of the total angular momentum onto the symmetry axis of the nucleus.

REFERENCES

1. O. T. Grudzevich, Yad. Fiz. **61**, 29 (1998) [Phys. At. Nucl. **61**, 24 (1998)].
2. O. T. Grudzevich, Yad. Fiz. **62**, 227 (1999) [Phys. At. Nucl. **62**, 192 (1999)].
3. S. G. Kadmensky, V. P. Markushev, and W. I. Furman, Yad. Fiz. **37**, 277 (1983) [Sov. J. Nucl. Phys. **37**, 165 (1983)].
4. E. S. Troubetzkoy, Phys. Rev. **122**, 212 (1961).
5. O. T. Grudzevich, A. V. Ignatyuk, and V. I. Plyaskin, in *Proceedings of International Conference on Nuclear Data for Science and Technology, Mito, Japan* (1988), p. 1221.
6. J. Voignier, S. Joly, and G. Greinier, Nucl. Sci. Eng. **93**, 43 (1986).
7. T. S. Belanova, A. V. Ignatyuk, A. B. Pashchenko, *et al.*, *Radiative Neutron Capture* (Énergoatomizdat, Moscow, 1986).
8. W. Grochulski *et al.*, Acta Phys. Pol. B **6**, 139 (1975).
9. A. Abboud *et al.*, Nucl. Phys. **A132**, 43 (1969).
10. W. Augustyniak *et al.*, Acta Phys. Pol. B **7**, 347 (1976).
11. S. A. Karamian, J. De Boer, Yu. Ts. Oganessian, *et al.*, Z. Phys. A **356**, 23 (1996).
12. F. G. Kodnev, Yu. P. Gangrsky, A. P. Tonchev, *et al.*, FLNR Scientific Report 1991–1992 (JINR, Dubna, 1992), p. 118.
13. Yu. Ts. Oganessian and S. A. Karamian, Hyperfine Interact. **107**, 43 (1997).
14. I. V. Bodrov, M. G. Davydov, I. B. Rakhmanov, *et al.*, Yad. Fiz. **57**, 1347 (1994) [Phys. At. Nucl. **57**, 1277 (1994)].
15. A. P. Tonchev, Yu. P. Gangrsky, A. G. Belov, *et al.*, *Heavy Ion Physics: FNLR Scientific Report* (JINR, Dubna, 1997), p. 149.
16. C. B. Collins, J. J. Carroll, and K. N. Taylor, Phys. Rev. C **46**, 952 (1992).

Translated by A. Isaakyan

Physics of Atomic Nuclei, Vol. 63, No. 3, 2000, pp. 422–430. From Yadernaya Fizika, Vol. 63, No. 3, 2000, pp. 492–500.

NUCLEI
Theory

On the Production Mechanism of Σ-Hypernuclear Systems in $A(K^-, \pi^\pm)$ Reactions*

O. D. Dalkarov and V. M. Kolybasov*****

Lebedev Institute of Physics, Russian Academy of Sciences, Leninskiĭ pr. 53, Moscow, 117924 Russia

Received December 28, 1998; in final form, March 18, 1999

Abstract—It is shown that the new data on the excitation energy E_{exc} spectrum of the residual nuclear system in the Σ-hypernuclear region in the reactions $(K^-, \pi^\pm)$ on ^{9}Be and in the reaction (K^-, π^+) on ^{4}He and ^{12}C can be described without assuming the existence of excited Σ-hypernuclear states. The basis is formed by a simultaneous consideration of the quasifree Σ production and Σ-nuclear rescattering (elastic and with $\Sigma \longrightarrow \Lambda$ conversion) with allowance for the interference of the respective amplitudes. To answer completely the question on the nature of the irregularities in E_{exc} spectrum, it is proposed to study the picture corresponding to the so-called moving complex singularity of the triangle graph with Σ rescattering: the position and the width of the peak in E_{exc} distribution should be appreciably changed with momentum transferred from the initial kaon to the final pion. © *2000 MAIK "Nauka/Interperiodica".*

1. INTRODUCTION

New BNL data on ^{9}Be$(K^-, \pi^\pm)$ reactions at 600 MeV/*c* in the Σ-hypernuclear region [1] transformed drastically the status on the problem of the excited states for Σ nuclei. As followed from the former data (see, for instance, review [2]), there were clear indications on the narrow peaks ($\Gamma < 10$ MeV) in the excitation energy spectrum of the residual nuclear systems in the region near Σ-hyperon production. For this reason, the idea about the creation of excited hypernuclear states seemed to be quite attractive. However, after its appearance, the problem of a small hypernuclear width was discussed, since due to $\Sigma N \longrightarrow \Lambda N$ conversion in the nuclear matter all estimations lead to the widths exceeding 20–40 MeV [2, 3]. Recent data [see Fig. 1, where circles correspond to ^{9}Be(K^-, π^-) reaction and squares to ^{9}Be(K^-, π^+) one] exclude overly narrow peaks but reveal the structures with the width up to 20 MeV for (K^-, π^-) and 30–40 MeV for the case of (K^-, π^+) reaction.

Several questions should be cleared up: Do these peaks call for the idea about the existence of Σ hypernuclei or are they caused by the reaction mechanism and, probably, by the near-threshold phenomena? If there is a way to understand the problem without Σ hypernuclei, then how will the natural and doubtless description be made through the simplest mechanisms? Finally, are there crucial tests to clear up the question about the nature of the irregularities in the excitation energy spectrum of Σ-hypernuclear systems? Below, we will try to answer these questions.

The first goal of this study is to show that there are the means to describe entirely a set of data on the reaction ^{9}Be(K^-, π^-) and the reactions (K^-, π^+) on ^{9}Be, ^{12}C, and ^{4}He nuclei without the idea on the existence of excited Σ-hypernuclear states (see Fig. 2*d*), but using the Feynman graphs and taking into account the quasifree Σ-hyperon production (Fig. 2*a*), the elastic rescattering of Σ (Fig. 2*b*), and final inelastic interaction of Σ hyperon with the $\Sigma \longrightarrow \Lambda$ conversion (Fig. 2*c*). In this approach, the interference of the pole graph of Fig. 2*a* and the triangle graph of Fig. 2*b* should be essential. We

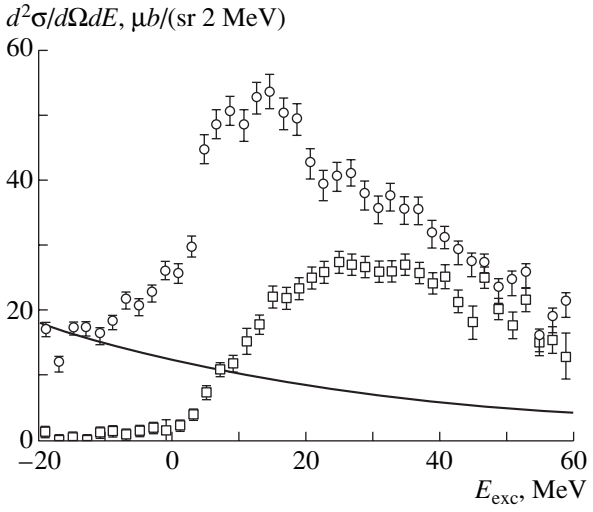

Fig. 1. The data of [1] on the differential cross sections of the reactions ^{9}Be(K^-, π^-) (circles) and ^{9}Be(K^-, π^+) (squares) at small angles at 600 MeV/*c*. The solid curve is the approximation of the tail of direct Λ production used in Section 3.

* This article was submitted by the authors in English.

** e-mail: dalkarov@sci.lebedev.ru
*** e-mail: kolybasv@sci.lebedev.ru

will also emphasize some characteristic features of the process ^{9}Be(K^-, π^+) distinguishing it against others.

Another purpose, and apparently the main one, is to advance a theoretical method for final revelation of the nature of the peaks in the excitation energy spectra in order to give a way to distinguish the peaks caused by the existence of Σ hypernuclei from the ones produced by the reaction mechanism. This method is based on the analytical properties of the Feynman graphs. In our case, the singularities of the nonrelativistic triangle graph (see Fig. 2*e*) are close to the physical region; this leads to the appearance of moving maxima in the excitation energy spectra as a function of the momentum transfer from an initial kaon to final π meson. Note that the extraction of this graph as a unique one is achieved within the experiment if the Λ hyperon, produced by the interaction of virtual Σ hyperon with the intermediate nucleus, is detected. Therefore, a study of the double differential cross sections (with and without Λ-hyperon detection in the final state) for $A(K, \pi)X$ reactions is an effective test to distinguish the main features of the reaction mechanism.

The theoretical model is described in Section 2. Kinematical relations between various differential cross sections are given, and the detailed properties of the amplitude for the triangle graph are discussed. Section 3 is devoted to the procedure of ^{9}Be data processing, in particular, to a difference method which was used to extract the contribution of the (K^-, π^-) process on the outer weakly bound neutron. The question about the role of relative phase between the amplitudes for pole and triangle graphs (see Figs. 2*a*, 2*b*) is also discussed.

The final results for the (K^-, π^-) reaction on ^{9}Be and (K^-, π^+) on ^{9}Be, ^{4}He, and ^{12}C nuclei, which are in good agreement with the experimental data, are given in Section 4. We also discuss possible reasons for the sizable difference between the excitation energy spectrum for ^{9}Be and the same quantities for ^{4}He and ^{12}C.

The picture of the moving triangle singularities is discussed in Section 5. We present results of the calculations for the excitation energy spectra for the channels with $\Sigma \longrightarrow \Lambda$ conversion for different momentum transfers from initial kaon to final pion. These results show that the moving peaks in the excitation energy spectra are observable experimentally. For comparison, the excitation energy spectra with a hypernuclear state production (see Fig. 2*d*) are also calculated. In this case, the position of the peak virtually does not depend on the momentum transfer.

The main results and concluding remarks are given in the Conclusion.

2. THEORETICAL MODEL

We will consider the graphs of Figs. 2*a*–2*c*, where the pole graph (Fig. 2*a*) represents the quasifree Σ-hyperon production. The triangle graphs correspond to the rescattering of a virtual Σ hyperon on the intermediate nuclear system without any conversion (Fig. 2*b*) and taking the conversion into account (Fig. 2*c*), excluding production of the Σ-hypernuclear bound or resonance states (this process would correspond to the graph of Fig. 2*d*). Let us analyze more accurately the general properties of triangle Feynman graphs before making the fitting procedure. We will consider the general form of Fig. 2*e* implying that the particle 2 is the Σ hyperon and that the particle 1 is the residual nuclear system and the lower vertex stands in principle for the aggregate of all the processes that occur when the Σ hyperon interacts with the residual nucleus. We denote by p_i and E_i the momentum and total energy of a particle i in the lab system and introduce the notation

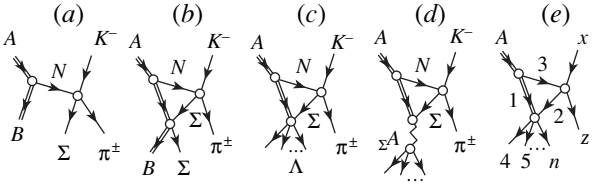

Fig. 2. The graphs for the processes (K^-, $\pi^\pm$) on nuclei (*a*–*d*) and a generic form of the triangle graph (*e*).

$$\mathbf{q} = \mathbf{p}_x - \mathbf{p}_z,$$
$$W = \sqrt{s_{12}} = [(m_A + E_x - E_z)^2 - q^2]^{1/2}. \quad (1)$$

Here, W is the invariant mass of the system $4 + \ldots + n$, consisting of the particles produced after Σ conversion in a nuclear medium. We shall henceforth be restricted by transfers q^2 small enough only and the quantity W from a region where Σ hyperon 2 can be assumed as nonrelativistic. If we neglect the complications caused by the spin structure of the amplitudes and restrict ourselves to the consideration of the triangle diagram only (Fig. 2*e*), then the quantity $d^2\sigma/dWdq^2$ can be expressed in terms of the differential cross section $d\sigma_{3x}/d\Omega$ of the elementary reaction $K^- + N \longrightarrow \pi + \Sigma$ (in c.m. frame of this reaction) and the total cross section $\sigma_{12}(W)$ for the interaction of the Σ hyperon and the nucleus 1 [4, 5]:

$$\frac{d^2\sigma}{dWdq^2} = \frac{m_1^2 m_2 s_{3x}}{4\pi^3 m_3 (m_1 + m_2)^2 p_x^2}\kappa\gamma^2 \times \left(\frac{p_1^{\text{c.m.}}}{m_{12}}\sigma_{12}(W)\right)\left(\frac{\tilde{p}_x}{\tilde{p}_z}\frac{d\sigma_{3x}}{d\Omega}\right)|M|^2. \quad (2)$$

Here, $s_{3x} = m_3^2 + m_x^2 + 2m_3E_x$; $p_1^{\text{c.m.}}$ is the momentum of the relative motion of the particles 1 and 2 in the c.m. frame of particles 4, …, n; and $\tilde{p}_x$ and $\tilde{p}_z$ are the momenta of particles x and z in the c.m. frame of the reaction $3 + x \longrightarrow 2 + z$. The quantities γ^2 and κ pertain to the nuclear vertex

$$A \longrightarrow 1 + 3, \quad (3)$$

γ^2 is the reduced vertex part [6] and determines the probability of the virtual disintegration (3), and $\kappa = \sqrt{2m_{13}\varepsilon}$, $\varepsilon = m_1 + m_3 - m_A$. The factor M is determined by the structure of the triangle graph.

We will also need the differential cross section $d^2\sigma/d\Omega dW$ for comparison with the experimental data. It can be obtained from (2) in the following manner:

$$\frac{d^2\sigma}{d\Omega dW} = \frac{W p_x p_z^2}{2\pi E_0 \left| p_z - \frac{E_z}{E_0} p_x \cos\theta \right|} \frac{d^2\sigma}{dW dq^2}, \quad (4)$$

where θ is the angle between particles z and x and E_0 is the total energy of all particles in the lab system.

We shall henceforth focus our attention on the quantity M which determines the behavior of differential cross section (2) as function of kinematical variables (1). It is convenient to introduce dimensionless variables [7]

$$\xi = \frac{m_2}{m_3 m_4 + \ldots + m_n} \frac{m_A}{} \frac{W - m_1 - m_2}{\varepsilon}, \qquad \lambda = \frac{m_1^2}{(m_1 + m_2)^2} \frac{q^2}{\kappa^2}. \quad (5)$$

The quantity M can be expressed through these variables in the form of a double integral in the momentum space

$$M = \frac{1}{\kappa} \int_0^\infty \int_{-1}^1 \frac{F_l(\kappa x) x^2 dx P_l(z) dz}{(1 + x^2)(x^2 + \lambda - \xi - 2x\sqrt{\lambda} z - i\eta)} \quad (6)$$

with $x = p/\kappa$. Here, $F_l(p)$ is the form factor of the vertex $A \longrightarrow 1 + 3$, normalized by the condition $F_l(i\kappa) = 1$; l is the angular momentum of the relative motion of particles 1 and 3 in the nucleus A; and P_l is the Legendre polynomial.

In practice, it is necessary to use the more general formulas taking into account the realistic nuclear form factor. In such a case, it is more profitable to operate into the coordinate space where M can be expressed as a single integral [4]

$$M = \frac{i^l}{2\pi} \int_0^\infty \Psi(r) j_l(\sqrt{\lambda}\kappa r) \exp(-A\kappa r + iB\kappa r) r dr. \quad (7)$$

Here, j_l is the spherical Bessel function, and the quantity $\Psi(r)$ is introduced by the equation

$$\Psi(r) = 4\pi i^l \int_0^\infty \frac{F_l(p)}{p^2 + \kappa^2} j_l(pr) p^2 dp \quad (8)$$

(in the single-particle model it would be proportional to the wave function for the relative motion of the particles 1 and 3). The quantities A and B are specified as

$$B = \sqrt{\xi}, \quad A = 0 \text{ at } \xi \geq 0, \qquad A = \sqrt{-\xi}, \quad B = 0 \text{ at } \xi < 0. \quad (9)$$

Hereinafter, except Section 5, we will take the amplitude of the lower vertex of Fig. 2*e* to be constant as we are first of all interested in the effects due to the structure and analytic properties of the graphs. We would like, whenever possible, to gain the results as model-independent ones. As there are no reliable data on sigma-nuclear interactions, we prefer not to rely on the calculations using a Σ–A optical potential. Let us point to the detailed research of K^-–^{4}He interactions with a variety of the forms for such potential [8]. In particular, it shows an appreciable dependence of the results on the potential parameters.

The amplitude M (6) for the graph of Fig. 2*e* has two kinds of singularities in W: (i) normal threshold at $W = m_1 + m_2$ and (ii) so-called triangle logarithmic singularity which appears in the complex plane. The position of the triangle singularity is determined by the value of q^2. In terms of the variables ξ and λ, the triangle singularity is found as

$$\xi_\Delta = \lambda - 1 + 2i\sqrt{\lambda}. \quad (10)$$

If we can approach closely to the position of the triangle singularity point in an experimental investigation, then the amplitude of a triangle graph would seem to be a sharp function. Thus, it is possible to expect that a bump in the W distribution will appear. The position and width of the bump should be varied with q^2. We will discuss in Section 5 how this property of a triangle graph can be verified.

3. PROCEDURE

Though the data [1] on the processes

$$^9\text{Be}(K^-, \pi^+) \quad (11)$$

and

$$^9\text{Be}(K^-, \pi^-) \quad (12)$$

(see Fig. 1) do not exhibit any narrow structures, these data, as we shall see below, contain a lot of physical information and unexpected features (positions of bump maxima, an absence of narrow near-threshold peaks due to channels with $\Sigma \longrightarrow \Lambda$ conversion, and so on). The channel (11) represents Σ production on the protons of the Be nuclei

$$K^- p \longrightarrow \pi^+ \Sigma^- \quad (13)$$

and the channel (12) can be realized on the protons

$$K^- p \longrightarrow \pi^- \Sigma^+ \quad (14)$$

as well as on the neutrons

$$K^- n \longrightarrow \pi^- \Sigma^0. \quad (15)$$

At 600 MeV/c, the cross section of the mode (14) is much less than that of the mode (15) [2]. The data for the channels (11) and (12) are quite different. The main reason, evidently, is the very small binding energy (1.67 MeV only) of the outer neutron in ^{9}Be. So it is useful to isolate the part of the channel (12) cross section which takes place on the outer neutron.

The zero in the excitation energy $E_{\rm exc}$ in the channel (11) corresponds to the invariant mass W of the final state consisting of Σ^- plus the ground state of ^{8}Li without relative motion, and in the channel (12) it corresponds to Σ^0 plus the ground state of ^{8}Be. Thus, $E_{\rm exc} \geq 0$ for events with the Σ hyperon in a final state. The left parts of the spectra in Fig. 1, related to $E_{\rm exc} < 0$, can have their origin in the process of Σ production followed by the conversion

$$\Sigma N \longrightarrow \Lambda N, \quad (16)$$

as well as (for the channel (12)) in the "tail" of direct Λ production. The estimation of this tail behavior in the model of a quasifree Λ production shows its sharp decrease in the interval of $E_{\rm exc}$ from –20 MeV to zero. It is inconsistent with the data on the channel (12). Therefore, we take the model of a quasifree Λ production followed by its rescattering. It leads to the result shown by the solid curve in Fig. 1 (the normalization of the curve is fixed by the experimental point at $E_{\rm exc}$ = –20 MeV). In the following, the corresponding values (the physical background due to the direct Λ production) will be subtracted from the data for channel (12).

The nucleus ^{9}Be has most probably a cluster structure consisting of the core (^{8}Be or two α particles) and the weakly bound outer neutron. So the reaction (12) can proceed through four protons and four neutrons of the core as well as through an outer neutron. The reaction (11) can proceed only through four core protons. We have simultaneously the data on both channels (11) and (12). This allows us to isolate the partial cross section for channel (12), which is specified by the outer neutron, in assuming that the wave functions of the core neutrons and protons are similar. For this purpose let us note that the sum of the cross sections of the processes (14) and (15) at 600 MeV/c are equal roughly to 90% of the cross section of process (13). Thus, we can believe that the contribution of the core neutrons and protons to the cross section of channel (12) is estimated as 90% of the cross section for channel (11). Then, the expression $(\sigma_2 - 0.9\sigma_1)$ gives the contribution of the outer neutron to the cross section of process (12). Here, σ_2 is the cross section of channel (12) minus the contribution of the tail from the direct Λ production. In the following, we will compare the results of our calculations of process (12) with the result just of this difference procedure (see below the points in Fig. 4*a*).

In the subsequent calculations, we will use the wave function (form factor) of the outer neutron in ^{9}Be from the n–α–α cluster model [9]. The corresponding form factor for the core proton was not calculated in the cluster model of [9]. At the first stage, we will use the p-wave oscillator wave function with the parameter p_0 = 130 MeV/c [10]. To estimate the sensitivity of our results to the shape of a wave function, we will also make some calculations with a model p-wave function of a "quasi-Hulthén" type

$$\psi(r) \sim \left(\frac{1}{\kappa r} + \frac{1}{\kappa^2 r^2}\right) \times (e^{-\kappa r} - 3e^{-(\kappa+\rho)r} + 3e^{-(\kappa+2\rho)r} - e^{-(\kappa+3\rho)r}), \quad (17)$$

which has a correct asymptotic behavior for $r \longrightarrow 0$ and for $r \longrightarrow \infty$. Note at once that it does not alter the results qualitatively.

Let us present at first several intermediate results for the reaction (11) at 600 MeV/c at small angles. Figure 3*a* shows the real and imaginary parts of the triangle graph for a secondary interaction of the Σ hyperon with the residual nuclear system (Figs. 2*b*, 2*c*) as functions of $E_{\rm exc}$. As was mentioned earlier, the calculations were carried out with constant amplitude of a secondary interaction in order to clarify, first of all, what results are connected to the structure of the graphs. Figure 3*b* demonstrates the modulus squared of the triangle graph amplitude. We can see that it has a sharp peak near $E_{\rm exc}$ = 0 with the width about 15 MeV. The cross section for the process represented by the graph in Fig. 2*b* includes the phase-space factor proportional to $\sqrt{E_{\rm exc}}$, and it leads to the smoothing and shifting of the peak. This is not so for the process with the conversion (16), and the corresponding peak must also appear in its cross section. Note that the peak of the same origin is well known for the process (K^-, π^-) on the deuteron [11]. The cusp structures are also distinctly seen in the results of calculations of stopped and in-flight K^- interactions with ^{4}He [8, 12].

The solid curve of Fig. 3*c* presents the $E_{\rm exc}$ distribution corresponding to the quasifree Σ production (the pole graph of Fig. 2*a*). The dotted curve shows the same for the triangle graph of Fig. 2*b*. We see that both the pole graph and the triangle graph separately lead to the bumps with the width 30–40 MeV but with maxima in the region of 10 MeV and it is inconsistent with the experimental data. However, the amplitudes of the graphs of Figs. 2*a* and 2*b* interfere with each other. Comparison of the real and imaginary parts of the triangle graph in Fig. 3*a* indicates that its phase varies quickly with $E_{\rm exc}$ and the result of the interference should be nontrivial. The dashed and dash-dotted curves in Fig. 3*c* are the results of calculations for the sum of the graphs of Figs. 2*a* and 2*b* with the relative phase equal to 0.4π and 0.9π, respectively. They demonstrate that the position and the shape of the resulting peak may be varied over a wide range as a result of rel-

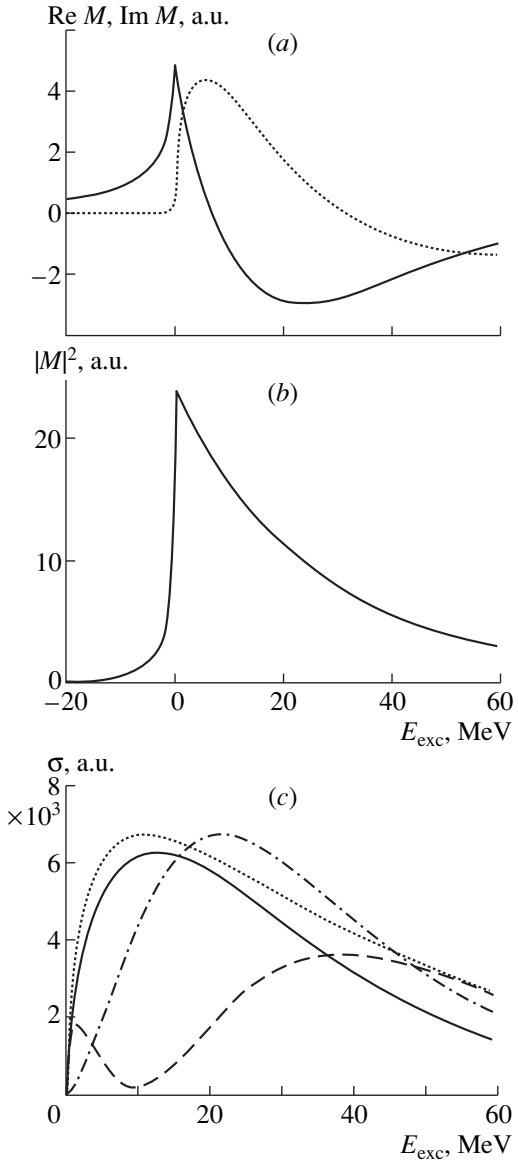

Fig. 3. The results of intermediate calculations for the process ^{9}Be(K^-, π^+): (*a*) real and imaginary parts of the triangle graph amplitude (solid and dotted curves, respectively); (*b*) modulus squared of the triangle graph amplitude; and (*c*) the shapes of the contributions to the cross section from the quasifree Σ production of Fig. 2*a* (solid curve), from the Fig. 2*b* triangle graph (dotted curve), and from two versions of the account of the interference of the Fig. 2*a* and 2*b* graphs with the relative phase 0.4π (dashed curve) and 0.9π (dash-dotted curve).

ative phase variation. (Note, that this phase is not known a priori because it is essentially determined by the phase of the elastic Σ-nucleus scattering amplitude and by the possible variation of the phases versus energy of the elementary processes (13)–(15).) Large interference effects were also noted in [8].

4. RESULTS

Let us go to the results for the best fit to the data on the channels (11) and (12). Firstly, we are interested in a principal possibility of the description without the introduction of Σ nuclei. Therefore, at this point, we did not try to estimate the absolute values of cross sections (at least, this demands that we account additionally for the absorption in initial and final states), but we concentrated on the description of the shape of the E_{exc} distributions at small pion angles. For this reason, the normalization factors of the Fig. 2*a* and 2*b* graphs and their relative phase were taken as free parameters. Here, it is necessary to make a few notes. As to an absolute normalization, [8] shows that the theoretical calculations for ^{4}He case lead to reasonable results when taking into account kaon and pion wave absorption. The relative contribution and phase of the Fig. 2*b* graph now cannot be evaluated reliably due to a lack of information on sigma-nuclear interactions. It is possible to invert a task into deriving information on sigma-nuclear interaction from outcomes of a comparison of calculations with experimental data. However, it is a theme of independent research.

The solid curve of Fig. 4*a* shows the result of the calculation for the sum of the Fig. 2*a* and 2*b* graphs with the relative phase 1.3π for the reaction ^{9}Be(K^-, π^+). It agrees with the data very well. The dashed curve corresponds to "switching off" the triangle graph of Fig. 2*b*; i.e. it represents the separate contribution of the quasifree Σ production (Fig. 2*a*). The contribution of the Fig. 2*c* graph was not taken into account since the experimental points at $E_{exc} < 0$ are virtually equal to zero.

Figure 4*b* deals with the difference data for the reaction ^{9}Be(K^-, π^-), which have their origin in the process on the outer neutron (see the preceding section). The dotted curve shows the supposed contribution from the process with the conversion $\Sigma \longrightarrow \Lambda$ (Fig. 2*c*). Essentially, it is an analog of the curve in Fig. 3*b* normalized to the point at $E_{exc} = 0$, where the contributions of the Fig. 2*a* and 2*b* processes go to zero. The solid curve is the result of a complete calculation with account of the interference of the Fig. 2*a* and 2*b* graphs with the relative phase 1.9π. The dashed curve is the separate contribution of the quasifree process. We notice that the cross section of the process (12) on the outer neutron has the appearance of the peak in E_{exc} with a maximum in the region of 8–10 MeV, the width of 15–20 MeV, and can be described very well by the combination of the Fig. 2*a*–2*c* graphs.

Having obtained the good results for the production of Σ-hypernuclear systems on ^{9}Be, we go now to the description by the same method of the new data on the reaction ^{4}He(K^-, π^+) at 600 MeV/*c* [13][1)] and on the reaction ^{12}C(K^-, π^+) at 715 MeV/*c* [14]. For ^{4}He, we use

[1)]We will not consider now the process ^{4}He(K^-, π^-) where the bound Σ-hypernuclear state of ^{4}He was discovered [13]. Here, the picture is more complicated due to presence of a resonance peak. In principle, our model must describe the background including, in particular, all data at $E_{exc} > 0$. We hope to discuss it in another work.

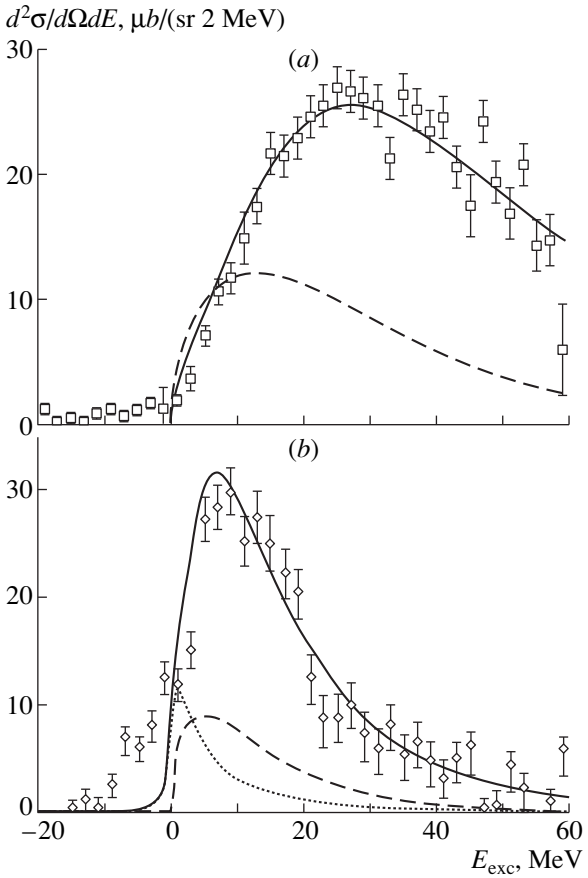

Fig. 4. (*a*) The excitation energy distribution in the reaction ^{9}Be(K^-, π^+). The data are from [1]. The solid curve is the result of a full calculation. The dashed curve shows the contribution only from the quasifree Σ production (Fig. 2*a*). (*b*) The excitation energy distribution in the reaction ^{9}Be(K^-, π^-) on the outer neutron. The experimental data are obtained from the data of [1] by means of the difference procedure described in Section 3. The solid curve is the result of a full calculation. The dotted curve is the contribution of the processes with the conversion Σ ⟶ Λ. The dashed curve shows the contribution only from the quasifree Σ production (Fig. 2*a*).

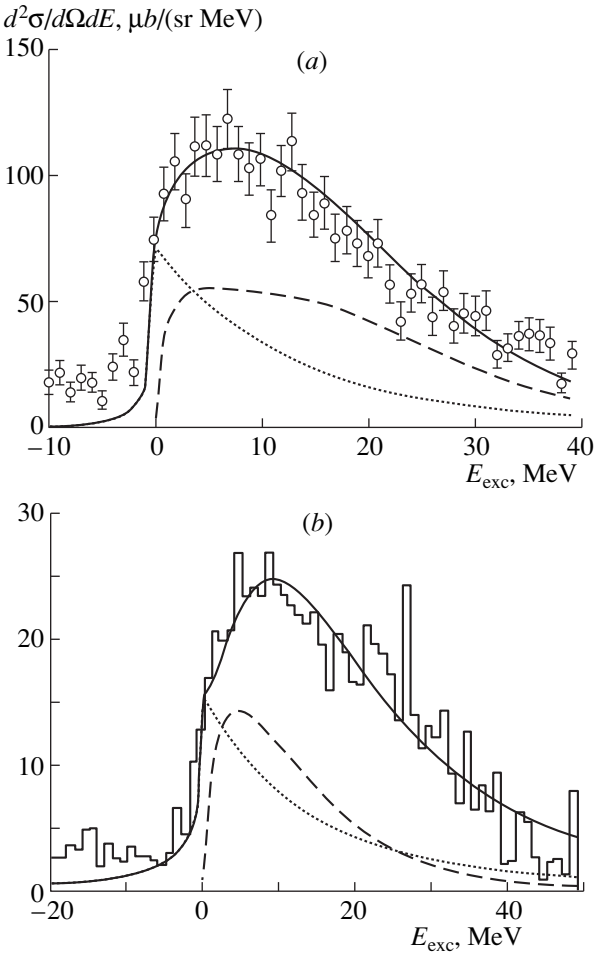

Fig. 5. (*a*) The excitation energy distribution in the reaction ^{12}C(K^-, π^+) at 715 MeV/*c* for 4°. The data are from [12]. The solid curve is the result of a full calculation. The dotted curve is the contribution of the process with the conversion Σ ⟶ Λ. The dashed curve shows the contribution only from the quasifree Σ production (Fig. 2*a*). (*b*) The excitation energy distribution in the reaction ^{4}He(K^-, π^+) at 600 MeV/*c* for small angles. The experimental histogram is from [11]. The meaning of the curves is the same as in Fig. 5*a*.

the *s*-wave oscillator wave function with the parameter p_0 = 90 MeV/*c* which gives the best fit to the data on the process ^{4}He(*e*, *ep*)^{3}H [15]. For ^{12}C, we use the *p*-wave oscillator wave function with the parameter p_0 = 80 MeV/*c* which gives the best fit to the data on the reaction ^{12}C(*e*, *ep*) in the ground and low-lying states of ^{11}B [16]. The results are shown in Fig. 5*a* for ^{12}C and in Fig. 5*b* for ^{4}He. Here, the dotted curves are the contributions of the processes with the conversion normalized to the points at E_{exc} = 0. The solid curves present the results of full calculations with account of the interference of the Fig. 2*a* and 2*b* graphs with the relative phase equal to 0.9π for Fig. 5*a* and 1.3π for Fig. 5*b*. The dashed curves are the separate contributions of the quasifree Σ production. One can see that our simple model provides a possibility to describe the data very well.

Certainly, owing to use of large number of fitting parameters, our description of the data on (K^-, $\pi^\pm$) reactions can be considered simply as a successful parametrization. However, the possibility of such parametrization was not obvious beforehand. We shall note that in sigma-nuclear physics the use of a large number of free parameters is not an unusual fact. Let us turn, for example, to [12], where four parameters were used for the description of stopped K^- interaction with ^{4}He.

It is necessary to emphasize also the following. In our calculations it was assumed that the residual nuclear system is in the ground state or in one of the low-excited states. There is direct experimental data on the reaction (*e*, *ep*) for ^{4}He and ^{12}C nuclei. It was found

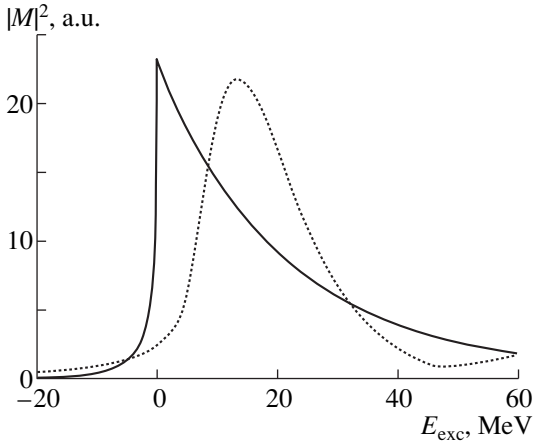

Fig. 6. $|M|^2$ for the triangle graph of Fig. 2*c* with two-particle (solid curve) and three-particle (dotted curve) intermediate states.

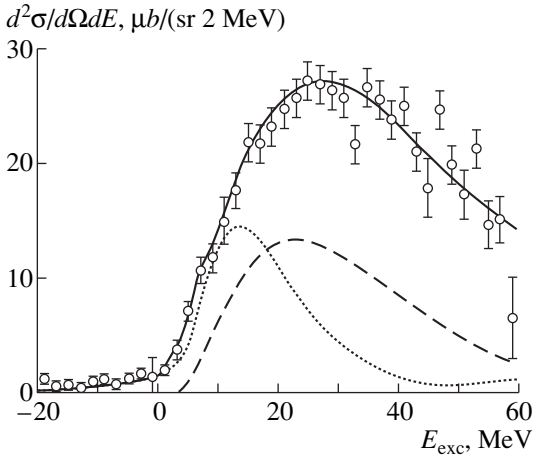

Fig. 7. The excitation energy distribution in the reaction ^{9}Be(K^-, π^+) with three-particle intermediate state in the Fig. 2*c* graph. The solid curve is the result of a full calculation. The dotted curve is the contribution of the processes with the conversion $\Sigma \longrightarrow \Lambda$. The dashed curve shows the contribution only from the quasifree Σ production.

that the vertices of a virtual breakup of these nuclei to proton and ground states of *t* and ^{11}B give the main contribution [17, 18]. The same is also noted for ^{12}C case in [19] devoted to the quasifree Σ production in (K^-, π^+) reactions. There are no electron data on the vertex $^9\text{Be} \longrightarrow n + {}^8\text{Be}$. However, the evaluation in the (2α + *n*) model [9] shows a preference of the transition to the ground state of ^{8}Be. Apparently, it is not so for the process ^{9}Be(K^-, π^+). This case will be considered separately in the following section.

5. THE CASE OF ^{9}Be(K^-, π^+) REACTION

The E_{exc} distribution for the ^{9}Be(K^-, π^+) reaction differs substantially from other cases in two aspects: (i) its maximum is shifted to higher energies at 25–30 MeV, whereas in all remaining cases it is found near 10 MeV; and (ii) it contains a few events at $E_{exc} \le 0$ and virtually does not leave a place for the contribution of the narrow near-threshold peak of Fig. 3*b*. Thus, the description presented in Fig. 4*a* was obtained without the contribution of the conversion process and used certainly too large a value for the oscillator parameter p_0 = 130 MeV/*c*. On the other hand, proceeding from known values of the cross sections of the elementary processes $\sigma(\Sigma^- p \longrightarrow \Sigma^- p)$ and $\sigma(\Sigma^- p \longrightarrow \Lambda n)$, each of which is about 150 mb in the Σ-momentum region 100–200 MeV/*c*, it is possible to evaluate that the cross sections of the processes of conversion and elastic Σ^- rescattering should be of the same order as the cross section of the quasifree production.

The contribution of the conversion process could be explained if we assumed that the secondary Σ interactions in the lower vertices of the Fig. 2*b* and 2*c* graphs proceed mainly in the *p* wave. It results in smoothening of the near-threshold peak and shifts it to the higher energies [20]. However, this explanation does not seem natural because there are no reasons for the special behavior in just the ^{9}Be(K^-, π^+) case. More plausible is another explanation. It is assumed that continuum states of the residual nuclear system ^{8}Li dominate in the breakup vertex $^9\text{Be} \longrightarrow p + {}^8\text{Li}$. As a difference to the ^{4}He and ^{12}C cases, there are no high precision data on the ^{9}Be(*e*, *ep*) reaction. It is possible only to state for which the available data [21] show a wide distribution with respect to the proton removal energy and do not contradict such a hypothesis. In that case, on the one hand, the E_{exc} distribution from the quasifree Σ production is shifted to the higher energies. On the other hand, the intermediate state in the Fig. 2*c* graph becomes three-particle or many-particle but not a two-particle one. It changes the shape of near-threshold behavior absolutely. Figure 6 shows the comparison of $|M|^2$ for the triangle graphs with two-particle (solid curve) and three-particle (dotted curve) intermediate states. The character of the dotted curve leaves room for the significant contribution of the conversion, keeping small number of events at $E_{exc} \le 0$. Figure 7 demonstrates an example of successful description of ^{9}Be(K^-, π^+) data with considerable contribution of the conversion process (dotted curve). Here, the dashed curve is the separate contribution of the quasifree Σ production. The solid curve is the summary result with account of interference of the Fig. 2*a* and 2*b* graphs, the relative phase being 0.35π. The value of the oscillator parameter p_0 = 115 MeV/*c* was used. It is close to the value of 110 MeV/*c* which is suggested in [21] for the region of large proton removal energies.

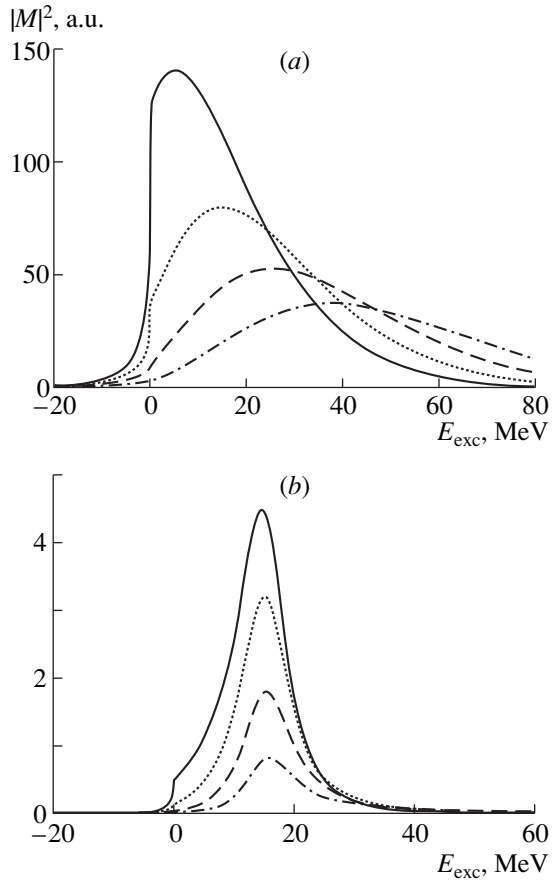

Fig. 8. (*a*) The modulus squared of the Fig. 2*c* graph amplitude for the reaction $^{12}C(K^-, \pi^+)$ at momentum-transfer values q = (solid curve) 200, (dotted curve) 250, (dashed curve) 300, and (dash-dotted curve) 350 MeV/*c*. (*b*) The same with the inclusion of the excited Σ-hypernuclear state (Fig. 2*d*) with the width 10 MeV and the mass corresponding to E_{exc} = 15 MeV.

6. MOVING SINGULARITIES AND THE MECHANISM OF Σ-HYPERNUCLEAR SYSTEM PRODUCTION

Strictly speaking, the good description of the data on the $(K^-, \pi^\pm)$ processes in the Σ-hypernuclear region by the simplest mechanisms does not exclude a possible contribution from Σ hypernuclei. For a complete and unambiguous solution of the reaction mechanism problem, it seems efficient to use the theoretical predictions which follow from the picture of moving complex triangle singularities described in Section 2. As mentioned above, the presence of these singularities near the physical region of a reaction should lead to a maximum for E_{exc} distribution. The position and the shape of the bump must be varied with the momentum q transferred from the initial kaon to the final pion [5]. Numerical calculations should show whether this effect is noticeable or not. The contribution of the quasifree Σ-hyperon production would conceal the above-mentioned effect. Therefore, it is more desirable to study it in the channels with the conversion $\Sigma \longrightarrow \Lambda$ (i.e., with the detection of Λ), where the Fig. 2*a* graph does not contribute. To investigate the discussed picture, one needs to measure the differential cross section $d^2\sigma/dE_{exc}dq^2$, which is directly expressed through the modulus squared of the matrix element (see equation (2)), in a wide range of E_{exc} and q.

For example, let us consider the reaction $^{12}C(K^-, \pi^+)$. Figure 8*a* shows the theoretical predictions for the modulus squared of the Fig. 2*c* graph amplitude as a function of E_{exc} for different values of q = 200, 250, 300, and 350 MeV/*c*. A distinct picture of moving and broadening of the peak is visible. This picture is quite available for an experimental observation.

The question is what would happen with the same distributions in the case of Σ-hypernucleus production (the graph of Fig. 2*d*)? To answer the question, calculations were made with inclusion of a resonance state (a Breit–Wigner pole was put in) with the width of 10 MeV and the mass which was 15 MeV larger than the sum of the masses of Σ and the ground state of the residual nucleus. Figure 8*b* shows the results for the same set of the momentum transfer. As could be expected, the position of the maximum remains constant in this case. It follows that the investigation of $d^2\sigma/dE_{exc}dq^2$ would make it possible to answer unambiguously the question about the nature of the irregularities in the excitation energy spectrum of the processes $(K^-, \pi^\pm)$: whether they appeared from the reaction mechanism or from the existence of Σ hypernuclei.

7. CONCLUSION

Thus, all considered data on the reactions $(K^-, \pi^\pm)$ in the Σ-hypernuclear region can be basically described without the supposition on the existence of Σ hypernuclei. The bumps in the excitation energy distributions of the residual nuclear systems are due to the peculiarities of the reaction mechanisms.

The successful description of the available data by means of the simplest mechanisms cannot completely exclude the existence of hypernuclei. We tried to emphasize that the decisive conclusion on this problem can be made only through detailed investigation of the Σ-hypernuclear system production mechanism. We propose to study the cross section $d^2\sigma/dE_{exc}dq^2$ at different values of momentum transfer q, since its behavior strongly depends on the existence of Σ hypernuclei. If the experimental investigations confirm the picture of moving singularities, predicted in Section 5, and thus the dominant contribution of the Fig. 3*c* graph in the channels with the conversion, then it would be possible to extract the cross section σ_{12} of the Σ-nucleus interaction using equation (2). In the future, this value of σ_{12} could be compared with dynamical calculations.

Note that the considered picture of moving singularities of triangle Feynman graphs in the case of rescattering effects for Σ-hypernuclear system production is

universal. The same phenomena could be observed at different kinematical conditions in other reactions, for instance, $A(e, e'K^-)X$.

ACKNOWLEDGMENTS

The authors are indebted to Prof. I.S. Shapiro for the attention to the investigation and discussions, to Profs. T. Nagae and R. E. Chrien for information on the experimental data, and to Profs. V. I. Kukulin, V. I. Pomerantsev, and M. A. Zhusupov for the advice and the data on the neutron form factor of ^{9}Be.

This work was supported in part by the Russian Foundation for Basic Research (project no. 99-02-17263).

REFERENCES

1. R. Sawafta, Nucl. Phys. **A585**, 103 (1995); T. Nagae, in *Abstracts of 25th INS International Symposium, Tokyo, 1996*, p. 130; *Nuclear and Particle Physics with High-Intensity Proton Accelerators*, Ed. by T. Komatsubara *et al.* (World Sci., 1998), p. 265.
2. C. B. Dover, D. J. Millener, and A. Gal, Phys. Rep. **184**, 1 (1989).
3. L. N. Bogdanova and V. E. Markushun, Part. Nucl. **15**, 808 (1984).
4. O. D. Dalkarov and V. M. Kolybasov, Yad. Fiz. **18**, 809 (1973) [Sov. J. Nucl. Phys. **18**, 416 (1973)].
5. O. D. Dalkarov, V. M. Kolybasov, and D. V. Voronov, Preprint No. 8, Lebedev Institute of Physics, Russian Academy of Sciences (Moscow, 1995).
6. I. S. Shapiro, Usp. Fiz. Nauk **92**, 549 (1967) [Sov. Phys. Usp. **10**, 515 (1967)].
7. E. I. Dubovoj and I. S. Shapiro, Zh. Éksp. Teor. Fiz. **51**, 1251 (1966) [Sov. Phys. JETP **24**, 839 (1966)].
8. T. Harada and Y. Akaishi, Prog. Theor. Phys. **96**, 145 (1996).
9. V. T. Voronchev, V. I. Kukulin, V. N. Pomerantsev, *et al.*, Yad. Fiz. **57**, 1964 (1994) [Phys. At. Nucl. **57**, 1890 (1994)]; M. A. Zhusupov, *et al.*, Izv. Akad. Nauk, Ser. Fiz. **58** (5), 55 (1994).
10. F. Ajzenberg-Selove, Nucl. Phys. **A490**, 1 (1988).
11. T. H. Tan, Phys. Rev. Lett. **23**, 395 (1969); R. H. Dalitz, *Strange Particles and Strong Interactions* (Oxford Univ. Press, Oxford, 1962); A. E. Kudryavtsev, Pis'ma Zh. Éksp. Teor. Fiz. **14**, 137 (1971) [JETP Lett. **14**, 91 (1971)].
12. R. H. Dalitz and A. Deloff, Nucl. Phys. **A585**, 303 (1995).
13. T. Nagae, *et al.*, Phys. Rev. Lett. **80**, 1605 (1998).
14. L. G. Tang, *et al.*, Phys. Rev. C **38**, 846 (1988).
15. J. M. Laget, Nucl. Phys. **A497**, 391 (1989).
16. G. van der Steenhoven *et al.*, Nucl. Phys. **A480**, 547 (1988).
17. J. F. J. van den Brand *et al.*, Phys. Rev. Lett. **60**, 2006 (1988); J. M. Le Goff *et al.*, Phys. Rev. C **50**, 2278 (1994).
18. J. Mougey *et al.*, Nucl. Phys. **A262**, 461 (1976).
19. R. E. Chrien *et al.*, Phys. Rev. C **35**, 1589 (1987).
20. V. M. Kolybasov, Preprint No. 42, Lebedev Institute of Physics, Russian Academy of Sciences (Moscow, 1997); Yad. Fiz. **62**, 998 (1999) [Phys. At. Nucl. **62**, 932 (1999)].
21. V. A. Goldshtein *et al.*, Pis'ma Zh. Éksp. Teor. Fiz. **19**, 695 (1974) [JETP Lett. **19**, 358 (1974)]; E. L. Kuplennikov *et al.*, Yad. Fiz. **25**, 1129 (1977) [Sov. J. Nucl. Phys. **25**, 599 (1977)].

Physics of Atomic Nuclei, Vol. 63, No. 3, 2000, pp. 431–439. Translated from Yadernaya Fizika, Vol. 63, No. 3, 2000, pp. 501–509.

NUCLEI
Theory

Microscopic Description of the Reactions $d + d \longrightarrow p + {}^3\mathrm{H}$ and $d + d \longrightarrow n + {}^3\mathrm{He}$ at Low Energies

A. M. Gorbatov, A. V. Germanov, D. V. Nechaev, P. V. Komarov, and P. Yu. Nikishov

Tver State University, ul. Zhelyabova 33, Tver, 170000 Russia

Received November 5, 1998; in final form, June 17, 1999

Abstract—A collective adiabatic approach is used to explore the total and differential cross sections for the reactions $d + d \longrightarrow p + {}^3\mathrm{H}$ and $d + d \longrightarrow n + {}^3\mathrm{He}$ at incident-deuteron energies of up to 6 MeV. All substantially contributing partial waves of order not higher than that of G waves are taken into account. The experimental value of the difference of the cross sections for the above mirror reactions is reproduced theoretically under the assumption that nuclear forces obey the condition of isotopic invariance. The positions and amplitudes of the maxima in the calculated total cross sections virtually coincide with those of the corresponding experimental values. It is shown that, around the maxima of the cross sections under study, dominant contributions to them come from the P wave. The sensitivity of observables to the parameters of nucleon–nucleon interaction is analyzed. © *2000 MAIK "Nauka/Interperiodica".*

1. INTRODUCTION

Inelastic collisions of two deuterons are interesting in that the experimental probability of $n + {}^3\mathrm{He}$ formation in such collisions differs considerably from the probability of $p + {}^3\mathrm{H}$ formation in analogous collisions. This leaves us on the horns of a dilemma as to whether so pronounced a difference is due to the Coulomb repulsion of protons exclusively or it results from violation of the isotopic invariance of nuclear forces. It is obvious that only by means of a precise microscopic calculation can we resolve this dilemma.

In this study, we use the dynamical equations of the collective adiabatic approach [1–3], which describe equally well problems of discrete and continuous spectra [3–7]. An algorithm developed previously for numerically solving these equations simplifies considerably the task at hand, enabling us to focus primarily on physical aspects of the problem.

Within the collective adiabatic approach, the fusion of two deuterons was analyzed in [8], where the $n + {}^3\mathrm{He}$ and $p + {}^3\mathrm{H}$ channels were combined into the unified $N + 3N$ channel, where $3N$ is treated as a system of three bound nucleons that is close either to ${}^3\mathrm{H}$ or to ${}^3\mathrm{He}$. In other words, the isospin T and its projection T_z were considered as conserved quantum numbers. In order to determine the difference of the cross sections between the above mirror processes that is due to the Coulomb interaction, we do not assume here isospin conservation.

2. CHOICE OF THE POTENTIAL

As in any microscopic calculation, we run here into an ambiguity in determining a phenomenological nucleon–nucleon potential. Moreover, no version of realistic nucleon–nucleon interaction is able to describe precisely both a two-nucleon problem and the properties of extremely light nuclei that appear to be the products of the reactions under consideration. The only way out of this situation consists in abandoning attempts at describing phase shifts for high-energy scattering in favor of a less ambitious task of constructing a potential that would reproduce the entire body of low-energy data.

Thus, it is necessary to choose a nucleon–nucleon potential that makes it possible to describe correctly the following properties of nucleon–nucleon scattering: (i) the triplet scattering length a_t; (ii) the triplet effective range r_t; (iii) the singlet scattering length a_s; (iv) the singlet effective range r_s; (v) the deuteron binding energy E_d; and (vi) the root-mean-square mass radius of the deuteron, R_d. In addition, it is required that the ${}^3\mathrm{H}$ and ${}^3\mathrm{He}$ binding energies, $E_{{}^3\mathrm{H}}$ and $E_{{}^3\mathrm{He}}$, also be reproduced.

This set of quantities can be closely approximated with the central component $\hat{V}_c$ of the nucleon–nucleon interaction alone. Moreover, we can use only the even components $\hat{V}_c^{31}$ and $\hat{V}_c^{13}$ because the contribution of the odd components $\hat{V}_c^{33}$ and $\hat{V}_c^{11}$ to the binding energies of extremely light nuclei is negligible. Following [3], we represent here the radial components $v_c^{\mu\tau}$ as

$$v_c^{\mu\tau} = A_1^{\mu\tau}\exp(-(r/a_1^{\mu\tau})^2) - A_2^{\mu\tau}\exp(-(r/a_2^{\mu\tau})^2). \quad (1)$$

The amplitudes $A_{1,2}^{\mu\tau}$ and radii $a_{1,2}^{\mu\tau}$ of the repulsive and attractive Gaussian potentials are specified as fol-

Table 1. Calculated and experimental parameters of low-energy two-nucleon scattering and of extremely light nuclei involved in the reaction under consideration

Parameters	Calculation	Measurement
Triplet scattering length a_t, fm	5.4122	5.41
Triplet effective range r_t, fm	1.7475	1.75
Singlet scattering length a_s, fm	–23.719	–23.719
Singlet effective range r_s, fm	2.76	2.76
Deuteron binding energy E_d, MeV	2.2246	2.224579
Root-mean-square radius R_d of the deuteron, fm	1.9667	1.9627
Triton binding energy $E_{^3\mathrm{H}}$, MeV	6.5502 (0) 8.491 (40)	8.4822
Root-mean-square radius $R_{^3\mathrm{H}}$ of the triton, fm	1.6546 (0) 1.814 (40)	1.5556
Binding energy $E_{^3\mathrm{He}}$ of the ^{3}He nucleus, MeV	5.7885 (0) 7.730 (40)	7.7184
Root-mean-square radius $R_{^3\mathrm{He}}$ of ^{3}He nucleus, fm	1.682 (0) 1.851 (40)	1.703

Note: The values of K_{max} are indicated in parentheses.

lows. First, we determine the amplitudes $A_{1,2}^{\mu\tau}$ by fitting parameters of the two-body problem at fixed radii $a_{1,2}^{\mu\tau}$. After that, the radii $a_{1,2}^{\mu\tau}$ are fitted to the binding energies of the ^{3}H and ^{3}He nuclei.

The binding energies of the extremely light nuclei were calculated by the method of hyperspherical functions, the fundamental harmonic and all the potential harmonics being taken into account in this calculation. Constructing the *NN*-interaction matrix in this physical basis is a crucial point in the present approach. One possible way of tackling the problem is to focus on analytic manipulations, but this would lead to a very cumbersome final result and to poorly controllable calculations. Choosing another way, we apply our experience gained in complicated computations of nuclear reactions to the case of bound states. Only the averaging of relative quantities over spin–isospin variables do we perform analytically in the proposed procedure, relying on an evaluation of remaining configuration integrals by the method of random walks on a hypersphere. A detailed account of the new approach will be given elsewhere.

Implemented on the basis of modern computing facilities, the Monte Carlo method is as good as analytic approaches, ensuring accurate numerical results at a comparatively small number N of random walks. For example, the number of $N = 50000$ is sufficient for calculating the properties of the ^{3}He nucleus, even though grand orbital values as high as $K = 40$ are operative here.

The best fit of the calculated values to experimental data (see Table 1) is achieved at the following values of the parameters in the potential (1):

$$A_1^{31} = 0.61127, \quad A_2^{31} = 3.67,$$

$$a_1^{31} = 0.95, \quad a_2^{31} = 1.5,$$

$$A_1^{13} = 10.3115, \quad A_2^{13} = 3.6463,$$

$$a_1^{13} = 0.7, \quad a_2^{13} = 1.5.$$

Here, the energies and distances are measured in so-called nuclear energy units (NUE; 1 NUE ≈ 20.738 MeV) and in fm, respectively.

Although the results for the d, ^{3}He, and ^{3}H radii were not fitted in determining the potential parameters, they agree well with the experimental values.

To describe the fusion of two deuterons, the unified pair nucleon–nucleon potential (1) will henceforth be used for the entire four-nucleon system without invoking additional free parameters, as should in fact be done in a consistent microscopic approach. In the calculations, we will also employ a realistic nucleon–nucleon interaction—specifically, its versions that provide the best description of the internal states of reaction products. This will enable us to assess the sensitivity of observables to the choice of nucleon–nucleon potential.

3. CONVENTIONAL METHOD FOR CONSTRUCTING THE MAIN CHANNEL HARMONICS

As soon as the Coulomb interaction V_{Coul} is taken into account, the protons cease to be identical to the

neutrons. Despite this, we can still employ the isospin formalism. It should only be borne in mind that V_{Coul} does not commute with squared-isospin operator T^2; therefore, the isospin is not conserved in the reactions being considered.

The simple form (1) that we chose for the interaction admits the conservation of the orbital angular momentum L and of the spin moment S separately. Therefore, all collision processes in the problem being considered are characterized by five conserved quantum numbers: L, L_z, S, S_z, and T_z (isospin projection).

All the reaction channels that are taken into consideration here are numbered in the order of increasing energy thresholds E_i for these channels:

$$\text{(i) } p + {}^3\text{H}, \quad E_1 = -8.4822 \text{ MeV},$$

$$\text{(ii) } n + {}^3\text{He}, \quad E_2 = -7.7142 \text{ MeV},$$

$$\text{(iii) } d + d, \quad E_3 = -4.4492 \text{ MeV}.$$

In the collective adiabatic approach, a specific function of the multidimensional angles $\Omega_{3A-3} \equiv \Omega_\rho$ that depends on the hyperradius ρ as a parameter is associated with each channel. This function obeys the equation

$$(\hat{Q} - I_i)U_i = 0, \tag{2}$$

where the operator $\hat{Q}$ has the form

$$\hat{Q} = \frac{1}{\rho^2}\left[-\Delta_{3A-3} + \frac{1}{4}(3A-6)(3A-4)\right] + \hat{V}. \tag{3}$$

The eigenfunctions $U_i \equiv U_i(\rho, \Omega)$ and the eigenvalues $I_i = I_i(\rho)$ are referred to, respectively, as the channel function and as the channel collective potential. These are associated with a specific ith channel by considering their asymptotic behavior on a hypersphere of large radius. As $\rho \longrightarrow \infty$, the collective potential I_i tends to the energy threshold E_i of the ith channel, while U_i is given by

$$U_i \underset{\rho \to \infty}{\sim} \hat{A}\rho_{\text{out}i}^{\mu_i} X_i^{ljJ}, \quad i = 1, 2, 3. \tag{4}$$

Here, the operator $\hat{A}$ permutes particles belonging to different fragments in accordance with the requirements of the Pauli exclusion principle, while the component X_i^{ljJ} describes the free motion of the fragments in the space of angles. The superscripts on this component represent the orbital angular momentum of relative motion, total internal angular momentum, and total angular momentum of the entire system. An analytic continuation of the expression on the right-hand side of (4) to the region of finite ρ yields the so-called cluster approximation U_i^{cl}, which was successfully used to describe the fusion reaction $d + {}^3\text{H} \longrightarrow n + \alpha$ [3]. The cluster approximation can be improved by supplementing it with a series of hyperspherical harmonics. Prior to this, however, the function U_i^{cl} is subjected to a harmonic analysis aimed at optimizing the way in which the functional space orthogonal to U_i^{cl} is to be extended in precisely solving equation (2) in the region where the fragments overlap.

In a harmonic analysis of U_i^{cl}, a key role is played by the so-called main channel harmonic U_i^{main} that appears to be an eigenfunction of the operator Δ_{3A-3} of multidimensional angles and which enters into U_i^{cl} with a maximum weight. Thus far, a particular form of U_i^{main} has been established by directly selecting the orbitals from the corresponding Slater determinant $A \times A$. Now that the range of the problems being considered has been expanded—and especially in connection with a partial-wave analysis with allowance for higher angular momenta—it is impossible to dispense with the universal technique for constructing the main harmonics.

We represent the function U_i^{cl} as a superposition of its projections onto the subspace of harmonics with a given value of K. For all channels that we know, this expansion is dominated by the $K = K_{\min}$ fundamental harmonic. If this component is normalized to unity, we obtain precisely the main harmonic U_i^{main}. A specific component is isolated by applying the projection operator $\hat{C}_K^\nu$ [9] as

$$U_{i,K}^{\text{cl}} = \hat{C}_K^\nu U_i^{\text{cl}}. \tag{5}$$

According to [10], the kernel $\hat{C}_K^\nu(\Omega_\rho, \Omega_\rho')$ of the integral operator $\hat{C}_K^\nu$ can be expressed in terms of the generating function as

$$C_K^\nu(\Omega_\rho, \Omega_\rho') \equiv \hat{D}_K^\nu \exp\left\{\frac{i\beta}{\rho^2}\sum_{i=1}^{A} \boldsymbol{\rho}_i \cdot \boldsymbol{\rho}_i'\right\}. \tag{6}$$

Here, $\hat{D}_K^\nu$ is the differential operator

$$\hat{D}_K^\nu \equiv \frac{N-1}{2\pi^{(3A-3)/2}} \times \lim_{\beta \to 0} \sum_{m=0}^{K/2} (-1)^m 2^{K-2m} \frac{\Gamma(N-1-m)}{m!\Gamma(K-2m+1)} \frac{\partial^{K-2m}}{\partial(i\beta)^{K-2m}}, \tag{7}$$

where $A = 4$, $N = K + (3A-3)/2$, $\nu = (3A-5)/2$, and $\boldsymbol{\rho}_i = \mathbf{r}_i - \mathbf{R}$ is the distance from the ith nucleon to the center of mass $\mathbf{R}$ of the entire system.

In the expanded form, relation (5) reads

$$U_{i,K}^{\text{cl}}(\rho, \Omega) = \int C_K^\nu(\Omega_\rho, \Omega_\rho') U_i^{\text{cl}}(\rho, \Omega_\rho) d\Omega_\rho. \tag{8}$$

In choosing the contour of integration in (8), we must take into account the cluster structure of $U_i^{\rm cl}$—that is, we must go over from the vectors $\boldsymbol{\rho}_i$ to cluster variables.

Let A_{a_j} be the number of particles in the a_j cluster, and let $\mathbf{R}_{a_j}$ be its center of mass. The position $\mathbf{r}_{i_{a_j}}$ of the i_{a_j} nucleon belonging to the a_j cluster is reckoned from $\mathbf{R}_{a_j}$,

$$\boldsymbol{\rho}_{i_{a_j}}^{(a_j)} = \mathbf{r}_{i_{a_j}} - \mathbf{R}_{a_j}, \tag{9}$$

and the vectors $\mathbf{R}_{a_j}$ are measured from the center of mass $\mathbf{R}$ of entire system,

$$\boldsymbol{\eta}_{a_j} = \mathbf{R}_{a_j} - \mathbf{R}. \tag{10}$$

We refer precisely to the vectors $\{\boldsymbol{\rho}_{i_{a_j}}^{(a_j)}\}$ and $\{\boldsymbol{\eta}_{a_j}\}$ as cluster variables. In terms of these variables, the exponent in the generating function in (6) can be represented in the form

$$\sum_{i=1}^{A} \boldsymbol{\rho}_i \cdot \boldsymbol{\rho}_i' = \sum_{j=1}^{q} A_{a_j} \boldsymbol{\eta}_{a_j} \cdot \boldsymbol{\eta}_{a_j}' + \sum_{j=1}^{q} \sum_{i_{a_j}}' \boldsymbol{\rho}_{i_{a_j}}^{(a_j)} \cdot \boldsymbol{\rho}_{i_{a_j}}'^{(a_j)}, \tag{11}$$

where the prime means that summation is performed only over structure fragments.

For binary channels, the first term on the right-hand side of (11) has the simple form

$$\sum_{j=1}^{2} A_{a_j} \boldsymbol{\eta}_{a_j} \cdot \boldsymbol{\eta}_{a_j}' = \frac{A_{a_1} A_{a_2}}{A} \boldsymbol{\xi} \cdot \boldsymbol{\xi}', \tag{12}$$

where ξ is the distance between the fragments. We then express the volume element in terms of the cluster variables as

$$d\Omega_\rho = \frac{1}{\rho^{3(A-q)}} \left(1 - \frac{1}{\rho^2} \sum_{j=1}^{q} \rho_{a_j}^2\right)^{(3q-5)/2} d\Omega_{\rho_{\rm out}} \times \prod_{j=1}^{q} \rho_{a_j}^{(3a_j-4)} d\rho_{a_j} d\Omega_{\rho_{a_j}}, \tag{13}$$

where $d\Omega_{\rm out}$ is the volume element of the multidimensional angles $\Omega_{\rm out}$ in the space of the centers of mass $\{\boldsymbol{\eta}_{a_j}\}$, while $\boldsymbol{\rho}_{a_j}$ is the hyperradius of the internal motion of the fragment a_j. From the general expression (13), we obtain the volume elements for the channels under consideration:

$$p + {}^3{\rm H}, \quad d\Omega_\rho = \left(1 - \frac{\rho_{^3{\rm H}}^2}{\rho^2}\right)^{1/2} \left(\frac{\rho_{^3{\rm H}}}{\rho}\right)^5 \frac{d\rho_{^3{\rm H}}}{\rho} d\Omega_{\rho_{^3{\rm H}}} d\Omega_\xi,$$

$$d + d, \quad d\Omega_\rho = \left(1 - \frac{\rho_{d_1}^2 + \rho_{d_2}^2}{\rho^2}\right)^{1/2} \left(\frac{\rho_{d_1}}{\rho}\right)^2 \frac{d\rho_{d_1}}{\rho} \times \left(\frac{\rho_{d_2}}{\rho}\right)^2 \frac{d\rho_{d_2}}{\rho} d\Omega_{\rho_{d_1}} d\Omega_{\rho_{d_2}} d\Omega_\xi.$$

According to the expansion in (11), we break down the generating function from (6) into factors and expand each factor in relevant hyperspherical harmonics as

$$\exp\left\{\frac{i\beta}{\rho^2} \frac{A_{a_1} A_{a_2}}{A} \boldsymbol{\xi} \cdot \boldsymbol{\xi}'\right\} = 4\pi \sum_{lm} i^l \sqrt{\frac{\pi A}{2\frac{\beta}{\rho^2} A_{a_1} A_{a_2} \boldsymbol{\xi} \cdot \boldsymbol{\xi}'}} \times J_{l+1/2}\left(\frac{\beta}{\rho^2} \frac{A_1 A_2}{A} \boldsymbol{\xi} \cdot \boldsymbol{\xi}'\right) Y_{lm}\left(\frac{\boldsymbol{\xi}}{\xi}\right) Y_{lm}^*\left(\frac{\boldsymbol{\xi}'}{\xi'}\right), \tag{14}$$

$$\exp\left\{\frac{i\beta}{\rho^2} \sum_{i_{s_j}} \boldsymbol{\rho}_{i_{a_j}}^{(a_j)} \cdot \boldsymbol{\rho}_{i_{a_j}}'^{(a_j)}\right\} = 2\pi^{(3A_{a_j}-3)/2} \times \sum_{K_{a_j}, \nu_{a_j}} \frac{i^{K_{a_j}}}{\left(\frac{\beta}{\rho^2} \boldsymbol{\rho}_{i_{a_j}} \cdot \boldsymbol{\rho}_{i_{a_j}}'\right)^{(3A_{a_j}-5)/2}} J_{\kappa_{i_{a_j}} + \frac{1}{2}}\left(\frac{\beta}{\rho^2} \boldsymbol{\rho}_{i_{a_j}} \cdot \boldsymbol{\rho}_{i_{a_j}}'\right) \times |U_{K_{a_j}}^{\nu_{a_j}}(\Omega_{\boldsymbol{\rho}_{a_j}})\rangle\langle U_{K_{a_j}}^{\nu_{a_j}}(\Omega_{\rho_{a_j}})|, \tag{15}$$

where $\kappa_{a_j} = K_{a_j} + (3A_{a_j} - 6)/2$, $J_s(x)$ is a Bessel function, $Y_{lm}(\mathbf{n})$ stands for spherical harmonics, and $U_{K_{a_j}}^{\nu_{a_j}}(\Omega_{\rho_{a_j}})$ is the hyperspherical harmonic for the internal motion of the fragment a_j.

The expansions in (14) and (15) and the expression on the right-hand side of (4) are further substituted into the integral in (8). We single out a polynomial in β of degree not higher than $K_{\min}$ (or $K_{\min} + 2$ in some cases that occur in constructing the superposition of $U_i^{\rm cl}$, $i = 1, 2, 3$). As a matter of fact, this polynomial is obtained from lower terms in the expansion of the Bessel function appearing in (14) and (15). The results obtained by further applying the differential operator $\hat{D}$ can be derived easily. Numerous required integrals are calculated analytically with allowance for orthonormalization in relevant spaces. As a result, we arrive at general expressions for main harmonics. For sake of brevity, we present here specific results only for the channels of our interest.

In order to implement this program, we need some preliminary information about these channels and, above all, about the values of the orbital angular momentum l that are allowed by the Pauli exclusion

principle and about $K_{\min}$ as a function of this orbital angular momentum (see Table 2).

We emphasize that all the structure fragments from Table 2 represent *S*-shell nuclei. To a high accuracy, the internal functions of these systems are reproduced by the harmonics $U^{\nu_{a_j}}_{K_{a_j}}(\Omega_{\rho_{a_j}})$ of minimum possible degree $K_{a_j} = 0$. For this reason, we restrict our consideration to this basic approximation, where the internal angular momentum j coincides with the total spin S of the system.

The eventual expressions for the main harmonics are given by

$$U_i^{\text{main}} = \hat{A}\rho_{\text{out}}^{\mu_i} Y_{ll}\left(\frac{\boldsymbol{\rho}}{\rho}\right) F_i(S), \quad \text{for } K = l, \tag{16}$$

$$U_i^{\text{main}} = \hat{A}\rho_{\text{out}}^{\mu_i}\left\{1 - \frac{(l+9/2)}{(l+3/2)}\left(\frac{\rho_{\text{out}}}{\rho}\right)\right\} Y_{ll}\left(\frac{\boldsymbol{\rho}}{\rho}\right) F_i(S), \tag{17}$$

$$\text{for } K = l+2.$$

They possess definite values of the orbital angular momentum (l) and of the spin moment (S). For the potential (1), the calculated observables are independent of the result of composition of l and S into the total angular momentum J; the expressions in (16) and (17) for U_i^{main} correspond to $J = l + S$. Because the processes under consideration are characterized by the isospin-projection value of $T_z = 0$, the quantum number of the isospin projection is indicated explicitly nowhere. The factor $F_i(S)$ in (16) and (17) is the spin–isospin component of the function U_i^{main} having the quantum numbers $S_z = S$ and $T_z = 0$. Specifically, we have

$$F_1(0) = \sqrt{\frac{1}{12\pi^3}}\left\{\left\|\begin{matrix}++\\-+\\+-\\--\end{matrix}\right\| - \left\|\begin{matrix}-+\\++\\+-\\--\end{matrix}\right\|\right\}, \tag{18}$$

$$F_1(1) = \sqrt{\frac{1}{6\pi^3}}\left\|\begin{matrix}++\\++\\+-\\--\end{matrix}\right\|. \tag{19}$$

Following [4, 7], we represent here the Slater determinant in the form of a column that involves the spin–isospin orbitals $\|\mu\tau\|$. Recall that, as usual, a horizontal line denotes the partition into clusters within which orbitals are permuted. The spin–isospin function $F_2(S)$ of the second channel is obtained from $F_1(S)$ by merely reversing the sign of the isospin τ. The functions $F_1(S)$ and $F_2(S)$ are superpositions of the $T = 0$ and $T = 1$ states with identical weights.

Table 2. Possible values of the quantum numbers in various binary channels

Channel	Total spin of the fragments, j	Orbital angular momentum of the relative motion of the fragments, l	Power of the main harmonic, K
$p + {}^3\text{H}$, $n + {}^3\text{He}$	0	Any	l
$p + {}^3\text{H}$, $n + {}^3\text{He}$	1	Any	l, for $l > 0$ 2, for $l = 0$
$d + d$	0	Even	l
$d + d$	1	Odd	l
$d + d$	2	Even	l, for $l > 0$ 2, for $l = 0$

The spin of the system consisting of two deuterons can take the values of $S = 0$, 1, and 2 (only elastic scattering is possible at $S = 2$). Therefore, the set of the factors $F_3(S)$ is somewhat wider:

$$F_3(0) = \frac{1}{8\pi\sqrt{3}}$$
$$\times\left\{\left\|\begin{matrix}++\\+-\\-+\\--\end{matrix}\right\| + \left\|\begin{matrix}-+\\--\\++\\+-\end{matrix}\right\| - \frac{1}{2}\left\|\begin{matrix}++\\--\\++\\--\end{matrix}\right\| - \frac{1}{2}\left\|\begin{matrix}+-\\-+\\+-\\-+\end{matrix}\right\| + \frac{1}{2}\left\|\begin{matrix}++\\--\\+-\\-+\end{matrix}\right\| + \frac{1}{2}\left\|\begin{matrix}+-\\-+\\++\\--\end{matrix}\right\|\right\},$$
$$F_3(1) = \frac{1}{16\pi}\left\{\left\|\begin{matrix}++\\+-\\++\\--\end{matrix}\right\| - \left\|\begin{matrix}++\\+-\\+-\\-+\end{matrix}\right\| - \left\|\begin{matrix}++\\--\\++\\+-\end{matrix}\right\| + \left\|\begin{matrix}+-\\-+\\++\\+-\end{matrix}\right\|\right\}, \tag{20}$$
$$F_3(2) = \frac{1}{8\pi}\left\|\begin{matrix}++\\+-\\++\\+-\end{matrix}\right\|.$$

It is assumed that the main harmonics U_i^{main} are always normalized to unity—that is, formulas (16) and (17) involve a normalization factor that is omitted here to avoid encumbering the presentation.

In order to evaluate the contribution of U_i^{main} to the normalization integral, we will need explicit expressions for the cluster channel functions. They are close in structure to their main harmonics, but the former also carry information about the hyperradial motion of the

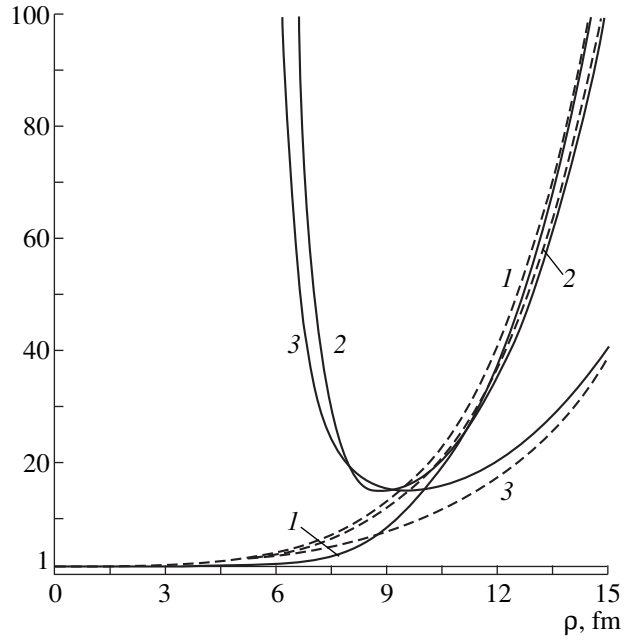

Fig. 1. Overlap integrals of superpositions (26) for $l = 0$ that are normalized by the condition $\langle U_i|U_0\rangle = 1$, where U_0 is the main harmonic of the ^{4}He nucleus. The curves are labeled with the channel numbers. The dashed curves differ from the solid curves by the substitution of $U_i^{\rm cl}$ for U_i.

fragments. For $i = 1, 2$, we have

$$U_i^{\rm cl} = \hat{A}\rho_{\rm out}^{\mu_i} Y_{ll}\left(\frac{\boldsymbol{\rho}}{\rho}\right)\rho_a^{-5/2}\varphi_0^{(a)}(\rho_a)F_i(S), \quad i = 1, 2, \tag{21}$$

where $\varphi_0^{(a)}$ is the hyperradial function of the tritium fragment ($i = 1$, $a = {}^3$H) or of ^{3}He ($i = 2$, $a = {}^3$He). Denoting by d_1 and d_2 two identical fragments of the third channel and by $\varphi(\rho_d)$ the function describing the hyperradial motion of the deuteron (the deuteron hyperradius is $\rho_d^2 = 1/2r^2$, where r is the distance between the deuteron nucleons), we obtain

$$U_3^{\rm cl} = \hat{A}\rho_{\rm out}^{\mu_3} Y_{ll}\left(\frac{\boldsymbol{\rho}}{\rho}\right)\rho_{d_1}^{-1}\varphi_0^{(d_1)}(\rho_{d_1})\rho_{d_2}^{-1}\varphi_0^{(d_2)}(\rho_{d_2})F_3(S). \tag{22}$$

Further, we assume that $U_i^{\rm cl}$ is normalized by the condition

$$\langle U_i^{\rm main}|U_i^{\rm cl}\rangle = 1. \tag{23}$$

(Hereafter, the symbol $\langle\ldots|\ldots\rangle$ denotes integration with respect to Ω_ρ and averaging over spin–isospin variables of all nucleons.) In the case of this normalization, an excess of the overlap integral $\langle U_i^{\rm main}|U_i^{\rm cl}\rangle$ over unity directly demonstrates the weight with which $U_i^{\rm main}$ enters into $U_i^{\rm cl}$.

In order to analyze these overlap integrals, which are shown by the dashed curves in Fig. 1, we indicate the critical values $\rho_{\rm cr}$ at which the collective form of motion gives way to a cluster form. We make use of the well-known representation of the hyperradius in the form

$$\rho^2 = \frac{A_{a_1}A_{a_2}}{A}\zeta^2 + \rho_{a_1}^2 + \rho_{a_2}^2. \tag{24}$$

Averaging this equality over the states $U_i^{\rm cl}$ and taking into account the relation $\overline{\rho_{a_j}^2} = A_j R_{a_j}^2$, where R_{a_j} is the root-mean-square radius of the fragment a_j, we obtain

$$\bar{\rho}_{\rm cr} = \begin{cases} \sqrt{\dfrac{15}{4}}R_{^3{\rm H}} \cong 3.02 \text{ fm}, & p + {}^3{\rm H} \quad \text{channel} \\ \sqrt{\dfrac{15}{4}}R_{^3{\rm He}} \cong 3.3 \text{ fm}, & n + {}^3{\rm He} \quad \text{channel} \\ \sqrt{8}R_d \cong 5.6 \text{ fm}, & d + d \quad \text{channel}. \end{cases} \tag{25}$$

It can be seen from Fig. 1 that, in the case of the S wave ($l = 0$), all three channels have a common main harmonic and that $U_i^{\rm cl} \sim U_i^{\rm main}$ in the region $\rho \le \rho_{\rm cr}$.

For higher partial waves ($l > 0$), we similarly have $U_i^{\rm cl} \sim U_i^{\rm main}$ in the region $\rho \le \rho_{\rm cr}$, but the difference between the main harmonics of different channels becomes ever more pronounced with increasing l.

4. VARIATIONAL SEARCH FOR CHANNEL FUNCTIONS

In [4], a solution to equation (2) was sought in the form of a superposition of $U_i^{\rm cl}$. In the more recent study [3], a series of hyperspherical harmonics was added to this superposition but the results for the calculated observables were found to be virtually unchanged. Bearing in mind this conclusion, we represent the sought channel function $U_i(\rho, \Omega_\rho)$ in the form

$$U_i(\rho, \Omega) = \sum_{j=1}^{3} C_{ij}(\rho)U_i^{\rm cl}(\rho)/\sqrt{\langle U_i^{\rm cl}|U_i^{\rm cl}\rangle}. \tag{26}$$

The coefficients $C_{ij}(\rho)$ are determined by minimizing the functional

$$\Phi = \frac{\langle U_i|\hat{Q}|U_j\rangle}{\langle U_i|U_j\rangle}. \tag{27}$$

The procedure of minimization was described in detail elsewhere [3]; for this reason, we present here only the final result for the case of the S wave ($l = 0$, $S = 0$). The resulting coefficients $C_{ij}(\rho)$ ensure orthogonality of different channels; that is, we have

$$\langle U_i|U_j\rangle = 0, \quad i \ne j. \tag{28}$$

Considering that, in the coefficients $C_{ij}(\rho)$, a constant factor remains free, we choose it in such a way that the diagonal coefficients $C_{ii}(\rho)$ are equal to unity for all ρ:

$$C_{ii}(\rho) = 1. \quad (29)$$

This means that the normalization condition $\langle U_i|U_i\rangle = 1$ is satisfied only in the asymptotic limit $\rho \longrightarrow \infty$, where $C_{ij}(\rho) = \delta_{ij}$. Owing to this, condition (29) makes it possible to evaluate quickly the interference of the cluster functions $U_i^{\rm cl}$ for finite ρ values. That the coefficients $C_{ij}(\rho)$, which are presented in Fig. 2, decrease rather slowly indicates that the cluster functions $U_i^{\rm cl}$ continue to interfere far from the region where the collective motion occurs ($\rho > \rho_{\rm cr}$).

Let us return to discussing data in Fig. 1. The solid curves represent the overlap integrals $\langle U_i|U_i\rangle/\langle U_i^{\rm main}|U_i\rangle^2$, $i = 1, 2, 3$. The behavior of these curves differs considerably from the behavior of the dashed curves. Whereas the three functions $U_i^{\rm cl}$ in the S-wave state have a common main harmonic of power $K_{\rm min} = 0$, the true channel functions (26) do not possess this property—the main harmonics of $U_i^{\rm cl}$ do not generally coincide with the main harmonics of superposition (26).

The importance of the data in Fig. 1 becomes obvious when we notice that the character of the solid curves allows us to draw some conclusions about the behavior of the total cross section prior to calculating it. Indeed, the orthogonality of the main harmonics $U_i(\rho, \Omega_\rho)$ indicates that they differ considerably in the space of multidimensional angles Ω_ρ. It is well known that the intensity of inelastic processes is determined exclusively by the overlap integrals of the partial derivatives of these functions with respect to hyperradius, $\left\langle \frac{\partial^m}{\partial\rho^m}U_i \middle| \frac{\partial^n}{\partial\rho^n}U_j \right\rangle$, where $m + n \le 2$. In the case where the main harmonics are different, these overlap integrals will obviously be small, and, accordingly, so will the integrated cross section. The analysis of the fusion reaction $d + {}^3\mathrm{H} \longrightarrow n + \alpha$ from [3] revealed that the main harmonics of the $d + {}^3\mathrm{H}$ and $n + \alpha$ channels coincide. As a result, the total cross section has a pronounced resonance with a large peak amplitude of about 5 b. On the basis of the data in Fig. 1, nothing similar should be expected in the total cross section for the fusion of two deuterons.

Figure 3 shows the collective potentials $I_i(\rho)$, strength channel features that correspond to the coefficients C_{ij} displayed in Fig. 2. Only the collective potential I_1 has the shape of a potential well, the remaining two potentials (I_2 and I_3) being monotonically decreasing functions over the entire region of the variable ρ. This behavior is fully consistent with the above harmonic analysis of $U_i(\rho, \Omega_\rho)$, reflecting the powers of the main harmonics ($K = 0$ for the first channel and $K > 0$ for the second and the third channel).

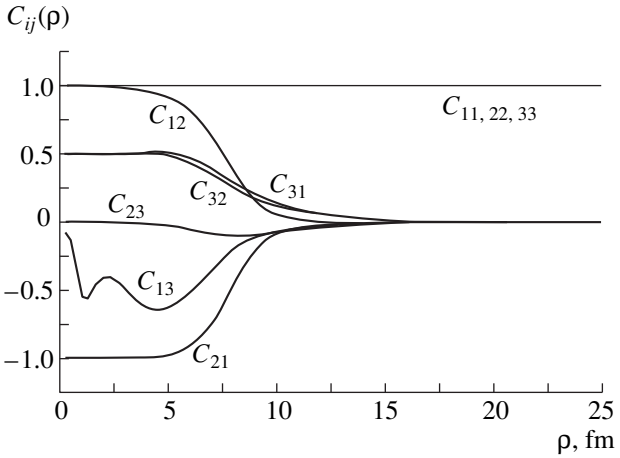

Fig. 2. Coefficients $C_{ij}(\rho)$ in the linear combination (26) for the S-wave state.

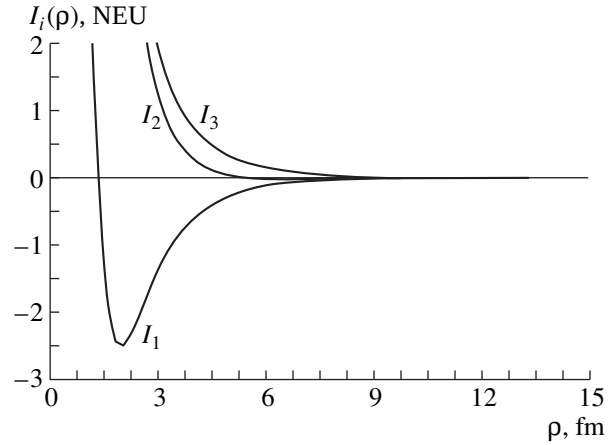

Fig. 3. Collective S-wave potentials $I_i(\rho)$ reckoned from the corresponding energy thresholds E_i.

5. FORMULAS FOR CALCULATING CROSS SECTIONS

In the collective adiabatic approach, the wave function is expanded in a series in terms of the eigenfunctions of the operator $\hat{Q}$ [see equation (3)]:

$$\Psi = \rho^{-(3A-4)/2}\sum_i \Phi_i(\rho)U_i(\rho, \Omega_\rho). \quad (30)$$

The hyperradial expansion coefficients $\Phi_i(\rho)$ satisfy the set of differential equations

$$\sum_i \left\langle U_j \middle| -\frac{\partial^2}{\partial\rho^2} + I_i(\rho) - E \middle| U_i \right\rangle \Phi_i(\rho) = 0. \quad (31)$$

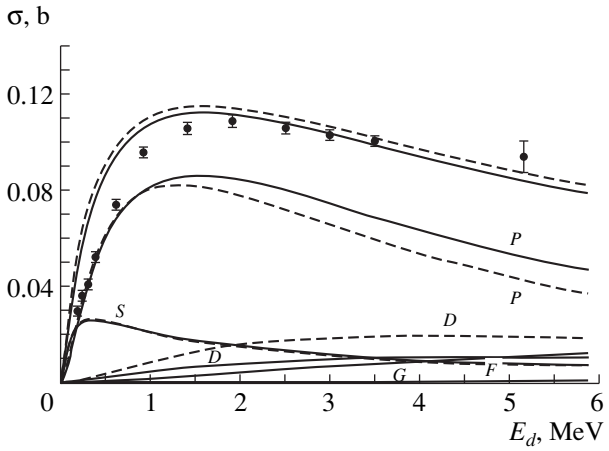

Fig. 4. Total cross section for the reaction $d + d \longrightarrow n + {}^3\mathrm{He}$ versus the incident-deuteron energy E_d (two upper curves) and the contributions of various partial waves (curves *S*, *P*, *D*, *F*, and *G*). Solid and dashed curves were calculated with the potential (1) and with the potential (42) from [3], respectively. Experimental data were borrowed from [11, 12].

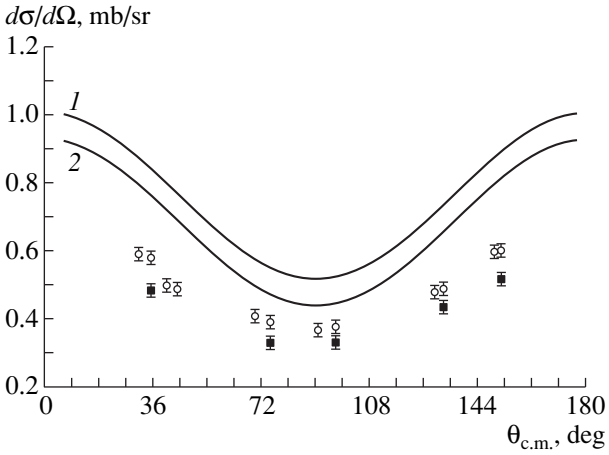

Fig. 5. Differential cross sections for the reactions (curve *1*) $d + d \longrightarrow p + {}^3\mathrm{H}$ and (curve *2*) $d + d \longrightarrow n + {}^3\mathrm{He}$ at E_d = 50 keV. Experimental data were borrowed from [13].

The real symmetric *K* matrix [4] and the corresponding unitary symmetric *S* matrix are determined by studying the asymptotic behavior of $\Phi_i(\rho)$ for $\rho \longrightarrow \infty$.

In expressing the cross sections for the relevant processes in terms of the *S* matrix, it is necessary to consider that identical particles collide in the input channel. As is well known, this leads to an additional factor of $\sqrt{2}$ in the expression for the amplitude whose parity coincides with the parity of the total spin *S* of the system of colliding deuterons. According to the numbering of the channels, the fusion processes are denoted symbolically as $3 \longrightarrow 1$ and $3 \longrightarrow 2$. The amplitudes $f^{(S)}_{i\to j}$ of these processes are related to the *S*-matrix elements $S^{(lS)}_{i\to j}$ by the equation

$$f^{(S)}_{3\to j} = \frac{1}{ik\sqrt{2}}\sum_l{}'(2l+1)e^{i(\delta_l(3)+\delta_l(j))}S^{(lS)}_{3\to j}P_l(\cos\theta), \quad (32)$$

where *k* is the wave vector of the relative motion of the two deuterons involved, $\delta_l(i)$ is the Coulomb phase shift in the *i*th channel, and $P_l(\cos\theta)$ is a Legendre polynomial. The primed sum is taken over *l* values whose parity coincides with the parity of *S*. We emphasize that $\delta_l(2) = 0$ in the case under consideration. The differential cross section for unpolarized deuterons is expressed in terms of the amplitude in (32) as

$$\frac{d\sigma_{3\to j}}{d\Omega} = \frac{3}{9}\left|f^{(1)}_{3\to j}\right|^2 + \frac{1}{9}\left|f^{(0)}_{3\to j}\right|^2. \quad (33)$$

As usual, the nuclear component of the cross section for a low-energy collision of charged particles can be conveniently represented in terms of the so-called astrophysical *S* factor defined as the ratio of the cross section to the quantity $e^{-2\pi\eta}/E$, where η is the Coulomb parameter, a quantity that specifies the energy dependence of the Coulomb cross section for low collision energies *E*. Thus, the *S* factor is given by

$$S(E) = Ee^{2\pi\eta}\sigma_{3\to j}, \quad (34)$$

where $\sigma_{3\to j}$ is the total cross section for the processes $d + d \longrightarrow p + {}^3\mathrm{H}$ and $d + d \longrightarrow n + {}^3\mathrm{He}$. In the case under consideration, this yields

$$S = 0.5E_d\exp(44.402E_d^{-1/2})\sigma_{3\to j}. \quad (35)$$

6. NUMERICAL RESULTS AND DISCUSSION

We first compare the calculated total cross section $\sigma_{3\to j}$ with experimental data in order to test the viability of the computational scheme used. There were several experiments that measured the total cross section for the reaction $d + d \longrightarrow n + {}^3\mathrm{He}$ and which produced consistent data. The results of our calculations are represented by the two upper curves in Fig. 4, which reproduce qualitatively the behavior of the experimental cross sections over a wide energy range, the calculated position and amplitude of the cross-section maximum being virtually coincident with corresponding experimental values. It is interesting to establish the hierarchy of the contributions to the total cross section from various partial waves. It can be seen that the main contribution to the cross section $\sigma_{3\to j}$ comes from the *P* wave. The reason why the *S*-wave contribution is suppressed was revealed via the above harmonic analysis (see Fig. 1). We now consider the difference of the cross sections between the reactions $d + d \longrightarrow p + {}^3\mathrm{H}$ and $d + d \longrightarrow n + {}^3\mathrm{He}$. A comparison of the calculated and measured cross sections shows their good agreement at all values of the collision energy and all values of the scattering angle. By way of illustration, Fig. 5 shows

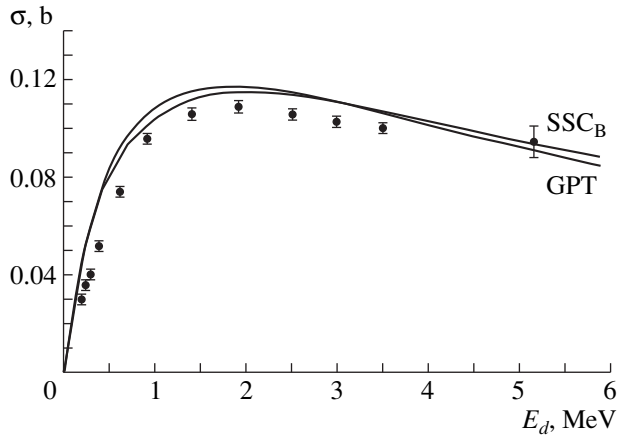

Fig. 6. As in Fig. 4, but for the realistic nucleon–nucleon potentials GPT [15] and SSC_B [16].

the differential cross sections for the two reactions under consideration at the incident deuteron energy of $E_d = 50$ keV. Thus, data on the fusion of two deuterons are compatible with the assumption of isotopic invariance of nuclear forces.

The trend of the calculated total cross section toward overestimating the experimental values at low energies is of particular interest for astrophysical processes. In the region $E_d < 60$ keV, the experimental S factor is a slowly decreasing function tending to a value of about 55 keV b for $E_d < 0$. The calculated S factor qualitatively reproduces this behavior, but its value is twice as large as that determined experimentally [14]. In order to clarify the reasons behind so pronounced a distinction, we considered a different version of nucleon–nucleon interaction, that which is given by equation (42) from [3] and which describes well experimental data on the discrete and continuous spectra of the five-nucleon system within the same collective adiabatic approach. This potential fails to reproduce data on low-energy *NN* scattering, but it describes correctly the internal states of the fragments. A calculation of the S factor with this potential changed next to nothing, but the relevant total cross section somewhat increased (Fig. 4, upper dashed curve). This indicates that the discrepancy between the calculated and experimental results at low energies is caused by the inadequacy of the cluster approximation (26), which should be improved by adding a hyperspherical series (see above). This is also confirmed by the curves in Fig. 6 that were obtained with realistic nucleon–nucleon forces. At the same time, we cannot rule out the possibility that, at low energies, experimental data require refinement.

REFERENCES

1. A. M. Gorbatov, Yad. Fiz. **55**, 44 (1992) [Sov. J. Nucl. Phys. **55**, 26 (1992)].
2. A. M. Gorbatov, Yad. Fiz. **55**, 1791 (1992) [Sov. J. Nucl. Phys. **55**, 991 (1992)].
3. A. M. Gorbatov, Yad. Fiz. **59**, 1761 (1996) [Phys. At. Nucl. **59**, 1702 (1996)].
4. A. M. Gorbatov, Yad. Fiz. **56** (8), 107 (1993) [Phys. At. Nucl. **56**, 1054 (1993)].
5. A. M. Gorbatov, Yad. Fiz. **57**, 651 (1994) [Phys. At. Nucl. **57**, 613 (1994)].
6. A. M. Gorbatov, Yad. Fiz. **57**, 1995 (1994) [Phys. At. Nucl. **57**, 1919 (1994)].
7. A. M. Gorbatov and A. Yu. Khazov, Yad. Fiz. **60**, 844 (1997) [Phys. At. Nucl. **60**, 751 (1997)].
8. A. M. Gorbatov, Yad. Fiz. **58**, 432 (1995) [Phys. At. Nucl. **58**, 381 (1995)].
9. A. M. Gorbatov, Yad. Fiz. **20**, 326 (1974) [Sov. J. Nucl. Phys. **20**, 174 (1975)].
10. A. V. Bursak, A. M. Gorbatov, Yu. N. Krylov, *et al.*, Yad. Fiz. **36**, 1138 (1982) [Sov. J. Nucl. Phys. **36**, 665 (1982)].
11. J. Fowler *et al.*, Rev. Mod. Phys. **28**, 103 (1956).
12. W. A. Wenzel and W. Whaling, Phys. Rev. **88**, 1149 (1952).
13. A. Krauss, H. W. Becker, H. P. Trautvetter, *et al.*, Nucl. Phys. **A465**, 150 (1987).
14. R. E. Brown and N. Jarmie, Phys. Rev. C **41**, 1391 (1990).
15. D. Gogny, P. Pires, and R. De Tourreil, Phys. Lett. B **32**, 591 (1970).
16. R. De Tourreil and D. W. L. Sprung, Nucl. Phys. **A201**, 193 (1973).

Translated by R. Tyapaev

Physics of Atomic Nuclei, Vol. 63, No. 3, 2000, pp. 440–444. Translated from Yadernaya Fizika, Vol. 63, No. 3, 2000, pp. 510–514.

NUCLEI
Theory

Separating the Contributions of Interaction Mechanisms in the Transverse-Momentum Distributions of Light Fragments

A. V. Burduli, I. F. Grishashvili, D. D. Djalagania, N. I. Kostanashvili, K. A. Maglakelidze, and T. A. Nikvashvili

Tbilisi State University, Universitetskaya ul. 9, Tbilisi, 380086 Republic of Georgia

Received March 11, 1998; in final form, April 14, 1999

Abstract—Transverse-momentum distributions of light spectator fragments are analyzed by representing them as superpositions of contributions from various interaction mechanisms. The temperatures and the collective transverse momenta of light projectile fragments formed in Ne + Em and Si + Em interactions at momenta of 4.1–4.5 GeV/*c* per projectile nucleon are estimated under the assumption that these spectators are compressed as the participant projectile nucleons traverse the target nucleus. This analysis reveals the important role of sound waves in the transfer of collective momenta to spectator fragments. © *2000 MAIK "Nauka/Interperiodica".*

1. INTRODUCTION

Investigation into processes occurring in participant and spectator parts of interacting nuclei and, in particular, into the interplay of such processes, which is due to a central character of interactions, is an important problem in establishing the mechanism of nucleus–nucleus interactions.

Photoemulsion experiments, which ensure a full 4π angular coverage and which make it possible to determine the charges of projectile fragments and identify particles, according to the commonly accepted classification, as *b*, *g*, and *s* particles [1] nearly without any threshold, can contribute significantly to resolving these problems. The intervals of momenta for particles classified as nonrelativistic *b* and *g* particles (with the exception of target fragments with charges $Z \geq 3$) are listed in Table 1.

In contrast to models that rely on the cascade–evaporation mechanism and which attribute fragment formation to the evaporation of the residual nucleus, hydrodynamic models [2] and microscopic dynamical models [3], which describe collective effects in nuclei, pay virtually no attention to the existence of spectator fragments in the nuclei involved. A comparison of experimental data coming from photoemulsion experiments at ultrarelativistic energies with the results of model calculations reveals that model descriptions usually oversimplify the production of nonrelativistic particles [4].

From photoemulsion data, it follows that, in collisions characterized by high multiplicities—and it is precisely these collisions that are analyzed in studying collective effects—the growth of the number of relativistic *s* particles is accompanied by the growth of the multiplicity of *b* and *g* particles [5, 6]. Here, it is necessary to consider that, according to investigations of the angular distributions within the above individual classes of particles, the coefficient of azimuthal asymmetry for *b* and *g* particles in the azimuthal plane is much greater than the corresponding coefficient for *s* particles [7].

In an alternative pattern of collective nuclear interactions that was proposed by Baumgardt *et al.* [8], the transfer of collective momenta to particles occurs owing to the compression of spectators in nucleus–nucleus collisions; it is important here that these collective momenta are carried predominantly by spectator fragments.

According to [8], the zone of a head shock is formed in the interaction of light projectile nuclei with heavy target nuclei; as this zone propagates in the target nucleus, cold nuclear matter of the spectator is pushed sideways, forming a Mach shock wave, which prompts the transfer of collective momenta to spectator fragments. This effect was studied in [8] by analyzing the angular distributions of the alpha-particle fragments of Ag and Cl target nuclei. The density of the compressed cold matter of the spectator, ρ, was estimated there at $\rho \sim 3.5\rho_N$, where ρ_N is the normal nuclear density.

In more recent experiments performed with photoemulsions, which contain light nuclei as well, the angular distributions of *b* particles proved to be more complicated [5, 9].

Table 1

Particle	Momentum, MeV/*c*	
	b particles	*g* particles
Alpha-particle fragment	0–900	>900
Proton	0–224	224–900
Pion	0–58.1	58.1–140

1063-7788/00/6303-0440$20.00

Within the above pattern, we have studied manifestations of collective momenta in the transverse-momentum distributions of light projectile fragments and connections between the fine structure of such distributions and the formation of compressed cold nuclear matter featuring components of different densities. With this aim in view, we have analyzed experimental data on the transverse-momentum distributions of protonic and alpha-particle projectile fragments formed in Ne + Em and Si + Em interactions. A detailed description of the experiments that furnished these data can be found in [7, 10].

2. TRANSVERSE-MOMENTUM DISTRIBUTIONS OF LIGHT PROJECTILE FRAGMENTS

The transverse-momentum distributions of alpha-particle projectile fragments from photoemulsion experiments are complicated by the presence of tails at high transverse momenta. Usually, such distributions are fitted to a superposition of two Rayleigh distributions (distribution of a two-component quantity whose components obey Gaussian distributions with identical variances); that is,

$$\frac{d\sigma}{dp_t} = p_t\left(\frac{1-a}{\sigma_1^2}\right. \times \exp(-p_t^2/2\sigma_1^2) + \left.\frac{a}{\sigma_2^2}\exp(-p_t^2/2\sigma_2^2)\right), \quad (1)$$

where σ_1^2 and σ_2^2 are the variances of these distributions, while a measures the weight of the second term.

In model descriptions of the transverse-momentum distributions of alpha-particle fragments, the temperatures of the sources of fast α-particle fragments are overly high for fragmentation processes both in the case of two particle sources at rest [11] and in the case of two [12] (or more [13]) systems moving at different velocities.

The existence of two partial transverse-momentum distributions of the fragments may be due to the contributions of two mechanisms of nucleus–nucleus interactions, the cascade–evaporation mechanism and the mechanism of collective interactions, which results in the transfer of collective momenta to the fragments.

In accordance with this, we consider two particle sources such that they have identical temperatures T and isotropic angular distributions in the azimuthal plane, the transverse-momentum distribution of particles within either source being of a Rayleigh form. Upon the transfer of a transverse collective momentum $\mathbf{p}_t^{\text{coll}}$ to the fragments, their transverse-momentum distribution assumes the form

$$\frac{d\sigma}{\sigma p_t} = \int_{(p_t^*)_{\min}}^{(p_t^*)_{\max}}\int_0^{\pi}\frac{d^2\sigma^*}{dp_t^* d\varphi^*}J(p_t^*, \varphi^*/p_t^*, p_t)dp_t^* d\varphi^*, \quad (2)$$

where quantities labeled with an asterisk are specified in the rest frame of the particle source, φ^* and $J(p_t^*, \varphi^*/p_t^*, p_t)$ being, respectively, the azimuthal angle and the Jacobian for the relevant transformation.

It can be shown easily that, at a fixed value of p_t^{coll}, the transverse-momentum distribution of the fragments has the form

$$\left(\frac{d\sigma}{dp_t}\right)_{p_t^{\text{coll}} = \text{const}} = \frac{p_t}{\sigma_1^2}\exp[-((p_t^{\text{coll}})^2 + (p_t)^2)/2\sigma_1^2]I_0\left(\frac{p_t^{\text{coll}}p_t}{\sigma_1^2}\right), \quad (3)$$

where $I_0\left(\frac{p_t^{\text{coll}}p_t}{\sigma_1^2}\right)$ is a Bessel function of an imaginary argument, and σ_1^2 is the variance of the transverse-momentum distribution of the fragments in the source rest frame.

If the transfer of the collective transverse momentum, p_t^{coll}, obeys a Rayleigh distribution with a variance $\sigma^2_{p_t^{\text{coll}}}$, the transverse-momentum distribution of the fragments is also of a Rayleigh form, its variance being $\sigma_2^2 = \sigma_1^2 + \sigma^2_{p_t^{\text{coll}}}$, where $\sigma_1^2 = mT$ (m is the fragment mass). In this case, the most probable value of the collective transverse momentum, $(p_t^{\text{coll}})_m$, must be equal to $\sigma_{p_t^{\text{coll}}}$.

The transverse-momentum distribution of alpha-particle fragments originating from nucleus–nucleus collisions then appears to be a superposition of two Rayleigh distributions (1) with the variances σ_1^2 and σ_2^2.

We have analyzed the transverse-momentum distributions of alpha-particle fragments from Ne + Em and Si + Em interactions and the transverse-momentum distributions of spectator protons from Ne + Em interactions. Data from [10] on the transverse-momentum distributions of spectator protons that were identified by studying multiple Coulomb scattering along the tracks of singly charged fragments within the fragmentation cone are unique.

The numbers of fragments, the values of the parameters T and p_t^{coll} (or $\sigma_{p_t^{\text{coll}}}$), and the relative contribution a of the collective-interaction mechanism were determined by fitting a superposition of two Rayleigh forms to the experimental transverse-momentum distributions of alpha-particle and protonic fragments. The results obtained in this way are listed in Table 2, along with the computed values of the collective momentum p^{coll}.

Table 2

Interaction type	Number of fragments, N	Temperature, T, MeV	Contribution of collective interactions, a	$(p_t^{\mathrm{coll}})_m$, MeV/c	Collective momentum of fragments, p^{coll}, MeV/c
Ne + Em $\longrightarrow p_f + X$	4275	7.86 ± 0.64	0.45 ± 0.06	136 ± 6.4	151.4 ± 6.9
Ne + Em $\longrightarrow \alpha_f + X$	3465	5.62 ± 0.40	0.29 ± 0.05	273 ± 29	302 ± 14
Si + Em $\longrightarrow \alpha_f + X$	1939	7.14 ± 2.9	0.27 ± 0.01	317 ± 58	302 ± 14

In Fig. 1, the transverse-momentum distributions of alpha-particle fragments from Ne + Em and Si + Em events generated according to the cascade–evaporation model are contrasted against the Rayleigh distributions at the values of the temperature T from Table 2. The agreement between the former and the latter confirms the assumption that the first Rayleigh distribution in (1) is associated with the cascade–evaporation mechanism.

In Fig. 2, the transverse-momentum distributions of (*a*) protons and (*b*) alpha-particle fragments from Ne + Em collisions and (*c*) alpha-particle fragments from Si + Em collisions are contrasted against the results of fitting in terms of two Rayleigh distributions. The dashed curves represent the contributions of the individual interaction mechanisms. According to the data in Fig. 2, the protons with transverse momenta in the range p_t = 250–500 MeV/c and the alpha-particle fragments with transverse momenta in the range p_t = 500–800 MeV/c can be produced only via the mechanism of collective interactions.

According to [14], the speed c_0 of the first sound in normal, cold nuclear matter is given by

$$c_0 = (1/3)\sqrt{K/m}, \qquad (4)$$

where K is the compressibility modulus.

In sound waves, the values of c_0 are close to the root-mean-square velocity $\langle v_T^2 \rangle^{1/2}$ of the thermal motion of fragments [15]. The values of c_0 as calculated at the compressibility modulus of K = 220 ± 20 MeV obtained from an analysis of data on giant monopole resonances [16] are given in Table 3, along with the values of $\langle v_T^2 \rangle^{1/2} = \sqrt{3T/m}$. It can be seen that these velocities are nearly identical. The proximity of collective fragment velocities to the speed of sound is also manifested in a comparison of collective fragment momenta $p^{\mathrm{coll}} = mc_0$ with the results that the fitting to data yields for the most probable values of the projections of collective fragment momenta onto the azimuthal plane, $(p_t^{\mathrm{coll}})_m$. The predicted fragment-mass dependence of collective momenta is also confirmed (see Table 1).

That the absolute values of the velocities of protonic and alpha-particle fragments are close to the corresponding speeds of the first sound in cold nuclear matter suggests that, in noncentral interactions of asymmetric nuclei—this is precisely the case that is under analysis here—there arise conditions for the formation of sound waves in the spectator part of the projectile nucleus.

Table 3

Interaction type	Thermal velocity of fragments, $\langle v_T^2 \rangle^{1/2}$	Speed of sound, c_0
Ne + Em $\longrightarrow p_f + X$	0.158 ± 0.007	0.161 ± 0.015
Si + Em $\longrightarrow \alpha_f + X$	0.067 ± 0.002	0.081 ± 0.007
Si + Em $\longrightarrow \alpha_f + X$	0.076 ± 0.004	0.081 ± 0.007

Table 4

Interaction type	N_α/N_p	
	experimental data	cascade–evaporation model
Ne + Em	0.521 ± 0.011	0.118 ± 0.007
Si + Em	0.429 ± 0.012	0.110 ± 0.002

3. SPECIAL FEATURES OF DISSOCIATION OF PROJECTILE SPECTATORS AND FORMATION OF COMPRESSED COLD MATTER IN COLLECTIVE INTERACTIONS OF NUCLEI

That spectator fragmentation cannot be described completely on the basis of the cascade–evaporation model (there must exist a mechanism that results in the copious production of alpha-particle fragments) is illustrated by the data from Table 4, where the relative numbers of the alpha-particle and protonic spectator fragments of projectile nuclei in live events are contrasted against the corresponding values in events generated according to the cascade–evaporation model.

The most probable channels of the dissociation of spectators from Ne and Si projectile nuclei [17, 18]—these channels were selected according to the criterion $n_i/\langle n \rangle \geq 1.5$, where n_i is the number of events where these spectators dissociate through the ith channel, while $\langle n \rangle$ is the number of events per dissociation channel—are presented in Table 5 versus the total charge of projectile fragments (Q).

From this table, it can be seen that events involving a heavy fragment, which are usually associated with the

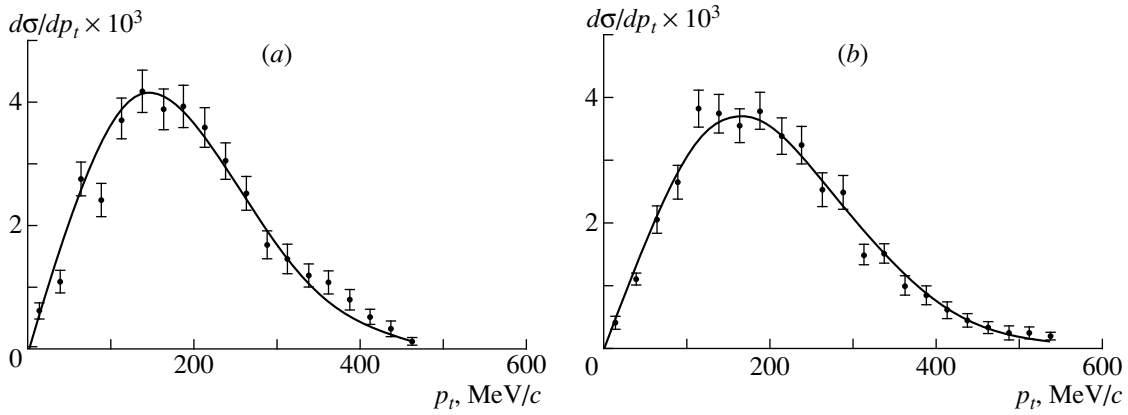

Fig. 1. Transverse-momentum distributions of alpha-particle fragments from (*a*) Ne + Em and (*b*) Si + Em interactions generated according to the cascade–evaporation model. The curves represent Rayleigh distributions at the temperature values from Table 2.

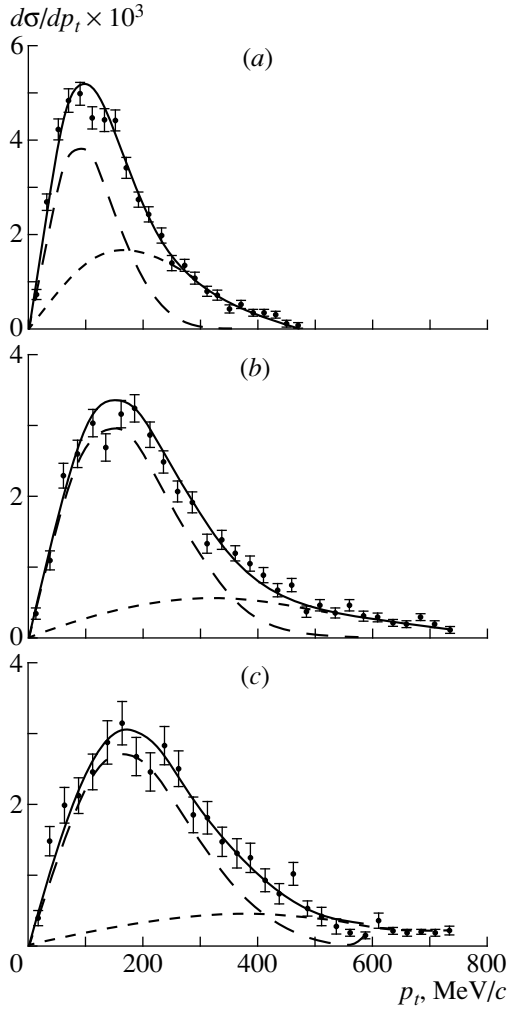

Fig. 2. Transverse-momentum distributions of spectator fragments of projectile nuclei: (*a*) distribution of protons from Ne + Em collisions, (*b*) distribution of alpha-particle fragments from Ne + Em collisions, and (*c*) distribution of alpha-particle fragments from Si + Em collisions. Dashed curves represent the contributions of the individual mechanisms (long and short dashes correspond, respectively, to the cascade–evaporation and collective-interaction mechanisms), while solid curves show their sums.

cascade–evaporation mechanism, emerge predominantly from peripheral interactions at large Q values. As the impact parameter is reduced, the number of events where only light fragments appear to be dissociation products grows. At identical values Q, an increase in the number of interacting nucleons leads to the growth of the multiplicity of light fragments owing to the dissociation of alpha-particle fragments into nucleons. This suggests that processes occurring in spectators depend on the number of interacting nucleons.

The spectators are compressed not only because of the effect of a greater number of interacting projectile nucleons but also because of the expansion of the participant part of the projectile moderated down to stopping in the target nucleus. The probability of the latter process is expected to be sizable even at ultrarelativistic energies. This is due to a large fraction of the stoppings of projectiles in heavy nuclei (according to data presented in [19], this fraction is about 8.5% in the interactions of Si nuclei with heavy targets at a projectile momentum of 200 GeV/c per projectile nucleon). Within the pattern being considered, the spectator and participant parts of nuclei are interrelated even in this process because of finite dimensions of nuclei.

That the spectator density may undergo jumplike changes is suggested by the data from [20] on the transverse-momentum distribution of alpha-particle fragments formed in Au + Em interactions at a momentum of 10.6 GeV/c per projectile nucleon. These data were found there to be adequately fitted, at high transverse momenta, to a superposition of two Rayleigh distributions with $\sigma_1 = 606 \pm 84$ MeV/c and $\sigma_2 = 1620 \pm 828$ MeV/c.

It is of crucial importance to obtain strongly compressed cold nuclear matter in order to observe, under laboratory conditions, a phase transition from hadronic matter to cold quark–gluon plasma (this phase transition is expected to occur at densities $\rho \geq 3$–$5\rho_N$).

Table 5. Most probable channels of dissociation of Ne and Si spectators

Q	Dissociation channel								
	^{28}Si + Em						^{22}Ne + Em		
14	p + Al	2p + C	p + α + B	α + C					
	3.33 ± 0.63	2.84 ± 0.59	1.98 ± 0.49	1.73 ± 0.46					
13	p + C	2p + B							
	3.58 ± 0.66	2.59 ± 0.56							
12	2p + α + O	p + α + Be	2p + Ne	p + B	3p + Be	2p + 2α + C			
	3.09 ± 0.61	2.59 ± 0.56	2.47 ± 0.55	2.22 ± 0.52	1.98 ± 0.49	1.73 ± 0.46			
11	3p + 4α	5p + 3α	p + Ne	p + p + F	2p + α + N				
	2.22 ± 0.52	2.22 ± 0.52	2.10 ± 0.50	1.98 ± 0.49	1.85 ± 0.47				
10	4p + 3α	6p + 2α					α + O	α + p + N	p + F
	3.21 ± 0.62	1.73 ± 0.46					4.21 ± 0.40	2.19 ± 0.29	2.06 ± 0.28
9	3p + 3α	5p + 2α					α + N	p + O	p + α + C
	2.72 ± 0.57	2.72 ± 0.57					2.57 ± 0.31	2.19 ± 0.29	1.93 ± 1.27
8	4p + 2α	2p + 3α	6p + α				2p + 3α	α + C	
	4.07 ± 0.70	2.59 ± 0.56	1.85 ± 0.47				1.99 ± 0.28	1.74 ± 0.26	
7	3p + 2α	5p + α	p + 3α				p + 3α	3p + 2α	
	4.57 ± 0.74	2.84 ± 0.59	1.60 ± 0.44				2.44 ± 0.31	2.44 ± 0.31	
6	4p + α	2p + 2α	6p				2p + 2α	4p + α	
	4.69 ± 0.75	2.96 ± 0.60	1.85 ± 0.47				3.28 ± 0.36	2.12 ± 0.29	
5	3p + α	5p					3p + α	p + 2α	
	3.83 ± 0.68	2.96 ± 0.60					3.38 ± 0.36	2.80 ± 0.33	
4	4p	2p + α					2p + α	2α	
	6.30 ± 0.87	5.18 ± 0.79					4.34 ± 0.41	1.61 ± 0.25	

ACKNOWLEDGMENTS

We are indebted to the physicists from JINR (Dubna) who are involved in photoemulsion experiments for many years of fruitful collaboration and for kind permission to use their data in our analysis presented in this article.

REFERENCES

1. ABGDDEKKLMTTU Collab. (A. Vokolova *et al.*), Kratk. Soobshch. OIYaI (Dubna), No. 12-85 (1085).
2. I. N. Mishustin *et al.*, Yad. Fiz. **54**, 429 (1991) [Sov. J. Nucl. Phys. **54**, 260 (1991)].
3. Q. Pan and P. Danielewicz, Phys. Rev. Lett. **70**, 2062 (1993).
4. EMU01 Collab. (M. I. Adamovich *et al.*), Phys. Lett. B **243**, 180 (1990).
5. A-ABGDDEKKMRS-PSTTU-BU Collab. (N. P. Andreeva *et al.*), Yad. Fiz. **55**, 1010 (1992) [Sov. J. Nucl. Phys. **55**, 569 (1992)].
6. EMU01 Collab. (N. P. Andreeva *et al.*), Yad. Fiz. **58**, 1024 (1995) [Phys. At. Nucl. **58**, 951 (1995)].
7. A-ABDDEKLMRST Collab. (B. U. Ameeva *et al.*), Yad. Fiz. **51**, 1047 (1990) [Sov. J. Nucl. Phys. **51**, 669 (1990)].
8. H. C. Baumgardt *et al.*, Z. Phys. A **273**, 359 (1975).
9. A-ABGDDEKKLMRTTU-B Collab. (N. P. Andreeva *et al.*), Yad. Fiz. **45**, 123 (1987) [Sov. J. Nucl. Phys. **45**, 78 (1987)].
10. A-ABGDDEZKKLMTTU-B Collab. (S. A. Krasnov *et al.*), Yad. Fiz. **47**, 949 (1988) [Sov. J. Nucl. Phys. **47**, 605 (1988)].
11. JJL Collab. (K. B. Bhalla *et al.*), Nucl. Phys. **A367**, 446 (1981).
12. JJL Collab. (Y. Prakash *et al.*), in *Contributed Papers of the Second International Conference on Nucleus–Nucleus Collisions, Visby, Sweden, 1985*, Ed. by B. Jacobsson and K. Aleklett, Vol. 1, p. 19.
13. S. Nagamiya, VII International Seminar on High Energy Physics Problems (Dubna, 1984).
14. M. I. Sobel *et al.*, Nucl. Phys. **A251**, 502 (1975).
15. R. P. Feynman, R. B. Leighton, and M. Sands, *The Feynman Lectures on Physics* (Mir, Moscow, 1965, 1966, 1978; Addison-Wesley, Reading, 1963, 1964, 1965).
16. J. Treiner *et al.*, Nucl. Phys. **A371**, 253 (1981).
17. ABGDDEKKLM Collab. (N. P. Andreeva *et al.*), Kratk. Soobshch. OIYaI (Dubna), No. R1-85-692 (1985).
18. ABDDEKL Collab. (S. A. Krasnov *et al.*), Kratk. Soobshch. OIYaI (Dubna), No. R1-88-252 (1988).
19. J. Stachel and P. Braun-Munziger, Phys. Lett. B **216**, 1 (1989)
20. KLM Collab. (B. Wilezynska *et al.*), in *Contributed Papers of the 25th Cosmic Ray Conference, Durban, South Africa, 1997*, Vol. 6, sessions He 1-C, p. 13.

Translated by A. Isaakyan

Physics of Atomic Nuclei, Vol. 63, No. 3, 2000, pp. 445–447. From Yadernaya Fizika, Vol. 63, No. 3, 2000, pp. 515–518.

ELEMENTARY PARTICLES AND FIELDS
Experiment

Study of Correlation of Production and Decay Planes in $\pi \longrightarrow 3\pi$ Diffractive Dissociation Process on Nuclei*

A. V. Efremov, Yu. I. Ivanshin, L. G. Tkatchev, and R. Ya. Zulkarneev
Joint Institute for Nuclear Research, Dubna, Moscow oblast, 141980 Russia
Received January 5, 1999

Abstract—A large correlation of production and decay planes of the $\pi^-\pi^+\pi^-$ system in dissociation of a 40-GeV/c π^- beam on nuclear targets was observed. The dependence of the correlation on atomic number, Feynman variable, and transversal momentum, as well as on invariant mass of the pion triple and neutral pion pair, was investigated. It was shown that the phenomenon has a clear dynamical origin and resembles the single-spin asymmetry behavior. © *2000 MAIK "Nauka/Interperiodica".*

1. INTRODUCTION

The measurement of polarization at high energies is a complicated problem since the observation of a spin or total angular momentum projection is a nondirect one as a rule and explore features such as angular distribution in secondary scattering or in decay process. For a strong interaction process, parity and Lorentz invariance require that at least three momenta of particles (either spinless or spin-averaged) in a final state be measured.

Some years ago, the concept of handedness was introduced[1)] as a measure of polarization of parent partons (or decaying hadrons) [1]. It was defined as an asymmetry of a process probability W with respect to a spatial component of an axial 4-vector $n_\mu \propto \epsilon_{\mu\nu\sigma\rho}k_1^\nu k_2^\sigma k^\rho$, where k^ρ is the 4-momentum of particle (or a system) in question ($k = k_1 + k_2 + k_3 + \ldots$), with respect to some direction $\mathbf{i}$ ($n_i = \mathbf{n}\cdot\mathbf{i}$)

$$H_i = \frac{W(n_i>0) - W(n_i<0)}{W(n_i>0) + W(n_i<0)} = \alpha_i P_i, \qquad (1)$$

which was shown to be proportional to polarization P_i of the system (at least for spin 1/2 and spin 1), provided the analyzing power α is not zero. The direction $\mathbf{i}$ could be chosen as longitudinal (L) with respect to the momentum $\mathbf{k}$ or as transversal ones ($T1$ or $T2$).

In the previous publication [5], the attention was drawn to the fact that in diffractive production of pion triples [6]

$$\pi^- + A \longrightarrow (\pi^-\pi^+\pi^-) + A \qquad (2)$$

by a 40-GeV/c π^- beam from a nucleus A, a noticeable asymmetry with respect to the triple production plane (transversal handedness H_{T1}) was observed. This paper is devoted to further experimental investigation of this phenomenon. It includes new information on the dependence of the transversal handedness on the variables:

(i) atomic number of the target;

(ii) transversal momenta of the pion triple;

(iii) Feynman variable x_F of the leading π^-;

(iv) invariant mass of the triple;

(v) invariant mass of neutral pairs $\pi^+\pi^-$.

Also the statistics were considerably increased.

2. DEFINITIONS AND NOTATION

For reaction (2), let us define the normal to the plane of production of a secondary pion triple $(\pi_f^-\pi^+\pi_s^-)$

$$\mathbf{N} = \mathbf{v}_{3\pi}\times\mathbf{v}_b, \qquad (3)$$

where $\mathbf{v}_b = \mathbf{k}_b/\epsilon_b$ and $\mathbf{v}_{3\pi} = \mathbf{k}_{3\pi}/\epsilon_{3\pi}$ are velocities of the initial π^- beam and the center of mass of the triple in laboratory frame, and indices f and s label fast and slow π^-'s. The normal to the "decay plane" of the triple in its center of mass is defined as

$$\mathbf{n} = (\mathbf{v}_f^- - \mathbf{v}^+)\times(\mathbf{v}_s^- - \mathbf{v}^+), \qquad (4)$$

where $\mathbf{v}_{f(s)}^-$ or $\mathbf{v}^+$ are velocities of the fast (slow) π^- or π^+.

The transversal handedness according to (1) is[2)]

$$H_{T1} = \frac{W(\mathbf{N}\cdot\mathbf{n}>0) - W(\mathbf{N}\cdot\mathbf{n}<0)}{W(\mathbf{N}\cdot\mathbf{n}>0) + W(\mathbf{N}\cdot\mathbf{n}<0)}. \qquad (5)$$

Two other components of the handedness connected with $\mathbf{n}\cdot\mathbf{v}_{3\pi}$ and $\mathbf{n}\cdot(\mathbf{v}_{3\pi}\times\mathbf{N})$ are forbidden by the parity conservation in the strong interaction.

* This article was submitted by the authors in English.

1) In fact, an idea similar to the handedness was earlier proposed in works [2]. Its application to certain heavy quark decay was studied in [3]. A similar technique was also studied in [4].

2) It is easy to show that this quantity is in fact Lorentz invariant.

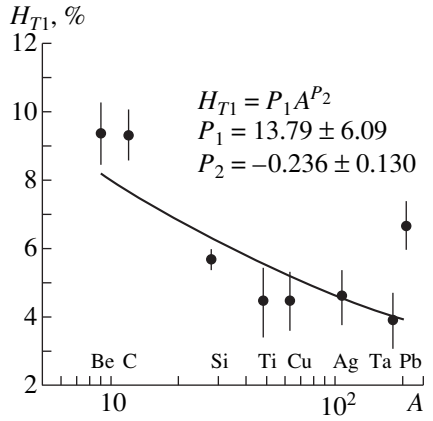

Fig. 1. The A dependence of the handedness.

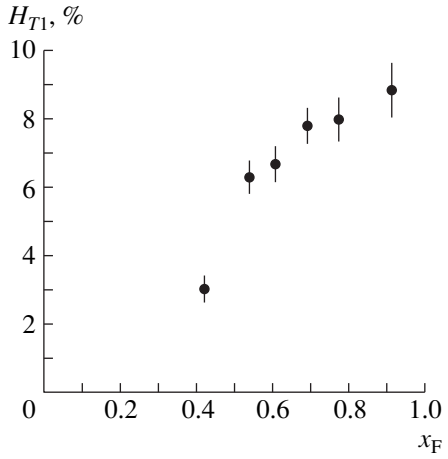

Fig. 2. The handedness dependence on x_F of the leading π^-.

3. EXPERIMENTAL RESULTS AND DISCUSSION

In this work the experimental material of the Bologna–Dubna–Milan collaboration for diffraction production of 40 GeV/c π^- into three pions was used. The details of the experiment were presented in the works [6]. Notice here that the admixture of nondiffractive events in the used set of experimental data was less than 1%.

The transversal handedness (5) was measured for a wide sample of nuclear targets: ^{9}Be, ^{12}C, ^{28}Si, ^{48}Ti, ^{63}Cu, ^{107}Ag, ^{181}Ta, and ^{207}Pb. The total number of selected events of pion triples with leading π^- was about 250000.

The dependence of H_{T1} on the atomic number A is presented in Fig. 1. One can see that the handedness systematically decreases with increasing A, which resembles a depolarization effect due to multiple scattering. That the effect magnitude decreases approximately in inverse proportion to the radius of the nucleus is an argument in support of this.

The value of the asymmetry (5) averaged over all nuclei is

$$H_{T1} = (5.96 \pm 0.21)\%. \quad (6)$$

Statistically, this is highly reliable verification of the existence of correlation of the triple production and decay planes in process (2).

The values of two other asymmetries with respect to correlations $\mathbf{n} \cdot \mathbf{v}_{3\pi}$ and $\mathbf{n} \cdot (\mathbf{v}_{3\pi} \times \mathbf{N})$ were found to be comparable to zero from the same statistical material: $H_L = (0.25 \pm 0.21)\%$ and $H_{T2} = (0.43 \pm 0.21)\%$, respectively. This is by no means surprising since they are forbidden by the parity conservation in process (2). Also, they show the order of magnitude of systematic errors.

A natural question is to what extent the effect observed is due to the kinematics or apparatus influence, in particular, due to acceptance of the experimental setup where the events have been registered. For this aim, the Monte Carlo events of reaction (2) were generated with a constant mass spectrum of the 3π system in the interval 0.6–2.5 GeV/c^2 and zero outside and with the exponential decrease of the cross section in $t' = t - t_{\min}$ with the slope (for beryllium) 40 (GeV/c)$^{-2}$ found experimentally. These events were traced through the apparatus simulation with the same trigger conditions as in [6] and the same selection of events and show no transversal handedness H_{T1},

$$H_{T1}^{\mathrm{MC}} = (0.20 \pm 0.28)\%. \quad (7)$$

For two other asymmetries, forbidden by the parity conservation, the result was $(0.00 \pm 0.28)\%$ and $(-0.14 \pm 0.28)\%$, respectively. Thus, the effect (6) cannot be explained by the kinematics or apparatus influence.

To understand the nature of the effect observed, the dependence of the handedness (5) on the Feynman variable $x_F = k_f/k_b$ of the leading π^-, on the invariant mass of the triple $m_{3\pi}$ and its neutral subsystem $m_{\pi^+\pi^-}$, and on the triple transversal momentum k_T was studied. From Fig. 2, one can see that the handedness (5) increases with x_F, which resembles the behavior of the single-spin asymmetry (e.g., the pion asymmetry or the Λ polarization [7]).

The dependence of H_{T1} on the triple invariant mass (Fig. 3*a*) is especially interesting. It clearly indicates two different sources of H_{T1} with comparable contributions: a resonance and nonresonance one. The resonance contribution is clearly seen at the mass of $a_1(1260)$ and $\pi_2(1670)$ region and by all means is due to a nonzero polarization of the resonances. The nonresonance background could also be polarized, provided that the 3π system is predominantly in a state with the total angular momentum $J \neq 0$, e.g., if a neutral pair $m_{\pi^+\pi^-}$ was predominantly produced from ρ decay. Some indication of this can be seen from Fig. 3*b*. In this context, the growth of H_{T1} in the region of small $m_{3\pi}$, i.e., in the region of small relative momenta of pions, looks quite intriguing.

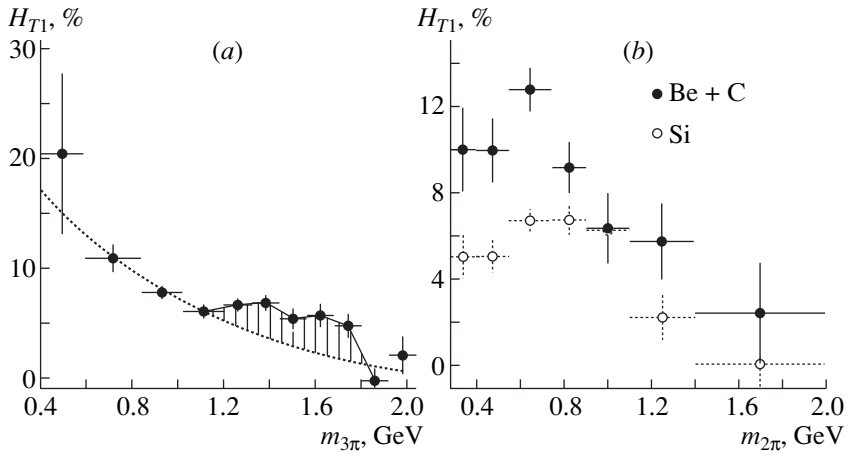

Fig. 3. The handedness dependence on (*a*) $m_{3\pi}$ and (*b*) $m_{\pi^+\pi^-}$.

A complicated picture of the k_T dependence with a sharp dip at k_T = 0.05–0.07 GeV/*c* (Fig. 4) reflects by all means the fact of interference of the resonance and nonresonance processes in the triple production. With further increase of k_T, the handedness increases, which resembles the single-spin asymmetry behavior too.

To check this assumption, the events with invariant mass $m_{3\pi}$ in the a_1 and π_2 resonance region 1.05–1.80 GeV were excluded from further analysis. This, however, does not lead us to a definite conclusion since, for Be and C, the dip disappears, but it is conserved for Si with some change of its form and width. The average value of the handedness stays at the same level 5–11% with high statistical significance.

Notice also that, in earlier study of reaction (2) at 4.5 GeV for the proton target at the hydrogen bubble chamber, no angular dependence of the normal **n** (4) was found, just as in the Regge pole exchange model, which provides a reasonable description of that experiment [8].

In conclusion, a rather large handedness transversal to the production plane was definitely observed in the diffractive production of $(\pi^-\pi^+\pi^-)$ triples in the π^--beam dissociation region. The phenomenon has a clear dynamical origin and in some features resembles the single-spin asymmetry behavior. For a more detailed study, a partial wave analysis of reaction (2) seems necessary for determination of different spin states contributing to the investigated effect.

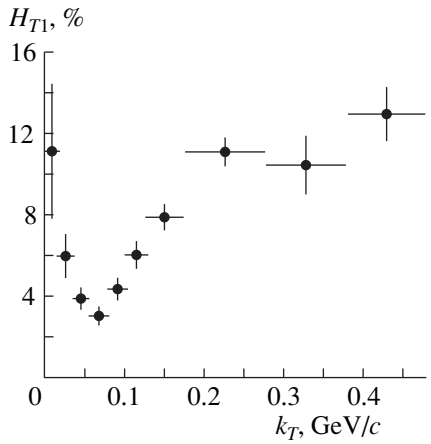

Fig. 4. The k_T dependence of the handedness for a ^{28}Si target.

ACKNOWLEDGMENTS

The authors sincerely thank the participants of the Bologna–Dubna–Milan collaboration, whose data were used in the present work.

This work was supported by the Russian Foundation for Basic Research (project nos. 98-02-16508 and 96-02-17631).

REFERENCES

1. A. Efremov, L. Mankiewicz, and N. Törnqvist, Phys. Lett. B **284**, 394 (1992).
2. O. Nachtmann, Nucl. Phys. B **127**, 314 (1997); A. V. Efremov, Yad. Fiz. **28**, 166 (1978) [Sov. J. Nucl. Phys. **28**, 83 (1978)].
3. R. H. Dalitz, G. Goldstein, and R. Marshall, Z. Phys. C **42**, 441 (1989).
4. J. C. Collins, Nucl. Phys. B **396**, 161 (1993); J. C. Collins *et al.*, Nucl. Phys. B **420**, 565 (1994); X. Artru and J. C. Collins, Z. Phys. C **69**, 277 (1996).
5. A. V. Efremov, Yu. I. Ivanshin, L. G. Tkatchev, *et al.*, JINR Rapid Commun., No. 3 (83), 5 (1997).
6. G. Bellini *et al.*, Nucl. Phys. B **199**, 1 (1982); Phys. Rev. Lett. **48**, 1697 (1982); Lett. Nuovo Cimento **38**, 433 (1983); Nuovo Cimento **A79**, 282 (1984).
7. A. Bravar, in *Proceedings of 13th International Symposium on High Energy Spin Physics, Protvino, 1998* (World Sci., 1999), p. 167.
8. G. V. Beketov *et al.*, Yad. Fiz. **19**, 424 (1974) [Sov. J. Nucl. Phys. **19**, 210 (1974)]; **20**, 709 (1974) [**20**, 379 (1975)].

Physics of Atomic Nuclei, Vol. 63, No. 3, 2000, pp. 448–454. Translated from Yadernaya Fizika, Vol. 63, No. 3, 2000, pp. 519–526.

ELEMENTARY PARTICLES AND FIELDS
Theory

Protonium Formation in Collisions of Antiprotons with Hydrogen Atoms

G. V. Avakov†, L. D. Blokhintsev, and E. N. Voronina

Institute of Nuclear Physics, Moscow State University, Vorob'evy gory, Moscow, 119899 Russia

Received November 4, 1998; in final form, May 11, 1999

Abstract—The formation of an antiprotonic hydrogen atom $\{p\bar{p}\}$ (protonium) in the ground state and in excited states (nlm) in collisions of 1- to 250-keV antiprotons with hydrogen atoms is considered theoretically. Partial cross sections (both differential and integrated ones) for this reaction are calculated for various values of n, l, and m up to $n \sim 100$; cross sections summed over l and m are also obtained. Statistical (polarization) tensors of the orbital angular momentum of protonium atoms are evaluated. Corrections due to strong proton–antiproton interaction in the protonium ground ($1s$) state are analyzed. © *2000 MAIK "Nauka/Interperiodica".*

1. INTRODUCTION

Investigation of antiprotonic atoms is a vigorously developing branch of modern physics (for an overview, see [1]). The majority of studies dealt with the states formed as the result of the capture of stopped antiprotons into highly excited atomic orbits that was followed by cascade transitions. In this process, the antiprotons could miss low-lying states of antiprotonic atoms—especially in medium-mass and heavy atoms—because of their absorption by nuclei from higher orbits. Consequently, it seems interesting to study the formation of antiprotonic atoms by antiprotons in flight.

Here, we consider theoretically the formation of the simplest antiprotonic atom, protonium $\{p\bar{p}\}$, in the interaction of an antiproton $\bar{p}$ with a ground-state hydrogen atom,

$$\bar{p} + \mathrm{H}(1s) \longrightarrow \{p\bar{p}\}_{nlm} + e, \qquad (1)$$

n, l, and m being protonium quantum numbers. We perform our calculations within the first Born approximation in Coulomb interaction. This approximation is quite accurate for incident-antiproton energies in the range E = 1–250 keV (in laboratory frame) considered here. For various values of n, l, and m up to $n \sim 100$, we calculate partial cross sections for reaction (1), both differential and integrated ones; we also determine the cross section summed over l and m. In addition, we derive the statistical tensors of the protonium orbital angular momentum. We also analyze corrections due to strong interaction in the protonium ground ($1s$) state.

For n = 1 and E = 50–250 keV, reaction (1) was considered by Roy and Deb [2], who disregarded strong-interaction effects. Their study is not free, however, from miscalculations, which those authors tried to correct in [3]. It should be noted that there are inaccuracies in [3] as well: the absolute values presented there for the differential and integrated cross sections do not comply with each other (possibly, this is because there were inconsistencies in units in which these cross sections were given).

At lower energies, the formation of mesic and antiprotonic atoms was considered in a series of studies of Korenman *et al.* (see [4] and references therein), who calculated the integrated partial cross sections for exotic-atom formation that were summed over m.

2. BASIC EQUATIONS

2.1. Born Approximation

In the first Born approximation, the amplitude of reaction (1) has the form

$$T(\mathbf{k}_f, \mathbf{k}_i) = \langle \mathbf{k}_f, \varphi_{12} | V_{23} + V_{31} | \mathbf{k}_i, \varphi_{23} \rangle = T^{(1)} + T^{(2)}, \qquad (2)$$

where the subscripts 1, 2, and 3 are associated with the particles $\bar{p}$, p, and e, respectively; $\mathbf{k}_i$ and $\mathbf{k}_f$ stand for, respectively, the proton and protonium 3-momenta in the c.m. frame; φ_{23} and φ_{12} are the hydrogen and protonium wave functions; V_{23} and V_{31} are the corresponding Coulomb interaction potentials; and $T^{(1)}$ and $T^{(2)}$ are determined by the interactions V_{23} and V_{31}, respectively.

The amplitude $T^{(1)}$ has the simple form

$$T^{(1)}(\mathbf{k}_f, \mathbf{k}_i) = -\frac{q_2^2 + \kappa_{23}^2}{2\mu_{23}} \tilde{\varphi}_{12}^*(\mathbf{q}_1)\tilde{\varphi}_{23}(\mathbf{q}_2), \qquad (3)$$

where $\tilde{\varphi}_{12}$ and $\tilde{\varphi}_{23}$ are, respectively, the protonium and hydrogen-atom wave functions in the momentum representation; $\mu_{ij} = m_i m_j/(m_i + m_j)$; $\kappa_{ij} = Z_i Z_j e^2 \mu_{ij}/n$; m_i ($Z_i e$) is the mass (charge) of the particle i; and n is the prin-

† Deceased.

cipal quantum number. The relative momenta on the right-hand side of (3) are[1)]

$$\mathbf{q}_1 = \mathbf{k}_i - \frac{1}{2}\mathbf{k}_f, \quad \mathbf{q}_2 = \lambda\mathbf{k}_i - \mathbf{k}_f, \qquad \lambda = \frac{m_3}{m_2 + m_3} \ll 1. \tag{4}$$

For the purely Coulomb interaction, the momentum-representation wave function of the two-particle i–j bound state characterized by the quantum numbers n, l, and m has the form [5]

$$\tilde{\varphi}_{ij}(\mathbf{q}) = \tilde{R}_{nl}(q)Y_{lm}(\hat{q}),$$
$$\tilde{R}_{nl}(q) = \tilde{N}_{nl}\frac{q^l}{(q^2+\kappa_{ij}^2)^{l+2}}C_{n-l+1}^{l+1}\left(\frac{q^2-\kappa_{ij}^2}{q^2+\kappa_{ij}^2}\right), \tag{5}$$
$$\tilde{N}_{nl} = (2\pi)^{3/2}\left[\frac{2^{2l+5}n(n-l-1)!}{\pi(n+l)!}\right]^{1/2} l!\,\kappa_{ij}^{(2l+5)/2},$$

where $C_{n-l+1}^{l+1}(x)$ are Gegenbauer polynomials. In this study, we assume that the hydrogen target is in the ground state.

The amplitude $T^{(2)}$ is given by

$$T^{(2)}(\mathbf{k}_f, \mathbf{k}_i) = 4\pi\int\frac{d^3p}{(2\pi)^3}\tilde{\varphi}_{12}^*(\mathbf{q}_{12})\frac{1}{q_{31}^2}\tilde{\varphi}_{23}(\mathbf{p}), \tag{6}$$
$$\mathbf{q}_{12} = \mathbf{q}_1 - \mathbf{q}_2 + \mathbf{p}, \quad \mathbf{q}_{31} = \mathbf{q}_2 - \mathbf{p}.$$

Employing the explicit form of the Gegenbauer polynomials [6], we express (6) as

$$T^{(2)}(\mathbf{k}_f, \mathbf{k}_i) = 32\pi^{3/2}\kappa_{23}^{5/2}\tilde{N}_{nl}\frac{(n+l)!}{(n-l-1)!(2l+1)!} \times \sum_{k=0}^{n-l-1} a_k(n,l)\int\frac{d^3p}{(2\pi)^3}\frac{q_{12}^l}{(q_{12}^2+\kappa_{12}^2)^L} \times \frac{1}{q_{31}^2}\frac{1}{(p^2+\kappa_{23}^2)^2}Y_{lm}^*(\hat{q}_{12}), \tag{7}$$

where n, l, and m are the protonium quantum numbers; $L = l + k + 2$; and the coefficients $a_k(n, l)$ are determined by the recursion relations

$$a_0 = 1, \quad a_k = -a_{k-1}\kappa_{12}^2\frac{(n+l+k)(n-l-k)}{k(l+k+1/2)}. \tag{8}$$

By applying the Feynman integral representation

$$\frac{1}{A^{N_1}B^{N_2}C} = \frac{(N_1+N_2)!}{(N_1-1)!(N_2-1)!} \times \int_0^1 d\alpha_1\alpha_1^{N_1-1}(1-\alpha_1)^{N_2-1}\int_0^1 d\alpha_2\alpha_2^{N_1+N_2-1}\frac{1}{D^{N_1+N_2+1}}, \tag{9}$$
$$D = \alpha_1\alpha_2 A + (1-\alpha_1)\alpha_2 B + (1-\alpha_2)C,$$
$$A = q_{12}^2 + \kappa_{12}^2, \quad B = p^2 + \kappa_{23}^2, \quad C = q_{31}^2,$$

to the integrand on the right-hand side of (7), we can recast the integral in (7) with respect to $\mathbf{p}$ into the form

$$I_p = L(L+1)(L+2)\int_0^1 d\alpha_1\alpha_1^{L-1}(1-\alpha_1) \times \int_0^1 d\alpha_2\alpha_2^{L+1}\int\frac{d^3k}{(2\pi)^3}\frac{1}{(\kappa^2+d)^{L+3}}q_{12}^2Y_{lm}^*(\hat{q}_{12}), \tag{10}$$

where

$$d = a - b^2,$$
$$a = \alpha_1\alpha_2(q^2+\kappa_{12}^2) + (1-\alpha_1)\alpha_2\kappa_{23}^2 + (1-\alpha_2)q_2^2, \tag{11}$$
$$\mathbf{b} = \alpha_1\alpha_2\mathbf{q} - (1-\alpha_2)\mathbf{q}_2, \quad \mathbf{q} = \mathbf{q}_1 - \mathbf{q}_2,$$
$$\mathbf{k} = \mathbf{p} + \mathbf{b}.$$

Employing the well-known transformation

$$q_{12}^l Y_{lm}^*(\hat{q}_{12}) = \sqrt{4\pi}\sum_{l_1+l_2=l,\,m_1,m_2} Q^{l_1}k^{l_2}\left[\frac{(2l+1)!}{(2l_1+1)!(2l_2+1)!}\right]^{1/2} \times (l_1m_1l_2m_2|lm)Y_{l_1m_1}^*(\hat{Q})Y_{l_2m_2}^*(\hat{k}), \tag{12}$$
$$\mathbf{q}_{12} = \mathbf{Q} + \mathbf{k},$$
$$\mathbf{Q} = \mathbf{q} - \mathbf{b} = (1-\alpha_1\alpha_2)\mathbf{q}_1 - \alpha_2(1-\alpha_1)\mathbf{q}_2,$$

where $(a\alpha b\beta|c\gamma)$ stands for Clebsch–Gordan coefficients, we can perform integration in (10) first with respect to $\mathbf{k}$ and then with respect to α_2. As a result, we obtain

$$I_p = \frac{1}{4\pi}\frac{\Gamma(L+3/2)}{(L-1)!} \times \sum_{l_1+l_2=l}(-1)^{l_2}q_1^{l_1}q_2^{l_2}\left[\frac{(2l+1)!}{(2l_1+1)!(2l_2+1)!}\right]^{1/2} \times\left\{\sum_{m_1m_2}(l_1m_1l_2m_2|lm)Y_{l_1m_1}^*(\hat{q}_1)Y_{l_2m_2}^*(\hat{q}_2)\right\} \times\int_0^1 d\alpha_1\alpha_1^{L-1}(1-\alpha_1)^{l_2+1} \times\frac{1}{U^{L+3/2}(1+W/U)^{l_1+k+3}(2l_2+1)} \tag{13}$$

[1)]Below, we employ the atomic system of units in which $\hbar = e = m_e\ (\equiv m_3) = 1$.

$$\times F_1\Big(l_2+1/2,-l_1,-k-2,l_2+3/2;$$

$$\alpha_1-(1-\alpha_1)\frac{W}{U},-\frac{W}{U}\Big),$$

$$U = \alpha_1(1-\alpha_1)q^2+\alpha_1\kappa_{12}^2+(1-\alpha_1)\kappa_{23}^2,$$

$$W = (\alpha_1\mathbf{q}+\mathbf{q}_2)^2,$$

where $F_1(a, b, b', c; x, y)$ is a hypergeometric function of two variables [6]; in the case being considered, it takes the form of a finite sum.

Eventually, the amplitude $T^{(2)}$ is expressed in terms of a one-dimensional integral with respect to the variable α_1. If the quantization axis is aligned with the 3-momentum vector $\mathbf{k}_i$, the absolute value of the amplitude T is independent of the azimuthal angle of the 3-momentum vector $\mathbf{k}_f$.

2.2. Multipole Expansion

In order to optimize an approximate calculation of the cross sections, we will recast the amplitude T into a different form. For this, we represent the right-hand side of (2) as the integral

$$T(\mathbf{k}_f,\mathbf{k}_i) = \int d^3r_{12}d^3r_{23}e^{i\mathbf{k}_f\cdot\boldsymbol{\rho}_3}\varphi_{12}^*(\mathbf{r}_{12}) \times\left(\frac{1}{r_{31}}-\frac{1}{r_{23}}\right)\varphi_{23}(\mathbf{r}_{23})e^{i\mathbf{k}_i\cdot\boldsymbol{\rho}_1}, \quad (14)$$

where $\mathbf{r}_{ij}=\mathbf{r}_i-\mathbf{r}_j$ is the relative coordinate of the particles i and j, while $\boldsymbol{\rho}_i$ is the coordinate of the particle i with respect to the center of mass of the particles j and k ($\boldsymbol{\rho}_1=\mathbf{r}_{12}+\lambda\mathbf{r}_{23}$ and $\boldsymbol{\rho}_3=-\frac{1}{2}\mathbf{r}_{12}-\mathbf{r}_{23}$). Considering that the protonium size, which specifies, through the function $\varphi_{12}^*(\mathbf{r}_{12})$, the effective range of the variable in the integral in (14), is much less than that of the hydrogen atom, which is described by the function $\varphi(\mathbf{r}_{23})$, and employing the constraint $\mathbf{r}_{31}=-(\mathbf{r}_{12}+\mathbf{r}_{23})$, we can represent the sum of the potentials in (14) as a multipole expansion in powers of the small ratio r_{12}/r_{23}. Specifically, we have

$$\frac{1}{r_{31}}-\frac{1}{r_{23}} = \frac{1}{r_{23}}\sum_{L=1}^{\infty}(-1)^L\left(\frac{r_{12}}{r_{23}}\right)^L P_L(\hat{r}_{12}\cdot\hat{r}_{23}), \quad (15)$$

where P_L stands for Legendre polynomials. The first term on the right-hand side of (15) ($L = 1$) corresponds to the dipole approximation.

In specific calculations, the infinite sum in (15) is replaced by a finite one, with an upper limit $L_{\max}$ being determined by the desired accuracy of cross-section estimations. Substituting (15) into (14), we can approximate T by T^a as

$$T\approx T^a = 4\pi\sum_{L=1}^{L_{\max}}(-1)^L\frac{1}{2L+1}\sum_{M=-L}^{L}T_{LM}^{(12)}(\mathbf{q}_1)T_{LM}^{(23)}(\mathbf{q}_2), \quad (16)$$

where

$$T_{LM}^{(12)}(\mathbf{q}_1) = \int d^3r_{12}e^{i\mathbf{q}_1\cdot\mathbf{r}_{12}}\varphi_{12}^*(\mathbf{r}_{12})r_{12}^L Y_{LM}(\hat{r}_{12}), \quad (17)$$

$$T_{LM}^{(23)}(\mathbf{q}_2) = \int d^3r_{23}e^{i\mathbf{q}_2\cdot\mathbf{r}_{23}}\varphi_{23}(\mathbf{r}_{23})r_{12}^{-L-1}Y_{LM}^*(\hat{r}_{23}). \quad (18)$$

In the coordinate representation, the Coulomb wave functions of the i–j bound state with quantum numbers n, l, and m are given by [5]

$$\varphi_{ij}(\mathbf{r}_{ij}) = i^l R_{nl}(r_{ij})Y_{lm}(\hat{r}_{ij}),$$

$$R_{nl}(r_{ij}) = N_{nl}(2\kappa_{ij}r_{ij})^l e^{-\kappa_{ij}r_{ij}} \times\Phi(-n+l+1,2l+2;2\kappa_{ij}r_{ij}), \quad (19)$$

$$N_{nl} = \frac{1}{(2l+1)!}\left[\frac{(n+l)!}{2n(n-l-1)!}\right]^{1/2}(2\kappa_{ij})^{3/2},$$

where $\Phi(a, c; x)$ is a confluent hypergeometric function; in the case being considered, it represents a finite sum. Suppose that the hydrogen target is in the ground state, which is described by the wave function

$$\varphi_{23}(\mathbf{r}_{23}) = \frac{\mu_{23}^{3/2}}{\sqrt{\pi}}e^{-\mu_{23}r_{23}}. \quad (20)$$

From (18), we then obtain

$$T_{LM}^{(23)}(\mathbf{q}_2) = 4\pi i^L\mu_{23}^{3/2}\frac{q_2^{L-2}}{2^L}\left(1+\frac{\mu_{23}^2}{q_2^2}\right)^{L-1} \times\left[\frac{1}{\Gamma(L+1/2)}F\left(L,-\frac{1}{2};\frac{1}{2};-\frac{\mu_{23}^2}{q_2^2}\right)-\frac{\sqrt{\pi}}{(L-1)!}\frac{\mu_{23}}{q_2}\right] \times Y_{LM}^*(\hat{q}_2). \quad (21)$$

Since $\mu_{23}^2/q_2^2 \ll 1$, the hypergeometric series on the right-hand side of (21) converges fast.

Performing integration in (17) with respect to r_{12} and employing a finite-sum representation for the function Φ, which appears in expression (19) for the protonium wave function $\varphi_{12}(\mathbf{r}_{12})$, we can easily obtain

$$T_{LM}^{(12)}(\mathbf{q}_1) = i^{-1}\pi\sqrt{\frac{2L+1}{2l+1}}N_{nl}\times 2^l\kappa_{12}^{-(L+3)}$$

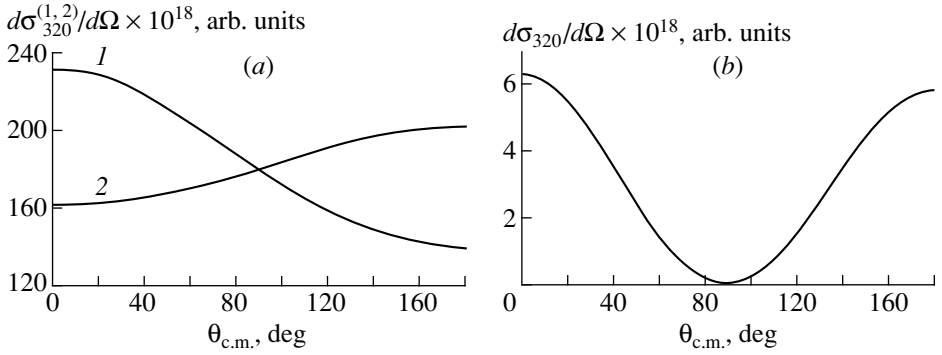

Fig. 1. (*a*) Partial differential cross section $d\sigma_{320}/d\Omega$ calculated at $E = 50$ keV with (curve *1*) the amplitudes $T^{(1)}$ and (curve *2*) the amplitude $T^{(2)}$; (*b*) same cross section calculated with the summed amplitude $T = T^{(1)} + T^{(2)}$.

$$\times\left(1+\frac{q_1^2}{\kappa_{12}^2}\right)^{-(L+l+2)}\sum_{\lambda,\nu} i^{\lambda}\sqrt{2\lambda+1}\,\frac{1}{2^{\lambda}}(L0\lambda0|l0) \tag{22}$$

$$\times(LM\lambda\nu|lm)Y^*_{\lambda\nu}(\hat{q}_1)\sum_{k=0}^{n-l-1} b_k(n,l)\cdot 2^k\Gamma(N+\lambda+2)$$

$$\times\left(1+\frac{q_1^2}{\kappa_{12}^2}\right)^{-k} F\left(\frac{\lambda-N}{2},\frac{\lambda-N+1}{2};\,\lambda+3/2;\,-\frac{q_1^2}{\kappa_{12}^2}\right),$$

where $N = l + L + k + 1$ and the coefficients $b_k(n, l)$ are determined by the recursion relations

$$b_0 = 1, \quad b_k = b_{k-1}\frac{-n+l+k}{k(2l+k+1)}. \tag{23}$$

It should be emphasized that the hypergeometric function F in (22) reduces to a finite sum.

3. RESULTS AND DISCUSSION

3.1. Differential and Total Cross Sections

Employing the above expressions for the amplitudes T and T^a, we have calculated the partial differential and integrated cross section ($d\sigma_{nlm}/d\Omega$ and σ_{nlm}, respectively) for reaction (1), which leads to protonium formation in states that are characterized quantum numbers n, l, and m.[2)] In addition, we have calculated the cross sections

$$\sigma_{nl} = \sum_m \sigma_{nlm}, \quad \sigma_n = \sum_{lm}\sigma_{nlm}. \tag{24}$$

Our calculations were performed for incident-antiproton energies in the range E = 1–250 keV (in laboratory frame).[3)]

As can be seen from (2), the amplitude T is given by the sum of two amplitudes representing two different mechanisms of reaction (1). The amplitude $T^{(1)}$ corresponds to the pole mechanism of proton pickup by the antiproton, while $T^{(2)}$ describes protonium formation via the exchange scattering of the incident antiproton by the target electron (this mechanism can be represented by a triangle Feynman diagram). By way of example, the cross sections $d\sigma_{nl|m|}/d\Omega$ for $n = 3$, $l = 2$, and $|m| = 0, 1, 2$ at $E = 50$ keV are presented in Figs. 1–3 as functions of the scattering angle θ in the c.m. frame. Figure 1*a* shows the cross sections $d\sigma^{(1)}_{320}/d\Omega$ and $d\sigma^{(2)}_{320}/d\Omega$ calculated with the amplitudes $T^{(1)}$ and $T^{(2)}$, respectively, while Fig. 1*b* displays the cross section $d\sigma_{320}/d\Omega$ corresponding to the summed amplitude T. It should be noted that the cross section $d\sigma_{320}/d\Omega$ is much smaller than each of the cross sections $d\sigma^{(1)}_{320}/d\Omega$

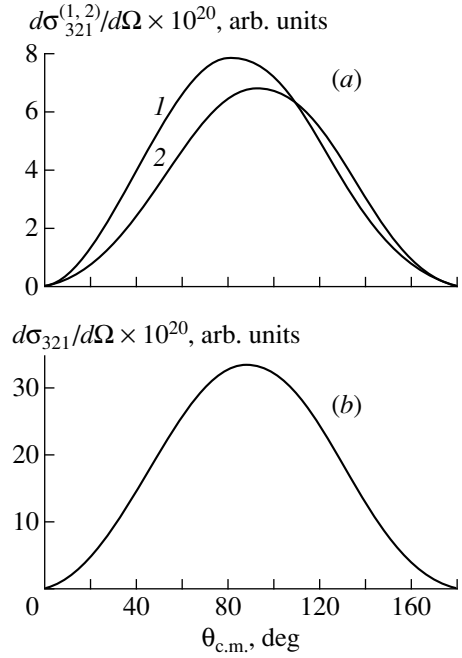

Fig. 2. As in Fig. 1, but for the cross section $d\sigma_{321}/d\Omega$.

[2)]We note that these cross sections depend only on $|m|$.
[3)]Presently, there are no relevant data.

Table 1. Partial cross sections $\sigma_{nl|m|}(E)$ (in a.u.)

nlm	Energy, keV						
	1	10	50	100	150	200	250
100	1.22×10^{-13}	5.62×10^{-14}	9.12×10^{-16}	4.72×10^{-17}	6.53×10^{-18}	1.48×10^{-18}	4.54×10^{-19}
200	1.40×10^{-10}	2.34×10^{-14}	3.26×10^{-16}	1.15×10^{-17}	1.32×10^{-18}	2.69×10^{-19}	7.68×10^{-20}
210	2.82×10^{-12}	1.12×10^{-12}	4.30×10^{-16}	5.71×10^{-18}	4.03×10^{-19}	5.91×10^{-20}	1.31×10^{-20}
211	8.68×10^{-11}	1.54×10^{-13}	2.29×10^{-17}	2.64×10^{-19}	1.77×10^{-20}	2.54×10^{-21}	5.56×10^{-22}
300	8.29×10^{-10}	7.60×10^{-14}	1.21×10^{-16}	3.90×10^{-18}	4.30×10^{-19}	8.57×10^{-20}	2.41×10^{-20}
310	2.18×10^{-9}	5.05×10^{-13}	1.94×10^{-16}	2.30×10^{-18}	1.56×10^{-19}	2.23×10^{-20}	4.89×10^{-21}
311	4.34×10^{-10}	8.12×10^{-14}	9.72×10^{-18}	1.03×10^{-19}	6.69×10^{-21}	9.42×10^{-22}	2.04×10^{-22}
320	1.09×10^{-11}	1.05×10^{-12}	2.51×10^{-17}	1.35×10^{-19}	5.89×10^{-21}	6.25×10^{-22}	1.08×10^{-22}
321	1.52×10^{-9}	1.73×10^{-13}	2.42×10^{-18}	1.21×10^{-20}	5.15×10^{-22}	5.39×10^{-23}	9.27×10^{-24}
322	4.99×10^{-15}	8.05×10^{-20}	4.87×10^{-25}	2.03×10^{-27}	8.05×10^{-29}	8.14×10^{-30}	1.39×10^{-30}
400	2.09×10^{-9}	6.84×10^{-14}	5.57×10^{-17}	1.73×10^{-18}	1.87×10^{-19}	3.70×10^{-20}	1.04×10^{-20}
410	1.00×10^{-9}	2.24×10^{-13}	9.43×10^{-17}	1.08×10^{-18}	7.16×10^{-20}	1.02×10^{-20}	2.22×10^{-21}
411	2.06×10^{-10}	4.14×10^{-14}	4.63×10^{-18}	4.76×10^{-20}	3.05×10^{-21}	4.27×10^{-22}	9.22×10^{-23}
420	1.12×10^{-8}	7.84×10^{-13}	1.65×10^{-17}	8.52×10^{-20}	3.66×10^{-21}	3.85×10^{-22}	6.65×10^{-23}
421	1.13×10^{-9}	1.28×10^{-13}	1.56×10^{-18}	7.56×10^{-21}	3.18×10^{-22}	3.30×10^{-23}	5.66×10^{-24}
422	4.13×10^{-15}	5.66×10^{-20}	3.07×10^{-25}	1.25×10^{-27}	4.92×10^{-29}	4.97×10^{-30}	8.42×10^{-31}
430	1.22×10^{-9}	2.40×10^{-13}	6.23×10^{-19}	1.52×10^{-21}	4.29×10^{-23}	3.35×10^{-24}	4.62×10^{-25}
431	8.91×10^{-9}	4.51×10^{-14}	8.33×10^{-20}	1.95×10^{-22}	5.41×10^{-24}	4.20×10^{-25}	5.74×10^{-26}
432	6.97×10^{-14}	5.53×10^{-20}	4.88×10^{-26}	9.83×10^{-29}	2.58×10^{-30}	1.94×10^{-31}	2.63×10^{-32}
433	2.70×10^{-16}	2.97×10^{-22}	4.52×10^{-27}	1.04×10^{-30}	2.86×10^{-32}	2.21×10^{-33}	3.02×10^{-34}

and $d\sigma^{(2)}_{320}/d\Omega$; this indicates that the two mechanisms of the reaction under consideration interfere destructively. Figures 2 and 3 present the cross sections for transitions into the (321) and (322) states, respectively. From these figures, it can be seen that, at $|m| \neq 0$, the cross sections $d\sigma^{(1,2)}_{32|m|}/d\Omega$ have a peak, which becomes narrower with increasing $|m|$. It can also be seen that the interference of the amplitudes $T^{(1)}$ and $T^{(2)}$ is constructive at $|m| = 1$ and destructive at $|m| = 2$. The results of the calculations for transitions into other protonium states at various energies reveal that the shape of the differential cross sections is weakly sensitive to variations in the quantum numbers n and l.

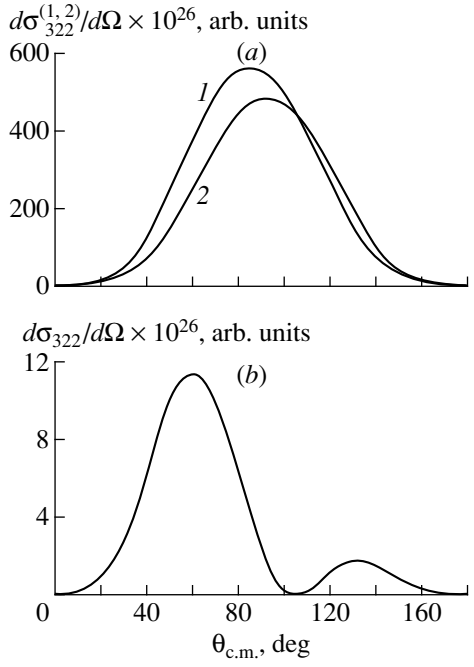

Fig. 3. As in Fig. 1, but for the cross section $d\sigma_{322}/d\Omega$.

Table 1 quotes the integrated partial cross sections $\sigma_{nl|m|}$ for the four lowest shells (n = 1–4) calculated with the amplitude T (see Section 2.1). It can be seen that, for $E \geq 100$ keV, the maximum values of $\sigma_{nl|m|}$ at fixed n are achieved for transitions to the $l = 0$ states. For $E \leq 50$ keV, $\sigma_{nl|m|}$ can peak either at $l = 1$ or at $l = 2$, with m always being zero. At fixed values of n and l, the cross section $\sigma_{nl|m|}$ decreases with increasing $|m|$. Among data presented in Table 1, this is not so only at $E = 1$ keV, in which case $\sigma_{431} > \sigma_{430}$. Finally, all the cross sections decrease monotonically with increasing energy.

A calculation of the cross sections according to the expressions from Section 2.1 is disadvantageous in that it consumes a great amount of machine time at large values of n and l. The calculations can be considerably simplified by using the multipole expansion described in Section 2.2 (amplitude T^q). Within this approach, the

Table 2. Cross sections $\sigma_n(E)$ (in a.u.)

n	Energy, keV						
	1	10	50	100	150	200	250
1	1.23×10^{-13}	5.62×10^{-14}	9.11×10^{-16}	4.72×10^{-17}	6.54×10^{-18}	1.48×10^{-18}	4.51×10^{-19}
2	3.17×10^{-10}	1.45×10^{-12}	8.01×10^{-16}	1.77×10^{-17}	1.76×10^{-18}	3.33×10^{-19}	9.07×10^{-20}
3	6.96×10^{-9}	2.14×10^{-12}	3.64×10^{-16}	6.56×10^{-18}	6.06×10^{-19}	1.11×10^{-19}	2.96×10^{-20}
4	3.62×10^{-8}	1.75×10^{-12}	1.80×10^{-16}	3.00×10^{-18}	2.70×10^{-19}	4.86×10^{-20}	1.28×10^{-20}
5	9.06×10^{-8}	1.24×10^{-12}	9.89×10^{-17}	1.59×10^{-18}	1.41×10^{-19}	2.54×10^{-20}	6.68×10^{-21}
6	1.51×10^{-7}	8.66×10^{-13}	5.96×10^{-17}	9.41×10^{-19}	8.30×10^{-20}	1.48×10^{-20}	3.90×10^{-21}
7	1.97×10^{-7}	6.11×10^{-13}	3.85×10^{-17}	6.00×10^{-19}	5.27×10^{-20}	9.39×10^{-21}	2.47×10^{-21}
8	2.23×10^{-7}	4.43×10^{-13}	2.62×10^{-17}	4.05×10^{-19}	3.55×10^{-20}	6.33×10^{-21}	1.66×10^{-21}
9	2.30×10^{-7}	3.27×10^{-13}	1.86×10^{-17}	2.86×10^{-19}	2.50×10^{-20}	4.45×10^{-21}	1.17×10^{-21}
10	2.24×10^{-7}	2.47×10^{-13}	1.37×10^{-17}	2.09×10^{-19}	1.83×10^{-20}	3.25×10^{-21}	8.52×10^{-22}
20	7.79×10^{-8}	3.49×10^{-14}	1.75×10^{-18}	2.65×10^{-20}	2.31×10^{-21}	4.09×10^{-22}	1.07×10^{-22}
30	2.47×10^{-8}	1.06×10^{-14}	5.21×10^{-19}	7.87×10^{-21}	6.84×10^{-22}	1.21×10^{-22}	3.14×10^{-22}
40	1.12×10^{-8}	4.50×10^{-15}	2.20×10^{-19}	3.32×10^{-21}	2.89×10^{-22}	5.13×10^{-23}	1.34×10^{-23}
50	6.84×10^{-9}	2.31×10^{-15}	1.13×10^{-19}	1.70×10^{-21}	1.48×10^{-22}	2.62×10^{-23}	6.86×10^{-24}
60	4.03×10^{-9}	1.34×10^{-15}	6.53×10^{-20}	9.85×10^{-22}	8.56×10^{-23}	1.52×10^{-23}	3.97×10^{-24}
70	2.57×10^{-9}	8.45×10^{-16}	4.11×10^{-20}	6.20×10^{-22}	5.39×10^{-23}	9.55×10^{-24}	2.50×10^{-24}
80	1.73×10^{-9}	5.67×10^{-16}	2.75×10^{-20}	4.16×10^{-22}	3.61×10^{-23}	6.40×10^{-24}	1.67×10^{-24}
90	1.23×10^{-9}	3.98×10^{-16}	1.94×10^{-20}	2.92×10^{-22}	2.54×10^{-23}	4.49×10^{-24}	1.18×10^{-24}
100	8.96×10^{-10}	2.90×10^{-16}	1.41×10^{-20}	2.13×10^{-22}	1.85×10^{-23}	3.28×10^{-24}	8.57×10^{-25}

accuracy of the calculations is determined by the number of terms, L_{max}, retained in the sum over L on the right-hand side of (16). A comparison of the results of calculations that rely on the amplitude T^a with those that employ the exact amplitude T demonstrates that, for the cross sections σ_{nl} and σ_n, the first (dipole) term in expansion (16) ($L_{max} = 1$) ensures a precision no poorer than 1%. In order to achieve the same accuracy in calculating the partial cross sections $\sigma_{nl|m|}$, it is usually sufficient to take two terms ($L_{max} = 2$), but there are exceptions—for example, a 2% accuracy in σ_{322} requires $L_{max} = 4$, in which case, however, the cross section σ_{322} does not make noticeable contributions to σ_{32} and σ_3.

Table 2 lists the values of the cross section σ_n for $n \le 100$ that were calculated on the basis of expression (16) with $L_{max} = 3$. At $E = 1$ and 10 keV, σ_n peaks at $n = 9$ and 3, respectively. At higher energies, σ_n is maximal at $n = 1$, showing a monotonic decrease with increasing n. All values of $\sigma_n(E)$ decrease monotonically as the energy E is increased.

To conclude this section, we would like to indicate that, for reaction (1), we have tested the validity of the well-known $1/n^3$ rule for the cross sections σ_n. It turned out that, at $E = 1$ keV, the decrease in σ_n with increasing n complies well with this rule from $n \approx 60$. At $E = 10$ keV, the $1/n^3$ rule holds for $n \ge 30$. Finally, the $1/n^3$ behavior of the cross section σ_n at $E = 250$ keV set in from $n = 3$.

3.2. Inclusion of Strong Interaction

In the above calculations, we have taken no account of strong proton–antiprotonic interaction. Its effect on the features of the antiprotonic atoms was considered in a number of studies (see, for example, [7–9] and references therein). In order to assess roughly the implications of this effect for the cross sections considered here, we make use of the circumstance that the range of strong interaction is much less than the protonium size. In a rough approximation, we can assume that the strong-interaction effect reduces to a shift of protonium levels in relation to those in a purely Coulomb field. According to experimental data reported in [1], this shift is sizable only for the protonium ground (1s) state, $\Delta E_{12} = -0.73 \pm 0.04$ keV. For other levels, it is negligible.

The effect of strong proton–antiproton interaction on the cross section for protonium formation in the ground state ($nlm = 100$) is illustrated in Table 3. There, the cross section $\tilde{\sigma}_{100}$ differs from the cross section σ_{100}, which was considered above, only in that, in the matrix element (17), the purely Coulomb wave function of the protonium ground (1s) state, $\varphi_{12} = Ce^{-\kappa r}$, is replaced by the function $\tilde{\varphi}_{12} = \tilde{C}(\tilde{\kappa} r)^{\eta - 1} e^{-\tilde{\kappa} r}$; in these

Table 3. Inclusion of strong interaction

Energy, keV	$\tilde{\sigma}/\sigma$
1	1.28
10	1.16
50	0.97
100	0.9
150	0.85
200	0.83
250	0.81

Table 4. Statistical tensors $\rho_{k0}(l)$

n	$\rho_{k0}(l)$	Energy, keV				$\lvert\rho_{k0}(l)\rvert_{\max}$
		1	10	50	100	
2	$\rho_{20}(1)$	0.66	−0.94	−1.2	−1.24	1.41
3	$\rho_{20}(1)$	−0.8	−0.9	−1.21	−1.24	1.41
	$\rho_{20}(2)$	−0.6	−1.06	−1.1	−1.12	1.2
	$\rho_{40}(2)$	−1.08	−1.49	−1.53	−1.54	1.6

expressions, C and $\tilde{C}$ are normalization factors; $\kappa^2 = m_p\epsilon$ and $\tilde{\kappa}^2 = m_p\tilde{\epsilon}$, ϵ and $\tilde{\epsilon}$ being, respectively, the purely Coulomb binding energy of the ground (1*s*) state and the experimental binding energy of the protonium 1*s* state; and $\eta = (1/137)(e^2 m_p/2\hbar\tilde{\kappa}) \approx 1.03$.[4)]

The data in Table 3 show that the effect in question is not negligible. Its magnitude and even sign (we imply the difference $\tilde{\sigma}_{100} - \sigma_{100}$) are dependent on energy.

3.3. Evaluation of Statistical Tensors for Reaction (1)

The results of our calculations reveal that the cross sections $\sigma_{nl|m|}$ depend greatly on $|m|$ (see Table 1). This suggests a noticeable alignment of the orbital angular momentum $\mathbf{l}$ of the protonium for $l \neq 0$. This effect is commonly described in terms of the statistical tensors (see, for example, [10])

$$\rho_{k\kappa}(l) = \sqrt{2l+1}\sum_{m,\,m'}(-1)^{l-m'}(lm'l-m|k\kappa)\rho_l(m,m'), \quad (25)$$

where $\rho_l(m, m')$ is the angular-momentum density matrix satisfying the condition $\mathrm{tr}\rho_l = \sum_m \rho_l(m, m) = 1$.

If the system possesses cylindrical symmetry, as it does in the case under consideration, the density matrix is diagonal in m. By averaging the density matrix for reaction (1) over the scattering angle, we can obtain

$$\rho_{nl}(m, m') = \delta_{mm'}\frac{\sigma_{nlm}}{\sigma_{nl}}. \quad (26)$$

Taking into account the definition in (25), we can conclude that, in the case of a diagonal density matrix, the statistical tensors $\rho_{k\kappa}(l)$ vanish for $\kappa \neq 0$. There is an additional constraint on the density matrix: from the relation $\sigma_{nl-m} = \sigma_{nlm}$, it follows that $\rho_{k\kappa}(l)$ can be nonzero only for even k.

For reaction (1), the statistical-tensor components $\rho_{k0}(l)$ calculated according to (25) and (26) at $n = 2$ and 3 for energies in the range $E = 1$–100 keV are presented in Table 4. We note that the $\rho_{k0}(l)$ values calculated for energies of $E \geq 100$ keV virtually coincide with those calculated at $E = 100$ keV; therefore, they are not presented here. The maximal possible values $|\rho_{k0}(l)_{\max}|$ satisfying the definition in (25) are quoted in the last column of Table 4. It can be seen that the computed values of $|\rho_{k0}(l)|$ are sufficiently close to the maximal possible ones. It follows that the angular distributions of photons emitted from the excited states of protonium that are formed in process (1) should be pronouncedly anisotropic.

ACKNOWLEDGMENTS

We are grateful to G.Ya. Korenman for stimulating discussions.

This work was supported in part by the Russian Foundation for Basic Research (project no. 98-02-16275).

REFERENCES

1. C. J. Batty, Rep. Prog. Phys. **52**, 1165 (1989).
2. P. Roy and N. C. Deb, Indian J. Phys. B **68**, 245 (1994).
3. P. Roy and N. C. Deb, Indian J. Phys. B **69**, 443 (1994).
4. G. Ya. Korenman and S. I. Rogovaya, J. Phys. B **13**, 641 (1980).
5. H. A. Bethe and E. E. Salpeter, *Quantum Mechanics of One- and Two-Electron Atoms* (Fizmatgiz, Moscow, 1960; Academic, New York, 1957).
6. I. S. Gradshteĭn and I. M. Ryzhik, *Table of Integrals, Sums, Series, and Products* (5th ed., Nauka, Moscow, 1971; Transl. of 4th Russ. ed., Academic, New York, 1980).
7. V. S. Popov, A. E. Kudryavtsev, and V. D. Mur, Zh. Éksp. Teor. Fiz. **77**, 1727 (1979) [Sov. Phys. JETP **50**, 865 (1979)].
8. I. S. Shapiro, Phys. Rep. **35**, 129 (1978).
9. I. L. Grach, V. O. Kebrikov, and Yu. A. Simonov, Phys. Lett. B **208**, 309 (1988).
10. N. S. Zelenskaya and I. B. Teplov, *Features of Excited Nuclear States and Angular Correlations in Nuclear Reactions* (Énergoatomizdat, Moscow, 1995).

Translated by O. Chernavskaya

[4)]Strictly speaking, the Coulomb level shifted owing to strong interaction is described by the Whittaker function, but it differs insignificantly from $\tilde{\varphi}_{12}$ in the range of r values that make a substantial contribution to the matrix element of the process under consideration.

Physics of Atomic Nuclei, Vol. 63, No. 3, 2000, pp. 455–463. From Yadernaya Fizika, Vol. 63, No. 3, 2000, pp. 527–535.

ELEMENTARY PARTICLES AND FIELDS
Theory

Excited Strange Mesons and Their Decays in a Chiral $U(3) \times U(3)$ Lagrangian*

M. K. Volkov and V. L. Yudichev*****

Joint Institute for Nuclear Research, Dubna, Moscow oblast, 141980 Russia

Received December 2, 1998; in final form, March 19, 1999

Abstract—We bosonize the Nambu–Jona-Lasinio quark model with separable nonlocal interactions in order to derive a chiral $U(3) \times U(3)$ Lagrangian, containing, besides the usual meson fields, their first radial excitations. The spontaneous breaking of chiral symmetry is governed by the Nambu–Jona-Lasinio gap equation. The first radial excitations of the kaon, K^*, and φ are described with the help of two form factors. The decays $K^{*\prime} \longrightarrow \rho K$, $K^{*\prime} \longrightarrow K^*\pi$, $K^{*\prime} \longrightarrow K\pi$, $\varphi' \longrightarrow K^*K$, $\varphi' \longrightarrow \bar{K}K$, $K' \longrightarrow K\rho$, $K' \longrightarrow K^*\pi$, and $K' \longrightarrow K2\pi$ are considered, and a qualitative agreement of our results with the experimental data is found. © *2000 MAIK "Nauka/Interperiodica".*

1. INTRODUCTION

In our previous papers [1–3], the chiral quark model of the Nambu–Jona-Lasinio (NJL) type with separable nonlocal interactions was proposed. This model is a nonlocal extension of the standard NJL model [4–9]. The first radial excitations of the scalar, pseudoscalar, vector, and axial-vector mesons were described with the help of the form factors corresponding to 3-dimensional ground- and excited-state wave functions. The meson masses, weak-decay constants, and a set of decay widths of nonstrange mesons were calculated.

The theoretical foundations for the choice of polynomial pion–quark form factors were discussed in [1], and it was shown that we can choose these form factors in such a way that the mass-gap equation holds its usual form and has a solution with a constant constituent quark mass. Moreover, the quark condensate is not modified after including the excited states in the model, because the tadpoles, connected with the excited scalar fields, vanish. Thus, in this approach, it is possible to describe radially excited mesons above the usual NJL vacuum, preserving the usual mechanism of chiral symmetry breaking. Finally, it has been shown that one can derive an effective meson Lagrangian for the ground and excited meson states directly in terms of the local fields and their derivatives. A nonlocal separable interaction is defined in the Minkowski space in a 3-dimensional (yet covariant) way, whereby form factors depend only on the part of the quark–antiquark relative momentum transverse to the meson momentum. This ensures the absence of spurious relative-time excitations [10].

In paper [2], the meson-mass spectrum for the ground and excited pions, kaons, and the vector meson nonet in the $U(3) \times U(3)$ model of this type has been obtained. By fitting the meson-mass spectrum, all parameters in this model are fixed. This then allows one to describe all the strong, electromagnetic, and weak interactions of these mesons without introducing any new additional parameter.

In paper [3], it was shown that this model satisfactorily describes two types of decay. This concerns the strong decays like $\rho \longrightarrow 2\pi$, $\pi' \longrightarrow \rho\pi$, and $\rho' \longrightarrow 2\pi$ associated with divergent quark diagrams, as well as the decays $\rho' \longrightarrow \omega\pi$ and $\omega' \longrightarrow \rho\pi$ defined by anomalous quark diagrams. Here, we continue the similar calculations for the description of the decay widths of strange pseudoscalar and vector mesons.

In Section 2, we introduce the effective quark interaction in the separable approximation and describe its bosonization. In Section 3, we derive the effective Lagrangian for the pions and kaons and perform the diagonalization procedure leading to the physical pion and kaon ground and excited states. In Section 4, we carry out the diagonalization for the K^* and φ mesons. In Section 5, we give the parameters of our model and the masses of the ground and excited states of kaons, K^* and φ mesons, and the weak-decay constants F_π, $F_{\pi'}$, F_K, and $F_{K'}$. In Section 6, we evaluate the decay widths of the processes $K^{*\prime} \longrightarrow K^*\pi$, $K^{*\prime} \longrightarrow \rho K$, $K^{*\prime} \longrightarrow K\pi$, $\varphi' \longrightarrow K^*K$, and $\varphi' \longrightarrow \bar{K}K$. In Section 7, we calculate the decay widths of the processed $K' \longrightarrow \rho K$, $K' \longrightarrow K^*\pi$, and $K' \longrightarrow K2\pi$. The results obtained are discussed in Section 8.

* This article was submitted by the authors in English.

** e-mail: volkov@thsun1.jinr.ru
*** e-mail: yudichev@thsun1.jinr.ru

2. $U(3) \times U(3)$ CHIRAL LAGRANGIAN WITH THE EXCITED MESON STATES

We shall use a separable interaction, which is still of current–current form, but allows for nonlocal vertices (form factors) in the definition of the quark currents,

$$L[\bar{q}, q] = \int d^4x \bar{q}(x)(i\partial\!\!\!/ - m^0)q(x) + \tilde{L}_{\rm int}, \quad (1)$$

$$\tilde{L}_{\rm int} = \int d^4x \sum_{a=0}^{8}\sum_{i=1}^{N}\Big[\frac{G_1}{2}[j^a_{S,i}(x)j^a_{S,i}(x) + j^a_{P,i}(x)j^a_{P,i}(x)] - \frac{G_2}{2}[j^{a,\mu}_{V,i}(x)j^{a,\mu}_{V,i}(x) + j^{a,\mu}_{A,i}(x)j^{a,\mu}_{A,i}(x)]\Big], \quad (2)$$

$$j^a_{S,i}(x) = \int d^4x_1 \int d^4x_2 \bar{q}(x_1)F^a_{S,i}(x; x_1, x_2)q(x_2), \quad (3)$$

$$j^a_{P,i}(x) = \int d^4x_1 \int d^4x_2 \bar{q}(x_1)F^a_{P,i}(x; x_1, x_2)q(x_2), \quad (4)$$

$$j^{a,\mu}_{V,i}(x) = \int d^4x_1 \int d^4x_2 \bar{q}(x_1)F^{a,\mu}_{V,i}(x; x_1, x_2)q(x_2), \quad (5)$$

$$j^{a,\mu}_{A,i}(x) = \int d^4x_1 \int d^4x_2 \bar{q}(x_1)F^{a,\mu}_{A,i}(x; x_1, x_2)q(x_2). \quad (6)$$

Here, m^0 is the current quark mass matrix (we suppose that $m^0_u \approx m^0_d$), $j^a_{S,P,V,A}(x)$ denote, respectively, the scalar, pseudoscalar, vector, and axial-vector currents of the quark field; $F^{a,\mu}_{U,i}(x; x_1, x_2)$, $i = 1, \ldots, N$, are a set of nonlocal scalar, pseudoscalar, vector, and axial-vector quark vertices (in general, momentum- and spin-dependent), which will be specified below.

Upon bosonization, we obtain [1, 2]

$$\begin{aligned} &L_{\rm bos}(\bar{q}, q; \sigma, \phi, P, A) \\ &= \int d^4x_1 \int d^4x_2 \bar{q}(x_1)[(i\partial\!\!\!/_{x_2} - m^0)\delta(x_1 - x_2) \\ &+ \int d^4x \sum_{a=0}^{8}\sum_{i=1}^{N}(\sigma^a_i(x)F^a_{\sigma,i}(x; x_1, x_2) \\ &+ \phi^a_i(x)F^a_{\phi,i}(x; x_1, x_2) + V^{a,\mu}_i(x)F^{a,\mu}_{V,i}(x; x_1, x_2) \\ &+ A^{a,\mu}_i(x)F^{a,\mu}_{A,i}(x; x_1, x_2))]q(x_2) \\ &- \int d^4x \sum_{a=0}^{8}\sum_{i=1}^{N}\Big[\frac{1}{2G_1}(\sigma^{a2}_i(x) + \phi^{a2}_i(x)) \\ &- \frac{1}{2G_2}(V^{a,\mu 2}_i(x) + A^{a,\mu 2}_i(x))\Big]. \end{aligned} \quad (7)$$

This Lagrangian describes a system of local meson fields, $\sigma^a_i(x)$, $\phi^a_i(x)$, $V^{a,\mu}_i(x)$, and $A^{a,\mu}_i(x)$, $i = 1, \ldots, N$, which interact with the quarks through nonlocal vertices. These fields are not yet to be associated with physical particles, which will be obtained after determining the vacuum and diagonalizing the effective meson Lagrangian.

In order to describe the first radial excitations of mesons ($N = 2$), we take the form factors (see [1]) as

$$\begin{aligned} &F^a_{\sigma,2}(\mathbf{k}) = \lambda^a f^P_a(\mathbf{k}), \quad F^a_{\phi,2}(\mathbf{k}) = i\gamma_5\lambda^a f^P_a(\mathbf{k}), \\ &F^{a,\mu}_{V,2}(\mathbf{k}) = \gamma^\mu\lambda^a f^V_a(\mathbf{k}), \quad F^{a,\mu}_{A,2}(\mathbf{k}) = \gamma_5\gamma^\mu\lambda^a f^V_a(\mathbf{k}), \end{aligned} \quad (8)$$

$$f^U_a(\mathbf{k}) = c^U_a(1 + d_a\mathbf{k}^2), \quad (9)$$

where λ^a are the Gell-Mann matrices. We consider here the form factors in the momentum space and in the rest frame of the mesons ($\mathbf{P}_{\rm meson} = 0$; k and P are the relative and total momentum of the quark–antiquark pair). For the ground states of the mesons, the functions $f^{U,0}_a(\mathbf{k}) = 1$.

After integrating over the quark fields in (7), one obtains the effective Lagrangian of the σ^a_1, σ^a_2, ϕ^a_1, ϕ^a_2, $V^{a,\mu}_1$, $V^{a,\mu}_2$, $A^{a,\mu}_1$, and $A^{a,\mu}_2$ fields:

$$\begin{aligned} &L(\sigma', \phi, V, A, \bar{\sigma}, \bar{\phi}, \bar{V}, \bar{A}) = -\frac{1}{2G_1}(\sigma'^2_a + \phi^2_a + \bar{\sigma}^2_a + \bar{\phi}^2_a) \\ &+ \frac{1}{2G_2}(V^2_a + A^2_a + \bar{V}^2_a + \bar{A}^2_a) - iN_c\,\mathrm{tr}\log[i\partial\!\!\!/ - m^0 \\ &+ (\sigma'_a + i\gamma_5\phi_a + \gamma_\mu V^\mu_a + \gamma_5\gamma_\mu A^\mu_a \\ &+ (\bar{\sigma}_a + i\gamma_5\bar{\phi}_a)f^P_a + (\gamma_\mu\bar{V}^\mu_a + \gamma_5\gamma_\mu\bar{A}^\mu_a)f^V_a)\lambda^a], \end{aligned} \quad (10)$$

where we have set $\sigma_1 = \sigma'$, $\sigma_2 = \bar{\sigma}$, $\pi_1 = \pi$, $\pi_2 = \bar{\pi}$, etc.

Let us define the vacuum expectation of the σ'_a fields[1)]

$$\begin{aligned} &\left\langle \frac{\delta L}{\delta\sigma'_a} \right\rangle_0 = -iN_c \\ &\times \mathrm{tr}\int_{\Lambda_3} \frac{d^4k}{(2\pi)^4}\frac{1}{(k\!\!\!/ - m^0 + \langle\sigma'_a\rangle_0)} - \frac{\langle\sigma'_a\rangle_0}{G_1} = 0. \end{aligned} \quad (11)$$

Introduce the new sigma fields whose vacuum expectations are equal to zero

$$\sigma_a = \sigma'_a - \langle\sigma'_a\rangle_0 \quad (12)$$

and redefine the quark masses

$$m_a = m^0_a - \langle\sigma'_a\rangle_0. \quad (13)$$

Then equation (11) can be rewritten in the form of the usual gap equation

$$m_i = m^0_i + 8G_1 m_i I_1(m_i) \quad (i = u, d, s), \quad (14)$$

[1)]We can derive this form of the gap equation only if the condition $\langle\bar{\sigma}_a\rangle_0 = 0$ is fulfilled (see [1–3] and equations (17)).

where

$$I_n(m_i) = -iN_c\int_{\Lambda_3}\frac{d^4k}{(2\pi)^4}\frac{1}{(m_i^2-k^2)^n} \tag{15}$$

and m_i are the constituent quark masses.

3. THE EFFECTIVE LAGRANGIAN FOR THE GROUND AND EXCITED STATES OF THE PIONS AND KAONS

To describe the first excited states of all the meson nonets, it is necessary to use three different slope parameters d_a in the form factors $f_a^U(\mathbf{k})$ [see (9)]:

$$\begin{aligned} f_{uu}^{P,V}(\mathbf{k}) &= c_{uu}^{P,V}(1+d_{uu}\mathbf{k}^2),\\ f_{us}^{P,V}(\mathbf{k}) &= c_{us}^{P,V}(1+d_{us}\mathbf{k}^2),\\ f_{ss}^{P,V}(\mathbf{k}) &= c_{ss}^{P,V}(1+d_{ss}\mathbf{k}^2). \end{aligned} \tag{16}$$

Following our works [1, 2], we can fix the parameters d_{uu}, d_{us}, and d_{ss} by using the conditions

$$I_1^{f_{uu}^P}(m_u) = 0,\quad I_1^{f_{us}^P}(m_u)+I_1^{f_{us}^P}(m_s) = 0,\quad I_1^{f_{ss}^P}(m_s) = 0, \tag{17}$$

where

$$I_1^{f_a\cdots f_a}(m_i) = -iN_c\int_{\Lambda_3}\frac{d^4k}{(2\pi)^4}\frac{f_a\cdots f_a}{(m_i^2-k^2)}. \tag{18}$$

Equations (17) allow us to reduce the gap equations to the form usual for the NJL model [see (14)] because the tadpoles with the excited scalar external field do not contribute to the quark condensates and to the constituent quark masses.

Using (17), we obtain close values for all d_a

$$d_{uu} = -1.784\ \text{GeV}^{-2},\quad d_{us} = -1.7565\ \text{GeV}^{-2},\quad d_{ss} = -1.727\ \text{GeV}^{-2}. \tag{19}$$

Now, let us consider the free part of the Lagrangian (10). For the pions and kaons, we obtain

$$L^{(2)}(\phi) = \frac{1}{2}\sum_{i,j=1}^{2}\sum_{a=1}^{7}\phi_i^a(P)K_{ij}^{ab}(P)\phi_j^b(P). \tag{20}$$

Here,

$$\sum_{a=1}^{3}(\phi_i^a)^2 = (\pi_i^0)^2+2\pi_i^+\pi_i^-,\qquad (\phi_i^4)^2+(\phi_i^5)^2 = 2K_i^+K_i^-,\quad (\phi_i^6)^2+(\phi_i^7)^2 = 2K_i^0\bar{K}_i^0. \tag{21}$$

The quadratic form $K_{ij}^{ab}(P)$ in (20) is obtained as

$$\begin{aligned} K_{ij}^{ab}(P) &\equiv \delta^{ab}K_{ij}^a(P),\\ K_{ij}^a(P) &= -\delta_{ij}\frac{1}{G_1}-iN_c\,\mathrm{tr}\int_{\Lambda_3}\frac{d^4k}{(2\pi)^4}\\ &\times\left[\frac{1}{\not k+\frac{1}{2}\not P-m_q^a}i\gamma_5 f_i^a\frac{1}{\not k-\frac{1}{2}\not P-m_{q'}^a}i\gamma_5 f_j^a\right], \end{aligned} \tag{22}$$

$$\begin{aligned} f_1^a &\equiv 1,\quad f_2^a \equiv f_a^P(\mathbf{k});\\ m_q^a &= m_u\ (a=1,\ldots,7);\\ m_{q'}^a &= m_u\ (a=1,\ldots,3);\\ m_{q'}^a &= m_s\ (a=4,\ldots,7), \end{aligned} \tag{23}$$

m_u and m_s being the constituent quark masses ($m_u\approx m_d$). The integral (22) is evaluated by expanding in the meson field momentum P. To order P^2, one obtains

$$\begin{aligned} K_{11}^a(P) &= Z_1^a(P^2-M_1^{a2}),\quad K_{22}^a(P) = Z_2^a(P^2-M_2^{a2}),\\ K_{12}^a(P) &= K_{21}^a(P) = \gamma^a(P^2-\Delta^2\delta_{ab}|_{b=4,\ldots,7})\\ &(\Delta = m_s-m_u), \end{aligned} \tag{24}$$

where

$$Z_1^a = 4I_2^aZ,\quad Z_2^a = 4I_2^{ff_a}\bar{Z},\quad \gamma^a = 4I_2^{f_a}Z, \tag{25}$$

$$M_1^{a2} = (Z_1^a)^{-1}\left[\frac{1}{G_1}-4(I_1^a(m_q^a)+I_1^a(m_{q'}^a))\right] + Z^{-1}\Delta^2\delta_{ab}|_{b=4,\ldots,7}, \tag{26}$$

$$M_2^{a2} = (Z_2^a)^{-1}\left[\frac{1}{G_1}-4(I_1^{ff_a}(m_q^a)+I_1^{ff_a}(m_{q'}^a))\right] + \bar{Z}^{-1}\Delta^2\delta_{ab}|_{b=4,\ldots,7}. \tag{27}$$

Here, $Z=1-6m_u^2/M_{a_1}^2\approx 0.7$ and $\bar{Z}=1-\Gamma^2\cdot 6m_u^2/M_{a_1}^2\approx 1$ (see (32)), Z being the additional renormalization of the ground pseudoscalar meson states, taking into account the $\phi^a\longrightarrow A^a$ transitions (see [2, 3]). I_n^a, $I_n^{f_a}$, and $I_n^{ff_a}$ denote the usual loop integrals arising in the momentum expansion of the NJL quark determinant, but now with zero, one, or two factors $f_a(\mathbf{k})$ [see equation (16)], in the numerator [see (18) and below]:

$$I_2^{f\cdots f_a}(m_q,m_{q'}) = -iN_c\int_{\Lambda_3}\frac{d^4k}{(2\pi)^4}\frac{f_a(\mathbf{k})\cdots f_a(\mathbf{k})}{(m_q^{a2}-k^2)(m_{q'}^{a2}-k^2)}. \tag{28}$$

After the renormalization of the meson fields

$$\phi_i^{ar} = \sqrt{Z_i^a}\phi_i^a, \tag{29}$$

the part of the Lagrangian (20) describing the pions and kaons takes the form

$$L_\pi^{(2)} = \frac{1}{2}[(P^2 - M_{\pi_1}^2)\pi_1^2 + 2\Gamma_\pi P^2\pi_1\pi_2 + (P^2 - M_{\pi_2}^2)\pi_2^2], \tag{30}$$

$$L_K^{(2)} = \frac{1}{2}[(P^2 - M_{K_1}^2 - \Delta^2)K_1^2 + (P^2 - M_{K_2}^2 - \Delta^2)K_2^2 + 2\Gamma_K(P^2 - \Delta^2)K_1K_2]. \tag{31}$$

Here,

$$\Gamma_a = \frac{\gamma_a}{\sqrt{Z_1^a Z_2^a}} = \frac{I_2^{f_a}\sqrt{Z}}{\sqrt{I_2^a I_2^{f f_a}\bar{Z}}}. \tag{32}$$

After the transformations of the meson fields

$$\phi^a = \cos(\theta_a - \theta_a^0)\phi_1^{ar} - \cos(\theta_a + \theta_a^0)\phi_2^{ar},$$
$$\phi'^a = \sin(\theta_a - \theta_a^0)\phi_1^{ar} - \sin(\theta_a + \theta_a^0)\phi_2^{ar}, \tag{33}$$

the Lagrangians (30) and (31) take the diagonal forms

$$L_\pi^{(2)} = \frac{1}{2}(P^2 - M_\pi^2)\pi^2 + \frac{1}{2}(P^2 - M_{\pi'}^2)\pi'^2, \tag{34}$$

$$L_K^{(2)} = \frac{1}{2}(P^2 - M_K^2)K^2 + \frac{1}{2}(P^2 - M_{K'}^2)K'^2. \tag{35}$$

Here,

$$M^2_{(\pi,\pi')} = \frac{1}{2(1-\Gamma_\pi^2)} \times \left[M_{\pi_1}^2 + M_{\pi_2}^2 \mp \sqrt{(M_{\pi_1}^2 - M_{\pi_2}^2)^2 + (2M_{\pi_1}M_{\pi_2}\Gamma_\pi)^2}\right], \tag{36}$$

$$M^2_{(K,K')} = \frac{1}{2(1-\Gamma_K^2)}\left[M_{K_1}^2 + M_{K_2}^2 + 2\Delta^2(1-\Gamma_K^2) \mp \sqrt{(M_{K_1}^2 - M_{K_2}^2)^2 + (2M_{K_1}M_{K_2}\Gamma_K)^2}\right], \tag{37}$$

and

$$\tan 2\bar{\theta}_a = \sqrt{\frac{1}{\Gamma_a^2} - 1}\left[\frac{M_{\phi_1^a}^2 - M_{\phi_2^a}^2}{M_{\phi_1^a}^2 + M_{\phi_2^a}^2}\right], \quad 2\theta_a = 2\bar{\theta}_a + \pi, \tag{38}$$

$$\sin\theta_a^0 = \sqrt{\frac{1+\Gamma_a}{2}}, \tag{39}$$

$$M_{\pi_1}^2 = (4ZI_2(m_u, m_u))^{-1}\left[\frac{1}{G_1} - 8I_1(m_u)\right] = \frac{m_u^0}{4Zm_uI_2(m_u, m_u)G_1}, \tag{40}$$

$$M_{\pi_2}^2 = (4I_2^{ff}(m_u, m_u))^{-1}\left[\frac{1}{G_1} - 8I_1^{ff}(m_u)\right],$$

$$M_{K_1}^2 = (4ZI_2(m_u, m_u))^{-1}\left[\frac{1}{G_1} - 4(I_1(m_u) + I_1(m_s))\right]$$

$$+ (Z^{-1} - 1)\Delta^2 = \frac{m_u^0/m_u + m_s^0/m_s}{4ZI_2(m_u, m_s)G_1} + (Z^{-1} - 1)\Delta^2, \tag{41}$$

$$M_{K_2}^2 = (4I_2^{ff}(m_u, m_s))^{-1}\left[\frac{1}{G_1} - 4(I_1^{ff}(m_u) + I_1^{ff}(m_s))\right].$$

4. THE EFFECTIVE LAGRANGIAN FOR THE GROUND AND EXCITED STATES OF THE VECTOR MESONS

The free part of the effective Lagrangian (10) describing the ground and excited states of the vector mesons has the form

$$L^{(2)}(V) = -\frac{1}{2}\sum_{i,j=1}^{2}\sum_{a=0}^{8} V_i^{\mu a}(P)R_{ij}^{\mu\nu a}(P)V_j^{\nu a}(P), \tag{42}$$

where

$$\sum_{a=0}^{3} V_i^{\mu a} = (\omega_i^\mu)^2 + (\rho_i^{0\mu})^2 + 2\rho_i^{+\mu}\rho_i^{-\mu},$$
$$(V_i^{4\mu})^2 + (V_i^{5\mu})^2 = 2K_i^{*+\mu}K_i^{*-\mu}, \tag{43}$$
$$(V_i^{6\mu})^2 + (V_i^{7\mu})^2 = 2K_i^{*0\mu}K_i^{*0\mu}, \quad (V_i^{8\mu})^2 = (\varphi_i^\mu)^2$$

and

$$R_{ij}^{\mu\nu a}(P) = -\frac{\delta_{ij}}{G_2}g^{\mu\nu} - iN_c\,\mathrm{tr}\int_{\Lambda_3}\frac{d^4k}{(2\pi)^4} \times \left[\frac{1}{\not k + \frac{1}{2}\not P - m_q^a}\gamma^\mu f_i^{a,V}\frac{1}{\not k - \frac{1}{2}\not P - m_{q'}^a}\gamma^\nu f_j^{a,V}\right], \tag{44}$$

$$f_1^{a,V} \equiv 1, \quad f_2^{a,V} \equiv f_a^V(\mathbf{k}).$$

To order P^2, one obtains

$$R_{11}^{\mu\nu a} = W_1^a[P^2 g^{\mu\nu} - P^\mu P^\nu - g^{\mu\nu}(\bar{M}_1^a)^2],$$
$$R_{22}^{\mu\nu a} = W_2^a[P^2 g^{\mu\nu} - P^\mu P^\nu - g^{\mu\nu}(\bar{M}_2^a)^2],$$
$$R_{12}^{\mu\nu a} = R_{21}^{\mu\nu a} \tag{45}$$
$$= \bar{\gamma}^a\left[P^2 g^{\mu\nu} - P^\mu P^\nu - \frac{3}{2}\Delta^2 g^{\mu\nu}\delta^{ab}\big|_{b=4,\ldots,7}\right].$$

Here,

$$W_1^a = \frac{8}{3}I_2^a, \quad W_2^a = \frac{8}{3}I_2^{ff_a}, \quad \bar{\gamma}^a = \frac{8}{3}I_2^{f_a}, \tag{46}$$

$$(\bar{M}_1^a)^2 = (W_1^a G_2)^{-1} + \frac{3}{2}\Delta^2\delta^{ab}\big|_{b=4,\ldots,7}, \tag{47}$$

$$(\bar{M}_2^a)^2 = (W_2^a G_2)^{-1} + \frac{3}{2}\Delta^2\delta^{ab}\big|_{b=4,\ldots,7}. \tag{48}$$

After renormalization of the meson fields

$$V_i^{\mu ar} = \sqrt{W_i^a}V_i^{\mu a}, \tag{49}$$

we obtain the Lagrangians

$$\begin{aligned} L_\rho^{(2)} = -\frac{1}{2}[&(g^{\mu\nu}P^2 - P^\mu P^\nu - g^{\mu\nu}M_{\rho_1}^2)\rho_1^\mu\rho_1^\nu \\ &+ 2\Gamma_\rho(g^{\mu\nu}P^2 - P^\mu P^\nu)\rho_1^\mu\rho_2^\nu \\ &+ (g^{\mu\nu}P^2 - P^\mu P^\nu - g^{\mu\nu}M_{\rho_2}^2)\rho_2^\mu\rho_2^\nu], \end{aligned} \tag{50}$$

$$\begin{aligned} L_\varphi^{(2)} = -\frac{1}{2}[&(g^{\mu\nu}P^2 - P^\mu P^\nu - g^{\mu\nu}M_{\varphi_1}^2)\varphi_1^\mu\varphi_1^\nu \\ &+ 2\Gamma_\varphi(g^{\mu\nu}P^2 - P^\mu P^\nu)\varphi_1^\mu\varphi_2^\nu \\ &+ (g^{\mu\nu}P^2 - P^\mu P^\nu - g^{\mu\nu}M_{\varphi_2}^2)\varphi_2^\mu\varphi_2^\nu], \end{aligned} \tag{51}$$

$$\begin{aligned} L_{K^*}^{(2)} = -\frac{1}{2}\Big[&\Big(g^{\mu\nu}P^2 - P^\mu P^\nu - g^{\mu\nu}\Big(\frac{3}{2}\Delta^2 + M_{K_1^*}^2\Big)\Big)K_1^{*\mu}K_1^{*\nu} \\ &+ 2\Gamma_{K^*}\Big(g^{\mu\nu}P^2 - P^\mu P^\nu - g^{\mu\nu}\frac{3}{2}\Delta^2\Big)K_1^{*\mu}K_2^{*\nu} \\ &+ \Big(g^{\mu\nu}P^2 - P^\mu P^\nu - g^{\mu\nu}\Big(\frac{3}{2}\Delta^2 + M_{K_2^*}^2\Big)\Big)K_2^{*\mu}K_2^{*\nu}\Big]. \end{aligned} \tag{52}$$

Here,

$$\begin{aligned} M_{\rho_1}^2 &= \frac{3}{8G_2I_2(m_u, m_u)}, \quad M_{K_1^*}^2 = \frac{3}{8G_2I_2(m_u, m_s)}, \\ M_{\varphi_1}^2 &= \frac{3}{8G_2I_2(m_s, m_s)}, \quad M_{\rho_2}^2 = \frac{3}{8G_2I_2^{ff}(m_u, m_u)}, \\ M_{K_2^*}^2 &= \frac{3}{8G_2I_2^{ff}(m_u, m_s)}, \quad M_{\varphi_2}^2 = \frac{3}{8G_2I_2^{ff}(m_s, m_s)}, \end{aligned} \tag{53}$$

$$\Gamma_{a_{i,j}} = \frac{I_2^{f_a}(m_i, m_j)}{\sqrt{I_2^a(m_i, m_j)I_2^{ff_a}(m_i, m_j)}}. \tag{54}$$

After transformations of the vector meson fields, similar to (33) for the pseudoscalar mesons, the Lagrangians (50)–(52) take the diagonal form

$$\begin{aligned} L_{V^a,\bar{V}^a}^{(2)} = -\frac{1}{2}[&(g^{\mu\nu}(P^2 - M_{V^a}^2) - P^\mu P^\nu)V^{a\mu}V^{a\nu} \\ &+ (g^{\mu\nu}(P^2 - M_{\bar{V}^a}^2) - P^\mu P^\nu)\bar{V}^{a\mu}\bar{V}^{a\nu}], \end{aligned} \tag{55}$$

where V^a and $\bar{V}^a$ are the physical ground- and excited-state vector mesons

$$\begin{aligned} M_{\rho,\bar{\rho}}^2 &= \frac{1}{2(1-\Gamma_\rho^2)} \\ &\times\Big[M_{\rho_1}^2 + M_{\rho_2}^2 \mp \sqrt{(M_{\rho_1}^2 - M_{\rho_2}^2)^2 + (2M_{\rho_1}M_{\rho_2}\Gamma_\rho)^2}\Big], \end{aligned} \tag{56}$$

$$\begin{aligned} M_{\varphi,\bar{\varphi}}^2 &= \frac{1}{2(1-\Gamma_\varphi^2)} \\ &\times\Big[M_{\varphi_1}^2 + M_{\varphi_2}^2 \mp \sqrt{(M_{\varphi_1}^2 - M_{\varphi_2}^2)^2 + (2M_{\varphi_1}M_{\varphi_2}\Gamma_\varphi)^2}\Big], \end{aligned} \tag{57}$$

$$\begin{aligned} M_{K^*,\bar{K}^*}^2 = \frac{1}{2(1-\Gamma_{K^*}^2)}\Big[&M_{K_1^*}^2 + M_{K_2^*}^2 + 3\Delta^2(1-\Gamma_{K^*}^2) \\ &\mp \sqrt{(M_{K_1^*}^2 - M_{K_2^*}^2)^2 + (2M_{K_1^*}^2M_{K_2^*}^2\Gamma_{K^*})^2}\Big]. \end{aligned} \tag{58}$$

5. MODEL PARAMETERS AND MESON MASSES

In the paper [2], there were obtained numerical estimations for the model parameters, meson masses, and weak-decay constants in our model. Here, we only give the values: the constituent quark masses are $m_u \approx m_d \approx 280$ MeV, $m_s \approx 455$ MeV; the cutoff parameter $\Lambda_3 = 1.03$ GeV; the four-quark coupling constants $G_1 = 3.47$ GeV^{-2} and $G_2 = 12.5$ GeV^{-2}; the slope parameters in the form factors $d_{uu} = -1.784$ GeV^{-2}, $d_{us} = -1.757$ GeV^{-2}, $d_{ss} = -1.727$ GeV^{-2}; the external parameters in the form factors $c_{uu}^\pi = 1.37$, $c_{uu}^\rho = 1.32$, $c_{us}^K = 1.45$, $c_{us}^{K^*} = 1.54$, and $c_{ss}^\varphi = 1.41$.

With the model parameters fixed, we obtain the angles θ_a and θ_a^0:

$$\begin{aligned} &\theta_\pi = 59.48^\circ, \quad \theta_\pi^0 = 59.12^\circ, \quad \theta_\rho = 81.8^\circ, \\ &\theta_\rho^0 = 81.5^\circ, \quad \theta_K = 60.2^\circ, \quad \theta_K^0 = 57.13^\circ \\ &\theta_{K^*} = 84.7^\circ, \quad \theta_{K^*}^0 = 59.14^\circ, \quad \theta_\varphi = 68.4^\circ, \\ &\theta_\varphi^0 = 57.13^\circ, \end{aligned} \tag{59}$$

and the meson masses are

$$\begin{aligned} M_\pi &= 136\ \text{MeV}, & M_{\pi'} &= 1.3\ \text{GeV}, \\ M_\rho &= 768\ \text{MeV}, & M_{\rho'} &= 1.49\ \text{GeV}, \\ M_K &= 496\ \text{MeV}, & M_{K'} &= 1.45\ \text{GeV}, \\ M_{K^*} &= 887\ \text{MeV}, & M_{K^{*'}} &= 1.479\ \text{GeV}. \end{aligned} \tag{60}$$

The experimental values are [11]

$$\begin{aligned} M_{\pi^\pm}^{\exp} &= 134.9764 \pm 0.0006\ \text{MeV}, \\ M_{\pi'}^{\exp} &= 1300 \pm 100\ \text{MeV}, \\ M_\rho^{\exp} &= 768.5 \pm 0.6\ \text{MeV}, \\ M_{\rho'}^{\exp} &= 1465 \pm 25\ \text{MeV}, \end{aligned} \tag{61}$$

$$M_{K^\pm}^{\exp} = 493.677 \pm 0.016\ \text{MeV}, \quad M_{K'}^{\exp} \approx 1460\ \text{MeV},$$

$$M_{K^{*\pm}}^{\exp} = 891.59 \pm 0.24\ \text{MeV}, \quad M_{K^{*'}}^{\exp} = 1412 \pm 12\ \text{MeV}.$$

For the weak decay constants, we have

$$\begin{aligned} F_\pi &= 93\ \text{MeV}, \quad F_{\pi'} = 0.57\ \text{MeV}, \\ F_K &= 108\ \text{MeV} \approx 1.16 F_\pi, \quad F_{K'} = 3.3\ \text{MeV}. \end{aligned} \tag{62}$$

Now, we can calculate the strong-decay widths of K' and $K^{*'}$.

6. DECAYS $K^{*'} \longrightarrow K\rho$, $K^{*'} \longrightarrow K^*\pi$, $K^{*'} \longrightarrow K\pi$, $\varphi' \longrightarrow K^*K$, AND $\varphi' \longrightarrow \bar{K}K$

In the framework of our model, the decay modes of the excited strange vector mesons $K^{*'}$ and φ' are represented by the triangle diagrams shown in Figs. 1 and 2. When calculating these diagrams, we keep the lowest possible dependence on the external momenta: squared for the anomaly-type graphs and linear for another type. We omit here the higher order momentum dependence.

As has been mentioned in this paper, every vertex is now momentum dependent and includes form factors defined in Section 3 (see equation (16)). In Figs. 1 and 2, the presence of form factors is marked by black shaded angles in vertices. Each black shaded vertex with a pseudoscalar meson is implied to contain the following linear combination for the ground state

$$\bar{f}_a = \frac{1}{\sin 2\theta_a^0}\left[\frac{\sin(\theta_a + \theta_a^0)}{\sqrt{Z_1^a}} + \frac{\sin(\theta_a - \theta_a^0)}{\sqrt{Z_2^a}} f_a\right] \tag{63}$$

and for an excited state

$$\bar{f}_a' = -\frac{1}{\sin 2\theta_a^0}\left[\frac{\cos(\theta_a + \theta_a^0)}{\sqrt{Z_1^a}} + \frac{\cos(\theta_a - \theta_a^0)}{\sqrt{Z_2^a}} f_a\right], \tag{64}$$

where θ_a and θ_a^0 are the angles defined in Section 3 [see equations (38) and (39)] and f_a is one of the form factors defined in Section 3 [equation (16)]. In the case of vector meson vertices, we have the same linear combinations except that Z_i^a are to be replaced by W_i^a (46), and the related angles and form-factor parameters must be chosen.

Now, we can calculate the decay widths of the excited mesons. Let us start with the process $K^{*'} \longrightarrow K^*\pi$. The corresponding amplitude, $T_{K^{*'} \to K^*\pi}$, has the form

$$T_{K^{*'} \to K^*\pi} = g_{K^{*'} \to K^*\pi} \epsilon_{\mu\nu\alpha\beta} p^\alpha q^\beta \xi^\mu(p|\lambda) \xi^\nu(q|\lambda'), \tag{65}$$

where p and q are the momenta of the $K^{*'}$ and K^* mesons, respectively, and $g_{K^{*'} \to K^*\pi}$ is the (dimensional) coupling constant, which follows from the combination of one-loop integrals

$$\begin{aligned} g_{K^{*'} \to K^*\pi} &= \frac{8 m_s}{m_u^2 - m_s^2} \\ &\times \left(I_2^{\bar{f}_{K^*}' \bar{f}_{K^*} \bar{f}_\pi}(m_u) - I_2^{\bar{f}_{K^*}' \bar{f}_{K^*} \bar{f}_\pi}(m_u, m_s) \right). \end{aligned} \tag{66}$$

Note that in (66), the integrals $I_2^{f \ldots f}$ are defined in the same way as in Section 3, equation (28), except that the form factors f in (28) are replaced by the expressions of type (63) and (64). $\xi_\mu(p|\lambda)$ and $\xi_\nu(q|\lambda')$ are polarized vector wave functions ($\lambda, \lambda' = 1, 2, 3$).

Using (63) and (64), we expand the above expression and rewrite it in terms of I_2^{ff} defined in (28). The

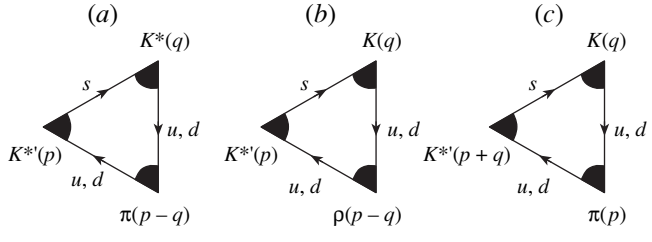

Fig. 1. The one-loop diagram set for the decays of $K^{*'}$.

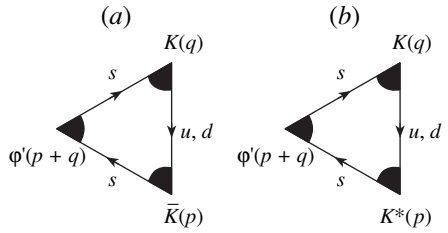

Fig. 2. The one-loop diagram set for the decays of φ'.

result is too lengthy, so we omit it here. For the parameters given in Section 5, we find

$$g_{K^{*\prime}\to K^*\pi}\approx 4\ \text{GeV}^{-1} \tag{67}$$

and the decay width

$$\Gamma_{K^{*\prime}\to K^*\pi} = \frac{g^2_{K^{*\prime}\to K^*\pi}}{4\pi}|\mathbf{p}|^3\approx 90\ \text{MeV}. \tag{68}$$

Here,[2)] $|\mathbf{p}|$ is the 3-momentum of a produced particle in the rest frame of the decaying meson. The lower limit for this value coming from the experiment is ~91 ± 9 MeV [11].

A similar calculation has to be performed for the rest of the $K^{*\prime}$-decay modes under consideration. The coupling constant $g_{K^{*\prime}\to K\rho}$ is derived in the same way as in (66), with the only difference that $\bar f_\pi$ and $\bar f_{K^*}$ are to be replaced by $\bar f_\rho$ and $\bar f_K$. The corresponding amplitude, $T_{K^{*\prime}\to K\rho}$, takes the form

$$T_{K^{*\prime}\to K\rho} = g_{K^{*\prime}\to K\rho}\epsilon_{\mu\nu\alpha\beta}p^\alpha q^\beta\xi^\mu(p|\lambda)\xi^\nu(p-q|\lambda'), \tag{69}$$

where p and q are the momenta of $K^{*\prime}$ and K mesons, respectively, and

$$g_{K^{*\prime}\to K\rho} = \frac{8m_s}{m_u^2-m_s^2} \times\left(I_2^{\bar f'_{K^*}\bar f_K\bar f_\rho}(m_u) - I_2^{\bar f'_{K^*}\bar f_K\bar f_\rho}(m_u, m_s)\right). \tag{70}$$

The corresponding decay width follows from (69) and (70) via integration of the squared module of the decay amplitude over the phase space of the final state

$$\Gamma_{K^{*\prime}\to K\rho} = \frac{g^2_{K^{*\prime}\to K\rho}}{4\pi}|\mathbf{p}|^3. \tag{71}$$

For the parameters given in Section 5, one has

$$g_{K^{*\prime}\to K\rho}\approx 3\ \text{GeV}^{-1}, \tag{72}$$

$$\Gamma_{K^{*\prime}\to K\rho}\approx 20\ \text{MeV}. \tag{73}$$

From the experiment, the upper limit for this process is $\Gamma^{\text{exp}}_{K^{*\prime}\to K\rho} < 16\pm 1.5$ MeV.

The process $K^{*\prime}\longrightarrow K\pi$ is described by the amplitude

$$T_{K^{*\prime}\to K\pi} = i\frac{g_{K^{*\prime}\to K\pi}}{2}(q-p)^\mu\xi_\mu(p+q|\lambda), \tag{74}$$

where p and q are the momenta of π and K, and ξ_μ is the $K^{*\prime}$ wave function. The coupling constant $g_{K^{*\prime}\to K\pi}$ is presented by the one-loop integral

$$g_{K^{*\prime}\to K\pi} = 4I_2^{\bar f'_{K^*}\bar f_K\bar f_\pi}(m_u, m_s)\approx 2, \tag{75}$$

and the decay width is

$$\Gamma_{K^{*\prime}\to K\pi} = \frac{g^2_{K^{*\prime}\to K\pi}|\mathbf{p}|^3}{8\pi M^2_{K^{*\prime}}}\approx 20\ \text{MeV}. \tag{76}$$

The experimental value is 15 ± 5 MeV [11].

The mesons with hidden strangeness (φ') are treated in the same way as $K^{*\prime}$. We consider the two decay modes: $\varphi'\longrightarrow KK^*$ and $\varphi'\longrightarrow \bar K K$. Their amplitudes are

$$T_{\varphi'\to KK^*} = g_{\varphi'\to KK^*}\epsilon_{\mu\nu\alpha\beta}p^\alpha q^\beta\xi^\mu(p+q|\lambda)\xi^\nu(p|\lambda'), \tag{77}$$

$$T_{\varphi'\to\bar KK} = ig_{\varphi'\to\bar KK}(p-q)_\mu\xi^\mu(p+q|\lambda). \tag{78}$$

Here, ξ_μ and ξ_ν are the wave functions of the φ' and K^* mesons, and p and q are the momenta of the K and K^* mesons. The related coupling constants are

$$g_{\varphi'\to KK^*} = \frac{8m_u}{m_s^2-m_u^2} \times\left(I_2^{\bar f'_\phi\bar f_{K^*}\bar f_K}(m_s) - I_2^{\bar f'_\phi\bar f_{K^*}\bar f_K}(m_u, m_s)\right), \tag{79}$$

$$g_{\varphi'\to\bar KK} = 4I_2^{\bar f'_\phi\bar f_{K^*}\bar f_K}(m_s). \tag{80}$$

Thus, the decay widths are estimated as

$$\Gamma_{\varphi'\to KK^*}\approx 90\ \text{MeV}, \tag{81}$$

$$\Gamma_{\varphi'\to\bar KK}\approx 10\ \text{MeV}. \tag{82}$$

Unfortunately, there are no reliable data from the experiment on the partial decay widths for $\varphi'\longrightarrow KK^*$ and $\varphi'\longrightarrow\bar KK$ except the total width of φ' being estimated as 150 ±50 MeV [11]. However, the dominance of the process $\varphi'\longrightarrow KK^*$ is observed, which is in agreement with our result.

7. DECAYS $K'\longrightarrow K^*\pi$, $K'\longrightarrow K\rho$, AND $K'\longrightarrow K\pi\pi$

Following the scheme outlined in the previous section, we first estimate the $K'\longrightarrow K^*\pi$ and $K'\longrightarrow K\rho$ decay widths (see Fig. 3). Their amplitudes are

$$T_{K'\to K^*\pi} = ig_{K'\to K^*\pi}(p+q)^\mu\xi_\mu(p-q|\lambda), \tag{83}$$

$$T_{K'\to K\rho} = ig_{K'\to K\rho}(p+q)^\mu\xi_\mu(p-q|\lambda). \tag{84}$$

Here, p is the momentum of K', q is the momentum of $\pi(K)$, and ξ_μ is the vector-meson wave function. The

[2)] The value for $|\mathbf{p}|$ can be obtained from the formula $|\mathbf{p}| = \sqrt{(M^2_{K^{*\prime}}-(M_{K^*}+M_\pi)^2)(M^2_{K^{*\prime}}-(M_{K^*}-M_\pi)^2)}/2M_{K^{*\prime}}$.

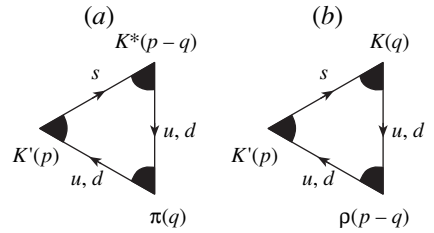

Fig. 3. The one-loop diagram set for the decays of K'.

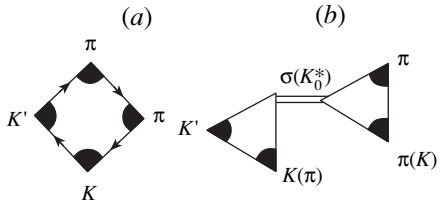

Fig. 4. The one-loop diagram set for the decay $K' \longrightarrow K2\pi$.

coupling constants are

$$g_{K' \to K^*\pi} = 4I_2^{\bar{f}'_K \bar{f}_{K^*} \bar{f}_\pi}(m_u, m_s), \quad (85)$$

$$g_{K' \to K\rho} = 4I_2^{\bar{f}'_K \bar{f}_K \bar{f}_\rho}(m_u, m_s). \quad (86)$$

By calculating the integrals in the above formulas, we have $g_{K' \to K^*\pi} \approx -1.4$ and $g_{K' \to K\rho} \approx -1.2$. The decay widths thereby are

$$\Gamma_{K' \to K^*\pi} \approx 100 \text{ MeV}, \quad (87)$$

$$\Gamma_{K' \to K\rho} \approx 50 \text{ MeV}. \quad (88)$$

These processes have been seen in the experiment and the decay widths are[3)] [11]

$$\Gamma^{\text{exp}}_{K' \to K^*\pi} \sim 109 \text{ MeV}, \quad (89)$$

$$\Gamma^{\text{exp}}_{K' \to K\rho} \sim 34 \text{ MeV}. \quad (90)$$

The remaining decay $K' \longrightarrow K\pi\pi$ into three particles requires more complicated calculations. In this case, one must consider a box diagram Fig. 4*a* and two types of diagrams Fig. 4*b* with intermediate σ and K_0^* resonances. The diagrams for resonant channels are approximated with the use of the relativistic Breit–Wigner function. The integration over the kinematically relevant range in the phase space for final states gives

$$\Gamma_{K' \to K\pi\pi} \sim 1 \text{ MeV}. \quad (91)$$

[3)]The accuracy of the measurements carried out for the decays of K' is not given in [11].

8. SUMMARY AND CONCLUSIONS

In the standard NJL model for the description of the interaction of mesons, it is conventional to use the one-loop quark approximation, where the external momentum dependence in quark loops is neglected. This allows one to obtain, in this approximation, the chiral symmetric phenomenological Lagrangian [4–9], which gives a good description of the low-energy meson physics in the energy range of an order of 1 GeV [12]. In this paper, we have used a similar method for describing the interaction of the excited mesons. Insofar as the masses of the excited mesons noticeably exceed 1 GeV, we claim only a qualitative description rather than quantitative agreement with the experiment. For the light excited mesons, we have achieved results closer to the experiment [3], while for heavier strange mesons we are only in qualitative agreement with experimental data. One should note that the description of all the decays has been obtained without introducing new parameters, besides those used for the description of the mass spectrum.

In this work, we have shown that the dominant decays of the excited vector mesons $K^{*\prime}$ and φ' are the decays $K^{*\prime} \longrightarrow K^*\pi(\rho K)$ and $\varphi' \longrightarrow KK^*$, which go through the triangle quark loops of the anomaly type. These results are close to the experiment [11]. The decays of the type $K^{*\prime} \longrightarrow K\pi$ and $\varphi' \longrightarrow K\bar{K}$, going through the other (not anomaly type) quark diagrams, have smaller decay widths, which is also in agreement with the experiment.

On the other hand, the main decays of the K' meson $K' \longrightarrow K^*\pi$, $K' \longrightarrow K\rho$, and $K' \longrightarrow K\pi\pi$ are described by the quark diagrams, which are similar to those for the decay $\pi' \longrightarrow \rho\pi$ (see [3]). The dominant decays here are the decays $K' \longrightarrow K^*\pi$ and $K' \longrightarrow K\rho$. These results do not contradict (qualitatively) the recent experimental data. So one can see that our model satisfactorily describes not only the masses and weak-decay constants of the radially excited mesons [1, 2] but also their decay widths.

We would like to emphasize once more that we did not use any additional parameter for description of the decays (see also [3]). The model is too simple to claim a more exact quantitative description of the meson-decay widths.

A similar calculation has also been made in the $3P_1$ potential model [13]. Nonlocal versions of chiral quark models for the description of excited meson states have also been considered in various works (see, for instance, [7, 14]). In [15], a generalized NJL model including a relativistic model of confinement was used to study the radial excitations of pseudoscalar and vector mesons.

In our further work, we are going to describe the masses and decay widths of the excited states of η and η' mesons.

ACKNOWLEDGMENTS

The work was supported by the Heisenberg–Landau Program 1998 and by the Russian Foundation for Basic Research, project no. 98-02-16135.

REFERENCES

1. M. K. Volkov and Ch. Weiss, Phys. Rev. D **56**, 221 (1997); hep-ph/9608347.
2. M. K. Volkov, Yad. Fiz. **60**, 2094 (1997).
3. M. K. Volkov, D. Ebert, and M. Nagy, hep-ph/9705334; Int. J. Mod. Phys. A **13**, 5443 (1998).
4. M. K. Volkov and D. Ebert, Yad. Fiz. **36**, 1265 (1982); Z. Phys. C **16**, 205 (1983); M. K. Volkov, Ann. Phys. (New York) **157**, 282 (1984).
5. M. K. Volkov, Sov. J. Part. Nucl. **17**, 186 (1986).
6. D. Ebert and H. Reinhardt, Nucl. Phys. B **271**, 188 (1986).
7. A. A. Andrianov and V. A. Andrianov, Int. J. Mod. Phys. A **8**, 1981 (1993); Nucl. Phys. B (Proc. Suppl.) **39**, 257 (1995).
8. H. Vogl and W. Weise, Prog. Part. Nucl. Phys. **27**, 195 (1991).
9. S. P. Klevansky, Rev. Mod. Phys. **64**, 649 (1992).
10. R. P. Feynman, M. Kislinger, and F. Ravndal, Phys. Rev. D **3**, 2706 (1971).
11. Review of Particle Properties (C. Caso *et al.*), Eur. Phys. J. C **3**, 1 (1998).
12. S. Gasiorovicz and D. A. Geffen, Rev. Mod. Phys. **41**, 531 (1969).
13. S. B. Gerasimov and A. B. Govorkov, Z. Phys. C **32**, 405 (1986).
14. V. Ja. Burdanov, G. V. Efimov, S. N. Nedelko, *et al.*, Phys. Rev. D **54**, 4483 (1996).
15. L. S. Celenza, Bo Huang, and C. M. Shakin, Preprint Nos. BCCNT 97/071/271, BCCNT 97/091/266.

Physics of Atomic Nuclei, Vol. 63, No. 3, 2000, pp. 464–469. From Yadernaya Fizika, Vol. 63, No. 3, 2000, pp. 536–541.

ELEMENTARY PARTICLES AND FIELDS
Theory

Chiral $SU(2) \times SU(2)$ Model with Infrared Quark Confinement*

M. K. Volkov and V. L. Yudichev

Joint Institute for Nuclear Research, Dubna, Moscow oblast, 141980 Russia

Received January 20, 1999

Abstract—An $SU(2) \times SU(2)$ chiral quark model describing the properties and interaction of pions and scalar and vector mesons is considered. The confinement of quarks is introduced in the model by means of an infrared cut-off in the one-loop quark diagrams. This cutoff gives rise to the elimination of the unphysical thresholds of the quark–antiquark pair production. The π–a_1 transitions are taken into account. The model conserves all low-energy theorems. The masses of mesons and the widths of the decays $\rho \longrightarrow 2\pi$ and $\sigma \longrightarrow 2\pi$ are calculated.

1. INTRODUCTION

The Nambu–Jona-Lasinio (NJL) model is a convenient semiphenomenological quark model for the description of low-energy meson physics [1–5]. Within this model, the mechanism of spontaneous breaking of chiral symmetry (SBCS) is realized in a simple and transparent way, and the low-energy theorems are fulfilled.

Unfortunately, the ordinary NJL model fails to prevent hadrons from decaying into free quarks, which makes the realistic description of hadron properties on their mass shell questionable. The exact solution of this problem seems to be a very difficult task. However, different methods have been proposed for its solution [6–10]. In the present work, we discuss a new approach which is similar to that suggested in [10] where an infrared (IR) cutoff has been used to develop a quark propagator without poles. In our approach, the quark propagator is of the usual form (with quasiparticle pole), but due to the IR cutoff, the pole does not lie within the integration interval for the quark loops. This method of taking into account the phenomenon of confinement is based on the idea of combining the NJL and bag models [11].

Thus, together with the ultraviolet (UV) cutoff, which is necessary for the elimination of the UV divergences, we introduce the IR cutoff and thereby divide the momentum space into three domains. In Fig. 1, these domains are represented in the coordinate space.

The first domain corresponds to short distances (large momenta), where quarks are not confined and the chiral symmetry is not spontaneously broken. This domain is withdrawn by the UV cutoff Λ.

The second domain corresponds to long distances (IR region), and here we have the confinement of quarks. We truncate this region from the integration over the internal momenta in quark loops, following thereby the idea of the bag model. For this purpose, we introduce a new parameter λ.

Finally, there remains only the third domain ($\lambda^2 \le \mathbf{p}^2 \le \Lambda^2$), where SBCS takes place, the quark condensate exists, and the quark loops have no imaginary parts. In other words, quark–antiquark thresholds do not appear when calculating quark loops even if the mass of the decaying meson exceeds the effective mass of the free quark–antiquark state. Therefore, we can use quark propagators with constant, momentum independent masses (constituent masses).

The first attempt to produce an NJL model of this type has been made in [12], where only the scalar and pseudoscalar mesons were considered. Now, we suggest a more general version of this model where the scalar, pseudoscalar, and vector mesons can be described, and the possibility of π–a_1 transitions is taken into account.

In Section 2, we give the effective chiral quark Lagrangian and the gap equation describing SBCS. The pion-mass formula is also deduced, and it is shown that the pion is a Goldstone boson in the chiral limit. In Sec-

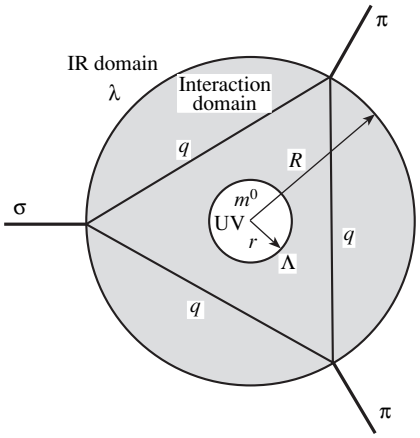

Fig. 1. Three domains in the momentum space, defined by the UV and IR cutoffs.

* This article was submitted by the authors in English.

Model parameters, the mass of the σ meson and first decay width for different values of the ratio λ/m of the IR cutoff to the constituent quark mass

λ/m	m, MeV	m^0, MeV	Λ, GeV	G_1, GeV^{-2}	G_2, GeV^{-2}	$-\langle\bar{q}q\rangle^{1/3}$, MeV	M_σ, MeV	Γ, MeV
0.7	330	1.54	1.11	3.108	9.683	298	670	1280
0.8	310	1.58	1.13	2.967	8.629	296	630	970
0.9	300	1.49	1.18	2.698	8.949	302	608	830
1.0	290	1.45	1.21	2.555	9.222	304	590	721
1.1	280	1.37	1.26	2.339	9.322	309	570	614
1.2	270	1.32	1.33	2.079	9.273	318	550	536

tion 3, the scalar meson (σ) is considered, and it is demonstrated that the quark loop with two σ-meson legs does not have the imaginary part if we use the IR cutoff. The model parameters are fitted in Section 4. There we consider the decay $\rho \longrightarrow 2\pi$ through the triangle quark loop where the quark–antiquark threshold does not appear when the IR cutoff is applied. In Section 5, the σ-meson mass and the decay $\sigma \longrightarrow 2\pi$ width are estimated. In the last section, we discuss the obtained results and give some proposals for applying this model in the investigation of the behavior of mesons in a hot and dense medium in the vicinity of the critical point. The values of the model parameters, the σ-meson mass, and the $\sigma \longrightarrow 2\pi$ decay width are given in the table for different values of λ.

2. $SU(2) \times SU(2)$ LAGRANGIAN, GAP EQUATION, AND PION MASS FORMULA

Let us consider an $SU(2) \times SU(2)$ NJL model defined by the Lagrangian

$$\mathcal{L}_q = \bar{q}(i\partial\!\!\!/ - m^0)q + \frac{G_1}{2}[(\bar{q}q)^2 + (\bar{q}i\gamma_5\boldsymbol{\tau}q)^2] - \frac{G_2}{2}[(\bar{q}\gamma_\mu\boldsymbol{\tau}q)^2 + (\bar{q}\gamma_5\gamma_\mu\boldsymbol{\tau}q)^2]. \quad (1)$$

After the bosonization of the four-fermion model (1), one obtains its equivalent representation in terms of the scalar (σ), pseudoscalar (**π**), vector ($\boldsymbol{\rho}_\mu$), and axial-vector ($\mathbf{a}_{1\mu}$) mesons

$$\mathcal{L}_{\text{meson}} = -\frac{\tilde{\sigma}^2 + \boldsymbol{\pi}^2}{2G_1} + \frac{\boldsymbol{\rho}_\mu^2 + \mathbf{a}_1^2}{2G_2} - i\,\mathrm{tr}\ln\left\{1 + \frac{1}{i\partial\!\!\!/ - m}[\sigma + i\gamma_5\boldsymbol{\tau}\cdot\boldsymbol{\pi} + \boldsymbol{\tau}\cdot\hat{\boldsymbol{\rho}}_\mu + \gamma_5\tau\hat{\mathbf{a}}_{1\mu}]\right\}. \quad (2)$$

Here, the scalar fields σ and $\tilde{\sigma}$ satisfy the relation

$$-m^0 + \tilde{\sigma} = -m + \sigma, \quad (3)$$

where m^0 is the current-quark mass, m is the constituent quark mass, and the vacuum expectation of σ vanishes: $\langle\sigma\rangle_0 = 0$. Then, from the condition

$$\left.\frac{\delta\mathcal{L}}{\delta\sigma}\right|_{\sigma=0,\,\pi=0} = 0, \quad (4)$$

one obtains the gap equation[1)]

$$m^0 = m(1 - 8G_1 I_1^{(\lambda\Lambda)}(m)) \approx m(1 - 8G_1 I_1^{(0\Lambda)}(m)) = m + 2G_1\langle\bar{q}q\rangle_0, \quad (5)$$

where $\langle\bar{q}q\rangle_0$ is the quark condensate. $I_1^{(ab)}(m)$ is obtained from the Λ^2-divergent integral

$$I_1(m) = -i\frac{N_c}{(2\pi)^4}\int\frac{d^4k}{m^2 - k^2 - i\varepsilon} \quad (6)$$

by applying the three-dimensional UV ($b = \Lambda$) and IR ($a = \lambda$) cutoffs

$$I_1^{(\lambda\Lambda)}(m) = \frac{N_c}{(2\pi)^2}\int_\lambda^\Lambda dk\frac{k^2}{E(k)} = \frac{N_c m^2}{8\pi^2}[x\sqrt{x^2+1} - \ln(x + \sqrt{x^2+1})]\Big|_{\lambda/m}^{\Lambda/m}, \quad (7)$$

where $E(k) = \sqrt{k^2 + m^2}$ and N_c is the number of colors.

Now, let us consider the free part of the Lagrangian (2) for pion fields in the quark one-loop approximation (see Fig. 2)[2)]

$$\mathcal{L}_\pi^{(2)} = -\frac{\pi^2}{2}\left\{\frac{1}{G_1} - 8I_1^{(\lambda\Lambda)}(m) - 4p^2 I_2^{(\lambda\Lambda)}(p^2, m)\right\}, \quad (8)$$

[1)]Here, the dependence of the integral $I_1(m)$ on λ can be neglected since (1) the value of the integral is defined by the UV cutoff Λ and (2) $I_1(m)$ does not depend on external momenta and, therefore, does not have the imaginary part. Hence, there is no need for an IR cutoff.

[2)]The braced expression can be written as $1/G_1 + \Pi_\pi(p)$, where $\Pi_\pi(p)$ is the polarization operator of the pion.

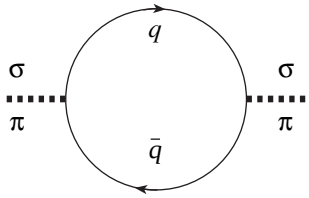

Fig. 2. The quark-loop diagram for the polarization operator of σ and π.

where $I_2^{(\lambda\Lambda)}(p^2, m)$ is a logarithmically growing integral:

$$I_2^{(\lambda\Lambda)}(p^2, m) = -i\frac{N_c}{(2\pi)^4} \times \int \frac{d^4k}{(m^2 - k^2 - i\varepsilon)(m^2 - (k-p)^2 - i\varepsilon)} = \frac{N_c}{2\pi^2}\int_\lambda^\Lambda dk \frac{k^2}{E(4E^2 - p^2 + i\varepsilon)}. \quad (9)$$

In order to express (8) through physical fields, we renormalize the pions

$$\boldsymbol{\pi} = g_\pi(M_\pi)\boldsymbol{\pi}^r, \qquad g_\pi(M_\pi) \approx g_\pi(0) = [4I_2^{(\lambda\Lambda)}(0, m)]^{-1/2}. \quad (10)$$

Here, as the pion mass M_π is small, we can neglect $p^2 \sim M_\pi^2$ in $I_2^{(\lambda\Lambda)}(p^2, m)$:

$$I_2^{(\lambda\Lambda)}(p^2, m) \approx I_2^{(\lambda\Lambda)}(0, m) = \frac{N_c}{8\pi^2}[\ln(x + \sqrt{x^2+1}) - (1 + 1/x^2)^{-1/2}]\Big|_{\lambda/m}^{\Lambda/m}. \quad (11)$$

Moreover, an additional renormalization factor $\sqrt{Z}$ appears for pions when we take into account the π–a_1 transitions [3]:

$$\bar{g}_\pi = g_\pi\sqrt{Z}, \quad Z^{-1} = 1 - 6m^2/M_{a_1}^2, \quad (12)$$

where $M_{a_1} = 1230$ MeV is the mass of the a_1 meson. Thus, we obtain the following expression for the pion mass:

$$M_\pi^2 = \bar{g}_\pi^2\left[\frac{1}{G_1} - 8I_1^{(\lambda\Lambda)}(m)\right], \quad (13)$$

which can be given the form of the Gell-Mann–Oakes–Renner relation

$$M_\pi^2 \approx -2\frac{m^0\langle\bar{q}q\rangle_0}{F_\pi^2}, \quad (14)$$

where the Goldberger–Treiman relation (21) and the gap equation (5) have been used. We can see that this pion-mass formula is in accordance with the Goldstone theorem since, for $m^0 = 0$, the pion mass vanishes and a pion plays the role of the Goldstone boson.

3. THE σ MESON AND IR CONFINEMENT

The free part of the Lagrangian (2) for the σ meson in the one-loop approximation (see Fig. 2) has the following form:

$$\mathcal{L}_\sigma^{(2)} = -\frac{\sigma^2}{2} \times \left\{\frac{1}{G_1} - 8I_1^{(\lambda\Lambda)}(m) - 4(p^2 - 4m^2)I_2^{(\lambda\lambda)}(p^2, m)\right\}. \quad (15)$$

After the renormalization of the σ field

$$\sigma = g_\sigma(M_\sigma)\sigma^r, \qquad g_\sigma(M_\sigma) = [4I_2^{(\lambda\Lambda)}(M_\sigma^2, m)]^{-1/2}, \quad (16)$$

we obtain the expression for the σ-meson mass

$$M_\sigma^2 = g_\sigma^2(M_\sigma)\left[\frac{1}{G_1} - 8I_1^{(\lambda\Lambda)}(m)\right] + 4m^2 = r^2M_\pi^2 + 4m^2, \qquad r = \frac{g_\sigma(M_\sigma)}{g_\pi(M_\pi)}. \quad (17)$$

Now, let us consider more carefully the integral $I_2^{(\lambda\Lambda)}(p^2, m)$:

$$I_2^{(\lambda\Lambda)}(M_\sigma^2, m) = \frac{N_c}{2\pi^2}\int_\lambda^\Lambda dk \frac{k^2}{E(4E^2 - M_\sigma^2 + i\varepsilon)}. \quad (18)$$

When $\lambda = 0$, this integral aquires an imaginary part. Indeed, the integrand in (18) is singular when its denominator is equal to zero:

$$4E^2 - M_\sigma^2 = 4k^2 - r^2M_\pi^2 = 0. \quad (19)$$

The imaginary part appears if the singularity ($k = rM_\pi/2$) lies within the integration interval. Therefore, if we apply the IR cutoff

$$\lambda = cm, \quad \text{where} \quad c > rM_\pi/2m, \quad (20)$$

then $\Lambda > k > \lambda > rM_\pi/2$ and the integral is real, which is equivalent to the absence of the quark–antiquark threshold, or confinement.

4. MODEL PARAMETERS

In this model we have four input parameters [13]:

(1) the pion-decay constant $F_\pi = 92.4$ MeV describing the weak-decay process $\pi \longrightarrow \bar{\mu}\nu$;

(2) the ρ-meson-decay constant $g_\rho^{\exp} = 6.14$ describing the decay $\rho \longrightarrow 2\pi$;

(3) the pion mass $M_\pi = 140$ MeV;

(4) the ρ-meson mass $M_\rho = 770$ MeV.

The output parameters are

(1) the constituent quark mass m,

(2) the 3-momentum UV cutoff parameter Λ,

(3) the scalar (pseudoscalar) four-quark coupling constant G_1,

(4) the vector (axial-vector) four-quark coupling constant G_2.

The IR cutoff λ is an arbitrary parameter of our model which is to satisfy the condition (20).

In order to fix the output parameters, we use the following four equations:

(1) The Goldberger–Treiman relation

$$m/F_\pi = \bar{g}_\pi(0) = g_\pi(0)\sqrt{Z}. \tag{21}$$

(2) The decay width of the process $\rho \longrightarrow 2\pi$. The amplitude of this process is of the form

$$T_{\rho\to 2\pi} = i\frac{g_\rho^{\exp}}{2}(p_{\pi^+} - p_{\pi^-})^\nu \rho_\nu^0 \pi^+ \pi^-. \tag{22}$$

In the one-loop approximation (see Fig. 3), we obtain the following expression for $g_\rho^{\exp}$:

$$\begin{aligned} g_\rho^{\exp} &= Z^{-1} g_\rho(M_\rho)\bar{g}_\pi^2(M_\pi)[4I_2^{(\lambda\Lambda)}(0, m) + \Delta] \\ &= \left(\frac{2}{3}I_2^{(\lambda\Lambda)}(M_\rho^2, m)\right)^{-1/2}\left[1 + \frac{\Delta}{4I_2^{(\lambda\Lambda)}(0, m)}\right], \end{aligned} \tag{23}$$

where $g_\rho(M_\rho) = \left[\frac{2}{3}I_2^{(\lambda\Lambda)}(M_\rho^2, m)\right]^{-1/2}$ (see [3]) and $\Delta = \frac{3}{8\pi^2}\left(1 + \frac{2M_\pi^2}{3m^2}\right)$ is the finite part of the quark triangle diagram (Fig. 3). The factor Z^{-1} appears due to the π–a_1 transitions (see [3]). From these two equations one can find m and Λ.

(3) The coupling constant G_1 is defined by the mass formula

$$M_\pi^2 = \bar{g}_\pi^2\left[\frac{1}{G_1} - 8I_1^{(\lambda\Lambda)}(m)\right]. \tag{24}$$

(4) The coupling constant G_2 is found from the mass formula for M_ρ [3]

$$M_\rho^2 = \frac{g_\rho^2(M_\rho)}{G_2} = \frac{3}{8G_2 I_2^{(\lambda\Lambda)}(M_\rho^2, m)}. \tag{25}$$

By means of the gap equation (5), we define the current quark mass m^0.

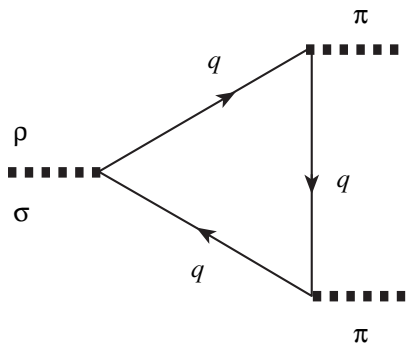

Fig. 3. The triangle quark diagram describing the decay of the ρ and σ mesons into two pions.

5. THE σ-MESON MASS AND THE DECAY $\sigma \longrightarrow 2\pi$

The mass of the σ-meson is given by (17). Using this formula for the IR cutoff $\lambda = m$, we obtain[3)]

$$M_\sigma = 590 \text{ MeV}. \tag{26}$$

The decay $\sigma \longrightarrow 2\pi$ occurs through the quark triangle diagram (see Fig. 3). This diagram also satisfies the confinement condition (20) if we use the IR cutoff $\lambda = m$. The amplitude of the process $\sigma \longrightarrow 2\pi$ has the form

$$\begin{aligned} T_{\sigma\to 2\pi} &= 8mg_\sigma(M_\sigma)\bar{g}_\pi^2(M_\pi) \\ &\times [I_2^{(\lambda\Lambda)}(M_\sigma^2, m) + \mathcal{T}(M_\sigma, M_\pi, m)]\sigma\pi^2, \end{aligned} \tag{27}$$

where

$$\begin{aligned} &\mathcal{T}(M_\sigma, M_\pi, m) \\ &= \frac{1}{2}(M_\sigma^2 - 2M_\pi^2)I_3(p_1, p_2, m)\Big|_{p_1^2 = p_2^2 = M_\pi^2} \end{aligned} \tag{28}$$

and

$$\begin{aligned} I_3(p_1, p_2, m) &= -i\frac{N_c}{(2\pi)^4} \\ &\times \int \frac{d^4k}{(k^2 - m^2)((k + p_1)^2 - m^2)((k - p_2)^2 - m^2)}. \end{aligned} \tag{29}$$

Neglecting the external pion momenta in $I_3(p_1, p_2, m)$, we obtain

$$\begin{aligned} I_3(p_1, p_2, m) &\approx -i\frac{N_c}{(2\pi)^4}\int \frac{d^4k}{(k^2 - m^2)^3} = -\frac{3N_c}{32\pi^2}\int_\lambda^\Lambda dk\frac{k^2}{E^5} \\ &= -\frac{N_c}{32\pi^2 m^2}\left[\left(1 + \frac{m^2}{\Lambda^2}\right)^{-3/2} - \left(1 + \frac{m^2}{\lambda^2}\right)^{-3/2}\right]. \end{aligned} \tag{30}$$

[3)]See table for different choices of the ratio λ/m.

Then the decay width of the σ meson is found to be

$$\Gamma_{\sigma\to 2\pi} = \frac{3}{2\pi}\left(\frac{m^3}{g_\sigma(M_\sigma)F_\pi^2}\right)^2 \times \frac{(1+\delta)^2}{M_\sigma^2}\sqrt{M_\sigma^2 - 4M_\pi^2} \approx 720\ \text{MeV}, \quad (31)$$

where

$$\delta = \frac{\mathcal{T}(M_\sigma, M_\pi, m)}{I_2^{(\lambda\Lambda)}(0, m)} \approx -0.22. \quad (32)$$

Therefore, one can see that our estimates for the σ-meson mass and its decay width are in agreement with the experimental data [13] (see also [14, 15]):

$$M_\sigma^{\exp} = 400\text{–}1200\ \text{MeV},\ \Gamma_\sigma^{\exp} = 600\text{–}1000\ \text{MeV}. \quad (33)$$

From this, one can conclude that the NJL model with the IR cutoff satisfies both of the low-energy theorems together with SBCS and describes the low-energy physics of the scalar, pseudoscalar, and vector mesons.

6. DISCUSSION AND CONCLUSION

In this paper, we have investigated the extension of the NJL model for the light-nonstrange-meson sector of QCD, where the interaction of *u* and *d* quarks is represented by four-fermion vertices and the phenomenon of quark confinement is taken into account. This extension of the NJL model describes the properties of the π, ρ, and σ mesons in good agreement with the experiment and with the low-energy theorems. The model parameters are obtained by fitting the model so that it reproduces the experimental values of the pion and ρ-meson masses, the pion-decay constant F_π-, and the $\rho \longrightarrow \pi\pi$ decay constant g_ρ. Moreover, it was shown that, for the π, ρ, and σ mesons, the nonphysical quark–antiquark thresholds do not appear if the IR cutoff is applied.

The prediction of the σ-meson mass and its decay width for different values of IR cutoff is given in the table, together with the model parameters. From this table and the experimental data [13], one can conclude that the parameter λ is allowed to have values within the interval $0.8 \le \lambda \le 1.2$. The value of the current-quark mass turned out to be too low because, in our model, the quark condensate exceeds its conventional value—$(250\ \text{MeV})^3$. This can be seen from (14).

Insofar as the NJL model is a semiphenomenological model based on the effective chiral four-quark interaction motivated by QCD on the phenomenological level, the introduction of quark confinement in our model through IR cutoff (without considering the gluon exchanges, instanton interactions, etc.) is in the spirit of this model.

An important application of our model is the description of the meson properties in a hot and dense medium. The standard NJL model has been already used for this purpose [5, 16, 17], where the temperature dependence of the masses of quarks and mesons and of the Yukawa coupling constants was found. The IR cutoff λ is expressed through the constituent quark mass *m* (or the quark condensate $\langle\bar{q}q\rangle_0$), which is lowered when the temperature (*T*) and chemical potential (μ) increase. Therefore, the IR cutoff will also reduce with *T* and μ. This will at length result in the deconfinement of quarks near the critical point. The temperature at which deconfinement takes place can be found from the condition [see also (19)]

$$4E_{\text{low}}^2 - M_{\text{meson}}^2 = 4(1+c^2)m^2 - M_{\text{meson}}^2 \le 0, \quad (34)$$

where E_{low} is the lowest energy of the quark in the quark loop. Then, for the pion, the temperature of deconfinement follows from the condition (34)

$$m(T_\pi^{\text{dec}}) \approx M_\pi/2\sqrt{1+c^2}. \quad (35)$$

In the vicinity of the critical point, the constituent quark mass is reduced with *T* too suddenly, and the pion mass increases gradually (see [17]). Therefore, when the constituent quark mass is as light as 40–50 MeV, the decay of a pion into free quarks becomes possible.

For the σ meson, we obtain a lower value of T^{dec}:

$$m(T_\sigma^{\text{dec}}) \approx M_\pi r/c. \quad (36)$$

The decay channel $\sigma \longrightarrow 2\pi$ is closed when $M_\sigma \le 2M_\pi$ [see (31)] and then

$$m(T_{\sigma \not\to 2\pi}) \approx \frac{\sqrt{3}}{2}M_\pi r \sim 100\ \text{MeV}. \quad (37)$$

Note that, first of all, the quark deconfinement occurs for the ρ meson, where we have the lowest T^{dec} {see (34) and [17]}

$$m(T_\rho^{\text{dec}}) \approx \frac{M_\rho}{2\sqrt{1+c^2}} \approx 250\ \text{MeV}. \quad (38)$$

Thus, we come to the following picture. At low *T* and μ, the σ meson is unstable since it has a large decay width (31) into two pions. The pion is stable since electroweak-decay channels can be neglected here, in comparison to the strong ones. The ρ meson takes an intermediate position between σ and π, having the $\rho \longrightarrow 2\pi$ strong decay width 150 MeV. When *T* increases, an extra channel emerges: $\rho \longrightarrow \bar{q}q$. At higher *T*, there is a temperature range where the decays of σ both into 2π and into $\bar{q}q$ are forbidden, and the σ meson turns out to be a stable particle. For $T > T_\sigma^{\text{dec}}$, the σ meson is allowed to decay into a $\bar{q}q$ pair, and only the pion remains stable. Finally, near the critical point, when $T \ge T_\pi^{\text{dec}}$, all the particles decay into free quarks.

The process of deconfinement is entirely reflected in the following sequence of inequalities

$$T_\rho^{\rm dec} < T_{\sigma \to 2\pi} < T_\sigma^{\rm dec} < T_\pi^{\rm dec}, \quad (39)$$

where we have four different temperatures separating different phases. Therefore, one can see that the transition of the hadron matter to the quark–gluon plasma occurs, not suddenly, but in a smooth manner.

In our further work, we are going to make a more careful investigation of these processes, which can play an important role for the explanation and prediction of the signals coming from ultrarelativistic heavy-ion collisions, as well as ensuring restoration to the chiral symmetry and the quark deconfinement in the hadron matter at the transition to the quark–gluon plasma. For example, among the possible visible effects associated with the quark deconfinement, there is the low-mass dilepton enhancement observed by the CERES collaboration [18].

ACKNOWLEDGMENTS

This work has been supported by the Russian Foundation for Basic Research, project no. 98-02-16135, and the Heisenberg–Landau program, 1998–1999.

REFERENCES

1. T. Eguchi, Phys. Rev. D **14**, 2755 (1976); K. Kikkawa, Prog. Theor. Phys. **56**, 947 (1976).
2. M. K. Volkov and D. Ebert, Yad. Fiz. **36**, 1265 (1982); Z. Phys. C **16**, 205 (1983); M. K. Volkov, Ann. Phys. (New York) **157**, 282 (1984).
3. M. K. Volkov, Sov. J. Part. Nucl. **17**, 186 (1986).
4. D. Ebert and H. Reinhardt, Nucl. Phys. B **271**, 188 (1986).
5. H. Vogl and W. Weise, Prog. Part. Nucl. Phys. **27**, 195 (1991); S. P. Klevansky, Rev. Mod. Phys. **64**, 649 (1992).
6. G. V. Efimov and M. A. Ivanov, *The Quark Confinement Model of Hadrons* (IOP Publ., Bristol, 1993).
7. F. Gross and J. Milana, Phys. Rev. D **43**, 2401 (1991); **45**, 969 (1992).
8. L. S. Celenza, C. M. Shakin, Wei-Dong Sun, *et al.*, Phys. Rev. D **51**, 3638 (1995); L. S. Celenza, X.-D. Li, and C. M. Shakin, Phys. Rev. C **55**, 3083 (1997).
9. A. Bender, D. Blaschke, Yu. L. Kalinovsky, *et al.*, Phys. Rev. Lett. **77**, 3724 (1996).
10. D. Ebert, T. Feldmann, and H. Reinhardt, Phys. Lett. B **388**, 154 (1996).
11. P. N. Bogoliubov, Ann. Inst. Henri Poincaré **8**, 163 (1967); A. Chodos, R. L. Jaffe, C. B. Thorn, *et al.*, Phys. Rev. D **9**, 3471 (1974); A. E. Dorokhov, Yu. A. Zubov, and N. I. Kochelev, Part. Nucl. **23**, 1192 (1992).
12. D. Blaschke, G. Burau, M. K. Volkov, *et al.*, Preprint No. E2-98-227 (JINR, Dubna, 1998); Yad. Fiz. **62**, 2071 (1999).
13. Review of Particle Properties (C. Caso *et al.*), Eur. J. Phys. C **3**, 1 (1998).
14. S. Ishida *et al.*, Prog. Theor. Phys. **95**, 745 (1996).
15. M. Svec, Phys. Rev. D **53**, 2343 (1996); Phys. Rev. D **55**, 5727 (1997).
16. T. Hatsuda and T. Kunihiro, Phys. Lett. B **145**, 7 (1984).
17. D. Ebert, Yu. L. Kalinovsky, L. Münchov, *et al.*, Int. J. Mod. Phys. A **8**, 1295 (1993).
18. G. Agakishiev *et al.*, Phys. Rev. Lett. **75**, 1272 (1995); CERES Collab. (A. Dress *et al.*), Nucl. Phys. **A610**, 536 (1997).

Physics of Atomic Nuclei, Vol. 63, No. 3, 2000, pp. 470–479. Translated from Yadernaya Fizika, Vol. 63, No. 3, 2000, pp. 542–551.

ELEMENTARY PARTICLES AND FIELDS
Theory

Magnetic Catalysis and Magnetic Oscillations in the Nambu–Jona-Lasinio Model

M. A. Vdovichenko, A. S. Vshivtsev†, and K. G. Klimenko[1), *]

Moscow Institute of Radio Engineering, Electronics, and Automatics (Technical University), pr. Vernadskogo 78, Moscow, 117454 Russia

Received September 30, 1998; in final form, February 26, 1999

Abstract—The phase structure of the four-dimensional Nambu–Jona-Lasinio model in the presence of a chemical potential μ and an external magnetic field H is investigated at comparatively small values of the bare coupling constant ($G < G_c$). It is shown that only for magnetic-field strengths in excess of some critical value $H_c(\mu)$ does the magnetic field induce a spontaneous breakdown of chiral symmetry. On the phase portrait of the model, there are infinitely many massless chiral-invariant phases; in addition, there is one massive phase characterized by spontaneously broken chiral invariance. It is because of this phase structure of the system that some physical features of its ground state, including magnetization, pressure, and particle density, oscillate as $H \longrightarrow 0$. Changes in the vacuum properties of the model are accompanied by first- or second-order phase transitions.

1. INTRODUCTION

A magnetic catalysis represents dynamical chiral-symmetry (flavor-symmetry) breaking induced by an external magnetic or an external chromomagnetic field.

For the first time, this property of a uniform external magnetic field was discovered in studying the (2 + 1)-dimensional Gross–Neveu model featuring discrete chiral symmetry [1, 2]. It is well known [3] that, at $H = 0$, two phases are possible in this model. Of these, one possesses chiral symmetry for $G < G_c$, where G is a bare coupling constant; in the other, chiral invariance is spontaneously broken for $G > G_c$. Even at arbitrarily small (but nonzero) values of H and arbitrary values of $G > 0$, the model does not have, however, a symmetric ground state, and chiral invariance is spontaneously broken [1, 2].[2)] In [1], special attention was of course given to the case of $G < G_c$, where the magnetic field causes a dynamical breakdown of chiral symmetry even at arbitrarily small values of G. It was shown in [4] that an external chromomagnetic field leads to similar consequences.

Later on, this effect was explained in [5, 6] by considering that, in an external magnetic field, the dimension of spacetime is effectively reduced (dimensional reduction), which enhances the role of infrared divergences in the rearrangement of the vacuum. In those studies, as well as in [7–10], it was proven[3)] that the effect of magnetic catalysis is peculiar not only to various three-dimensional models like the continuous-symmetry Gross–Neveu model, QED_3, and free-fermion models but also to four-dimensional theories like those that are based on the Nambu–Jona-Lasinio (NJL) models. Of such four-dimensional theories, the simplest one is that which is specified by the Lagrangian

$$L_\psi = \sum_{k=1}^{N} \bar\psi_k i\hat\partial \psi_k + \frac{G}{2N}\left[\left(\sum_{k=1}^{N}\bar\psi_k\psi_k\right)^2 + \left(\sum_{k=1}^{N}\bar\psi_k i\gamma_5\psi_k\right)^2\right], \quad (1)$$

which is invariant under the continuous chiral transformation

$$\psi_k \longrightarrow e^{i\theta\gamma_5}\psi_k \quad (k = 1, \ldots, N). \quad (2)$$

(In order that the nonperturbative method of $1/N$ expansion could be used, we will consider the N-fermion version of the NJL model.) It was shown in [11] that, at

† Deceased.

1) Institute for High Energy Physics, Moscow oblast, Protvino, 142284 Russia.

* e-mail: kklim@mx.ihep.ru

2) The analysis in [1] was performed in terms of the parameter g such that $1/g = 1/g(m) - 2m/\pi$, where m is a normalization point and $g(m)$ is the renormalized coupling constant. The relation between g and G has the form $1/g = 1/G - 1/G_c$ [4]. It is clear that, for $g < 0$ ($g > 0$), we have $G > G_c$ ($G < G_c$). It is also obvious that g is independent of either the normalization point of the theory or the ultraviolet-cutoff parameter.

3) The authors of [7, 9] assert that only the fact of an increase in the dynamical fermion mass in the presence of an external magnetic field was established in [1, 2]; that is, they are confident that only the case of $G > G_c$ was considered in [1, 2]. In fact, the effect of an external (chromo)magnetic field on the (2 + 1)-dimensional Gross–Neveu model was studied in [1, 2, 4] for arbitrary values of the bare coupling constant. It was also shown in those studies that, at $H \neq 0$, chiral symmetry is spontaneously broken for all $G \in (0, \infty)$, including the case of $G < G_c$ and the case of arbitrarily small positive values of G (magnetic catalysis of dynamical symmetry breaking proper).

1063-7788/00/6303-0470$20.00 © 2000 MAIK "Nauka/Interperiodica"

$H = 0$, the chiral symmetry (2) in the theory specified by equation (1) is spontaneously broken (phase B) when the coupling constant G exceeds the critical value G_c ($G > G_c$). If $G < G_c$, the vacuum of the model is invariant under transformations (2) (phase A). Under the effect of an external magnetic field, the vacuum of the phase B changes its symmetry properties at no values of H [12].[4)] For $G < G_c$, however, the ground state of the model ceases to be symmetric even at arbitrarily small values of G and H [6]; that is, there is no A phase in the NJL model for $H \neq 0$ (effect of magnetic catalysis). Within three-dimensional QED, a generalization of the effect to the case of a nonuniform magnetic field was performed in [14].

From quite general heuristic considerations, it follows that, in all probability, the effect of a magnetic catalysis is universal—that is, it is expected to manifest itself in the majority of models featuring fermion fields. In order to demonstrate this, we note that, for any quantum system of fermions interacting with one another and with other particles in a chirally invariant way, the effective fermion Lagrangian must involve a term proportional to $G(\bar{\psi}\psi)^2$. (In order to find the effective Lagrangian, it is sufficient to perform integration in the generating functional for Green's functions with respect to all fields, except for spinor ones.) By analogy with the NJL model, we can therefore conclude that, in the presence of a catalyst (external magnetic field), chiral invariance will inevitably be broken in the system at an arbitrarily small value of the effective constant G. It goes without saying that, in each specific model, the effect of magnetic catalysis has individual features inherent in this model.

As a matter of fact, many physical processes occur at nonzero values of temperature and particle-number density; for this reason, much attention is given to the dependence of the effect of magnetic catalysis on these and on some other factors. By way of example, we indicate that the effect of temperature, a chemical potential, and a magnetic field on the properties of the (2 + 1)-dimensional Gross–Neveu model was considered in [15, 16] and that the effect of temperature on the catalysis in the NJL model and in QED_4 was studied in [8, 10, 17]; in addition, the concerted effect of gravity and magnetic fields on the critical properties of various theories featuring four-fermion interaction was analyzed in [18, 19].

In the present article, we proceed along the above lines, pursuing further the investigation of magnetic catalysis. Specifically, the properties of the vacuum of the NJL theory whose Lagrangian is given by (1) are considered here in the presence of a chemical potential μ and a uniform external magnetic field H. On this basis, it is shown that, with increasing magnetic field, oscillations of pressure, magnetization (de Haas–Van Alphen effect), and particle-number density (analog of the Shubnikov–de Haas effect of electric-conductivity oscillations in metals) may occur in the system.

2. $\mu \neq 0$, $H = 0$ CASE

We begin by recalling the properties of the NJL model (1) at $\mu = 0$. For this purpose, we consider, instead of (1), the auxiliary Lagrangian

$$L_\sigma = \bar{\psi} i\hat{\partial}\psi - \bar{\psi}(\sigma_1 + i\sigma_2\gamma_5)\psi - \frac{N}{2G}(\sigma_1^2 + \sigma_2^2) \quad (3)$$

(on the field ψ, we suppressed here, for the sake of simplicity, the index k numbering fermion fields). On the manifold specified by the equations of motion for auxiliary boson fields $\sigma_{1,2}$, the Lagrangian in (3) is equivalent to the original Lagrangian (1).

In the leading order of $1/N$ expansion, the effective action of the model is given by

$$\begin{aligned} \exp(iNS_{\text{eff}}(\sigma_{1,2})) &= \int D\bar{\psi} D\psi \exp\left(i\int L_\sigma d^4x\right), \\ S_{\text{eff}}(\sigma_{1,2}) &= -\int d^4x \frac{\sigma_1^2 + \sigma_2^2}{2G} \\ &\quad - i\ln\det(i\hat{\partial} - \sigma_1 - i\gamma_5\sigma_2). \end{aligned} \quad (4)$$

Further, we assume that the fields $\sigma_{1,2}$ are independent of spacetime coordinates. By definition, we have

$$S_{\text{eff}}(\sigma_{1,2}) = -V_{\text{eff}}(\sigma_{1,2})\int d^4x, \quad (5)$$

where

$$\begin{aligned} V_{\text{eff}}(\sigma_{1,2}) &= \frac{\Sigma^2}{2G} \\ &\quad + 2i\int \frac{d^4p}{(2\pi)^4}\ln(\Sigma^2 - p^2) \equiv V_0(\Sigma) \end{aligned} \quad (6)$$

with $\Sigma = \sqrt{\sigma_1^2 + \sigma_2^2}$.

Going over to the Euclidean metric ($p_0 \longrightarrow ip_0$) in the function appearing in (6) and introducing a Lorentz invariant cutoff ($p^2 \leq \Lambda^2$) in the domain of integration, we obtain

$$\begin{aligned} V_0(\Sigma) &= \frac{\Sigma^2}{2G} - \frac{1}{16\pi^2}\left\{\Lambda^4\ln\left(1 + \frac{\Sigma^2}{\Lambda^2}\right)\right. \\ &\quad \left. + \Lambda^2\Sigma^2 - \Sigma^4\ln\left(1 + \frac{\Lambda^2}{\Sigma^2}\right)\right\}. \end{aligned} \quad (7)$$

[4)] This is at odds with expectations based on the analogy with the theory of superconductivity, where the symmetry of the model must be restored with increasing H. Calculations reveal that, in all of the models listed above, the fermion mass grows with increasing H; therefore, a transition to a chiral-symmetric, massless, phase occurs at no value of the magnetic field H. Of particular interest is the investigation performed in [13], where the growth of the quark condensate with increasing external magnetic field was proven within QCD, as well as within the generalized chiral model, which describes the low-energy region of QCD.

The points of extrema of the function in (7) are determined by the equation

$$\frac{\partial V_0(\Sigma)}{\partial \Sigma} \equiv \frac{\Sigma}{4\pi^2}F(\Sigma)$$
$$\equiv \frac{\Sigma}{4\pi^2}\left\{\frac{4\pi^2}{G} - \Lambda^2 + \Sigma^2 \ln\left(1 + \frac{\Lambda^2}{\Sigma^2}\right)\right\} = 0. \quad (8)$$

From (8), it can be seen that, for $G < G_c = 4\pi^2/\Lambda^2$, equation (8) does not have solutions, with the exception of the trivial solution $\Sigma = 0$; that is, fermions prove to be massless in this case, and invariance under the chiral transformations (2) is not violated.

If $G > G_c$, equation (8) has one nontrivial solution corresponding to the global minimum of the potential $V_0(\Sigma)$; this implies a spontaneous breakdown of chiral symmetry and emergence of a nonzero fermion mass.

Let us now assume that $\mu > 0$. This case was considered in detail in [20], where the expression for the corresponding effective potential $V_\mu(\Sigma)$ [the expression for $V_0(\Sigma)$ is given in (7)] was obtained in the form

$$V_\mu(\Sigma) = V_0(\Sigma)$$
$$-2\int \frac{d^3p}{(2\pi)^3}\theta(\mu - \sqrt{\Sigma^2 + p^2})(\mu - \sqrt{\Sigma^2 + p^2}), \quad (9)$$

with $\theta(x)$ being a Heaviside step function. Evaluating the integral on the right-hand side of (9), we arrive at

$$V_\mu(\Sigma) = V_0(\Sigma) - \frac{\theta(\mu - \Sigma)}{16\pi^2}\left\{\frac{10}{3}\mu(\mu^2 - \Sigma^2)^{3/2}\right.$$
$$\left. - 2\mu^3\sqrt{\mu^2 - \Sigma^2} + \Sigma^4 \ln[(\mu + \sqrt{\mu^2 - \Sigma^2})^2/\Sigma^2]\right\}. \quad (10)$$

It can easily be shown that, for $G < G_c$ and for any value of μ, the absolute minimum of the function in (10) is always attained at the origin—that is, the symmetry under the transformations in (2) is not broken.

For $G > G_c$, previously unknown properties of the NJL model were discovered in [20] on the basis of an analysis of the point where the potential (10) attains the absolute minimum. Among other things, it was shown there that, at nonzero values of the chemical potential, the state featuring massive fermions is described, in that case, by two different phases that go over to each other via a first-order phase transition. It was also shown in [20] that the chiral symmetry of the model can be restored by means of either a first-order or a second-order phase transition, depending on the values of the model parameters. The phase portrait of the NJL model was constructed in the (μ, M) plane, where M is the dynamical fermion mass at $\mu = 0$, and it was found that there are two tricritical points on this phase portrait.

3. MAGNETIC CATALYSIS AT $H \neq 0$ AND $\mu = 0$

In a nonzero external magnetic field, the effective potential of the NJL model can be derived by the well-known proper-time method [21] or by no less elegant methods relying on calculations in momentum space [22]:

$$V_H(\Sigma) = \frac{\Sigma^2}{2G} + \frac{eH}{8\pi^2}\int_0^\infty \frac{ds}{s^2}\exp(-s\Sigma^2)\coth(eHs).$$

Upon an identical transformation of this expression, we arrive at

$$V_H(\Sigma) = V_0(\Sigma) + \tilde{V}_H(\Sigma) + Z(\Sigma), \quad (11)$$

where

$$V_0(\Sigma) = \frac{\Sigma^2}{2G} + \frac{1}{8\pi^2}\int_0^\infty \frac{ds}{s^3}\exp(-s\Sigma^2),$$

$$Z(\Sigma) = \frac{(eH)^2}{24\pi^2}\int_0^\infty \frac{ds}{s}\exp(-s\Sigma^2),$$

$$\tilde{V}_H(\Sigma) = \frac{1}{8\pi^2}\int_0^\infty \frac{ds}{s^3}\exp(-s\Sigma^2) \quad (12)$$
$$\times\left[(eHs)\coth(eHs) - 1 - \frac{(eHs)^2}{3}\right].$$

Apart from an immaterial infinite term, which is independent of Σ, the potential $V_0(\Sigma)$ in (12) is equal to the function in (6); therefore, the regularized expression for $V_0(\Sigma)$ has the form (7).

In just the same way as the potential $V_0(\Sigma)$, the integral $Z(\Sigma)$ diverges at its lower limit. Upon isolating a finite component in $Z(\Sigma)$ by means of identical transformations in (12), we arrive at

$$Z(\Sigma) = \frac{(eH)^2}{24\pi^2}\int_0^\infty \frac{ds}{s}(\exp(-s\Sigma^2) - \exp(-s\Lambda^2))$$
$$+ \frac{(eH)^2}{24\pi^2}\int_0^\infty \frac{ds}{s}\exp(-s\Lambda^2) \quad (13)$$
$$= -\frac{(eH)^2}{24\pi^2}\ln\frac{\Sigma^2}{\Lambda^2} + \frac{(eH)^2}{24\pi^2}\int_0^\infty \frac{ds}{s}\exp(-s\Lambda^2),$$

where Λ appears to be the same cutoff parameter as in (7). As to the last, divergent, term in (13), it contributes to the renormalization of the electric charge e and to the renormalization of the external magnetic field H; therefore, we disregard this term in the following (we are dealing with a similar situation in calculating the effective action in QED [21, 23], where it is also necessary

to renormalize e and H in order to obtain a finite expression for the effective action).

The last potential in (12), $\tilde{V}_H(\Sigma)$, features no divergences; it can be evaluated easily by using standard integrals that are presented in [24]. Taking into account (11)–(13), we obtain

$$V_H(\Sigma) = V_0(\Sigma) - \frac{(eH)^2}{2\pi^2}\left\{\zeta'(-1, x) - \frac{1}{2}[x^2 - x]\ln x + \frac{x^2}{4}\right\}, \quad (14)$$

where $x = \Sigma^2/(2eH)$, $\zeta(\nu, x)$ is a generalized Riemann zeta function [25], and $\zeta'(-1, x) = d\zeta(\nu, x)/d\nu|_{\nu=-1}$. The following relations [25] will be useful in the ensuing calculations:

$$\frac{d}{dx}\zeta(\nu, x) = -\nu\zeta(\nu + 1, x),$$
$$\frac{d}{d\nu}\zeta(\nu, x)|_{\nu=0} = \ln\Gamma(x) - \frac{1}{2}\ln(2\pi). \quad (15)$$

With the aid of equations (14) and (15), we can find easily that the point at which the potential $V_H(\Sigma)$ achieves the global minimum satisfies the equation

$$\frac{\partial}{\partial\Sigma}V_H(\Sigma) = \frac{\Sigma}{4\pi^2}\{F(\Sigma) - I(\Sigma)\} = 0, \quad (16)$$

where $F(\Sigma)$ is given by (8) and where

$$I(\Sigma) = 2eH\left\{\ln\Gamma(x) - \frac{1}{2}\ln(2\pi) + x - \frac{1}{2}(2x - 1)\ln x\right\} \quad (17)$$
$$= \int_0^\infty \frac{ds}{s^2}\exp(-s\Sigma^2)[eHs\coth(eHs) - 1]$$

[the parameter x has been defined immediately after equation (14)]. Now, it can be shown easily that, for $\Sigma \in (0, +\infty)$, the function $I(\Sigma)$ decreases monotonically from $+\infty$ to 0; on the contrary, the function $F(\Sigma)$ increases monotonically, within this interval, from $4\pi^2/G - \Lambda^2$ to $4\pi^2/G$. For any nonzero value of the external magnetic field H, there therefore exists a unique nonzero function $\Sigma_0(H)$ (both for $G < G_c$ and $G > G_c$) such that it satisfies equation (16) and that it corresponds to the global minimum of the potential $V_H(\Sigma)$. Physically, the solution denoted by $\Sigma_0(H)$ represents a fermion mass [in Fig. 1, which illustrates the case of $G < G_c$, it appears to be the point where the graphs of the functions $F(\Sigma)$ and $I(\Sigma)$ intersect].

Thus, we can see that, for $G < G_c$ and $H = 0$, the vacuum of the NJL model possesses chiral invariance, but that, at arbitrarily small nonzero values of the magnetic-field strength, this symmetry is spontaneously broken, which means that a magnetic field appears to be a catalyst of a spontaneous breakdown of invariance under the chiral transformations (2) (this result was first obtained in [6]). In the following, the properties of the vacuum of the model specified by equation (1) will be studied only in the case of $G < G_c$.[5)]

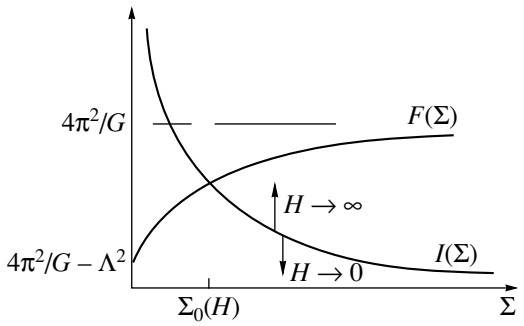

Fig. 1. Graphs of the functions $F(\Sigma)$ and $I(\Sigma)$. The point of their intersection determines a nontrivial solution to equation (16) for the points of extrema of the effective potential. Errors indicate the directions in which the graph of the function $I(\Sigma)$ is displaced when the external-magnetic-field strength is increased or decreased.

Listed below are some properties of the function $\Sigma_0(H)$. From the integral representation (17) of $I(\Sigma)$, it follows that $\partial I/\partial H > 0$; at fixed values of Σ, the graph of the function $I(\Sigma)$ are therefore shifted upward with increasing H and downward (toward the Σ axis) with decreasing H (see Fig. 1). It is obvious that $\Sigma_0(H)$ then increases or decreases, respectively, since the graph of the function $F(\Sigma)$ undergoes no changes; that is, $\Sigma_0(H)$ appears to be a monotonically increasing function of the magnetic-field strength.

Let us now study the asymptotic behavior of this function for $H \longrightarrow \infty$. We assume that

$$\Sigma_0(H) \longrightarrow \infty, \quad \Sigma_0^2(H)/(eH) \longrightarrow \infty \text{ for } H \longrightarrow \infty. \quad (18)$$

By using equations (8) and (17) and taking into account (18), we find that, at large values of the magnetic-field strength, the functions F and I are given by

$$F(\Sigma_0) \approx 4\pi^2/G, \quad I(\Sigma_0) \approx 4(eH)^2/(12\Sigma_0^2).$$

It follows that, for $H \longrightarrow \infty$, the leading term in the asymptotic expansion of the solution to the equation $F(\Sigma) = I(\Sigma)$ is given by

$$\Sigma_0(H) \approx \frac{eH}{\pi}\sqrt{\frac{G}{12}}. \quad (19)$$

[It can be seen easily that the solution in (19) satisfies the conditions in (18).]

In a similar way, we can determine the asymptotic behavior of the solution $\Sigma_0(H)$ for $H \longrightarrow 0$. Indeed, it can be shown that, if only the leading terms in the

[5)] It was indicated in the Introduction that, for $G > G_c$, the symmetry of the model under chiral transformations (2) is spontaneously broken at any value of the magnetic-field strength [12].

asymptotic expansions on the two sides of the equation $F(\Sigma) = I(\Sigma)$ are retained under the condition that $H \longrightarrow 0$, $\Sigma \longrightarrow 0$, and $\Sigma^2/(eH) \longrightarrow 0$, we arrive at an equation whose solution

$$\Sigma_0^2(H) = \frac{eH}{\pi}\exp\left\{-\frac{1}{eH}\left(\frac{4\pi^2}{G} - \Lambda^2\right)\right\} \tag{20}$$

is consistent with the constraints imposed in deriving it. Hence, the expression on the right-side of (20) is precisely the leading term in the asymptotic expansion of the nontrivial solution to the equation for the points of extrema in the limit $H \longrightarrow 0$.

Thus, we conclude that, for $G < G_c$, even an arbitrarily small external magnetic field induces a spontaneous breakdown of chiral invariance in the NJL model.

4. MAGNETIC CATALYSIS AT $H \neq 0$ AND $\mu \neq 0$

Suppose that $G < G_c$ and $\mu \neq 0$. It is well known that, in contrast to a magnetic field, the chemical potential facilitates the restoration of chiral symmetry. It is therefore natural to expect that, at a fixed nonzero value of μ, the opposing trends due to the above two factors will result in that only for magnetic fields whose strength exceeds some finite threshold critical value $H_c(\mu)$ will a dynamical breakdown of symmetry under transformations (2) be induced in the case being considered. If $H < H_c(\mu)$, the chemical potential must have a more pronounced effect on the vacuum; hence, chiral symmetry is expected to be preserved. Below, these qualitative considerations will be supported by a calculation of the phase structure of the NJL model for $H \neq 0$ and $\mu \neq 0$.

The effective potential in the three-dimensional Gross–Neveu model was obtained in [16] at nonzero values of an external magnetic field H, temperature T, and the chemical potential μ. In a similar way, we can derive the effective potential in the model considered here, that specified by equation (1), for nonzero values of H, T, and μ. The result is

$$V_{H\mu T}(\Sigma) = V_H(\Sigma) - \frac{TeH}{4\pi^2} \times \sum_{k=0}^{\infty}\alpha_k\int_{-\infty}^{\infty} dp \ln\{[1 + \exp(-\beta(\varepsilon_k + \mu))] [1 + \exp(-\beta(\varepsilon_k - \mu))]\}, \tag{21}$$

where $\beta = 1/T$, $\alpha_k = 2 - \delta_{0k}$, $\varepsilon_k = \sqrt{\Sigma^2 + p^2 + 2eHk}$, and the function $V_H(\Sigma)$ is defined in (11). In the limit $T \longrightarrow 0$, expression (21) takes the form

$$V_{H\mu}(\Sigma) = V_H(\Sigma) - \frac{eH}{4\pi^2}\sum_{k=0}^{\infty}\alpha_k\int_{-\infty}^{\infty} dp(\mu - \varepsilon_k)\theta(\mu - \varepsilon_k). \tag{22}$$

Evaluating the integral in (22), we arrive at

$$V_{H\mu}(\Sigma) = V_H(\Sigma) - \frac{eH}{4\pi^2}\sum_{k=0}^{\infty}\alpha_k\theta(\mu - s_k) \times \left\{\mu\sqrt{\mu^2 - s_k^2} - s_k^2\ln\left[\frac{\mu + \sqrt{\mu^2 - s_k^2}}{s_k}\right]\right\}, \tag{23}$$

where $s_k = \sqrt{\Sigma^2 + 2eHk}$. With the aid of (16), the equation that determines the points of extrema of the potential (23) can be written as

$$\frac{\partial}{\partial\Sigma}V_{H\mu}(\Sigma) = \frac{\Sigma}{4\pi^2}\left\{F(\Sigma) - I(\Sigma) + 2eH\sum_{k=0}^{\infty}\alpha_k\theta(\mu - s_k)\ln\left[\frac{\mu + \sqrt{\mu^2 - s_k^2}}{s_k}\right]\right\} = 0. \tag{24}$$

Our attention being focused on the phase structure of the model specified by equation (1), each point of that region of the (μ, H) plane where $\mu \geq 0$ and $H \geq 0$ must be associated with some phase that is unambiguously determined by the global minimum of the potential (23). The procedure that we believe to be optimal for implementing this construction and which is dictated by the structure of expressions (23) and (24) is as follows. We break down the above region of the (μ, H) plane into domains ω_k $(\mu, H \geq 0)$ defined as

$$(\mu, H) = \bigcup_{k=0}^{\infty}\omega_k; \quad \omega_k = \{(\mu, H): 2eHk \leq \mu^2 \leq 2eH(k+1)\}. \tag{25}$$

It is obvious that, in the region ω_0, the quantities in (23) and (24) receive contributions only from the first terms in the corresponding sums; that two terms in each of these sums—those that correspond to $k = 0$ and 1—are nonzero in the region ω_1; and so on. (A similar approach was adopted in studying the effective potentials in the three-dimensional Gross–Neveu model for $\mu, H \geq 0$ [16] and in the NJL model with a chemical potential and one compactified spatial coordinate—that is, in spacetime of the form $R^3 \times S^1$ [26, 27].)

Let us now consider the phase structure of the NJL model in the region ω_0 under the condition $G < G_c$. In this case, equation (24), which determines the points of extrema of the potential (23), takes the form

$$\frac{\Sigma}{4\pi^2}\left\{F(\Sigma) - I(\Sigma) + 2eH\theta(\mu - \Sigma)\ln\left[\frac{\mu + \sqrt{\mu^2 - \Sigma^2}}{\Sigma}\right]\right\} = 0. \tag{26}$$

External-magnetic-field values H^* at which the graph of the function $\Sigma_0(H)$ intersects the boundary of the domain ω_0

G_c/G	1.01	1.1	1.5	2.5	3	11	101
$2eH^*/\Lambda^2$	11.97	13.12	18.18	30.64	36.84	135.65	1245.96

A numerical investigation of equation (26) reveals that, for points of the region ω_0 that lie above the curve $L = \{(\mu, H) : \mu = \Sigma_0(H)\}$, the potential (23) attains the global minimum at the point $\Sigma = 0$. From the asymptotic behavior of the solution $\Sigma_0(H)$ [see equations (19) and (20)], it follows that, at sufficiently small values of the magnetic-field strength, the curve L lies within the region ω_0. However, it intersects the boundary of ω_0 at some value H^* dependent on G and Λ and goes beyond this region. At some values of G and Λ, $H^*(G, \Lambda)$ can be determined easily on the basis of the data from the table, whose upper and lower rows quote, respectively, several values of the ratio G_c/G and the corresponding values of $2eH^*(G, \Lambda)/\Lambda^2$. It can be seen that, as G approaches zero, the magnetic-field-strength value at which the curve L leaves the region ω_0 increases, the parameter Λ being fixed. Specifically, we have

$$2eH^* \underset{G\to 0}{\approx} (487.01\ldots)G^{-1};$$
$$\lim_{G\to G_c}(2eH^*) = (11.84\ldots)\Lambda^2.$$

As soon as we reduce the value of μ and intersect the curve L within the region ω_0, the potential $V_{H\mu}(\Sigma)$ develops a second nonzero, local, minimum—the point $\Sigma_0(H)$—which becomes the global minimum when μ decreases further. The critical chemical-potential value $\mu_c(H)$ at which the system goes over from the chiral-invariant phase to a phase where chiral symmetry is spontaneously broken is determined from the equation

$$V_{H\mu}(0) = V_{H\mu}(\Sigma_0(H)). \qquad (27)$$

In the region ω_0, it has the solution

$$\mu_c(H) = \frac{2\pi}{\sqrt{eH}}[V_H(0) - V_H(\Sigma_0(H))]^{1/2}. \qquad (28)$$

By integrating equation (16) with respect to Σ from 0 to $\Sigma_0(H)$ and going over to the limit $H \longrightarrow 0$ in the resulting expression, we can find that the asymptotic behavior of $\mu_c(H)$ at small H is given by

$$\mu_c(H) \approx \sqrt{\frac{eH}{2\pi}}\exp\left\{-\frac{1}{2eH}\left(\frac{4\pi^2}{G} - \Lambda^2\right)\right\}.$$

Thus, we can see that, in the model specified by equation (1) and considered at $G < G_c$, the curve $\mu = \mu_c(H)$ divides the (μ, H) plane into two regions. In the first of these—that is, at $\mu > \mu_c(H)$—the vacuum of the system is invariant under chiral transformations, while, in the second—that is, at $\mu < \mu_c(H)$—the invariance of the theory under the chiral transformations (2) is spontaneously broken. The two phases go over to each other via a first-order phase transition occurring upon the intersection of the curve $\mu = \mu_c(H)$ separating these phases.

It is obvious that, at $\mu = \text{const}$ and $H < H_c(\mu)$ [here, $H_c(\mu)$ is obtained by inverting the function $\mu_c(H)$], the condition $\mu > \mu_c(H)$ holds; that is, chiral symmetry is not broken. The case of $H > H_c(\mu)$ corresponds to the region where chiral symmetry is broken. At $\mu = \text{const}$, this means that, for $H > H_c(\mu)$, an external magnetic field catalyzes a spontaneous breakdown of invariance under the chiral transformations (2).

It is also interesting to note that, in the region below the critical curve $\mu = \mu_c(H)$, the order parameter—for this, we can take either the fermion mass or the point of the global minimum, $\Sigma_0(H)$—is independent of μ; in other words, the amount of chiral-symmetry breaking in the model by a magnetic field is independent here of μ.

5. OSCILLATION PHENOMENA AT $H \neq 0$ AND $\mu \neq 0$

In the preceding section, we have shown that, on the (μ, H) phase plane, the chiral-invariant ground state of the NJL model specified by equation (1) corresponds to points lying above the critical curve $\mu = \mu_c(H)$. Single-particle fermion excitations above this vacuum are massless. At first glance, the properties of this vacuum are weakly dependent on μ and H, and that part of the (μ, H) plane where $\mu > \mu_c(H)$ is entirely occupied by the symmetric phase of the theory. But in fact, infinitely many critical phenomena occur in the region $\mu > \mu_c(H)$ at an infinite number of points in response to variations in external parameters. This is because the ground state of the model changes abruptly its properties with increasing μ at fixed H or with decreasing H at fixed μ. At the above points, there occur second-order phase transitions that do not violate, however, the chiral invariance of the vacuum. These critical phenomena can manifest themselves as oscillations of pressure and magnetization; oscillations of the particle-number density in ground-state of the system are also possible in this case. Below, we consider all these possibilities.

The state of thermodynamic equilibrium (ground state) of any quantum field theory is unambiguously characterized by the thermodynamic potential defined as the value of the effective potential at the point of the global minimum. The thermodynamic potential coincides with pressure in absolute value, differing from it in sign (see Appendix). In the case considered here, the

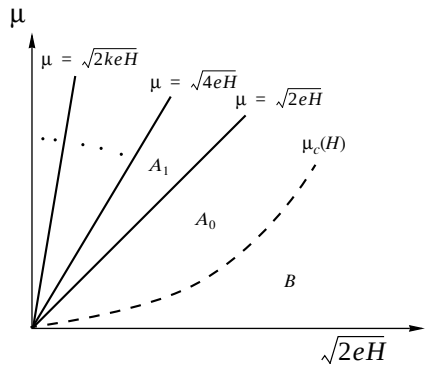

Fig. 2. Phase portrait of the Nambu–Jona-Lasinio model for $G < G_c$. Solid lines are those of second-order phase transitions, while the dashed curve is drawn through the points of first-order phase transitions. In the phase B, the chiral symmetry of the model is spontaneously broken, and fermions have a mass $\Sigma_0(H)$. In each of an infinite set of chiral invariant phases A_0, A_1,…, fermions are massless.

expression for the thermodynamic potential $\Omega(\mu, H)$ in the region $\mu > \mu_c(H)$ has the form

$$\Omega(\mu, H) \equiv V_{H\mu}(0) = V_H(0) - \frac{eH}{4\pi^2}\sum_{k=0}^{\infty}\alpha_k\theta(\mu-\epsilon_k) \times\{\mu\sqrt{\mu^2-\epsilon_k^2} - \epsilon_k^2\ln[(\sqrt{\mu^2-\epsilon_k^2}+\mu)/\epsilon_k]\}, \quad (29)$$

where $\epsilon_k = \sqrt{2eHk}$. It is well known that, at the points of first-order (second-order) phase transitions, the first-order (second-order) partial derivative of the thermodynamic potential with respect to one of the arguments develops a discontinuity, and so naturally do all the corresponding partial derivatives of orders higher than one (two) with respect to the same argument. On the basis of this criterion of phase transitions, we will analyze the phase structure of the model under investigation for $\mu > \mu_c(H)$. We will show that the boundaries between the regions ω_k (25)—that is, the lines $l_k = \{(\mu, H) : \mu = \sqrt{2eHk}\}$ $(k = 1, 2, \ldots)$—represent the critical lines of second-order phase transitions. In order to do this, we will consider the function given by (29) in one of the regions ω_k:

$$\Omega(\mu, H)\big|_{\omega_k} \equiv \Omega_k = V_H(0) - \frac{eH}{4\pi^2}\sum_{i=0}^{k}\alpha_i\theta(\mu-\epsilon_i) \times\left\{\mu\sqrt{\mu^2-\epsilon_i^2} - \epsilon_i^2\ln\left[\frac{(\sqrt{\mu^2-\epsilon_i^2}+\mu)}{\epsilon_i}\right]\right\}. \quad (30)$$

Evaluating the first- and second-order derivatives of expression (30) with respect to μ, we obtain

$$\left.\frac{\partial\Omega_k}{\partial\mu}\right|_{(\mu, H)\to l_{k+}} - \left.\frac{\partial\Omega_{k-1}}{\partial\mu}\right|_{(\mu, H)\to l_{k-}} = 0, \quad (31)$$

$$\left.\frac{\partial^2\Omega_k}{(\partial\mu)^2}\right|_{(\mu, H)\to l_{k+}} - \left.\frac{\partial^2\Omega_{k-1}}{(\partial\mu)^2}\right|_{(\mu, H)\to l_{k-}} = -\left.\frac{eH\mu}{2\pi^2\sqrt{\mu^2-\epsilon_k^2}}\right|_{\mu\to\epsilon_{k+}} \longrightarrow -\infty. \quad (32)$$

The equality in (31) means that the first-order derivative of the thermodynamic potential Ω with respect to μ is continuous on all curves l_k. From (32), it follows, however, that a second-order phase transition occurs on each line l_k, since the second-order derivative of the thermodynamic potential with respect to μ undergoes there infinite jumps. Similarly, it can be shown that the second-order derivatives $\partial^2\Omega/(\partial H)^2$ and $\partial^2\Omega/\partial\mu\partial H$ are also discontinuous (have infinite jumps) on each of the curves l_n.[6)]

For the case of $G < G_c$, which is considered here, the phase portrait of the model is depicted in Fig. 2, where solid lines (lines l_k) represent lines of second-order phase transitions, while the dashed curve is that of first-order phase transitions. In the phase B, chiral symmetry is spontaneously broken, and fermions have a mass $\Sigma_0(H)$. The figure also shows an infinite sequence of massless chiral-invariant phases A_0, A_1, …, which generate oscillations of some physical quantities in the model. We also note that, in the phase B, the fermion density $n = -\partial\Omega/\partial\mu$ is identically equal to zero. Upon traversing the critical line (28), the fermion density n undergoes a jump, taking a finite nonzero value.

Let us set μ = const. In the (μ, H) plane, this corresponds to the straight line that intersects the critical curves l_1, …, l_k, … at the points H_1, …, H_k, …, respectively. At μ = const, we now consider the external-magnetic-field dependence of the particle-number density, $n(H)$, and of the magnetization of the system, $m(H) = -\partial\Omega/\partial\mu$. From the above properties of the thermodynamic potential (29), it follows that the functions $n(H)$ and $m(H)$ are continuous for $H \geq 0$ and that their graphs have characteristic cusps at an infinite number of the points H_1,…. Functions that behave in this way will henceforth be referred to as oscillating functions. Thus, we can say that, in the NJL model, the fermion concentration $n(H)$ and the magnetization $m(H)$ of the ground state oscillate as functions of the magnetic field.

Of course, smoother functions can also oscillate; therefore, the above definition should be further clarified. The point is that, at zero temperature and nonzero chemical potential, oscillations of physical quantities usually satisfy this definition. This is because the number of the filled energy levels of the system that are below the Fermi surface as a function of external parameters has discontinuities at an infinite number of points. By way of example, we indicate that, at zero

[6)] In the Appendix, we consider relations between the second-order derivatives of the thermodynamic potential and thermodynamic coefficients, the latter being determined, for the majority of systems, from an analysis of experimental data.

temperature, the first-order derivatives of the magnetization $m(H)$ and the particle-number density $n(H)$ of a free fermion gas in an external magnetic field H with respect to H have discontinuities at an infinite number of points [28–30]. According to the above definition, oscillating parameters of the NJL model include the quark condensate, the fermion-number density, and the critical curve of chiral phase transitions in the case where one of the spatial coordinates is compactified and where the compactification radius appears to be a variable [27]. (Oscillations of various physical quantities become smoother at nonzero temperature, but this case is not considered here.)

It turns out that, in the NJL model, the oscillations of the functions $n(H)$ and $m(H)$ can be obtained in an explicit form. For this purpose, we make use of the technique proposed in [30], where the oscillating component of the thermodynamic potential of the relativistic electron–positron gas was isolated exactly. This technique is applicable to the thermodynamic potential in the form (29). By analogy with what was done in [30], we represent it as[7)]

$$\Omega(\mu, H) = \Omega_{\text{mon}}(\mu, H) + \Omega_{\text{osc}}(\mu, H), \tag{33}$$

where

$$\Omega_{\text{mon}} = V_H(0) - \frac{\mu^4}{12\pi^2} - \frac{(eH)^2}{4\pi^3}\int_0^\nu dy \sum_{k=1}^{\infty}\frac{1}{k}P(\pi k y), \tag{34}$$

$$\Omega_{\text{osc}} = \frac{\mu}{4\pi^{3/2}}\sum_{k=1}^{\infty}\left(\frac{eH}{\pi k}\right)^{3/2}[Q(\pi k\nu)\cos(\pi k\nu + \pi/4) + P(\pi k\nu)\cos(\pi k\nu - \pi/4)] \tag{35}$$

with $\nu = \mu^2/(eH)$.

Expressions (34) and (35) involve the functions $P(x)$ and $Q(x)$ that are related to the well-known Fresnel integrals $C(x)$ and $S(x)$ [25] by the equations

$$C(x) = \frac{1}{2} + \sqrt{\frac{x}{2\pi}}[P(x)\sin x + Q(x)\cos x],$$

$$S(x) = \frac{1}{2} - \sqrt{\frac{x}{2\pi}}[P(x)\cos x - Q(x)\sin x].$$

For $x \longrightarrow \infty$, the asymptotic expansions of these functions are [25]

$$P(x) = x^{-1} - \frac{3}{4}x^{-3} + \ldots, \quad Q(x) = -\frac{1}{2}x^{-2} + \frac{15}{8}x^{-4} + \ldots.$$

From (35), it can be seen that the thermodynamic potential of the NJL model, along with the pressure in the system, oscillates at large values of the variable $(eH)^{-1}$, the frequency of these oscillations being $\mu^2/2$. Although the function $\Omega(\mu, H)$ oscillates explicitly as a function of H at a constant value of the chemical potential, it does not belong to the class of oscillating functions that was defined above. However, the partial derivatives of this function with respect to μ and H—that is, the quantities $n(H)$ and $m(H)$—belong to this class and oscillate at large value of $(eH)^{-1}$, the oscillation frequency being again $\mu^2/2$. The explicit expressions for the oscillating components of $n(H)$ and $m(H)$ can be found by using equations (33)–(35), but we do not present them here to avoid encumbering the article with unwieldy expressions.

6. CONCLUSION

The effect of an external magnetic field on the NJL model in the presence of a chemical potential has been considered for $G < G_c$. At $\mu = 0$, arbitrarily small values of the magnetic-field strength induce a spontaneous breakdown of the chiral invariance of the model considered here [6], but, for $\mu \neq 0$ and sufficiently small values of H, it has been shown here that the system occurs in the symmetric state. As soon as the magnetic-field strength achieves some critical value $H_c(\mu)$, there occurs a first-order phase transition from the massless symmetric phase A_0 to the massive phase B (see phase portrait of the model in Fig. 2), where the chiral symmetry is spontaneously broken (we can then say that a dynamical breakdown of symmetry is induced by an external magnetic field).

It has also been proven that, as the magnetic-field strength is decreased at $\mu = \text{const}$, there occurs an infinite cascade of second-order phase transitions in the system, each leaving the chiral properties of the ground state of the model unchanged [that is, invariance under the chiral transformations (2) is preserved]; at the same time, thermodynamic features of the system like isothermal compressibility and magnetic susceptibility undergo discontinuities (see Appendix). These critical properties of the model are illustrated by its phase portrait in Fig. 2, where we can see an infinite number of massless chiral-invariant phases A_k ($k = 0, 1, 2, \ldots$) in the (μ, H) plane. Owing to this phase structure, oscillations of the magnetization (de Haas–Van Alphen effect) and oscillations of the fermion-number density in the ground state (analog of the Shubnikov–de Haas effect, which consists in oscillations of the electric conductivity of metals in external magnetic fields at low temperatures) can be observed in the NJL system as the magnetic-field strength tends to zero.

ACKNOWLEDGMENTS

We are grateful to A.K. Klimenko for performing some numerical calculations.

This work was supported by the Russian Foundation for Basic Research (project no. 98-02-16690).

[7)] For this, it is sufficient to make the electron mass tend to zero in equation (19) from [30].

APPENDIX

Thermodynamic Coefficients and Their Relation to $\Omega(\mu, H)$

By thermodynamic coefficients, we mean expressions of the form $(\partial x/\partial y)_{z, \ldots}$, where x, y, z, … are thermodynamic features of the system like temperature T, volume V, pressure p, the total number N of particles, the total magnetization M, and an external magnetic field H [29]. It is the jumps in thermodynamic coefficients that are used in practice to establish the occurrence of second-order phase transitions.

Suppose that T, V, H, and μ (chemical potential) are independent parameters of the system. The thermodynamic potential (more precisely, its density) then has the form $\Omega(\mu, T, H) = -p \equiv -p(\mu, T, H)$ [29, 31]. It follows that

$$-d\Omega = dp = nd\mu + sdT + mdH, \qquad \text{(A.1)}$$

where $n = N/V$ is the particle-number density, s is the density of the entropy, and $m = M/V$ is the density of the magnetization. Here, we aim at establishing relations between the second-order derivatives of the thermodynamic potential $\Omega(\mu, T, H)$ and some thermodynamic coefficients.

By definition, the isothermal compressibility is the thermodynamic coefficient (supplemented with a factor V^{-1})

$$\kappa_T \equiv -\frac{1}{V}\left(\frac{\partial V}{\partial p}\right)_{T, N, H}, \qquad \text{(A.2)}$$

which can be measured directly in many experiments peculiar to the physics of condensed states [29, 31]. From (A.1), it follows that $n = -\partial\Omega/\partial\mu$ and that, at constant H and T, $dp = nd\mu$. Taking these relations into account, we can reduce κ_T to the form

$$\kappa_T \equiv -\frac{1}{V}\left(\frac{\partial V}{\partial p}\right)_{T, N, H} = -\frac{1}{V}\left(\frac{\partial (N/n)}{n\partial\mu}\right)_{T, N, H} = n^{-2}\frac{\partial n}{\partial\mu} = -n^{-2}\frac{\partial^2\Omega}{(\partial\mu)^2}; \qquad \text{(A.3)}$$

that is, $\partial^2\Omega/(\partial\mu)^2$ is proportional to the isothermal compressibility κ_T of the system.

The magnetic susceptibility κ_m, another thermodynamic coefficient, is proportional to $\partial^2\Omega/(\partial H)^2$. Indeed, we have

$$\kappa_m \equiv \frac{1}{V}\left(\frac{\partial M}{\partial H}\right)_{T, V, \ldots} = \frac{\partial m}{\partial H} = -\frac{\partial^2\Omega}{(\partial H)^2},$$

where we have used the definition of magnetic susceptibility, the identity $M = mV$, and the relation $m = -\partial\Omega/\partial H$ [which follows from (A.1)].

Finally, we consider the thermodynamic coefficient $(\partial M/\partial p)_{T, V, H}$. It is obvious that

$$-\frac{1}{V}\left(\frac{\partial M}{\partial p}\right)_{T, V, H} = -\frac{1}{V}\left(\frac{\partial (Vm)}{n\partial\mu}\right)_{T, V, H} = -n^{-1}\frac{\partial m}{\partial\mu} = n^{-1}\frac{\partial^2\Omega}{\partial\mu\partial H},$$

where we have used, in just the same way as in deriving (A.3), the relation $dp = nd\mu$.

REFERENCES

1. K. G. Klimenko, Teor. Mat. Fiz. **89**, 211 (1991); Z. Phys. C **54**, 323 (1992).
2. I. V. Krive and S. A. Naftulin, Yad. Fiz. **54**, 1471 (1991) [Sov. J. Nucl. Phys. **54**, 897 (1991)]; Phys. Rev. D **46**, 2737 (1992).
3. D. J. Gross and A. Neveu, Phys. Rev. D **10**, 3235 (1974).
4. K. G. Klimenko, A. S. Vshivtsev, and B. V. Magnitsky, Nuovo Cimento **A107**, 439 (1994); A. S. Vshivtsev, K. G. Klimenko, and B. V. Magnitsky, Teor. Mat. Fiz. **101**, 391 (1994); Yad. Fiz. **57**, 2260 (1994) [Phys. At. Nucl. **57**, 2171 (1994)]; A. S. Vshivtsev, V. Ch. Zhukovsky, K. G. Klimenko, and B. V. Magnitsky, Fiz. Élem. Chastits At. Yadra **29**, 1259 (1998) [Phys. Part. Nucl. **29**, 523 (1998)].
5. V. P. Gusynin, V. A. Miransky, and I. A. Shovkovy, Phys. Rev. Lett. **73**, 3499 (1994).
6. V. P. Gusynin, V. A. Miransky, and I. A. Shovkovy, Phys. Lett. B **349**, 477 (1995).
7. A. Yu. Babansky, E. V. Gorbar, and G. V. Shchepanyuk, Phys. Lett. B **419**, 272 (1998).
8. V. P. Gusynin, hep-ph/9709339; I. A. Shovkovy, hep-ph/9709340.
9. V. A. Miransky, hep-th/9805159.
10. D. Ebert and V. Ch. Zhukovsky, Mod. Phys. Lett. A **12**, 2567 (1997).
11. Y. Nambu and G. Jona-Lasinio, Phys. Rev. **122**, 345 (1961); V. G. Vaks and A. I. Larkin, Zh. Éksp. Teor. Fiz. **40**, 282 (1961) [Sov. Phys. JETP **13**, 192 (1961)]; B. A. Arbuzov, A. N. Tavkhelidze, and R. N. Faustov, Dokl. Akad. Nauk SSSR **139**, 345 (1961) [Sov. Phys. Dokl. **6**, 598 (1961)].
12. S. P. Klevansky and R. H. Lemmer, Phys. Rev. D **39**, 3478 (1989).
13. I. A. Shushpanov and A. V. Smilga, Phys. Lett. B **402**, 351 (1996).
14. R. R. Parwani, Phys. Lett. B **358**, 101 (1995); W. Dittrich and H. Gies, Phys. Lett. B **392**, 182 (1997).
15. K. G. Klimenko, Teor. Mat. Fiz. **90**, 3 (1992); A. S. Vshivtsev, K. G. Klimenko, and B. V. Magnitsky, Pis'ma Zh. Éksp. Teor. Fiz. **62**, 265 (1995) [JETP Lett. **62**, 283 (1995)]; S. Kanemura and H.-T. Sato, Nucl. Phys. B **517**, 567 (1998).
16. A. S. Vshivtsev, K. G. Klimenko, and B. V. Magnitsky, Teor. Mat. Fiz. **106**, 390 (1996).
17. V. P. Gusynin and I. A. Shovkovy, Phys. Rev. D **56**, 5251 (1997).

18. T. Inagaki, T. Muta, and S. D. Odintsov, Prog. Theor. Phys. (Suppl.) **127**, 93 (1997).
19. D. M. Gitman, S. D. Odintsov, and Yu. I. Shil'nov, Phys. Rev. D **54**, 2968 (1996); B. Geyer, L. N. Granda, and S. D. Odintsov, Mod. Phys. Lett. A **11**, 2053 (1996); T. Inagaki, S. D. Odintsov, and Yu. I. Shil'nov, hep-th/9709077; E. Elizalde, Yu. I. Shil'nov, and V. V. Chitov, Class. Quantum Grav. **15**, 735 (1998).
20. A. S. Vshivtsev, V. Ch. Zhukovsky, and K. G. Klimenko, Zh. Éksp. Teor. Fiz. **111**, 1921 (1997) [JETP **84**, 1047 (1997)]; A. S. Vshivtsev and K. G. Klimenko, Pis'ma Zh. Éksp. Teor. Fiz. **64**, 313 (1996) [JETP Lett. **64**, 338 (1996)].
21. J. Schwinger, Phys. Rev. **82**, 664 (1951).
22. M. R. Brown and M. J. Duff, Phys. Rev. D **11**, 2124 (1975); W. Dittrich, Fortschr. Phys. **26**, 289 (1978).
23. I. M. Ternov, V. Ch. Zhukovsky, and A. V. Borisov, *Quantum Processes in Strong External Fields* (Mosk. Gos. Univ., Moscow, 1989).
24. A. P. Prudnikov, Yu. A. Brychkov, and O. I. Marichev, *Integrals and Series*, Vol. 1 (Nauka, Moscow, 1981; Gordon and Breach, New York, 1986).
25. A. Erdélyi, *Higher Transcendental Functions (Bateman Manuscript Project)*, Ed. by A. Erdélyi (Nauka, Moscow, 1965, 1966; McGraw-Hill, New York, 1953, 1953), Vols. 1, 2.
26. M. A. Vdovichenko, A. S. Vshivtsev, and K. G. Klimenko, Preprint No. 97-59, IHEP (Institute for High Energy Physics, 1997); A. S. Vshivtsev, A. K. Klimenko, and K. G. Klimenko, Yad. Fiz. **61**, 543 (1998) [Phys. At. Nucl. **61**, 479 (1998)].
27. A. S. Vshivtsev, M. A. Vdovichenko, and K. G. Klimenko, Zh. Éksp. Teor. Fiz. **114**, 418 (1998) [JETP **87**, 229 (1998)].
28. L. D. Landau and E. M. Lifshitz, *Statistical Physics* (Nauka, Moscow, 1976; Pergamon, Oxford, 1980); I. M. Lifshits, *Collected Works* (Nauka, Moscow, 1994); D. Persson and V. Zeitlin, Phys. Rev. D **51**, 2026 (1995).
29. Yu. B. Rumer and M. Sh. Ryvkin, *Thermodynamics, Statistical Physics, and Kinetics* (Nauka, Moscow, 1977).
30. K. G. Klimenko and A. S. Vshivtsev, Zh. Éksp. Teor. Fiz. **109**, 954 (1996) [JETP **82**, 514 (1996)].
31. P. M. Chaikin and T. C. Lubensky, *Principles of Condenced Matter Physics* (Cambridge Univ. Press, Cambridge, 1995).

Translated by A. Isaakyan

Physics of Atomic Nuclei, Vol. 63, No. 3, 2000, pp. 480–488. From Yadernaya Fizika, Vol. 63, No. 3, 2000, pp. 552–560.

ELEMENTARY PARTICLES AND FIELDS
Theory

Strangeness, Charm, and Bottom in a Chiral Quark–Meson Model*

V. B. Kopeliovich and M. S. Sriram[1)]

Institute for Nuclear Research, Russian Academy of Sciences, ul. Shestidesyatiletiya Oktyabrya 7a, Moscow, 117312 Russia

Received November 27, 1998; in final form, June 6, 1999

Abstract—In this paper, we investigate an $SU(3)$ extension of the chiral quark–meson model. The spectra of baryons with strangeness, charm, and bottom are considered within a "rigid oscillator" version of this model. The similarity between the quark sector of the Lagrangian in the model and the Wess–Zumino term in the Skyrme model is noted. The binding energies of baryonic systems with baryon numbers $B = 2$ and 3 possessing strangeness or heavy flavor are also estimated. The results are in good qualitative agreement with those obtained previously in the chiral soliton (Skyrme) model. *© 2000 MAIK "Nauka/Interperiodica".*

1. INTRODUCTION

The chiral soliton models, Skyrme model first of all [1], are attractive because they are simple and elegant and allow us to describe the properties of lowest baryons with a rather good accuracy. At the same time, since the quark degrees of freedom are excluded from the beginning, the Skyrme model is not completely realistic: it is generally believed that quarks should be explicitly present in the baryons. Consideration of more realistic models with explicit quark degrees of freedom included in the Lagrangian seems to be necessary.

For the case of nonstrange baryons, this was done in [2–6] within the chiral quark–meson (CQM) model, where the mean-field approximation for the quark wave functions was an important ingredient. From a theoretical point of view, CQM models have an advantage that there is no question about the choice of the terms in the Lagrangian responsible for the stability of the soliton: the stabilization is due to the quark–meson interaction. Such models are minimal in the sense that only the second-order terms in chiral-field derivatives are present in the effective Lagrangian [2–5].

Here, we extend such models for the consideration of baryons with strangeness, charm, and bottom for the sector with $B = 1$, first of all. These degrees of freedom are treated in the same manner as in the bound-state approach to heavy flavors proposed in [7, 8] and a "rigid oscillator" version of which was developed in [9–11]. Within this model, the deviations of quark fields and solitons into "strange" ("charm" or "bottom") directions are considered as small ones, and a corresponding expansion of the Lagrangian is made. The results obtained confirm the assumption concerning the smallness of these deviations. Also, the deformations according to, e.g., "cranking" [3] into the strange or other directions are neglected within the rigid oscillator version of the model.

The sectors with $B = 2$ and 3 are also briefly discussed. Previously, the question of existence of baryonic systems with strangeness different from zero was a subject of intensive studies originated with papers [12–15]. Some review of theoretical predictions, mainly for the sector with $B = 2$, can be found in [16]. The question of whether a baryonic system with flavor different from u and d exists is quite general. Charm, bottom, or top quantum numbers are also of interest, and their consideration can be performed in the framework of chiral soliton models, in particular, the bound-state approach to heavy flavors [7–10]. As was shown recently within the rigid oscillator model, the baryonic systems with charm or bottom have even more chances to be stable with respect to strong interactions, in comparison with strange baryonic systems [11]. Here, we present some estimates for the binding energies of the lightest baryonic system with nontrivial flavor in the chiral quark–meson model and show that these estimates are in qualitative agreement with those obtained in [10, 11].

In Section 2, we consider the $SU(3)$ extension of the chiral quark–meson Lagrangian. In the next section, we give an explicit expression for the Hamiltonian of the baryonic system in the leading order in N_c in terms of the flavor (antiflavor) excitation frequencies. In Section 4, the $B = 1$ sector is considered and hyperon–nucleon mass differences are estimated, including the zero-mode corrections of order $1/N_c$. In Section 5, the sectors with $B \geq 2$ are discussed, and binding energies of some few-baryonic systems are estimated.

* This article was submitted by the authors in English.

[1)] Department of Theoretical Physics, University of Madras, Guindy Campus, 600025 Madras, India.

1063-7788/00/6303-0480$20.00

2. *SU*(3) EXTENSION OF THE CHIRAL QUARK–MESON LAGRANGIAN

The *SU*(3) extension of the chiral quark–meson Lagrangian density can be written in the following way [2, 3]:

$$\mathcal{L} = i\overline{\Psi}\hat{\partial}\Psi - gF_\pi(\overline{\Psi}_L U\Psi_R + \overline{\Psi}_R U^\dagger\Psi_L)$$
$$-\frac{\alpha_F}{3}gF_\pi[\overline{\Psi}_L(1-\sqrt{3}\lambda_8)U\Psi_R + \overline{\Psi}_R U^\dagger(1-\sqrt{3}\lambda_8)\Psi_L]$$
$$+\frac{F_\pi^2}{16}\mathrm{tr}\,l_\mu l^\mu + \frac{F_\pi^2 m_\pi^2}{16}\mathrm{tr}(U+U^\dagger-2) \quad (1)$$
$$+\frac{F_D^2 m_D^2 - F_\pi^2 m_\pi^2}{24}\mathrm{tr}(1-\sqrt{3}\lambda_8)(U+U^\dagger-2)$$
$$+\frac{F_D^2 - F_\pi^2}{48}\mathrm{tr}(1-\sqrt{3}\lambda_8)(Ul_\mu l^\mu + l_\mu l^\mu U^\dagger).$$

Here, Ψ is a triplet of quark fields: (*u*, *d*, *s*), (*u*, *d*, *c*), or (*u*, *d*, *b*); λ_k are the Gell-Mann matrices; $U \in SU(3)$ is a unitary matrix incorporating chiral (meson) fields; and $l_\mu = U^\dagger\partial_\mu U$. In this model, F_π is fixed at the physical value, $F_\pi = 186$ MeV, and $gF_\pi \simeq 500$ MeV appears as the effective bare *u*- and *d*-quark masses. The interaction between quarks is not considered explicitly, but it is present in this mean-field description of the quarks due to the quark–meson coupling. Here, we have included terms in the Lagrangian which describe flavor symmetry breaking (FSB) in bare constituent quark masses, $\sim(F_D^2 m_D^2 - F_\pi^2 m_\pi^2)$, as well as in the quark–meson coupling which is proportional to a parameter α_F. The FSB in the meson sector of the Lagrangian is of usual form and was sufficient to describe the mass splittings of the octet and decuplet of baryons [17]. Here, we consider first a case of flavor symmetry in decay constants, i.e., $F_D = F_\pi$. Even for realistic values of F_D, the last term in (1) is small and can be omitted for estimates we are making here.

The importance of the quark sector of the Lagrangian is that it reproduces the properties of the Wess–Zumino (WZ) term written in the simple form by Witten [18]. First, the baryon number is given by this term, and second, when the field Ψ is turned into "strange" or other direction, the quark Lagrangian gives the contribution coinciding with that coming from the WZ term in the Skyrme model [9, 10].

We shall consider the collective-coordinate rotation of the quark field Ψ and the meson fields incorporated into the matrix *U*, in the spirit of the bound-state approach to the description of strangeness proposed in [7–9] and used in [10, 11]:

$$\Psi(r,t) = R(t)\Psi_0(O(t)\mathbf{r}),$$
$$U(r,t) = R(t)U_0(O(t)\mathbf{r})R^\dagger(t), \quad R(t) = A(t)S(t), \quad (2)$$

where Ψ_0 is originally a two-component spinor in the (*u*, *d*) *SU*(2) subgroup; U_0 is the *SU*(2) soliton embedded into *SU*(3) in the usual way (into left upper corner); $A(t) \in SU(2)$ describes *SU*(2) rotations; $S(t) \in SU(3)$ describes rotations in the "strange," "charm," or "bottom" direction; and $O(t)$ describes rigid rotations in coordinate space. To be more specific, we shall consider the extension of the (*u*, *d*) *SU*(2) Skyrme model in strange direction, when *D* is the field of *K* mesons. But it is evident that a similar extension can be made in the charm or bottom directions also:

$$S(t) = \exp(i\mathcal{D}(t)), \quad \mathcal{D}(t) = \sum_{a=4,\ldots,7} D_a(t)\lambda_a, \quad (3)$$

where λ_a are Gell-Mann matrices of (*u*, *d*, *s*), (*u*, *d*, *c*), or (*u*, *d*, *b*) *SU*(3) groups. The (*u*, *d*, *c*) and (*u*, *d*, *b*) *SU*(3) groups are quite similar to the (*u*, *d*, *s*) one. For the (*u*, *d*, *c*) group, a simple redefinition of hypercharge should be made. For the (*u*, *d*, *s*) group, we have $D_4 = (K^+ + K^-)/\sqrt{2}$, $D_5 = i(K^+ - K^-)/\sqrt{2}$, etc. For the (*u*, *d*, *c*) group $D_4 = (D^0 + \bar{D}^0)/\sqrt{2}$, etc.

Consider first the contribution due to the time dependence of the collective rotations in the quark sector of the Lagrangian:

$$\mathcal{L}_q = \left[\sum_q i\overline{\Psi}\hat{\partial}\Psi\right]_{\mathrm{coll}}$$
$$= \sum_q \Psi^\dagger\left[iS^\dagger\dot{S} + \frac{1}{2}S^\dagger\boldsymbol{\tau}\cdot\boldsymbol{\omega}S + i(\mathbf{r}\cdot\boldsymbol{\Omega}\cdot\boldsymbol{\partial})\right]\Psi. \quad (4)$$

Here, $\boldsymbol{\omega}$ and $\boldsymbol{\Omega}$ are the vectors of angular velocities for the isospin and usual space rotations, respectively, defined in the standard way:

$$A^\dagger\dot{A} = -i\boldsymbol{\omega}\cdot\boldsymbol{\tau}/2, \quad \dot{O}_{in}O_{kn} = \epsilon_{ikm}\Omega_m.$$

The field *D* is small in magnitude, of order $1/\sqrt{N_c}$, where N_c is the number of colors in QCD. Therefore, an expansion of the matrix *S* in *D* powers can be made. Taking into account all the terms up to $O(1/N_c)$, we can represent $\mathcal{L}_q$ in the form

$$\mathcal{L}_q \simeq \sum_q \Psi_0^\dagger\left[\frac{i}{2}(\dot{D}^\dagger D - D^\dagger\dot{D})\left(1 - \frac{2}{3}D^\dagger D - \frac{1}{2}\boldsymbol{\tau}D^\dagger\cdot\boldsymbol{\tau}D\right)\right.$$
$$+\frac{1}{2}(\boldsymbol{\omega}-\boldsymbol{\beta})\cdot\boldsymbol{\tau} - \frac{1}{2}(\boldsymbol{\omega}\cdot\boldsymbol{\tau}D^\dagger D + \boldsymbol{\omega}D^\dagger\cdot\boldsymbol{\tau}D) \quad (5a)$$
$$\left.+\frac{1}{12}D^\dagger D\boldsymbol{\tau}\cdot\boldsymbol{\beta} + i(\mathbf{r}\cdot\boldsymbol{\Omega}\cdot\boldsymbol{\partial})\right]\Psi_0.$$

Here,

$$\boldsymbol{\beta} = i(D^\dagger \boldsymbol{\tau} \dot{D} - \dot{D}^\dagger \boldsymbol{\tau} D) \tag{5b}$$

is the angular velocity of rotation in the "flavor" direction, D is the doublet of heavy-meson fields, kaons, and D or B mesons. Lagrangian (5a) does not depend on the quark orientation in isospace or on their radial wave functions, which are not the same for different quarks. However, for arbitrary B, we always find the following term containing the factor N_c, after summing over quark colors and flavors and integrating with respect to space coordinates:

$$L_q = \frac{N_c B s_d^2}{2} \frac{}{d^2} [i(\dot{D}^\dagger D - D^\dagger \dot{D}) - (\boldsymbol{\omega} D^\dagger \cdot \boldsymbol{\tau} D)], \tag{6}$$

which is valid in any order in $d^2 = 2D^\dagger D$. It is assumed in (6) that the quark wave functions Ψ are properly normalized, $\int \Psi^\dagger \Psi d^3 r = 1$. This contribution coincides with that obtained from the Wess–Zumino term in the action in the bound-state approach of the topological soliton (Skyrme) model [8–10].

The general parametrization of U_0 for the $SU(2)$ soliton we use here is given by $U_0 = c_f + s_f \boldsymbol{\tau} \cdot \mathbf{n}$ with $n_z = c_\alpha$, $n_x = s_\alpha c_\beta$, $n_y = s_\alpha s_\beta$, $s_f = \sin f$, $c_f = \cos f$, etc. The mass term in Lagrangian (1) can be calculated exactly, without expansion in the field D because the matrix S is $S = 1 - i\mathcal{D} \sin d/d - \mathcal{D}^2(1 - \cos d)/d^2$ with $d^2 = \mathrm{tr}\mathcal{D}^2$:

$$\Delta \mathcal{L}_M = -\frac{F_D^2 m_D^2 - F_\pi^2 m_\pi^2}{4} (1 - c_f) s_d^2. \tag{7}$$

The expansion of this term can be done easily up to any order in d. The comparison of this expression with ΔL_M within the collective-coordinate approach of the quantization of $SU(2)$ solitons in $SU(3)$ configuration space allows us to deduce an equality $\sin^2 d = \sin^2 \nu$, where ν is the angle of the λ_4 rotation, or rotation into "strange" direction. The so-called strangeness (or flavor) content of the quark fields can be calculated easily as $C_s \simeq D^\dagger D$. It should be kept in mind that in the collective-coordinate method the scalar strangeness content of the soliton $C_s = (\sin^2 \nu)/2$.

The time-dependent part of the second-order term in the Lagrangian density (1) due to rotations in the $SU(3)$ configuration space leads to the following contribution:

$$\begin{aligned} \mathcal{L}_2 = 2\mathrm{tr}[&\dot{S}\dot{S}^\dagger + S^\dagger \dot{S} U_0^\dagger S^\dagger \dot{S} U_0 + \dot{A}\dot{A}^\dagger + 2A^\dagger \dot{A} S \dot{S}^\dagger \\ &+ S^\dagger A^\dagger \dot{A} S U_0^\dagger S^\dagger A^\dagger \dot{A} S U_0 + S^\dagger \dot{S} U_0^\dagger S^\dagger A^\dagger \dot{A} S U_0 \\ &+ S^\dagger A^\dagger \dot{A} S U_0^\dagger S^\dagger \dot{S} U_0]. \end{aligned} \tag{8}$$

Making an expansion of the matrix S and also adding together contributions from the usual space rotations we obtain

$$\begin{aligned} \mathcal{L}_2 \simeq \frac{F_\pi^2}{8} \Big\{ &4(1 - c_f) \Big[\dot{D}^\dagger \dot{D} \Big(1 - \frac{2}{3} D^\dagger D \Big) \\ &- \frac{2}{3} (D^\dagger \dot{D} \dot{D}^\dagger D - (D^\dagger \dot{D})^2 - (\dot{D}^\dagger D)^2) + \boldsymbol{\omega} \cdot \boldsymbol{\beta}/2 \Big] \\ &+ s_f^2 [(\boldsymbol{\omega} - \boldsymbol{\beta})^2 - (\boldsymbol{\omega} \cdot \mathbf{n} - \boldsymbol{\beta} \cdot \mathbf{n})^2] + (\boldsymbol{\partial} f \mathbf{r} \cdot \boldsymbol{\Omega})^2 \\ &+ s_f^2 (\boldsymbol{\partial} n_i \mathbf{r} \cdot \boldsymbol{\Omega})^2 + 2 s_f^2 (\boldsymbol{\omega} \cdot \mathbf{n} \partial_i \mathbf{n}) \epsilon_{ikl} r_k \Omega_l \Big\}. \end{aligned} \tag{9}$$

The moments of inertia of the configuration can be extracted easily from (9) as the coefficients in the quadratic form in angular velocities of rotation.

The interaction of quarks and mesons gives the contribution proportional to the new parameter α_F, after integrating over space:

$$L_{\mathrm{int}} \simeq -\alpha_F E_{qm} D^\dagger D \Big(1 - \frac{2}{3} D^\dagger D \Big), \tag{10}$$

where, according to [2, 3], $E_{qm} < 0$ is the quark–meson interaction energy.

An expression (9) can be simplified considerably for spherically symmetrical configurations (hedgehogs) for $B = 1$, as well as for $B \geq 2$ solitons described by axially symmetrical configurations (see Sections 4 and 5 for details).

After some calculation, the Lagrangian of the chiral quark–meson model in the lowest order in field D can by written in the form below which is similar to that of the bound state approximation to the topological soliton model [7–10]:

$$\begin{aligned} L = &-M_{\mathrm{cl},B} + 4\Theta_{F,B} \dot{D}^\dagger \dot{D} \\ &- [\Gamma_B (m_D^2 - m_\pi^2) + \alpha_F E_{qm}] D^\dagger D - i \frac{N_c B}{2} (D^\dagger \dot{D} - \dot{D}^\dagger D). \end{aligned} \tag{11}$$

We have ignored the difference between F_K and F_π through the last term in (1) in the above expression and kept our former notation for the moment of inertia under rotation into "strange," "charm," or "bottom" direction $\Theta_c = \Theta_b = \Theta_s = \Theta_F$ [15] (the subscript c indicates the charm quantum number everywhere, except in N_c). In the present model, this moment of inertia has a simple analytical form for an arbitrary initial $SU(2)$ skyrmion, regardless of its symmetry properties:

$$\Theta_{F,B} = \frac{F_\pi^2}{8} \int (1 - c_f) d^3 r. \tag{12}$$

Note, that since the Skyrme term is absent in the CQM model, this formula is especially simple. Some contribution to Θ_F originates from deformations, or "cranking" of the quark fields into strange, or other directions,

similar to the isotopic inertia Θ_T [3], but it can be neglected in the spirit of the rigid oscillator model.

The quantity Γ_B defines the contribution of the mass term in the Lagrangian (1),

$$\Gamma_B = \frac{F_\pi^2}{2}\int(1-c_f)d^3r, \tag{13}$$

so, the following relation is valid in CQM:

$$\Gamma_B = 4\Theta_{F,B}. \tag{14}$$

The term proportional to N_cB in (11), which comes from the quark sector here, is responsible for the splitting between excitation energies of strangeness and antistrangeness (flavor and antiflavor in general case) [8–10].

3. FLAVOR EXCITATION FREQUENCIES

As a result of the canonical quantization procedure, the Hamiltonian of the system including the terms of order N_c^0 takes a form similar to that in the topological soliton models [9, 10]:

$$\begin{aligned} H_B &= M_{\mathrm{cl},B} + \frac{1}{4\Theta_{F,B}}\Pi^\dagger\Pi \\ &+ \left[\Gamma_B\bar{m}_D^2 + \alpha_F E_{qm} + \frac{N_c^2B^2}{16\Theta_{F,B}}\right]D^\dagger D \\ &+ i\frac{N_cB}{8\Theta_{F,B}}(D^\dagger\Pi - \Pi^\dagger D), \end{aligned} \tag{15}$$

$\bar{m}_D^2 = m_D^2 - m_\pi^2$. A momentum Π is conjugated canonically to variable D [see (23) below]. Hamiltonian (15) corresponds to the oscillator-type motion of the field D against the background formed by the (u, d) $SU(2)$ soliton. A diagonalization of H_B can be done explicitly according to [9, 10], and the normal-ordered Hamiltonian can be written as

$$H_B = M_{\mathrm{cl},B} + \omega_{F,B}a^\dagger a + \bar{\omega}_{F,B}b^\dagger b + O(1/N_c), \tag{16}$$

with $a^\dagger$ and $b^\dagger$ being the operators of creation of the strangeness (i.e., antikaons) and the antistrangeness (flavor and antiflavor) quantum number, $\omega_{F,B}$ and $\bar{\omega}_{F,B}$ being the frequencies of flavor (antiflavor) excitation. D and Π are related to a and b in the following way [9, 10]:

$$\begin{aligned} D^i &= \frac{1}{\sqrt{N_cB\mu_{F,B}}}(b^i + a^{\dagger i}), \\ \Pi^i &= \frac{\sqrt{N_cB\mu_{F,B}}}{2i}(b^i - a^{\dagger i}) \end{aligned} \tag{17}$$

with

$$\mu_{F,B} = \left[1 + 16(\bar{m}_D^2\Gamma_B + \alpha_F E_{qm})\Theta_{F,B}/(N_cB)^2\right]^{1/2}.$$

For the lowest states, the values of D are small,

$$D \sim [16\Gamma_B\Theta_{F,B}\bar{m}_D^2 + N_c^2B^2]^{-1/4},$$

and increase with $|F|$ as $(2|F|+1)^{1/2}$. As was noted in [10], deviations of the field D from the vacuum decrease with increasing mass m_D, as well as the number of colors N_c, and the method works for any m_D—for charm and bottom quantum numbers also.

The excitation frequencies ω and $\bar{\omega}$ are

$$\begin{aligned} \omega_{F,B} &= \frac{N_cB}{8\Theta_{F,B}}(\mu_{F,B} - 1), \\ \bar{\omega}_{F,B} &= \frac{N_cB}{8\Theta_{F,B}}(\mu_{F,B} + 1). \end{aligned} \tag{18}$$

As was observed in [11], the difference $\bar{\omega}_{F,B} - \omega_{F,B} = N_cB/(4\Theta_{F,B})$ coincides in the leading order in N_c with that obtained in the collective-coordinate approach [15].

To get an idea about the value of the parameter α_F, we can use a relation between $\alpha_F gF_\pi$ and the effective quark mass:

$$(1+\alpha_F)gF_\pi \simeq m_F^{\mathrm{eff}}. \tag{19}$$

Since the quark–meson interaction energy is negative—it leads to the stability of the whole configuration—the term $\alpha_F E_{qm}$ makes the flavor excitation frequencies smaller. The relative role of this effect decreases with increasing mass of the flavor and is more important for strange baryons. For the $B = 1$ configuration, the quark–meson interaction energy $E_{qm} = -1.127$ GeV [3]. For strange baryons to have bare constituent strange quark mass greater than that of nonstrange quarks by about 0.2 GeV, we should take $\alpha_s \simeq 0.4$. Similarly, we can obtain the crude estimates $\alpha_c \simeq 2.7$ and $\alpha_b \simeq 9.4$.

The FSB in the flavor decay constants, i.e., the fact that $F_K/F_\pi \simeq 1.23$ and $F_D/F_\pi = 1.7 \pm 0.2$, should be taken into account as well. In the Skyrme model, it leads to the increase of the flavor excitation frequencies, which modifies the spectra of flavored baryons in better agreement with data [19, 20], and leads also to some changes of the binding energies of baryonic system [11]. It was mainly due to the large contribution of the Skyrme term in the Lagrangian to the inertia Θ_F. Since the Skyrme term in the CQM model under consideration is absent—we obtain the relation $\Gamma_B = 4\Theta_{F,B}$ as a result—the effect of FSB in decay constants is of minor importance in the chiral quark–meson model.

The terms of the order N_c^{-1} in the Hamiltonian depending on the angular velocities of rotations in the isospin and the coordinate space, describing the zero-mode contributions, are not crucial, but they are important for numerical estimates of the baryon spectra. They will be considered in the next sections.

4. $B = 1$ HEDGEHOG AND ESTIMATES OF BARYON SPECTRA

The $B = 1$ hedgehog configuration in the chiral quark–meson model can be treated in the same manner as in the topological (Skyrme) model. The unit vector $\mathbf{n}$ describing the chiral meson-field configuration is $\mathbf{n} = \hat{\mathbf{r}} = \mathbf{r}/r$, and the spinor Ψ_0 has the structure [2, 3]

$$\Psi_0 = \begin{pmatrix} G(r)\chi_h \\ i\boldsymbol{\sigma}\cdot\mathbf{n}F(r)\chi_h \end{pmatrix},$$

where χ_h is the hedgehog spinor

$$\chi_h = \frac{1}{\sqrt{2}}(u\downarrow - d\uparrow). \tag{20}$$

It can be examined for hedgehogs that the terms in (5) that depend on the orientation of the quarks in isospin and spin space, being proportional to $\boldsymbol{\tau}$, make zero contribution to the Lagrangian. Rotations in the iso- and coordinate spaces are equivalent for hedgehogs, and the contribution to the energy depends on one common moment of inertia, $\Theta_{T,B}$.

From equations (1), (6), (9), and (10) in Section 2, we obtain the following expression for the Lagrangian including all the terms up to $O(1/N_c)$:

$$\begin{aligned} L \simeq -M_{\rm cl} &+ 4\Theta_F\Big[\dot{D}^\dagger\dot{D}\Big(1-\frac{2}{3}D^\dagger D\Big) \\ &-\frac{2}{3}(D^\dagger\dot{D}\dot{D}^\dagger D - (D^\dagger\dot{D})^2 - (\dot{D}^\dagger D)^2)\Big] + 2\Theta_F(\boldsymbol{\omega}\cdot\boldsymbol{\beta}) \\ &+ \frac{\Theta_T}{2}(\boldsymbol{\omega}-\boldsymbol{\beta})^2 - (\Gamma_B\bar{m}_F^2 + \alpha_F E_{qm})D^\dagger D\Big(1-\frac{2}{3}D^\dagger D\Big) \\ &+ i\frac{N_cB}{2}\Big(1-\frac{2}{3}D^\dagger D\Big)(\dot{D}^\dagger D - D^\dagger\dot{D}) - \frac{N_cB}{2}\boldsymbol{\omega}\cdot D^\dagger\boldsymbol{\tau}D. \end{aligned} \tag{21}$$

By means of this Lagrangian, we can introduce the canonical variables

$$\begin{aligned} \Pi &= \frac{\partial L}{\partial\dot{D}^\dagger} \\ &= 4\Theta_F\Big[\dot{D}\Big(1-\frac{2}{3}D^\dagger D\Big) - \frac{2}{3}D^\dagger\dot{D}D + \frac{4}{3}\dot{D}^\dagger DD\Big] \\ &\quad + i(\Theta_T - 2\Theta_F)\boldsymbol{\omega}\cdot\boldsymbol{\tau}D - i\Theta_T\boldsymbol{\beta}\cdot\boldsymbol{\tau}D \\ &\quad + i\frac{N_cB}{2}\Big(1-\frac{2}{3}D^\dagger D\Big)D, \end{aligned} \tag{22}$$

$$\begin{aligned} \mathbf{I}_{bf} &= \partial L/\partial\boldsymbol{\omega} \\ &= \Theta_T\boldsymbol{\omega} + (2\Theta_F - \Theta_T)\boldsymbol{\beta} - \frac{N_cB}{2}D^\dagger\boldsymbol{\tau}D \end{aligned} \tag{23a}$$

or

$$\mathbf{I}_{bf} = \Theta_T\boldsymbol{\omega} + \Big(1-\frac{\Theta_T}{2\Theta_F}\Big)\langle\mathbf{I}_F\rangle - \frac{N_cB\Theta_T}{4\Theta_F}D^\dagger\boldsymbol{\tau}D, \tag{23b}$$

where $\langle\mathbf{I}_F\rangle$ is matrix element of the operator $\mathbf{I}_F = (b^\dagger\boldsymbol{\tau}b - a\boldsymbol{\tau}a^\dagger)/2$ taken between states with flavor F.

Using the relations

$$-i\boldsymbol{\beta}\cdot\boldsymbol{\tau}D = 2D^\dagger D\dot{D} - (\dot{D}^\dagger D + D^\dagger\dot{D})D$$

and

$$\boldsymbol{\beta}^2 = 4D^\dagger D\dot{D}^\dagger\dot{D} - (\dot{D}^\dagger D + D^\dagger\dot{D})^2,$$

one can see that L, Π, and $\mathbf{I}_{bf}$ have essentially the same structures as the appropriate expressions in [10]. This is true for the Hamiltonian also, and we find that the $1/N_c$ zero-mode quantum correction to the energies of hedgehogs in the CQM model has a structure which is quite similar to the correction term in the Skyrme model. It can be estimated according to the expression [9, 10]

$$\begin{aligned} \Delta E_{1/N_c} &= \frac{1}{2\Theta_{T,B}}[c_{F,B}T_r(T_r+1) \\ &+ (1-c_{F,B})I(I+1) + (\bar{c}_{F,B} - c_{F,B})I_F(I_F+1)], \end{aligned} \tag{24}$$

where $I = I_{bf}$ is the isospin of the baryon or baryonic system, T_r is the quantity analogous to the "right" isospin T_r in the collective-coordinate approach [21, 22], and $\mathbf{T}_r = \mathbf{I}_{bf} - \mathbf{I}_F$, the operator $\mathbf{I}_F = \frac{1}{2}(b^\dagger\boldsymbol{\tau}b - a\boldsymbol{\tau}a^\dagger)$,

$$\begin{aligned} c_{F,B} &= 1 - \frac{\Theta_{T,B}}{2\Theta_{F,B}\mu_{F,B}}(\mu_{F,B}-1), \\ \bar{c}_{F,B} &= 1 - \frac{\Theta_{T,B}}{\Theta_{F,B}(\mu_{F,B})^2}(\mu_{F,B}-1). \end{aligned} \tag{25}$$

In the case of antiflavor excitations, we have the same formula (24), with the substitution $\mu \longrightarrow -\mu$ in (25). For example,

$$\bar{c}_{\bar{F},B} = 1 + \frac{\Theta_{T,B}}{\Theta_{F,B}\mu_{F,B}^2}(\mu_{F,B}+1). \tag{26}$$

According to (9), the isotopic inertia is

$$\Theta_T = \frac{F_\pi^2}{6}\int s_f^2 d^3r, \tag{27}$$

but it acquires the same contribution (about 30%) also from the quark sector of the Lagrangian due to the cranking procedure described in [3]. For numerical estimates here, we take the value of Θ_T obtained in [3] in the linear σ model since the differences of all calculated quantities in the linear and nonlinear versions of the σ model are negligible.

The excitation frequencies for flavor F, ω_F, antiflavor, $\bar{\omega}_F$, and the energy differences of baryons with different flavors and the nucleon, in GeV; ω_{Sk} are the flavor excitation frequences in the Skyrme model shown here for comparison

F	ω_F	ω_{Sk}	$\bar{\omega}_F$	$\langle D^\dagger D\rangle$	$\Delta M_{\Lambda_F - N}$	$\Delta M^{exp}_{\Lambda_F - N}$	$\Delta M_{\Sigma_F - N}$	$\Delta M^{exp}_{\Sigma_F - N}$	$\Delta M_{Z_F - N}$	$\bar{c}_F$
s	0.326	0.20	0.69	0.120	0.28	0.177	0.44	0.254	0.78	0.34
c	1.687	1.18	2.05	0.032	1.67	1.346	1.89	1.516	2.07	0.75
b	5.098	3.66	5.46	0.011	5.09	4.702	5.32	–	5.47	0.90

Note: For $B = 1$ soliton, we use the values of mass $M_1 = 1149$ MeV, flavor inertia $\Theta_F = 2.06$ GeV^{-1} [23], and isotopic inertia $\Theta_T = 5.93$ GeV^{-1} [3]. The estimate used here, $\langle D^\dagger D\rangle = (N_c B\mu)^{-1}$, is valid for the lowest state of oscillator with $|F| = 0$, i.e., for the nucleon.

In the rigid oscillator model, the states predicted are not identified with definite $SU(3)$ or $SU(4)$ representations. However, it can be done, as shown in [10]. The quantization condition $(p + 2q)/3 = B$ [21] for arbitrary N_c is changed to $(p + 2q) = N_c B + 3n_{q\bar{q}}$, where $n_{q\bar{q}}$ is the number of additional quark–antiquark pairs present in the quantized states. For example, the state with $B = 1$, $|F| = 1$, $I = 0$, and $n_{q\bar{q}} = 0$ should belong to the octet of (u, d, s), or (u, d, c), etc., $SU(3)$ group if $N_c = 3$ (see also [10]). In limiting case $\Theta_F \longrightarrow \infty$, (24) turns into the expression obtained within the collective-coordinate approach [15, 21]. In a realistic case with $\Theta_T/\Theta_F \simeq 2.9$, the structure of (24) is more complicated.

We will first summarize the results for $B = 1$ in the "rigid oscillator" approach to heavy flavors in CQM, without including the effect of flavor symmetry breaking in the quark–meson couplings (that is, $\alpha_F = 0$). We find that the excitation frequencies ω_F are, in general, higher than in the Skyrme model. This can be attributed to the fact that the value of Γ_B in the present model is higher than the same parameter in the Skyrme model. The mass difference $M_\Lambda - M_N$ comes out to be 284 MeV compared to the experimental value of 176 MeV. However, it is to be noted that the value of ω_S in the rigid oscillator approach used here is close to the value of 315 MeV obtained in a random phase approximation to the CQM model with broken $SU(3)$ [4].

It should be noted that the values of inertia obtained within the chiral quark–meson model are close to those obtained in the Skyrme model. For example, the flavor inertia $\Theta_F = 1.86$ GeV^{-1} in the Skyrme model with $F_\pi = 108$ MeV and $e = 4.84$ (nucleon and Δ-isobar masses are fitted), and $\Theta_F = 2.03$ GeV^{-1}, $\Theta_T = 5.55$ GeV^{-1} in the Skyrme model version with $F_\pi = 186$ MeV and $e = 4.12$.

The Z_F baryons included in the table have $\bar{F}$ quantum number and are truly exotic because they cannot be made of N_c valence quarks only: one $\bar{q}q$ pair is needed for this purpose. These states belong to the $\overline{10}$ representation of the corresponding $SU(3)$ (the upper state with isospin $I = 0$). The mass of the state with $S = +1$, which was calculated first in [24] within the collective-coordinate approach of the quantization of zero modes in the Skyrme model, was found to be ~740 MeV above the nucleon. Later, this antistrange baryon was considered in more detail in [25], where the $M_Z - M_N$ mass difference was found to be ~590 MeV, also within Skyrme model, but with the additional assumption that the $N^*(1710)$ resonance is the nonstrange component of the antidecuplet of baryons. The CQM model prediction for the $S = +1$ baryon (see table) is in better agreement with predictions of the collective-coordinate method [16, 24].

The inclusion of FSB in the quark–meson coupling improves the situation. We take the values of the parameter α_F to be $\alpha_s = 0.4$, $\alpha_c = 2.7$, and $\alpha_b = 9.4$, which allow us to obtain the effective quark masses in the Lagrangian close to the known values. Then, we obtain $\omega_s = 0.27$ GeV, $\omega_c = 1.58$ GeV, and $\omega_b = 4.97$ GeV. The values of the mass differences now are (in GeV) $\Delta M_{\Lambda - N} = 0.229(0.176)$, $\Delta M_{\Sigma - N} = 0.371(0.254)$, $\Delta M_{\Lambda_c - N} = 1.57(1.346)$, $\Delta M_{\Sigma_c - N} = 1.788(1.516)$, $\Delta M_{\Lambda_b - N} = 4.968(4.702)$, and $\Delta M_{\Sigma_b - N} = 5.196$, where the figures in parentheses correspond to the experimental values. We see that the values are now in better agreement with data. The difference of masses of exotic Z baryons and the nucleon also is lowered slightly but remains well above the threshold for strong decay: $\Delta M_{Z_F - N} \simeq 0.74$, 1.97, and 5.35 GeV for $\bar{s}$, $\bar{c}$, and $\bar{b}$ quantum numbers. A role of the α_F term is lost with increasing mass of the quark, as expected.

5. BINDING-ENERGY ESTIMATES FOR DIBARYONS WITH STRANGENESS, CHARM, AND BOTTOM

It was shown in [5, 6] that in the chiral quark–meson model there are bound states of solitons with $B = 2$ and more, similar to the topological soliton models [26]. Therefore, one should expect the prediction of the dibaryons, tribaryons, etc., with different values of flavor quantum number, s, c, or b, stable against the strong interactions, similar to the Skyrme model.

The structure of the toruslike configurations with $B = 2$ should be described first. For $B = 2$, Ψ_0 has the

structure

$$\Psi_0 = \begin{pmatrix} G(\rho, z)\chi_{1,2} \\ i\boldsymbol{\sigma}\cdot\mathbf{r}F(\rho, z)\chi_{1,2}\end{pmatrix},$$

where

$$\chi_1 = \frac{1}{\sqrt{2(1-\cos\theta\cos\alpha)}}$$
$$\times[\sin\alpha u\downarrow - \sin\theta e^{i\phi}d\uparrow - (\cos\alpha-\cos\theta)e^{2i\phi}d\downarrow]$$

and

$$\chi_2 = \frac{1}{\sqrt{2(1-\cos\theta\cos\alpha)}} \quad (28)$$
$$\times[\sin\alpha d\uparrow - \sin\theta e^{-i\phi}u\downarrow + (\cos\alpha-\cos\theta)e^{-2i\phi}u\uparrow],$$

r and z are cylindrical variables, $\theta = \arctan(r/z)$ is the polar angle, and α is the angular profile of the soliton. For $\alpha = \theta$, equation (28) is similar to the corresponding expression (20) for the hedgehog.

In the $B = 2$ soliton, N_c quarks are in the state χ_1 and N_c quarks are in the state χ_2. Similar considerations apply for higher B. Then, equations (5) and (9) for the Lagrangian are simplified substantially; in particular, the terms in (5) proportional to $\Psi^\dagger\boldsymbol{\tau}\Psi$ cancel, similarly to the hedgehog case.

In [6, 23], the following values of the binding energy of quark–meson solitons have been obtained: $\epsilon_2 = 279$ MeV, $\epsilon_3 = 226$ MeV, and $\epsilon_4 = 192$ MeV for two, three, and four baryons. These quantities can be compared with the values of binding energy in the Skyrme model, 72, 70, and 10 MeV, for smaller value of the constant, $F_\pi = 108$ MeV [26]. For $F_\pi = 186$ MeV and $e = 4.12$, $\epsilon_2 = 142$ MeV. It makes sense to give the binding energies in units, e.g., of the mass of the $B = 1$ soliton: although the symmetry-violating mass terms in the Lagrangian violate the scaling, such comparison provides information which does not depend noticeably on the value of F_π. In the CQM model, $\epsilon_2 = 0.24M_1$, $\epsilon_3 = 0.20M_1$, and $\epsilon_4 = 0.17M_1$ to be compared with 0.083, 0.081, and $0.012M_1$ in the Skyrme model [26].

Let us consider here the state with $B = 2$ and $|F| = 2$ with the lowest value of isospin, $I = 0$, which can belong to the 27-plet of the corresponding $SU(3)$ group, (u, d, s) or (u, d, c), etc. For 27-plet of dibaryons, we have $T_r = 1$; for antidecuplet, $T_r = 0$. The quantum correction due to usual space rotations (also of order $1/N_c$) is exactly of the same form as obtained in [15] (see [9, 10]). Since we are interested here in the lowest states, we shall consider the baryonic systems with the lowest allowed angular momentum, $J = 0$ for $B = 2$, and $J = 3/2$ for $B = 3$. The latter value is due to the constraint because of symmetry properties of the configuration. The value $J = 1/2$ is allowed for the configuration found in [27].

For the state with $B = |F| = 2$, its mass is equal to [10]

$$M(B = 2, |27;\ Y = 0, I = 0\rangle)$$
$$= M_{\rm cl} + 2\omega_{F,2} + \frac{\bar{c}_{F,2}}{\Theta_{T,2}}. \quad (29)$$

The binding energy of this state as a system of two Λ_F particles is

$$\epsilon(|27;\ Y = 0, I = 0\rangle)$$
$$= \epsilon_2 + 2(\omega_{F,1} - \omega_{F,2}) + \frac{3\bar{c}_{F,1}}{4\Theta_{T,1}} - \frac{\bar{c}_{F,2}}{\Theta_{T,2}}. \quad (30)$$

As always, we define the binding energies relative to appropriate thresholds for the decay into B baryons, nucleons, or flavored hyperons.

If the moments of inertia of the baryonic system at small values of B are proportional to the baryon number B, then the values of μ, excitation frequencies ω_F, and coefficients c would not depend on B at all. In this case, the binding energy consisted only of its classical part and some contribution from zero modes; the difference of ω's would not contribute. Within the CQM model, the moments of inertia for $B \geq 2$ have still not been calculated. Therefore, we shall make a natural assumption that the ratios of moments of inertia for different values of B in the CQM model are the same as in the Skyrme model [26]. For $B = 2$, $\Theta_{F,2}/\Theta_{F,1} = 2.038$ and $\Theta_{T,2}/\Theta_{T,1} = 2.053$ [26].

With this assumption, we obtain the following numerical values: $\epsilon_{\Lambda\Lambda(s=-2)} = 0.29$ GeV, $\epsilon_{\Lambda\Lambda(c=2)} = 0.31$ GeV, and $\epsilon_{\Lambda\Lambda(b=-2)} = 0.32$ GeV from expression (30). It should be compared with the binding energy of the deuteron $\epsilon_D = 351$ MeV and the binding energy of the NN scattering state with $J = 0$ and isospin $I = 1$, and $\epsilon_{D'} = 321$ MeV. After renormalization, which is necessary to produce the NN scattering state on the right place, i.e., near threshold, we find that the strange dibaryon with $s = -2$ is unbound, but that it is close to the threshold; charmed, as well as bottomed, dibaryons are also unbound, but they are even closer to the $\Lambda_F\Lambda_F$ threshold. This renormalization procedure is justified by the fact that a number of quantum effects like loop corrections and nonzero-mode contributions have not been, but should be taken into account (see also discussion of Casimir energy in Conclusions). The binding energy of the deuteron is 30 MeV instead of measured 2.23 MeV, so ~30 MeV is the uncertainty of our approach.

The dibaryons with $|F| = 1$ should be considered also. The lowest states belong to antidecuplet of corresponding $SU(3)$, $(p, q) = (0, 3)$, and have isospin $I = 1/2$. They all are bound within the developed approach and come close to the threshold, even unbound after the renormalization procedure.

For $\overline{35}$ -plet of tribaryons, $T_r = 1/2$ (for arbitrary (p, q) irrep which the baryonic system belongs to $T_r = p/2$ if

$n_{q\bar{q}} = 0$). I and T take the lowest possible values, 0 and 1/2 for $|F| = 1$, and 1/2, 0 for $|F| = 2$. The binding energies take the same order of magnitude as for the $B = 2$ case if we make a similar assumption on the behavior of moments of inertia. But after renormalization, the flavored states become unbound, although rather close to thresholds.

These results are in qualitative agreement with those obtained in the chiral soliton (topological) models. However, it should be noted that in the Skyrme model the quantized states with charm and bottom remain bound after such renormalization [11].

6. CONCLUSIONS

We found that, as far as we are concerned with the spectra of baryons, there is no difference of principle between topological (Skyrme) soliton models and the chiral quark meson model [2, 3]. The CQM model is more realistic, but, as is usual for more realistic models, it involves an additional parameter α_F which specifies the flavor symmetry breaking in the sector of the Lagrangian describing the quark–meson interaction. When this parameter is omitted, the flavor excitation frequencies are too large in comparison with the data and with the topological Skyrme model also. Reasonable values of this parameter make the excitation frequencies smaller, in better agreement with data.

We have estimated the spectra of baryons with flavor different from u and d in the simplest $SU(3)$ extension of the chiral quark–meson model proposed in [2, 3]. One can note that the approach developed here—the rigid oscillator version of the CQM model—works even better for c and b flavor in comparison with strangeness.

There are predictions of the baryonic systems with $B = 2, 3\ldots$ and flavors s, c, and b similar to that in topological soliton (Skyrme) models [10, 11, 15]. In the CQM model, due to the absence of the Skyrme term in the Lagrangian, after all the renormalization procedures, the attraction of heavy flavors by (u, d) solitons is somewhat weaker than in topological models. Similar predictions can also be made for systems with top-number. However, because of the large width of the t quark, the spectroscopy of the baryonic systems as well as hadrons containing the t quark will not be available, most probably.

The apparent deficiency of the approach employed in the present paper is that the motion of the system into the "strange," "charm," or "bottom" direction is considered independently of other motions. Consideration of the baryonic system with "mixed" flavors is possible in principle, but it demands a more complicated treatment, technically.

There is a difference between the rigid oscillator version of the CQM model we considered here and the collective-coordinate approach to soliton models widely exploited previously. In the collective-coordinate approach to the zero modes of solitons with a rigid- or a soft-rotator variant of the model, the masses of baryons are usually considerably greater than in the bound-state approach, when the Casimir energies are not taken into account [28, 29]. One of the sources of this difference is the presence of a term of order N_c/Θ_F in the zero-mode contribution to the rotation energy, which is absent in the bound-state model. It was shown recently by Walliser for the $B = 1$ sector within the $SU(3)$ symmetrical ($m_K = m_\pi$) version of the Skyrme model [29] that this large contribution is canceled almost completely by the kaonic one-loop correction to the zero-point Casimir energy, which is of the same order of magnitude, N_c^0 [29]. This correction has been calculated recently also within the bound-state approach to the Skyrme model [30]. Taking into account loop corrections to the energies of quantized states is needed also in the hybrid models similar to CQM model.

Recently, it was shown within the Skyrme model [31] that one should expect the existence of strange-baryonic systems close to the strong decay threshold, for baryon numbers up to 17. They are obtained by means of quantization of bound $SU(2)$ skyrmions found previously in [27, 32]. The charmed baryonic systems with $B = 3, 4$ were considered in [33] within a potential approach. The $B = 3$ systems were found to be very close to the threshold, and the $B = 4$ system was found to be stable to the strong decay, with a binding energy of ~10 MeV.

Experimental searches for the baryonic systems with flavor different from u and d could shed more light on the dynamics of heavy flavors in few-baryonic systems. The threshold for charm production on a free nucleon is about 12 GeV, and for double charm it is ~25.2 GeV. For bottom production, the threshold on nucleon is about 70 GeV. However, for nuclei as targets, the thresholds are much lowered due to two-step processes with mesons in intermediate states and due to normal Fermi motion of nucleons inside the target nucleus (see, e.g., [34]). Therefore, the production of baryons or baryonic systems with charm and bottom will be possible on accelerators with energy of several tens of GeV.

ACKNOWLEDGMENTS

The authors are very much indebted to J. Segar for help in numerical computations and to H. Walliser and H. Weigel for useful discussions.

MSS thanks the Russian Academy of Sciences and the Indian National Science Academy for financial support which enabled him to work at INR, Moscow. VBK is indebted to the Institute for Nuclear Theory at the University of Washington for its hospitality and the Department of Energy for partial support.

REFERENCES

1. T. H. R. Skyrme, Proc. R. Soc. London, Ser. A **260**, 127 (1961); Nucl. Phys. **31**, 556 (1962).
2. S. Kahana, G. Ripka, and V. Soni, Nucl. Phys. **A415**, 351 (1984); M. C. Birse and M. K. Banerjee, Phys. Rev. D **31**, 118 (1985).
3. T. D. Cohen and W. Broniowski, Phys. Rev. D **34**, 3472 (1986); M. K. Banerijee, W. Broniowski, and T. D. Cohen, *A Chiral Quark Soliton Model* (Univ. of Maryland Preprint, 1986).
4. J. A. McGovern and M. C. Birse, Nucl. Phys. **A506**, 392 (1990).
5. J. Segar, M. Sripriya, and M. S. Sriram, Int. J. Mod. Phys. E **3**, 769 (1994).
6. J. Segar, M. Sripriya, and M. S. Sriram, Phys. Lett. B **342**, 201 (1995).
7. C. G. Callan and I. R. Klebanov, Nucl. Phys. B **262**, 365 (1985).
8. N. Scoccola, H. Nadeau, M. Nowak, *et al.*, Phys. Lett. B **201**, 425 (1988); C. G. Callan, K. Hornbostel, and I. R. Klebanov, Phys. Lett. B **202**, 269 (1988); J. P. Blaizot, M. Rho, and N. Scoccola, Phys. Lett. B **209**, 27 (1988); N. Scoccola, D. P. Min, H. Nadeau, *et al.*, Nucl. Phys. **A505**, 497 (1989).
9. D. Kaplan and I. R. Klebanov, Nucl. Phys. B **335**, 45 (1990).
10. K. M. Westerberg and I. R. Klebanov, Phys. Rev. D **50**, 5834 (1994); I. R. Klebanov and K. M. Westerberg, Phys. Rev. D **53**, 2804 (1996).
11. V. B. Kopeliovich, Pis'ma Zh. Éksp. Teor. Fiz. **67**, 854 (1998) [JETP Lett. **67**, 896 (1998)].
12. R. L. Jaffe, Phys. Rev. Lett. **38**, 195 (1977); R. L. Jaffe and C. L. Kopra, Nucl. Phys. B **258**, 468 (1985).
13. A. P. Balachandran, A. Barducci, F. Lizzi, *et al.*, Phys. Rev. Lett. **52**, 887 (1984); A. P. Balachandran *et al.*, Nucl. Phys. B **256**, 525 (1985).
14. J. Kunz and P. Mulders, Phys. Lett. B **215**, 449 (1988); Nucl. Phys. **A497**, 339 (1989).
15. V. B. Kopeliovich, Yad. Fiz. **51**, 241 (1990) [Sov. J. Nucl. Phys. **51**, 151 (1990)]; Phys. Lett. B **259**, 234 (1991); V. B. Kopeliovich, B. Schwesinger, and B. E. Stern, Nucl. Phys. **A549**, 485 (1992).
16. V. B. Kopeliovich, Genshikaku Kenkyu **41**, 171 (1997); Nucl. Phys. **A639**, 75 (1998); Zh. Éksp. Teor. Fiz. **112**, 1941 (1997) [JETP **85**, 1060 (1997)]; Yad. Fiz. **56** (8), 160 (1993) [Phys. At. Nucl. **56**, 1084 (1993)].
17. B. Schwesinger and H. Weigel, Phys. Lett. B **267**, 438 (1991); H. Weigel, Int. J. Mod. Phys. A **11**, 2419 (1996).
18. E. Witten, Nucl. Phys. B **223**, 422, 433 (1983).
19. D. O. Riska and N. N. Scoccola, Phys. Lett. B **265**, 188 (1991).
20. M. Bjornberg, K. Dannbom, D. O. Riska, *et al.*, Nucl. Phys. **A539**, 662 (1992).
21. G. Guadagnini, Nucl. Phys. B **236**, 35 (1984).
22. G. S. Adkins, C. R. Nappi, and E. Witten, Nucl. Phys. B **228**, 552 (1983); G. S. Adkins and C. R. Nappi, Nucl. Phys. B **233**, 109 (1984).
23. J. Segar, PhD Thesis (Univ. of Madras, 1994).
24. H. Walliser, Nucl. Phys. **A548**, 649 (1992).
25. D. Diakonov, V. Petrov, and M. Polyakov, Z. Phys. A **359**, 305 (1997).
26. V. B. Kopeliovich and B. E. Stern, Preprint No. 83-34 NORDITA (Copenhagen, 1989); Pis'ma Zh. Éksp. Teor. Fiz. **45**, 165 (1987) [JETP Lett. **45**, 203 (1987)].
27. E. Braaten, S. Townsend, and L. Carson, Phys. Lett. B **235**, 147 (1990).
28. B. Moussalam, Ann. Phys. (New York) **225**, 264 (1993); F. Meier and H. Walliser, Phys. Rep. **289**, 383 (1997).
29. H. Walliser, Phys. Lett. B **432**, 15 (1998).
30. N. Scoccola and H. Walliser, hep-ph/9805340.
31. M. Schvellinger and N. Scoccola, Phys. Lett. B **430**, 32 (1998); V. B. Kopeliovich and W. J. Zakrzewski, Pis'ma Zh. Éksp. Teor. Fiz. **69**, 675 (1999) [JETP Lett. **69**, 721 (1999)].
32. R. A. Battye and P. M. Sutcliffe, Phys. Lett. B **391**, 150 (1997); Phys. Rev. Lett. **79**, 363 (1997).
33. B. F. Gibson, C. B. Dover, G. Bhamathi, *et al.*, Phys. Rev. C **27**, 2085 (1983).
34. V. B. Kopeliovich, Phys. Rep. **139**, 51 (1986); Yad. Fiz. **42**, 854 (1985) [Sov. J. Nucl. Phys. **42**, 542 (1985)].

Physics of Atomic Nuclei, Vol. 63, No. 3, 2000, pp. 489–498. Translated from Yadernaya Fizika, Vol. 63, No. 3, 2000, pp. 561–570.

ELEMENTARY PARTICLES AND FIELDS
Theory

Off-Diagonal Quark Distributions in Pions in the Effective Single-Instanton Approximation

I. V. Anikin, A. E. Dorokhov, A. E. Maximov, and L. Tomio[1)]

Joint Institute for Nuclear Research, Dubna, Moscow oblast, 141980 Russia

Received January 10, 1999; in final form, April 5, 1999

Abstract—Nonperturbative functions that parametrize off-diagonal hadronic matrix elements of the light-cone leading-twist quark operators are considered. These functions are calculated within the proposed relativistic quark model allowing for the nontrivial structure of the QCD vacuum, special attention being given to gauge invariance. Hadrons are treated as bound states of quarks; strong-interaction quark–pion vertices are described by effective interaction Lagrangians generated by instantons. The parameters of the instanton vacuum, such as the effective radius of the instanton and the quark mass, are related to the vacuum expectation values of the quark–gluon operators of the lowest dimension and to low-energy pion observables. © *2000 MAIK "Nauka/Interperiodica".*

1. INTRODUCTION

The distributions of quarks and gluons (or their structure functions) that form hadrons play an important role in investigations of the complicated hadron structure. Perturbative QCD makes it possible to calculate the Q^2 evolution of these functions by using operator-product expansion and renormalization-group methods. However, the functions themselves cannot be calculated from the first principles of QCD because the problem of strong coupling has yet to be solved. This situation gives strong incentives to developing effective approaches that are based on the fundamental principles of QCD, on the one hand, and which enable a calculation of features associated with long-distance dynamics [1–4], on the other hand.

In recent years, much attention has been given to quark distributions that parametrize asymmetric hadronic matrix elements $\langle p'|\ldots|p\rangle$ (these distributions are referred to as off-diagonal ones). Off-diagonal distributions generalize conventional quark distributions, carrying more information about the structure of particles and providing a link between conventional distributions measured in deep-inelastic scattering and elastic form factors of hadrons.

In the present study, we calculate off-diagonal quark distributions in the pion that correspond to the leading twist. We use an approach that represents the bosonized version of the instanton-liquid model developed in [5–7]. The model is based on nonlocal effective quark–hadron Lagrangians, with nonlocality being generated by instantons. The parameters of the instanton vacuum (effective instanton size and quark mass) are determined in terms of low-energy pion observables and the vacuum expectation values of quark–gluon operators of the lowest dimension. The quark–hadron (in particular, quark–pion) coupling constants are calculated by using the condition requiring that the renormalization constant for hadron fields be equal to zero (composeteness condition). This condition also guarantees fulfillment of momentum sum rules. In formulating the model, we pay special attention to gauge invariance of Lagrangians and of quark Green's functions in the external field of instantons and anti-instantons.

The proposed effective model is applicable up to relative quark momenta of $p \sim \rho_c^{-1} \approx 0.5$–$1$ GeV. Quark distributions are also determined for the renormalization point $\mu_0 \sim \rho_c^{-1}$.

2. DESCRIPTION OF THE MODEL

In dealing with hadronic processes in QCD, much attention is given to studying the ground state of the system. Presently, investigations into the intricate structure of the vacuum most often rely either on approaches employing the semiclassical approximation, or on approaches invoking the Wilson operator-product expansion, or on lattice models. It is well known that the gravest difficulty in applying semiclassical approaches to (3 + 1)-dimensional Yang–Mills theory is that the gas approximation cannot be used to calculate the amplitude of the vacuum–vacuum transitions in the field of large-scale fluctuations of the QCD vacuum. Since the dimensions of vacuum fluctuations can be arbitrarily large in scale-invariant theories, the density of media formed by pseudoparticles grows indefinitely (infrared catastrophe). Diakonov and Petrov [8] proposed an original way to stabilize pseudoparticle media. Their idea amounted to using the Feynman variational principle in calculating the QCD

[1)] Instituto de Física Teórica, UNESP, Rua Pamplona 145, BR-01405-900 São Paulo, Brazil.

1063-7788/00/6303-0489$20.00

partition function for a trial ansatz representing a superposition of instantons and anti-instantons. As a result, a new small parameter (packing parameter) that characterizes the stable media of pseudoparticles and which coincides with the phenomenological parameter in the instanton-liquid model [6, 7] is introduced in a natural way. In the present study, we develop some ideas proposed by Diakonov and Petrov [5] in an attempt at constructing effective quark–hadron Lagrangians by applying the bosonization procedure to the four-fermion interaction generated by instantons.

A correct description of the vacuum in the form of a stable medium consisting of instantons and anti-instantons is possible only in the strictly fixed singular gauge where (anti)instantons decay at infinity sufficiently fast. Within a completely gauge-invariant approach (for details, see sections that follow the present one), it is possible, however, to go over to other gauges, if this is dictated by considerations of convenience.

The generating QCD functional (QCD partition function in the Euclidean signature) can be represented in the form [9]

$$Z_{\mathrm{QCD}} = \int D\bar{\psi} D\psi \langle \exp(-W^I[\bar{\psi}, \psi]) \rangle, \tag{1}$$

where angular brackets denote averaging over the ensemble of (anti)instantons and where the effective fermion action is given by

$$\begin{aligned} &\exp(-W^I[\bar{\psi}, \psi]) \\ &= \exp\left(\int dx \bar{\psi}(x) i\hat{\partial} \psi(x)\right)(im - K^I[\bar{\psi}, \psi]) \end{aligned} \tag{2}$$

with

$$\begin{aligned} &K^I[\bar{\psi}, \psi] \\ &= \int\int dx dy (\bar{\psi}(x) i\hat{\partial} \Phi_0^I(x))(\Phi_0^I(y) i\hat{\partial} \psi(y)). \end{aligned} \tag{3}$$

In (3), the notation $\Phi_0(x)$ is used for quark zero modes of the Dirac operator in the external field of an (anti)instanton. Relation (2) describes the interaction of quarks via the 't Hooft's vertex K^I [10]. We assume that the entire set of topological singularities is a stable medium similar to a liquid with an average density (ratio of the average size to the average distance between the particles) of about 1/3 [5–8]. In other words, a medium formed by pseudoparticles is quite dilute. In addition, Diakonov and Petrov [8] showed that, in the $N_c \longrightarrow \infty$ approximation, where N_c is the number of colors, the distribution of instantons with respect to size ρ has a sharp delta-function peak near the average instanton size ρ_c; therefore, all instanton sizes can be replaced by this average size. It follows that, instead of taking an average over the entire ensemble of pseudoparticles, we can perform independent averaging over the position and orientation of an individual (anti)instanton. The generating functional (1) then assumes the form

$$\begin{aligned} Z_{\mathrm{QCD}} &= \int D\bar{\psi} D\psi \exp\left[\int dx \bar{\psi}(x) i\hat{\partial} \psi(x)\right] \\ &\times \left(im - \overline{K^I[\bar{\psi}, \psi]}\right)^{N_I} \left(im - \overline{K^I[\bar{\psi}, \psi]}\right)^{N_{\bar{I}}}, \end{aligned} \tag{4}$$

where an overbar denotes averaging over an individual (anti)instanton, while N_I ($N_{\bar{I}}$) is the number of instantons (anti-instantons). It follows that, by taking into account the one-(anti)instanton contribution N_I ($N_{\bar{I}}$) times, we take effectively into account multi-instanton configurations (effective one-instanton approximation) if it is adopted that correlations between (anti)instantons are small to the same degree as the medium packing parameter $\bar{\rho}/\bar{R}$ ($\bar{\rho}$ is the mean pseudoparticle size, while $\bar{R}$ is the mean distance between pseudoparticles) and that, in the limit $N_c \longrightarrow \infty$, the sizes of all (anti)instantons can be taken to be equal to $\bar{\rho}$ (these are basic approximations of our approach).

The functional in (4) generates a nonlocal $2N_f$-fermion vertex that, in the chiral limit, assumes the form

$$V^{I(\bar{I})} = \int d^4 z_{I(\bar{I})} \int dU_{I(\bar{I})} \prod_f K^{I(\bar{I})}[\bar{\psi}_f, \psi_f]. \tag{5}$$

For the particular case of two quark flavors, the expression for the generating QCD functional (4) in the leading order in $1/N_c$ is given by

$$Z_{\mathrm{QCD}} = \int D\bar{\psi} D\psi \exp(-S_I), \tag{6}$$

where

$$\begin{aligned} S_I &= \int dx \bar{\psi}(x) i\hat{\partial} \psi(x) \\ &+ \int d^4x \ldots d^4y' K(x, x'; y, y') \frac{1}{4(N_c^2 - 1)} \left\{ \frac{2N_c - 1}{2N_c} \right. \\ &\left. \times (\bar{\psi}_R(x') \tau^a \psi_L(x))(\bar{\psi}_R(y') \tau^a \psi_L(y)) + O\left(\frac{1}{N_c}\right) \right\}. \end{aligned} \tag{7}$$

Here, $\tau^a = (1, i\boldsymbol{\tau})$ is a matrix in flavor space, $N_c = 3$ is the number of quark colors, and

$$\psi_{R(L)}(x) = \frac{1 \pm \gamma_5}{2} \psi(x)$$

are quark fields of definite helicity. In the local limit, this action functional reduces to the Nambu–Jona-Lasinio model (a model of spontaneously broken chiral symmetry), which describes effectively low-energy chiral dynamics. In contrast to the Nambu–Jona-Lasinio model, however, the action functional in (7) has the natural regularization parameter $\bar{\rho}^{-1} \sim \Lambda_{\mathrm{cut}}$, so that the four-fermion coupling constant is expressed in terms of

physical parameters and the density of the instanton–anti-instanton medium. The action functional (7) is invariant under the global group of chiral-symmetry transformations, $U_L(N_f) \otimes U_R(N_f)$; at the quantum level, it describes the Adler–Bell–Jackiw anomaly breaking $U_A(1)$ symmetry.

The integral kernel of the four-quark interaction, $K(\ldots)$, characterizes the region of nonlocality that is induced by the interaction of quarks and antiquarks with (anti)instantons. It is expressed in terms of the profile functions of quark zero modes, Φ_0, and depends on the phenomenological parameters of the QCD vacuum ($n_c = 1$ fm^{-4} and $\rho_c = 1.6$–2 GeV^{-1}). We emphasize that the mean instanton size ρ_c determines the dimension of nonlocality and provides a natural cutoff parameter for effective low-energy theory.

In order to ensure gauge invariance, we go over from the conventional field functions to the Mandelstam field functions [11]:

$$\psi(x) \longrightarrow E(0, x)\psi(x),$$
$$E(0, x) = P\exp\left(ieQ\int_0^x dz_\mu A_\mu(z)\right). \quad (8)$$

Here, $Q = \mathrm{diag}(2/3, -1/3, -1/3)$, A_μ is a gauge field, and P denotes ordering along the trajectory. The gauge-invariant quark Green's function then assumes the form

$$S_g(x, y) = \langle\psi(x)E(x, y)\bar{\psi}(y)\rangle$$
$$= \int DA\int D\bar{\psi}D\psi e^{-S_{\mathrm{QCD}}(A, \bar{\psi}, \psi)}\bar{\psi}(x)\psi(y)P \quad (9)$$
$$\times\exp\left(ieQ\int_x^y dz_\mu A_\mu(z)\right).$$

The functional integral in (9) is calculated by the Laplace method near the one-instanton configuration; as a result, we obtain

$$S_g(x, y)$$
$$= \mathrm{tr}_c\left[P\exp\left(ieQ\int_0^x dz_\mu A_\mu^I(z)\right)\bar{\Phi}_0(x)\Phi_0(y)\right], \quad (10)$$

where A_μ^I is the (anti)instanton field, while Φ_0 is the quark zero mode in an arbitrary gauge. The gauge-invariant quark Green's function (10) assumes the simplest form in the axial gauge $n_\mu A_\mu = 0$ ($n_\mu = y_\mu - x_\mu$) because, in this gauge, the Schwinger factor $E(x, y)$ is equal to unity. In the coordinate frame where the (anti)instanton is at the origin of coordinates and where the vector $x - y$ is aligned with the time axis at $\mathbf{x} = \mathbf{y} = \mathbf{z}$, the P-ordered exponential reduces to an ordinary exponential. The gauge function $R(x)$ corresponding to the transition from the regular gauge to the axial one was considered in detail elsewhere [12]. For the quark zero modes Φ_0^{ax} in the axial gauge, we have

$$\Phi_0^{\mathrm{ax}}(x) = \sqrt{2}\phi^{\mathrm{ax}}(x)U^+ = \sqrt{2}\phi(x)R^+(x)U^+, \quad (11)$$

where

$$\phi(x) = \frac{\rho}{\pi(x^2 + \rho^2)^{3/2}},\ R(x) = \exp[i\boldsymbol{\tau}\cdot\hat{\mathbf{x}}\alpha(x)],$$
$$\alpha(x) = \frac{|\mathbf{x}|}{\sqrt{x^2 + \rho^2}}\arctan\frac{x_4}{\sqrt{x^2 + \rho^2}}, \quad (12)$$

and U is the rotation matrix in color space (the plus sign in the superscript on U corresponds to the instanton configuration).

The nonlocal four-fermion action functional (7) is linearized with the aid of auxiliary fields interpreted as meson fields. In the literature, this procedure is referred to as bosonization.

Upon explicitly evaluating the integral with respect to the (anti)instanton position, that part in the action functional (7) which describes the interaction assumes the following form in the momentum representation:

$$S_{\mathrm{eff}}^{(4)} = \frac{G}{2}\int\prod_{i=1}^4\frac{dk_i}{4\pi^2 i}f(k_i)\delta(k_1 - k_2 + k_3 - k_4)$$
$$\times(\bar{\psi}(k_1)\Gamma\psi(k_2))(\bar{\psi}(k_3)\Gamma\psi(k_4)). \quad (13)$$

Here, $G \simeq (N/V)^{-1}$ is the coupling constant for the four-fermion interaction, while Γ is the corresponding flavor matrix. The functions $f(k)$ represent normalized zero modes in the momentum representation. For these, we use the approximation (see [13])

$$f(k)$$
$$\approx 2\pi\rho_c(2.25\exp\{-\rho_c|k|\} - 1.25\exp\{-3\rho_c|k|\}). \quad (14)$$

Making the relevant change of variables and going back to the coordinate representation, we obtain the action functional (13) in the form

$$S_{\mathrm{eff}}^{(4)} = G\int dx(\bar{\Psi}(x)\Gamma\Psi(x))^2, \quad (15)$$

which the most convenient for linearization. In expression (15), we have introduced the notation

$$\Psi(x) = \int dp e^{-ipx}f(p)\psi(p).$$

Without changing the dynamics of the system, we can replace the action functional (15) by an alternative action functional of the form

$$S[\varphi]$$
$$= S_{\mathrm{eff}}^{(4)} - \frac{1}{2}\frac{N_c}{g}\int dx\left(\varphi(x) + \frac{g}{N_c}\varphi(x)\Psi(x)\Gamma\Psi(x)\right)^2, \quad (16)$$

where we have redefined the coupling constant as $g = GN_c$. Upon integration with respect to quark fields, the generating functional can then be recast into the form (for the sake of convenience, we formally go over to the Minkowski signature)

$$\begin{aligned} Z[\bar{\eta}, \eta, J] &= \int D\varphi \exp[-iN_c\tilde{S}[\varphi] + i\int dx J(x)\varphi(x)], \\ \tilde{S}[\varphi] &= \frac{1}{2g}\int dx\varphi^2(x) + i\mathrm{tr}\ln G(x,y) \\ &\quad - \frac{1}{N_c}\int dxdy\bar{\eta}(x)G^{-1}(x,y)\eta(y), \end{aligned} \tag{17}$$

where the symbol tr denotes the functional, group, and spinor trace and

$$\begin{aligned} G(x,y) &= i\hat{\partial}_x\delta(x-y) - \varphi(x,y), \\ \varphi(x,y) &= \int d\xi\varphi(\xi) f(x-\xi) f(\xi-y). \end{aligned}$$

The auxiliary fields φ are interpreted as composite meson fields. The transition to the action functional (17) resulted in the rearrangement of the vacuum state owing to a spontaneous breakdown of chiral symmetry [14].

In the limit $N_c \longrightarrow \infty$, the integral with respect to the fields φ in (17) is calculated by the stationary-phase method. In order to implement this, we must find a solution φ_0 to the equation

$$\delta\hat{S}/\delta\varphi = 0 \tag{18}$$

and expand the action functional (17) in a functional series in the vicinity of this solution as

$$\begin{aligned} Z[\bar{\eta}, \eta, J] &= \exp\left(iN_c\tilde{S}[\varphi_0] - \frac{1}{2}\mathrm{tr}\ln\tilde{S}''[\varphi_0]\right) \\ &\quad \times \exp\left(iN_c\sum_{n=3}^{\infty}\frac{\tilde{S}^{(n)}[\varphi_0]}{n!}\frac{\delta^n}{\delta J^n}\right) \\ &\quad \times \exp\left(-\frac{i}{2N_c}\int dxdyJ(x)(\tilde{S}''[\varphi_0])^{-1}J(y)\right). \end{aligned} \tag{19}$$

Differentiating the generating functional (19) with respect to the currents $\bar{\eta}$, η, and J, we obtain the corresponding Green's functions in various orders in $1/N_c$. By way of example, we indicate that the propagator of the field φ in the first order in $1/N_c$ is

$$\begin{aligned} D(x,y) &= \frac{1}{i}\frac{\delta^2 Z[\bar{\eta}, \eta, J]}{\delta J(x)\delta J(y)}\bigg|_{\bar{\eta}=\eta=J=0} \\ &= -\frac{1}{N_c}(\tilde{S}''[\varphi_0])^{-1}(x,y), \end{aligned} \tag{20}$$

where

$$\begin{aligned} \frac{\delta^2\tilde{S}[\varphi_0]}{\delta\varphi(x)\delta\varphi(y)} &= \frac{1}{g}\delta(x-y) \\ &\quad - \mathrm{tr}\frac{f(\xi_1-y)f(y-\xi_2)f(\xi_1-x)f(x-\xi_2)}{(i\hat{\partial}_{\xi_1}\delta(\xi_1-\xi_2) - \varphi(\xi_1,\xi_2))^2}. \end{aligned}$$

Instead of (17), it is more convenient to use, in actual practice, the effective-action representation that also describes the interaction of the composite fields through quark loops, but which is based on the quark–hadron Lagrangian of the $\varphi(\bar{\psi}\psi)$ type. For this, it is necessary, however, to determine the physical coupling constant for quark–hadron interaction. We will now show the way in which this can be done. Let us consider the amplitude $T_{\bar{\psi}\psi\to\bar{\psi}\psi}$ for elastic fermion–fermion scattering. We assume that fermion interaction results in the formation of a boson (for example, pion) bound state with the quantum numbers of the $(\bar{\psi}\psi)$ pair. In other words, a pole at $p^2 = m_M^2$ appears in the amplitude $T_{\bar{\psi}\psi\to\bar{\psi}\psi}$. In the momentum representation, the elastic-fermion-scattering amplitude has the form

$$T_{\bar{\psi}\psi\to\bar{\psi}\psi} \sim \Gamma D(p^2)\Gamma, \tag{21}$$

where Γ stands for the corresponding flavor and Dirac matrices, while $D(p^2)$ is the meson propagator [see (20)]. In the momentum representation, this propagator is given by

$$\begin{aligned} D(p^2) &= \frac{g}{1-g\Pi(p^2)}, \\ \Pi(p^2) &= \int\frac{d^4k}{(2\pi)^4 i} \\ &\quad \times f^2(k)f^2(k+p)\mathrm{tr}(\gamma_5 S(k)\gamma_5 S(k+p)). \end{aligned} \tag{22}$$

Expanding the denominator in (22) in a Taylor series near the physical meson mass, we can the recast the elastic-fermion-scattering amplitude into the form

$$T_{\bar{\psi}\psi\to\bar{\psi}\psi} \sim \Gamma\frac{g}{1 - g\Pi(m_M^2) - (p^2 - m_M^2)g\Pi'(m_M^2) - \Pi^{\mathrm{reg}}(p^2)}\Gamma. \tag{23}$$

It is obvious from (23) that, in the meson Green's function, the condition

$$1 - g\Pi(m_M^2) = 0 \tag{24}$$

corresponds to the pole associated with the mass of the physical particle. If, in addition, the pion mass in (24) is set to zero, we arrive at the mass-gap equation, thereby reproducing the Goldstone theorem.

Let us recast the elastic-scattering amplitude into the form

$$T_{\bar{\psi}\psi\to\bar{\psi}\psi}\sim\Gamma\frac{g^2_{M\bar{\psi}\psi}}{p^2-m^2_M}\Gamma, \tag{25}$$

where the physical quark–meson coupling constant $g^2_{M\bar{\psi}\psi}$ is given by

$$g^2_{M\bar{\psi}\psi} = \frac{1}{\Pi'(m^2_M)}. \tag{26}$$

The last equality is usually written in the form of the compositeness condition [15–19]

$$Z_M = 1-g^2_{M\bar{\psi}\psi}\Pi'(m^2_M) = 0, \tag{27}$$

where Z_M is the constant of meson-field renormalization. Physically, the condition $Z_M = 0$ implies that the meson field is always in a dressed state. As a matter of fact, the compositeness condition is equivalent to the strong-coupling condition, because it determines forces responsible for the formation of bound states.

Thus, the proposed approach relies on effective quark–meson Lagrangians written in the gauge-invariant form

$$\begin{aligned}\mathcal{L}^{\rm int}_M(x) &= g_{M\bar{\psi}\psi}\int d\xi_1 d\xi_2 f(\xi_1)f(\xi_2)\bar{\psi}(x+\xi_1)\\ &\times E(x+\xi_1,x)\Gamma_M M(x)E(x,x-\xi_2)\psi(x-\xi_2),\end{aligned} \tag{28}$$

where Γ_M is the flavor matrix corresponding to the meson being considered and

$$\begin{aligned}E(x,y) &= \exp\left\{ieQ\int_x^y dz_\mu A^\mu(z)\right\},\\ Q &= \frac{1}{2}\left(\lambda^3+\frac{1}{\sqrt{3}}\lambda^8\right) = \mathrm{diag}(2/3,-1/3,-1/3),\end{aligned} \tag{29}$$

and on the connectivity condition (27), which makes it possible to calculate the physical values of the quark–hadron coupling constants and which plays an important role in proving momentum sum rules for the distributions of interest.

3. MODEL PARAMETERS

In this section, we will discuss model parameters. Owing to a spontaneous breakdown of chiral symmetry, the quark mass is a function of momentum; in other words, it appears to be an effective mass. It can be determined by solving the mass-gap equation (Schwinger–Dyson equation):[2)]

$$\int\frac{d^4k}{(2\pi)^4}\frac{M^2(k)}{k^2+M^2k} = \frac{n_c}{4N_c}, \tag{30}$$

where $M(k)$ is the effective quark mass, while n_c is the instanton-medium density, which is expressed in terms of $M^2(0)/G$, G being the coupling constant for four-fermion interaction. A solution to equation (30) can be represented as

$$M(k) = M(0)f^2(k) = Mf^2(k). \tag{31}$$

The quark condensate and the quark virtuality are also important quantities. The former plays the role of the order parameter in chiral-symmetry breaking; it is determined as the nonperturbative part of the quark propagator,

$$\langle\bar{q}q\rangle = \lim_{y\to x}\mathrm{tr}S_F(x-y) = -4N_c\int\frac{d^4k}{(2\pi)^4}\frac{M(k)}{k^2+M^2(k)}. \tag{32}$$

The latter specifies the mean value of the squared momentum of a virtual quark; it is given by (see [20, 21])

$$\lambda^2_q = \frac{\langle\bar{q}D^2q\rangle}{\langle\bar{q}q\rangle} = -\frac{4N_c}{\langle\bar{q}q\rangle}\int\frac{d^4k}{(2\pi)^4}k^2\frac{M(k)}{k^2+M^2(k)}. \tag{33}$$

In the approximation of a sufficiently dilute instanton medium, the assumption that $\langle k^2\rangle\sim\lambda^2_q \gg M^2(\lambda^2_q)$ does not lead to significant errors. Therefore, the momentum dependence of the effective mass in the denominator of the integrands in (32) and (33) can be neglected against k^2. At the same time, the use of expression (31) for the effective mass in the numerators of (32) and (33) leads to the quark-condensate and quark-virtuality values of, respectively,

$$\langle\bar{q}q\rangle = -\frac{N_cM}{2\pi^2\rho^2_c} \text{ and } \lambda^2_q = \frac{2}{\rho^2_c}. \tag{34}$$

By using the values from (34) and expressing the parameters of the instanton vacuum model in terms of the fundamental QCD-vacuum parameters, we obtain

$$\rho^2_c = \frac{2}{\lambda^2_q},\ M_q = -\frac{4\pi^2}{N_c}\frac{\langle\bar{q}q\rangle}{\lambda^2_q}. \tag{35}$$

With aid of expressions (35), we can determine the model parameters ρ_c and M on the basis of the quark-condensate value

$$\langle\bar{q}q\rangle\approx-(230\ \mathrm{MeV})^3$$

and the quark-virtuality value

$$\lambda^2_q = (0.4\pm0.2)\text{–}(0.55\pm0.05)\ \mathrm{GeV}^2,$$

which were obtained in [22–24]. As a result, we arrive at

$$\rho_c\sim1.7\ \mathrm{GeV}^{-1},\quad M\sim0.3\ \mathrm{GeV}.$$

The global analysis of the vacuum and low-energy pion properties from [13] confirms these estimates, setting the following constraints on the above parameters:

$$\rho_c = 1.5\text{–}2.0\ \mathrm{GeV}^{-1},\quad M = 0.22\text{–}0.26\ \mathrm{GeV}.$$

[2)]Hereafter, we use the Euclidean signature.

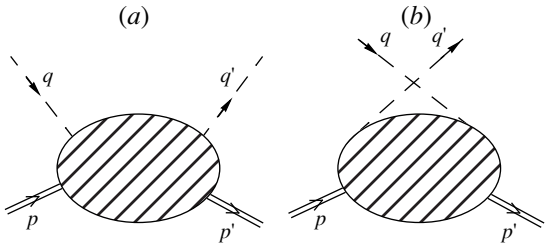

Fig. 1. Compton scattering of a virtual photon with a momentum q by a pion with a momentum p.

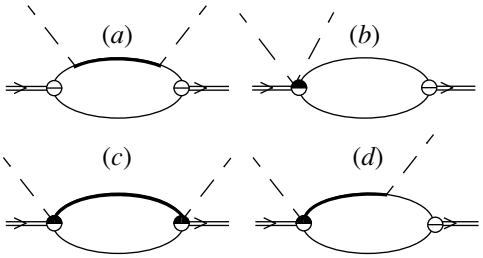

Fig. 2. Diagrams for the Compton scattering amplitude: (*a*) main type and (*b–d*) additional types.

We note that the condition

$$\eta = M^2(\lambda_q^2)/\lambda_q^2 \ll 1,$$

which ensures the applicability of the dilute-medium approximation, holds in the entire parameter region.

4. OFF-DIAGONAL DISTRIBUTIONS

Let us now consider the off-diagonal quark distributions that parametrize the asymmetric hadron matrix elements of a nonperturbative origin. These matrix elements are used, for example, in studying hard exclusive processes like elastic electroproduction. We will dwell at some length on one such process, deep virtual Compton scattering represented in Fig. 1, where the pion, with a momentum p, absorbs a virtual photon with a momentum q, whereby a real photon with a momentum $q' = q + r$, is emitted, the remaining recoil pion having the momentum $p' = p - r$. The momentum q is considered in the deep virtual kinematical region—that is, in the Bjorken limit $Q^2 = -q^2 \longrightarrow \infty$ and $p \cdot q \longrightarrow \infty$ at finite $Q^2/(p \cdot q)$.

We distinguish two cases, $t = 0$ and $t \neq 0$, where $t = r^2$. Let us first consider the more general second case. The amplitude for the Compton scattering of a photon on a pion at the momenta p and q in the initial state and the momenta p' and q' in the final state (see Fig. 1) is given by

$$T_{\mu\nu}(p, q) = \int d\xi_1 d\xi_2 d\xi_3 d\xi_4 \times \exp(iq\xi_1 - iq'\xi_2 + ip\xi_3 - ip'\xi_4) \times \left\langle \frac{\delta^4 S}{\delta A_\mu(\xi_1)\delta A_\mu(\xi_2)\delta M_{(\pi)}(\xi_3)\delta M_{(\pi)}(\xi_4)} \right\rangle_0. \quad (36)$$

The scattering matrix has the conventional form

$$S = T\exp\left(i\int dx[\mathcal{L}_{\text{eff}}(x) + \mathcal{L}_{\text{em}}(x)]\right). \quad (37)$$

The Compton amplitude is described by an entire set of diagrams. The basic types of these are displayed in Fig. 2. Diagrams of the 2*c* and 2*d* types are suppressed in the Bjorken limit; therefore, we will restrict our consideration to the 2*a* and 2*b* types. The main contribution to the amplitude comes from the diagram in Fig. 2*a*, and not from the diagram in Fig. 2*b*.

A general method for separating off-diagonal distributions was developed in [4, 25]. In the momentum representation, the contribution of the diagram in Fig. 2*a* to the reaction amplitude can be represented as

$$T_{\mu\nu}^{\text{main}}(p, q) = \frac{g_{\pi\bar{q}q}^2}{4\pi^2}\int\frac{dk}{4\pi^2 i} f(k^2) f^2((k-p)^2) f((k-r)^2) \times \text{tr}(\gamma_5 S(k-p)\gamma_5 S(k)\gamma_\mu S(k+q)\gamma_\nu S(k-r)). \quad (38)$$

In order to determine the asymptotic behavior at large Q^2, it is convenient to use the Sudakov variables. For the lightlike vectors m_μ and n_μ, we choose the vector of the target-pion momentum p_μ ($p^2 = 0$ for a Goldstone particle) and $\hat{n}_\mu = q'/(p \cdot q')$, where q' is the real-photon momentum. The momenta involved can then be expanded as

$$p'_\mu = \bar{\zeta} p_\mu - \frac{t}{2}\hat{n}_\mu + p'^{\perp}_\mu, \quad r_\mu = \zeta p_\mu + \frac{t}{2}\hat{n}_\mu + r^\perp_\mu,$$
$$q_\mu = -\zeta p_\mu + (p \cdot q)\hat{n}_\mu + q^\perp_\mu, \quad \zeta = r_\parallel \cdot \hat{n} = 1 - p' \cdot \hat{n}, \quad p \cdot q = p \cdot q' + t/2, \quad (39)$$

where ζ is the asymmetry parameter, which, in the Bjorken limit, is an analog of the scaling variable

$$x_B = -\frac{q^2}{2pq} = \frac{Q^2}{2pq}.$$

Introducing expansion (39) into (38) and performing invariant integration with respect to k, we arrive at the expression

$$\int\frac{dk}{4\pi^2 i} I_{\mu\nu}(k, p, \hat{n}) = p_\mu \hat{n}_\nu C_1(k, p, \hat{n}) + \hat{n}_\mu p_\nu C_2(k, p, \hat{n}) + g_{\mu\nu} C_3(k, p, \hat{n}), \quad (40)$$

where $I_{\mu\nu}(k, p, \hat{n})$ and $C_n(k, p, \hat{n})$ ($n = 1, 2, 3$) are some typical functions. In the above expression, we have omitted terms that are suppressed at large Q^2. With the

aid of the relation

$$\int_{-1}^{1} d\tilde{X}\delta(\tilde{X} - k\hat{n}) = 1, \tag{41}$$

an integral representation of unity, we reduce the amplitude to the form

$$T_{\mu\nu}(p, q, r) = (p_\mu \hat{n}_\nu + \hat{n}_\mu p_\nu - g_{\mu\nu}) \times \int_0^1 dX\left(\frac{1}{X-\zeta} - \frac{1}{X}\right)\mathcal{F}_\zeta(X, t). \tag{42}$$

By definition, the function $\mathcal{F}_\zeta(X, t)$, which appears in expression (42), represents the contribution of the basic diagrams to the off-diagonal distribution of quarks in the pion and has the form

$$\mathcal{F}_\zeta^\Delta(X, t) = \frac{1}{2-\zeta}\frac{g_{\pi\bar{q}q}^2}{4\pi^2}\int\frac{dk}{2(4\pi^2 i)} f(k) f^2(k-p) \times f(k-r)\mathrm{tr}(\gamma_5 S(k-p)\gamma_5 S(k)\hat{n}\gamma S(k-r)) \times \delta(X - k\hat{n}) + (X \longrightarrow \bar{X}). \tag{43}$$

The variable X in expressions (42) and (43) ranges between zero and unity. Physically, it appears to be the common fraction of the initial-hadron momentum p. It can be represented as a linear superposition of the conventional fraction x of the momentum p for the case of zero momentum transfer and the fraction y of the nonzero momentum transfer r: $X = xp + yr$.

The contributions to the off-diagonal distribution from the additional diagrams (see Fig. 2*b*) can be singled out in a similar way. As a result, we obtain

$$\mathcal{F}_\zeta^\circ(X, t) = \frac{1}{2-\zeta}\frac{g_{\pi\bar{q}q}^2}{4\pi^2}\int\frac{dk}{4\pi^2 i} f(k) f^2(k+p') \times \int_0^1 d\tau f'((k-r\tau)^2 + r^2\tau(1-\tau)) \times \mathrm{tr}(\gamma_5 S(k)\gamma_5 S(k+p'))\left(2X - \frac{3}{2}\zeta\right) \times (\delta(X - k\hat{n}) + \delta(X - \zeta + k\hat{n})) + (X \longrightarrow \bar{X}). \tag{44}$$

The structure integrals in (43) and (44) are calculated in the Euclidean signature, where the form factors $f(k^2)$ are well defined. In this calculation, we also use the α representation for the propagators that relies on integral representations of the gamma and the delta function,

$$\frac{1}{A^n} = \frac{1}{\Gamma(n)}\int_0^\infty d\alpha\alpha^{n-1}e^{-\alpha A}, \quad \delta(X) = \frac{1}{(2\pi)^4}\int_{-\infty}^{+\infty} d\gamma e^{i\gamma X}, \tag{45}$$

and the Laplace transform of the nonlocal vertex form factors.

The eventual expressions for these functions in the α representation are given in the Appendix. Integration of the sum of the functions in (43) and (44) with respect to the common momentum fraction X yields the hadronic electromagnetic form factor (pion form factor in the case under study); that is,

$$\int_0^1 dX(\mathcal{F}_\zeta^\Delta(X, t) + \mathcal{F}_\zeta^\circ(X, t)) = \int_0^1 dX\mathcal{F}_\zeta(X, t) = F_\pi(t), \tag{46}$$

where the hadronic form factor is normalized to unity. The behavior of the function $F_\pi(t)$ (see Fig. 3) agrees with experimental values; numerically, it virtually coincides with the results of the calculations performed in [26, 27].

In order to derive asymmetric distribution functions (for the definition, see [4]), it is necessary to set the squared momentum transfer in (43) and (44) to zero, $t = 0$. In this way, we obtain the family of functions $\mathcal{F}_\zeta(X)$ depending on the asymmetry parameter ζ (in contrast to the double distribution functions in [4], which are universal and which are independent of ζ). It follows from (46) that the function $\mathcal{F}_\zeta(X)$ satisfies the sum rule

$$\int_0^1 dX\mathcal{F}_\zeta(X) = 1 \tag{47}$$

and possesses the following properties. In the region $X \geq \zeta$, the parton returning to the hadron carries a positive fraction $(X - \zeta)p$ of the primary-hadron momentum. Therefore, the asymmetric function can be interpreted as a function similar to the conventional distribution function. In the region $X \leq \zeta$, the parton returning to the hadron carries the negative momentum fraction $(X - \zeta)p$; therefore, it can be interpreted as a parton emitted by the final hadron and traveling together with the parton that has left the initial hadron. If X is represented in the form $X = Y\zeta$, we can see that either parton of the two emitted by the primary and the final hadron carries a positive fraction of the momentum transfer r, Y and $\bar{Y}$, respectively. In this case, the asymmetric distribution function $\mathcal{F}_\zeta(X)$ is similar to the amplitude for the decay of the bound state with total momentum $r = \zeta p$ into two parts. In particular, we can show in a model-independent way that the asymmetric distribution of quarks in the pion at $\zeta = 1$ reduces to the pion wave function. For this, we consider the hadronic matrix element of an arbitrary operator that parametrizes the distribution functions:

$$\langle\pi(p')|\mathbb{O}(0)|\pi(p)\rangle. \tag{48}$$

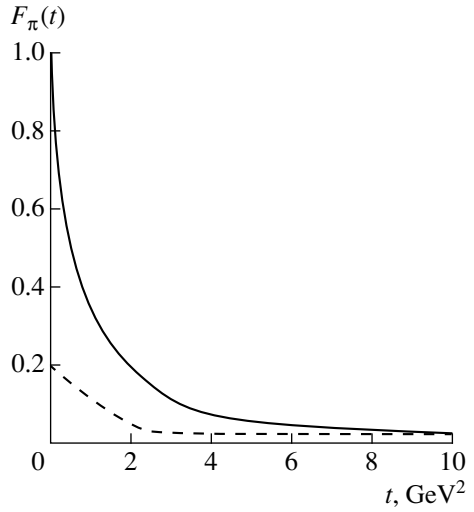

Fig. 3. Electromagnetic form factor for the pion: (solid curve) total contribution from the main and additional diagrams and (dashed curve) contribution from the additional diagrams.

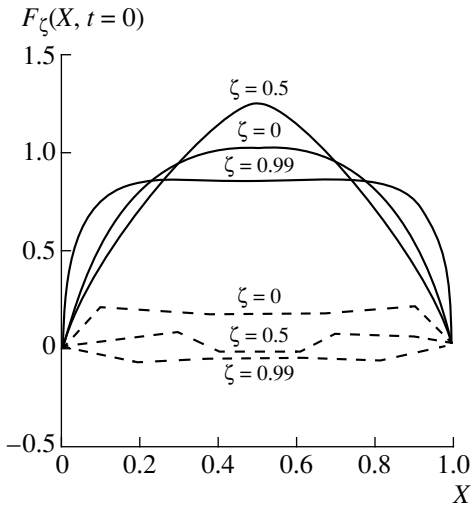

Fig. 4. Family of the curves for the asymmetric distribution at various values of the asymmetry parameter ζ: (solid curves) total contributions from the main and additional diagrams and (dashed curves) contributions from the additional diagrams.

By using the reduction relations and the PCAC theorem, we arrive at

$$\frac{p'^2 - m_\pi^2}{m_\pi^2 f_\pi}\int dx e^{ip'x}\langle 0|T\partial\cdot\mathcal{A}(x)\mathbb{C}(0)|\pi(p)\rangle. \qquad (49)$$

At $\zeta = 1$, the recoil-pion momentum p' is zero [see equation (39)]; taking into account the result of commuting ∂_0 with the chronological product, we therefore find that the hadronic matrix element of an arbitrary operator is given by

$$\frac{1}{f_\pi}\langle 0|[\mathcal{Q}_5(0), \mathbb{C}(0)]|\pi(p)\rangle, \qquad (50)$$

where $\mathcal{Q}_5$ is the axial charge. Using current algebra, we can now substitute the electromagnetic current for $\mathbb{C}(0)$, as is required in our case. This yields

$$\frac{1}{f_\pi}\langle 0|\mathcal{A}_\mu(x)|\pi(p)\rangle = \phi_\pi(x), \qquad (51)$$

where ϕ_π is the pion wave function. Thus, we have shown that, if the asymmetry parameter ζ is equal to unity—this is equivalent to zero momentum of the final pion—the asymmetric function $\mathcal{F}_\zeta(X)$ coincides with the pion wave function. Figure 4 displays the graphs of the asymmetric functions at various values of the parameter ζ. It can be seen that the contributions of the additional diagrams decrease with increasing asymmetry parameter ζ (we recall that the maximum contribution of the additional diagrams corresponds to $\zeta = 0$ and amounts to about 20%).

5. CONCLUSION

We have predicted general properties of the off-diagonal distributions of valence quarks in the pion.[3)] These off-diagonal distributions are of particular interest because they relate conventional (diagonal) distributions to hadron form factors. Our calculations have been performed within the proposed model that relies on gauge-invariant nonlocal quark–hadron Lagrangians and on the compositeness condition, which permits computing physical coupling constants for quark interaction with hadrons. Nonlocal vertices are fully generated by instantons and are characterized by the mean instanton size. We have shown that, if gauge invariance is strictly respected within the approach used, parton sum rules for the distribution of the total hadron momentum among valence quarks follow from the compositeness condition. It has been found that the parameters of the instanton vacuum, such as the effective radius of the instanton and the quark mass, are related to the vacuum expectation values of quark–gluon operators of the lowest dimension and to low-energy pion observables.

ACKNOWLEDGMENTS

We are grateful to M.K. Volkov, S.B. Gerasimov, N.I. Kochelev, S.V. Mikhailov, O.V. Teryaev, and V.L. Yudichev for numerous stimulating discussions.

This work was supported by the Russian Foundation for Basic Research (project nos. 96-02-18096 and 96-02-18097), by the St. Petersburg Center for Basic Research (grant no. 95-0-6.3-20), and by the Heisenberg–Landau program.

APPENDIX

Presented below for an arbitrary value of the asymmetry parameter ζ are the parametric α representations

[3)]Here, we have taken into account only the leading twist and neglected the effects of the quark–gluon sea.

for typical integrals in the expressions for quark distributions.

We have

$$\mathcal{F}_\zeta^\Delta(X,t) = \frac{1}{2-\zeta}\frac{g_{\pi\bar{q}q}^2}{4\pi^2}\mathcal{J}_\zeta^\Delta(\alpha,t),$$

where

$$\mathcal{J}_\zeta^\Delta(\alpha,t) = \frac{1}{2}\int_0^\infty d\alpha_1\ldots d\alpha_4 \tilde{f}_1(\alpha_1)\tilde{f}_2(\alpha_2)\tilde{f}_1(\alpha_3)e^{\alpha_4 M^2}$$

$$\times\left[\frac{Xe^{\tilde{\alpha}_1 M^2}\Theta(\tilde{\alpha}_1)}{\alpha_2+\alpha_{34}\zeta}\exp\left(-tX\frac{\alpha_{34}(\alpha_1+\tilde{\alpha}_1)}{\alpha_2+\alpha_{34}\zeta}\right)\right.$$

$$\left.+\frac{(1-\zeta)e^{\tilde{\alpha}_2 M^2}\Theta(\tilde{\alpha}_2)}{\alpha_1+\alpha_{34}(1-\zeta)}\exp\left(-t(1-X)\frac{\alpha_{34}\alpha_1}{\alpha_1+\alpha_{34}(1-\zeta)}\right)\right]$$

$$-\frac{1}{2}\int_0^\infty d\alpha_1\ldots d\alpha_5 \tilde{f}_1(\alpha_1)\tilde{f}_2(\alpha_2)\tilde{f}_1(\alpha_3)$$

$$\times\frac{(1-\zeta)(1-X)t\alpha_{35}\Theta(\tilde{\alpha}_3)}{(\alpha_{14}+\alpha_{35}(1-\zeta))^2}$$

$$\times\exp\left(-M^2(\alpha_{45}+\tilde{\alpha}_3)-t(1-X)\frac{\alpha_{35}\alpha_{14}}{\alpha_{14}+\alpha_{35}(1-\zeta)}\right),$$

for the main diagram in Fig. 2*a* and

$$\mathcal{F}_\zeta^\circ(X,t) = \frac{1}{2-\zeta}\frac{g_{\pi\bar{q}q}^2}{4\pi^2}(\mathcal{J}_\zeta^{\circ(1)}(\alpha,t)+\mathcal{J}_\zeta^{\circ(2)}(\alpha,t)),$$

where

$$\mathcal{J}_\zeta^{\circ(1)}(\alpha,t) = \int_0^\infty d\alpha_1\ldots d\alpha_3\alpha_3\tilde{f}_1(\alpha_1)\tilde{f}_2(\alpha_2)\tilde{f}_1(\alpha_3)$$

$$\times\int_0^1 d\tau\frac{2X-1.5\zeta}{\alpha_3\zeta\tau-\alpha_2(1-\zeta)}$$

$$\times\left[\Theta(\hat{\alpha}_1)\exp\left(\hat{\alpha}_1 M^2 - t\tau\alpha_3\frac{\alpha_1+\hat{\alpha}_1+\alpha_3(1-\tau)}{\alpha_{123}+\hat{\alpha}_1}\right)\right.$$

$$\left.+\Theta(\hat{\alpha}_2)\exp\left(\hat{\alpha}_2 M^2 - t\tau\alpha_3\frac{\alpha_1+\hat{\alpha}_2+\alpha_3(1-\tau)}{\alpha_{123}+\hat{\alpha}_2}\right)\right],$$

$$\mathcal{J}_\zeta^{\circ(2)}(\alpha,t) = \int_0^\infty d\alpha_1\ldots d\alpha_3\alpha_3\tilde{f}_1(\alpha_1)\tilde{f}_2(\alpha_2)\tilde{f}_1(\alpha_3)$$

$$\times\int_0^1 d\tau\frac{2X-1.5\zeta}{\alpha_{13}(1-\zeta)+\alpha_3\zeta\tau}$$

$$\times\left[\Theta(\hat{\alpha}_3)\exp\left(\hat{\alpha}_3 M^2 - t\tau\alpha_3\frac{\alpha_1+\alpha_3(1-\tau)}{\alpha_{123}+\hat{\alpha}_3}\right)\right.$$

$$\left.+\Theta(\hat{\alpha}_4)\exp\left(\hat{\alpha}_4 M^2 - t\tau\alpha_3\frac{\alpha_1+\alpha_3(1-\tau)}{\alpha_{123}+\hat{\alpha}_4}\right)\right],$$

for the additional diagram in Fig. 2*b*.

In the above expressions $\tilde{f}_n(\alpha)$ stands for the Laplace transform of the form factor raised to the *n*th power, and we have also introduced the notation

$$\alpha_{n_1\ldots n_i} = \alpha_{n_1}+\ldots+\alpha_{n_i},$$

$$\tilde{\alpha}_1 = \alpha_2\frac{1-X}{X}-\alpha_{34}\frac{X-\zeta}{X}-\alpha_1,$$

$$\tilde{\alpha}_2 = \alpha_1\frac{X}{1-X}+\alpha_{34}\frac{X-\zeta}{1-X}-\alpha_2,$$

$$\tilde{\alpha}_3 = \alpha_{14}\frac{X}{1-X}+\alpha_{35}\frac{X-\zeta}{1-X}-\alpha_2,$$

$$\hat{\alpha}_1 = \alpha_3\frac{\zeta\tau-X}{X}-\alpha_2\frac{1-\zeta+X}{X}-\alpha_1,$$

$$\hat{\alpha}_2 = -\alpha_3\frac{\zeta(1-\tau)-X}{\zeta-X}-\alpha_2\frac{1-X}{\zeta-X}-\alpha_1,$$

$$\hat{\alpha}_3 = -\alpha_3\frac{\zeta(1-\tau)-X}{1-X}-\alpha_1\frac{\zeta-X}{1-X}-\alpha_2,$$

$$\hat{\alpha}_4 = -\alpha_3\frac{X-\zeta\tau}{1-\zeta+X}-\alpha_1\frac{X}{1-\zeta+X}-\alpha_2.$$

REFERENCES

1. C. Best *et al.*, Phys. Rev. D **56**, 2743 (1997).
2. A. V. Belitsky, Phys. Lett. B **386**, 359 (1996).
3. V. M. Belyaev and M. B. Johnson, Phys. Rev. D **56**, 1481 (1997).
4. A. V. Radyushkin, Phys. Rev. D **56**, 5524 (1997).
5. D. I. Diakonov and V. Yu. Petrov, Zh. Éksp. Teor. Fiz. **89**, 361 (1985) [Sov. Phys. JETP **62**, 204 (1985)].
6. E. V. Shuryak, Nucl. Phys. B **203**, 93, 116, 140 (1982).
7. E. V. Shuryak, Nucl. Phys. B **214**, 237 (1983).
8. D. I. Diakonov and V. Yu. Petrov, Nucl. Phys. B **245**, 259 (1984).
9. D. I. Diakonov, *Lectures at the Enrico Fermi School in Physics, Varenna, 1995*.
10. G. 't Hooft, Phys. Rev. D **14**, 3432 (1976).
11. S. Mandelstam, Ann. Phys. (New York) **19**, 1, 25 (1962).
12. M. Hutter, LMU 95-03 (1995).
13. A. E. Dorokhov and L. Tomio, hep-ph/9803329.
14. M. K. Volkov, Ann. Phys. (New York) **157**, 282 (1984); Fiz. Élem. Chastits At. Yadra **17**, 433 (1986) [Sov. J. Part. Nucl. **17**, 186 (1986)].
15. B. Jouvet, Nuovo Cimento **5**, 1 (1957).
16. M. T. Vaughn, R. Aron, and R. D. Amado, Phys. Rev. **124**, 1258 (1961).
17. A. Salam, Nuovo Cimento **25**, 224 (1962).
18. S. Weinberg, Phys. Rev. **130**, 816 (1963).

19. K. Hayashi *et al.*, Fortschr. Phys. **15**, 625 (1967).
20. S. V. Mikhailov and A. V. Radyushkin, Yad. Fiz. **49**, 794 (1989) [Sov. J. Nucl. Phys. **49**, 494 (1989)].
21. S. V. Mikhailov and A. V. Radyushkin, Phys. Rev. D **45**, 1754 (1992).
22. T. Schäfer and E. V. Shuryak, Rev. Mod. Phys. **70**, 323 (1998).
23. V. M. Belyaev and B. L. Ioffe, Zh. Éksp. Teor. Fiz. **83**, 867 (1982) [Sov. Phys. JETP **56**, 493 (1982)].
24. M. Kramer and G. Schierholtz, Phys. Lett. B **194**, 283 (1987).
25. X. Ji, Phys. Rev. Lett. **78**, 610 (1997).
26. I. Anikin *et al.*, Z. Phys. C **65**, 681 (1995).
27. I. Anikin *et al.*, Yad. Fiz. **57**, 1082 (1994) [Phys. At. Nucl. **57**, 1021 (1994)].

Translated by M. Kobrinsky

Physics of Atomic Nuclei, Vol. 63, No. 3, 2000, pp. 499–501. Translated from Yadernaya Fizika, Vol. 63, No. 3, 2000, pp. 571–574.

ELEMENTARY PARTICLES AND FIELDS
Theory

Box Anomaly and Decay $\eta' \longrightarrow \pi^+\pi^-\gamma$

A. V. Kisselev and V. A. Petrov

Institute for High Energy Physics, Protvino, Moscow oblast, 142284 Russia

Received April 21, 1999

Abstract—The amplitude of the decay $\eta' \longrightarrow \pi^+\pi^-\gamma$ is derived in the soft limit of the current scheme of η–η' mixing. The results are compared with experimental values of the phenomenological contribution additive to the ρ-meson contribution. © *2000 MAIK "Nauka/Interperiodica".*

1. INTRODUCTION

According to the precise results of the LEPTON-F experiment [1], which studied the decay process $\eta' \longrightarrow \pi^+\pi^-\gamma$, the inconsistencies found in a fit of the two-pion spectrum in terms of the purely ρ-meson-decay contribution can be removed by supplementing it with a constant additive term. A thorough reanalysis of the relevant world data at CERN [2] confirmed this conclusion. More recently, the Crystal Barrel measurement [3] of the invariant-mass distribution of the two-pion system from the decay process $\eta' \longrightarrow \pi^+\pi^-\gamma$ provided further evidence for a nonresonance contribution to this spectrum. The analysis of this process from [4] yielded similar results.

It has long since been known that the amplitude of the decay $\eta' \longrightarrow \pi^+\pi^-\gamma$ is affected by the AVV and AAAV chiral anomalies (see, for example, [5]). As a result, this amplitude depends on the quark charges, providing the possibility of determining (see [6] and references therein) whether they are fractional [7] or integral [8].

That the two-pion mass spectrum observed in the decay process being discussed is dominated by the ρ-meson contribution—in contrast to what occurs in the two-photon decays of either η and η'—complicates the use of the soft limit for the term generated by the anomaly in the lowest order. In [6], the ρ-meson contribution was taken into account by multiplying the low-energy amplitude by the corresponding Breit–Wigner factor. According to Benayoun *et al.* [2], it is the non-ρ term that must be identified with the anomalous contribution to the amplitude in the soft limit. (For a detailed analysis of the ρ-meson contribution to η' decays, the reader is referred to [2].)

In the soft limit, the anomalous contributions to the $\pi^+\pi^-\gamma$ decays of either η and η' were estimated in [9] for two theoretical schemes of η–η' mixing [10].

Assuming the current-mixing scheme, we derive here the anomalous contribution to the amplitude of the decay $\eta' \longrightarrow \pi^+\pi^-\gamma$ and then compare our results with experimental data quoted in [2, 3].

2. η–η' MIXING

The amplitude being discussed receives contributions from anomalies through the coupling of the Heisenberg fields η and η' to the divergences of $SU(3)$-octet and $SU(3)$-singlet currents. For the interpolating fields η and η', we obtained [10]

$$\begin{aligned}\eta &= \frac{1}{m_\eta^2}\left(\frac{D_8}{F_8}\cos\theta - \frac{D_0}{F_0}\varepsilon\sin\theta\right),\\ \eta' &= \frac{1}{m_{\eta'}^2}\left(\frac{D_8}{\varepsilon F_8}\sin\theta + \frac{D_0}{F_0}\cos\theta\right),\end{aligned} \tag{1}$$

where $D_a = \partial_\mu A_a^{\mu 5}$ with $a = 8\ (0)$, $A_a^{\mu 5}$ being octet (singlet) currents ($\langle\Omega|A_a^{\mu 5}|\eta(\eta')(p)\rangle = ip_\mu f_a$); $F_a = f_a/\cos\theta$; and θ is the mixing angle. In the so-called current-mixing scheme, the quantity ε in (1) is equal to $m_\eta/m_{\eta'}$.

In using expressions of the type (1), we imply a subtraction of anomalous terms, whereby the Lorentz invariant form factors of the divergences vanish in the soft limit, so that we arrive at the anomalous contribution in its pure form (apart from the sign).

3. BASIC FORMULAS

The amplitude of the decay $\eta' \longrightarrow \pi^+\pi^-\gamma$ depends on the decay constants f_8 and f_0 and on the mixing angle θ; these parameters can be inferred from the two-photon widths of η and η'. From (1), we obtain

$$\begin{aligned}R_\eta &\equiv \left[\frac{3\Gamma(\eta \longrightarrow \gamma\gamma)}{\Gamma(\pi^0 \longrightarrow \gamma\gamma)}\right]^{1/2}\left(\frac{m_\pi}{m_\eta}\right)^{3/2}\\ &= \frac{f_\pi}{F_8}\cos\theta - \sqrt{8}\frac{f_\pi}{F_0}\varepsilon\sin\theta,\\ R_{\eta'} &\equiv \left[\frac{3\Gamma(\eta' \longrightarrow \gamma\gamma)}{\Gamma(\pi^0 \longrightarrow \gamma\gamma)}\right]^{1/2}\left(\frac{m_\pi}{m_{\eta'}}\right)^{3/2}\end{aligned} \tag{2}$$

1063-7788/00/6303-0499$20.00

Table 1. Mixing angle and decay constants as obtained from the measured $\eta/\eta' \longrightarrow \gamma\gamma$ and $J/\psi \longrightarrow \eta/\eta'\gamma$ decay widths

θ, deg	f_8/f_π	f_0/f_π
-19.62 ± 2.33	0.84 ± 0.05	0.88 ± 0.07

$$= \frac{f_\pi}{F_8}\frac{1}{\varepsilon}\sin\theta + \sqrt{8}\frac{f_\pi}{F_0}\cos\theta.$$

The parameters f_8, f_0, and θ can also be related to the features of the decays $J/\psi \longrightarrow \eta\gamma$ and $J/\psi \longrightarrow \eta'\gamma$. Following [11], we assume that the radiative decays of J/ψ are determined primarily by $c\bar{c}$ annihilation into $gg\gamma$. For the cases being considered, the gluon pair occurs in a pseudoscalar state. According to [10], the ratio of the widths with respect to the decays $J/\psi \longrightarrow \eta'\gamma$ and $J/\psi \longrightarrow \eta\gamma$ can be expressed in terms of the corresponding matrix elements $\langle 0|G\tilde{G}|\eta'\rangle$ and $\langle 0|G\tilde{G}|\eta\rangle$ of the gluon-anomaly operator $G\tilde{G} = G_{\mu\nu}\tilde{G}^{\mu\nu}$ [11]; that is,

$$\begin{aligned} R &\equiv \left[\frac{\Gamma(J/\psi \longrightarrow \eta'\gamma)}{\Gamma(J/\psi \longrightarrow \eta\gamma)}\right]^{1/2}\left(\frac{p_{\eta'}}{p_\eta}\right)^{3/2}\left(\frac{m_\eta}{m_{\eta'}}\right)^2 \\ &= \left|\frac{\langle 0|G\tilde{G}|\eta'\rangle}{\langle 0|G\tilde{G}|\eta\rangle}\right|\left(\frac{m_\eta}{m_{\eta'}}\right)^2 \\ &= \varepsilon\frac{\sqrt{2}f_0\cos\theta + \varepsilon f_8\sin\theta}{-\sqrt{2}f_0\sin\theta + \varepsilon f_8\cos\theta}, \end{aligned} \tag{3}$$

where $p_{\eta'}/p_\eta = (1 - m_{\eta'}^2/m_{J/\psi}^2)/(1 - m_\eta^2/m_{J/\psi}^2)$.

The mixing angle and the decay constants can also be expressed in terms of R_η, $R_{\eta'}$, and R. This was done and discussed in [10]. The experimental data quoted in [12] for the decays $\eta/\eta' \longrightarrow \gamma\gamma$ and $J/\psi \longrightarrow \eta/\eta'\gamma$ make it possible to obtain the estimates presented in Table 1.

The value of $\theta = -19.7^\circ \pm 2.2^\circ$ is consistent with the estimate $\theta \approx -(19^\circ\text{–}20^\circ)$ from [13].

We have also obtained the expressions

$$\begin{aligned} \tan\theta &= [2\varepsilon(R_\eta - 4R_{\eta'}R)]^{-1}\{5(\varepsilon^2 R_{\eta'} + R_\eta R) \\ &- [9(R_\eta R - \varepsilon^2 R_{\eta'})^2 + 16(R_\eta^2 + \varepsilon^2 R_{\eta'}^2)(\varepsilon^2 + R^2)]^{1/2}\}, \end{aligned} \tag{4}$$

$$\begin{aligned} \frac{f_\pi}{f_8} &= R_\eta + \varepsilon R_{\eta'}\tan\theta, \\ \frac{f_\pi}{f_0} &= \frac{-R_\eta\tan\theta + \varepsilon R_{\eta'}}{\sqrt{8}\varepsilon}. \end{aligned} \tag{5}$$

From (4), it follows that the mixing angle θ depends only on R and on the ratio $R_\eta/R_{\eta'}$.

It should be emphasized that the above expressions for the decay-width ratios—they have been used to estimate the mixing angle θ and the decay constants f_8 and f_0—are not identical to those from [2] and from the references quoted therein, but they reduce to them upon setting $\varepsilon = 1$ in (1)–(5).

4. DEPENDENCE ON THE RENORMALIZATION SCALE

The renormalization-group properties of the decay constants f_0 and f_8 should be discussed separately. Since our analysis is restricted to the lowest order of QED, the anomalous divergences D_8 and D_0 are virtually independent of the QED renormalization point. However, the effects of QCD renormalization cannot be neglected: that the singlet current is not conserved—that is, it shows an anomaly—renders it strongly dependent on the renormalization scale (the corresponding anomalous dimension was found in [14]), whence it follows that D_0 and f_0 are also dependent on the renormalization scale.

Owing to a multiplicative character of renormalization, the matrix element for D_0 decay into $\pi^+\pi^-\gamma$ can be represented in the form

$$\begin{aligned} &\langle\pi(p_+)\pi(p_-)\gamma(k)\big|D_0(\mu^2)\big|\Omega\rangle \\ &= Z(\mu^2/q^2)\langle\pi(p_+)\pi(p_-)\gamma(k)\big|D_0(q^2)\big|\Omega\rangle, \end{aligned} \tag{6}$$

where $q = p_+ + p_- + k$.

The same factor $Z(\mu^2/q^2)$ renormalizes $f_0(q^2)$ into $f_0(\mu^2)$. Since the expression for η' features only the ratio D_0/f_0 [see equation (1)], the amplitude of the decay $\eta' \longrightarrow \pi^+\pi^-\gamma$ then proves to be independent of the renormalization point.

Upon isolating the pole at $m_{\eta'}^2$, the matrix element $\langle\pi\pi|D_0(q^2)|\Omega\rangle$ is computed in the soft limit ($q^2 \longrightarrow 0$), whereas $f_0(q^2)$ is taken at the point $q^2 = m_{\eta'}^2$. It is usually assumed that $\langle\pi\pi|D_0(0)|\Omega\rangle \simeq \langle\pi\pi|D_0(q_0^2)|\Omega\rangle$, where $q_0 \simeq 1$ GeV. Since the q^2 evolution of the factor $Z(\mu^2/q^2)$ is slow (its anomalous dimension is on the order of α_s^2 [14]), the difference between $D_0(q_0^2)$ and $D_0(m_{\eta'}^2)$ is negligibly small. We may conclude that $\langle\pi\pi|D_0(0)|\Omega\rangle/f_0(m_{\eta'}^2) \simeq \langle\pi\pi|D_0(m_{\eta'}^2)|\Omega\rangle/f_0(m_{\eta'}^2)$.

The renormalization-invariant properties of some other matrix elements involving η'—in particular, those of the amplitude for the decay $\eta' \longrightarrow \gamma\gamma$—have been analyzed in [15].

5. DECAY $\eta' \longrightarrow \pi^+\pi^-\gamma$ IN THE SOFT LIMIT

The amplitude for the decay of either η or η' into $\pi^+\pi^-\gamma$ has the Lorentz structure

$$\begin{aligned} &M(\eta' \longrightarrow \pi(p_+)\pi(p_-)\gamma(k)) \\ &= E_P(p_+k, p_-k)\varepsilon_{\mu\nu\rho\sigma}\varepsilon^\mu k^\nu p_+^\rho p_-^\sigma, \end{aligned} \tag{7}$$

Table 2. Experimental values of the extra additive term in the resonance background for two assumed forms of this background

Model	$E_{\eta'}$, GeV^{-3}	
	[2]	[3]
M1	$5.06^{0.53}_{0.54}$	-4.46 ± 0.51
M2	$2.17^{0.49}_{0.46}$	-1.78 ± 0.53

where $P = \eta$ or η' and ε^μ is the photon polarization vector. Using equation (1) and taking into account all comments to it, we are now able to obtain E_P in the soft limit (contributions from the box and triangular anomalies [5, 6]),

$$E_P(0) = -\frac{e}{4\pi^2\sqrt{3}f_\pi^2}\left(\frac{\sin\theta}{\varepsilon F_8} + \sqrt{2}\frac{\cos\theta}{F_0}\right), \quad (8)$$

where $E_P(0) \equiv E_P(0, 0)$ and $e^2 = 4\pi\alpha_{em}$.

Substituting the parameter values quoted in Table 1 into (8), we finally obtain

$$E_{\eta'}(0) = -4.17 \pm 0.57 \text{ GeV}^{-3}. \quad (9)$$

In deriving this estimate, we employed the world-average data on the decay $\eta \longrightarrow \gamma\gamma$ [12] and data on production processes induced by the Primakoff mechanism. By invoking only the data on the two-photon processes, we obtain a slightly lower estimate:

$$E_{\eta'}(0) = -4.01 \pm 0.38 \text{ GeV}^{-3}. \quad (10)$$

The estimates in (9) and (10) should be regarded as the foremost results of the present analysis.

In [2, 3], the phenomenological parameter $E_{\eta'}$ of the contribution additive to the ρ-meson background, which the authors of [2, 3] propose to identify with $E_{\eta'}(0)$, depends on this background and was estimated from the data for two schemes, M1 and M2 (see [2] for details). The results obtained in this way for $E_{\eta'}$ are quoted in Table 2.

Our basic results as given by (9) and (10) were obtained within the current-mixing scheme. Previously, [9], we used the same scheme to derive the value of $E_{P(0)}$ for the decay $\eta \longrightarrow \pi^+\pi^-\gamma$ and obtained

$$E_\eta(0) = -7.37 \pm 0.77 \text{ GeV}^{-3}. \quad (11)$$

This result agrees well with the estimate given in [16]:

$$|E_\eta(0)| = 6.9 \pm 0.7 \text{ GeV}^{-3}. \quad (12)$$

To conclude, we have derived the nonresonance (anomalous) contribution to the amplitude of the decay $\eta' \longrightarrow \pi^+\pi^-\gamma$. The results are consistent with the empirical estimates of the parameter $E_{\eta'}$ that assume the M1 scheme. The theoretical prediction obtained in the soft limit, which is rather far from the realistic situation, proves to be surprisingly close to the experimental estimate of $E_{\eta'}$.

REFERENCES

1. S. I. Bityukov *et al.*, Z. Phys. C **50**, 451 (1991).
2. M. Benayoun *et al.*, Z. Phys. C **58**, 31 (1993); **65**, 399 (1995).
3. A. Abele *et al.*, Phys. Lett. B **402**, 195 (1997).
4. M. A. Ivanov and T. Mizutani, hep-ph/9710514.
5. M. S. Chanowitz, Phys. Rev. Lett. **35**, 977 (1975); **44**, 59 (1980).
6. M. S. Chanowitz, in *Proceedings of the VI International Workshop on Photon–Photon Collisions*, Ed. by R. L. Lander (World Sci., Singapore, 1985).
7. M. Gell-Mann, Phys. Lett. **8**, 214 (1964); G. Zweig, Preprint Nos. TH-401, TH-412, CERN (Geneva, 1964); W. A. Bardeen, H. Fritsch, and M. Gell-Mann, Preprint No. TH-1538, CERN (Geneva, 1972).
8. N. N. Bogoluybov, B. V. Struminsky, and A. N. Tavkhelidze, Preprint No. D-1958, JINR (Dubna, 1965); M. Y. Han and Y. Nambu, Phys. Rev. B **139**, 1006 (1965); Y. Miyamoto, Prog. Theor. Phys. Suppl. (Extra Number) 187 (1965).
9. A. V. Kisselev and V. A. Petrov, Preprint No. TH 7184/94, CERN (Geneva, 1994).
10. A. V. Kisselev and V. A. Petrov, Z. Phys. C **58**, 595 (1993).
11. V. A. Novikov *et al.*, Nucl. Phys. B **165**, 55 (1980).
12. R. M. Barnett *et al.*, Particle Data Group, Phys. Rev. D **54**, 1 (1996).
13. J. Donoghue, B. Holstein, and Y. Lin, Phys. Rev. Lett. **55**, 2766 (1985); J. Gasser and H. Leutwyler, Nucl. Phys. B **250**, 465 (1985); F. J. Gilman and R. Kauffman, Phys. Rev. D **36**, 2761 (1987); M. L. Nekrasov and V. E. Rochev, Teor. Mat. Fiz. **74**, 171 (1988); D. Coffman *et al.*, Phys. Rev. D **38**, 2695 (1988); R. Akhoury and J.-M. Frére, Phys. Lett. B **220**, 258 (1989); R. Akhoury and M. Leurer, Z. Phys. C **43**, 145 (1989); Kuang-Ta Chao, Nucl. Phys. B **335**, 101 (1990); N. A. Roe *et al.*, Phys. Rev. D **41**, 17 (1990); J. Jousset *et al.*, Phys. Rev. D **41**, 1389 (1990); T. N. Pham, Phys. Lett. B **246**, 175 (1990); N. Morisita *et al.*, Phys. Rev. D **44**, 175 (1991); C. Picciotto, Phys. Rev. D **45**, 1569 (1992); P. Ball, J.-M. Frére, and M. Tytgat, Phys. Lett. B **365**, 367 (1996); E. P. Venugopal and B. R. Holstein, Phys. Rev. D **57**, 4397 (1998).
14. J. Kodaira, Nucl. Phys. B **165**, 129 (1980).
15. A. V. Kisselev and V. A. Petrov, Teor. Mat. Fiz. **91**, 234 (1992).
16. D. V. Amelin *et al.*, Preprint No. 98-62, IHEP (Protvino, 1998).

Translated by A. Asratyan

Physics of Atomic Nuclei, Vol. 63, No. 3, 2000, pp. 502–519. From Yadernaya Fizika, Vol. 62, No. 4, 1999, pp. 697–714.

ELEMENTARY PARTICLES AND FIELDS
Theory

On Radiative Corrections to the Strangeness-Conserving β-Decay of Free Baryons*, **

G. G. Bunatian
Joint Institute for Nuclear Research, Dubna, Russia
Received December 30, 1997; in final form June 26, 1998

Abstract—In the work presented, the effect of electromagnetic interactions on the strangeness-conserving β-decay of baryons: neutron, $n \longrightarrow p + e^- + \bar{\nu} + \gamma$, and hyperon, $\Sigma^\pm \longrightarrow \Lambda^0 + e^\pm + \nu(\bar{\nu}) + \gamma$, is visualized. The polarized baryon decay studied, the total decay probability modification, as well as the modifications of the $e^\pm$ spectrum and the angular distribution with respect to the polarization vector $\boldsymbol{\xi}$ of the initial baryon (coefficient A), have been calculated. Dependence of the results on the value of the ultraviolet cut-off parameter Λ is elucidated. The spectrum and yield of the γ-radiation accompanying the β-decay is acquired, with special attention being paid to the infrared (soft-photon) radiation. The photon radiation of pions constituting the baryon's "pion cloud" is investigated. The radiative corrections to the total β-decay probability and to the electron energy and angular distributions found in this work proves to be of pivotal importance for obtaining the main characteristics of the weak interaction from experimental data processing. © *2000 MAIK "Nauka/Interperiodica".*

1. INTRODUCTION. THE CONCEPT OF ELECTROMAGNETIC INTERACTIONS IN β-DECAY

As charged particles are involved in β-decay, electromagnetic interactions are bound to be taken into consideration in describing such phenomenon. γ-radiation accompanying the β-decay of neutron, hyperons, and nuclei was investigated as far back as in the 'fifties [1, 2], and even in the 'thirties [3]. In so far as a mere bremsstrahlung of an outgoing electron (or positron) with sufficiently large energy was considered in those early works, the familiar perturbation theory in the fine structure constant α was perfectly applicable in treating such γ-radiation and its influence on $e^\pm$-spectra and the total decay probability [4]. Afterwards, allowing for the electromagnetic interactions having embraced the γ-radiation of any permitted energies including soft-photon radiation, the general physical problem of the infrared divergency emerged. An approach beyond the reach of the common perturbation theory in α was to be pursued, the virtual photons coming into the picture as well. The relevant methods elaborated in the profound works [5, 6] are to be consistently applied in treating electromagnetic interactions in β-decay. Aforementioned accounting for the virtual photons entails, in turn, the onset of the ultraviolet divergence while calculating the radiative corrections to baryon (and nucleus) β-decay. Nowadays, Sirlin's comprehensive investigations [7] in the framework of the Weinberg–Salam $SU_L(2) \times U(1)$ gauge model [8] provide two rather different recipes for removing the ultraviolet divergence that appears when treating the radiative β-decay. After all, baryons being far from to be point-like, its intrinsic structure has an effect on the β-decay, especially on the radiative corrections to it, and this fact needs to be properly accounted for [9, 10].

Thus, there exist nowadays several substantial grounds and purposes for an inquiry into the radiative corrections to baryon β-decay.

(i) First, in so far as correct acquiring the Cabibbo–Kobayashi–Maskawa (CKM) [11] quark-mixing matrix elements and invariant amplitudes (form-factors) [12, 13], determining the weak interactions, from the experimental data goes, the radiative corrections to β-decay have to be scrutinized. By now, the accuracy of the most precise experimental data on decay probability and on the energy and angular lepton distributions is known to amount to ≈0.1% for neutron data [14–22] and ≈2–3% for hyperon data [23]. Consequently, if the radiative corrections are strictly calculated, the CKM-matrix elements and invariant amplitudes of weak interactions can be disentangled, in the long run, from the experimental data with the same high accuracy, which is substantial to comprehend to what extent the weak interaction universality holds true [8, 11, 12]. What must be proclaimed from the very first is that we focus solely on the radiative corrections themselves, all other problems not associated with electromagnetic interactions immediately being put aside, significant though they may be in their own right. In particular, we do not deal with the induced terms and the momentum-transferred dependence of the form-factors (invariant amplitudes) incorporated in the general effective weak interaction Lagrangian [12, 13] (see the next Section).

* This article was submitted by the author in English.

** This paper, which was originally submitted by the author in English, was first published in *Physics of Atomic Nuclei*, 1999, vol. 62, no. 4, p. 648. Due to the errors made in the course of its language editing and upon the author's demand, this paper is republished in its original version.

Even so, we restrict ourselves for the sake of definiteness to treating the strangeness-conserving semileptonic decays of neutron, $n \longrightarrow p + e^- + \bar{\nu} + \gamma$, and $\Sigma^\pm$-hyperons, $\Sigma^\pm \longrightarrow \Lambda^0 + e^\pm + \nu(\bar{\nu}) + \gamma$ only, to sidestep and avoid, according to our lights, the highbrow discussion about the peculiarities of CKM-matrix elements [11], right-handed currents [24, 25], and so on.

During last three decades, many a calculation has been pursuing the Sirlin's simplified approach [9, 26, 27], treating the radiative corrections as a sum of the so-called "model-dependent" (MD) and "model-independent" (MI) parts, which had been managed, initially, to describe the electron spectrum modification in neutron β-decay and then was generalized to treat the modifications of the total decay probability and the lepton energy-angular distributions for neutron [28, 29] and hyperons [30–32]. In this rather untenable handling, the MI part renders some finite part of the radiative corrections, independent of strong interactions, as well as of the interactions mediated by vector bosons, and is calculated for point-like baryons within the familiar $(V-A)$ theory. The whole remnant, the MD part, is suggested to be absorbed into the effective form-factors, causing their redefinition. The key point is that the transition amplitude M is presumed to be a multiple of M_0, the uncorrected one. These main features of the original treatment have been retained, though some improvements and generalizations were undertaken in [33–35], with the explicit dependence of the MI part on the ultraviolet cutoff parameter Λ emerging instead of the original mere redefinition of the effective amplitudes. As our calculations do not utilize the aforesaid simplifications, the results obtained prove to be rather different. We shall trace the origin of these differences in Sections 3, 4 and discuss their consequences in Sections 5, 7.

(ii) In studying the radiative corrections to baryon β-decay, the general physical problem of soft-photon radiation emerges, which purports to be an important feature of the phenomenon, especially for hyperon decay, because of the large energy released. Treating the infrared divergence and double-logarithmic asymptotic behavior in radiative β-decay typifies the case of working beyond the usual perturbation theory in the fine structure constant α [5, 6]. Thus, visualization of the true behavior of the baryon radiative β-decay probability when the γ-radiation energy tends to zero, offered in Sections 4, 5, is of physical interest in its own right, which warrants our plunge into radiative β-decay if only for this reason. Certainly, we need this to repose full confidence in the actual accuracy of our calculations as well.

(iii) Inquiring into the γ-radiation accompanying β-decay, one becomes conscious of the fact that side by side with the familiar bremsstralung of outgoing charged particles, there exists a γ-radiation straightforward from baryon interior, as being due to the baryon intrinsic structure, and, especially, due to the baryon's internal pionic degrees of freedom. Thus, the study of this phenomenon provides a tool for investigating the baryon structure within the framework of low-energy physics.

(iv) As far as treating the ultraviolet divergence is concerned, we are to realize (see Section 5) what is the sensitivity of the ultimate results of our calculations on the choice of different prescriptions elaborated in Sirlin's investigations [7].

All of the enumerated tasks (i)–(iv) being closely related to each other are of long-standing and ever-increasing significance. Keeping in mind the aforesaid agenda we make bold to launch our present study of the radiative corrections to baryon β-decay.

2. GENERAL LAGRANGIAN FORMULATION

First and foremost, we set out the general effective Lagrangian (see [12, 13, 36–38]) relevant to describe the strangeness-conserving baryon β-decay,

$$n \longrightarrow p + e^- + \bar{\nu} + \gamma, \quad \Sigma^\pm \longrightarrow \Lambda^0 + e^\pm + \nu(\bar{\nu}) + \gamma,$$

accounting for the electromagnetic interactions which we are about to consider,

$$L_{\rm int} = L_{BfBiw} + L_{e\gamma} + L_{B\gamma} + L_{\pi\pi w} + L_{\pi w} + L_{BfBi\pi}, \quad (1)$$

where

$$\begin{aligned} L_{BfBiw}(x) &= \frac{G}{\sqrt{2}}(\bar{\psi}_e(x)\gamma^\alpha(1+\gamma^5)\psi_\nu(x)) \\ &\times \bar{\Psi}_{Bf}(x)[\gamma_\alpha g_V^B(q) + g_{\rm WM}^B\sigma_{\alpha\nu}q_\nu \\ &+ (g_A^B(q)\gamma_\alpha + g_{\rm IP}^B q_\alpha)\gamma^5]\Psi_{Bi}(x) \end{aligned} \quad (2)$$

renders the $(V-A)$ baryon-lepton weak interaction, q being the four-momentum transfer in β-decaying. The expression

$$L_{e\gamma}(x) = -e\bar{\psi}_e(x)\gamma^\mu\psi_e(x)A_\mu(x) \quad (3)$$

stands for electromagnetic field interaction with leptons and $L_{B\gamma}$, likewise, with baryons. The electro-weak pion interactions are described by

$$\begin{aligned} L_{\pi\pi w}(x) &= (\partial_\mu\pi^a(x) + \epsilon^{bac}\mathscr{A}_\mu^b(x)\pi^c(x))^2, \\ L_{\pi w}(x) &= f_\pi\sqrt{2}\mathscr{A}_\mu^a(x)(\partial^\mu\pi^a(x) + \epsilon^{bac}\mathscr{A}^{b\mu}(x)\pi^c(x)), \end{aligned} \quad (4)$$

where $(a, b, c) = (1, 2, 3)$, whereas $\mu = (1, 2, 3, 4)$, $f_\pi = f_{\pi NN} = 93$ MeV, and

$$\mathscr{A}_\mu^0 = eA_\mu, \quad \mathscr{A}_\mu^- = \frac{G}{\sqrt{2}}\bar{\psi}_e\gamma_\mu(1+\gamma^5)\psi_\nu,$$

$$\mathscr{A}^+ = -(\mathscr{A}^-)^*.$$

Lastly, the effective pion interaction with the three-

quark bag-baryon can be presented in the form [38]

$$L_{BfBi\pi}(x) = \frac{1}{2f_{\pi BfBi}}\int\frac{d^4q}{(2\pi)^4 i}(\boldsymbol{\sigma}\cdot\mathbf{q})u(\mathbf{q})\Psi^{+}_{Bf}(x) \times(\boldsymbol{\pi}(x)\boldsymbol{\tau})\Psi_{Bi}(x)e^{iqx}, \quad (5)$$

$$u(\mathbf{q}) = -2\mathcal{N}^2R^3\frac{5}{3}j_1(pR)j_0(pR)\frac{j_1(qR)}{|\mathbf{q}|\cdot|\mathbf{x}|},$$

where $\mathcal{N}$, R, p are the normalization factor, baryon-bag radius, and quark momentum, respectively [38], and $f_{\pi NN}/f_{\pi\Sigma\Lambda} \approx 11/14$ [12, 13]. In the aforesaid formulae (2)–(5), the γ-matrices are defined accordingly [36], $\sigma_{\alpha\nu} = (\gamma_\alpha\gamma_\nu - \gamma_\nu\gamma_\alpha)/2$, and the system of units $h = c = 1$ is adapted; $\Psi_{Bi}(x)$, $\Psi^{+}_{Bf}(x)$ render baryon fields in the initial and final states, and ψ_e, ψ_ν, π^α, A_μ stand for the electron (positron), (anti)neutrino, pion, and electromagnetic fields, respectively. The particle masses (in MeV) occurring in (1)–(5) are $M_p = 938.2723$, $M_n = 939.5656$, $M_{\Sigma^+} = 1189.4$, $M_{\Sigma^-} = 1197.3$, $M_{\Lambda^0} = 1115.6$, $m_{\pi^0} = 134.98$, $m_{\pi^\pm} = 139.57$ and $m = m_e = 0.5110$ [37]. As we are inquiring into the strangeness-conserving β-decay only, we henceforth adapt, for our numerical calculations, the effective value $G = G^{00} = G_F|V_{ud}| = 1.1365(11) \times 10^{-5}$ GeV^{-2} [11, 37, 39, 40], where $G_F = 1.16639(2)\times10^{-5}$ GeV^{-2} and G^{00} are acquired from the muon decay and super-allowed ($0^+ \longrightarrow 0^+$) nuclear Fermi transitions, respectively. Here, the radiative corrections in both cases have been thoroughly accounted for and disentangled, and $|V_{ud}| = 0.9744 \pm 0.001$ is an element of the KM-matrix which mixes the u-, d-quarks, related to the Cabibbo angle θ_C by $|V_{ud}| = \cos\theta_C$. We also prescribe for the effective amplitudes in (2) the values $g_V^n = 1$, $g_A^n = 1.266$ in the neutron decay case [14], [21], and $g_V^\Sigma = 0$, $g_A^\Sigma = \sqrt{2/3}\,D$, $D \approx 0.74$ [12, 13] for Σ-hyperon one. However, as we shall treat in our further calculations the relative radiative corrections that is, the radiative corrections divided by the uncorrected bulk decay probability, the G value itself does not influence the results set forth anywhere, but in Section 7.

The amplitudes g_V, g_A determine the main bulk $(V-A)$ weak interaction, whereas g_{IP} represents the induced pseudoscalar, and $g_{WM} = (\tilde{\mu}_i - \tilde{\mu}_f)/2M_B$ stands for "weak magnetism," where $\tilde{\mu}_f$, $\tilde{\mu}_i$ are the anomalous magnetic moments of initial and final baryons; for neutron $g_{WM} = -3.70/2M_p$. Certainly, as the ratio $\sqrt{q^2}/M_p$ is known to be small enough even in the Σ-decay case, accounting for the q^2-dependence of the effective form-factors g_V, g_A, as well as retaining the terms with g_{WM}, g_{IP}, when calculating the radiative corrections to the bulk β-decay process caused by $g_V(0)$, $g_A(0)$ in equation (2), would have provided superfiuous corrections to corrections. Furthermore, the baryon mass is thought to be so large that we have the right to neglect the baryon recoil, the final baryon velocity in the rest frame of the initial baryon, and all of the quantities which are multiples of the ratios q_μ/M_B, Δ/M_B, m/M_B, ($\Delta = M_i - M_f$, and m is electron mass). Thus, in (2), we abandon from outset the weak magnetism and the induced pseudoscalar, and neglect the q^2-dependence of g_V, g_A. This does not mean to say the additional corrections due to accounting for the form-factors q^2-dependence and the terms with g_{WM}, g_{IP} in (2) must be conceived as being quite negligible. It is only that the evaluation of those quantities is not our task here. However, when we try to gain the correct values of the quantities G, g from experimental data processing, it will be necessary, of course, to take into account side by side with the radiative corrections all the others, as well, these second being comparable with the first and substantial in their own right, especially in the case of Σ-decay because of the large mass difference $\Delta = M_\Sigma - M_\Lambda \approx 80$ MeV [37].

3. TRANSITION AMPLITUDES

The effective interactions (2), (3) are known to give rise to both the real γ-radiation of charged particles involved in β-decaying and virtual photon exchanging between them. The matrix elements of the transition amplitude to be calculated are presented, to the lowest order in electric charge e, by diagrams, as shown in Figs. 1, 2. All of the notations in the figures, being familiar, need not to be explained. The diagram *a* in Figs. 1, 2 presents uncorrected bulk β-decay, and *b* describes the common $e^\pm$-bremsstrahlung. It is worth to take the view of the fact that in the Σ-decay case, incoming and outgoing charged particles interchange a virtual photon, diagram *d*, Fig. 2, whereas the virtual photon exchange holds in the neutron case between two charged particles in the final state, diagram *d*, Fig. 1. In so far as the baryon γ-radiation presented by the diagrams *c* of the Figs. 1, 2 goes, one need not to take this into account, with baryons masses being suggested to be infinitely large (see discussion in the end of the previous Section 2).

Side by side with the aforesaid γ-radiation which has been treated in many papers, we allow for that caused by the internal structure of the baryon, treated as consisting of the heavy and tough three-quark bag and a pion cloud surrounding it [38]. During β-decaying, the correspondent interactions (3)–(5) carry the γ-radiation from the baryon interior into effect. We account for the γ-radiation of the relatively light particles, pions, coming into picture, but not of the heavy three-quark bag itself. To the lowest order in e, the corresponding graphs of the transition amplitude are displayed in Fig. 3.

The diagrams *a* in Fig. 3 render the processes when a charged or neutral virtual pion, having been emitted

by the initial baryon, undergoes the β-decay as follows:

$$\pi^{\pm} \longrightarrow \pi^0 + e^{\pm} + \nu(\bar{\nu}), \quad \pi^0 \longrightarrow \pi^{+(-)} + e^{-(+)} + \bar{\nu}(\nu),$$

and then is reabsorbed by the baryon with producing the final baryon state, a charged pion emitting a photon. The β-decay of the virtual pion and the photon emission occur in case *b* simultaneously:

$$\pi^{\pm} \rightleftharpoons \pi^0 + e^{\pm} + \nu(\bar{\nu}) + \gamma,$$

$$\pi^0 \longrightarrow \pi^{+(-)} + e^{-(+)} + \bar{\nu}(\nu) + \gamma,$$

In the case presented in the diagram *d*, a virtual charged pion emitted by the initial baryon emits a photon and suffers β-decay; in case *c* β-decay and γ-radiation occur simultaneously:

$$\pi^{\pm} \longrightarrow e^{\pm} + \nu(\bar{\nu}) + \gamma.$$

γ-radiation directly from baryon interior is a subject of great conceptual interest in its own right, irrespective of how much it contributes to the total γ-radiation accompanying β-decay.

Now, we shall obtain the values of the matrix elements discussed above.

Renormalization of the outer charged particles states, that is accounting for diagrams *e*, *f* in Figs. 1, 2, having been carried out, the uncorrected, zerothorder in *e*, transition amplitude, presented by diagrams *a*,

$$M_0^B = \frac{G}{\sqrt{2}}\bar{u}_e(\mathbf{p}_e)l_0^{\lambda}u_{\nu}(\mathbf{p}_{\nu})\bar{U}_{Bf}(\mathbf{p}_f)h_{0\lambda}^B U_{Bi}(\mathbf{p}_i), \qquad (6)$$

$$l_0^{\lambda} = \gamma^{\lambda}(1+\gamma^5), \quad h_{0\lambda}^B = \gamma_{\lambda}(g_V^B + g_A^B\gamma^5), \qquad (7)$$

is known to be replaced by (see, for instance [36])

$$\tilde{M}_0^B \approx M_0^B + M_R^B, \quad M_R^B = M_0^B(Z_e^{(1)} + Z_B^{(1)})/2,$$
$$Z_i^{(1)} = -\frac{\alpha}{2\pi}[\ln(\Lambda/m_i) + 9/4 + 2\ln(\lambda/m_i)]. \qquad (8)$$

In (6), p_e, p_ν, p_i, p_f are the momenta of the electron, (anti)neutrino, initial and final baryons, respectively, and $u_e, u_\nu, U_{Bi}, U_{Bf}$ indicate their Dirac spinors. The photon mass λ is introduced, as usually, to treat the soft (infrared) γ-radiation. The cut-off parameter Λ, emerging ad hoc in (8), formally prevents an ultraviolet divergence. The up-to-date genuine treatment [7] of the ultraviolet divergence and the respective Λ values are properly discussed later on.

The matrix element presented by diagrams *d* involving the internal photon line takes the form

$$M_{2\gamma}^B = \pm\frac{i}{(2\pi)^4}\frac{e^2G}{\sqrt{2}}\int d^4k(\bar{u}_e(\mathbf{p}_e)\mathcal{P}^{\mu\lambda}u_{\nu}(\mathbf{p}_{\nu}))$$
$$\times(\bar{U}_{Bf}(\mathbf{p}_f)(h_{\gamma}^B)_{\mu\lambda}U_{Bi}(\mathbf{p}_i))F_B(k). \qquad (9)$$

Here, $B = p$ and the "+" sign correspond to the neutron decay case, where $Bi = n$, $Bf = p$, whereas $B = \Sigma$ and the "–" sign correspond to the hyperon one, where $Bi = \Sigma^{\pm}$,

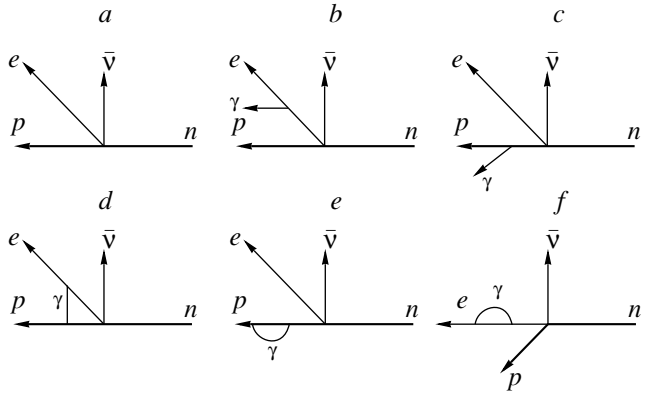

Fig. 1. Diagrams describing the radiative neutron β-decay, $n \longrightarrow p + e^- + \bar{\nu} + \gamma$, to the lowest *e*-order.

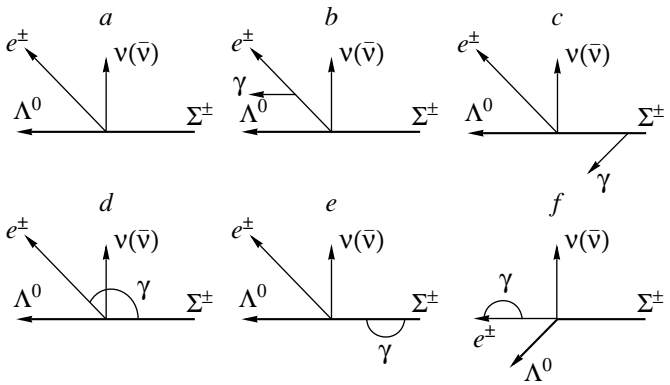

Fig. 2. The same as Fig. 1 for $\Sigma^{\pm} \longrightarrow \Lambda^0 + e^{\pm} + \nu(\bar{\nu}) + \gamma$.

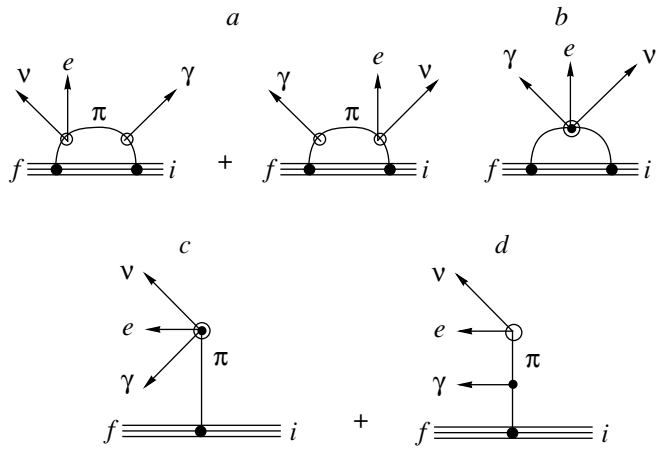

Fig. 3. Diagram describing the γ-radiation of the virtual pions from the baryon interior during β-decaying, the triple lines standing for the three-quark baryon-bag.

$Bf = \Lambda^0$. The following notations are introduced in (9):

$$F_B(k) = 1/[(P^2 - m^2 + i0) \times (Q_B^2 - M_B^2 + i0)(k^2 - \lambda^2 + i0)],$$

$$(h_\gamma^p)^{\mu\lambda} = \gamma^\mu(\hat{Q}_p + M_p)\gamma^\lambda(g_V^n + g_A^n\gamma^5),$$

$$(h_\gamma^\Sigma)^{\mu\lambda} = \gamma^\lambda(g_V^\Sigma + g_A^\Sigma\gamma^5)(\hat{Q}_\Sigma + M_\Sigma)\gamma^\mu, \qquad (10)$$

$$\mathcal{P}^{\mu\lambda} = \gamma^\mu(\hat{P} + m)\gamma^\lambda(1 + \gamma^5),$$

$$P = p_e - k, \quad Q_p = p_p + k,$$

$$Q_\Sigma = p_\Sigma - k, \quad \hat{O} \equiv O_\alpha\gamma^\alpha.$$

Obviously, to the first order in α, the expression (9) lumps together all of the effects of the electromagnetic interactions between charged particles involved in the β-decay, the so called "Coulomb corrections" being not separated as against that what have been expounded in some papers [41]. Let us emphasize that though the outer baryons are nonrelativistic and even have the negligible velocity, the virtual baryon in the intermediate state in diagrams *d* must be described by the relativistic propagator

$$G(Q) = \frac{\hat{Q} + M}{Q^2 - M^2 + i0} \qquad (11)$$

because integrating over d^4k in (9) involves arbitrarily large values of the virtual photon momentum k and, consequently, of the virtual baryon momentum Q_B. If anything, it might be pertinent to point out that if we had replaced the function G (11) by the nonrelativistic value, the calculation of the radiative corrections to the transition amplitudes and, thereafter, to the β-decay probability would have reduced, for all intents and purposes, to handling their so-called MI parts [26–35] mentioned in Section 1 (see, also, the discussion below, in Section 5).

The total amplitude of the bremsstrahlung is the sum of the amplitudes presented by diagrams *b*, *c* in Figs. 1, 2. The contributions of baryon γ-radiation, diagrams *c*, prove to be negligible because of the large baryon mass (the vanishing baryon velocity), as was asserted above. The transition amplitude corresponding to diagram *b* in Figs. 1, 2 is

$$M_{1\gamma}^{B(l)} = \frac{eG}{\sqrt{2}}\epsilon_m^{(l)} \times (\bar{u}_e(\mathbf{p}_e)\mathcal{P}^{m\alpha}u_\nu(\mathbf{p}_\nu))(\bar{U}_{Bf}(\mathbf{p}_f)h_{0\alpha}^B U_{Bi}(\mathbf{p}_i)), \quad (m, l) = (1, 2, 3), \qquad (12)$$

where $\boldsymbol{\epsilon}^{(l)}$ is the photon polarization vector.

Next, what we are to do now is to inquire for the transition amplitudes describing the direct γ-radiation from baryon interior as being due to the pionic degrees of freedom of a baryon. After the due calculations utilizing equations (4), (5), relativistic pion propagators and nonrelativistic baryon propagators in the intermediate states, we obtain for the amplitude presented by two diagrams *a* in Fig. 3 together:

$$M_{\pi a}^{B(l)} = i\frac{1}{(2\pi)^4}\frac{e}{(2f_{\pi BfBi})^2}\frac{\sqrt{4\pi}}{\sqrt{k}} \times \epsilon_m^{(l)}(\bar{u}_e(\mathbf{p}_e)\mathcal{A}^-_\alpha u_\nu(\mathbf{p}_\nu))\int d^4k_1\mathbf{k}_1^2u(\mathbf{k}_1)u(\mathbf{k}_3) \times \left[\frac{(k_1^\alpha + k_2^\alpha)(k_2^m + k_3^m)}{(\delta_f + k_{10} - i0E_f)(\omega_{01}^2 - k_{10}^2 - i0)} \times \frac{1}{(\omega_2^2 - k_{20}^2 - i0)(\omega_3^2 - k_{30}^2 - i0)} - \frac{(k_1^\alpha + \tilde{k}_2^\alpha)(\tilde{k}_2^m + k_3^m)}{(\delta_i + k_{10} - i0E_i)(\omega_1^2 - k_{10}^2 - i0)} \times \frac{1}{(\omega_2^2 - \tilde{k}_{20}^2 - i0)(\omega_{03}^2 - k_{30}^2 - i0)}\right], \qquad (13)$$

$$\delta_f = E_f(\mathbf{P}) - E_f(\mathbf{p}_f), \quad \delta_i = E_i(\mathbf{P}) - E_f(\mathbf{p}_f).$$

Here, the indices i, f denote the initial and final sorts of baryons (for neutron decay $i = n, f = p$, and for hyperon decay $i = \Sigma^\pm, f = \Lambda^0$), E is the baryon energy, $P = p_f - k_1$ is the momentum of an intermediate baryon. The following notations were also introduced in (13):

$$k_3 = k_1 + K, \quad k_2 = k_1 + Q,$$

$$\tilde{k}_2 = k_1 + k, \quad \omega_{n,0n}^2 = \mathbf{k}_n^2 + m_{\pi^{\pm,0}}^2,$$

where $m_{\pi\pm}, m_0$ are the masses of the charged and neutral pion, respectively, $Q = p_e + p_\nu$ is the sum of electron and neutrino momenta, and $K = Q + k = p_e + p_\nu + k$. The matrix element corresponding to diagram *b* in Fig. 3 results as

$$M_{\pi b}^{B(l)} = i\frac{1}{(2\pi)^4}\frac{e}{(2f_{\pi BfBi})^2}\frac{\sqrt{2\pi}}{\sqrt{k}} \times \epsilon_m^{(l)}(\bar{u}_e(\mathbf{p}_e)(\mathcal{A}^-)^m u_\nu(\mathbf{p}_\nu))\int d^4k_1\mathbf{k}_1^2u(\mathbf{k}_1)u(\mathbf{k}_2) \times \left[\frac{1}{(\delta_f + k_{10} - i0E_f)(\omega_{01}^2 - k_{10}^2 - i0)(\omega_2^2 - k_{20}^2 - i0)} - \frac{1}{(\delta_i + k_{10} - i0E_i)(\omega_1^2 - k_{10}^2 - i0)(\omega_{02}^2 - k_{20}^2 - i0)}\right], \qquad (14)$$

the notations being the same as in (13).

The sum of the matrix elements presented by dia-

grams c and d in Fig. 3 appears to be

$$M^{B(l)}_{\pi cd} = \frac{e\sqrt{2\pi}}{\sqrt{k}}\frac{u(|\mathbf{K}|)(\bar{U}_{Bf}(\mathbf{p}_f)\boldsymbol{\sigma}\mathbf{K}U_{Bi}(\mathbf{p}_i))}{(K^2-m_\pi^2)} \times\left[\epsilon^{m(l)}\bar{u}_e(\mathbf{p}_e)\mathcal{A}^-_m u_\nu(\mathbf{p}_\nu)\right. \left.+\frac{\epsilon^{(l)}_n(2Q^n+k^n)Q^\mu(\bar{u}_e(\mathbf{p}_e)\mathcal{A}^-_\mu u_\nu(\mathbf{p}_\nu))}{Q^2-m_\pi^2}\right]. \quad (15)$$

After all, lumping all of the terms of (6)–(15) together we are left with the corrected transition amplitude accounting for electromagnetic interactions to the lowest order in electric charge e:

$$M^{B(l)}_{\rm tot} = M^B_0 + M^{B(l)}_{1\gamma} + M^{B(l)}_\pi + M^B_2, \quad (16)$$

where

$$M^B_2 = M^B_R + M^B_{2\gamma} \quad (17)$$

is proportional to e^2, whereas $M^{B(l)}_{1\gamma}$ and

$$M^{B(l)}_\pi = M^{B(l)}_{\pi a} + M^{B(l)}_{\pi b} + M^{B(l)}_{\pi cd} \quad (18)$$

are linear in e.

The physical nature of the phenomenon described by the amplitude (18) being different from that described by (8)–(12), the main features of (18) are also unlike those of (8)–(12). Especially, by treating the γ-radiation described by (18), we do not encounter the problems of infrared and ultraviolet divergences. Let us also be conscious of the absence of the quantities g^B_V, g^B_A in (18). The contribution of M^B_π (18) in the total γ-radiation turns out to be very small, rather negligible, when compared with that caused by the amplitude $M^B_2 + M^B_{1\gamma}$. Nevertheless, the inquiry into γ-radiation associated with M^B_π (18) is of a great conceptual interest in its own right as being due to the intrinsic structure of baryons. Therefore, we set forth this γ-radiation separately after the main calculation of the radiative β-decay probability that makes allowance for the amplitudes $M^B_2 + M^B_{1\gamma}$ presented by Figs. 1, 2. The transition amplitudes having been acquired, we are now in position to calculate the decay probability accounting for electromagnetic interactions.

4. THE β-DECAY PROBABILITY ACCOUNTING FOR ELECTROMAGNETIC INTERACTIONS

The decay probability we take up to calculate is expressed through the square of the absolute value

$$\left|M'^{B(l)}_{\rm tot}\right|^2 = \left|M^B_0 + M^B_2 + M^{B(l)}_{1\gamma}\right|^2, \quad (19)$$

which reduces in the first α-order to

$$\left|M'^{B(l)}_{\rm tot}\right|^2 = \left|M^B_0\right|^2 + M^{B*}_0 M^B_R + M^B_0 M^{B*}_R + \left|M^{B(l)}_{1\gamma}\right|^2 + M^{B*}_0 M^B_{2\gamma} + M^B_0 M^{B*}_{2\gamma}. \quad (20)$$

Allowing for the polarizations of the various particles involved in the process considered, we rewrite, as usually (see, for instance [36]), the terms incorporated in (20), making use of the polarization matrices ρ_e, ρ_ν, ρ_{Bi}, ρ_{Bf} of the electron, neutrino, and the initial and final baryons, respectively. The value of the first term in (20) is, of course, well known,

$$\left|M^B_{0if}\right|^2 = \frac{G}{2}\mathrm{tr}[\rho_{Bf}h^{B\alpha}_0\rho_{Bi}\bar{h}^{B\beta}_0]\mathrm{tr}[\rho_e l_{0\alpha}\rho_\nu \bar{l}_{0\beta}], \quad (21)$$

and to gain the value of

$$[M^{B*}_0 M^B_R + M^B_0 M^{B*}_R]_{if} \quad (22)$$

in (20) is straightforward according to equation (8). The quantities $h^{B\alpha}_0$, $l_{0\alpha}$ are defined in (6), (7), and, as usual, $\bar{a} \equiv \gamma^0 a^+ \gamma^0$.

The fourth term in (20) is

$$\left|M^{B(l)}_{1\gamma}\right|^2 = \frac{\alpha G^2}{2}\epsilon^{(l)}_\mu \epsilon^{(l)*}_\kappa \times \mathrm{tr}[\rho_{Bf}h^B_{0\alpha}\rho_{Bi}\bar{h}^B_{0\beta}]\mathrm{tr}[\rho_e \mathcal{P}^{\mu\alpha}\rho_\nu \bar{\mathcal{P}}^{\kappa\beta}], \quad (23)$$

where $\mathcal{P}^{\mu\alpha}$ is defined by (10). With equations (9), (10) being accounted for, the sum of the last two terms in (20) can be presented in the following form

$$(M^B_S)^2_{if} \equiv (M^{B*}_0 M^B_{2\gamma} + M^B_0 M^{B*}_{2\gamma})_{if} = \pm\frac{\alpha G^2}{2}\frac{i}{(2\pi)^4}\int d^4k F_B(k)[T^{\mu\lambda\alpha}_B S_{\mu\lambda\alpha} + (T^{\mu\lambda\alpha}_B S_{\mu\lambda\alpha})^*], \quad (24)$$

$$T^{\mu\lambda\alpha}_B = \mathrm{tr}[\rho_{Bf}(h^B_\gamma)^{\mu\lambda}\rho_{Bi}(h^B_0)^\alpha], \quad S_{\mu\lambda\alpha} = \mathrm{tr}[\rho_e \mathcal{P}^{\mu\lambda}\rho_\nu l^\alpha_0]. \quad (25)$$

As explained above, we study the decay of the polarized baryon at rest, the velocity of the final baryon being considered as negligible. In this work, we inquire into total decay probability, the γ-radiation and electron spectra, and electron angular distribution with respect to the initial baryon polarization vector $\boldsymbol{\xi}$, that is the correlation between the vector $\boldsymbol{\xi}$ and the electron velocity $\mathbf{v}$. All of the other correlations between the particles involved in the β-decay and their polarizations, as well as the neutrino and final baryon spectra, are unobservable. Consequently, the aforesaid polarization matri-

ces, (21)–(24), are given as follows:

$$\rho_{Bf} = M_{Bf}\begin{pmatrix} 1 & 0 \\ 0 & 0 \end{pmatrix}, \quad \rho_{Bi} = M_{Bi}(1+\boldsymbol{\sigma}\cdot\boldsymbol{\xi})\begin{pmatrix} 1 & 0 \\ 0 & 0 \end{pmatrix}, \quad \rho_e = (\hat{p}_e + m)/2, \quad \rho_\nu = \hat{p}_\nu, \tag{26}$$

and we evaluate the β-decay probability integrated over the final baryon and (anti)neutrino momenta, and over the photon emission directions, and summarized over the polarizations of all of the final particles.

As a matter of course, the quantity $|M_0|^2$ in (20) is well known to provide the uncorrected bulk baryon β-decay probability with the $e^{\pm}$ energy-momentum (ε, **p**),

$$d\mathbf{W}^{B0} = d\mathbf{w}[w_0^{B0} + (\mathbf{v}\cdot\boldsymbol{\xi})w_\xi^{B0}], \tag{27}$$

where the following notations are introduced:

$$d\mathbf{w} = \frac{G^2}{2\pi^3}\varepsilon p\omega_{\nu 0}^2 d\varepsilon\frac{d\mathbf{n}}{4\pi}, \quad \mathbf{n} = \frac{\mathbf{p}}{p}, \quad \mathbf{v} = \frac{\mathbf{p}}{\varepsilon},$$

$$\omega_{\nu 0} = \Delta^B - \varepsilon, \quad \Delta^B = M_{Bi} - M_{Bf}, \tag{28}$$

$$w_0^{B0} = (g_V^B)^2 + 3(g_A^B)^2, \quad w_\xi^{B0} = 2g_A^B(g_V^B - g_A^B).$$

The probability of γ-radiation, accompanying the β-decay, with an absolute value of the momentum $k = |\mathbf{k}|$ proves to be

$$d\mathbf{W}_\gamma^B(\varepsilon, \mathbf{p}, k; \lambda) = d\mathbf{W}_{0\gamma}^B(\varepsilon, \mathbf{p}, k; \lambda) + \mathbf{v}\cdot\boldsymbol{\xi}\, d\mathbf{W}_{\xi\gamma}^B(\varepsilon, \mathbf{p}, k; \lambda) = d\mathbf{w}dk[W_{0\gamma}^B(\varepsilon, \mathbf{p}, k; \lambda) + \mathbf{v}\cdot\boldsymbol{\xi} W_{\xi\gamma}^B(\varepsilon, \mathbf{p}, k; \lambda)], \tag{29}$$

where

$$W_{0\gamma}^B = w_0^{B0}\frac{2\alpha}{\pi}\left\{\frac{1}{\varepsilon}\left[\mathcal{L}(p) + \frac{k}{2\varepsilon}(\mathcal{L}(p)+1)\right]\frac{\omega_\nu^2}{\omega_{\nu 0}^2} + \frac{k-2\omega_{\nu 0}}{\omega_{\nu 0}^2}\mathcal{L}(p) + \mathcal{R}(k)\right\}, \tag{30}$$

$$W_{\xi\gamma}^B = w_\xi^{B0}\frac{2\alpha}{\pi}\times\left\{\mathcal{L}(p)\left[\frac{1}{\varepsilon v^2}\left(1+\frac{k}{2\varepsilon}\right)\frac{\omega_\nu^2}{\omega_{\nu 0}^2} + \frac{k-2\omega_{\nu 0}}{\omega_{\nu 0}^2}\right] + \mathcal{R}(k)\right\}. \tag{31}$$

Here, the following notations were introduced:

$$\mathcal{R}(k) = \frac{1}{2kv}\ln\left|\frac{\sqrt{\lambda^2+k^2}+vk}{\sqrt{\lambda^2+k^2}-vk}\right| - \frac{1}{\sqrt{\lambda^2+k^2}} + \frac{\lambda^2}{2\sqrt{k^2+\lambda^2}}\left(\frac{1}{k^2+\lambda^2} + \frac{1}{k^2+\lambda^2-v^2(k^2+\lambda^2)+v^2\lambda^2} + \frac{1}{kv\sqrt{k^2+\lambda^2}}\ln\left|\frac{\sqrt{\lambda^2+k^2}-vk}{\sqrt{\lambda^2+k^2}+vk}\right|\right), \tag{32}$$

$$\omega_\nu = \omega_{\nu 0} - k, \quad \mathcal{L} = \frac{1}{v}\ln\left(\frac{p+\varepsilon}{m}\right) - 1.$$

In so far as γ-radiation with the energies k beyond the infrared domain goes, $\alpha\ln(\Delta/k) \ll 1$, the familiar perturbation theory holds true, there is no reason for imposing λ in (29)–(32), and equations (30), (31) reduce to

$$W_{0\gamma}'^B = w_0^{B0}\frac{2\alpha\omega_\nu^2}{k\pi\omega_{\nu 0}^2}\left\{\mathcal{L}(p)\left(1+\frac{k}{\varepsilon}\right) + \frac{k^2}{2p\varepsilon}\ln\left(\frac{p+\varepsilon}{m}\right)\right\}, \tag{33}$$

$$W_{\xi\gamma}'^B = w_\xi^{B0}\frac{2\alpha\omega_\nu^2}{\pi\omega_{\nu 0}^2}\mathcal{L}(p)\left(\frac{1}{pv} + \frac{1}{2p^2} + \frac{1}{k}\right), \tag{34}$$

which were handled long before in [1–4]. They proved to be success in describing the experimental data of the nuclei radiative β-decay as far as γ-radiation beyond the infrared domain is concerned. The possibility of observing such photons in neutron β-decay was discussed recently in [42]. As we shall become convinced after due calculations, the main modifications of the total decay probability, and of the electron energy and angular distributions prove to be caused by soft (infrared) γ-radiation, $k \longrightarrow 0$, whereas the influence of emitting the aforesaid "high energy" photons appears to be too small.

The contribution to the decay probability caused by (24) can be set as:

$$d\mathbf{W}_{2\gamma}^B(\varepsilon, \mathbf{p}; \lambda, \Lambda) = d\mathbf{w}W_{2\gamma}^B(\varepsilon, \mathbf{p}; \lambda, \Lambda) = d\mathbf{W}^{B0}B_{2\gamma}^B(\varepsilon, \mathbf{p}; \lambda) + d\mathbf{w}(C_{02\gamma}^B(\varepsilon, \mathbf{p}; \Lambda) + C_{\xi 2\gamma}^B(\varepsilon, \mathbf{p}; \Lambda)), \tag{35}$$

with $d\mathbf{w}$, $d\mathbf{W}^{B0}$ from (27), the quantities B, C being expressed through integrals of the type

$$\int d^4k F_B(k)k_\alpha^n k_\beta^m, \quad (n, m = 0, 1), \tag{36}$$

where the function F_B is defined in (9), (10). In the course of treating these integrals, we utilize the validity of the relations $\Delta/M_B \longrightarrow 0$, $(\Delta/M_B)\ln(\Delta/M_B) \longrightarrow 0$ which simplifies the calculations, as all of the integrals (36), but those set out below, vanish thereby. Subsequently,

$$I^B = 2M_B\int d^4k F_B(k) \approx i\pi^2\frac{1}{v\varepsilon}\left[\ln(x)\ln\left(\frac{\lambda}{m}\right) - \mathcal{J}_B\right],$$

$$\mathcal{J}_B \approx \frac{1}{4}(\ln(x))^2 - F(x-1) + \pi^2\left(\frac{v}{\tilde{v}}\right)\delta_{Bn}, \quad x = \frac{1-v}{1+v},$$

$$\tilde{v} = \sqrt{v^2 + [(\Delta - \varepsilon - k)^2 + k^2]/M_B^2},$$

$$2M_B\int d^4k k_\alpha F_B(k) = p_\alpha I_1 + \delta_{\alpha 0} I_{10}^B,$$

$$I_1 \approx -i\pi^2\frac{1}{v\varepsilon}\ln(x),$$

$$I_{10}^B = i\pi^2\left(-2\ln(m/M_B) + \frac{1}{v}\ln(x)\right),$$

$$2M_B\int d^4k F_B k_\alpha k_\beta = -g^{\alpha\beta}(I_2^B - \delta_{0\alpha} I_{20}),$$

$$I_2^B = -\frac{i\pi^2}{4}(3/2 + 2\ln(\Lambda/M_B)),$$

$$I_{20} = -\frac{i\pi^2}{2}, \qquad (37)$$

$$B_{2\gamma}^B(\varepsilon, \mathbf{p}; \lambda) = \frac{i\alpha}{2\pi^3}[\varepsilon(2I^B - I_1) - I_{10}^B],$$

$$C_{02\gamma}^B(\varepsilon, \mathbf{p}; \Lambda) = \frac{i\alpha}{2\pi^3}\{-I_1\varepsilon v^2[(g_V^B)^2 + 3(g_A^B)^2]$$

$$+ 2I_2[5(g_V^B)^2 + 12g_V^B g_A^B + 15(g_A^B)^2]$$

$$- 2I_{20}[2(g_V^B)^2 + 3g_V^B g_A^B + 3(g_V^B)^2]\},$$

$$C_{\xi 2\gamma}^n(\varepsilon, \mathbf{p}; \Lambda) = \frac{i\alpha}{2\pi^3}\{-I_1\varepsilon 2g_A^n(g_V^n - g_A^n)$$

$$+ 2I_2[3(g_V^n)^2 + 4g_V^n g_A^n - 7(g_A^n)^2]$$

$$- 2I_{20}[(g_V^n)^2 + g_V^n g_A^n - 2(g_A^n)^2]\},$$

$$C_{\xi 2\gamma}^\Sigma(\varepsilon, \mathbf{p}; \Lambda) = \frac{i\alpha}{2\pi^3}(g_A^\Sigma)^2\{2I_1\varepsilon + 4I_{20} - 26I_2\}.$$

Here, the Spens-function [43] is

$$F(z) = \int_0^z \frac{dt}{t}\ln(1+t).$$

The cut-off parameter Λ emerging in equations (35) via the integral I_2^B from (37) prevents the ultraviolet divergence in much the same way as above in (8).

The contributions from the first three terms in (20), if combined, result in

$$d\mathbf{W}_R^B(\varepsilon, \mathbf{p}; \lambda, \Lambda) = d\mathbf{W}_0 W_R^B(\varepsilon, \mathbf{p}; \lambda, \Lambda),$$

$$W_R^B = 1 - \frac{\alpha}{2\pi}[2\ln(\Lambda/M_B) \qquad (38)$$

$$+ 4\ln(\lambda/m) + 9/2 - \ln(M_B/m)].$$

The sum of (24) and (38),

$$d\mathbf{W}^B(\varepsilon, \mathbf{p}; \lambda, \Lambda)$$
$$= d\mathbf{W}_{2\gamma}^B(\varepsilon, \mathbf{p}; \lambda, \Lambda) + d\mathbf{W}_R^B(\varepsilon, \mathbf{p}; \lambda, \Lambda), \qquad (39)$$

gives the β-decay probability with the $e^\pm$ energy-momentum $(\varepsilon, \mathbf{p})$, accounting for the electromagnetic corrections to the α-order due to the virtual photons. It is pertinent to rewrite the sum (39) as follows:

$$d\mathbf{W}^B(\varepsilon, \mathbf{p}; \lambda, \Lambda) = d\mathbf{W}^{B0}(\varepsilon, \mathbf{p})[1 + B^B(\varepsilon, \mathbf{p}; \lambda)]$$
$$+ d\mathbf{w}[C_0^B(\varepsilon, \mathbf{p}; \Lambda, g_V^B, g_A^B) + \boldsymbol{\xi}\mathbf{v}C_\xi^B(\varepsilon, \mathbf{p}; \Lambda, g_V^B, g_A^B)], \qquad (40)$$

where

$$B^B = \frac{2\alpha}{\pi}\left[\mathcal{L}\ln\left(\frac{\lambda}{m}\right) + \frac{\mathcal{J}_B(\varepsilon)}{2v} + \frac{1}{4}\left(3\ln\left(\frac{M_B}{m}\right) - \frac{9}{2}\right)\right],$$

$$C_0^B = \frac{\alpha}{2\pi}\left[2\ln\left(\frac{\varepsilon + p}{m}\right)v((g_V^B)^2 + 3(g_A^B)^2)\right.$$

$$+ \frac{33(g_A^B)^2}{4} + 6g_A^B g_V^B + \frac{7(g_V^B)^2}{4}$$

$$\left. + \ln\left(\frac{\Lambda}{M_B}\right)(3(g_V^B)^2 + 12g_V^B g_A^B + 9(g_A^B)^2)\right], \qquad (41)$$

$$C_\xi^n = \frac{\alpha}{2\pi}\left[\frac{4g_A^n(g_V^n - g_A^n)}{v}\ln\left(\frac{\varepsilon + p}{m}\right) + \frac{5}{4}g_V^{n2} + 2g_V^n g_A^n\right.$$

$$\left. - \frac{13}{4}g_A^{n2} + \ln\left(\frac{\Lambda}{M_B}\right)3(g_V^{n2} - g_A^{n2})\right],$$

$$C_\xi^\Sigma = -\frac{\alpha}{2\pi}(g_A^\Sigma)^2\left[\frac{4}{v}\ln\left(\frac{\varepsilon + p}{m}\right) - \frac{31}{4} - 9\ln\left(\frac{\Lambda}{M_\Sigma}\right)\right].$$

The quantity B^B in (40), (41) apparently does depend on the artificially introduced "photon mass" λ to prevent the infrared divergence of equation (39). To eliminate this dependence, the probability of γ-radiation (29) of momenta k less than some given value k_m, $k \le k_m \le \Delta^B - \varepsilon$,

$$\int_0^{k_m} d\mathbf{W}_\gamma^B = d\mathbf{w}\int_0^{k_m} dk W_\gamma^B(\varepsilon, \mathbf{p}, k; \lambda), \qquad (42)$$

is known to be added to (39), and, after all, we treat, in

α-order, the radiative decay probability

$$d\mathbf{W}^B(\varepsilon, \mathbf{p}; \Lambda) = d\mathbf{W}^B(\varepsilon, \mathbf{p}; \lambda, \Lambda) + \int_0^{k_m} d\mathbf{W}^B_\gamma(\varepsilon, \mathbf{p}, k; \lambda). \quad (43)$$

It is expedient to present equation (42) in the following form:

$$d\mathbf{w}\left[\int_0^{k_m} dk W^B_{0\gamma}(\varepsilon, \mathbf{p}, k; \lambda) + \int_0^{k_m} dk W^B_{\xi\gamma}(\varepsilon, \mathbf{p}, k; \lambda)\right] = d\mathbf{W}^{B0}\tilde{B}(\varepsilon, \mathbf{p}, k_m; \lambda) \quad (44)$$

$$+ d\mathbf{w}\left[w_0^{B0}\tilde{C}'_0(\varepsilon, \mathbf{p}, k_m) + w_\xi^{B0}\tilde{C}'_\xi(\varepsilon, \mathbf{p}, k_m)\right],$$

where

$$\tilde{B} = \frac{2\alpha}{\pi}\left(\mathcal{L}\ln\left(\frac{2k_m}{\lambda}\right) - \frac{\mathcal{H}(\varepsilon)}{2v}\right),$$

$$\tilde{C}'_0 = \frac{2\alpha}{\pi\omega_{v0}^2}\left[\frac{\mathcal{L}}{\varepsilon}T_1(k_m, \varepsilon) + \frac{1}{2v\varepsilon^2}\ln\left(\frac{p+\varepsilon}{m}\right)T_2(k_m, \varepsilon) + \mathcal{L}\left(\frac{k_m^2}{2} - 2k_m\omega_{v0}\right)\right],$$

$$\tilde{C}'_\xi = \frac{2\alpha}{\pi\omega_{v0}^2}\mathcal{L}\left[\frac{1}{\varepsilon v^2}\left(T_1 + \frac{T_2}{2\varepsilon}\right) + \frac{k_m^2}{2} - 2k_m\omega_{v0}\right], \quad (45)$$

$$\mathcal{H} = \frac{1}{2}\left(F(x) - F(1/x) - \ln(1/x)\ln\left(\frac{1-v^2}{4}\right)\right) - v + \frac{1}{2}\ln(x) + F(v) - F(-v),$$

$$T_1 = [(\Delta-\varepsilon)^3 - (\Delta-\varepsilon-k_m)^3]/3,$$

$$T_2 = k_m^2[(\Delta-\varepsilon)^2/2 + k_m^2/4 - 2k_m(\Delta-\varepsilon)/3].$$

The expressions (29)–(31), (35), (37)–(41), (44), and (45) having been substituted into (43), the probability of the β-decay with the $e^\pm$ energy-momentum (ε, **p**), accompanied by the γ-radiation of energies k less than some given value k_m, $k \le k_m \le \Delta^B - \varepsilon$, takes the form

$$d\mathbf{W}^B(\varepsilon, \mathbf{p}; \Lambda) = d\mathbf{W}^{B0}(\varepsilon, \mathbf{p})[1 + \mathcal{B}(\varepsilon, \mathbf{p}, k_m)] + d\mathbf{w}[w_0^{B0}\tilde{C}_0(\varepsilon, \mathbf{p}, k_m) + \mathbf{v}\cdot\boldsymbol{\xi}w_\xi^{B0}\tilde{C}_\xi(\varepsilon, \mathbf{p}, k_m) + C_0(\varepsilon, \mathbf{p}; \Lambda, g_V^B, g_A^B) + \mathbf{v}\cdot\boldsymbol{\xi}C_\xi(\varepsilon, \mathbf{p}; \Lambda, g_V^B, g_A^B)], \quad (46)$$

where

$$\mathcal{B} = \frac{2\alpha}{\pi}\mathcal{L}\ln\left(\frac{2k_m}{m}\right), \quad \tilde{C}_0 = \tilde{C}'_0 + \tilde{C}_1^B, \quad \tilde{C}_\xi = \tilde{C}'_\xi + \tilde{C}_1^B,$$
$$\tilde{C}_1^B = \frac{2\alpha}{\pi}\left[\frac{\mathcal{J}_B}{2v} - \frac{\mathcal{H}}{2v} + \frac{1}{4}(3\ln(M_B/m) - 9/2)\right], \quad (47)$$

all the other quantities herein having been specified above.

The cut-off parameter Λ emerges in these expressions to formally preclude the divergences occurring in various integration over the virtual photon four-momentum d^4k.

In the early works [9, 27], the cut-off mass Λ was adapted to be of the nucleon mass order, $\Lambda \approx M_N$. Under the assumption that weak interactions are mediated by heavy vector bosons [44], the mass of these mesons provided the effective cut-off $\Lambda = M_V \gg M_N$.

Here, it is instructive to take cognizance of the fact that if the relation $g_V^n = -g_A^n$ had been valid, the parameter Λ would have disappeared from the eventual result (46), likewise in the case of μ-meson decay [45], in perfect agreement with the general assertion of [46].

Nowadays, after advent of the profound Sirlin's works [7], carried out in the framework of the $SU(2)_L \times U(1)$ gauge model [8], we get two rather different recipes for treating the ultraviolet divergence in the course of calculating the radiative corrections. Working in the framework of the effective lagrangian (2), we are not on the point to discuss obtaining the results of [7]. We just take for granted these results and only recall that, first (according to [7]), if the simplest model of $SU(2)_L \times U(1)$ symmetry breaking via the single Higgs isospinor is used, the mass $M_Z \approx 91$ GeV will be substituted for the cut-off Λ, and, secondly, in the case of arbitrary symmetry breaking (via, for example, several Higgs multiplets) the mass $M_W \approx 80$ GeV is substituted for Λ. In addition, the weak coupling constant G would be replaced by the corrected one,

$$G_{\mathrm{cor}} \approx G\left[1 - \frac{\alpha}{\pi}\ln(\cos\theta_w)\right], \quad (48)$$

but the correction to G amounts to no more than a few hundredths of a percent (~0.01%). Our numerical calculations in Section 5 show the dependence of the total radiative corrections on the Λ-value to be not negligible.

The radiative β-decay probability presented by (43), (46) as the sum of the β-decay probability (39) including virtual photons only, but no real γ-radiation, and the probability of one photon emission (42), turns out to be divergent logarithmically when the boundary photon energy k_m in equations (46), (47) tends to zero, $k_m \longrightarrow 0$, or(and) when the emitted electron energy ε increases infinitely, $\varepsilon \longrightarrow \infty$, $v \longrightarrow 1$. This manifests the well-known fact that the familiar perturbation theory in α is

not applicable to treat the infrared (soft) bremsstrahlung, and the bremsstrahlung of an ultra-relativistic electron (double-logarithmic asymptomatic) (see [5, 6, 36, 47]). To comprehend the β-decay consistently accounting for electromagnetic interactions, we are drawn into considering the processes to arbitrary high order in α, with infinite numbers of both real and virtual photons which are displayed by the diagrams with infinite numbers of internal and external photon lines in addition to those given in Figs. 1, 2, the final state being specified by fixing the summary total γ-radiation energy as less than the given value k_m. Thoroughly pursuing the general treatment of the infrared divergence phenomena step by step, as perfectly worked out in [39], we express the arbitrarily high α-order infrared contributions to the transition amplitudes and, consequently, to the decay probability through the first order in α quantities B, $\tilde{B}$, $\mathcal{B}$, C_0, C_ξ, $\tilde{C}_0$, $\tilde{C}_\xi$ (39)–(47). All of the contributions having been summarized, we arrive, instead of equation (46), at the eventual complete result

$$d\mathbf{W}^B(\varepsilon, \mathbf{p}, k_m; \Lambda) = d\mathbf{w} W_0^B(\varepsilon, k_m; \Lambda) + (\mathbf{v}\cdot\boldsymbol{\xi}) d\mathbf{w} W_\xi^B(\varepsilon, k_m; \Lambda),$$

$$W_0^B = e^{\mathcal{B}(\varepsilon, k_m)}[((g_V^B)^2 + 3(g_A^B)^2) \times (1 + \tilde{C}_0(\varepsilon, \mathbf{p}, k_m)) + C_0(\Lambda, g_V^B, g_A^B; \varepsilon, \mathbf{p})], \quad (49)$$

$$W_\xi^B = e^{\mathcal{B}(\varepsilon, k_m)}[2g_A^B(g_V^B - g_A^B) \times (1 + \tilde{C}_\xi(\varepsilon, \mathbf{p}, k_m)) + C_\xi(\Lambda, g_V^B, g_A^B; \varepsilon, \mathbf{p})],$$

$$d\mathbf{w} = \frac{G^2}{2\pi^3}\varepsilon p(\Delta^B - \varepsilon)^2 d\varepsilon \frac{d\mathbf{n}}{4\pi}, \quad \mathbf{n} = \frac{\mathbf{p}}{p}, \quad \mathbf{v} = \frac{\mathbf{p}}{\varepsilon},$$

where the infrared contributions arising from both real and virtual photons are explicitly factored out in exponential form. The exponent, emerging in (49) with the quantity $\mathcal{B}$ from equation (47), governs the true infrared behavior of equation (49): $W_{0,\xi}^B \longrightarrow 0$, when the boundary γ-radiation energy $k_m \longrightarrow 0$. This means, in accordance with the general theory [6, 36, 47], that there is no β-decay without the infrared γ-radiation. For now, we can deal with β-decay accompanied by γ-radiation of arbitrary small energy.

Thus, we have acquired the baryon β-decay probability (49) with the $e^\pm$ energy-momentum (ε, **p**) accompanied by γ-radiation of the summary total energy k less than some given value k_m, $k \le k_m$, the number of photons and the directions of their emissions being not fixed. Certainly, the k_m value cannot exceed $\Delta^B - \varepsilon$. Having obtained the general result (49), we are able to calculate the total β-decay probability, the electron energy and angular distributions, and the γ-radiation spectrum and yield, which is what we turn to now.

5. THE TOTAL β-DECAY PROBABILITY AND ELECTRON ENERGY-MOMENTUM DISTRIBUTION

Before to discuss the numerical results obtained according to equation (49), we are to visualize some features of this. Let us note that the functions (40), (41), $C_0(\Lambda, g_V^B, g_A^B; \varepsilon, \mathbf{p})$, $C_\xi(\Lambda, g_V^B, g_A^B; \varepsilon, \mathbf{p})$ do incorporate the cut-off Λ and quantities g_V^B, g_A^B, whereas $\tilde{C}_0(\varepsilon, \mathbf{p}, k_m)$, $\tilde{C}_\xi(\varepsilon, \mathbf{p}, k_m)$, $\mathcal{B}(\varepsilon, k_m)$ do not. Thus, our final expression (49) is seen to involve, firstly, the part which shows the same familiar dependence on g_V^B, g_A^B as the uncorrected bulk β-decay probability (27) does, and, secondly, the part which appears to depend on g_V^B, g_A^B via the functions $C_0(\Lambda, g_V^B, g_A^B; \varepsilon, \mathbf{p})$, $C_\xi(\Lambda, g_V^B, g_A^B; \varepsilon, \mathbf{p})$, (40), (11) in much more complicated way, as compared to equation (27). This result appears immediately from the straightforward calculations of (37), (36), (24) and (8), (7), (38) which, in turn, are due to the diagrams *d*, *e*, *f* in Figs. 1, 2 with internal photon lines. If the quantities $C_0(\Lambda, g_V^B, g_A^B; \varepsilon, \mathbf{p})$, $C_\xi(\Lambda, g_V^B, g_A^B; \varepsilon, \mathbf{p})$ in (49) had been omitted and the exponent replaced by $\exp(\mathcal{B}) \approx 1 + \mathcal{B}$, our result (49) would have been reduced to one, corresponding at $k_m = \Delta^B - \varepsilon$, to all intents and purposes, to the so-called MI part of the radiative corrections invented in [26] and applied to calculate the modifications of the electron spectrum and total decay probability [26, 31], and then to the electron angular distribution modification as well [28–39, 32]. According to the key assertion of this approach, the remainder of the radiative corrections after the MI part is removed, the MD part, might affect, at most, the magnitudes of g_V^B, g_A^B only, these quantities being replaced by primed ones, $g_V^B, g_A^B \longrightarrow g_V'^B, g_A'^B$.

Some improvements of the original method of [26] seem to be managed in [33, 34], where the well-known renormalizations (8) and, consequently, the contribution of the (38) in decay probability were accounted for, but the contributions to $C_0(\Lambda, g_V^B, g_A^B; \varepsilon, \mathbf{p})$, $C_\xi(\Lambda, g_V^B, g_A^B; \varepsilon, \mathbf{p})$ in equation (49) originating from equations (24), (35), (37) were still neglected. The main general feature of this approach [26–35] as a whole is that the corrected transition amplitude (9) $M_{2\gamma}^B$ is thought to be a multiple of uncorrected one M_0^B (6), and, consequently, the quantities W_0^B, W_ξ^B (49) are multiples of w_0^{B0}, w_ξ^{B0} (27), which is obviously not our case. Handy as this very treatment is, we decided to refrain from it and pursue calculating set forth along the work presented, according to our lights. If anything, it is pertinent to recall that the authors of [30, 33, 34] themselves were in-

clined to regard the separation of the MD and MI parts and practically handling the MI parts only as being rather untenable, and so do we.

We would like to mention that, unlike what was adapted in some papers [26, 35, 41] until a little while ago, our calculations lump together all of the radiative corrections, without dividing them into the "Coulomb," "inner," "outer." Let us also note the $|\mathcal{B}|$ value enhancement and, consequently, the increase of the deviation of $\exp(\mathcal{B})$ from $(1 + \mathcal{B})$, as being due to both tiny small $k_m \longrightarrow 0$ and (or) sufficiently large electron energy $\varepsilon \gg m$, which may be case in hyperons decay, where $\varepsilon \sim 100$ MeV $\gg m$ at the end point of electron spectrum.

Substituting the maximum k_m value at the given electron energy ε, $k_{m(\max)} = \Delta^B - \varepsilon$, in the equation (49), we arrive at the β-decay probability with the electron energy-momentum $(\varepsilon, \mathbf{p})$, including the γ-radiation of all energies compatible to the given ε value. The deviations of the functions, $W_0^B(\varepsilon, \mathbf{p})$, $W_\xi^B(\varepsilon, \mathbf{p})$ in (49) from the $w_0^{B0}(\varepsilon, \mathbf{p})$, $w_\xi^{B0}(\varepsilon, \mathbf{p})$ in (27) render the distinction between the corrected electron energy-momentum distribution accounting for electromagnetic interactions and the uncorrected one. The modification of the electron spectrum integrated over the electron emission directions $d\mathbf{n}$ is naturally reflected by the quantity

$$\frac{W_0^B(\varepsilon, k_m = \Delta^B - \varepsilon)}{(g_V^B)^2 + 3(g_A^B)^2} - 1 = S_0^B(\varepsilon), \qquad (50)$$

whereas the quantity

$$\frac{W_\xi^B(\varepsilon, k_m = \Delta^B - \varepsilon)}{2g_A^B(g_V^B - g_A^B)} - 1 = S_\xi^B(\varepsilon) \qquad (51)$$

is pertinent to characterize the modification of the energy dependence of the electron angular distribution. These S_0^B, S_ξ^B are presented in Fig. 4 by solid and short-dashed lines, respectively, as functions of the electron kinetic energy $E = \varepsilon - m$ for neutron decay, the upper picture, and Σ^--decay, the lower one. Both functions S_0^B, S_ξ^B culminate at the beginning and the end of the electron spectrum, that is, at $E = 0$ and $E = \Delta^B - m$, their mean values being $\bar{S}_0^n \approx 0.08$, $\bar{S}_\xi^n \approx 0.06$ for neutron decay and $\bar{S}_0^\Sigma \approx \bar{S}_\xi^\Sigma \approx 0.007$ for Σ^- decay. The numerical results in the Figs. 4–6 are obtained for $\Lambda = M_W$. The S_0^B, S_ξ^B enhancement at $\varepsilon \longrightarrow m$, $k_m \longrightarrow \Delta^B - m$ is as a matter of course, due to the increasing quota of the γ-radiation energy in the total energy release Δ^B. As seen, the corrected decay probability exceeds the uncorrected one along all the electron energies E, except for limiting case $E \longrightarrow \Delta^B - m$, $\varepsilon \longrightarrow \Delta^B$, $k_m \longrightarrow 0$, where $W_0^B \longrightarrow 0$, $W_\xi^B \longrightarrow 0$, due to $\exp(\mathcal{B}) \longrightarrow 0$,

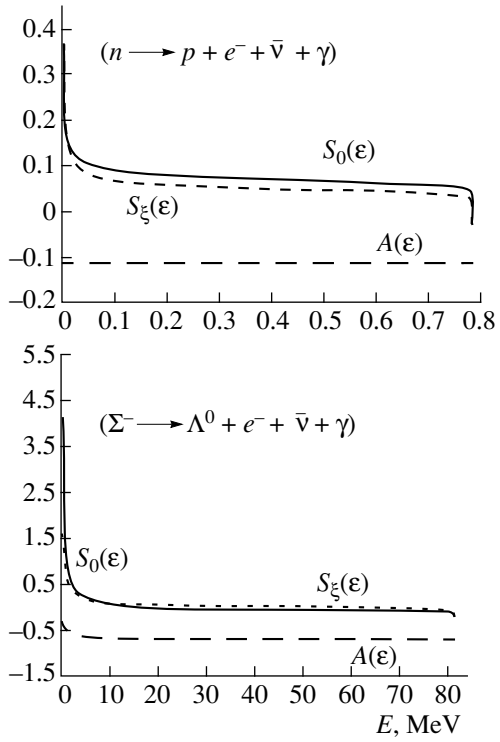

Fig. 4. Quantities S_0^B, S_ξ^B, A^B (see text), for neutron and Σ^--hyperon decays as functions of electron kinetic energy $E = \varepsilon - m$. For the sake of simplicity, we have dropped the superscripts "B" from the quantities in the pictures.

and we arrive at S_0, $S_\xi \longrightarrow -1$. This behavior may be substantial in treating the phenomena, where just such a limiting electron energy turns out to be of crucial importance.

The uncorrected asymmetry factor of the electron angular distribution A_0^B is replaced by corrected one $A^B(\varepsilon, k_m = \Delta^B - \varepsilon)$ accounting for the radiative corrections,

$$A_0^B = \frac{2g_A^B(g_V^B - g_A^B)}{(g_V^B)^2 + 3(g_A^B)^2} \longrightarrow \frac{W_\xi^B(\varepsilon, k_m = \Delta^B - \varepsilon)}{W_0^B(\varepsilon, k_m = \Delta^B - \varepsilon)} = A^B(\varepsilon, k_m = \Delta^B - \varepsilon), \qquad (52)$$

which is presented in Fig. 4 by long-dashed lines for the neutron and Σ^- decays. The differences $\delta A^B = A^B(\varepsilon) - A_0^B$ amount to $\delta A^{(n)} \approx -1.9\%$ for the neutron and $\delta A^{(\Sigma)} \approx 1.8\%$ for the Σ decay. It is to score under the disparate dependencies of A_0^B and $A^B(\varepsilon)$ on the quantities g_V^B, g_A^B, as being due to the functions $C_0(\Lambda, g_V^B, g_A^B; \varepsilon, \mathbf{p})$, $C_\xi(\Lambda, g_V^B, g_A^B; \varepsilon, \mathbf{p})$, (40), (41) in equation (49). Cer-

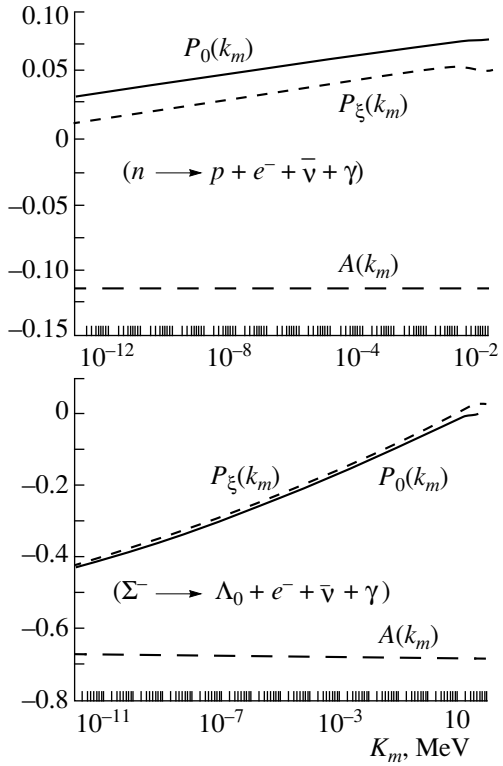

Fig. 5. Quantities $P_0^B(k_m)$, $P_\xi^B(k_m)$, $A^B(k_m)$ (see text), for neutron and Σ^--hyperon decays as functions of k_m, the boundary γ-radiation energy (see text). For the sake of simplicity, we have dropped the superscripts "B" from the quantities in the pictures.

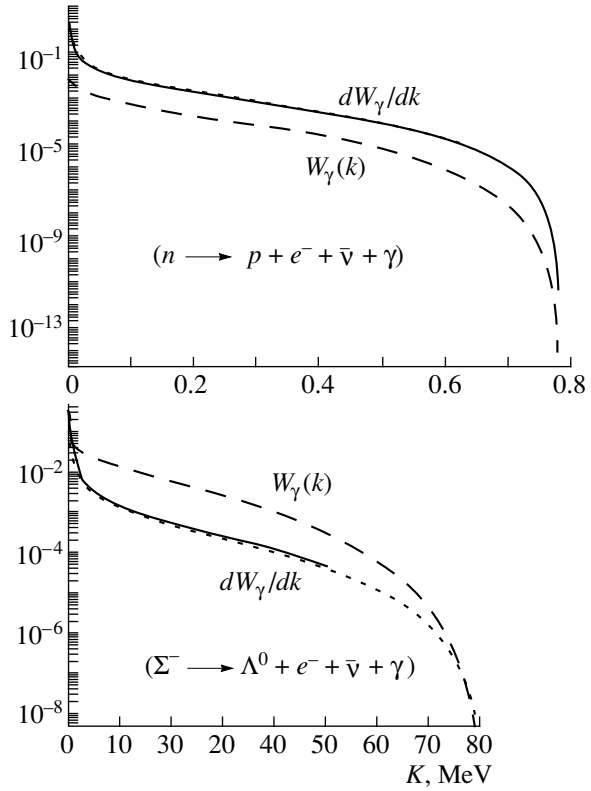

Fig. 6. Differential relative spectra $dW_\gamma^B(k)/dk$ and yields $W_\gamma^B(k)$ of electron bremsstrahlung for neutron and Σ^--hyperon decays as functions of γ-radiation energy k. For the sake of simplicity, we have dropped the superscripts "B" from the quantities in the pictures.

tainly, this fact is of the great importance for acquiring g_V^B, g_A^B from experimental data (see [14, 16, 22]).

Next, we inquire into the β-decay probability integrated over the electron energy-momentum. Having at our disposal equation (49), we treat the quantity

$$\frac{\left(\int\limits_m^{\Delta^B - k_m} d\mathbf{w} W_0^B(\varepsilon, k_m) + \int\limits_{\Delta^B - k_m}^{\Delta^B} d\mathbf{w} W_0^B(\varepsilon, \Delta^B - \varepsilon)\right)}{w_0^{B0} \int\limits_m^{\Delta^B} d\mathbf{w}} - 1 = P_0^B(k_m), \tag{53}$$

which determines the relative probability of the γ-radiation of the energies $|\mathbf{k}|$ less than the given k_m value, $|\mathbf{k}| \le k_m$, $(0 \le k_m \le \Delta^B - m)$. The function $P_0^B(k_m)$ is plotted in Fig. 5 by solid lines for neutron and Σ^- decay in the upper and lower parts of the figure, respectively. For the γ-radiation of the energies $k \le k_m$, we also displayed in Fig. 5 (short-dashed lines) the relative probability of the electron emission under the angle θ ($\cos\theta = \boldsymbol{\xi}\mathbf{v}/v|\boldsymbol{\xi}|$) to the polarization vector $\boldsymbol{\xi}$ of the initial baryon,

$$\frac{\left(\int\limits_m^{\Delta^B - k_m} d\mathbf{w} v W_\xi^B(\varepsilon, k_m) + \int\limits_{\Delta^B - k_m}^{\Delta^B} d\mathbf{w} v W_\xi^B(\varepsilon, \Delta^B - \varepsilon)\right)}{w_\xi^{B0} \int\limits_m^{\Delta^B} d\mathbf{w} v} - 1 = P_\xi^B(k_m). \tag{54}$$

As one can see, both functions (53), (54) show the very steep growth with k_m at the extremely small k_m, within the infrared domain, being varied rather negligibly beyond that: for instance, in the neutron decay case $P_0^n(k_m = 0) = 0$, whereas $P_0^n(k_m \approx 10^{-2}\ \text{MeV}) \approx P_0^n(k_m = \Delta^n - m)$. Thus, the radiative corrections to the β-decay prove to reach saturation at $k_m \ll \Delta^B - m$, or, approximately, in the infrared domain. So, we infer from this Fig. 5, as well as from the previous one, that, in actual

The modifications of the total β-decay probability δW and asymmetry factor of the $e^{\pm}$ angular distribution δA for neutron (n) and Σ^--hyperon at various values of the ultraviolet cut-off Λ, M_W, M_Z, M_N denoting W-, Z-bosons and nucleon masses, respectively

Λ	n			Σ^-		
	M_W	M_Z	M_N	M_W	M_Z	M_N
δW, %	7.94	8.05	5.04	0.50	0.55	−1.70
δA, %	−1.86	−1.91	−0.47	1.74	1.77	0.70

fact, the crucial effect on the β-decay is just due to the infrared γ-radiation.

In Fig. 5, we also offer the asymmetry factor of the electron angular distribution, averaged over the electron energy,

$$\left(\int\limits_{m}^{\Delta^B - k_m} \frac{W_\xi^B(\varepsilon, k_m)}{W_0^B(\varepsilon, k_m)} d\varepsilon + \int\limits_{\Delta^B - k_m}^{\Delta^B} \frac{W_\xi^B(\varepsilon, \Delta^B - \varepsilon)}{W_0^B(\varepsilon, \Delta^B - \varepsilon)} d\varepsilon \right) \Big/ (\Delta^B - m) = A^B(k_m), \tag{55}$$

which is the contribution to the asymmetry of the electron angular distribution associated with the γ-radiation of the energies less than the given k_m. This quantity appears to be, as a matter of fact, independent of k_m, likewise (52) is of ε, and, consequently, the modifications δA^B are as good as constant. Obviously, the relative modification of the total decay probability δW^B is given simply by equation (53) at $k_m = \Delta^B - m$: $\delta W^B = P_0^B(\Delta^B - m)$.

After all, the results summarized in Table emerge from the calculations we have carried out.

In Table, we present the modifications of the total decay probability δW and asymmetry factor δA (in percents) for the neutron and Σ^--hyperon cases calculated at the various cut-off Λ values, M_W, M_Z, M_N, which stand for W-, Z-bosons, and nucleon masses, respectively. The results for Σ^+ coincide with those for Σ^-, for all intents and purposes; for example, instead of the data in Table, we have at $\Lambda = M_W$ the magnitudes $\delta W = 0.56\%$, $\delta A = 1.70\%$ for Σ^+ case.

Let us expose the dependence of the results on the ultraviolet cut-off parameter Λ. Certainly, the value $\Lambda = M_N$ is understood nowadays as being not eligible. Yet the relatively small differences between the results for $\Lambda = M_W$ and $\Lambda = M_Z$ prove to be very significant reflecting the uncertainties of principle occurring in the present-day general approaches to treating the ultraviolet divergence [7] (recall the discussion above equation (48)).

Our results for δW^B, δA^B differ appreciably from ones presented in [26, 28–35, 41]. In particular, for the neutron case, our values $\delta W^n \approx 8\%$, $\delta A^n \approx 1.9\%$ (see Table) do not coincide apparently with the values $\delta W^n \approx 5\%$, $\delta A^n \approx 0\%$ asserted in those papers. This fact is thought to be substantial in the course of processing the up-to-date experimental data on the neutron lifetime (see [14–20]), and electron angular distribution (see [14, 17–22]). Keeping in mind the arguments set forth in the discussion at the beginning of this Section, we realize the origin of these noticeable distinctions. So, we are not taken aback by this mismatch. If anything, it is instructive to note that our values δW^B, δA^B would have come much closer to those of [28–35], if the cut-off Λ had been equal to the nucleon mass M_N. It is not surprising because the substantial pieces of the very functions $C_0(\Lambda, g_V^B, g_A^B; \varepsilon, \mathbf{p})$, $C_\xi(\Lambda, g_V^B, g_A^B; \varepsilon, \mathbf{p})$, (40), (41), depending on Λ via $\ln(\Lambda/M_B)$, vanish at $\Lambda = M_N$ for neutron case and become very small (negative) for Σ. Also for that matter, if we had omitted the term $\pi^2(v/\tilde{v})$ in the functions $\tilde{C}_0(\varepsilon, \mathbf{p}, k_m)$, $\tilde{C}_\xi(\varepsilon, \mathbf{p}, k_m)$, (37), (46), (47), in the neutron case, the value δW^n would have been reduced to ≈4.6% instead of ≈8% in Table. The difference amounting to ≈3.5% might be, properly speaking, conceived as the "Coulomb correction", which would be in accordance with the assertions of some previous papers [26, 29–35, 41].

The feasible consequence of our results for acquiring the G, g_V, g_A values from processing the up-to-date experimental data are discussed in Section 7. Now let us proceed to the inquiry for the spectrum and yield of the γ-radiation accompanying β-decay.

6. THE γ-RADIATION SPECTRUM AND YIELD

The relative differential probability of γ-radiation is obtained simply by differentiating the aforesaid function $P_0^B(k)$ (53) with respect to its argument k

$$\frac{dP_0^B(k)}{dk} = \frac{1}{\int\limits_m^{\Delta^B} d\mathbf{w} W_0^B(\varepsilon, \mathbf{p}, k = \Delta^B - \varepsilon)} \times \int\limits_m^{\Delta^B - k} d\mathbf{w} \frac{dW_0^B(\varepsilon, \mathbf{p}, k)}{dk} \equiv \frac{dW_\gamma^B(k)}{dk}. \tag{56}$$

This quantity is presented in Fig. 6 by solid lines, the domain of the extremely small k values, $k \longrightarrow 0$, set out thoroughly in Fig. 5, escaping our attention here in Fig. 6. The short-dashed lines render the calculation of the same quantity, but merely in the framework of the familiar perturbation theory in α [1–4, 42], that is ac-

cording equation (33):

$$\frac{dW_\gamma^{B0}(k)}{dk} = \frac{1}{w_0^{B0}\int\limits_m^{\Delta^B} d\mathbf{w}} \int\limits_m^{\Delta^B - k} d\mathbf{w} W_{0\gamma}^{'B}(\varepsilon, \mathbf{p}, k) \qquad (57)$$

descending from equations (49), (53), (56) when $\mathcal{B} \ll 1$, $\exp(\mathcal{B}) \longrightarrow (1 + \mathcal{B})$. In Fig. 6, beyond infrared asymptotic onset, the distinction between the solid and short-dashed curves is virtually invisible for the neutron decay, whereas the difference between these curves, though being very small, is still observable in the Σ case. It is due to sufficiently large $\Delta^{(\Sigma)} \approx 82$ MeV $\gg m$ which entails $v \approx 1$ and $\mathcal{L} \approx 5$ (see (32)), in contrast to the neutron case, where $\mathcal{L} < 1$. Consequently, the $\mathcal{B}$ value for the Σ decay is appreciably greater than for the neutron decay, and, therefore, the replacement $\exp(\mathcal{B}) \longrightarrow (1 + \mathcal{B})$ is valid in the neutron case with much better accuracy than in the Σ case.

Though the functions (56) and (57) coincide, as a matter of fact, beyond the infrared domain, their infrared asymptotic behaviors prove to be significantly different:

$$\frac{dP_0^B(k)}{dk} \equiv \frac{dW_\gamma^B(k)}{dk} \asymp \frac{2\alpha}{\pi m} \int\limits_{\mathbf{m}}^{\Delta^B - k} d\mathbf{w} \mathcal{L} \left(\frac{m}{k}\right)^{(1-x)}, \qquad (58)$$

$$\frac{dW_\gamma^{B0}(k)}{dk} \asymp \frac{2\alpha}{\pi k} \int\limits_m^{\Delta^B - k} d\mathbf{w} \mathcal{L},$$
$$\mathcal{L} = \frac{\ln[(\varepsilon + p)/m]}{v} - 1, \quad x = \frac{2\alpha}{\pi}\mathcal{L}. \qquad (59)$$

Indeed, small as the positive quantity x is (even for the Σ decay $x \approx 0.02$), the behaviors of (58) and (59) differ crucially at small k. Though the both diverge at $k \longrightarrow 0$, the first one has the integratable singularity, whereas the second posses the singularity causing the logarithmic divergency by integrating over the γ-energy k.

The yield of γ-radiation can be estimated using the quantity

$$W_\gamma^B = \int\limits_k^{\Delta^B} (dW_\gamma^B/dk)dk \qquad (60)$$

drawn in the Fig. 6 by the long-dashed line and the quantity $P_0^B(k_m)$ (53) presented in Fig. 5. The quantity (60) renders the number of photons emitted in one β-decay event with the energies exceeding the given value k. For instance, one can infer from these figures that, in the neutron case, one photon with the energy $k \geq 0.1$ MeV is expected to be radiated along $\approx 10^3$ β-decay events, and one photon of the energy $k \geq 10^{-6}$ MeV (optical red photon energy) per ≈ 50 events. We can also expect in neutron decay case that the optical photons yield to be one optical photon per ≈ 200 events. In the Σ case, one can expect one photon with $k \geq 40$ MeV, to be emitted per $\approx 10^3$ events.

Now, we proceed to expounding the spectrum and yields of the γ-radiation from interior of a baryon which is brought into being by the baryon's pionic degrees of freedom, see Fig. 3, equations (13), (14), (15).

Though the ultraviolet divergence problem has been perfectly solved [7] without allowing for baryon's pionic degrees of freedom, without virtual pion cloud, these are known to be substantial to comprehend β-decay. The actual deviation g_A^n from g_V^n, the appearance of the amplitudes g_{IP}, g_{SM}, and the dependence of all the form-factors involved in the process on momentum transfer are thought to be due to the pion degrees of freedom. Certainly, these virtual pions give rise to the real γ-radiation in β-decaying as well, which we have been treating in this work. We are to inquire for the desirable γ-radiation spectrum, using the amplitudes (13)–(15). As before, we evaluate the β-decay probability, integrated over the final baryon and (anti)neutrino momenta as well as photon and electron emission directions, and summarized over the polarizations of all final particles, the equation (26) being put to use. In the course of calculating, the ratios

$$\frac{(m_{\pi^\pm} - m_{\pi 0})}{m_{\pi 0}}, \quad \frac{m_e}{m_{\pi 0}}, \quad \frac{\Delta^B}{M_B}, \quad \frac{|\mathbf{Q}|}{M_B}, \quad \frac{k}{M_B}$$

(see the definitions following (13)) occur which obviously are small. We simplify the calculations, retaining only the terms linear in these ratios. Also, we replace in equation (15) the quantity $|\mathbf{K}|^2$ by its value averaged over angles between $\mathbf{p}_e$, $\mathbf{p}_\nu$, $\mathbf{k}$, namely $|\mathbf{K}|^2 \longrightarrow |\hat{\mathbf{K}}|^2 = \omega_\nu^2 + \mathbf{p}_e^2 + \mathbf{k}^2$. After a good deal of tedious work, we are left with the electron and photon distributions accounting for the processes presented in Fig. 3 by diagrams *a* plus *b*,

$$W_\gamma^{B(ab)}(k, \varepsilon)d\varepsilon dk \approx \frac{\alpha p k \omega_\nu G^2}{\pi^{10} f_{BfBi\pi}^4 2^{18}}$$
$$\times 128\left[\frac{2}{3}(V_2 - V_1/3)^2\left(\omega_\nu\varepsilon(\omega_\nu^2 + \varepsilon^2 + m^2) + \frac{2}{3}\omega_\nu^2 p^2\right)\right.$$
$$+ \omega_\nu\varepsilon\left(U_2 - \frac{2}{3}(3U_1 + (\omega_\nu + \varepsilon - k)V_1)\right)^2 \qquad (61)$$
$$+ \frac{4}{3}(V_2 + V_1/3)\left(U_2 - \frac{2}{3}(3U_1 + (\omega_\nu + \varepsilon - k)V_1)\right)$$
$$\left.\times (p^2 + \varepsilon\omega_\nu)\omega_\nu\right]d\varepsilon dk,$$

and by diagrams *c* plus *d*,

$$W_\gamma^{B(cd)}(k,\varepsilon)d\varepsilon dk \approx \frac{\alpha G^2 u^2\left(\sqrt{|\hat{\mathbf{K}}|^2}\right)}{\pi^4(|\hat{\mathbf{K}}|^2 - m_\pi^2)^2} \times kp\varepsilon\omega_\nu^2(p^2 + \omega_\nu^2 + k^2)d\varepsilon dk, \quad (62)$$

where $\omega_\nu = \Delta^B - \varepsilon - k$ and

$$V_1 = \int_0^\infty dk k^6 u^2(k)\frac{y^2 + 4y\omega + 5\omega^2}{\omega^5(y+\omega)^4} \approx 1.96,$$

$$U_1 = \int_0^\infty dk k^6 u^2(k)\delta E(k)\frac{y^2 + 4y\omega + 5\omega^2}{\omega^5(y+\omega)^4} \approx 2.07\Delta^B,$$

$$V_2 = \int_0^\infty dk k^4 u^2(k)\frac{3\omega + y}{\omega^3(y+\omega)^3} \approx 1.7,$$

$$U_2 = \int_0^\infty dk k^4 u^2(k)\delta E(k)\frac{3\omega + y}{\omega^3(y+\omega)^3} \approx 1.83\Delta^B,$$

$$\omega = \sqrt{k^2 + m_{\pi 0}^2}, \quad y(k) = \sqrt{k^2 + M_B} - M_B,$$

$$\delta E(k) = \frac{\Delta^B M_f}{\sqrt{M_f^2 + k^2}}.$$

In Fig. 7, we present by solid lines the relative differential spectrum of the γ-radiation corresponding to (61) plus (62):

$$\frac{W_\gamma^{B\pi}(k)}{dk} = \frac{1}{\int_m^{\Delta^B} d\mathbf{w} W_0^B(\varepsilon, \mathbf{p}, k = \Delta^B - \varepsilon)} \times \int_m^{\Delta^B - k} d\varepsilon [W_\gamma^{B(ab)}(k,\varepsilon) + W_\gamma^{B(cd)}(k,\varepsilon)]. \quad (63)$$

The yield of the photons with energies exceeding the given value k;

$$W_\gamma^{B\pi}(k) = \int_m^{\Delta^B - k} dq \frac{W_\gamma^{B\pi}(q)}{dq}, \quad (64)$$

is depicted in Fig. 7 by the long-dashed lines. This γ-radiation apparently has no singularity at $k \longrightarrow 0$, and the γ-spectrum as a whole shows a quite different behavior with k increasing as compared with the one set out in Figs. 5, 6. In particular, the photons with the relatively large energies are presented here, in Fig. 7, with much more weight.

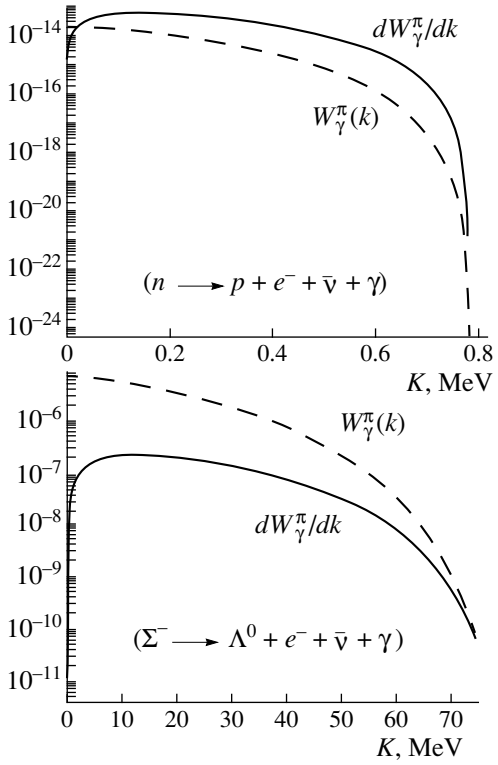

Fig. 7. Differential relative spectra $dW_\gamma^{B\pi}(k)/dk$ and yields $W_\gamma^{B\pi}(k)$ of virtual pion γ-radiation (see text) for neutron and Σ^--hyperon decays as functions of γ-radiation energy k. For the sake of simplicity, we have dropped the superscripts "B" by quantities in the pictures.

Though in the strangeness-conserving baryon β-decay considered here the quantities $d\,W_\gamma^{B\pi}(k)/dk$, $W_\gamma^{B\pi}(k)$ in Fig. 7 turn out to be small, rather negligible, as compared to those presented in Fig. 6, they are thought, nevertheless, to be of a great conceptual importance in their own right. Having become conscious of the strong dependence of these quantities on the energy Δ^B released in the β-decay, one may expect they will grow up substantially and become immediately observable in cases with greater Δ^B, for instance, in hyperon strangeness-nonconserving β-decay ($\Delta S \neq 0$), such as $\Sigma^+ \longrightarrow n + e^+ + \gamma + \nu$. We are on the point of studying in a subsequent work the γ-radiation of the virtual "pion cloud" in such decays, where it may be expected to become comparable to the electron bremsstrahlung.

Certainly, for now, allowing for this intrinsic g-radiation of virtual pions cannot alter the aforesaid results concerning the decay probability and angular correlations.

7. CONCLUDING REMARKS

In conclusion, some remarks are thought to be relevant and instructive. Let us recall the influence of elec-

tromagnetic interactions on β-decay has been considered in the work presented solely, all the other corrections to the main bulk β-decay process, described by (2), had been put aside, important as they may be in their own right to disentangle the g_V, g_A values from processing the up-to-date experimental data. For instance, accounting for the finiteness of the baryon mass, entailing, in turn, the weak magnetism and baryon recoil [48], is known to be necessary when treating the electron angular distribution in polarized neutron β-decay to deduce the precise g_A^n/g_V^n value [14, 16–26]. Still more, such corrections are to be important in treating hyperon decay. Thus, according to our lights, we are not about to acquire the G, g_V, g_A values from processing experimental data immediately, yet we can evaluate the G, g_A modifications associated with the modifications δW^B, δA^B calculated above and given in Table.

Let the "uncorrected" G, g_A values have been obtained from the experimental data on decay probability $W_{\exp}$ and the asymmetry coefficient $A_{\exp}$ without accounting for δW^B, δA^B from Table. The "corrected" values

$$\tilde{G} = G(1+\delta_G), \quad \tilde{g}_A^B = g_A^B(1+\delta_g^B) \tag{65}$$

are acquired from the same $W_{\exp}$, $A_{\exp}$, yet the modifications δW^B, δA^B have been allowed for. The general expressions (49), (53), (52) for the quantities W^B, A^B being put to use, the equations for the quantities δ_g^B, δ_G in (65) are deduced rather simply. In the neutron decay case, we have got

$$\delta_g^n = -\delta A^n \frac{(g_A^n-1)(3g_A^{n2}+1)}{3g_A^{n2}+2g_A^n-1}, \tag{66}$$

$$\delta_G = \delta A^n \frac{3g_A^{n2}(g_A^n-1)}{3g_A^{n2}+2g_A^n-1} - \frac{\delta W^n}{2}. \tag{67}$$

(It is to recall that according to the notations adapted in (2) $g_V^n = 1$.) If there were no other corrections to W^n, A^n addition to ones given in Table, the corrections to G, g_A^n according to (66), (67) would be: $\delta_g^n \approx 0.47\%$, $\delta_G \approx -4.4\%$.

Let us inquire into how the results gained in the current work affect the values of G, g_A^n acquired in some papers (see [14, 21, 22]) from processing the up-to-date experimental data, the values $\delta A \approx 1\%$ [48] and $\delta W \approx 5.4\%$ [28–35, 41] having been utilized. This quantity δW is due to radiative corrections as our δW^n is, yet the δA has quite a different nature, as being due to allowing for a finite baryon mass [48]. Thus, consequently, we shall acquire the corrections to the G, g_A^n values obtained in [14, 21, 22], if we substitute in equations (66), (67) our $\delta A^n \approx -1.9\%$, and instead of our value $\delta W^n \approx 8\%$, the value reduced by the δW, that is, replacing $\delta W^n \longrightarrow (\delta W^n - \delta W) \approx 2.6\%$. So, we adapt the G, g_A^n values of [14, 21, 22], as though they had been obtained from experimental data immediately, without any corrections, and the corrections must be calculated according to equations (65), (66), (67) with these last δA^n, δW^n values. Then equations (65), (66), (67) give $\delta_g^n \approx 0.47\%$, $\delta_G \approx -1.7\%$, and, subsequently, the $G = 1.1511(28) \times 10^{-5}\ \mathrm{GeV}^{-2}$, $g_A^n = 1.266 \pm 0.004$ asserted, for instance, in [21] are replaced by $\tilde{G} = 1.1318(28) \times 10^{-5}\ \mathrm{GeV}^{-2}$, $\tilde{g}_A^n = 1.272 \pm 0.004$. Let us remark that the last $\tilde{G}$ value appears to be very close to one gained in [39, 40] (see also [37]) from the nuclear super-allowed $(0^+ - 0^+)$ Fermi transitions, namely $G^{00} = G_F|V_{ud}| = 1.1365(11) \times 10^{-5}\ \mathrm{GeV}^{-2}$, the deviation being only ≈0.4%.

In the case of Σ-decay, as $g_V^\Sigma = 0$ (see (2)), the relation $A_{\exp} = -2/3\ (1 + \delta A^\Sigma)$ holds, and we can consider the modification of the product (Gg_A^Σ) only. The equation for δ_g^Σ, δ_G gives

$$\delta_g^\Sigma = -\delta W^\Sigma - \delta_G, \tag{68}$$

where δW^Σ, δA^Σ are given in Table. Certainly, to handle hyperon decay, one ought to allow for the finiteness of the baryon mass, likewise it has been done in [48] for the neutron case, and also account for the form-factors $g_V(q^2)$, $g_A(q^2)$, $g_{\mathrm{IP}}(q^2)$, $g_{\mathrm{WM}}(q^2)$, as the momentum transfer q is appreciable in this case, the plausible approach from [38] being relevant here. In spite of the lack of experimental data on the strangeness-conserving Σ-hyperon decays, we hope our results are thought to be instructive, the investigation of Σ decay with $\Delta S \neq 0$ being bound to be studied in another work.

In so far as the restrictions on the permissible G, g_A values go, the up-to-date situation is thought to be not perfectly visualized. Indeed, if we had taken for granted that acquiring the quantity $G^{00} = G_F|V_{ud}|$ from the super-allowed $(0^+ - 0^+)$ nuclear Fermi transitions had been reliable to an accuracy better than 1% [40], the G value would have proved to be fixed with the same precision. However, this is hardly the case in actual fact. Nowadays, such a high precision in the theoretical treatment of the β-decay of complex nuclei (even of the simplest aforesaid transitions) is known to be rather as good as impossible because one ought to deal thereby with the finite many-strong-interacting-fermion system in all of its complexity. For instance, among others, the following phenomena have to be strictly allowed for, to an accuracy as good as ~1%: electron and photon rescattering with exciting intermediate (virtual) nuclei complex states [4]; a knowledge of the precise values of nuclear (many-body) various form-factors (elec-

trons, photons, weak) with properly accounting for nuclear collective states; admixture of the axial-vector interaction to the vector interaction via the re-scattering processes; a thorough description of the nuclear charge density and its alternation in β-decaying, and so on.

For that matter, to acquire the G, g_A values from neutron β-decay data processing solely, without plunging into the nuclear many-body problem, is thought to be preferable, as was argued a little while ago in [14, 17, 21], and we are there. Of course, beside δA^B, the radiative corrections to the correlations between $\boldsymbol{\xi}$ and $\mathbf{v}(\delta B)$, $\mathbf{v}$ and $\mathbf{v}(\delta a)$ are very desirable, and we are about to study these in a next work. Certainly, the identity $|V_{ud}|^2 + |V_{sd}|^2 + |V_{bd}|^2 = 1$ inferred according to unitarity of the Kobayashi–Maskawa matrix [11] must hold true any way, yet its alignment and confirmation is beyond our objective here, so far as we restricted ourselves in this work from the very first by treating strangeness-conserving decay solely. To inquire into the aforecited identity, we ought to have launched into investigations of the processes involving high generations of quarks.

ACKNOWLEDGMENTS

Author is thankful to Yu.V. Gaponov, V.G. Nikolenko and, especially profoundly, to Yu.N. Pokatilovsky for the invaluable discussions and encouragements.

The work is supported by Russian Foundation for Fundamental Research, project no. 96-02-18826.

REFERENCES

1. R. R. Levis and G. W. Ford, Phys. Rev. **107**, 756 (1957).
2. S. Barshay and R. Behrends, Phys. Rev. **114**, 931 (1959).
3. J. K. Knipp and G. E. Uhlenbeck, Physica **3**, 425 (1936); F. Bloch, Phys. Rev. **50**, 272 (1936).
4. I. S. Batkin and Yu. G. Smirnov, Sov. J. Part. Nucl. **11**, 564 (1980).
5. A. A. Abrikosov, Zh. Éksp. Teor. Fiz. **30**, 96 (1956); B. B. Sudakov, Zh. Éksp. Teor. Fiz. **30**, 87 (1956).
6. D. R. Yennie, S. C. Frautschi, and H. Suura, Ann. Phys. (New York) **13**, 379 (1961); N. Meister and D. R. Yennie, Phys. Rev. **130**, 1210 (1963).
7. A. Sirlin, Nucl. Phys. B **71**, 29 (1974); **100**, 291 (1975); **196**, 83 (1982); Rev. Mod. Phys. **50**, 573 (1978); Phys. Rev. D **22**, 971 (1980).
8. S. Weinberg, Phys. Rev. Lett. **19**, 1264 (1967); Rev. Mod. Phys. **46**, 255 (1974); A. Salam, in *Elementary Particle Physics*, Ed. by N. Svartholm (Almquist and Wiksells, Stockholm, 1968), p. 367.
9. S. M. Berman and A. Sirlin, Ann. Phys. **20**, 20 (1962).
10. G. Kölen, Nucl. Phys. B **1**, 225 (1967).
11. N. Cabibbo, Phys. Rev. Lett. **10**, 531 (1963); M. Kobayashi and T. Maskawa, Prog. Theor. Phys. **49**, 625 (1973).
12. E. D. Commins and P. H. Bucksbaum, *Weak Interactions of Leptons and Quarks* (Cambridge Univ. Press, Cambridge, 1983); E. D. Commins, *Weak Interactions* (McGraw-Hill Book Company, 1973); P. H. Frampton and W. K. Tung, Phys. Rev. D **3**, 1114 (1971).
13. M. M. Nagels *et al.*, Nucl. Phys. B **147**, 189 (1979); G. Gustafson *et al.*, Phys. Scr. **15**, 289 (1977); J. J. de Swart, Rev. Mod. Phys. **35**, 916 (1963).
14. Yu. A. Mostovoĭ, Yad. Fiz. **59**, 1013 (1996).
15. P. E. Spivak, Zh. Éksp. Teor. Fiz. **94**, 1 (1988); V. I. Morozov, Nucl. Instrum. Methods A **284**, 108 (1989); J. Last *et al.*, Phys. Rev. Lett. **60**, 995 (1988); Yu. Yu. Kosvincev *et al.*, Pis'ma Zh. Éksp. Teor. Fiz. **44**, 444 (1986); R. Kossakowski *et al.*, Nucl. Phys. **A503**, 473 (1989); W. Paul *et al.*, Z. Phys. C **45**, 25 (1989); W. Mampe *et al.*, Phys. Rev. Lett. **63**, 593 (1989); J. Byrne *et al.*, Phys. Rev. Lett. **65**, 289 (1990); V. P. Alfimenkov *et al.*, Zh. Éksp. Teor. Fiz. **102**, 740 (1992); W. Mampe *et al.*, Pis'ma Zh. Éksp. Teor. Fiz. **57**, 77 (1993).
16. B. G. Erozolimsky, Contem. Phys. **35**, 191 (1994).
17. K. Schreckenbach *et al.*, J. Phys. G **18**, 1 (1992).
18. C. Stratowa *et al.*, Phys. Rev. D **18**, 3970 (1978); D. Dubbers *et al.*, Europhys. Lett. **11**, 195 (1990); Prog. Part. Nucl. Phys. **26**, 173 (1991).
19. B. G. Erozolimsky *et al.*, Yad. Fiz. **30**, 692 (1979).
20. B. G. Erozolimsky *et al.*, Yad. Fiz. **52**, 1583 (1990); **53**, 418 (1991); Phys. Lett. B **263**, 33 (1991).
21. K. Scheckenbach *et al.*, Phys. Lett. B **349**, 427 (1995); H. Abele *et al.*, *IV Int. Sem. on Int. of Neutrons with Nuclei*, E3-96-336, Dubna, Russia, 1996, p. 133.
22. A. P. Serebrov, Pis'ma Zh. Éksp. Teor. Fiz. **54**, 490 (1991); V. P. Alfimenkov *et al.*, Pis'ma Zh. Éksp. Teor. Fiz. **52**, 984 (1990); P. Bopp *et al.*, Phys. Rev. Lett. **56**, 919 (1986); Nucl. Instrum. Methods A **267**, 436 (1988); E. Klemt *et al.*, Z. Phys. C **37**, 179 (1988); I. A. Kuznetzov *et al.*, Pis'ma Zh. Éksp. Teor. Fiz. **60**, 311 (1994).
23. J. Wise *et al.*, Phys. Lett. B **91**, 165 (1980); **98**, 123 (1981); M. Bourquin *et al.*, Z. Phys. C **12**, 307 (1982); **21**, 1, 17, 27 (1983); S. Y. Hsueh *et al.*, Phys. Rev. Lett. **54**, 2399 (1985); Phys. Rev. D **38**, 2056 (1988); J. Dworkin *et al.*, Phys. Rev. D **41**, 780 (1990).
24. M. A. Beg *et al.*, Phys. Rev. Lett. **38**, 1252 (1977); B. R. Holstein and S. B. Treiman, Phys. Rev. D **16**, 2369 (1977).
25. Yu. V. Gaponov, *Proc. of III Int. Sym. on Weak and Elect. Int. in Nucl.*, Dubna, Russia, 1992, p. 87.
26. A. Sirlin, Phys. Rev. **164**, 1767 (1967).
27. T. Kinoshita and A. Sirlin, Phys. Rev. **113**, 1652 (1959).
28. R. T. Shan, Nuovo Cimento **5**, 591 (1971).
29. A. García and M. Maya, Phys. Rev. D **17**, 1376 (1978).
30. F. Glück and K. Tóth, Phys. Rev. D **46**, 2090 (1992).
31. A. García and W. Juárez, Phys. Rev. D **22**, 1132 (1980).
32. A. García, Phys. Rev. D **25**, 1348 (1982); **35**, 232 (1987).
33. K. Tóth, K. Szegö, and A. Margaritis, Phys. Rev. D **33**, 3306 (1986).
34. F. Glück and K. Tóth, Phys. Rev. D **41**, 2160 (1990).
35. F. Glück, Phys. Rev. D **47**, 2840 (1993).
36. V. B. Berestetskiĭ, E. M. Lifshitz, and L. P. Pitaevskiĭ, *Relativistic Quantum Field Theory* (Nauka, Moscow, 1971).
37. L. Montanet *et al.*, Review of Particle Properties, Phys. Rev. D **50**, 1173 (1994).

38. A. W. Thomas, Adv. Nucl. Phys. **13**, 1 (1984).
39. W. J. Marciano and A. Sirlin, Phys. Rev. Lett. **61**, 1815 (1988).
40. W. J. Marciano and A. Sirlin, Phys. Rev. Lett. **56**, 22 (1986); A. Sirlin and R. Zucchini, Phys. Rev. Lett. **57**, 1994 (1986); W. Jaus and G. Rasche, Phys. Rev. D **35**, 3420 (1987); A. Sirlin, Phys. Rev. D **35**, 3423 (1987); J. C. Hardy *et al*., Nucl. Phys. **A509**, 429 (1990).
41. D. H. Wilkinson, Nucl. Phys. **A377**, 474 (1982); Z. Phys. A **348**, 129 (1994).
42. Yu. V. Gaponov and R. U. Khafizov, Phys. Lett. B **379**, 7 (1996).
43. R. Mathuse, Philos. Mag. **40**, 351 (1949).
44. T. D. Lee, Phys. Rev. **128**, 899 (1962); R. A. Shaffer, Phys. Rev. **128**, 1452 (1962); G. Dorman, Nuovo Cimento **32**, 1226 (1964); D. Bailin, Phys. Rev. B **135**, 166 (1964).
45. S. M. Berman, Phys. Rev. **112**, 267 (1958).
46. R. P. Feynman and M. Gell-Mann, Phys. Rev. **109**, 193 (1958); Ya. A. Smorodinsky and Ho Tso-Hsin, Zh. Éksp. Teor. Fiz. **38**, 1007 (1960).
47. F. Bloch and A. Nordsieck, Phys. Rev. **52**, 54 (1937).
48. S. M. Bilin'ky, R. M. Rydin, Ya. A. Smorodinsky, and Ho Tso-Hsin, Zh. Éksp. Teor. Fiz. **37**, 1758 (1959).

Physics of Atomic Nuclei, Vol. 63, No. 3, 2000, pp. 520–521. Translated from Yadernaya Fizika, Vol. 63, No. 3, 2000, pp. 575–576.

LETTERS TO THE EDITOR

Fragmentation of Relativistic Oxygen Nuclei on Protons

V. V. Glagolev[1)], K. G. Gulamov, V. D. Lipin, S. L. Lutpullaev, K. Olimov, A. A. Yuldashev, and B. S. Yuldashev[2)]

Fizika–Solntse Research and Production Association, Institute for Physics and Technology, Uzbek Academy of Sciences, ul. Timiryazeva 2b, Tashkent, 700084 Uzbekistan

Received July 8, 1999

1. The mechanisms of nuclear fragmentation in hadron–nucleus and nucleus–nucleus collisions can be studied by measuring the yields of various multinucleon fragments emitted in these interactions. Our earlier studies demonstrated that, in collisions with a proton target, a relativistic oxygen nucleus disintegrates predominantly into alpha particles. We also found that, in those cases where all constituent nucleons were distributed among two or more multiply charged fragments, the oxygen nucleus broke up either to four α particles or to ^{12}C and ^{4}He [1–3].

In principle, a nucleus of oxygen may disintegrate into unstable nuclei ^{5}He, ^{5}Li, ^{8}Be, and ^{9}B in their ground or excited states. Although the binding energies of these nuclei exceed 5 MeV per nucleon, they allow ^{8}Be decay into two alpha particles, ^{5}He and ^{5}Li decay into an alpha particle and a nucleon, and ^{9}Be decay into two alpha particles and a nucleon.

This article reports our new results on the breakup of ^{16}O into multiply charged fragments and, in particular, on the yield of the short-lived nucleus ^{5}Li in oxygen–proton collisions at an incident momentum of 3.25 GeV/c per projectile nucleon. The data subjected to the present analysis were collected by using the 1-m hydrogen bubble chamber installed at the Joint Institute for Nuclear Research (JINR, Dubna). The procedures for data treatment, event reconstruction, and fragment-mass separation were described in [1–3]. In all, over 11000 events of ^{16}Op collisions were fully measured and reconstructed.

2. Listed in the table are the measured cross sections for those channels of ^{16}O fragmentation where all constituent nucleons are carried away by the multinucleon fragments formed. Of all events in this category, more than 80% feature only the even–even nuclei ^{4}He and ^{12}C among the fragments. A few detected candidates for the final states ^{13}C^{3}He, ^{12}C^{2}H^{2}H, and ^{11}C^{3}H^{2}H (one per channel)—these are not listed in the table—yield an upper limit of 80 μb on the total cross section for these channels of ^{16}O fragmentation.

The breakup of a ^{16}O nucleus into multinucleon fragments may proceed via a collective excitation resulting from the diffractive elastic scattering of this nucleus on a proton [4]. In principle, multinucleon fragments may also be formed through the coalescence of cascade nucleons or through a pickup reaction. In this case, the excited residual nucleus characterized by $A \leq 14$ may either break up into lighter multinucleon fragments or remain intact, as is exemplified by the final state ^{14}N^{2}H.

In the ^{4}He^{12}C fragmentation channel, which has the largest cross section, the azimuthal angle of the alpha particle proves to be correlated with that of the recoil proton: these particles are preferentially emitted in opposite directions. This suggests that the fragments in question are formed through the quasielastic knockout of an alpha cluster from the ^{16}O projectile.

3. The fragmentation of a ^{16}O nucleus into an unstable nucleus ^{5}Li was sought by trying to detect the decay $^{5}\mathrm{Li} \longrightarrow \alpha + p$. {This is the only allowed decay channel for the ground $[(3/2)^{-}, 1/2]$ state and for the first excited $[(1/2)^{-}, 1/2]$ state of the ^{5}Li nucleus with an excitation energy between 5 and 10 MeV, as well as a dominant channel for higher excitations [5].}

Since projectile fragments are largely emitted with small transverse momenta and, hence, at small emission angles in the laboratory frame (on the order of a few degrees), no event-by-event reconstruction of the decays $^{5}\mathrm{Li} \longrightarrow \alpha + p$ is possible under the conditions of our experiment. For this reason, the yield of ^{5}Li nuclei was studied by comparing the distribution of the angle between the alpha-particle and proton momenta,

Table

Breakup channel	Cross section, mb
^{12}C^{4}He	6.61 ± 0.66
^{4}He^{4}He^{4}He^{4}He	2.10 ± 0.38
^{14}N^{2}H	1.47 ± 0.29
^{6}Li^{4}He^{4}He^{2}H	0.27 ± 0.12
^{10}B^{4}He^{2}H	0.16 ± 0.10

[1)] Joint Institute for Nuclear Research, Dubna, Moscow oblast, 141980 Russia.

[2)] Institute of Nuclear Physics, Uzbek Academy of Sciences, pos. Ulughbek, Tashkent, 702132 Uzbekistan.

1063-7788/00/6303-0520$20.00

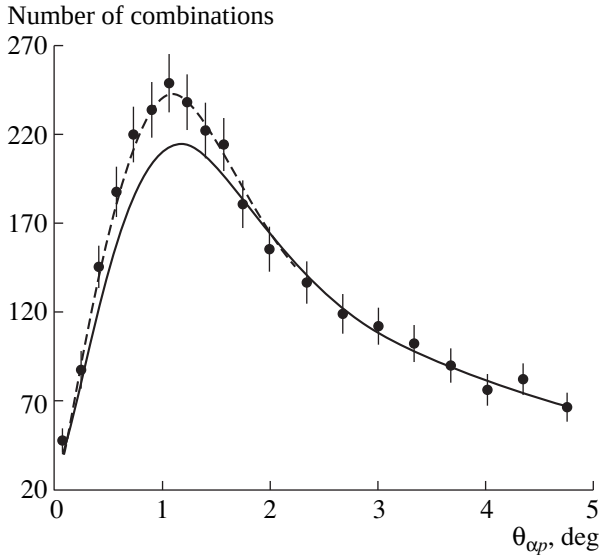

Distribution of the angle between the alpha-particle and proton momenta.

$\theta_{\alpha p}$, with the background distribution obtained with allowance for fractions of individual topological channels (recall that the angular distributions of fragments depend on these topological channels). The background distribution was constructed by pairing at random an alpha particle and a proton from different events. It should be noted that azimuthal correlations of a kinematical origin may result from the breakup of an excited residual nucleus. In order to take them into account, the transverse momenta of the alpha particle and the proton were determined preliminarily with respect to the total transverse momentum of all fragments detected in each event.

The results obtained in this way are illustrated in the figure. The background distribution (solid curve) was normalized to the number of events for $\theta_{\alpha p} > 2°$. It can be seen that the background distribution closely reproduces live events (points with error bars) at large angles, but that a significant excess over the background distribution is observed at small angles, where $\theta_{\alpha p}$ correlations are expected in the case of ^{5}Li production in the ground state. The excess as a function of $\theta_{\alpha p}$ agrees well ($\langle\chi^2\rangle < 0.5$) with the distribution calculated for the breakup of the ground-state ^{5}Li nucleus with allowance for the resonance width of $\Gamma = 1.5$ MeV. The sum of the background $\theta_{\alpha p}$ distribution and the computed spectrum is represented by the dashed curve.

The cross section for ^{5}Li formation proved to be $\sigma(^5\text{Li}) = 8.4 \pm 0.5$ mb, which does not differ significantly from the excitation-function values obtained in [1] for stable isotopes of lithium:

$$\sigma(^6\text{Li}) = 12.0 \pm 1.1 \text{ mb} \quad \text{and} \quad \sigma(^7\text{Li}) = 9.6 \pm 1.0 \text{ mb}.$$

An alternative approach to detecting the decay $^5\text{Li} \longrightarrow \alpha + p$ is to analyze the distribution of $Q_{\alpha p} = M_{\alpha p} - M_\alpha - M_p$, where $M_{\alpha p}$ is the effective mass of the αp system, while M_α and M_p are, respectively, the alpha-particle and the proton mass. The $Q_{\alpha p}$ spectrum is indeed enhanced with respect to the background distribution in the region $Q_{\alpha p} \leq 4$ MeV. The mean value of $Q_{\alpha p}$ for the background-subtracted enhancement is estimated at 2.14 ± 0.17 MeV, which is consistent with the amount of energy released in the αp decay of the ground-state ^{5}Li nucleus. The cross section for ^{5}Li formation as derived from the magnitude of the $Q_{\alpha p}$ enhancement, $\sigma(^5\text{Li}) = 8.3 \pm 0.6$ mb, compares well with the above estimate based on the $\theta_{\alpha p}$ distribution. That $\sigma(^5\text{Li})$ proves to be relatively large suggests that, in ^{16}Op collisions, the unstable nucleus ^{5}Li is largely formed from the α clusters of the projectile nucleus [2, 3].

REFERENCES

1. V. V. Glagolev, K. G. Gulamov, M. Yu. Kratenko, *et al.*, Pis'ma Zh. Éksp. Teor. Fiz. **58**, 497 (1993) [JETP Lett. **58**, 497 (1993)]; **59**, 316 (1994) [**59**, 336 (1994)].
2. V. V. Glagolev, K. G. Gulamov, M. Yu. Kratenko, *et al.*, Yad. Fiz. **58**, 2005 (1995) [Phys. At. Nucl. **58**, 1896 (1995)].
3. V. V. Glagolev, K. G. Gulamov, S. L. Lutpullaev, *et al.*, Yad. Fiz. **60**, 575 (1997) [Phys. At. Nucl. **60**, 500 (1997)].
4. I. Ya. Pomeranchuk and E. L. Feinberg, Dokl. Akad. Nauk SSSR **53**, 439 (1953).
5. F. Aizenberg-Selove, Nucl. Phys. **A490**, 1 (1988).

Translated by A. Asratyan